

Monitoring Snow Cover and
Modelling Catchment Discharge
With Remote Sensing in the Upper
Waitaki Basin, New Zealand

Pascal Sirguey

a thesis submitted for the degree of
Doctor of Philosophy
at the University of Otago, Dunedin,
New Zealand.

23 December 2009


Preliminaries



1. Introduction



2. Context of the research



3. Initial processing steps



4. Atmospheric and topographic correction




5. Snow classification



6. Accuracy assessment of the snow maps



7. Modelling the snowpack



8. Snowmelt Runoff Model



9. Conclusion



References



Appendices



Abstract

Because New Zealand relies heavily on water for electricity generation, it requires strong and reliable information about its water supplies as well as better knowledge about the processes that affect them. Situated in the Southern Alps, the Waitaki basin is the most important hydro catchment in New Zealand. Three alpine sub-catchments, namely Ohau, Pukaki, and Tekapo, provide most of the discharge to the Waitaki River. In this alpine region a large part of the water resource is temporarily stored as seasonal snow cover. To utilize better the value of water in hydro lakes, improving knowledge of the timing and supply of water from seasonal snow is a priority.

It has been long established that satellite remote sensing is a powerful tool to monitor snow cover in remote and inaccessible areas. In New Zealand, this technology has received only scant consideration. In addressing the remote sensing of the seasonal snow cover in the alpine catchments of the Waitaki basin, this thesis aims at filling a considerable void. This is achieved through the implementation of routine monitoring of the snow cover dynamics with the MODerate Imaging Spectro-radiometer (MODIS). Towards this goal, several advanced remote sensing techniques that are novel to MODIS are integrated in a single and operational algorithm.

This research demonstrates the desirable performance of an image fusion algorithm. The algorithm enables the mapping of snow with MODIS at 250m spatial resolution instead of the 500m spatial resolution imagery currently available. Furthermore, MODIS images are standardized by means of a physically-based atmospheric and topographic correction (ATOPCOR) approach. Finally, the radiometric normalization of the time series permits the design of a robust spectral unmixing technique. This allows further enhancement of the spatial details of the snow maps through the determination of sub-pixel snow fractions at 250m spatial resolution. Together, the combination of these techniques forms a processing chain, well suited

to the mountainous environment, to map snow with the highest possible amount of spatial detail. A careful assessment of the quality of the maps of snow fractions is conducted by means of comparison with high resolution reference snow maps obtained from the Advanced Spaceborne Thermal Emission and Reflection Radiometer (ASTER).

The processing of seven years of MODIS observations covering the 2000–2006 hydrological years permitted the creation of a new dataset that depicts the spatial distribution of snow. Based on this dataset, this thesis demonstrates that the current modelling approach of the snowpack by the model SnowSim tends to propagate errors that increase to an important level. Every year by the end of the ablation season SnowSim models nearly a quarter of the total water storage in locations that are free of snow according to observations from MODIS. Finally, the hydrological modelling approach enabled by the Snowmelt Runoff Model (SRM) is revisited. Daily meteorological data (i.e., temperature and precipitation) and the frequent observations of the snowpack provided by MODIS enable the daily discharge to be simulated. Unprecedented performance in the simulation of daily inflows are obtained for the three largest water reservoirs in New Zealand. This sheds new light on the relative contribution of seasonal snowmelt and ice melt to the discharge.

In revealing the large daily variability of the snowmelt, new estimates of its contribution to the lake inflows are obtained. Over the study period, snowmelt accounted for 37%, 40%, and 31% of the discharge in the Lakes Ohau, Pukaki, and Tekapo catchments, respectively. Finally, this research documents the severe drought of 2005. It strongly suggests that inflows were largely mitigated by ice melt from glaciers in the Pukaki basin. A contribution of glacier melt much larger than usual is believed to have sustained the discharge to within 17% of the mean annual flow, although precipitation was reduced by 34%. This mitigating factor was less marked in Tekapo and not observed in the Ohau basin, in accordance with the relative proportion of glacierized areas in the catchments. This potentially provides a striking example of the contribution of long term storage to inflows during dry periods.

Acknowledgments

More than a personal challenge, this PhD is also the work of many who contributed both professionally and personally to its completion, and to whom I am indebted in many ways.

First of all, I owe my deepest gratitude to my first class supervisors Renaud Mathieu, Yves Arnaud, and Blair Fitzharris, without whom this thesis would not have been possible. They provided constant help and unconditional support, while enduring my sometimes passionate and complicated nature. They must know, as they read these words, that I consider them simply as friends.

I feel honoured by the unconditional trust I received from Brent Hall who has made available his support in a number of ways and reviewed my manuscript more than thoroughly. I am also indebted to many of my colleagues of the School of Surveying who have expressed a sustained interest in my research during all these years. Among them, John Hannah and Chris Hoogsteden have been the first supporters of my endeavour. Geoffrey Hay and Robert Tenzer have been very good friends and succeeded in making me leave my office sometimes.

I am grateful to Anne Coudrain and Pierre Chevalier who made possible my visit at the *Maison des Sciences de l'Eau* at the early start of my research. I also thank Michel Fily who, as the director of the *Laboratoire de Glaciologie et de Géophysique de l'Environnement*, gave me the opportunity to conduct two study periods in Grenoble. There I found inspiration and friendship from Paulina Lopez and Alvaro Soruco with whom I wish to collaborate again in the future.

I also want to thank Trevor Chinn for his kindness and invaluable knowledge about New Zealand's glaciers. Jocelyn Chanussot helped on image fusion. Tim Kerr provided me with outputs from the SnowSim model. He also participated in fieldwork on Tasman glacier with Bryan Moore. I also wish to show my gratitude to Laimonis Kavalieris and Gerrard Liddell for their assistance with statistics, and Bojun for her various help.

I cannot forget the encouragement and support from Leo Vincent. As a matter of fact, Leo was the first informed when I reconsidered my early career as an engineer. He made me realize that there is no worst fear than the fear to change one's own life.

Life during these years has been punctuated by memorable surf sessions in the cold pacific waters. I thank my dear friends and surf buddies Michael, Jean-Marc (aka Tchatchi), and all the sea lions who shared this passion with me.

My parents Christiane and Daniel deserve far more than gratitude for their education, affection, and constant support despite the distance. This encompasses the regular food supplies from my beloved France. I thank my sisters Marion and Fanny who made me the invaluable gift to travel so far to share my love of Aotearoa, and Noëlle for her regular news about my nephews and niece.

Most importantly, Marine deserves the highest honour for the unmatched patience and affection she gave me, and to whom the completion of this thesis represents a new and more specific direction to our future in common.

Finally, I am thankful to the three examiners of this manuscript, Prof. Jeff Dozier from the University of Santa Barbara (USA), Dr. Christian Puech from the agricultural and environmental research institute (CEMAGREF, France), and Dr. Andrew Tait from the National Institute for Weather & Atmospheric research (NIWA, New Zealand), who kindly offered their valuable time to review this dissertation.

Funding and other resources for this research were acquired from several sources. To all of which, I am indebted. The University of Otago and the School of Surveying allotted funding to conduct this research. GIS data are sourced from the Land Information New Zealand NZTopo Database (Crown Copyright Reserved). The MODIS Level-1B data were processed by the MODIS Adaptive Processing System (MODAPS) and Goddard Distributed Active Archive Center (DAAC), and are archived and distributed by the Goddard DAAC. ASTER images were obtained with support from the Global Land Ice Measurement from Space. Eddy Stead from Meridian Energy Ltd and Kathy Walter from NIWA kindly supplied climatic and inflow data.

Contents

Abstract	v
Acknowledgments	vii
Contents	xvi
List of Tables	xviii
List of Figures	xxv
List of Abbreviations	xxvii
List of Symbols	xxxii
1 Introduction	1
1.1 Scope	1
1.2 Research objectives	4
1.2.1 General objectives	4
1.2.2 Methodological goals	4
1.2.3 Hydrological goals	5
1.3 Thesis structure	6
2 Context of the research	9
2.1 Introduction	9
2.2 The upper Waitaki catchment	10
2.2.1 Situation	10
2.2.2 General climate	10
2.2.3 Glaciers and landscape	14
2.2.4 Hydrological regime	16
2.2.5 Hydroelectricity	19
2.3 Study of snow in New Zealand	22
2.3.1 Overview	22
2.3.2 Snowpack modelling	24
2.3.3 The contribution of remote sensing	27
2.4 The satellite tool	30

2.4.1	Optical remote sensing of snow	30
2.4.1.1	Optical properties of snow	30
2.4.1.2	Mapping of snow with optical satellites	34
2.4.1.3	Use of snow covered area (SCA) observations in snow models	37
2.4.2	The EOS AM-1/TERRA platform	39
2.4.2.1	MODIS	41
2.4.2.2	ASTER	44
2.4.3	The MOD10 Snow product	45
2.4.3.1	Design	45
2.4.3.2	Limitations	46
2.5	Summary	50
3	Initial processing steps	53
3.1	Introduction	53
3.2	Digital elevation model	54
3.2.1	Source of elevation data and interpolation methods	54
3.2.2	Accuracy assessment of the DEMs	57
3.2.2.1	Common statistical measures	57
3.2.2.2	DEM derivatives and contour bias	59
3.2.2.3	Check points (CPs)	60
3.2.2.4	Quality of the DEMs and choice of a method	62
3.3	Projection and geo-location of MODIS data	65
3.3.1	The MODIS scan geometry	65
3.3.2	Projection of MODIS L1B data	67
3.3.3	Retrieval of physical values	69
3.4	Multispectral fusion	70
3.4.1	Motivation	70
3.4.2	Principle and methods	73
3.4.2.1	Substitution methods	74
3.4.2.2	Multi-resolution methods	76
3.4.2.3	A brief description of 2-D wavelet transform	76
3.4.3	The ARSIS concept	78
3.4.3.1	Implementation	78
3.4.3.2	Assessing the quality of the fused images	80
3.5	Cloud detection and masking	85
3.5.1	Discrimination of snow and clouds	85
3.5.1.1	In the reflective domain	85
3.5.1.2	In the emissive domain	87
3.5.1.3	Alternative technique	89
3.5.2	Cloud detection and masking design	89
3.5.2.1	Group 1, thick water clouds	90
3.5.2.2	Group 2 & 3, thick water clouds	90
3.5.2.3	Group 4, cirrus clouds	91

3.5.2.4	Group 5, strong Brightness Temperature Difference	91
3.5.2.5	Final mask	92
3.6	Summary	92
4	Atmospheric and TOPographic CORrection (ATOPCOR)	95
4.1	Introduction	95
4.2	Radiative transfer	96
4.2.1	Generalities	96
4.2.2	Bidirectional Reflectance Distribution Function	100
4.2.3	Model equations	102
4.3	Topographic considerations	103
4.3.1	Illumination angle	104
4.3.2	Sky-view factor and terrain configuration factor	104
4.3.2.1	Sky-view factor	104
4.3.2.2	Terrain configuration factor	111
4.3.2.3	Computation	113
4.3.3	Shadows	113
4.3.3.1	Self and cast shadows	113
4.3.3.2	Fractional shadow map	115
4.3.3.3	Final cleaning	117
4.3.4	Reflected terrain irradiance	118
4.3.4.1	First-order approximation	119
4.3.4.2	Multiple reflections model	119
4.4	Atmospheric model	120
4.4.1	SPECTRAL2 constituents	123
4.4.1.1	Rayleigh scattering	123
4.4.1.2	Water vapour absorption	125
4.4.1.3	Ozone absorption	125
4.4.1.4	Uniformly mixed gas absorption	126
4.4.1.5	Aerosol absorption and scattering	127
4.4.2	Radiation quantities	129
4.4.2.1	Diffuse irradiance	129
4.4.2.2	Atmosphere intrinsic radiance	132
4.4.2.3	Background radiance	133
4.4.3	Accuracy assessment of the atmospheric model	133
4.4.3.1	Comparison with 6S	133
4.4.3.2	Correction for the atmosphere intrinsic radiance	135
4.4.3.3	Performance of SPECTRAL2 in the seven MODIS land bands	136
4.5	Performance of ATOPCOR	139
4.5.1	Stability and convergence of the iterative process	139
4.5.2	Assessment of the correction	140
4.5.3	Critical assessment of the model of multiple reflections	144
4.5.3.1	Theoretical considerations	144

4.5.3.2	Practical application	145
4.6	Summary	147
5	Snow classification	149
5.1	Introduction	149
5.2	A matter of scale	150
5.2.1	The raster representation	150
5.2.2	Fractal considerations	151
5.2.3	The fractal nature of the snowpack	155
5.3	Binary and sub-pixel classification	160
5.3.1	Pixel-wise binary classification	160
5.3.2	Intuitive justification of binary mapping	160
5.3.3	Distribution of sub-pixel snow fractions	161
5.3.4	Limitations of the binary representation and need for sub-pixel mapping	165
5.4	Spectral mixture analysis	167
5.4.1	Mixing models description	167
5.4.2	Spectral unmixing of snow	170
5.4.3	Linear mixing model	171
5.4.4	End-members	173
5.4.4.1	Different approaches of selection	173
5.4.4.2	Strategy of selection	176
5.4.4.3	Additional criterion	178
5.5	Post processing of the snow maps	179
5.5.1	Cleaning of the snow maps	179
5.5.2	Completing snow maps under clouds	183
5.6	Summary	185
6	Accuracy assessment of the snow maps	187
6.1	Introduction	187
6.2	Context	188
6.2.1	The need for references	188
6.2.2	Assessment of the performance of the fusion	191
6.3	Assessment metrics and multi-scale issues	193
6.3.1	Snow cover area (SCA)	193
6.3.2	Pixel-based statistics	194
6.3.3	Feature-based metric: the Hausdorff Distance	196
6.3.3.1	Object representation	196
6.3.3.2	The Hausdorff Distance	197
6.3.3.3	Modified Hausdorff Distance (MDHD)	198
6.4	Assessment strategy	200
6.4.1	Initial argument	200
6.4.2	Reference images	201
6.4.2.1	Snow classification from ASTER	202

6.4.2.2	Aggregation	204
6.4.2.3	Mapping of the snowline	205
6.5	Pixel-based measures	208
6.5.1	Statistical and spatial structure of the error	208
6.5.2	Common statistical measures	213
6.5.2.1	Description	213
6.5.2.2	Overall measures	214
6.5.2.3	Results of the statistical measures	215
6.5.3	Global quality or <i>Q</i> Index	220
6.5.3.1	Description	220
6.5.3.2	Results of the <i>Q</i> index	220
6.5.4	Receiver Operating Characteristics curves	221
6.5.4.1	Description	221
6.5.4.2	Results of ROC curve analysis	225
6.6	Feature-based measure	227
6.6.1	Methodology	228
6.6.1.1	Calculation of Euclidean distance	228
6.6.1.2	Theoretical behaviour of the MDHD based on ASTER reference data	229
6.6.1.3	Empirical application of the MDHD to fused and non fused MODIS snow maps	231
6.6.2	Results and discussion	233
6.6.2.1	Metric behaviour	233
6.6.2.2	Application to MODIS-derived snow maps	233
6.7	Error sources and method limitations	236
6.8	Summary	237
7	Modelling the snowpack	241
7.1	Introduction	241
7.2	The energy budget of the snowpack	242
7.2.1	The energy balance equation	242
7.2.2	General considerations	244
7.2.3	Energy balance measurements in New Zealand	245
7.3	Modelling the snow pack	247
7.3.1	Energy balance models	247
7.3.2	The degree-day approach	248
7.3.3	The degree-day factor	251
7.3.4	Modelling the snowpack in the Southern Alps of New Zealand	253
7.4	SnowSim	255
7.4.1	Principle	255
7.4.2	SnowSim outputs and performance	258
7.5	Assessment of SnowSim	260
7.5.1	Method and data	261
7.5.2	Results and discussion	262

7.6	Summary	267
8	Snowmelt Runoff Model (SRM)	269
8.1	Introduction	269
8.2	General principle of SRM	270
8.2.1	Main assumption	270
8.2.2	The SRM formulation	272
8.2.2.1	Foundation	272
8.2.2.2	Zonal definition	273
8.3	Forcing data	275
8.3.1	Source of climatic data	275
8.3.2	Distributed temperature field	277
8.3.2.1	Review of techniques	277
8.3.2.2	Temperature interpolation method	278
8.3.2.3	Assessment of the accuracy of the temperature field	281
8.3.3	Distributed precipitation field	283
8.3.3.1	Review of techniques	283
8.3.3.2	Precipitation interpolation method	284
8.3.3.3	The long term annual precipitation surface	285
8.3.3.4	Assessment of the accuracy of the precipitation field	287
8.3.4	Snow cover area curves	292
8.3.4.1	Least-squares fitting and adaptation to the lower envelope	294
8.3.5	Forcing the melt factor	296
8.4	Estimation of model parameters	299
8.4.1	Goodness of fit measures	299
8.4.2	Time lag	300
8.4.3	Recession coefficient	303
8.4.4	Estimation of the runoff coefficient c_r and c_s	303
8.4.5	SRM, the critical temperature and the “new snow reservoir”	306
8.5	Simulation Results	309
8.5.1	Verification of the model performance	309
8.5.2	Interpretation of the model performance	311
8.5.3	Final adjustment of SRM and determination of the stored water component	314
8.5.3.1	Model adjustments	314
8.5.3.2	The long term storage	318
8.5.3.3	The seasonal snow	320
8.5.3.4	The short-lived snow	322
8.5.4	Study of the errors of modelling	323
8.5.4.1	Error <i>vs.</i> discharge	323
8.5.4.2	The statistical structure of the error	324
8.5.4.3	Towards providing confidence intervals with the predicted discharge	327

8.6	Summary	327
9	Conclusion, and future work	331
9.1	Methodological contributions	332
9.1.1	Multispectral fusion of MODIS bands	332
9.1.2	Atmospheric and topographic correction of MODIS data	333
9.1.3	Snow mapping	334
9.1.4	MODImLab	336
9.2	Hydrological contributions	336
9.2.1	Performance and pitfalls of the SnowSim model	336
9.2.2	Hydrological simulations with SRM	338
9.3	Future work	339
9.3.1	Image fusion	339
9.3.2	ATOPCOR	340
9.3.3	Snow mapping from MODIS/AQUA data	341
9.3.4	Hydrological modelling	341
	References	343
	Appendices	381
A	Thin plate spline	383
A.1	Problem statement	383
A.2	Interpolating <i>vs.</i> smoothing thin plate spline	383
A.3	Multivariate TP(S)S	385
A.4	Solution	385
B	Confidence intervals	387
B.1	Mean Absolute Error (MAE)	387
B.2	Root Mean Square Error (RMSE)	388
C	Illumination angle	393
D	Analytical integration of Equation (4.25)	395
E	Atmospheric absorption coefficients	397
F	Snow maps for accuracy assessment	399
G	Note about the recession law	417
G.1	The Snowmelt Runoff Model (SRM) and the recession law	417
G.2	The “reservoir” conceptualization of the recession	419
G.3	Non linear systems	420
G.4	SRM and the linear assumption	422

H	Simulation results without long term storage	427
I	Simulation results with long term storage adjustment	431
J	MODImLab	435

List of Tables

Chapter 2

2.1	Alpine catchments of the upper Waitaki basin.	17
2.2	Hydroelectric plants and capacity of generation of the upper Waitaki catchment (Meridian Energy Ltd, 2009).	22
2.3	Selected references about remote sensing of snow.	29
2.4	Spectral characteristics of MODIS [adapted from Barnes <i>et al.</i> (1998)].	42
2.5	Spectral characteristics of ASTER.	45

Chapter 3

3.1	Description of the three interpolation methods tested.	56
3.2	RMSE values as compared to the reference images for the images obtained from the fusion and those obtained by a resampling with cubic convolution (CC).	84

Chapter 4

4.1	Range of values for the parameters used in the comparison between atmospheric models 6S and SPECTRAL2.	134
4.2	Comparison of E_s , E_d , E_m , T_s , T_v , and L_p estimated from SPECTRAL2 and 6S.	138
4.3	Mean extraterrestrial solar irradiance values for MODIS spectral bands.	138
4.4	Proportion of saturated pixels for ASTER bands 1–4.	147

Chapter 6

6.1	Pairs of simultaneous ASTER/MODIS acquisitions used for the accuracy assessment of the snow maps.	203
6.2	Value of NDSI thresholds used for each image.	204
6.3	Mean of the sub-pixel snow fraction fra for strictly mixed pixels (i.e., $fra_{\text{ASTER}} \in]0, 100\%[$) at both 500 and 250m spatial resolution.	212
6.4	Comparison of ASTER- and MODIS-derived snow maps.	216

6.5	Descriptive statistics of the distribution of Euclidean distances between the test snowlines derived from MODIS and the reference snowline obtained from ASTER.	235
-----	---	-----

Chapter 8

8.1	Climate stations at high elevation (see location in Figure 8.3).	276
8.2	Results of the cross validation from the interpolation of the daily temperature over the period 2001–2007.	282
8.3	Results of the cross validation for the interpolation of daily precipitation over the period 2001–2007.	287
8.4	Mean annual values of the components of the water balance computed over the hydrological years 1994–2006.	290
8.5	Parameters of the recession coefficient, k	303
8.6	Performance criteria obtained from the calibration of the runoff coefficients.	307
8.7	Performances obtained over the calibration and verification periods.	310
8.8	Performances obtained after manually adjusting the snow runoff coefficient during the ablation season.	317
8.9	Parameters of the t location-scale distributions fitted to the experimental distribution of modelling errors.	326

Appendices

E.1	Extraterrestrial solar spectrum and atmospheric absorption coefficients at 122 wavelengths from Leckner (1978) with few additions and modification from Bird and Riordan (1986)	398
-----	---	-----

List of Figures

Chapter 1

- 1.1 View in perspective of the upper Waitaki catchment in the central South Island 2

Chapter 2

- 2.1 Limits of the study area overlaid on a hillshaded DEM. 11
- 2.2 Climatic conditions in the upper Waitaki catchment. 13
- 2.3 (a) Geology of New Zealand (Map reproduced with permission from the institute of Geological & Nuclear Sciences). (b) Major Land cover types (Ministry of the Environment, 2004, Land cover database version 2). 15
- 2.4 Runoff regimes of the three alpine catchments. 18
- 2.5 Main controllable storage capacity for hydroelectric generation [adapted from Fitzharris (1992)]. 21
- 2.6 Annual electricity generation by fuel type (Ministry of Economic Development, 2009). 21
- 2.7 Spectral signature for various snow and ice targets. 32
- 2.8 Spectral emissivity of snow, ice, and water. 33
- 2.9 The TERRA platform and its orbit (the satellite model on the left is reproduced from NASA). 40
- 2.10 MODIS relative spectral response for ‘land bands’ b1–b7. 42
- 2.11 Sinusoid projection with Tissot’s indicatrix to illustrate the distortions due to map projection. 44
- 2.12 Examples of MOD10 Snow product (9 September 2000, 22:55 GMT). 48

Chapter 3

- 3.1 Geoid heights above the WGS84/GRS80 ellipsoid (HAE). 57
- 3.2 Comparison of the three interpolated DEMs with respect to first order (i.e., slope and aspect) and second order (i.e., curvature) derivatives. 61

3.3	(a) Frequency distribution of CPs heights relative to the DEM's heights. (b) Spatial distribution of check points (CPs) over the study area.	63
3.4	Scatter plot of DEM errors <i>vs.</i> elevation.	64
3.5	(a) Histogram of errors for the four DEMs considered. (b) Comparative results of the statistical measures.	64
3.6	Ground projection of three consecutive MODIS scans showing the scan geometry and the panoramic "bow-tie" effect (adapted from Wolfe <i>et al.</i> , 2002).	66
3.7	Spatial mis-registration of images projected with the MRT software as a function of the requested cell size.	68
3.8	(a) ASTER image of the upper Pukaki basin draped over the DEM. (b) The MOD10 snow product of the corresponding MODIS acquisition.	71
3.9	Example of spectral coverage of multispectral and panchromatic channels in modern sensors (e.g., IKONOS, QuickBird).	73
3.10	Concept of image fusion.	74
3.11	Principle of fusion by band substitution method.	75
3.12	Correlations between the reflectance in MODIS Low Resolution bands 3-7 and the reflectance in the High Resolution bands 1-2 for a scene acquired on May, 16 th 2006.	76
3.13	Single level 2-D wavelet decomposition illustrating the approximation and coefficients of detail.	78
3.14	ARSIS concept as implemented in the case of MODIS using the undecimated wavelet transform, adapted from Ranchin and Wald (2000)	79
3.15	Example of multispectral fusion.	81
3.16	Comparison between the multispectral image fusion and the cubic convolution resampling.	83
3.17	(a) Absorption coefficient of water. (b) Bivariate distribution of MODIS band 4 (Green) <i>vs.</i> band 6 (SWIR) for ten scenes featuring snow and various types of clouds.	86
3.18	Example of MODIS band 2 (NIR) and 6 (SWIR) of a snowy scene (9 September 2005, 22:40 GMT).	86
3.19	Example of NDSI and infrared brightness temperature difference for the image shown in Figure 3.18 (9 September 2005, 22:40 GMT).	87
3.20	Histograms of the infrared brightness temperature difference of the image shown in Figure 3.18.	88

Chapter 4

4.1	Radiation components in rugged terrain.	97
4.2	Relative geometry of the sun, the sensor, and the target.	101
4.3	Sky obstruction by surrounding slopes.	105
4.4	(a) Parameterization in spherical coordinates. (b) The trigonometric approach for determining V_d	106

4.5	V_d computed from the unit-sphere method.	108
4.6	Computation of the sky-view factor.	110
4.7	Topographic parameters in the study area.	114
4.8	Self and cast shadowing in rugged terrain.	114
4.9	Example of computation of shadows (7 April 2001, 22:53 GMT).	116
4.10	Example of computation of shadows (5 May 2006, 22:35 GMT).	117
4.11	Phase function for Rayleigh scattering.	124
4.12	Phase function for Mie type of scattering.	128
4.13	Decay of the atmosphere spherical albedo with elevation.	132
4.14	Scatter plot of the predicted values retrieved from the SPECTRAL2 model versus the value obtained from the 6S model for MODIS bands 1–7.	136
4.15	Dependence of the relative error $\epsilon_{\%}$ of L_p to various parameters.	137
4.16	Linearization of the relative error of L_p	137
4.17	Convergence of reflectance values (MODIS band 2) for various targets.	140
4.18	Example of the atmospheric and topographic correction.	142
4.19	Scatter plot of MODIS band 2 and $\cos \gamma$ before and after correction.	143
4.20	Theoretical overestimation of ground reflectance for varying terrain configuration factor (C_t).	145
4.21	ASTER image of a rugged terrain covered with snow draped over a Digital Elevation Model.	146
4.22	Overestimation of reflectance ρ_1 corrected using ATOPCOR and the first-order model, according to the reflectance ρ_{∞} obtained using the multiple reflections correction for ASTER band 1.	147

Chapter 5

5.1	Characterization of the fractal behaviour of snow depth, reproduced from Deems <i>et al.</i> (2006).	159
5.2	Empirical distribution of fractional snow cover at the edge of a “toy” snow patch.	162
5.3	Example of beta distributions for various shape parameters.	163
5.4	Conceptualization of (a) a snow field with bare patches, and (b) a bare field with snow patches.	164
5.5	Two mixing models.	168
5.6	Spectral signature of the end-members used in the linear unmixing.	178
5.7	Relationship between the sub-pixel snow fractions and the NDSI value for the eight test images.	180
5.8	Error of modelling of the linear unmixing.	181
5.9	Series of morphological and logical operations to remove spurious ‘snow’ pixels outside a snow entity, while retaining small ‘snow-free’ patches inside.	183
5.10	Examples of spatial distribution of the three snow end-members.	184

Chapter 6

6.1	Example of map of sub-pixel snow fractions created from MODIS imagery.	192
6.2	Sub-pixel abundance mapping at two spatial resolutions.	195
6.3	Computation of the Hausdorff distance as the largest of both directed Hausdorff distances.	198
6.4	Mapping of boundaries extracted from low and high resolution imagery.	199
6.5	Histogram of the NDSI values for all sample pixels retained in the reference ASTER images.	204
6.6	Schematic illustration of the aggregation process.	205
6.7	Example of simultaneous ASTER and MODIS imagery (31 December 2002 22:35 GMT).	206
6.8	Subset of Figure 6.7.	207
6.9	Distribution of the error between MODIS-derived and ASTER sub-pixel snow fraction for each date.	209
6.10	Distribution of the error between MODIS-derived and ASTER sub-pixel snow fractions for all samples from the eight images combined.	210
6.11	(a) Relationship between the error of sub-pixel snow fraction and ASTER reference value for all eight images combined. (b) Variogram of ASTER reference value for a subset of image № 1.	211
6.12	Distribution of sub-pixel snow fraction in ASTER and MODIS images.	212
6.13	Illustration of ordinary (a) and standard weighted (b) least squares linear regression.	214
6.14	Scatter plots of the fractional snow cover retrieved from MODIS versus the reference snow fractions obtained from ASTER, for all pixels of the eight test images.	218
6.15	Results of pixel-based metrics: (a) MAE, (b) RMSE, and (c) R^2	219
6.16	Results of Q index.	221
6.17	(a) Confusion matrix for a binary classifier. (b) Representation of the classifier performance in the ROC space.	222
6.18	(a) Membership to class according to classifier continuous outcome value. (b) Representation of the classifier performance in the ROC space.	224
6.19	Distribution of MODIS sub-pixel snow fractions relative to thresholds defined on ASTER reference snow map (G500 maps for image № 7: April 3 rd , 2002).	225
6.20	Receiver Operating Characteristics (ROC) curves and Area Under (ROC) Curve and non-Discrimination line (AUCD) obtained for snow maps M500, M250, and G500 (image № 7: April 3 rd , 2002).	226
6.21	Results of AUCD.	226
6.22	Minimum Euclidean distance $d(p, S)$ between a point p on the 'test snowline' and the 'reference snowline' S	228

6.23	Example of reference snowline and corresponding Euclidean distance raster image created at 12.5m pixel size and computed from the ASTER-derived (15m) reference snowline.	229
6.24	Example of snowlines extracted from an ASTER image at different spatial resolutions.	231
6.25	Illustration of the influence of small patches on the determination of snowlines at various spatial resolutions.	232
6.26	Sensitivity of the MDHD to the sub-pixel snow fractions and the spatial resolution.	234
6.27	Distributions of Euclidean distances.	235
6.28	Time series of MODIS-derived snow cover area.	239
Chapter 7		
7.1	Processes contributing to the global energy budget of the snowpack.	243
7.2	(a) The long term annual rain surface used in SnowSim-Pukaki and the situation of climate stations. (b) Comparison of the mean precipitation profile suggested by Kerr (2005) and the NZMS rain surface.	257
7.3	Flowchart of the SnowSim model.	258
7.4	Example of an output from SnowSim compared with the simultaneous observation from MODIS.	259
7.5	Confusion matrix for a binary classification with associated performance measures.	262
7.6	Animation of the dynamic of the snow cover distribution as modelled by SnowSim (left) and observed by MODIS (right) in the Pukaki catchment over the period 2000-2007.	263
7.7	(top) MODIS- and SnowSim-derived snow cover area in the Pukaki catchment depending on the SWE threshold indicated by the colour bar. (bottom) Total storage in the modelled snowpack and in pixels not mapped as snow by MODIS.	264
7.8	Mean accuracy of the classification of snowy pixels by SnowSim depending on the threshold of SWE.	266
7.9	Classification performance of SnowSim.	266
Chapter 8		
8.1	The basin hydrograph, recession, and lag.	271
8.2	Zonal definition of the upper Waitaki catchments in SRM.	274
8.3	Situation of climate stations used to spatially distribute temperature and precipitation in the upper Waitaki catchment.	276
8.4	Examples of temperature interpolation.	280
8.5	Monthly variation of the cross validation errors for the temperature.	282
8.6	New Zealand Meteorological Service (NZMS) normal rain surface 1951–80.	284

8.7	Rain profiles along a transect normal to the main divide.	286
8.8	Examples of interpolation of the precipitation field.	288
8.9	(a) Monthly variation of the cross validation errors for the precipitation. (b) RMSE error versus mean annual precipitation.	289
8.10	Interpolation of the snow cover area from MODIS using Savitzky-Golay filtering with adaptation to the lower envelope.	295
8.11	Average ground NIR reflectance (MODIS band 2, 858 nm) of not shaded, fully snow covered pixels versus altitude for selected dates.	298
8.12	Time series of ground NIR reflectance (MODIS band 2, 858 nm) of not shaded, fully snow covered pixels.	299
8.13	Lag between the precipitation and the discharge.	302
8.14	Runoff coefficients.	305
8.15	Observed and modelled hydrographs over the calibration period.	307
8.16	Goodness of fit criteria averaged over all catchments and calibration years depending on the critical temperature T_c	309
8.17	Cumulative discharge in the Pukaki (top) and the Tekapo (bottom) catchments for hydrological year 2005 and 2006.	312
8.18	Total precipitation and discharge in each catchment during the study period.	313
8.19	Growth of the glacier terminal lakes in the Pukaki catchment between 2003 and 2007.	315
8.20	Growth of Tasman Lake as interpreted from ASTER and Landsat imagery.	316
8.21	Modelled and observed annual discharge showing the relative share of stored water components.	319
8.22	Monthly distribution of the inflow from the seasonal snow cover in the catchments of the upper Waitaki.	322
8.23	Correlation between the total snow melt simulated by SRM and the observed runoff volume.	323
8.24	Scatter plot of the errors of modelling.	324
8.25	Density of probability of the modelling error.	325
8.26	Modelled discharge with confidence intervals for the hydrological years 2000–2002.	328

Appendices

B.1	Empirical distribution of RMSE values obtained from 50,000 independent random vectors of errors for various values of n , μ , and σ	389
B.2	Probability density function of the non-central chi distribution for several degrees of freedom and non-centrality parameters.	390
B.3	Example of the distribution of RMSE values.	392
C.1	Relative geometry of the sun, the sensor, and the target.	393
C.2	Decomposition of the geometry using Euler's angles.	393

E.1	Typical irradiance spectrum calculated with the atmospheric model described in Section 4.4 [adapted from Slater (1980)]. Absorption coefficients are provided on the verso of the page.	397
F.1	Snow maps on 31 December 2002, 22:35 GMT.	400
F.2	Snow maps on 29 January 2002, 22:35 GMT.	402
F.3	Snow maps on 11 September 2000, 22:55 GMT.	404
F.4	Snow maps on 16 May 2006, 22:35 GMT.	406
F.5	Snow maps on 7 April 2001, 22:50 GMT.	408
F.6	Snow maps on 9 September 2005, 22:40 GMT.	410
F.7	Snow maps on 3 April 2002, 22:35 GMT.	412
F.8	Snow maps on 24 January 2006, 22:35 GMT.	414
G.1	The basin hydrograph, recession, and lag.	418
G.2	Conceptualisation of Equation G.5 by a reservoir.	420
G.3	Recession analysis.	424
G.4	Flow recessions after calibration of the non linear recession relationship. The non null horizontal asymptote must be lower than the minimum flow expected in each catchment.	425
H.1	Results of discharge simulation without long term storage in Ohau 2000–2007	428
H.2	Results of discharge simulation without long term storage in Pukaki 2000–2007	429
H.3	Results of discharge simulation without long term storage in Tekapo 2000–2007	430
I.1	Results of discharge simulation with long term storage adjustment in Ohau 2000–2007	432
I.2	Results of discharge simulation with long term storage adjustment in Pukaki 2000–2007	433
I.3	Results of discharge simulation with long term storage adjustment in Tekapo 2000–2007	434
J.1	Front panel of the MODImLab toolbox.	435
J.2	Flowchart of the MODImlab Toolbox.	436

List of Abbreviations

6S	Second Simulation of the Satellite Signal in the Solar Spectrum
AMSR-E	Advanced Microwave Scanning Radiometer
ARSIS	<i>Amélioration de la Résolution Spatiale par Injection de Structures</i> (Spatial Resolution Enhancement by Injection of Structures)
ASTER	Advanced Spaceborne Thermal Emission and Reflection Radiometer
ATCOR3	Atmospheric and Topographic Correction algorithm
ATOPCOR	Atmospheric and TOPographic CORrection algorithm
ATSR	Along Track Scanning Radiometer
AUC	Area Under (ROC) Curve
AUCD	Area Under (ROC) Curve and no-Discrimination line
AVHRR	Advanced Very High Resolution Radiometer
AVIRIS	Airborne Visible/Infrared Imaging Spectrometer
AWS	Automatic Weather Station
BRDF	Bidirectional Reflectance Distribution Function
BT	Brightness Temperature
BTD	Brightness Temperature Difference
BV	Bivariate interpolation
BVLR	Bivariate interpolation with specified Lapse Rate
CC	Cubic Convolution
CERES	Clouds and the Earth's Radiant Energy System
CI	Confidence Interval
Cliflo	New Zealand Climate Database
CP	Check Point
CV	Cross Validation
CWT	Continuous Wavelet Transform
DAAC	NASA Distributed Active Archive Centers
DEM	Digital Elevation Model
DGPS	Differential Global Positioning System
DISORT	Discrete Ordinates Radiative Transfer model
DN	Digital Number
DU	Dobson Unit (1 DU = 0.001 atm-cm)
DWT	Discrete Wavelet Transform
EGM	Earth Gravitational Model

EOS	NASA's Earth Observing System
ERS-AMI	European Remote Sensing - Active Microwave Instrument
ET	Evapo Transpiration
FAR	False Alarm Rate
FCLS	Fully Constrained Least Squares
FN	False Negative
FP	False Positive
G500	Aggregation of the M250 map at 500 m spatial resolution
GCOS	Global Climate Observing System
GCP	Ground Control Points
GCV	Generalized Cross Validation
GLIMS	Global Land Ice Measurements from Space
GOES	GEOstationary Satellite
GPS	Global Positioning System
GRS	Geodetic Reference System
GTOPO30	Global Topography model
HAE	Height Above Ellipsoid
HASL	Height Above mean Sea Level
HBV	Hydrologiska Byråns Vattenbalansmodell
HDRF	Hemispherical Distribution Reflectance Factor
HR	Hit Rate or High Resolution (depending on context)
HRU	Hydrological Response Unit
IDW	Inverse Distance Weighted interpolation
IFOV	Instantaneous Field Of View
IHS	Intensity Hue Saturation
IRS	Indian Remote Sensing satellite
ISODATA	Iterative Self-Organizing Data Analysis algorithm
KS-test	Kolmogorov-Smirnov test
L1B	Level-1B
Landsat ETM	Landsat Enhanced Thematic Mapper
Landsat MSS	Landsat MultiSpectral Scanner
Landsat TM	Landsat Thematic Mapper
LDR	Lauder Station
LIDAR	Light Detection And Ranging
LINZ	Land Information New Zealand
LMM	Linear Mixing Model
LR	Low Resolution
LUT	Look Up Table
M250	Map of sub-pixel snow fractions at 250 m spatial resolution
M500	Map of sub-pixel snow fractions at 500 m spatial resolution
MAD	Mean Absolute Deviation
MAUP	Modifiable Areal Unit Problem
MDHD	Modified Directed Hausdorff Distance

MEMSCAG	Multiple End-Member Snow Covered Area and Grain size algorithm
MESMA	Multiple End-member Spectral Mixture Analysis
MISR	Multiangle Imaging Spectro Radiometer
MLC	Maximum Likelihood
MODAPS	MODIS Adaptive Processing System
MODImLab	MODIS Imagery Laboratory
MODIS	MODERate Resolution Imaging Spectroradiometer
MODSCAG	MODIS Snow Covered Area and Grain size algorithm
MODTRAN	MODERate resolution atmospheric TRANsmission model
MOPITT	Measurements Of Pollution In The Troposphere
MRE	Mean Relative Error
MRSE	Mean Relative Square Error
MRT	MODIS Reprojection Tool
MS	Multispectral channel
MS2GT	MODIS Swath-to-Grid Toolbox
NASA	National Aeronautics and Space Administration
NDSI	Normalized Difference Snow Index
NDVI	Normalized Difference Vegetation Index
NEM	Normalized Error of Modelling
NIR	Near InfraRed
NIWA	National Institute of Water & Atmospheric Research
NN	Nearest Neighbour
NOAA	National Oceanic and Atmospheric Administration
NSIDC	National Snow and Ice Data Center
NZMS	New Zealand Meteorological Service
NZTM	New Zealand Transverse Mercator
NZTopo	New Zealand Topographic Database
OLS	Ordinary Least Squares
OMI	Ozone Monitoring Instrument
OZVW	Ozone & Water Vapour Group (National Oceanic and Atmospheric Administration).
PAN	Panchromatic channel
PCA	Principal Component Analysis
PCLS	Partially Constrained Least Squares
PSE	Point Spread Function
RMRSE	Root Mean Relative Square Error
RMSE	Root Mean Square Error
ROC	Receiver operating characteristic
RSR	Relative Spectral Response
SAR	Synthetic Aperture Radar
SCA	Snow Cover Area
SCS	Sun Canopy Sensor model

SDC	Snow cover Depletion Curve
SI	Scaled Integer
SIN	Sinusoidal projection
SL-M250	Snowline extracted from the M250 map
SL-M500	Snowline extracted from the M500 map
SNOMAP	Snow Mapping Algorithm
SPOT	Satellite Probatoire pour l'Observation de la Terre
SRM	Snowmelt Runoff Model
SRTM	Shuttle Radar Topography Mission
SSAR	Stremlow Synthesis And Reservoir Regulation Model
SSM/I	Special Sensor Microwave/Imager
SST	Snow Surface Temperature
SWE	Snow Water Equivalent
SWIR	ShortWave InfraRed
TIN	Triangulated Irregular Network
TIR	Thermal InfraRed
TIROS	Television Infrared Observation Satellites
TN	True Negative
TP	True Positive
TPS	Thin Plate Spline interpolation
TPSS	Thin Plate Smoothing Spline interpolation
TV	Trivariate interpolation
UBC	University of British Columbia hydrological model
ULS	Unconstrained Least Squares
VIC	Variable Infiltration Capacity hydrological model
WGS	World Geodetic System
WRC	World Radiation Center
WT	Wavelet Transform

List of Symbols

$\mathbf{1}^T$	$[1, 1, \dots, 1]$ is a $1 \times N$ vector	
${}_2F_1(a, b; c; z)$	Standard hyper geometric series	
$(a)_k$	Pochhammer symbol	
a	Melt factor	$[\text{mm} \cdot ^\circ\text{C}^{-1} \cdot \text{day}^{-1}]$
a_o	Ozone absorption coefficient	$[\text{m}^{-1}]$
a_u	Uniformly mixed gas absorption coefficient	
a_w	Water absorption coefficient	$[\text{m}^{-1}]$
b	Sub-pixel fraction of shadow	dimensionless
c	Speed of light in vacuum (299, 792, 458)	$[\text{m} \cdot \text{s}^{-1}]$
c_s, c_r	Snowmelt and rain runoff coefficients	dimensionless
d	Earth-Sun distance	dimensionless
	Day	
	Euclidean distance	
$d_H(X, Y)$	Hausdorff distance between two compact sets X and Y of the Euclidean space E	
dS, dA	Surface element	$[\text{m}^2]$
\mathbf{f}	Vector of abundance	
$f_{\alpha, \beta}$	Density function of the Beta distribution $Beta(\alpha, \beta)$	
fra	Sub-pixel fraction of snow	$[\%]$
f_ρ	Bidirectional Reflectance Distribution Function	$[\text{sr}^{-1}]$
$f_s(\cos \theta_s)$	Aerosol forward scattering	dimensionless
g	Aerosol asymmetry factor	dimensionless
j	Julian day	
k	Boltzmann constant (1.380658×10^{-23})	$[\text{J} \cdot \text{K}^{-1}]$
	Fractal dimension	
	Runoff recession coefficient	dimensionless
h	Planck constant (6.626×10^{-34})	$[\text{J} \cdot \text{s}]$
	Directed Hausdorff distance	$[\text{m}]$
h_o	Altitude of the maximum ozone concentration	$[\text{km}]$
l	Distance traversed in medium	$[\text{m}]$
$m(A, B)$	Modified Hausdorff distance between two countable sets of points A and B	
n	Number of samples	
p	Surface pressure	$[\text{mb}]$

$p(\vec{r}, \vec{\Omega}, \vec{\Omega}')$	Aerosol phase function	
r	Radius in spherical coordinates	[m]
\hat{s}	Estimator of statistics s	
t	Air temperature	[°C]
	Threshold in binary mapping	dimensionless
	Student's t-distribution	
$t_d(\theta_v)$	Ground to sensor diffuse transmittance	dimensionless
x, y	Parameters of a non-linear flow recession	dimensionless
z	Elevation	[m]
z_R	Fisher's z -transformation of the Pearson correlation coefficient R	
A_i	Area of zone i	[m ²]
B	Thermal quality of snow	dimensionless
$\mathcal{B}(n, p)$	Bernoulli binomial distribution of a sequence of n independent experiments, of which yields success with probability p	
$Beta(\alpha, \beta)$	Beta distribution	
C	Wavelet coefficients	
\overline{C}_t	Terrain configuration factor	dimensionless
\overline{C}_t	Mean terrain configuration factor in neighbourhood R_1	dimensionless
D	Topological dimension	
D_v	Normalized deviation between predicted and modelled runoff	[%]
E	Euclidean space	
E_0	Extraterrestrial solar irradiance	[W.m ⁻²]
$E_a \downarrow$	Downward aerosol scattering	[W.m ⁻²]
$E_a \uparrow$	Upward aerosol scattering	[W.m ⁻²]
E_d	Diffuse solar irradiance at ground level on a horizontal surface	[W.m ⁻²]
E_d^*	Total diffuse irradiance on tilted plane	[W.m ⁻²]
\overline{E}_d	Diffuse solar irradiance at ground level on a horizontal and unobstructed surface	[W.m ⁻²]
E_g	Global irradiance on a horizontal surface	[W.m ⁻²]
E_m	Diffuse environmental irradiance at ground level on a horizontal surface	[W.m ⁻²]
$E_r \downarrow$	Downward Rayleigh scattering	[W.m ⁻²]
$E_r \uparrow$	Upward Rayleigh scattering	[W.m ⁻²]
E_s	Direct beam solar irradiance at ground level	[W.m ⁻²]
E_t	Terrain reflected irradiance	[W.m ⁻²]
$E[X]$	Expected value of random variable X	
$H(\varphi), H_\varphi$	Horizon angle in azimuth direction φ	[degrees]
Q	Runoff	[m ³ .s ⁻¹]

	Q index	dimensionless
Q_m	Heat energy	[J.m ⁻²]
L_f	Enthalpy of fusion of water (335×10^3)	[J.kg ⁻¹]
L_g	Pixel radiance at ground level	[W.m ⁻² .sr ⁻¹]
L_k	Background radiance at sensor level	[W.m ⁻² .sr ⁻¹]
L_p	Atmospheric intrinsic radiance (Path radiance) at sensor level	[W.m ⁻² .sr ⁻¹]
L_{TOA}	Calibrated spectral radiance at the top of atmosphere	[W.m ⁻² .sr ⁻¹]
M	Relative optical air mass	dimensionless
M'	Pressure-corrected optical air mass	dimensionless
M_o	Stratospheric ozone relative optical air mass	dimensionless
O_3	Total ozone amount	[atm-cm]
P	Precipitation	[mm]
$P_\alpha(\mathfrak{A})$	α -th percentile of a countable set of real numbers \mathfrak{A}	
R	Mean radius of earth	[km]
	Pearson correlation coefficient	
	Total runoff	[m ³]
\mathbf{R}	Matrix of the spectral signature of the end-members	
R^2	Coefficient of determination	
	Nash-Sutcliffe efficiency coefficient	
R_{14d}^2	14-day moving average of R^2	
R_1	Contributing neighbourhood of E_t	[m]
R_2	Contributing neighbourhood of E_m and L_k	[m]
S	Set of the Euclidean space	
∂S	Boundary of a set S of the Euclidean space	
S_{stor}	Snow storage (SWE)	[mm]
T	Temperature	[°C]
T_a	Transmittance attributed to aerosol absorption and scattering	dimensionless
T_{aa}	Transmittance attributed to aerosol absorption	dimensionless
T_{as}	Transmittance attributed to aerosol scattering	dimensionless
T_c	Critical temperature	[°C]
T_o	Transmittance attributed to ozone absorption	dimensionless
T_r	Transmittance attributed to Rayleigh scattering	dimensionless
T_s	Sun to ground atmospheric transmittance	dimensionless
T_u	Transmittance attributed to uniformly mixed gas absorption	dimensionless
T_v	Ground to sensor atmospheric transmittance	dimensionless
T_w	Transmittance attributed to water absorption	dimensionless

$\frac{\partial U_i}{\partial t}$	Rate of change of the internal energy of the snow-pack	[W.m ⁻²]
Var[X]	Variance of random variable X	
V_d	Sky-view factor	dimensionless
W	Precipitable water vapour	[cm]
W_s	Amount of snowmelt	[mm]
α	Ångström turbidity exponent	
	Statistical significance level	dimensionless
$\alpha(\lambda)$	Spectral albedo	[%]
β	Ångström turbidity coefficient	
δ	Pixel size	[m]
ϵ	Error, residue	
	Emissivity	dimensionless
$\bar{\epsilon}$	Vector of residuals	
ϕ	Day angle	[rad]
ϕ^*	Net radiation	[W.m ⁻²]
ϕ_g	Conductive heat flux	[W.m ⁻²]
ϕ_h	Sensible heat flux	[W.m ⁻²]
ϕ_l	Longwave radiation	[W.m ⁻²]
ϕ_m	Heat flux	[W.m ⁻²]
ϕ_p	Advective heat flux	[W.m ⁻²]
ϕ_s	Shortwave radiation	[W.m ⁻²]
φ_n	Terrain aspect	[degrees]
φ_s	Solar azimuth	[degrees]
φ_v	Sensor azimuth	[degrees]
γ	Illumination angle	[degrees]
λ	Wavelength	[m]
μ	Mean	
ν	Degrees of freedom	
θ_n	Terrain slope	[degrees]
θ_s	Solar zenith	[degrees]
θ_v	Sensor zenith	[degrees]
ρ	Ground spectral reflectance	[%]
	Density	[kg.m ⁻³]
$\boldsymbol{\rho}$	Vector of ground reflectance	
ρ^*	Calibrated spectral reflectance at the top of the atmosphere	[%]
ρ_1	Ground Reflectance using the first order reflection model	[%]
ρ_∞	Ground Reflectance using the multiple reflections model	[%]
$\bar{\rho}_e$	Mean terrain reflectance in neighbourhood R_2	[%]
ρ_s	Atmosphere spherical albedo	[%]

$\bar{\rho}_t$	Mean terrain reflectance in neighbourhood R_1	[%]
σ	Standard deviation	
σ_e	Extinction coefficient	[m ⁻¹]
τ_a	Aerosol optical depth	dimensionless
ω	Aerosol single scattering coefficient	dimensionless
ΔI	Long term ice storage	[m ³]
ΔT	Positive degree-day	[°C.day]
Φ	Radiant energy flux	[W]
Γ	Gamma function	
Π	Net water production	[m ³]
Ω	Solid angle	[sr]
$\Psi(\varphi)$	Cutting angle in azimuth direction φ	[degrees]

Chapter 1

Introduction

1.1 Scope

New Zealand relies largely on water as its main renewable energy source. More than one-quarter of New Zealand's total energy needs are provided by electricity generation, of which 60% to 70% comes from hydroelectric plants. Situated in the heart of the Southern Alps, the Waitaki basin is the most important hydroelectric catchment in New Zealand and provides approximately one-third of the hydro electricity production for the country (Meridian Energy Ltd, 2009). In the northern part of the basin, the sub-catchments of Lakes Ohau, Pukaki, and Tekapo supply most of the discharge to the Waitaki River (Figure 1.1¹). Large reservoir lakes in each catchment provide important capability of storage that is crucial to the generation of power during low flow periods.

In this alpine region, an important fraction of the annual precipitation falls as snow, which accumulates from April to October. Thus, a great part of the water resource is temporarily stored in the seasonal snow cover, as well as in long term storage in perennial snowfields and glaciers. In 1992, 2001, 2003, and 2006, severe drought led to power crises and stressed the dependence of New Zealand on water resources for electricity generation (Staley, 2005). The link between the water available in the reservoirs and the snow stored during the previous winter was identified by Fitzharris (1992). The amount of water locked up in the seasonal snow cover and the timing of its release have a strategic importance in terms of managing the sus-

¹A flythrough animation around Aoraki/Mt Cook illustrates the dramatic topography of the region. The animation is playable in the .pdf version of this thesis and available in the DVD enclosed at \\Animations\AOI.640x480.25fps.v1-0.twopass2000kbps.avi.



Figure 1.1 View in perspective of the upper Waitaki catchment in the central South Island. The yellow lines represent the boundaries of the main sub-catchments.

tainability of the country's energy production.

In the past two decades, increasing efforts have been invested in New Zealand to provide a better understanding of the snowpack formation and evolution (Fitzharris *et al.*, 1999; Cutler and Fitzharris, 2005). Several modelling attempts have provided valuable insights into water storage in the seasonal snowpack (Kerr, 2005). The combination of snowpack modelling with the analysis of time series of observed lake inflows enabled estimation of the long-term contribution of snowmelt to the water supply. Thus, between 1947 and 1994, the snowmelt from the three alpine catchments was estimated to contribute from 18% to 24% of the total annual runoff and up to 40% to 50% of the spring and summer inflows (McKerchar *et al.*, 1998).

The variability of snowmelt from year to year in response to changing weather patterns was identified by Fitzharris and Garr (1995). So far, the monitoring of the seasonal snow cover in New Zealand has only been addressed by several refinements of the accumulation-ablation model SnowSim (Fitzharris and Garr, 1995;

Kerr, 2005; Clark *et al.*, 2009), whose outputs are solely estimates of the snow water equivalent stored at regular time intervals. The partitioning of the daily lake inflows into seasonal snowmelt, ice melt, and direct rainfall remains a difficult problem. This situation arose due to the lack of an integrated hydrological model that combines the simulation of the seasonal snowpack with snowmelt-rainfall-runoff processes. This potentially limits the operational use of SnowSim by water managers.

Repetitive water shortages emphasise the need for New Zealand to develop a better understanding of inflows originating from stored water resources. Monitoring and forecasting of water availability, as well as the relative roles of rainfall, seasonal snowmelt, and glacier melt into the lake inflows, demand further attention. In this context, the use of remote sensing technology has been generally ignored in New Zealand and was identified as an obvious gap in research on snow in the mountain environment (Fitzharris *et al.*, 1999). This situation strongly contrasts with the considerable volume of research conducted in other countries where satellite remote sensing has long proven to be successful at monitoring and modelling snow in remote and poorly accessible areas (Dewalle and Rango, 2008, Chap. 5).

Recent technological advances and the multiplicity of sensors now available have made observations from satellites ever more successful for monitoring the properties of the snow cover (Dozier and Painter, 2004; Rees, 2006). The MODerate Resolution Imaging Spectro-radiometer (MODIS sensor) benefits from near-daily repeat time, multispectral capabilities, and medium spatial resolution that make it a powerful instrument to monitor the snow cover dynamics at both global and local scales (Hall *et al.*, 2002; Lopez *et al.*, 2008). Maps of snow cover parameters obtained from MODIS have been used to calibrate (Lavallée *et al.*, 2006), assess (Brown *et al.*, 2008), and improve snow models (McGuire *et al.*, 2006), and thus have successfully contributed to the better prediction of snow water equivalent in mountainous catchments of other countries.

In this context, the Snowmelt Runoff Model (SRM, Dewalle and Rango, 2008, Chap. 11) is among the few and better known hydrological models that were developed specifically to accept direct input from satellite observations of the snow cover. A great volume of research conducted worldwide over more than thirty years has reported on successful implementations of SRM in conjunction with maps of snow cover obtained from various spaceborne sensors. Recently, implementations of SRM with data from MODIS enabled satisfactory modelling of the hydrology of moun-

tainous catchments (Tekeli *et al.*, 2005; Li and Williams, 2008; Immerzeel *et al.*, 2009), and provided a suitable modelling framework for the forecast of short-term runoff (Nagler *et al.*, 2008). In New Zealand, the SRM model has never been implemented in conjunction with satellite observations of the snow cover. Preliminary attempts were made for selected years and catchments (e.g., Bowden, 1994) but lacked a suitable remote sensing dataset to fulfil the model's needs.

1.2 Research objectives

1.2.1 General objectives

In the context highlighted above, this thesis encompasses two main objectives. The first main objective is to develop the routine mapping of the seasonal snow cover from remotely sensed images in the alpine catchments of the Waitaki basin. This objective involves subsidiary methodological goals that are detailed below and related to the automatic processing of remotely sensed images. The aim is to enhance the contribution of remote sensing to monitor seasonal snow which has received very little attention in New Zealand.

The second main objective is to use the observed time series of snow spatial distribution retrieved from MODIS in the local context to assess and improve the modelling of the snowpack in the Waitaki basin. This objective aims at gaining a better understanding of the components and timing of the catchment discharge, and developing a model of snowmelt runoff that enables better management of water resources.

1.2.2 Methodological goals

The MODIS sensor is selected to support the frequent mapping of the snowpack in the alpine terrain because it provides a good compromise between spatial (250-500m), spectral (36 spectral bands), and temporal resolution (1-2 days). Snow maps processed by the MODIS team of scientists are readily available in the MOD10 Snow product provided by the National Snow and Ice Data Center (NSIDC). Despite the availability and general performance of this product (Hall and Riggs, 2007), obvious limitations presented in the next chapter compromise its use in the local environment. This highlights the need for developing an adapted and robust algorithm

to map snow cover with MODIS. The use of lower level products (Level-1B) at a local scale allows implementation of advanced and computationally demanding image processing techniques to map snow with the highest possible amount of spatial details. The development of a new automatic processing chain to create a time series of snow maps with MODIS images represents the main methodological goal of this research.

Improved spatial resolution as well as sub-pixel capability of the proposed method are highly desirable factors in rugged terrain. The seven land bands of MODIS (i.e., bands 1-7), designed for the classification of land cover, are not provided at the same spatial resolution. MODIS bands 1 and 2 have a spatial resolution of 250m, while bands 3-7 are sampled at 500m at nadir. So far, the detection of snow with MODIS has been achieved on the basis of 500m resolution pixels only, but ignores the better spatial details present in the 250m spatial resolution bands. Recent progress in image processing techniques enables the design of image fusion algorithms capable of merging the spatial content of high resolution bands with the spectral content of low resolution bands. In revisiting the mapping of snow with MODIS in the very rugged topography of the Southern Alps, one aim of this thesis is to explore the feasibility of implementing an image fusion algorithm to enable the determination of snow with MODIS at 250m spatial resolution. This approach is new and original to MODIS data and rarely implemented with other sensors in an automatic manner for the processing of time series data.

As an alternative to the classic binary representation of snow cover, maps of sub-pixel snow fractions are becoming increasingly popular ([Salomonson and Appel, 2006](#); [Dozier *et al.*, 2009](#)). They are recommended for mapping snow in alpine terrain because they limit the over-estimation error usually made by binary classification algorithms when applied on spatially highly-variable or patchy snow-cover ([Dozier and Painter, 2004](#)). However, there are few examples that consider the retrieval of sub-pixel snow fractions from time series of satellite images. This thesis aims to develop a comprehensive methodology that is well-suited to the mountainous environment. The idea is to address this challenge in an automatic fashion.

1.2.3 Hydrological goals

The creation of an unprecedented time series of observations of the snow cover in New Zealand allows new scientific investigations to be conducted. A first goal is to investigate the performance of the existing modelling approach of the snowpack

provided by SnowSim in the Pukaki catchment.

A second goal seeks to integrate the time series of satellite observations in a hydrological modelling framework so as to model catchment discharge. By incorporating remotely sensed data from MODIS as input into the SRM model, this research develops an integrated modelling environment capable of simulating daily inflows into Lakes Ohau, Pukaki, and Tekapo. Furthermore, by processing a seven year long time series of satellite and climatic observations, this research seeks new insights as to the relative roles for lake inflows of seasonal snowmelt and loss of long term storage from perennial snow and glaciers.

1.3 Thesis structure

The research presented in this thesis is divided into nine chapters. The next chapter provides some elements of context. It describes the three alpine sub-catchments of the upper Waitaki basin on which this thesis concentrates, namely those of Lakes Ohau, Pukaki, and Tekapo. The presentation of their geographical and climatic setting leads to the characterization of their hydrological regime and highlights their importance for the production of energy in New Zealand. In traversing a body of literature about snow research in New Zealand, the lack of consideration of remote sensing technology for the systematic monitoring of the snow cover dynamics is identified. This leads to a review of the fundamental properties of snow in the context of optical remote sensing, followed by a presentation of the sensors used in this thesis, namely MODIS and the Advanced Spaceborne Thermal Emission and Reflection Radiometer (ASTER) aboard the TERRA platform.

The thesis is structured into three substantive parts. The first and second parts cover Chapters 3 to 6 and are devoted to the development of the automatic processing chain applied to the MODIS Level-1B images to create detailed maps of snow cover distribution on a routine basis. The first part involves several pre-processing steps and the second the mapping of snow and the assessment of the quality of the snow maps. The third part covers Chapters 7 to 8 and accounts for the hydrological component of this research. It describes two applications of the time series of snow maps obtained from MODIS in the context of snowpack modelling.

In describing the initial processing steps needed to conduct this research, Chapter 3 first addresses the creation and assessment of a Digital Elevation Model (DEM). The DEM forms an essential layer of data that is required in many occasions

across the thesis to process and/or analyse spatial data. The projection of MODIS swath data onto the local geographic system and retrieval of physical values is then examined. This leads to the description of a multispectral fusion scheme whereby the MODIS land bands at 500m spatial resolution are merged with those available at 250m to enable more detailed mapping of snow in very steep terrain. Finally, the detection and masking of clouds is addressed.

In order to address the normalization of the multi-temporal dataset of images, Chapter 4 describes the implementation of the 3-D atmospherical correction model ATCOR3(Richter, 1998) to convert images of radiance at the top of the atmosphere to values of ground reflectance. This processing step explores a comprehensive and rigorous correction of atmospheric and topographic effects. The original design of ATCOR3 and its adaptation to MODIS data required improvements that are examined in the context of mapping snow in mountainous terrain.

In addressing the mapping of snow from the satellite images, Chapter 5 describes the issues associated with the traditional detection of snow on a per pixel basis. In particular, the chapter stresses and clarifies the implications of the fractal nature of the snowpack to its mapping and characterization from remotely sensed imagery. It leads to the presentation of a snow mapping technique at sub-pixel resolution by means of a constrained linear unmixing model applied to the corrected MODIS images of ground reflectance.

Chapter 6 covers the assessment of the accuracy of the snow maps. This is aimed at judging the quality of the MODIS-derived output on the basis of simultaneous observations at high spatial resolution from ASTER. In the context of multi-spectral fusion, this assessment also aims to demonstrate the relevance and performance of the image fusion technique to improve the mapping of snow at 250m spatial resolution. The pitfalls of traditional pixel-based metrics in a multi-resolution framework lead to the design of a new measure inspired from object recognition science to quantify objectively the gain of information that can be attributed to an increase in spatial resolution.

Chapter 7 presents the modelling principles of the snowpack and in particular describes the latest version of SnowSim refined by Kerr (2005) in the Pukaki catchment. The ability of this model to represent the snow pack realistically is examined by means of comparison of its outputs with the time series of observations derived from MODIS. This allows identification of severe pitfalls that stress the need for alternate modelling strategies.

Although the Snowmelt Runoff Model (SRM, [Dewalle and Rango, 2008](#), Chap. 3) was tested on a few occasions in New Zealand, no attempts involved a monitoring of the snow covered area based on repeated satellite observations. Hence, Chapter 8 revisits this modelling approach by bringing together the SRM model and the time series of MODIS-derived snow maps to simulate the inflows into Lakes Ohau, Pukaki, and Tekapo over the hydrological years 2000–2006. The outputs from SRM in the three sub-catchments over this period are then discussed to elucidate the timing and contribution of seasonal snow and long term storage to the water supply.

Finally, Chapter 9 provides a summary of the main results of the thesis and its contributions, and charts future directions for research.

Chapter 2

Context of the research

2.1 Introduction

The first section of this chapter provides a contextual overview by describing the study area with regard to its geographical and climatic setting. The importance of the water resource is highlighted by a presentation of the hydrological regime of the three main alpine catchments. A brief history of the development of the upper Waitaki hydroelectric scheme illustrates the significance of the water resource from these catchments for the production of energy in New Zealand.

The second section briefly reviews relevant research on snow in the region, with a specific emphasis on previous modelling attempts. An overview of the contribution of remote sensing to such research in New Zealand demonstrates the lack of consideration of this technology.

The third section reviews some fundamental aspects of the remote sensing of snow using optical sensors. A description of the MODerate Resolution Imaging Spectro-radiometer (MODIS) and the Advanced Spaceborne Thermal Emission and Reflection Radiometer (ASTER) sensors is given. The MODIS Snow product developed by the MODIS team of scientists and provided on a daily basis (MOD10 Snow product) is presented. Its limitations in the study area are discussed. This justifies the efforts described in the following chapters, which develops an alternative approach to map the snow cover automatically in the local mountain environment.

2.2 The upper Waitaki catchment

2.2.1 Situation

Situated in the heart of the South Island, the Waitaki catchment covers almost 12,000 km². The topography of the region is dominated by Kā Tiritiri o te Moana (the Southern Alps) whose highest peak Aoraki/Mt Cook reaches 3754m above sea level (asl). The main alpine range is one of the remarkable consequences of the tectonic setting of New Zealand and its location on the boundary of the Australian and Pacific plates. The Australian plate is forced beneath the Pacific plate to the south of the South Island and reciprocally along the eastern part of the North Island, less than 1000 km in a north-easterly direction. Between these two segments of subduction, the two plates collide and create the oblique alpine fault along the western side of the South Island (Okaya *et al.*, 2007). The tectonic pressure causes continuous horizontal and vertical deformations which gave rise to the alpine range. The uplift across the Southern Alps is estimated to reach up to 10 mm.year⁻¹ locally, based on geochronological data (Tippet and Kamp, 1993), a rate confirmed recently by continuous GPS measurements (Beavan *et al.*, 2004).

The main range of the Southern Alps runs in a north-easterly direction, parallel to the West Coast. The Waitaki catchment runs in a south-easterly direction away from the Main Divide (i.e., the main ridge separating the river systems of the West Coast from those of the Eastern side) to the outlet of the Waitaki River on the Pacific Ocean. The upper part of the Waitaki basin (i.e., upstream of Lake Waitaki) is composed of several sub catchments, among which Ohau, Pukaki, and Tekapo provide most of the discharge to the Waitaki River and form the focus of this research. The three lakes of the same name are important water storage lakes for the Waitaki hydroelectric schemes. Figure 2.1 shows a cartographic projection (New Zealand Transverse Mercator 2000) of the study area and these three alpine catchments.

2.2.2 General climate

The main islands of New Zealand lie in a mid-latitude location in the South Pacific Ocean (see Figure 2.1 for geographic coordinates). Low pressure systems or troughs generally migrate eastward between pairs of anticyclones and create fronts that approach the country typically from the west (Sturman and Tapper, 2006, Chap. 7). The South Island is exposed to prevailing westerly winds from the Tasman Sea

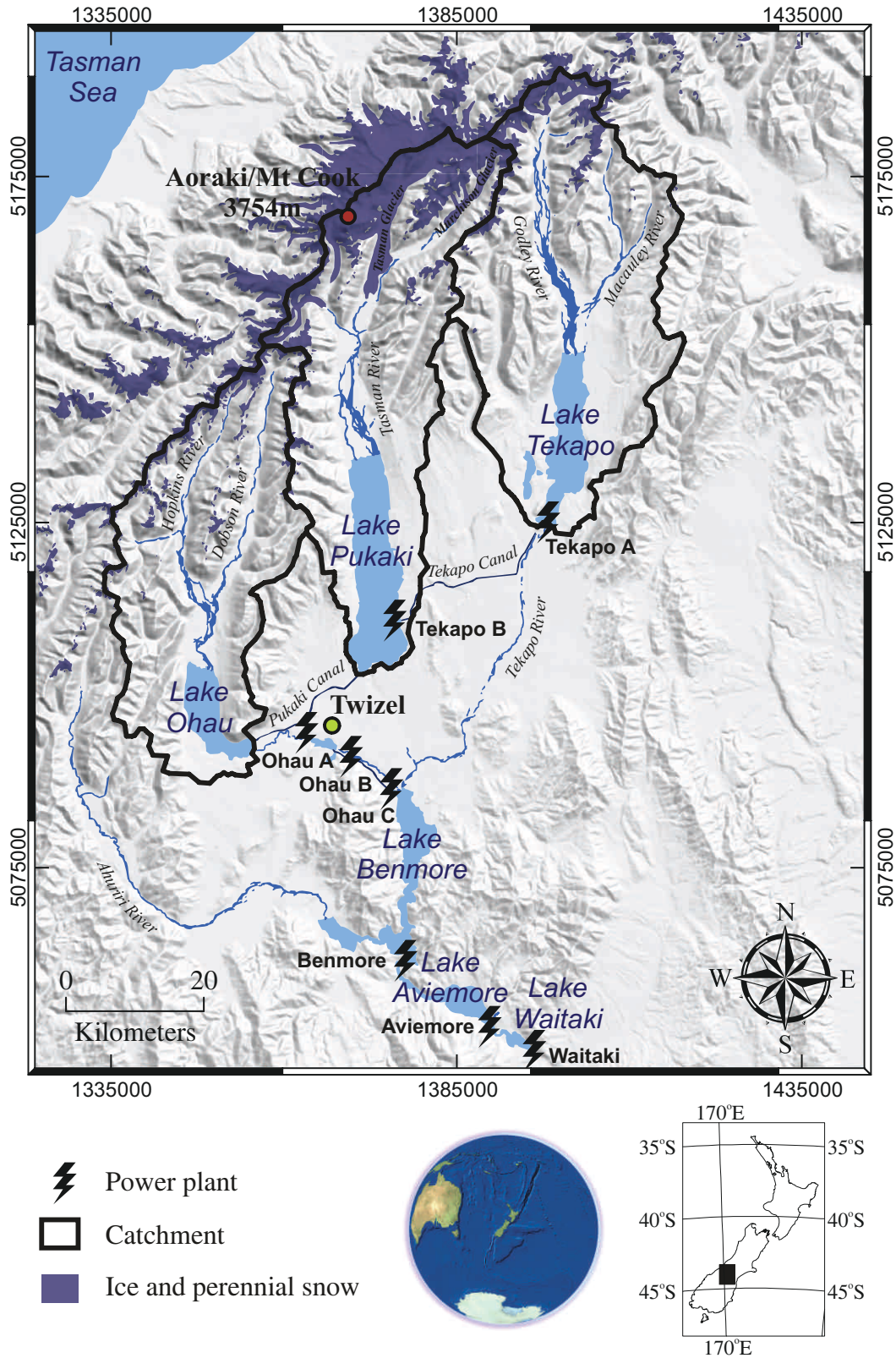


Figure 2.1 Limits of the study area overlaid on a hillshaded DEM (the coordinates are with respect to the New Zealand Transverse Mercator 2000). The catchment boundaries of the storage lakes are indicated as well as the hydro power plants.

that force the moist air mass to lift against the topographic barrier. The orographic effect caused by the alpine range divides the region into dramatically different climate zones (Salinger, 1980a,b). The adiabatic cooling of the large flow of humid air causes the release of enormous amounts of precipitation on the West Coast, making this region the wettest of New Zealand (Chinn, 1979). It results in an extremely variable spatial pattern of precipitation (Garnier, 1958; Griffiths and McSaveney, 1983), whereby the mean annual rainfall varies from 6000 mm along the western coast, to a maximum of over 10,000 mm just west of the Main Divide (Thompson, 1985; Kerr *et al.*, 2007), to only 600 mm.year⁻¹ 60 km south-east of the Main Divide in Twizel. The annual average precipitation at the Tasman névé (in the extreme north of the Pukaki catchment in Figure 2.1) is estimated to vary from 6,000 to 13,000 mm.year⁻¹ (Henderson and Thompson, 1999). Precipitation patterns across the Central Southern Alps are illustrated by the climatic graphs of selected weather stations shown in Figure 2.2.

The plentiful precipitation of the West Coast is evenly distributed throughout the year, while the temperature remains mild with only limited seasonal amplitude. Thus, the West Coast region has a humid maritime climate. The climate in the lee of the Southern Alps is dominated by the effect of their rain shadow and a strong Föhn effect when westerly conditions prevail. These give a semi-arid character to the eastern lowland areas of the upper Waitaki catchment. Only little precipitation occurs with limited or no seasonal variability. However, the temperature exhibits a more pronounced seasonal amplitude than that on the West Coast.

Snow can fall at any time of the year but accumulates principally during the winter months from April to October. The mild temperatures on the West Coast mean that snow seldom falls at sea level. On the high plains of the south-eastern part of the Waitaki catchment, occasional snowfalls can persist for several days due to sustained cold temperatures in winter (Hendrikx, 2007). Atmospheric freezing levels generally intercept the mountains at mid elevations but can rise or fall over several hundreds of meters within a few days. Accumulation of a persistent snow pack occurs above a well defined snow line that is typically located above the valley floor, even in winter (Fitzharris *et al.*, 1999). Mountain tops generally remain below freezing point, thus allowing the accumulation and carryover of snow from one year to the next and the formation of glaciers (Anderton, 1973; Chinn, 2001).

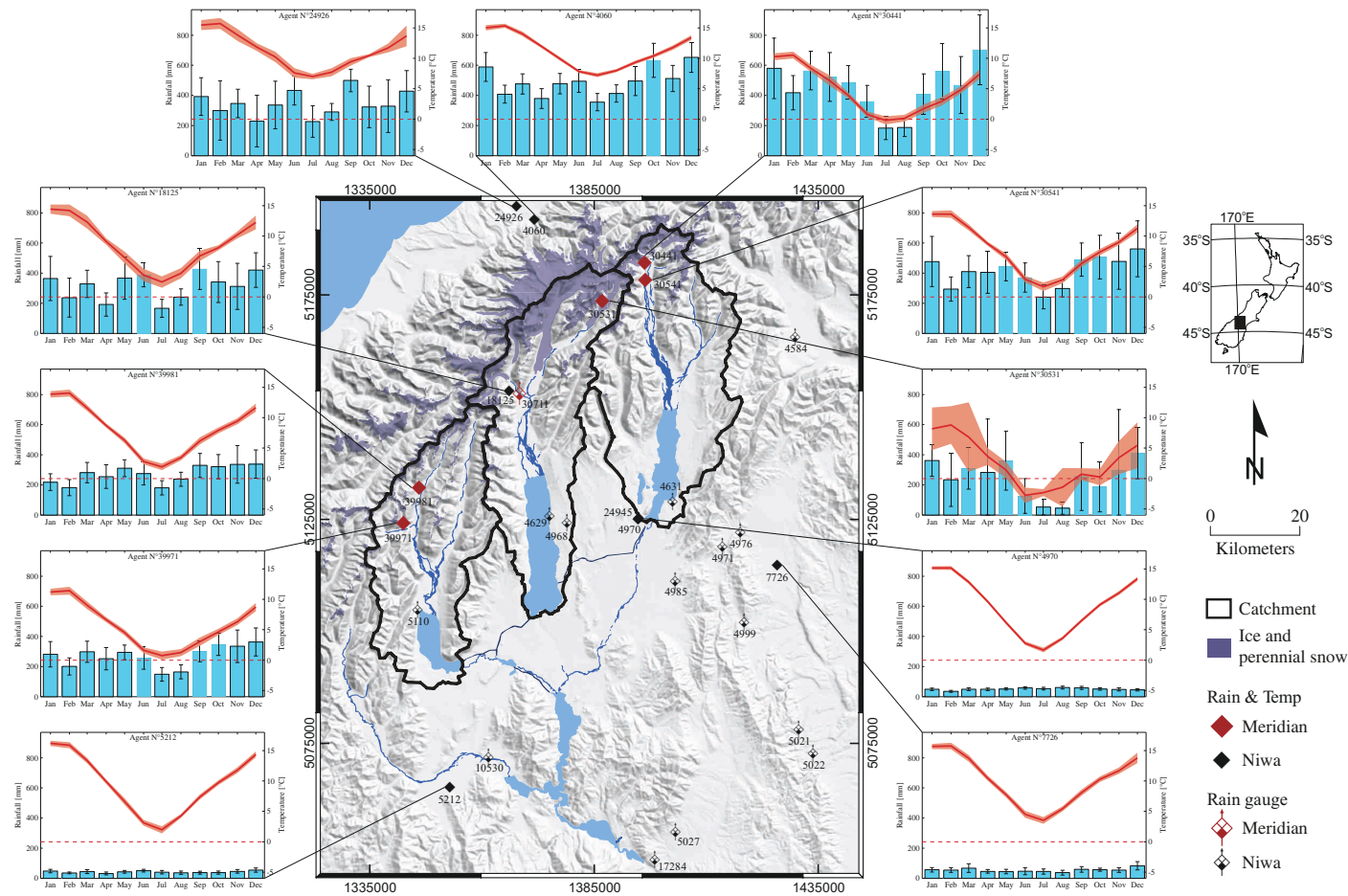


Figure 2.2 Climatic conditions in the upper Waitaki catchment. The envelopes around the mean temperature and error bars for the precipitation represent the 90% confidence standard error.^a

^aNote that the data from station N° 30531 installed by Meridian Energy in October 2002 Ltd at Rose Ridge (1980m asl) exhibits large standard errors due to a shorter time series. Rainfall and temperature records at high altitude sites belonging to Meridian Energy are also likely to be affected by snow during winter months.

2.2.3 Glaciers and landscape

The geology of the upper Waitaki catchment is dominated by Torlesse greywacke with occurrences of some Haast group schist on the northern part [Figure 2.3 (a)]. The southern part is a large and relatively flat inter-montane basin gently sloping southward from valley floors at about 700m to the southern edge of Lake Waitaki at around 300m asl. The basin is filled by gravels and alluvium originating from the exceptionally high erosion rate in the mountains (Hicks *et al.*, 1996) and deposited in extensive outwash plains by glacio-fluvial processes (Whitehouse, 1988). The landforms in the area are largely inherited from several sequences of glacier advances and retreats. Some remnants of the “Otira” glaciation at the late Pleistocene are well preserved. For instance, the deposits and moraines in the Mary Range on the south-eastern side of Lake Pukaki are associated with the Balmoral advance approximately 50,000 years ago (Wallace, 2001). Later, the Mt. John advance (17,000 years ago) and Tekapo advances (13,000 years ago) formed the major moraines that enclose lakes Ohau, Pukaki, and Tekapo (Fitzsimons, 1997). Evidence of additional sequences of glacier advance and recessions is widespread across the basin (Fitzsimons, 1997) including glacial erratic, recessional moraines, terraces, or trim lines across the valley walls.

Many glaciers remain in the catchments and continue to erode the hard rock mountain range aided by frequent and sometimes exceptionally large rock avalanches (Chinn *et al.*, 1992; Cox and Allen, 2009). This results in characteristic features such as glacial valleys, arêtes, horns, and cirques that contribute to the sharp topographic expression of the Southern Alps. Among about 3000 glaciers of over 1 ha inventoried in New Zealand (Chinn, 1989, 2001), the Ohau, Pukaki, and Tekapo catchments account for 206, 190, and 118 glaciers, respectively. The Ohau catchment has numerous but relatively small glaciers. It contrasts with the Pukaki and Tekapo catchments that account for 10 of the 55 largest (more than 300 ha) glaciers of New Zealand. The Pukaki catchment holds the two largest glaciers. The Tasman glacier is over 25 km long, while the Murchison glacier in the adjacent valley reaches nearly 15 km in length (see Figure 2.1). Together, these two have nearly two thirds of all the estimated ice volume of New Zealand (Chinn, 2001). The Tasman and Murchison glaciers, as well as other large debris-covered glaciers of the Pukaki and Tekapo catchments (e.g., the Muller, Hooker, Godley, Maud, or Classen glaciers), have undergone a massive down wasting since their last maximum at the end of the little ice age (Blair, 1994). For the last 50 years, formation and

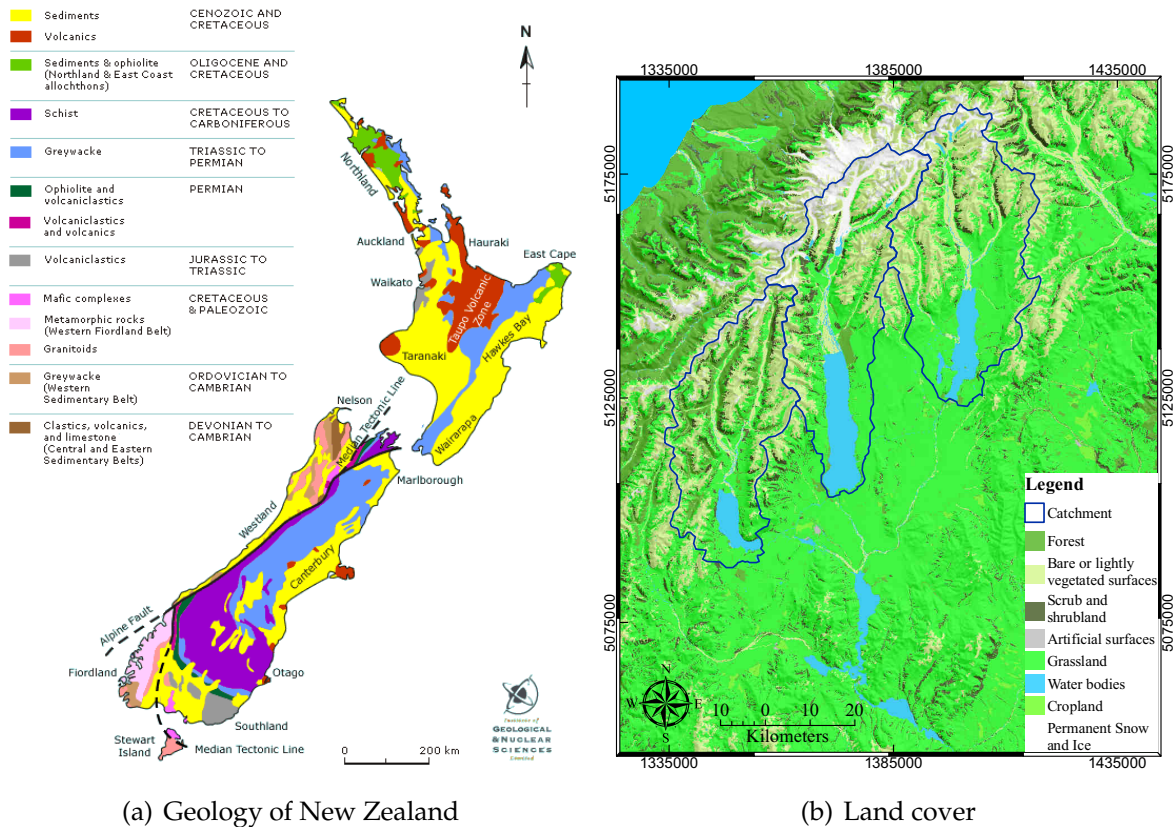


Figure 2.3 (a) Geology of New Zealand (Map reproduced with permission from the institute of Geological & Nuclear Sciences). (b) Major Land cover types (Ministry of the Environment, 2004, Land cover database version 2).

rapid growth of terminal lakes have led to the onset of calving processes that have further accelerated their ice loss and retreat (Purdie and Fitzharris, 1999; Rohl, 2006; Strong, 2008; Quincey and Glasser, 2009).

The massive areas of glacial outwashes downstream from the large glaciers are punctuated by wide and well-developed braided rivers. They are characterized by gently sloping gravel beds and many winding channels. The natural and highly variable flow of water has been artificially disturbed by the filling of lakes behind hydroelectric dams or the diversion of water from rivers to canals for electricity generation. Nevertheless, New Zealand's braided rivers remain incredibly dynamic environments. They provide great habitat opportunities and host unique plant and animal communities. During spring and summer, many species of water birds feed or nest on braided rivers, including both introduced and unique native species.

The vegetation in the three alpine catchments is mostly composed of grass-

land. Pastoral grazing dominates at low elevations, but give way to native tussocks at higher elevations [Figure 2.3 (b)]. Sub-alpine shrubland is often found on mountain slopes at the transition between the valley floor around 700m and the alpine grassland around 1200m. Typical species include *Olearia*, *Hebe*, or *Cassinia* with low canopy height ranging from 0.3 to 4m. Some patches of Manuka/Kanuka, riparian Matagouri, *Coprosma*, and broadleaved indigenous hardwoods are also present in some places. Forest communities are sparse in the Pukaki and Tekapo catchments. There are only scattered patches of indigenous forest in the Pukaki and Tekapo catchments, but with exotic conifers at mid-elevation. Indigenous forests are more widely spread within the Ohau catchment, where native silver beech forests can be found on the mountain slopes (Wardle, 1991). Areas above the tree line have a mixture of gravel, rocks, and low growing herbs and grasses and have little history of pastoral use. Finally, perennial snowfields and glaciers are generally found above 2000m although large glaciers such as the Tasman extend their terminal tongues to well below the tree line. In this environment of relatively low vegetation, the challenging mapping of snow under tree canopies is eliminated (Swanson, 1970). Although little studied, there appears to be no large aquifer in the catchments of the upper Waitaki (White and Reeves, 2002).

2.2.4 Hydrological regime

The outlet rivers of Lakes Ohau, Pukaki, and Tekapo alpine catchments combine with the waters of the Ahuriri River to form the Waitaki River, New Zealand's fourth largest. Sub-catchments of these three lakes are the wettest of the Waitaki basin, with precipitation mostly supplied by spill-over across the Main Divide. Together, they provide nearly 80% of the inflow to the Waitaki River (Leong and Chesterton, 2005, see Table 2.1).

The alpine nature of these sub-catchments means that an important fraction of precipitation falls as snow that accumulates. It is stored within a seasonal snowpack that builds during the winter months from April to October. Thereafter the snowpack tends to melt, although it is common to observe snow precipitation throughout the year at high elevations. The hydrological year in New Zealand ends at the time of minimum snow cover, generally the end of March. As stated in Section 2.2.2 and shown in Figure 2.2, there is no seasonal regime of precipitation in the catchments. Abundant rain or snowfall caused by the frequent westerly storms can occur at any time of the year (Henderson and Thompson, 1999). The mean tributary in-

Table 2.1 Alpine catchments of the upper Waitaki basin.

Catchment	Area [km ²]	Mean tributary inflow [m ³ .s ⁻¹] ^a	% Ice & perennial snow cover	Number of Glaciers ^b	Estimated ice volume [km ³] ^b
Ohau	1148	83.0	2.9	206	542
Pukaki	1372	128.4	15.7	190	6650
Tekapo	1457	85.9	4.4	118	2584
Waitaki	11908	379.0	2.6		

^a Calculated over the reference period 1980–2003 (Leong and Chesterton, 2005).

^b Data from the New Zealand glaciers inventory (Chinn, 2001).

flow to each lake is given in Table 2.1 and compared to the mean flow of the Waitaki River. However, such aggregated values conceal that catchment runoff exceeding 1000 m³.s⁻¹ is common during severe rain storms, possibly in combination with intense snowmelt (Moore and Prowse, 1988; Fitzharris *et al.*, 1999; Cutler and Fitzharris, 2005).

Figure 2.4 shows the mean daily inflow record for the hydrological years 2000 to 2007, which are selected as the study period for this thesis. It illustrates the highly dynamic nature of the discharge. Frequent rainstorms cause many short-lived peaks that complicate the hydrographs and challenge their modelling. Nonetheless, such stochastic events are of crucial importance since they make substantial contributions to the recharge of the storage lakes. For instance, maximum daily inflow during the study period reached as high as 813, 1473, and 893 m³.s⁻¹ in the Ohau, Pukaki, and Tekapo Lakes, respectively.

The records also have annual harmonics. The mean monthly discharge computed over the period of record since 1925 reveals systematic seasonal variations [Figure 2.4 (a-c)]. The three catchments exhibit a marked nivo-glacial regime characterized by single alternation of maximum and minimum discharge over the hydrological year. Low water generally remains above 40 m³.s⁻¹ and occurs during the winter months when snow accumulates. The maximum discharge occurs from December to January as the snowpack melts and is added to the release of ice-melt from glaciers. In the Pukaki catchment, the amplitude of the seasonal variation is double that of Ohau and Tekapo. The peak of discharge in the Pukaki catchment is reached later than that in the Ohau and Tekapo catchments, thus suggesting a larger amount of seasonal snow and/or a more pronounced effect of glaciers. Over the year, the snowmelt from these catchments is estimated to contribute from 18%

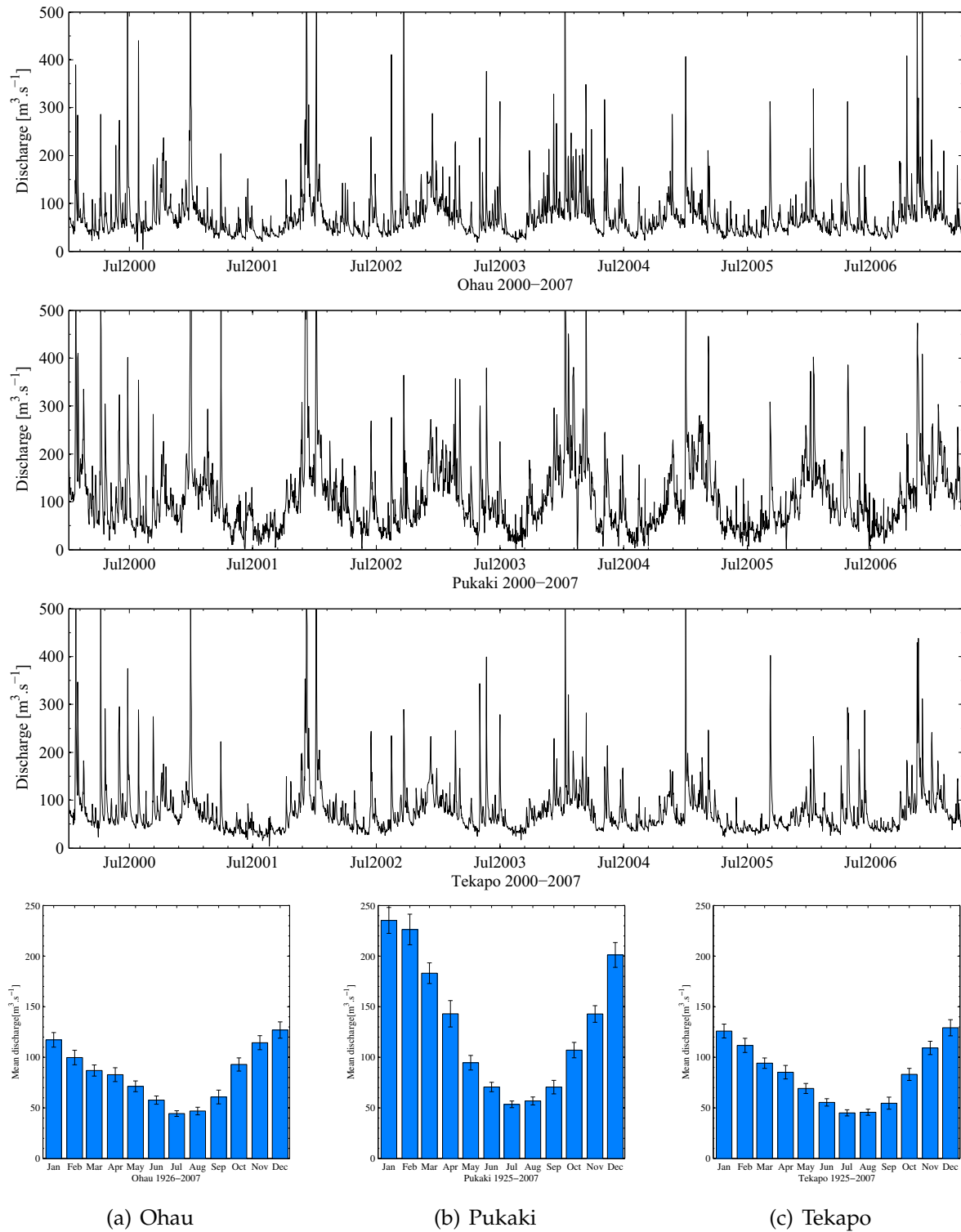


Figure 2.4 Runoff regimes of the three alpine catchments. (top) Daily inflow for the hydrological years 2000 to 2006, (bottom) mean monthly inflow computed over the full record from 1925. The error bars indicate the standard error at the 95% confidence interval (the inflow data were kindly provided by Meridian Energy Ltd.)

to 24% of the total annual runoff (McKerchar *et al.*, 1998) and up to 40% to 50% of the spring and summer inflows (Fitzharris and Garr, 1995). The amount of snow water equivalent stored in the seasonal snowpack is comparable to the size of the controlled lake storage (i.e., the water that can be released on demand by controlled gates as opposed to free flow) (Fitzharris *et al.*, 1999), thus stressing its importance in terms of optimal water management of the hydroelectric system.

2.2.5 Hydroelectricity

Only about six years after the *Thomas Edison Illuminating Company* had first begun to light the streets of New York in 1882, the little town of Reefton on the West Coast of New Zealand became the first in the country to turn to public electricity (Ministry of Economic Development, 2004). The city benefited from a generator brought by Walter Prince in 1886 and connected in 1888 to a turbine fed by the Inangahua River to become the Reefton Power Station. This was the first significant power plant in New Zealand. Quickly, the potential of hydro to generate the country's need for electric power was recognized. The government commissioned its first major hydroelectric power station at Lake Coleridge on the Rakaia River in 1914, with 4500 kW generators that provided regular supply to the city of Christchurch.

By 1920, the growth in electricity demand required the construction of new power capabilities. The availability of important water resources in the country encouraged the development of large state hydroelectric schemes. In 1928, a suitable site on the Waitaki River was selected for the building of a dam that would give birth to Lake Waitaki at 230m asl. The Waitaki station's powerhouse was completed in 1934 with two 15 MW generators. More units were added in 1940, 1944, 1949, and 1954 to meet the increasing demand and brought the generation capacity up to its present level at 105 MW (Meridian Energy Ltd, 2009). In 1938 construction started for the Tekapo power station which aimed at regulating the flow of water passing through the Waitaki power station. The Second World War and the lack of manpower forced construction to stop until it was resumed in 1944. The Tekapo A power station was finally commissioned in 1951 with a capacity of 25 MW. The level of Lake Tekapo was raised to its current maximum level of around 710m asl so as to provide a substantial storage capability.

The potential of the water resources in the Waitaki catchment was further exploited with the construction in 1958 and 1960 of the Benmore and Aviemore dams,

directly upstream of Lake Waitaki. Commissioned in 1965, the Benmore dam became the largest earth-filled structure in New Zealand and led to the creation of what is now the largest man-made lake of the country. It is at an elevation of 360m asl. The 540 MW capacity installed in the powerhouse provided essential supply to the North Island via the world's largest submarine cable beneath Cook Strait and allowed the development of the national electricity grid. At 270m asl, Lake Aviemore lies between Lakes Benmore and Waitaki. Its active production of hydroelectricity started in 1968 with 220 MW capacity, thus further increasing the importance of the Waitaki catchment to national power generation.

Electricity production of the upper Waitaki catchment increased in 1977 due to the diversion of water from Lake Tekapo to Lake Pukaki and the raising of the level of Lake Pukaki by 37m to reach 530m asl. This greatly increased its controllable storage capacity. Water from the Tekapo Canal runs through the Tekapo B power station that generates 160 MW (Figure 2.1). The water from Lake Pukaki was diverted to Lake Ohau at 520m asl via the Pukaki canal built in 1979 to feed the Ohau A power station equipped with 264 MW capacity. The development of the upper Waitaki hydro scheme was completed in 1985 by the canal diversion of water from Lake Ruataniwha to Lake Benmore and the commissioning of two "twin" stations Ohau B & C, each with 212 MW capacity.

The combined water storage of Lakes Tekapo, Pukaki, and Ohau linked together by dams and canals and the cascade of hydroelectric plants has a capacity of 1738 MW. The mean annual production reaches over 7700 GWh. A third of the capacity is controllable by gates and originates for the largest part from the Tekapo and Pukaki reservoirs (see Table 2.2). Overall, the three lakes of the upper Waitaki account for nearly 60% of the controllable storage available in the country (Figure 2.5). Moreover, the production from the Waitaki hydro scheme represents a third of all the hydroelectricity produced in New Zealand [Figure 2.6 (a)]. Despite the increase of generation by gas and coal in the last 20 years, hydroelectricity still accounts for around 60 to 70% of the total electricity generation [Figure 2.6 (b)]. New Zealand was the fifth ranked country in the world for hydroelectric consumption per capita in 2003.¹

This dependence on water has raised several issues with regard to energy policy and the sustainability of national electricity production. In 1992, 2001, 2003, and

¹Data from the Energy Information Administration, available online at <http://www.eia.doe.gov/>, last retrieved on October 9th, 2009.

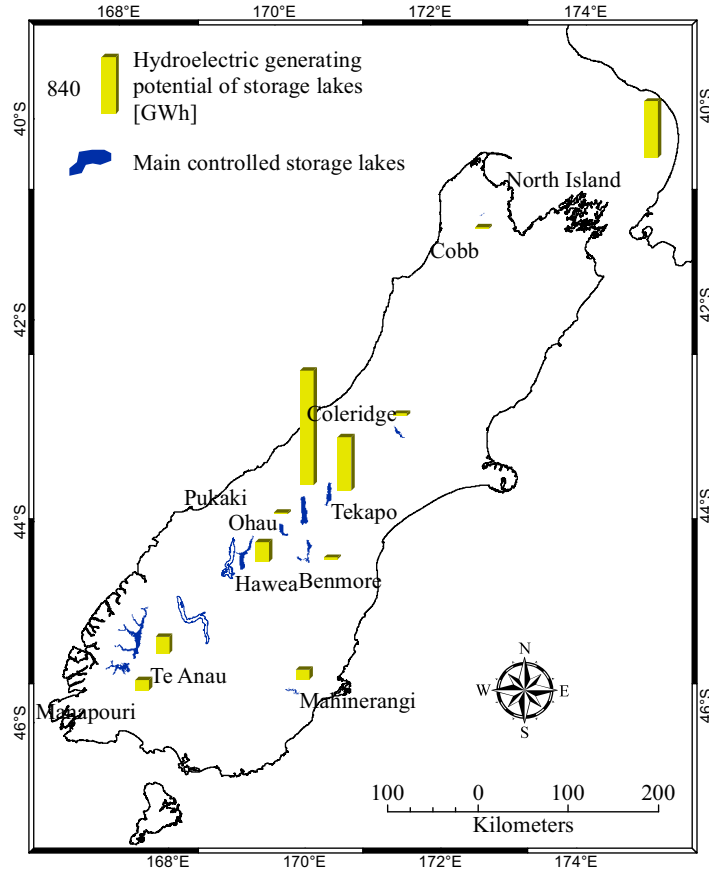


Figure 2.5 Main controllable storage capacity for hydroelectric generation [adapted from Fitzharris (1992)].

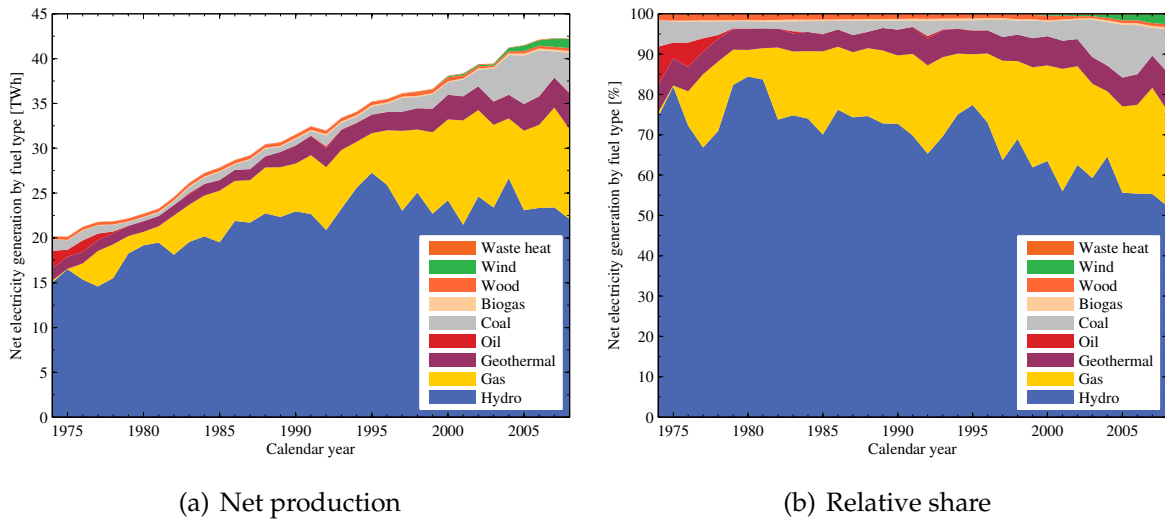


Figure 2.6 Annual electricity generation by fuel type (Ministry of Economic Development, 2009).

Table 2.2 Hydroelectric plants and capacity of generation of the upper Waitaki catchment (Meridian Energy Ltd, 2009).

Power station	Commissioned date	Lake area [km ²]	Capacity [MW]	Controllable storage [GWh]	Average annual generation [GWh]
<i>Tekapo</i>	-	96.2	-	782.4	-
Tekapo A	1951	-	25	-	160
Tekapo B	1977	-	160	-	833
<i>Pukaki</i>	-	172.8	-	1679.7	-
Ohau A	1979	59.3	264	22.0	1140
Ohau B	1984	canal feed	212	0.9	958
Ohau C	1985	canal feed	212	-	958
Benmore	1965	75.4	540	24.4	2215
Aviemore	1968	28.1	220	2.2	942
Waitaki	1935-54	5.6	105	0.5	496
Total			1738	2512.1	7702

2006 severe droughts led to water shortages in hydro catchments (Fitzharris, 1992; Staley, 2005) and required national energy saving campaigns. In June 2008, risk of shortages loomed large again and New Zealanders were, once more, urged to conserve power. Rising water demand and repetitive shortfalls sharpen the competition among water users, especially hydroelectric companies, agricultural industries, and domestic users. In this context, New Zealand requires strong and reliable information about its water supplies as well as a better knowledge about the processes that affect them. The report by the Ministry of Economic Development (2004) on sustainable energy explains how the careful planning for supply interruptions is now a necessary part of policy. One year later, the Ministry flagged systems simulation and modelling as priorities for energy research and to better utilize the value of water in hydro lakes. A critical component is the timing and supply of water from seasonal snow.

2.3 Study of snow in New Zealand

2.3.1 Overview

A comprehensive review on snow research in New Zealand can be found in Fitzharris *et al.* (1999). The first surveys of snow in the Southern Alps were conducted in the 1960s (Gillies, 1964; Morris and OLoughlin, 1965). Traditional sampling along snow courses aimed to assess the snow condition, estimate the snow

water equivalent of snow-fed river catchments, complete precipitation records, and forecast flood events (Chinn, 1969; Archer, 1970). A regular assessment of the snow pack at the névé of the Tasman glacier was also conducted between 1965 and 1973 in preparation for the hydro-electric development of the upper Waitaki (Ander-ton, 1975). Other sporadic surveys of snow accumulation were conducted within the framework of mass balance assessment of glaciers (e.g., Ruddell, 1995). Few snow courses were systematically surveyed. The longest systematic observations were conducted in the Craigieburn Range (Prowse, 1981), in the Two Thumb Range (Chinn, 1981), and in the Fraser catchment (Harrison, 1986). These covered a series from 12 to 19 winters. They demonstrated a large spatial and temporal variability of the snowpack and highlighted the relationship between dry winters and low annual runoff (Fitzharris *et al.*, 1999).

The 1992 national electricity crisis accentuated the role of the seasonal snow for water availability (Fitzharris, 1992) and two snow courses were initiated in the Pukaki catchment with measurement of snow depth and density four times a year so as to provide snow storage information to managers of hydroelectric plants (Kerr, 2005). Permanent climate stations were also installed at high altitude and included ultrasonic snow depth sensors at Panorama Ridge (station ID: 30441 in Figure 2.2, installed in 1997) and at Rose Ridge (station ID: 30531, installed in 2005) as well as a snow pillow at Rose Ridge. In 2007, an experiment was initiated by the National Institute of Water & Atmospheric Research (NIWA) in the Jollie catchment (a sub-catchment of the Pukaki basin) where a high number of snow cover samples were collected all across the basin at the time of maximum accumulation in September. This experiment was repeated in September 2008 and 2009 and aimed at getting a better understanding of the spatial variability of snow accumulation, as well as providing data to calibrate and assess modelling strategies in the future.

The hydrology of snow has been investigated on numerous occasions. For instance, energy balance measurements of the snow pack have been conducted at several locations (e.g., Prowse and Owens, 1982; Moore, 1983; Clark, 1993; Kelliher *et al.*, 1996; Neale and Fitzharris, 1997) and are reviewed in more detail in Chapter 7, Section 7.2.3. Moore and Prowse (1988) summarised research on snow in the Waimakariri catchment so as to understand better the processes of snow deposition, accumulation, melt, as well as water movement in the snowpack. The physical properties of new snow were documented by Prowse (1981) and Chinn (1981), revealing that new snow in New Zealand is generally ‘damp’ and its density often reaches

300 kg.m⁻³ (Fitzharris *et al.*, 1999). Other aspects of the physics of snow, such as the internal structure of the snowpack were investigated in the context of avalanche hazard understanding and mitigation (e.g., McNulty and Fitzharris, 1980; Ho, 1982; McGregor, 1990; Hendrikx, 2005).

2.3.2 Snowpack modelling

Several attempts have been made to model snow storage in the catchments of New Zealand. Archer (1970) fitted linear relationships between the measured snow water equivalent (SWE) and elevation in the Ben Ohau range (Pukaki catchment). Although he found significant correlations between both variables, the linear models were established on the basis of a very limited number of samples and varied according to time and location. The lack of robustness and limited spatial representativeness of this method clearly compromise its relevance for estimating snow storage over a whole basin. Fitzharris (1978) further stressed the difficulty of linking snow storage to elevation with simple empirical relationships in the Southern Alps of New Zealand. The mid-latitude maritime location of the mountainous range generally results in freezing levels that are highly variable in elevation, depending on the synoptic meteorological conditions. Elevation of the boundary between snow accumulation and ablation can vary within large amplitudes within and over the seasons. Mild conditions can occur even in winter and yield substantial snowmelt as high as 2500m, while snow may fall in summer as low as 500m. The succession of variable freezing markedly affects the accumulation of snow whose profile loses consistency with elevation (Fitzharris *et al.*, 1999), resulting in no consistent empirical relationship with elevation. For this reason, Fitzharris (1978) advocated the use of a more physically based approach for modelling snowpack accumulation, ablation, and snow storage in the Southern Alps.

In the Pukaki catchment, Anderton (1974a) analysed daily synoptic charts and provided snow storage estimates based on a classification of days. He used criteria as to whether days contributed to accumulation, or ablation, or status quo. Later, Fitzharris (1987) designed a weekly index of the storage of seasonal snow for all the Southern Alps based on precipitation and temperature records from twenty-one climate stations in the South Island. The index was developed as an arbitrary weighted sum of the departure of both physical variables from their long term normal value. Although this index could not provide an absolute estimation, the cumulative sum of the weekly values was designed to monitor the seasonal snow storage relative

to a normal situation. This method relied on the assumptions that mean weekly temperature and precipitation departures from normal levels always give an identical departure pattern of snow accumulation. This assumption is weakened by the lack of consideration of the timing between the precipitation and the temperature that give rise to snowfall events. [Fitzharris \(1987\)](#) admitted the difficulty of assessing the validity of this approach, but a qualitative historical investigation of well documented years known for their surplus or deficit of snow showed an acceptable agreement with his snow index.

[Moore and Owens \(1984a\)](#) developed a simple snow accumulation and ablation model based on a degree-day approach ([Hock, 2003](#)) for the Craigieburn Range in the Waimakariri River catchment, which is east of the Main Divide. [Moore and Owens \(1984b\)](#) then interfaced the snow model to a reservoir-based transformation model inspired by the Hydrologiska Byråns Vattenbalansmodell (HBV) hydrological model ([Bergström, 1976](#)) to simulate the streamflow from the small catchment. They obtained better results with the simple degree-day method than an energy budget approach, possibly due to an absence of good quality data to estimate the latter correctly (e.g., wind velocity, humidity profiles, and radiation measurements). [Barringer \(1989\)](#) refined the degree-day approach to model the snowline elevation in the Remarkables Range (Clutha River catchment, south of the Waitaki basin). [Barringer](#) did not consider the storage of snow but investigated the variability of the temperature lapse rate and its impact on the accurate modelling of the elevation of the snowline.

[Twaddle \(1995\)](#) produced a snow model whose ablation procedure was based on a simplified energy balance approach. The model was designed specifically for areas covered by tussock in the Pisa range (Central Otago), and was enhanced by an original approach that addressed the formation of hollows and the drifting of snow caused by vegetation and wind. The simulation of snow storage in New Zealand evolved following the 1992 national electricity crisis caused by the severe drought of 1991–92. [Fitzharris and Garr \(1995\)](#) developed an accumulation-ablation snow model for the main hydro catchments of the Southern Alps. The model called *SnowSim* implemented a similar accumulation-ablation approach to that used by [Moore and Owens \(1984a\)](#), but was semi-distributed to estimate the SWE in elevation bands of 300m with data from only five climate stations. Snow storage was reconstructed over the 1930–93 period. Mean snow storage provided a quantitative benchmark against which the yearly departure could be compared to facilitate op-

erational decisions by water managers. SnowSim was refined for the Waitaki catchments by [Thompson \(1997\)](#) so as to benefit from newly installed climatic stations at higher altitude. [McAlevy \(1998\)](#) extended SnowSim to the whole country in a distributed manner using a 1 km grid cell. Finally, [Kerr \(2005\)](#) adapted SnowSim specifically to the Pukaki catchment by implementing a new interpolation method for the precipitation (see Chapter 7, Section 7.4 for more details about the SnowSim model).

Of course, modelling the snowpack cannot be separated from wider attempts to simulate streamflow in catchments where the snow has a substantial contribution. The main characteristic of the hydrological modelling approach is that it aims at simulating streamflow rather than snow storage only. The transformation of the net production (i.e., liquid precipitations, snowmelt, and icemelt minus losses due to evapo-transpiration and ground recharge) into a delayed discharge can better support the need of water managers for forecasted inflows.

[Grimmond \(1980\)](#) followed by [Turner \(1986\)](#) applied the Snowmelt Runoff Model (SRM, [Martinec, 1975](#)) in the Fraser catchment (central Otago) but obtained poor performance. Although this could be explained by an inaccurate optimization of the calibration coefficients (e.g., melt factor, temperature lapse rate, recession coefficient), the quality of the input data could also have played a role. As explained in detail in Chapter 8, SRM relies on daily estimations of the snow cover fraction as an input to compute snowmelt, thus making the model specifically designed to take advantage of remotely sensed observations. No such data were available for the above-mentioned authors. They made subjective estimates of snow cover obtained from photographic panorama that could have introduced large uncertainties. [Bowden \(1994\)](#) applied SRM in the Jollie and Pukaki catchments during the winter of 1993. He also lacked appropriate observations of the snow cover fraction and relied on observations of the elevation of the snowline from the valley floor. The input data for SRM were estimated based on the hypsometric curve of the basin. [Bowden \(1994\)](#) simulated the discharge reasonably well except during low flow periods. Nevertheless, his experiment was only applied to an incomplete hydrological year and the robustness of his calibration was not tested on additional years.

The University of British Columbia watershed model (UBC, [Quick and Pipes, 1977](#)) was applied with reasonable success by [Peters \(1996\)](#) in the upper Waitaki catchments over the period 1973–80. [Islam \(2001\)](#) also tested the UBC model in glacierized catchments including the Hooker watershed (within the Pukaki catch-

ment) and modelled the streamflow of the Whataroa and Waiho Rivers on the West Coast, near Franz Joseph glacier. Thompson (2002) developed a simple semi-distributed hydrological model to forecast the discharge in mountainous catchments but disappointing performances were obtained from its application to the Tekapo basin. Lill (2003) applied the HBV-ETH9 model to four catchments with various levels of glacial cover (Hooker, Jollie, Rangitata, and Rakaia). A robust set of parameters permitted the streamflow to be modelled satisfactorily over a multi-year period and climate change scenarios were investigated to examine its impact on the availability of the water resources. Finally, an ongoing effort by NIWA is underway to model river flows in New Zealand using a networked version of the hydrological model TOPMODEL (TOPNET, Bandaragoda *et al.*, 2004; Clark *et al.*, 2008). The SnowSim model has been refined for the South Island (Clark *et al.*, 2009) whereby the storage and melt of snow remains addressed by an accumulation-ablation approach that implements a variable degree-day model. So far, none of the attempts were successful enough to enable an operational use of daily inflow forecasts. Furthermore, no model really took advantage of the power of remotely sensed data to map snow cover. It is this aspect that this thesis seeks to investigate.

2.3.3 The contribution of remote sensing

Remote sensing of the seasonal snow cover in New Zealand probably started with McKellar (Chinn, pers. comm.) who recorded repeated panorama photos of Tasman glacier from 1955 until 1971. Gillies (1964), who conducted the earliest measurements of seasonal snow in the country (Fitzharris *et al.*, 1999), linked traditional sampling across snow courses in the Fraser catchment (central Otago) with repeated aerial oblique photographs of the snow cover and panorama photos from the ground. Anderton initiated a more systematic photographic survey of the snow cover with nearly weekly panoramas of the mountains from Mt John observatory and the Hermitage near Aoraki/Mt Cook between 1971 and 1975 (Chinn, pers. comm.). Anderton (1974b) also tested the potential of multispectral aerial photography over the Tasman glacier during the winter 1974 and commented on the use of Landsat 1 to determine the areal extent of the melting area. Hickman (1972) attempted to retrieve the elevation of the snowline in the Southern Alps with meteorological satellite pictures, but was unsuccessful because of the very coarse spatial resolution available at the time in the context of the very rugged nature of the Southern Alps.

While he demonstrated the difficulty of estimating the accumulation of snow in New Zealand [Fitzharris \(1978\)](#) concluded that observations of the snowline based on aerial or satellite images could provide more reliable indices of snow accumulation. Around the same time [Thomas *et al.* \(1978\)](#) investigated the potential of the Landsat Multi Spectral Scanner (MSS) sensor for comparing the extent of the snowfields in the Mt Robert skifield and Six Mile Creek that became the Rainbow ski area. Ten years later, [Fitzharris and McGann \(1989\)](#) used 26 images of the Advanced Very High Resolution Radiometer (AVHRR) from NOAA satellites to estimate the snow covered area and snowline elevation of the Tararua and Ruahine Ranges in the South of the North Island. Satellite observations from AVHRR were also used by [McAlevey \(1998\)](#) and [Fitzharris and McAlevey \(1999\)](#) to assess the accuracy of the SnowSim model with respect to its ability to model the snow cover extent.

Despite the crucial importance of the snowpack to the water resource in New Zealand, it is obvious that the remote sensing of snow has received only introductory consideration. Although relatively simple, the retrieval of the snow cover extent over relatively short time periods (e.g., one or two years) to assess the accuracy of the SnowSim model ([Fitzharris and McAlevey, 1999](#)) appears to be the most advanced use of satellite imagery to study the country's snow cover. This situation strongly contrasts with other parts of the world where the remote sensing of snowpack has received much closer attention. For instance, since the first satellite observation of snow cover with the TIROS-1 meteorological satellite ([Singer and Popham, 1963](#)), the mapping of the snow cover and snow cover properties, such as grain size, albedo, snow water equivalent, or surface temperature, has been done in many areas in the world. [Table 2.3](#) provides a few examples of the abundant literature available on the subject. It contrasts with the scarcity of studies conducted in New Zealand despite the obvious advantages that remote sensing could bring to obtain a better understanding of the properties and dynamics of the snowpack in areas as remote and inaccessible as the Southern Alps. The potential contribution of satellite observations to the hydrological modelling of catchments dominated by snow melt has also been widely recognized (see [Hall and Martinec, 1985](#); [Rango and Martinec, 1997](#); [Seidel and Martinec, 2004](#), and references therein) and applied in many places (e.g., [Cline *et al.*, 1998](#); [Turpin *et al.*, 1999](#); [Molotch *et al.*, 2004](#); [Lavallée *et al.*, 2006](#); [Andreadis and Lettenmaier, 2006](#); [Brown *et al.*, 2008](#)). Successful applications of remote sensing to map snow cover in a wide range of global environments highlight the need to investigate this potential in New Zealand.

Table 2.3 Selected references about remote sensing of snow.

Site	Sensor	Type	Period	Reference
Worldwide	MODIS, Landsat TM & ETM+	Sub-pixel snow mapping and grain size		Painter <i>et al.</i> (2009)
Greenland	MODIS	Snow grain size retrieval	2004	Lyapustin <i>et al.</i> (2009)
Himalaya	MODIS	Snow mapping and snowmelt modelling	2000–2005	Immerzeel <i>et al.</i> (2009)
Northern Patagonia Icefield, Chile	MODIS, Landsat	Snow mapping	2000–2006	Lopez <i>et al.</i> (2008)
Liard and Athabasca Basins, Canada	MODIS	Snow mapping	2000–2001	Brown <i>et al.</i> (2008)
Kaidu River Basin, China	MODIS, ASTER, Landsat ETM+, CBERS	Snow mapping	2000–2005	Li <i>et al.</i> (2008)
Northern Xinjiang, China	MODIS	Snow mapping	2001–2005	Liang <i>et al.</i> (2008)
Himalaya, India	IRS-LISS-III	Mapping dry/wet snow	2000	Gupta <i>et al.</i> (2005, 2007)
Eurasia & Canada	SSM/I, AMSR-E	Snow water equivalent and snow depth	1993–94, 2004–05	Pulliainen (2006)
Canada	NOAA/AVHRR, SSM/I, Landsat TM	Snow mapping	1981–2000	Wang <i>et al.</i> (2005)
Ob River, Russia	SSM/I	Snow depth mapping	1989–2001	Grippa <i>et al.</i> (2005)
Tibetan Plateau	ASTER & MODIS	Sub-pixel snow mapping	2000 & 2001	Lina <i>et al.</i> (2005)
Tana River Basins, Fennoscandia	Landsat TM & SPOT VEGETATION	Snow mapping	1987, 1995, 1998–99	Dankers and De Jong (2004)
Austrian Alps	MODIS & MERIS	Snow mapping	2000 & 2003	Malcher <i>et al.</i> (2003)
Norway	MODIS & Landsat ETM+	Sub-pixel snow mapping	2000 & 2001	Vikhamar and Solberg (2003)
Mammoth Mountain, US	AVIRIS	Sub-pixel snow mapping and grain size	1994	Painter <i>et al.</i> (2003)
Himalaya, India	IRS-WiFS	Snow mapping and snowmelt modelling	2001	Kulkarni <i>et al.</i> (2002)
Austrian Alps	ERS-1	Wet snow mapping	1992–1993	Nagler and Rott (2000)
European Alps	NOAA/AVHRR	Snow mapping	1987–1998	Ranzi <i>et al.</i> (1999)
French Alps	Landsat TM	Snow grain size, snow surface temperature	1992	Fily <i>et al.</i> (1999)
Sierra Nevada, US	Landsat TM	Sub-pixel snow mapping	1983–1993	Rosenthal and Dozier (1996)
Ötztal Alps, Austria	AIRSAR and Landsat TM	Snow and glacier mapping	1989 & 1991	Shi <i>et al.</i> (1994)
Tioga Pass & Mammoth Mountain, US	AVIRIS	Sub-pixel snow mapping	1989 & 1991	Nolin <i>et al.</i> (1993)
Sierra Nevada, US	Landsat TM	Snow reflectance and snow mapping	1983	Dozier and Marks (1987)
Rocky Mountains, Canada	NOAA/AVHRR	Snow mapping and snowmelt modelling	1985–1986	Ferner and Sutherland (1987)
Rhine-Felsberg basin, Switzerland	Landsat MSS and NOAA/AVHRR	Snow mapping	1982 & 1985	Baumgartner <i>et al.</i> (1987)
Norway	TIROS-N & NOAA/AVHRR	Snow mapping	NA	Andersen (1982)

2.4 The satellite tool

2.4.1 Optical remote sensing of snow

In the context of remote sensing, the observation of the snowpack relies on the properties of snow with respect to reflection, absorption, and scattering of electromagnetic radiation. The snowpack is generally formed by a mixture of ice crystals, liquid water, and air (Colbeck *et al.*, 1998). Once deposited, the snowflakes transform due to the combined actions of mechanical compaction, melting, water movement, and processes of sublimation and condensation associated with thermal gradients within the snow layers (Colbeck, 1982; Armstrong and Brun, 2008, Chap. 2). The ageing of snow is characterized by the formation, coalescence, and growth of snow grains (Male and Gray, 1981), whose size can range from 50 μm for very fine snow up to several millimetres for old transformed snow.

2.4.1.1 Optical properties of snow

In the reflective domain (300–2500 nm). The coefficient of absorption of water and ice in the visible part of the spectrum (i.e., 400 to 700 nm) is low. Thus, when visible light travels through a dense layer of ice or water of 10m thickness, its intensity only reduces by a factor of about $e \approx 2.718$ (Hale and Querry, 1973; Warren, 1984). In addition, the granular structure of the snow medium, whose ice particles are large compared to the wavelength, enables multiple reflections at the interfaces between air, ice, and/or water (Rees, 2006, Chap. 4). Non-selective scattering properties combined with the limited absorption of light explain the high reflectance of snow across the visible domain. It explains why snow appears white to the human eye.

Towards the shortwave infrared range (SWIR), the properties of absorption of ice largely inherits that of liquid water and increases by a factor of about 10^4 to 10^5 between 600 nm and 2500 nm. Although the scattering properties remain substantial across the whole reflective domain, incoming photons are much more likely to be absorbed in the infrared. It causes a strong decrease of the snow reflectance from the visible to the longer wavelengths. As for liquid water, ice also accounts for strong absorption bands in the SWIR. However, unlike liquid water whose absorption coefficient peaks at about 1400 and 1900 nm, water in a crystalline lattice (i.e., ice) exhibits its maxima of absorption at about 1500 and 2000 nm (Dozier, 1989).

The shape of the grains is recognized to play a role in the scattering properties of snow (Picard *et al.*, 2009). However, grain size is largely considered to be the

dominant characteristic affecting the spectral reflectance. Thus, with regard to its spectral signature, snow is often idealized as a medium composed of spheres characterized by the grain radius (e.g., fine, medium, coarse) (Dozier *et al.*, 2009). As the size of snow grains increases, photons must travel longer distances within the absorbing medium, resulting in more photons being absorbed and a reduction of the upwelling radiation (Winther and Hall, 1999; Dozier and Painter, 2004). Such sensitivity of the spectral reflectance of snow to grain size is particularly pronounced in the NIR range and between absorption bands. Many studies have documented the sensitivity of the spectral reflectance of snow to grain size via experimental measurements (Aoki *et al.*, 2000; Painter and Dozier, 2004; Hudson *et al.*, 2006) and/or the implementation of the Mie scattering theory in radiative models (Wiscombe and Warren, 1980; Warren, 1982; Dozier, 1989). The theoretical approach has proven to be very successful in modelling the typical spectral reflectance of snow, such as that of pure snow shown in Figure 2.7 (a).¹

The reflectance of snow can also be affected by the deposition of aerosols such as soot, dust, and algae (Dozier *et al.*, 2009). These impurities generally affect the visible wavelengths and reduce the reflectance (Warren and Wiscombe, 1980). Fresh snow deposits of pure and generally fine grain snow typically exhibit a very high reflectance. As snow ages and transforms, grain growth and contaminants deposits tend to decrease the reflective properties. Although the effect of contaminants are not accounted for in the theoretical spectra shown in Figure 2.7 (a), they become evident in the spectra measured in real conditions [Figure 2.7 (b)]. These spectra measured at different locations on the névé of the Glenmary glacier in the Ohau catchment in March 2003 exhibited substantial differences with the theoretical spectra of pure snow. The spectrum of new fresh snow resembled that of coarse granular snow in the theoretical approach. Two additional types of older snow were measured and were assessed to have relatively fine (i.e., less than 1 mm) and relatively coarse grain size (i.e., more than 1 mm), respectively. Their spectra clearly illustrate the potential effect of contaminants in the visible domain with strong selective absorption in the blue and green range that can be attributed to the effect of dust (Warren and Wiscombe, 1980). The decrease of the reflectance due to larger grain size is also clearly visible in the near infrared (NIR) and SWIR domains. The increase of water content can also cause a decrease of the reflectance by clustering

¹Data obtained from the ASTER spectral library v2.0 available at <http://speclib.jpl.nasa.gov/>, last retrieved on October 23rd, 2009.

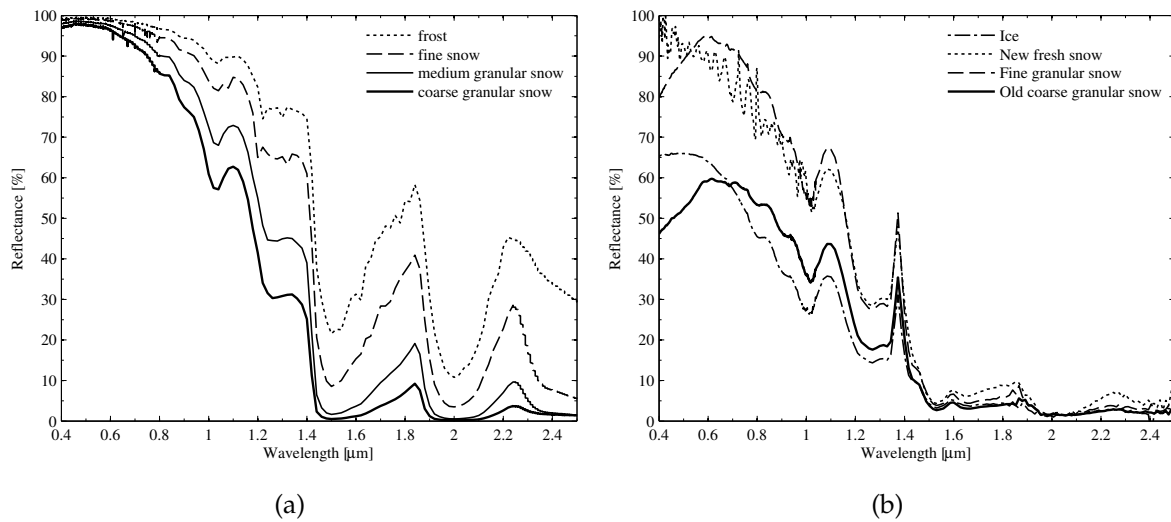


Figure 2.7 Spectral signature for various snow and ice targets. (a) Theoretical spectral reflectance of pure snow calculated using the optical constants of ice in a Mie theory and radiative transfer model (Warren, 1982). (b) Reflectance of various types of snow measured during fieldwork on Glenmary glacier, South Island of New Zealand, in March 2003.

individual snow grains, thus artificially increasing the effective grain size (Dozier, 1989; Winther and Hall, 1999; Dozier *et al.*, 2009).

Snow is a diffuse reflector that can exhibit a moderate to strong anisotropic behaviour. The angular distribution of the reflected light is characterized by the bidirectional reflectance distribution function (BRDF). The latter was established for various types of snow both experimentally (Leroux *et al.*, 1998; Hudson *et al.*, 2006) and theoretically (Leroux *et al.*, 1999). The BRDF of snow generally exhibits a strong forward scattering and an anisotropy that varies according to wavelength (Aoki *et al.*, 2000), grain size and shape (Painter and Dozier, 2004), and surface roughness (Warren *et al.*, 1998). Dumont *et al.* (2009) recently reported that the variations of the anisotropy factor with wavelength are controlled by the ice absorption coefficient. Dumont *et al.* (2009) also confirmed the results of Painter and Dozier (2004) showing that the dependence of the snow anisotropy to wavelength appears to be controlled by the dominance of multiple scattering within the snowpack at short wavelengths (i.e., smaller than 1 μm), while single scattering close to the surface dominates at longer wavelengths. Although the research presented in this thesis largely ignores the anisotropic behaviour of the snowpack, it is worth noting that the latter must be accounted for when properties such as broadband albedo are sought.

In the emissive domain (3–15 μm). With an emissivity close to 1 in the thermal infrared region (TIR, see Figure 2.8¹), snow has a behaviour that is sometimes considered to approach a black body (König *et al.*, 2001). However, some authors have pointed out that such an assumption can lead to errors since the emissivity of snow departs substantially from that of a black body in the 8–14 μm region (Warren, 1982; Salisbury and D’Aria, 1992; Hori *et al.*, 2006). It was also shown that viewing angle, grain size, or melting substantially affect the emissivity of snow (Dozier and Warren, 1982; Salisbury *et al.*, 1994). Hori *et al.* (2006) revealed the explicit dependence of snow emissivity to snow type, and in particular a decrease of emissivity with increasing grain size, ice producing the lowest values (see Figure 2.8). Nevertheless, with such high emissivity, the emission of radiation from the snowpack remains largely controlled by its surface temperature. The latter can be estimated from infrared measurement in atmospheric windows by inverting Planck’s law (Salisbury *et al.*, 1994; Fily *et al.*, 1999), as demonstrated later in Section 3.3.3. Although atmospheric scattering and emission are minimal in the 10.5–12.5 μm atmospheric window, absorption due to water vapour remains. Without an accurate radiative transfer model or atmospheric profile measurement, the retrieval of surface temperature from satellite sensors thus often relies on split-window algorithms that take advantage of the differential absorption in two adjacent infrared bands to account for atmospheric effects (Coll *et al.*, 1994; Wan and Dozier, 1996; Key *et al.*, 1997; Sobrino *et al.*, 2003).

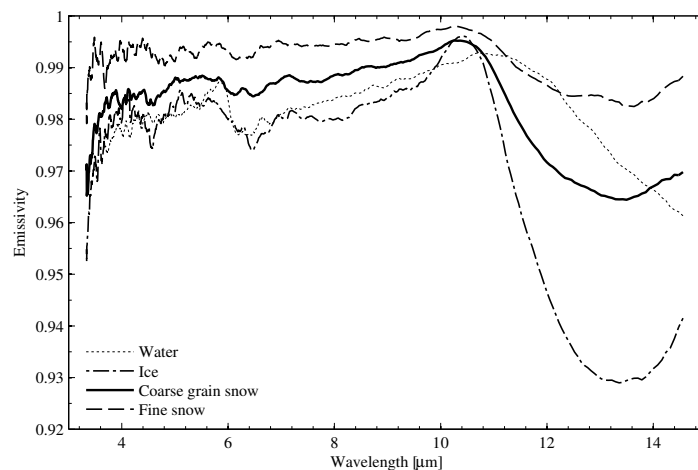


Figure 2.8 Spectral emissivity of snow, ice, and water.

¹Data obtained from the MODIS UCSB Emissivity Library available at <http://www.ices.ucsb.edu/modis/EMIS/html/em.html>, last retrieved on October 23rd, 2009.

2.4.1.2 Mapping of snow with optical satellites

The main use of airborne or spaceborne remote sensing to study snow involves mapping of the snow cover. Towards this goal, passive optical, as well as active and passive microwave technologies have been successful (Shi *et al.*, 1994; Nagler and Rott, 2000; König *et al.*, 2001; Hall *et al.*, 2002; Kelly *et al.*, 2003). Although microwave remote sensing has the undeniable advantage to allow observations at night and through cloud cover, the low level of energy radiated by the snowpack in the microwave region causes the available satellite sensors [e.g., the Advanced Microwave Scanning Radiometer (AMSR) or the Special Sensor Microwave/Imager (SSM/I)] to operate with relatively coarse spatial resolutions in the order of several kilometres. Although passive microwave technologies have revealed their potential to map directly snow depth and SWE (Foster *et al.*, 2005), the performance of retrieval algorithms remains affected by considerable bias (Pulliainen, 2006). In addition, the coarse spatial resolution compromises the accurate mapping of snow at a local scale in mountainous terrain (König *et al.*, 2001) and was therefore considered to be inappropriate for this research. Active radar and especially Synthetic Aperture Radar remote sensing (SAR) can achieve virtually any spatial sampling size but faces difficulties in mountainous regions due to strong topographic effects such as foreshortening, layover, or shadowing (Shi *et al.*, 1994). Although some of these limitations can be overcome by image processing techniques, the on-demand policy on image acquisition, as well as the price of individual images compromise the suitability of spaceborne SAR sensors [e.g., RADARSAT-2 or the Active Microwave Instrument (AMI) aboard ERS-2] for a frequent monitoring of the Earth surface at a daily or even weekly basis. Thus, their use for the routine mapping of the snow cover remains limited and was also discarded for this research.

Alternatively, progress in optical technologies has led to the miniaturization of detectors. In addition, satellites now implement a large bandwidth with regard to their capacity of telemetry that can support the transmission of large amounts of data. Both aspects allow the imaging of the entire Earth's surface at a near daily time scale with kilometre and sub-kilometre spatial resolution by sensors such as the Advanced Very High Resolution Radiometer (AVHRR, 5 spectral bands at 1 km spatial resolution and daily coverage), the Vegetation instrument aboard the Satellite Probatoire pour l'Observation de la Terre (SPOT 4/5-VEGETATION, 4 spectral bands at 1 km spatial resolution and near daily coverage), the MEdium Resolution Imaging Spectrometer aboard the Envisat platform (MERIS, 15 spectral bands at 300m spa-

tial resolution and 2-3 days coverage period), or the MODerate Resolution Imaging Spectroradiometer aboard the TERRA and AQUA platforms (MODIS, 36 spectral bands at resolution ranging from 250 to 1000m and 1-2 days coverage period).

Such repeated observations are essential to monitor the dynamic nature of the snow cover in areas of fast evolution and/or to accommodate regions with frequent cloud cover such as the alpine ranges of New Zealand. [Molotch and Margulis \(2008\)](#) recently discussed this aspect in the context of the contribution of satellite observations to the spatial modelling of snowmelt. [Molotch and Margulis](#) suggested that occasional observations with relatively high spatial resolution, such as that enabled by the Enhanced Thematic Mapper aboard Landsat 7 (ETM+, 7 spectral bands in the reflective and thermal domain with spatial resolutions ranging from 15 to 60m), are preferable to frequent observations at coarser resolution such as provided by MODIS. [Slater *et al.* \(2009\)](#) strongly disputed this counter-intuitive conclusion and demonstrated that it was compromised by the uncertainties associated with the modelling strategy of [Molotch and Margulis \(2008\)](#).

Only the techniques related to optical technologies were considered in this research. They take advantage of the fact that snow is among the most reflective targets on the Earth's surface and strongly contrasts with its neighbouring materials. Since the first successful mapping of snow from the meteorological satellite TIROS-1 ([Singer and Popham, 1963](#)), various techniques have been used to classify snow pixels automatically in satellite images. Whether they are unsupervised [e.g., K-means or Iterative Self-Organizing (ISODATA) clustering techniques] or supervised [e.g., Gaussian Maximum Likelihood Classifier (MLC)], pixel-wise classification techniques aim at recognising spectral patterns in the multispectral dataset so that individual pixels are assigned to a limited number of land cover classes. For instance, [Harrison and Lucas \(1989\)](#) used the ISODATA algorithm to discriminate snow from clouds in NOAA-AVHRR images. The same unsupervised classification strategy was chosen by [Slater *et al.* \(1999\)](#) to support the operational mapping of snow in a maritime sub-polar region (Scotland) from AVHRR, but concluded that the ISODATA classes had numerous confusions with clouds.

Alternatively, supervised techniques were preferred by [Baumgartner *et al.* \(1986\)](#) and [Swamy and Brivio \(1997\)](#) who used MLC to support the mapping of snow from Landsat MSS or AVHRR. In their comparison of both techniques for the classification of snow targets, [Rango and Itten \(1976\)](#) concluded that supervised classification was more accurate than unsupervised. However, the main advantage

of an unsupervised classification in an operational context remains the minimal requirement of manual intervention compared to supervised classification strategies. Indeed, the former only requires the user to label the classes appropriately subsequent to the classification, while the latter requires a time-consuming identification and definition of training areas for each image used.

Since [Crane and Anderson \(1984\)](#) and [Dozier \(1984\)](#) highlighted the potential of a spectral band in the SWIR range to discriminate snow from clouds, snow classification algorithms have relied heavily on the use of the Normalized Difference Snow Index (NDSI) ([Dozier and Marks, 1987](#)). This normalized band ratio takes advantage of the contrast between the high reflectance of snow in the green part of the visible spectrum and the low reflectance in the SWIR (see [Figure 2.7](#)). It is given by

$$\text{NDSI} = \frac{\rho_{\text{Green}} - \rho_{\text{SWIR}}}{\rho_{\text{Green}} + \rho_{\text{SWIR}}}, \quad (2.1)$$

where ρ is the reflectance of the pixel which can be either ground reflectance (i.e., after correction of topographic and atmospheric effects) or measured at the top of the atmosphere (i.e., ρ^* with no correction applied). The NDSI signal varies within the range $[-1, 1]$ and it generally increases as snow prevails within the pixel and/or when snow grains are finer ([Dozier, 1989](#)). The simple computational cost of the NDSI and its good performance at detecting snow make it an approach that is often preferred to other classification methods such as non supervised or supervised classification ([Wang and Li, 2003](#)). Although the NDSI was originally designed for Landsat TM data (Green: band 2 at 560 nm; SWIR: band 5 at 1650 nm), it has been used with many other sensors that implement the appropriate spectral bands, such as MODIS (Green: band 4 at 555 nm; SWIR: band 6 at 1640 nm) ([Hall et al., 2002](#); [Lopez et al., 2008](#)), ASTER (Green: band 1 at 560 nm; SWIR: band 4 at 1650 nm) ([Foppa et al., 2007](#)), SPOT ([Raup et al., 2007](#)), SPOT VEGETATION ([Xiao et al., 2001](#); [Dankers and De Jong, 2004](#)), Meteosat SEVIRI ([de Ruyter de Wildt et al., 2007](#)), AVHRR ([Gómez-Landesa et al., 2001](#); [Wang and Li, 2003](#)), GOES ([Romanov et al., 2000](#)), ATSR/2 ([Slater, 2001](#)), or IRS ([Gupta et al., 2005](#)).

However, with binary mapping, where pixels are crisply classified as being ‘snow’ or ‘no snow’, a level of generalization is introduced that fails to provide an insight with regard to the presence of other materials that may contribute to the pixel radiometry. Alternative techniques have been developed that ultimately aim to provide estimates of the abundance of snow within individual pixels (e.g., [Elder et al., 1998](#); [Nolin et al., 1993](#); [Painter et al., 2003](#); [Salomonson and Appel, 2006](#)). This approach is used in this research and is further detailed in [Chapter 5](#).

2.4.1.3 Use of snow covered area (SCA) observations in snow models

Various approaches have been investigated to make a practical use of the observed Snow Covered Area (SCA) and improve the performances of snow routines in hydrological models. These approaches are now summarized.

Direct insertion. [Turpin *et al.* \(1999\)](#) used Landsat-derived maps of SCA to update the distribution of snow water equivalent (SWE) predicted by the HBV model in Sweden. The SWE predicted for a day with observation of SCA was replaced by an anterior map of SWE whose modelled SCA matched better the observation. [Johansson *et al.* \(2001\)](#) and [Johansson *et al.* \(2003\)](#) applied a similar technique with the same model based on AVHRR observations of the snow cover extent. They demonstrated that this strategy can improve forecasts of runoff. Clearly, this approach relies on the disputable assumption that an exact correspondence exists between the spatial distribution of SWE and that of snow pixels. However, it is evident that the SCA is not necessarily indicative of the SWE, especially in mountainous regions where different states of storage may correspond to comparable extents of the snow cover. [McGuire *et al.* \(2006\)](#) used maps derived from MODIS to modify the maps of SWE modelled by the Variable Infiltration Capacity (VIC) hydrological model ([Liang *et al.*, 1994](#)). Their strategy consisted of removing all storage from the elevation bands with less than 50% SCA according to MODIS. Conversely, they added 5 mm of SWE in bands with null SWE but more than 50% observed SCA. This approach remains inconsistent because, although the departure of the spatial distribution of SWE from reality is acknowledged, not all locations are addressed. Moreover, the subjective and possibly unbalanced set of rules to update the SWE is based on the SCA, despite the inconsistency between both state variables.

Parameter calibration. [Lavallée *et al.* \(2006\)](#) designed a two-step method to improve a simple accumulation-ablation snow model similar to SnowSim with maps of snow cover from NOAA-AVHRR. Rather than a direct-insertion of the observed SCA in the snowmelt model to update the estimated SWE, [Lavallée *et al.* \(2006\)](#) used successive observations to determine the melt-factor for which there was an acceptable match between the modelled and the observed SCA. The SWE in the remaining snow-free pixels was redistributed to areas at higher elevations identified as snowy according to satellite observations. This strategy is believed to be more appropriate, at least for the first step, because it does not directly relate two inconsistent state

variables. The observation of one state variable (i.e., the SCA) is used to refine a model parameter in order to approach better reality, resulting in new estimates of both state variables (i.e., SCA and SWE). The SCA obtained from satellite observations was also used by [Udnæs *et al.* \(2007\)](#) to calibrate the HBV model. Although the modelled SCA benefitted from this strategy, no improvement was achieved in terms of modelled runoff. An additional updating technique of the model based on the SCA observations revealed contradictory results with the potential for improvement in years having unusual weather conditions.

Data assimilation. More sophisticated approaches based on a statistical data assimilation framework ([Evensen, 2006](#)) have been tested for incorporating SCA observations in snowmelt models. [Kolberg *et al.* \(2006\)](#) used observed SCA and a Bayesian approach to update the parameters of a statistical model that related a pixel's SCA and its SWE. [Andreadis and Lettenmaier \(2006\)](#) investigated the assimilation of MODIS-derived SCA into the VIC hydrological model using SCA information as part of an ensemble Kalman filter. They observed little improvement during the accumulation season, while the ablation of snow was better modelled. [Clark *et al.* \(2006\)](#) tested the same technique based on synthetic experiments without real observation of SCA. They demonstrated that the assimilation of SCA can affect substantially the state variables of the hydrological model. However, they obtained an improvement in terms of streamflow accuracy during periods of rapid depletion of the snow cover. Therefore, [Clark *et al.* \(2006\)](#) considered that such a technique would mostly benefit regions of ephemeral snow cover. [Hreinsson \(2008\)](#) implemented the methodology described by [Clark *et al.* \(2006\)](#) in the Jollie watershed (i.e., a sub-catchment of the Pukaki basin) based on the MODIS-derived snow maps created for this thesis (see Chapter 5). The modelled snow cover area largely benefitted from the assimilation strategy during the ablation season. However, improvements in terms of the modelled SWE and runoff were not investigated.

Forcing. Some models use observations about the snow extent as direct input to the snowmelt routine. For example, the “depletion curve” mode of the Streamflow Synthesis and Reservoir Regulation model (SSAR, [U.S. Army Corps of Engineers, 1991](#)) relies on a snow cover depletion relationship, whereby the SCA fraction of the catchment is related to the accumulated runoff or SWE. Although such a relationship is not necessarily uniform from year to year, observed SCA can be used

as an input variable on the basis of a calibrated curve to forecast runoff. For instance, [Dillard and Orwig \(1979\)](#) used timely spatial observations of the SCA from NOAA-AVHRR with this strategy, but only obtained marginal benefit. [Ferner and Sutherland \(1987\)](#) showed that better performances could be achieved when the observations were used to update the snow cover depletion relationship.

The Snowmelt Runoff Model (SRM, see [Martinec, 1975](#); [Hall and Martinec, 1985](#), Chap. 4; [Dewalle and Rango, 2008](#), Chap. 11) is among the few and better known hydrological models that were developed specifically to accept direct input of SCA, along with forcing from climatic data. It is a semi-distributed degree-day model that was designed to take advantage of frequent observations of the areal snow cover extent from aircraft or satellites, to simulate discharge in catchment where snowmelt has a substantial contribution. Successful applications with a variety of sensors over 30 years in many basins of various sizes worldwide made this approach a particularly suitable candidate for inclusion in this thesis (see for example [Martinec et al., 2005](#), and references therein). The few attempts to use SRM in New Zealand ([Grimmond, 1980](#); [Turner, 1986](#); [Bowden, 1994](#)), always lacked a suitable remote sensing dataset to fulfil the model's needs. This approach is revisited in Chapter 8 on the basis of detailed time series of MODIS-derived snow maps over the hydrological year 2000–2006.

2.4.2 The EOS AM-1/TERRA platform

Manufactured by Lockheed Martin, the EOS AM-1 spacecraft was launched on December 18th 1999 as the flagship of the Earth Observation System (EOS) of the National Aeronautics and Space Administration (NASA). Deployed on a near polar sun synchronous orbit at 705 km altitude (Figure 2.9), the satellite crosses the equator at the same local time around 10:30 in the morning as it descends on its orbit. This time generally corresponds to the minimal cloud cover on land and justifies the name TERRA given to the satellite. TERRA supports the operation of five scientific instruments mounted on the nadir-facing deck of the platform. They aim at providing a comprehensive monitoring of solar radiation, the atmosphere, the oceans, and the Earth's continents.

- The Advanced Spaceborne Thermal Emission and Reflection Radiometer (ASTER) acquires high-resolution images of the Earth in 14 spectral bands covering the visible to the thermal infrared spectrum. It is committed to the

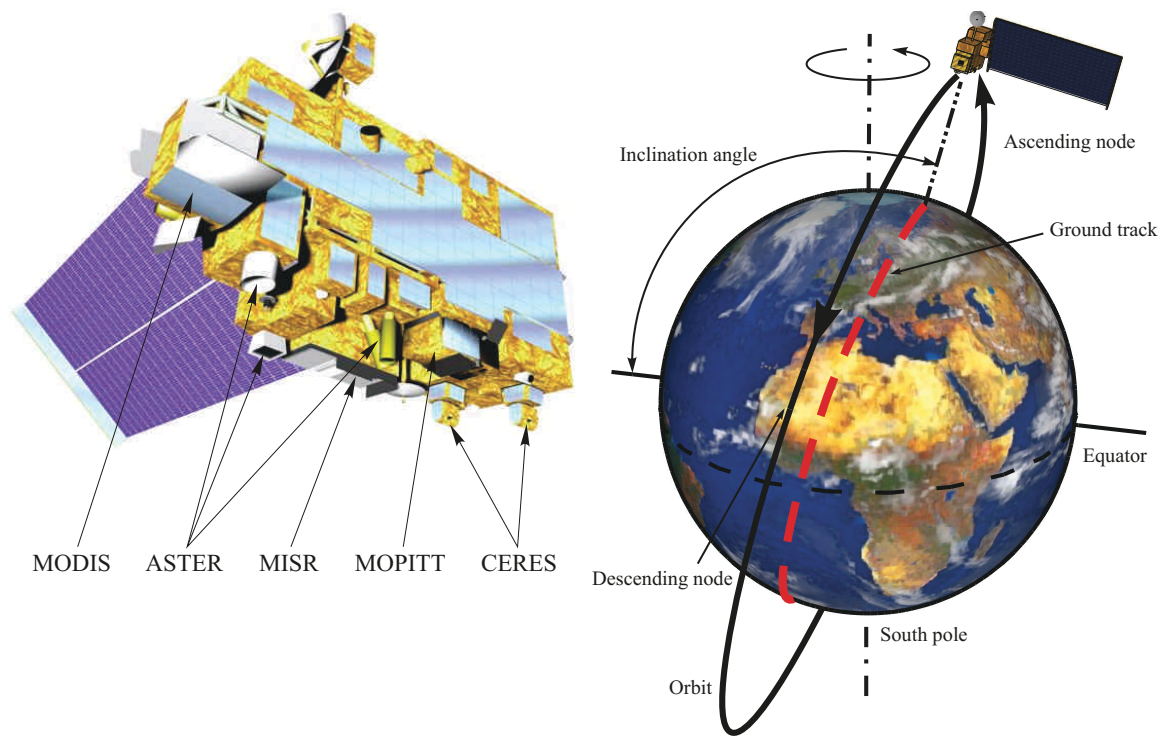


Figure 2.9 The TERRA platform and its orbit (the satellite model on the left is reproduced from NASA).

creation of detailed maps of land cover, surface temperature, or emissivity. Its backward looking telescope also enables the creation of Digital Elevation Models (DEM) by photogrammetric techniques.

- The Clouds and Earth's Radiant Energy System (CERES) consists of two radiometers measuring the radiant energy in three broadband spectral regions corresponding to the reflected, thermal and total radiation. One of the radiometers scans across track while the other rotates in an azimuth angle to sample the entire hemisphere of radiation. It aims at measuring cloud properties and their impact on the Earth's radiative balance.
- The Multi-angle Imaging Spectro-Radiometer (MISR) measures the reflected energy in four narrow bands covering the Blue, Green, Red, and Near Infrared (NIR) regions of the electromagnetic spectrum. Its original design enables the measurements to be done simultaneously in nine widely spaced angles to determine how the reflective energy is distributed in the upper hemisphere in order to estimate better the total amount of sunlight reflected by diverse surfaces and assess BRDF effects.

- The MODerate Resolution Imaging Spectro-radiometer (MODIS) captures radiant energy in 36 spectral bands ranging in wavelength from 0.4 μm to 14.4 μm at coarse spatial resolution. It is designed to enable an entire view of the Earth's surface every 1-2 days. Its comprehensive multispectral capability provides a unique vision of global dynamics including land surface cover change, land and ocean surface temperature, primary productivity, clouds, aerosols, water vapour, atmosphere gaseous profiles, or fires.
- The Measurements Of Pollution In The Troposphere (MOPITT) is a nadir sounding instrument that relies on gas correlation spectroscopy to estimate the profiles of concentration of methane and carbon monoxide in the lower atmosphere. It provides information about the patterns and transport of pollution and chemical reactions occurring in the troposphere.

The research in this thesis relies primarily on MODIS data to support the near-daily monitoring of the snow cover in the upper Waitaki catchment. ASTER does not acquire data continuously, but its much higher spatial resolution and simultaneous acquisition enabled it to serve as a 'zoom' lens for MODIS. It thus made ASTER an ideal tool for assessing the performance of snow cover mapping with MODIS source data.

2.4.2.1 MODIS

Overview. The MODIS sensor aboard TERRA has been continuously acquiring images since February 2000. A second identical MODIS instrument is also available aboard the EOS PM-1/AQUA satellite launched in May 2002. MODIS is an across track scanner with multispectral capabilities that make it one of the most advanced optical sensors for Earth observations currently operating in space. Its swath width of nearly 2400km on the Earth's surface along with the orbital period of the platform allow the successive scans almost to overlap and enable the whole Earth to be imaged within less than 2 days. The sensor has 36 bands covering wavelengths from the visible to thermal infrared at three spatial resolutions [250m at nadir: band 1 & 2; 500m at nadir: band 3 to 7; 1 km at nadir: all remaining channels in reflective and emissive domain, see Table 2.4] (Barnes *et al.*, 1998). The seven 'land bands' (b1–b7) cover wavelengths from the visible to the Short Wave Infrared (SWIR) and are specifically designed to measure land cover boundaries and properties. Their relative spectral response (RSR) and respective spatial resolution are shown in Figure 2.10.

Table 2.4 Spectral characteristics of MODIS [adapted from Barnes *et al.* (1998)].

Primary use	Band	Bandwidth [nm]	Primary use	Band	Bandwidth [nm]
Land/Cloud boundaries	1	620-670	Surface/Cloud temperature	20	3,660-3,840
	2	841-876		21	3,929-3,989
Land/Cloud/Aerosols properties	3	459-479	22	3,929-3,989	
	4	545-565	23	4,020-4,080	
Snow	5	1,230-1,250	Atmospheric temperature	24	4,433-4,498
	6	1,628-1,652	25	4,482-4,549	
Ocean colour/Phytoplankton/Biogeochemistry	7	2,105-2,155	Water vapour	27	6,535-6,895
	8	405-420	28	7,175-7,475	
Aerosol,cloud properties	9	438-448	Cloud properties	29	8,400-8,700
	10	482-493	Ozone	30	9,580-9,880
Atmospheric water vapour	11	526-536	Surface/Cloud temperature	31	10,780-11,280
	12	546-556	32	11,770-12,270	
Cirrus clouds	13	662-672	Cloud top altitude	33	13,185-13,485
	14	673-683	34	13,485-13,785	
	15	743-753	35	13,785-14,085	
	16	862-877	36	14,085-14,385	
	17	890-920			
	18	931-941			
	19	915-965			
	26	1,360-1,390			

Pixel size at nadir [m]
250
500
1000

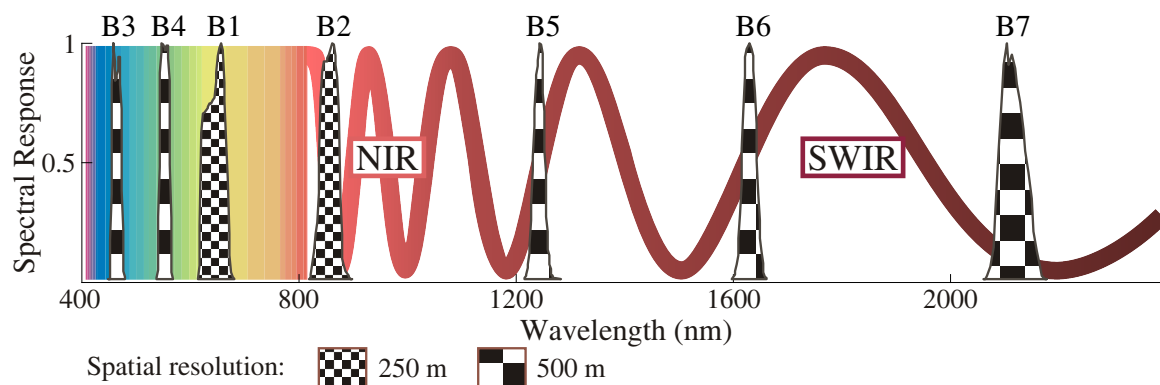


Figure 2.10 MODIS relative spectral response for ‘land bands’ b1–b7.

MODIS data products. Raw MODIS data are provided as Level-1A products and account for scans of non-calibrated radiance counts in the swath format. Calibrated at aperture radiance at the top of the atmosphere is provided as MODIS Level-1B (L1B) swath data products in granules consisting of five minutes acquisition. Products from MODIS/TERRA or AQUA are preceded by the MOD or MYD prefixes, respectively. Although this research exclusively relies on MODIS/TERRA data, the description of the products applies equally to both instruments and products are referred by the MxD prefix in this thesis. The bands 1 and 2 at 250m nadir resolution

are supplied in MxD02QKM files as arrays of 5416×8120 pixels. The bands 3 to 7 at 500m spatial sampling come in MxD02HKM files as arrays twofold smaller, along with bands 1 and 2 aggregated at 500m spatial resolution. All 36 bands acquired natively at 1 km nadir resolution (i.e., bands 8-36), as well as aggregated versions of the land bands 1-7, are provided in MxD021KM files as arrays of 1354×2030 pixels. A companion file referred to as MxD03 provides geolocation information about the centre of pixels in the swath products, as well as relative geometry parameters such as solar zenith (θ_s), solar azimuth (φ_s), sensor zenith (θ_v) and sensor azimuth (φ_v). A series of higher level MODIS products has been developed and the algorithms to generate them are continually updated, assessed and improved by the MODIS team of scientists (Masuoka *et al.*, 1998). They provide daily and sometimes multi-day composites of environmental variables and parameters such as cloud classification, atmospheric profiles, aerosols, snow classification, surface reflectance, and much more.

Swath vs. gridded products. Most of the higher level products (MODIS Level-2G, Level-3 and Level-4 data products) are gridded and provided in a Sinusoidal projection (SIN) that is suitable for the global mapping of geophysical parameters (Wolfe *et al.*, 1998). However, the SIN projection produces noticeable distortions in localities far from the central meridian (i.e., Greenwich). Khlopenkov and Trishchenko (2008) recently pointed out the pitfall of the SIN projection and its irrelevance for regional mapping in near Polar Regions. The SIN projection and its corresponding Tissot's indicatrix shown in Figure 2.11 reveal that New Zealand is situated at a location where the projection used for the MODIS gridded products produces the most severe distortions. Although the reprojection of gridded products is possible using widely available software packages, it can only propagate the distortions introduced by the gridding in the first place. Furthermore, it is generally accepted in remote sensing that reprojection and the associated resampling must be limited to a minimum to preserve the quality of the data. Thus, the use of gridded MODIS products for a local study in New Zealand was not suitable and the swath products were preferred for this research. Their projection on the local cartographic system (i.e., New Zealand Transverse Mercator 2000, NZTM2000¹) was addressed by specialized software and is described in the following chapter (Section 3.3).

¹The parameters of this projection are available at <http://www.linz.govt.nz/geodetic/datums-projections-heights/>, last retrieved on September 25th, 2009.

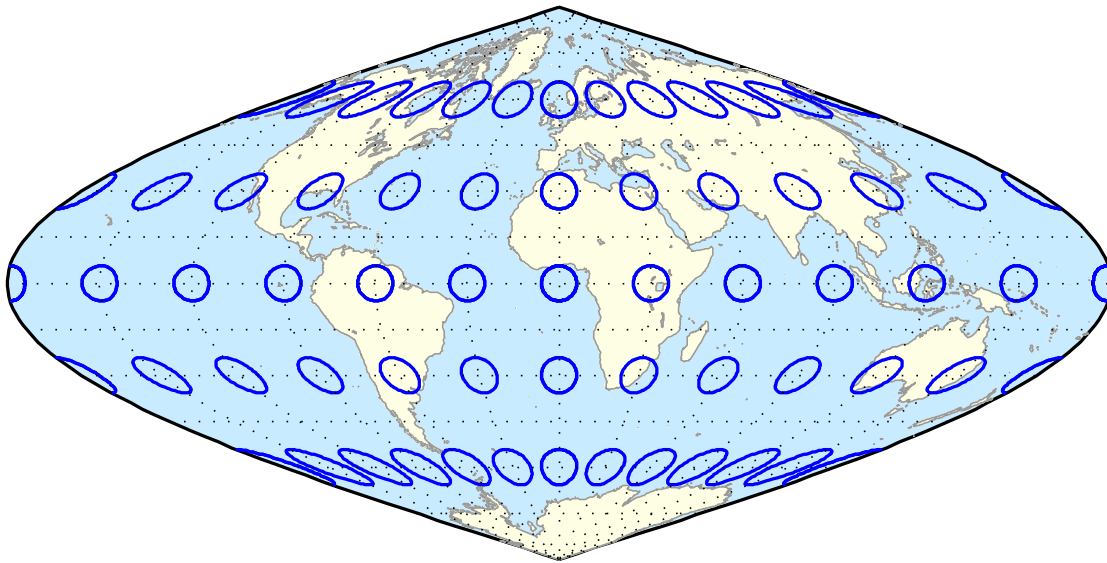


Figure 2.11 Sinusoide projection with Tissot's indicatrix to illustrate the distortions due to map projection. Note the severe distortions in New Zealand.

2.4.2.2 ASTER

ASTER is a high-resolution radiometer consisting of three instruments totalling 14 spectral bands that cover wavelengths from the visible to thermal infrared at three spatial resolutions (Table 2.5). The VNIR subsystem (i.e., Visible and Near Infrared) is an along-track scanner that has a nominal spatial resolution of 15m at nadir with spectral bands in the green, red, and NIR parts of the reflective spectrum. The band 3 in the NIR is duplicated by means of a telescope pointing backwards with an angle of 27.6° . This allows the acquisition of stereo pairs with a base-to-height ratio of about 0.6 that is suitable for performing the photogrammetric extraction of surface elevation and the creation of a DEM (Toutin, 2002). The SWIR subsystem holds bands 4 to 9 that cover wavelengths in the short-wave infrared domain with a nominal spatial resolution of 30m. Finally, the TIR subsystem stands for Thermal Infrared. It implements an across-track scanning design equipped with five spectral bands in the emissive part of the spectrum. The latter are provided with a coarser spatial sampling of 90m due to the lower energy level available in this spectral range.

The swath of ASTER is relatively narrow as it covers only 60 km. It produces a nominal repeat time of 16 days, although the three subsystems allow for cross-track pointing in order to reduce the revisit period. Furthermore, unlike MODIS,

Table 2.5 Spectral characteristics of ASTER.

Primary use	Band	Bandwidth [nm]	Primary use	Band	Bandwidth [nm]
Land/Cloud properties	1	520-600	Surface temperature/composition	10	8,125-8,475
	2	630-690		11	8,475-8,825
	3N	780-860		12	8,925-9,275
3B	780-860	13		10,250-10,950	
DEM	3B	780-860	14	10,950-11,650	
Surface composition	4	1,600-1,700	Pixel size at nadir [m]		
	5	2,145-2,185	15		
	6	2,185-2,225	30		
	7	2,235-2,285	90		
	8	2,295-2,365			
	9	2,360-2,430			

the acquisition from ASTER is not continuous and data are obtained based on an on-demand policy. It limits the availability of usable scenes especially at locations with frequent cloud cover such as in New Zealand. Thus, it prevents the use of ASTER images strictly as a monitoring tool for processes as dynamic as the snow cover in the Southern Alps. Nevertheless, the simultaneity of acquisition with MODIS data and the much finer spatial resolution make it an ideal tool for assessing the performance of snow cover mapping with MODIS. Its contribution is explored in Chapter 6.

2.4.3 The MOD10 Snow product

2.4.3.1 Design

Up to Collection 4, the MxD10 Snow Product delivered by the National Snow and Ice Data Center (NSIDC¹) provided only a binary classification of snow at 500m spatial resolution based on the NDSI approach (Klein *et al.*, 1998; Hall *et al.*, 2002). Hall *et al.* (1995) and Dozier (1989) showed that a threshold of 0.4 applied on the NDSI was efficient to discriminate snow and ice targets from most other surfaces. However, since water absorbs almost all SWIR radiation, it also exhibits a high NDSI. In addition, the denominator of the NDSI for very dark targets is small and only a small increase of visible reflectance can potentially make their NDSI value high enough to exceed the required threshold. Hence, unacceptable commission errors also can occur with shaded pixels, since they receive much more radiation in the visible wavelength relative to the SWIR due to the distorted spectral distribution

¹See <http://nsidc.org/>, last retrieved on October 14th,2009.

of diffuse sky irradiance. In order to mitigate such errors, the MxD10 algorithm implemented additional criteria applied to the reflectance at the top of the atmosphere (Hall *et al.*, 2002). Thus, the general form of the algorithm classifies a pixel as being snow covered when it fulfils the following conditions:

$$\text{NDSI threshold test} : \text{NDSI} > 0.4 \quad (2.2a)$$

$$\text{water exclusion test} : \rho_{0.86 \mu\text{m}}^* > 0.11 \quad (2.2b)$$

$$\text{dark pixel exclusion} : \rho_{0.55 \mu\text{m}}^* > 0.1. \quad (2.2c)$$

This original design had difficulties to map snow in forests due to the mixing of spectral signatures associated with bright snow and dark canopy (Klein *et al.*, 1997). It was addressed by relaxing the NDSI threshold when the vegetation activity measured by the Normalized Difference Vegetation Index (NDVI) was considered high enough. A crisp membership polygon was defined in the NDVI *vs.* NDSI feature space (Klein *et al.*, 1998). In this domain, pixels were considered as snow if:

$$\rho_{0.86 \mu\text{m}}^* > 0.11, \text{ and} \quad (2.3a)$$

$$\rho_{0.65 \mu\text{m}}^* > 0.1. \quad (2.3b)$$

Finally, residual spurious errors whereby pixels were classified as snow in well-known snow-free areas were addressed by means of a thermal test inspired from the work of Romanov *et al.* (2000). Barton *et al.* (2001) investigated a simple threshold of 277 K applied on the brightness temperature in MODIS band 31 at 11 μm ($\text{BT}_{11 \mu\text{m}}$, see Section 3.3.3 for more detail about the computation of brightness temperature). This thermal test was shortly replaced by an estimate of the snow surface temperature based on the split-window technique of Key *et al.* (1997). The threshold was increased to 283 K to prevent omission errors (Hall *et al.*, 2002; Riggs *et al.*, 2006).

The release by the NSIDC of the collection 5 of the MxD10 Snow Product in September 2006 brought a major innovation. In addition to the binary snow map described above, it provides an array with the sub-pixel snow fraction at 500m spatial resolution. The latter is estimated based on a linear relationship established between the value of the NDSI and the abundance of snow within a pixel (Salomonson and Appel, 2004, 2006). This relationship is discussed in more detail in Section 5.4.4.3.

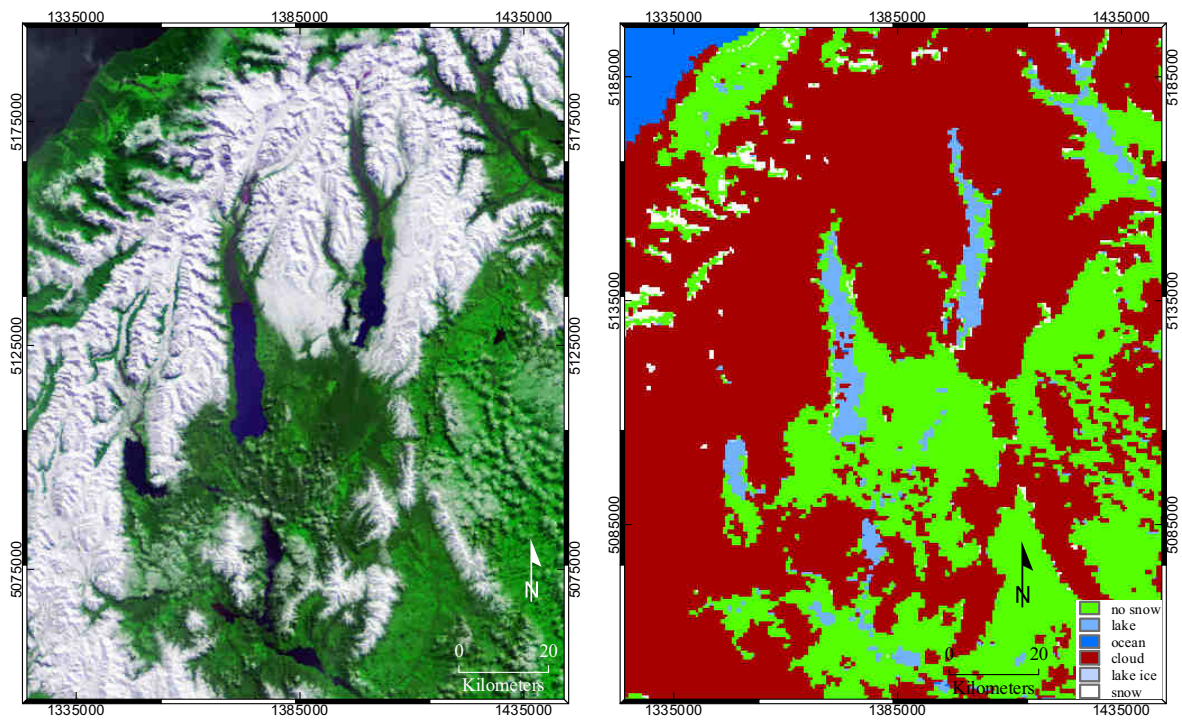
2.4.3.2 Limitations

The MxD10 MODIS snow product relies on the MxD35 cloud mask so the snow detection algorithm could be applied only to clear-sky pixels (Hall *et al.*, 2002; Riggs

et al., 2006). Despite the overall performance of the MxD35 cloud mask product at the global scale (Ackerman *et al.*, 2008) a number of issues have been raised by several researchers about its quality for studies at a local scale and/or specific environments, especially when the discrimination between cloud and snow is important (Stroeve *et al.*, 2006; Lopez *et al.*, 2008; Liang *et al.*, 2008; Luo *et al.*, 2008). In particular, the collection 4 of the MxD35 cloud mask product implemented a series of overly conservative tests that led to frequent misclassifications of snow pixels as clouds (Hall *et al.*, 2002). This issue was addressed in the Collection 4 of the MOD10 algorithm whereby two different layers of snow cover maps were provided:

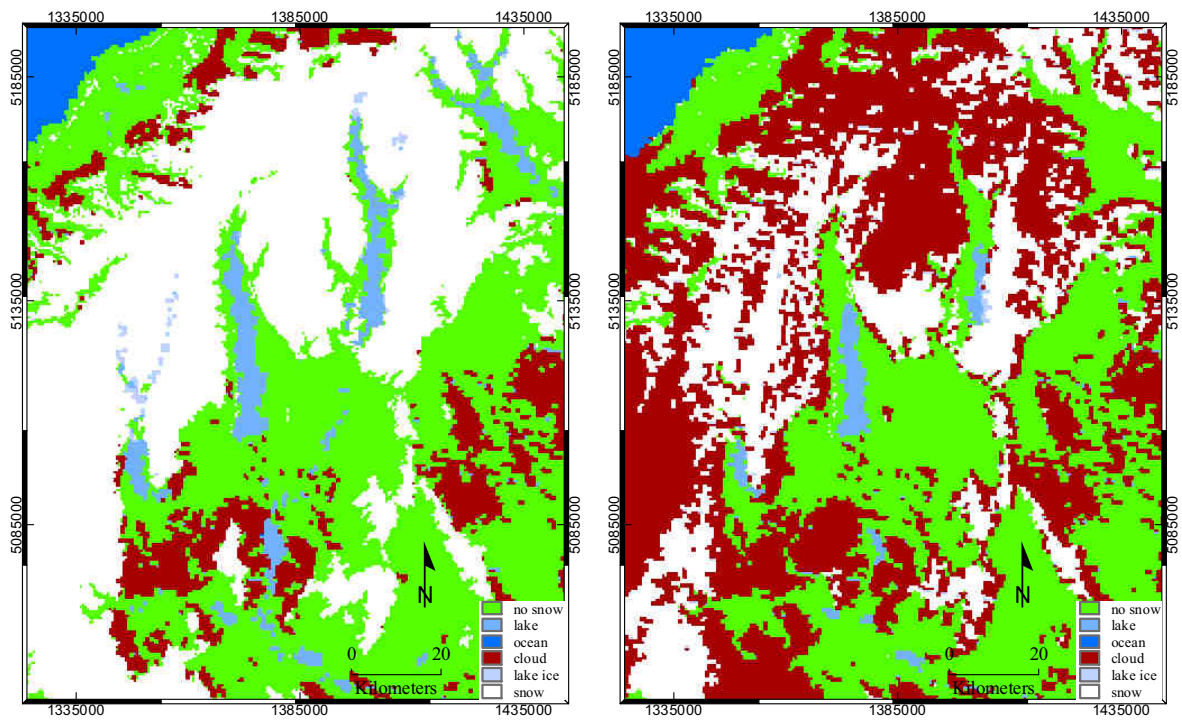
- the *snow cover* layer was processed according to the ‘cloud conservative’ MOD35 cloud product but had obvious, numerous and recurrent misclassifications, often showing snow cover classified as clouds [e.g., Figure 2.12 (b)];
- the *snow cover reduced cloud* layer was processed according to a more liberal cloud mask introduced by Riggs and Hall (2002) that limited omissions errors. This clearly improved the detection of snow in the study area [e.g., Figure 2.12 (c)]. However, this layer was available only in the swath product of version 4 (i.e., MxD10.L2-V4).

The Collection 5 of the MxD10 Snow product now relies on the collection 5 of the MOD35 cloud product and claims large improvements in cloud commission errors (Hall and Riggs, 2007). However, snow and cloud discrimination problems persist (Riggs *et al.*, 2006). A visual investigation of 12 different acquisitions revealed that misclassifications can still be important and frequently occur at the edges of the snowpack [e.g., Figure 2.12 (d, 7 April 2001)]. Riggs *et al.* (2006) suggested that this is related to the cloud spectral visible reflectance test of the MxD35 product that gives a confident outcome that such pixels are cloudy. Misclassifications within the snow cover are also recurrent [e.g., Figure 2.12 (d, 9 September 2000)] although possibly due to invisible cirrus clouds. In the context of monitoring the snow cover over a local and often cloudy area such as New Zealand, such recurrent misclassifications were considered to be too severe to enable the confident use of the MxD10 Snow product. Moreover, the examples shown in Figure 2.12 reveal a number of commission errors on the West Coast whereby a relatively high numbers of pixels are wrongly classified as snow. This may be due to the modification of the binary mapping in forest being inappropriate in this region. It further questions the usability of



(a) False colour RGB composite from MODIS bands 1, 2 and 3

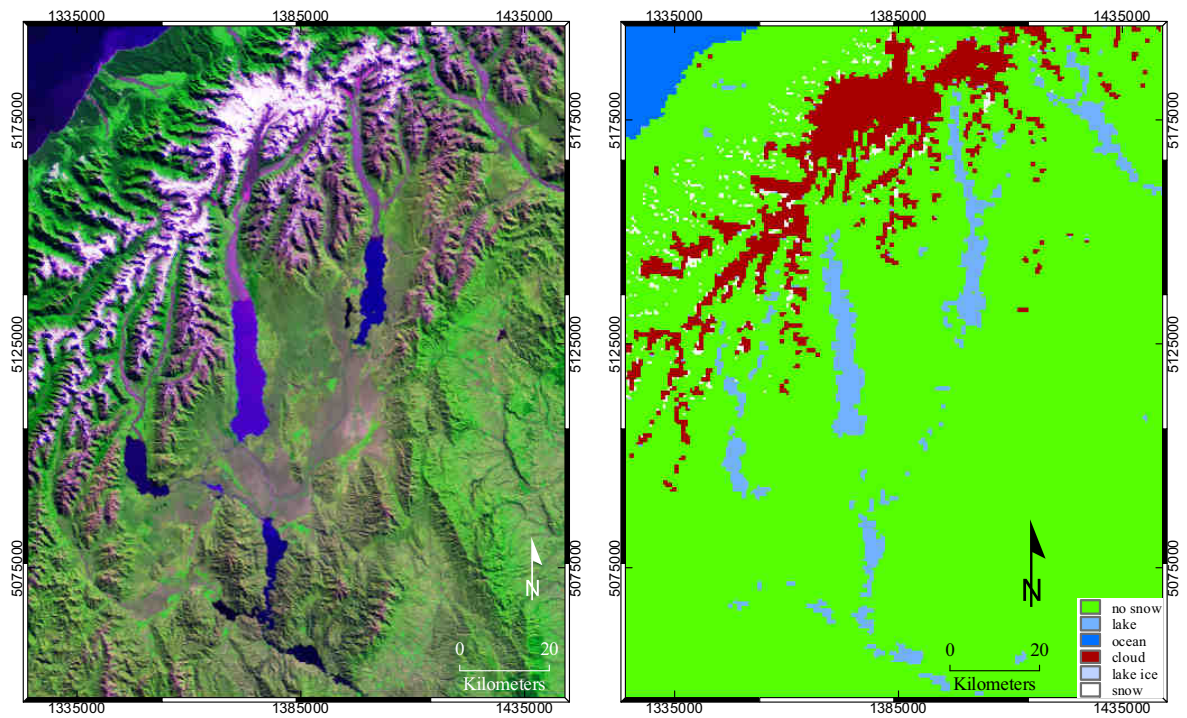
(b) MODIS Collection 4 MOD10.L2 Snow Product (conservative cloud mask)



(c) MODIS Collection 4 MOD10.L2 Snow Product (liberal cloud mask)

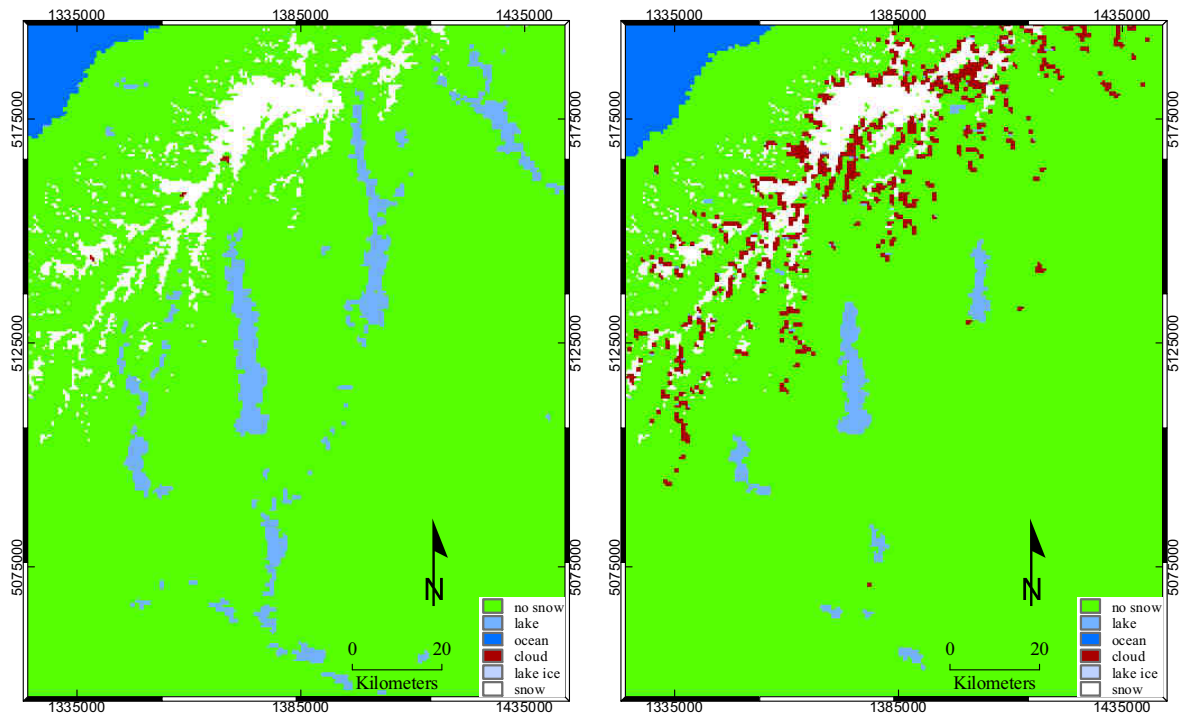
(d) MODIS Collection 5 MOD10.L2 Snow Product (classified)

Figure 2.12 Examples of MOD10 Snow product (9 September 2000, 22:55 GMT).



(a) False colour RGB composite from MODIS bands 1, 2 and 3

(b) MODIS Collection 4 MOD10.L2 Snow Product (conservative cloud mask)



(c) MODIS Collection 4 MOD10.L2 Snow Product (liberal cloud mask)

(d) MODIS Collection 5 MOD10.L2 Snow Product (classified)

Figure 2.12 (continued) MOD10 Snow product (7 April 2001 22:50 GMT).

the MxD10 product for this research and justifies that a more robust methodology is developed in this thesis for the mapping of the snow cover in the Southern Alps.

2.5 Summary

This chapter described the main characteristics of the upper Waitaki basin. In particular, it has highlighted the importance of the three sub-catchments of Lakes Ohau, Pukaki, and Tekapo with regard to their water supply. Most of the water that runs through the cascade of hydroelectric plants originates from these three alpine catchments. Nearly a third of the electricity production of New Zealand originates from this runoff, and thus is of considerable economic and strategic value. Accumulation and melt of the seasonal snow cover has a strong influence on the hydrology in this mountainous region. It appears that the snowpack can temporarily store nearly as much water as what is controllable in the reservoir storage lakes. In consequence, the water stored in the seasonal snow cover corresponds to the generation of about a third of the annual hydroelectric production of the Waitaki.

Despite the importance of the seasonal snow cover in this region, its modelling has received insufficient attention. The simple accumulation-ablation model SnowSim developed by [Fitzharris and Garr \(1995\)](#) and refined on several occasions ([Thompson, 1997](#); [McAlevey, 1998](#); [Kerr, 2005](#)) represents the main attempt to simulate the daily evolution of the snowpack in the region. However, SnowSim does not include any hydrological transformation processes. Therefore, it is not capable of simulating the daily contribution of snow melt to the lake inflow. Its use remains limited to providing estimates of the amount of snow water equivalent stored in the mountains. A limited number of other attempts to model the hydrology of selected sub-catchments in the region have had some success (e.g., [Peters, 1996](#); [Islam, 2001](#); [Lill, 2003](#)) but were not developed further, nor used practically by water managers.

Remote sensing has long proved to be successful for retrieving spatially distributed properties of the snowpack ([Dozier *et al.*, 2009](#)). Optical remote sensing applications in both the reflective and emissive domains has demonstrated its usefulness for estimating snow cover extent, snow grain size, snow albedo, or surface temperature. Passive and active microwave technologies proved their ability to support direct estimates of the snow water equivalent in certain conditions. Thus, remote sensing of snow has been used in many regions of the world to provide forcing and/or reference data to snowmelt models. A typical example of such a model is

the Snowmelt Runoff Model (SRM, [Martinec, 1975](#)) that was used in over 100 catchments ([Martinec et al., 2005](#)). The latter is specifically designed to take advantage of frequent observations of the areal snow extent to estimate the contribution of snowmelt to the catchment discharge.

Despite the desirable ability of remote sensing to operate in remote and poorly accessible regions, its potential to monitor and/or model the seasonal snow cover has barely been considered in New Zealand. Remote sensing of snow is limited to the creation of snow maps derived from the AVHRR sensor that were used to assess the performance of SnowSim at representing the snow cover area, and to monitor the snowline. Nevertheless, the potential of remote sensing technologies to assist with the monitoring and modelling of the snowpack in New Zealand has been identified ([Fitzharris, 1978](#)). Remote sensing was identified as an important domain of future research on seasonal snow and considered to be an important step towards achieving a better understanding of the snow cover dynamics ([Fitzharris et al., 1999](#)). The research undertaken in this thesis aims to address these issues by taking advantage of frequent satellite observations to monitor the dynamics of the seasonal snow cover, and thus improve the modelling of catchment discharge.

In this context, the daily repeat time, multispectral capabilities, and medium spatial resolution of the MODIS sensor make it suitable for supporting the routine mapping of the seasonal snow cover. Despite the availability and general performances of the MODIS MxD10 Snow product at providing daily maps of the snow cover distribution ([Hall et al., 2002](#); [Hall and Riggs, 2007](#)), its use has proved to be complicated in the local environment of the Southern Alps. In particular, it appears that the reliance of the MxD10 Snow product on the MxD35 Clouds product is the source of much confusion between cloudy and snowy pixels and compromises the use of the MxD10 products in the region. Hence, this thesis examines the development of a new automatic processing chain for mapping snow from MODIS L1B swath images adapted to local environments. The objective is to achieve more robust and accurate performance. Time series of snow maps are compared with output from the SnowSim model. They also provide input to the SRM model so as to simulate the discharge from the three very important alpine catchments of New Zealand presented in this chapter.

Chapter 3

Initial processing steps

3.1 Introduction

The previous chapter introduced the study area and identified the importance of the seasonal snow cover to the hydrology of the Waitaki catchment. It also demonstrated the need for considering remote sensing as a practical technology to monitor the dynamics of snow cover in the surrounding mountains. The MODerate Resolution Imaging Spectro-radiometer (MODIS) was identified as a suitable sensor to support the routine mapping of snow. However, it was shown that the MxD10 Snow product has limitations that compromise its use in the study area.

To develop a new method to map snow automatically from MODIS data, several initial steps were needed. These are described in this chapter. First, several aspects of the study required the use of a Digital Elevation Model (DEM) to represent the surface elevation required for the correction of topographic and atmospheric effects of the MODIS images detailed in Chapter 4. A DEM was also required for the orthorectification of terrain distortions in the ASTER images that were used as reference material for assessing the maps of snow distribution as detailed in Chapter 6. Finally, the spatial representation of climatic variables and the modelling of river discharge addressed in Chapter 8 also relies on the knowledge of terrain elevations. Hence, the first section of this chapter is devoted to the creation and assessment of a suitable DEM.

MODIS L1B data are provided in swath format, and thus are not readily usable for cartographic mapping. Thus, the second section of this chapter addresses the gridding of MODIS Level-1B (L1B) data on the projected geographic system of

New Zealand (New Zealand Transverse Mercator 2000, NZTM2000¹). This section outlines the geometric characteristics of MODIS as well as the method used to grid the data and to convert MODIS digital numbers into physical quantities such as radiance, reflectance, or brightness temperature.

The seven land bands of MODIS (i.e., bands 1-7) are not all available at the same spatial resolution. MODIS bands 1 and 2 in the red and near infrared (NIR) have a spatial resolution of 250m, while bands 3-7 are sampled at 500m pixel size at nadir. The third section of the chapter presents a method to merge the high spatial content of bands 1 and 2 into bands 3-7 using image fusion. This approach is new to MODIS data and relies on a multi-resolution decomposition using wavelet transform to extract the spatial information from bands 1 and 2. The fine spatial content is then injected into the lower resolution bands by means of the ARSIS concept (from its French name “Amélioration de la Résolution Spatiale par Injection de Structures” [Ranchin and Wald, 2000](#)). To assess the relevance of the fusion algorithm, the fused images are compared with images obtained from a pure interpolation. Finally, the last section of the chapter describes the detection and masking of clouds from MODIS radiance data.

3.2 Digital elevation model

3.2.1 Source of elevation data and interpolation methods

The principal source of topographic data in New Zealand is the Land Information New Zealand (LINZ) NZTopo database². This supplies a seamless coverage of the 1:50,000 scale topographic mapping of the country in industry standard digital format [Environmental Systems Research Institute (ESRI) shapefile]. The data are projected according to the NZTM 2000 system and comply with the following specifications ([LINZ, 2004b,a](#)):

- Planimetric accuracy (x Easting, y Northing): 90% of well-defined points³ are within $\pm 22\text{m}$;

¹the parameters of this projection are available at <http://www.linz.govt.nz/geodetic/datums-projections-heights/projections/new-zealand-transverse-mercator-2000/index.aspx>, last retrieved on September 25th, 2009.

²See <http://www.linz.govt.nz/topography/topographic-data/index.aspx>, last retrieved on September 22nd, 2009

³A well-defined point can be accurately identified both in the real world and in the digital data.

- Vertical accuracy (z Height): 90% of well-defined points are within $\pm 5\text{m}$; contour lines of 20m equidistance are within $\pm 10\text{m}$ in elevation.

Errors in the position of the data result from:

- errors inherent in the source map data resulting from the map production processes. This includes the cartographic principles of generalisation and displacement;
- errors in the digitising processes used to convert analog data to a digital format.

The topographic data available in the LINZ database for the study area were obtained by a stereo photogrammetric approach using aerial photographs acquired on February 1st, 1986. Topographic features such as contour lines or height points must be interpolated to create the raster image required in subsequent operations. Methods such as Inverse Distance Weighted (IDW) and Kriging were investigated for this purpose, although more specialized approaches of contour interpolators are recommended in the literature (Carrara *et al.*, 1997; Wise, 2000; Carlisle, 2002). For this research, three interpolators were considered for which the data sources are summarized in Table 3.1:

- The VDEMINT algorithm available in the PCI Geomatica software suite¹ can generate a raster DEM by interpolating elevation values of points and contours with additional constraints from 2-D break lines such as cliffs, ridges, and valleys. The algorithm initiates the grid by filling pixels whose elevation is known from the input data. The height of intermediate pixels is computed by a finite difference algorithm, thus enabling a very fast computation.
- ANUDEM v4.6 is a specific topographic interpolator that aims to generate a hydrologically correct DEM by removing spurious sinks in the surface (Hutchinson, 1989). Although it is primarily used with contour lines and height points, ANUDEM has the potential to be constrained by river paths and known sinkholes when such vector layers are available, in order to enforce hydrological correctness. It is supplied as a stand-alone program or in the 3-D Analyst extension of ESRI's ArcGIS 9.x software suite. ANUDEM accommodates data points by means of a 2-D thin plate smoothing spline (see

¹<http://www.pcigeomatics.com/cgi-bin/pci/pcihlp/VDEMINT>, last retrieved on September 22nd, 2009.

Table 3.1 Description of the three interpolation methods tested.

Interpolator	Data used	Comments
ANUDEM 4.6 (ArcGIS v9.x)	contour.cl coastline.cl height.pnt sinkhole.pnt river.cl lake.poly coastline.poly	19 DEMs have been interpolated with various degree of smoothing over a subset area comprising Aoraki/Mt Cook, the lower part of Tasman glacier, and a section of the typical flat and wide valleys (see Figure 3.2). The outputs were subjectively assessed and a roughness penalty of 0.5 along with 40 iterations was retained as a suitable set of parameters to accommodate the sharp changes of slope while minimizing artefacts over relatively flat areas.
VDEMINT (PCI v9.x,v10.x)	contour.cl coastline.cl height.pnt cliff_edge (as cliff 2-D) cutting_edge (as cliff 2-D) rivers.cl (as valley 2-D)	40 iterations were used for the finite difference algorithm, making VDEMINT a very fast method to interpolate DEMs from topographic features.
TIN (ArcGIS v9.x)	contour.cl (as soft lines) coastline.cl (as hard lines) height.pnt (as mass points) cliff_edge (as hard lines) cutting_edge (as hard lines)	The interpolation of a raster DEM from a TIN can be achieved with a linear or a natural neighbour method. Both were tested and the natural neighbour approach was retained as the technique provided less obvious artefacts.

Appendix A for a brief mathematical background about spline interpolation). The regularity of the spline is controlled by a user-defined *roughness penalty* that permits sharp changes occurring between slopes and valley floor to be accommodated, while minimizing interpolation artefacts.

- Finally, the use of a Triangular Irregular Network (TIN) is commonly used to represent a surface by a tessellation of contiguous triangles created from a set of nodes provided by contours and heights points (Li *et al.*, 2005, Chap. 4 & 5). The interpolation of a TIN into a raster format can be achieved by means of linear or natural neighbour techniques (Sibson, 1981).

In addition, a more recent DEM provided by the Shuttle Radar Topography Mission (SRTM) conducted in February 2000 was obtained from the Jet Propulsion Laboratory¹. The SRTM DEM is available with a grid cell resolution of 3 arc-second or about 90m over New Zealand (SRTM3). The SRTM3 heights are provided above mean sea level with respect to the EGM96 ellipsoid. Amos *et al.* (2005) pointed out that, because of its relatively low spatial resolution, the global geoid model EGM96 is not appropriate for local use. Considerable effort has recently been invested in

¹SRTM data are freely available at <http://www2.jpl.nasa.gov/srtm/>, last retrieved on September 22nd, 2009.

New Zealand to develop a new vertical datum based on improved knowledge of the geoid-ellipsoid separation using extensive gravity measurements in the region. It resulted in the creation of the New Zealand Quasigeoid 2005 (NZGeoid05)¹ that models the height above the WGS84/GRS80 ellipsoid (HAE) with better accuracy and more detail than EGM96 (Figure 3.1). In consequence, the SRTM3 elevations above mean sea level were corrected by the addition of the EGM96 grid and subsequent subtraction of the NZgeoid05 grid. The three DEMs interpolated from topographic features (i.e., VDEMINT, ANUDEM, and TIN) were produced at 15m spatial resolution over the study area, while the SRTM3 DEM, originally at 3 arc-second over WGS84, was reprojected over NZTM2000 at 15m spatial sampling using a cubic convolution kernel.

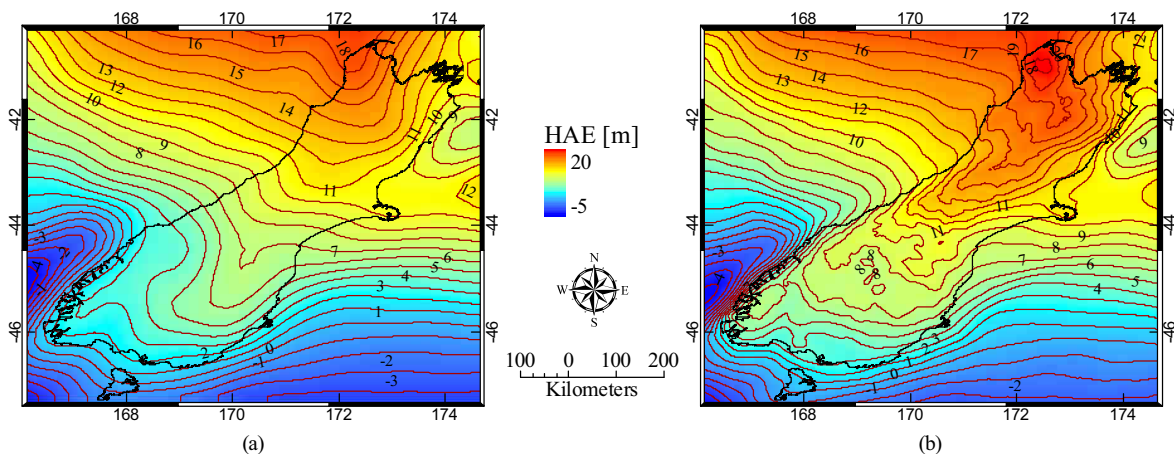


Figure 3.1 Geoid heights above the WGS84/GRS80 ellipsoid (HAE): (a) EGM96 model, (b) NZGeoid05 model.

3.2.2 Accuracy assessment of the DEMs

3.2.2.1 Common statistical measures

Description: The quality of a DEM is a relative concept that is assessed in accordance with its intended use (Wise, 2000). To describe the ability of a model to produce reliable observations Willmott *et al.* (1985) recommended the use of several

¹A grid of NZGeoid05 is freely available at <http://www.linz.govt.nz/geodetic/datums-projections-heights/vertical-datums/new-zealand-geoid-2005/index.aspx>, last retrieved on September 22nd, 2009. Note that as of September 2009, an updated version of the local geoid separation was released and referred to as the NZGeoid09.

measures to allow reliable conclusions about the performance. Given a set of control points (CP) of known elevation, the modelling error $\epsilon_i = P_i - O_i$ between the height P_i predicted by the DEM at the point i and the observed height O_i can be computed. The mean error (μ_ϵ), the mean absolute error (MAE), and the root mean square error (RMSE) often form the core of goodness-of-fit measures and model assessment (Li, 1994; Desmet, 1997; Venteris and Slater, 2005; Li *et al.*, 2005, Chap. 8). The estimator of the mean error is given by

$$\hat{\mu}_\epsilon = \frac{1}{n} \sum_{i=1}^n \epsilon_i, \quad (3.1)$$

where n is the total number of CPs. The MAE provides an overall indication of the average error regardless of whether it is positive or negative. The estimator of the MAE is given by

$$\text{M}\hat{\text{A}}\text{E} = \frac{1}{n} \sum_{i=1}^n |\epsilon_i|. \quad (3.2)$$

The estimator of the RMSE is written as

$$\text{R}\hat{\text{M}}\text{S}\text{E} = \sqrt{\frac{1}{n} \sum_{i=1}^n \epsilon_i^2}. \quad (3.3)$$

μ_ϵ , MAE, and RMSE have the advantage of being dimensioned measures, and thus are easily interpretable in terms of the modelled quantity. Willmott and Matsuura (2005) strongly criticized the RMSE on the basis that it is an ambiguous measure that does not describe the average error alone. Indeed, the RMSE is sensitive simultaneously to the bias and dispersion of errors (Stein, 2002). Clearly, if the error is unbiased (i.e., $\mu_\epsilon = 0$), then the RMSE identifies to the standard deviation of the error σ_ϵ . It can also be shown that the RMSE increases faster than the MAE as the dispersion of the error gets larger. Willmott and Matsuura (2005) estimated that such sensitivity to the dispersion is prejudicial and can lead to false interpretation of the modelling performance. Thus, they considered that only the MAE can assess the modelling performance genuinely and suggested dropping the RMSE from candidate measures.

Here, it is argued that there is no reason to disregard the RMSE and rely solely on the MAE. The dispersion of the error can be of importance when assessing the behaviour of a model. The larger sensitivity of the RMSE to the variability is a desirable attribute in the context of discriminating between two modelling strategies. There are cases when two dispersed datasets can behave identically in terms

of MAE, but can be discriminated by the RMSE because one model may account for more dispersion. [Willmott and Matsuura \(2005\)](#) provided two such datasets, one hypothetical and one real, but failed to recognize the discriminatory power of the RMSE in both cases.

Confidence Intervals: Since the purpose of the assessment seeks to discriminate between several DEMs, it was desirable to provide confidence intervals (CI) for each estimator. Despite the fact that the distribution of ϵ is not necessarily normal, $\hat{\mu}_\epsilon$ is an arithmetic mean. In accordance with the central limit theorem, the latter converges to a normal law of mean μ_ϵ and standard deviation $\frac{\sigma_\epsilon}{\sqrt{n}}$. Given a large number of samples (typically $n > 30$), the confidence interval for $\hat{\mu}_\epsilon$ can be approached using

$$\text{Prob}\left(\hat{\mu}_\epsilon - t_{\alpha/2} \frac{\hat{\sigma}_\epsilon}{\sqrt{n}} \leq \mu_\epsilon \leq \hat{\mu}_\epsilon + t_{\alpha/2} \frac{\hat{\sigma}_\epsilon}{\sqrt{n}}\right) = 1 - \alpha, \quad (3.4)$$

where $\hat{\sigma}_\epsilon^2 = \frac{1}{n-1} \sum_{i=1}^n (\epsilon_i - \hat{\mu}_\epsilon)^2$ is an estimator of the variance of ϵ and $t_{\alpha/2}$ is the critical value obtained from the Student's t distribution with $n - 1$ degrees of freedom for a given significance level α (e.g., $\alpha = 0.05$ corresponding to a 95% CI).

CI for MAE and RMSE are more difficult to address because their distribution is complicated by the use of absolute value and square root functions. [Willmott et al. \(1985\)](#) advocated the use of nonparametric methods such as *bootstrapping* ([Efron, 1979](#)) to estimate the CI for estimators whose distribution is not known or difficult to estimate by parametric approaches. Nevertheless, [Bonett and Seier \(2003\)](#) proposed a parametric method to compute the CI for the Mean Absolute Deviation (MAD) and MAE even under moderate non-normality (see Appendix B). No parametric method was found in the literature for computing the CI for RMSE, hence one is proposed in Appendix B for normally distributed errors. Since the assumption of normality was not always met, the CIs for RMSE were computed using the proposed method at the $\alpha = 0.01$ significance level (i.e., 99% confidence). Comparisons with a bootstrapping approach showed that this higher level of confidence corresponded well to the 95% confidence level under the experimental error distribution.

3.2.2.2 DEM derivatives and contour bias

In the context of assessing DEMs, [Wise \(2000\)](#) argued that standard statistical measures based on a limited sample of CPs such as the RMSE are too crude to assess truly the quality of DEMs, because they fail to indicate gross errors. Qualitative approaches based on the visual investigation of DEM-derived products such as

hill shade, slope, aspect, and curvature are, for instance, recommended due to the sensitivity of the first and second order derivatives to interpolation artefacts (Figure 3.2). In addition, Carrara *et al.* (1997) pointed out that the interpolated height should be uniformly distributed between the elevations of two bounding contours. In other words, when interpolating from 20m contour lines, 20% of the point heights should lie within $\pm 2\text{m}$ of a contour elevation. Carlisle (2002) strengthened this point and showed that some interpolators create DEMs where point elevations tend to be close to those of contour lines used as the primary source for the interpolation. Such artefacts are readily visible by the typical terracing effect in a hill shaded DEM [see Figure 3.2 (a)] and its uneven slope [see Figure 3.2 (g)]. Carlisle (2002) proposed to quantify this effect by means of the *contour bias* criterion that represents the proportion of points that lie within 10% of the height of a contour line.

3.2.2.3 Check points (CPs)

Geodetic survey marks ($n = 301$) and differentially corrected GPS measurement (DGPS, $n = 127$) were available for assessing the accuracy of the DEMs by statistical measures. Geodetic marks usually lay on a concrete block lower than 50 cm from the ground level. Since this order of magnitude is lower than the accuracy of the input data (i.e., contour lines and height points), those marks were not expected to introduce noticeable bias. Geodetic marks included different orders from 3mm up to 0.5m planimetric accuracy and order v1 to v4 with respect to elevation accuracy.¹ Geodetic marks of vertical order v5 were discarded since these station heights are of unknown reliability or doubtful accuracy.

GPS measurements were collected mostly on roads across relatively flat areas with a Leica GS20 receiver, and differentially corrected using the nearest reference station. Points on bridges or embankments were removed since such topographic features were not taken into account by the interpolation. All CPs closer than 30m (i.e., 2 pixels) from a height point used by the interpolation were also ignored to limit potential biases. DGPS surveyed points have a typical planimetric accuracy of 40 cm (1σ) and a vertical accuracy twice larger.

Among the 428 CPs, low and intermediate elevation terrain was over sampled in comparison to high mountains. Therefore, only a subset of 232 CPs was

¹See <http://www.linz.govt.nz/geodetic/datums-projections-heights/heights/normal-ortho-height-orders/index.aspx> for a description of normal orthometric height orders, last retrieved on September 23rd, 2009

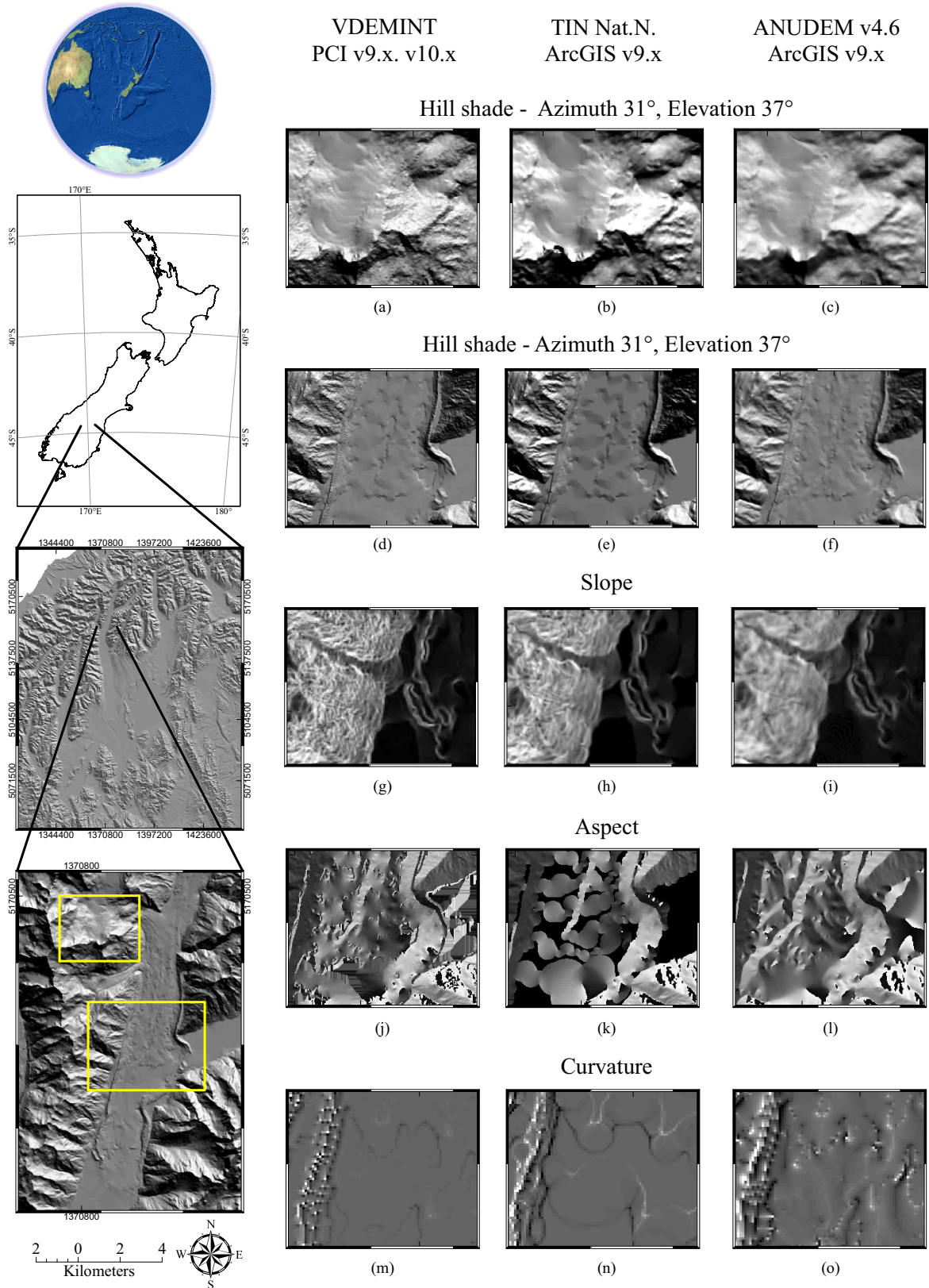


Figure 3.2 Comparison of the three interpolated DEMs with respect to first order (i.e., slope and aspect) and second order (i.e., curvature) derivatives.

retained so that the distribution of heights matched that of the terrain as shown in Figure 3.3 (a). Although such a reduction of the sample size would have the effect to increase the CI on statistics estimates, it was believed to be necessary in order to limit unwanted bias that could be attributed to the sampling strategy. Figure 3.3 (b) illustrates the spatial distribution of the final set of 232 CPs.

3.2.2.4 Quality of the DEMs and choice of a method

An intercontinental assessment of the SRTM was conducted by [Rodriguez *et al.* \(2005\)](#). In New Zealand, where 64,000 CPs were collected along State Highway 1, [Rodriguez *et al.* \(2005\)](#) reported a bias of 1.4m and a standard deviation of 5.9m, with 90% of all the absolute errors being within 10m. This error was found to be the largest of all geographic areas where such a survey was undertaken. [Rodriguez *et al.* \(2005\)](#) suggested that the discrepancy may be due to the rugged nature of the terrain in New Zealand. Based on the set of CPs described above, the distribution of SRTM3 errors was found to be more severe in the study area and appeared negatively biased by $\mu_{\text{SRTM3}} = -9.3\text{m}$. Further analysis revealed that this bias was not systematic and that a medium correlation exists between the SRTM3 error and the elevation with a coefficient of determination R^2 reaching $27\% \pm 10\%$ at the .05 significance level. Despite a slightly negative bias at low elevation, the heights were generally underestimated at higher altitude [Figure 3.4 (a)]. This corresponds to an altitudinal bias of -14 m.km^{-1} that compares well with other assessments of SRTM3 data in mountainous terrain (e.g., [Gerstenecker *et al.*, 2005](#); [Berthier *et al.*, 2006](#)). The standard deviation $\sigma_{\text{SRTM3}} = 14.9\text{m}$ was found to be nearly three times that provided by [Rodriguez *et al.* \(2005\)](#) with outliers as high as 60m away from the true elevation. Finally, this assessment confirmed the negatively skewed distribution of SRTM3 errors as reported by [Gerstenecker *et al.* \(2005\)](#) [see Figure 3.5 (a)].

Unlike the SRTM3, the interpolated DEMs (i.e., VDEMINT, ANUDEM, and TIN) exhibited a more typical bell-shaped distribution [Figure 3.5 (a)], although the hypothesis of normality was rejected at the .05 significance level according to the Kolmogorov-Smirnov test (KS-test). The correlation between error and elevation was weak for the interpolated DEMs with R^2 values less than 10% and a smaller altitudinal bias of -4 m.km^{-1} [Figure 3.4 (b)]. The performance in terms of standard statistical measures (i.e., μ , σ , RMSE, and MAE) outperformed significantly those obtained for the SRTM3 [Figure 3.5 (b)]. However, all interpolated DEMs obtained scores that could not be discriminated at the 95% confidence level on this basis.

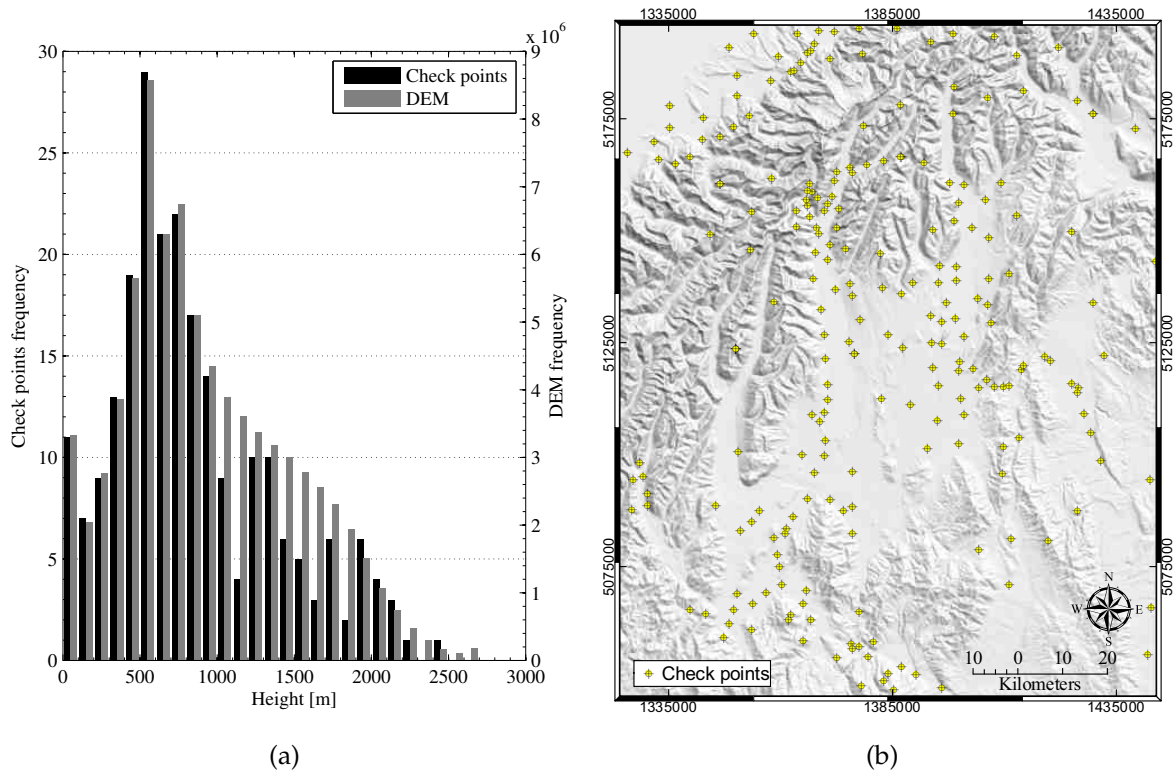


Figure 3.3 (a) Frequency distribution of CPs heights relative to the DEM's heights. (b) Spatial distribution of check points (CPs) over the study area.

Alternatively, Figure 3.2 (a-f) reveals noticeable differences between the three interpolators. For instance, the hill shaded subsets of the interpolated DEMs reveal marked terracing artefacts created by VDEMINT, and to a lesser extent by TIN and ANUDEM. This effect was quantified by a contour bias of 42%, 29%, and 24%, respectively, and is put into perspective with the ideal value of 20% achieved by SRTM3 [Figure 3.5 (b)]. This artefact of VDEMINT is also clearly visible in the slope derivative [Figure 3.2 (g)], whereby the pattern of original contour lines was apparent due to the tendency of the interpolator to flatten the surface near the contours. Comparatively, ANUDEM produced a contour bias corresponding to a more natural terrain due to the smoothing of the thin plate interpolation and its ability to accommodate contours with less rigidity. The better visual output of ANUDEM compared to VDEMINT and TIN is obvious on the debris covered parts of the Tasman glacier shown in Figure 3.2 (d-f). Aspects shown in Figure 3.2 (j-l) also confirmed the presence of substantial interpolation artefacts in VDEMINT and TIN. Horizontal and vertical stripes on flat areas in VDEMINT are caused by the algorithm searching the supporting data only in the cardinal directions to interpolate areas of low point den-

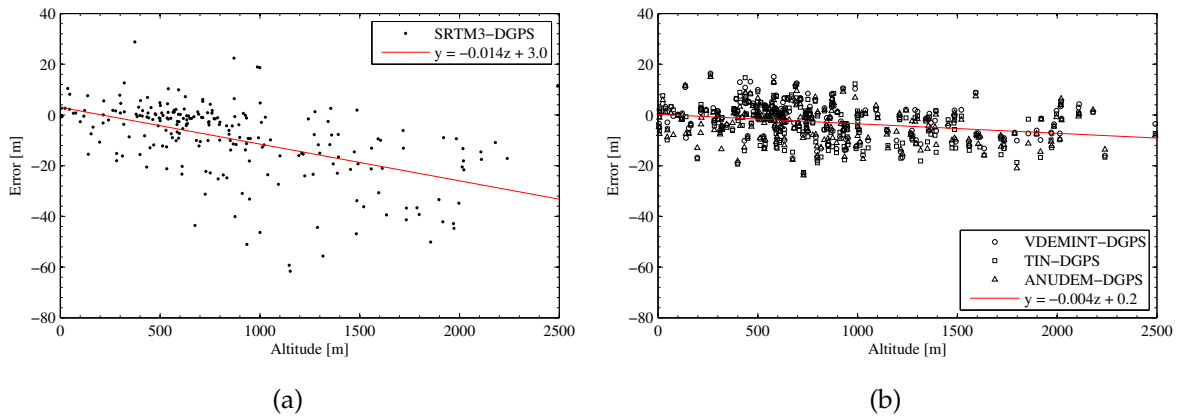


Figure 3.4 Scatter plot of errors *vs.* elevation of (a) SRTM3 revealing the altitudinal bias of SRTM data; (b) the three DEMs interpolated from topographic vector data.

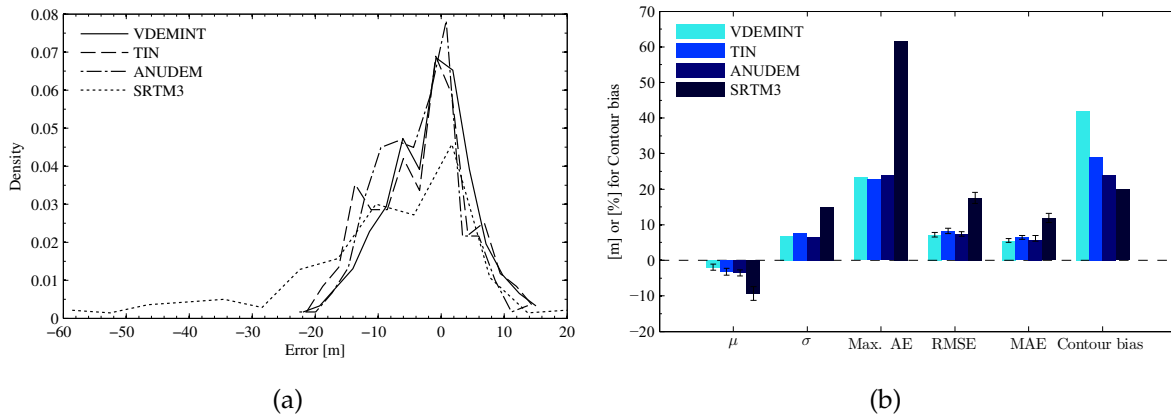


Figure 3.5 (a) Histogram of errors for the four DEMs considered. (b) Comparative results of the statistical measures.

sity. The search radius of the TIN natural neighbour algorithm is also revealed in the map of aspect and it introduces also visible artefacts in the map of curvature.

This comparison demonstrates that the interpolation from topographic data outperformed the SRTM3 DEM regardless of the interpolation technique. Despite its obvious quality, the SRTM3 DEM is tarnished by potentially large errors, significant altitudinal bias, as well as numerous data gaps in rugged terrain that further complicates its use. The SRTM3 DEM outperformed interpolation techniques only with regard to the contour bias. On the other hand, standard statistical measures failed to discriminate between the interpolation techniques. This confirms the need for additional criteria, both qualitative and quantitative towards the assessment of a DEM's quality. The contour bias proved to be very useful at quantifying the ter-

ancing effects of interpolators. In this context, ANUDEM obtained the best scores of all interpolation techniques. Finally, the examination of DEM derivatives proved to be desirable in terms of exposing additional artefacts, for example those related to the interpolation strategy in areas of poor density of points.

In summary, ANUDEM proved to provide a DEM with a competitive accuracy and limited artefacts compared to the two other methods. Given that it also had the advantage of producing a hydrologically correct DEM, it reinforced its relevance for this research. DEMs with various spatial resolutions were produced (i.e., 15m, 125m, 250m, and 500m) for different uses such as the ortho-rectification of the ASTER images, the automated computation of shadows, or the atmospheric and topographic corrections of the MODIS images as explained in the subsequent chapters.

3.3 Projection and geo-location of MODIS data

3.3.1 The MODIS scan geometry

The combination of tangential-scale distortion, panoramic distortion, and the effect of the Earth's surface curvature make the ground coverage of individual MODIS detectors vary across- and along-tracks as the view angle determined by the rotating mirror changes. Thus, the pixels towards the edges of a scan have a footprint increased fourfold in the across-track direction, and twofold in the along-track direction compared to their nominal dimensions at nadir (Toller *et al.*, 2006). This results in the ground projection of individual scans exhibiting a marked "bow-tie" effect with substantial overlaps between scans as the view angle exceeds 25° (see Figure 3.6).

In the MODIS L1B products, the imagery from the 36 spectral bands is provided in the swath format. In other words, this gridded information does not directly correspond to any cartographic projection system. Instead, the lines in the raster images account for the data measured by one detector as its field of view is swept across the terrain by the rotating mirror; the lines are stacked according to the series of scans made along-track to form the granule. Thus, the MODIS L1B products (i.e., MxD02 files) are not readily usable in a cartographic context since they still account for geometric distortions and overlapping pixels.

MODIS L1B image products also include geo-location data provided within the HDF-EOS file. These data document the longitude and latitude coordinates

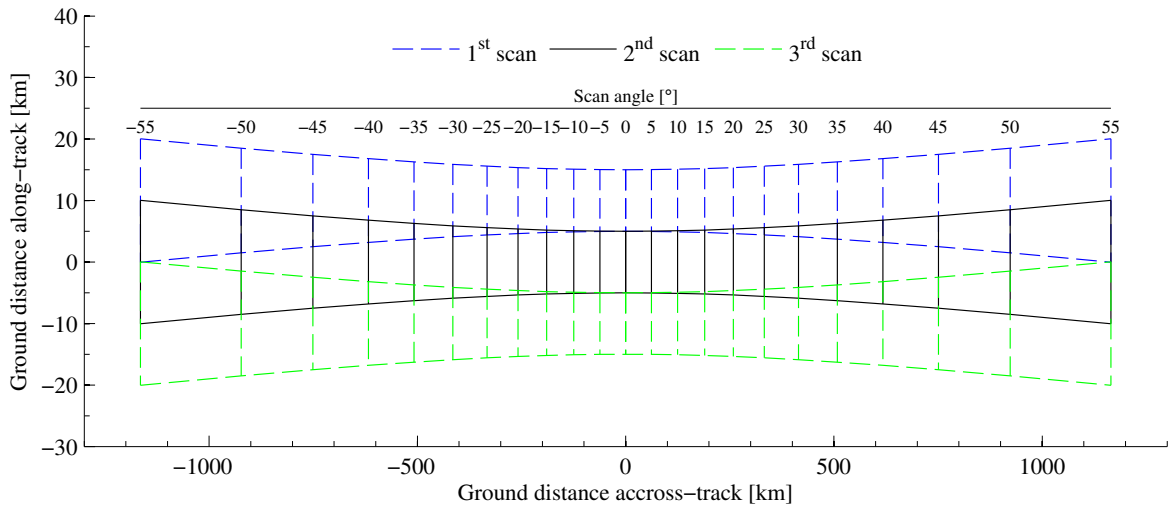


Figure 3.6 Ground projection of three consecutive MODIS scans showing the scan geometry and the panoramic “bow-tie” effect (adapted from Wolfe *et al.*, 2002).

(WGS84) of the centre points of pixels of the corresponding swath images. This information must be used to grid swath images onto a specified cartographic system. Alternatively, a MxD03 companion file exists for each granule that also contains these datasets, as well as the geometry parameters (e.g., solar zenith and azimuth, sensor zenith and azimuth). The geo-location data rely primarily on spacecraft attitude and orbit, and instrument telemetry. They also account for the deterministic “bow-tie” effect, the displacement due to the topography¹, as well as several static error terms attributed mainly to the assembly of the instrument. The geo-location accuracy of swath pixels is known within 47m (1σ) at nadir, and 166m (1σ) at 55° scan angle (Wolfe *et al.*, 2002). Given that the finest MODIS pixels have a footprint of 250m at nadir, this ensures sub-pixel accuracy, as well as sub-pixel band-to-band registration (Barnes *et al.*, 1998). Thus, once projected, the MODIS images do not require further orthorectification.

¹The surface elevation is retrieved from a global DEM at approximately 1km spatial resolution. Although no information was found about the source DEM provided in the MxD03 files, a comparison was done over New Zealand with the GTOPO30 DEM (<http://edc.usgs.gov/products/elevation/gtopo30/gtopo30.html>, last retrieved on August 25, 2009) and the SRTM30 DEM (i.e., the SRTM data gridded at 30 arc-second or about 1km pixel size) from the Shuttle Radar Topography Mission (<http://www2.jpl.nasa.gov/srtm/cbanddataproducts.html>, last retrieved on August 25, 2009). It suggested that the global DEM used for correcting the relief displacement on MODIS pixels and delivered in the MxD03 companion files corresponds to the SRTM30.

3.3.2 Projection of MODIS L1B data

The gridding of MODIS L1B swath products can be achieved by tools such as the MODIS Swath-to-Grid Toolbox¹ (Haran *et al.*, 2001) or the MODIS Swath Reprojection Tool (MRT Swath)² (Land Processes DAAC, 2006b). Recently, Khlopenkov and Trishchenko (2008) also designed a novel algorithm based on a concurrent gradient search for reprojecting MODIS L1B swath data. For the research in this thesis, the latest version of the MRT Swath Tool v2.1 released in January 2006 was used due to its ability to work in a MS WINDOWS[®] environment and because batch processing could readily be interfaced within MATLAB[®] software.

The MRT Swath Tool is primarily used to output GeoTIFF files.³ Khlopenkov and Trishchenko (2008) identified a bias of approximately 150m introduced by the MRT Swath Tool v2.1 when projecting a MODIS channel at 250m spatial resolution. This bias must be put into perspective with the fact that version 2.0 of the MRT Swath Tool incorrectly used GeoTIFF tags, resulting in the output images being shifted by a whole pixel size towards the south-east direction. Thus, an image projected with MRT Swath Tool v2.0 with different pixel sizes resulted in two non co-registered images. Although this inconsistency was supposed to be corrected in version 2.1 of the software (see Land Processes DAAC, 2006a), a shift of half a pixel size in the south-east direction remained.

In order to demonstrate this problem, one MODIS image was successively processed with the MRT Swath Tool v2.1 to output a subset of the same geographical extent at various spatial resolutions. A first subset was output with a 20m pixel size to serve as a master image. If an inconsistent projection was produced, the image would be shifted from its true position by 10m in both the south and east directions. Slave images of the same subset were outputted with increasing spatial resolutions s , so that $s \in \{20(2i + 1) : i \in \mathbb{N}^*\}$. The latter condition ensured that a slave image could be resampled to 20m spatial resolution, and that the expected shift compared to the master image was a multiple of 20 (e.g., an image gridded at 100m was expected to be shifted by 50m from its true position, thus 40m from the master image,

¹The MODIS Swath-to-Grid Toolbox (MS2GT) is available for download on <http://nsidc.org/data/modis/ms2gt/>, last retrieved on August 26, 2009.

²MRT Swath is distributed by the Land Processes Distributed Active Archive Center and is available for download on https://lpdaac.usgs.gov/lpdaac/tools/modis_reprojection_tool_swath, last retrieved on August 26, 2009.

³For more information about GeoTIFF, refer to <http://trac.osgeo.org/geotiff/>, last retrieved on August 26, 2009.

or two 20m pixels). For each slave image, the correlation with the master image was calculated as a function of the shift in both the south and the east directions. The peak of the correlation allowed the the co-registration error to be determined.

Figure 3.7 shows the distances in both the east and south directions corresponding to the maximum correlation between the master and the slave images as a function of the output cell size. It is evident that the MRT Swath Tool v2.1 remains inconsistent in terms of georeferences. The co-registration of the same image depends on the cell size specified for the projection, so that as the pixel size increases, so does the shift towards the south-east. At resolutions lower than 500m, this shift exactly matches the prediction based on the suggested half-pixel mismatch. Some digressions appeared for larger pixel sizes that can be attributed to the inherent uncertainty of the correlation estimate. As a consequence, Figure 3.7 demonstrates the inherent inconsistency of the MRT Swath Tool v2.1 for outputting GeoTIFF images. This error is likely to be due to the improper use of the GeoTIFF tags. This problem was remediated in the present application by automatically adjusting the georeferencing tags of the output image by half a pixel size in both directions within the GeoTIFF file.

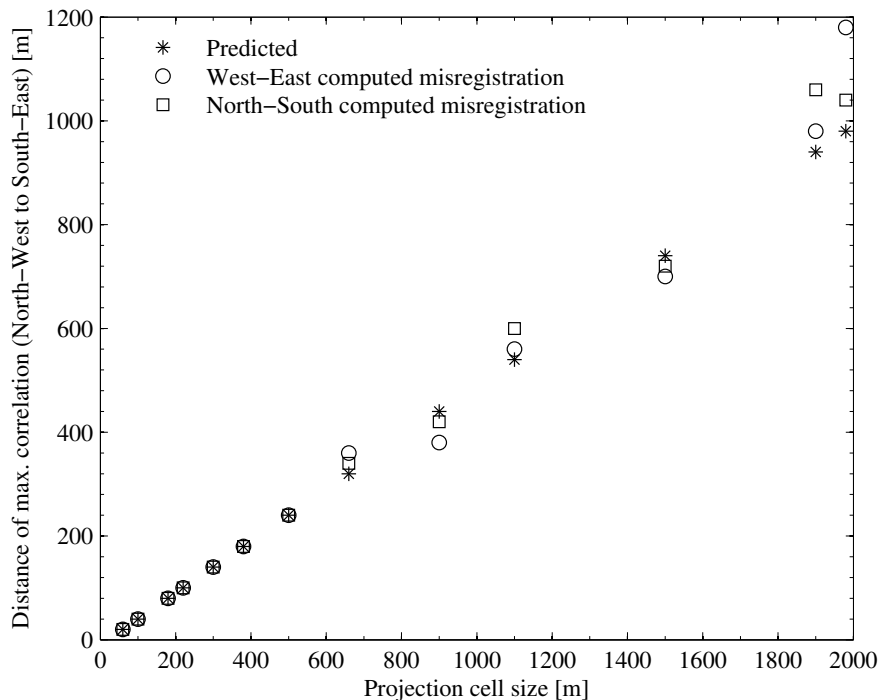


Figure 3.7 Spatial mis-registration of images projected with the MRT software as a function of the requested cell size.

Based on this adjustment, all imagery and geometric parameters (e.g., sun azimuth and elevation angles) were projected using the NZTM2000 projection. A Nearest Neighbour (NN) resampling method was used to preserve the integrity of the data. It also guaranteed that the values of pixels flagged as faulty detectors [i.e., when the most significant bit is set to 1 making the Digital Number (DN) value larger than 32768] were not merged with the radiometric information of the neighbouring pixels. Instead, faulty pixels were screened and replaced with a weighted sum of their linear interpolations from the nearest available points.

3.3.3 Retrieval of physical values

After the projection, all spectral bands were transformed into radiance at the top of the atmosphere L_{TOA} by means of the scale and offset coefficients provided for each image using

$$L_{\text{TOA}} = \text{radiance_scales} \cdot (\mathbf{SI} - \text{radiance_offsets}), \quad (3.5)$$

where \mathbf{SI} represents the scaled integer value in the range 0–32767 (i.e., coded with a radiometric resolution of 15 bits) (Toller *et al.*, 2006, section 5.4.1). For MODIS reflective solar bands, the reflectance at the top of the atmosphere ρ^* , at the centre wavelength λ , was obtained by

$$\rho^*(\lambda) = \frac{\pi d^2 L_{\text{TOA}}(\lambda)}{E_0(\lambda) \cos(\theta_s)}, \quad (3.6)$$

where d is the Earth-Sun distance, E_0 the extraterrestrial solar irradiance, and θ_s the local solar zenith, provided for each image within the corresponding MOD03 data product. In the emissive domain, the brightness temperature was computed by inverting Planck's law for a black body:

$$\text{BT}_\lambda = \frac{hc}{k\lambda \ln\left(\frac{2hc^2}{\lambda^5 L_{\text{TOA}}(\lambda)} + 1\right)}, \quad (3.7)$$

where BT_λ is the brightness temperature [degree Kelvin], k is the Boltzmann constant (1.380658×10^{-23} J.K⁻¹), h is the Planck constant (6.626×10^{-34} J.s), and c is the speed of light in a vacuum ($299,792,458$ m.s⁻¹).

3.4 Multispectral fusion¹

3.4.1 Motivation

In the context of remote sensing, many sensors have been made in the last ten years and provide imagery with various spatial, spectral, and temporal resolutions. The choice of the appropriate instrument(s) for a study is usually governed by trade-offs with respect to these competing characteristics. Clearly, it is desirable to obtain simultaneously a small pixel size to detect fine features, many spectral bands to identify targets reliably, and a frequent repeat time to resolve fast temporal changes. In reality, however, remote sensing technologies face what can be considered as a form of the “Heisenberg uncertainty principle”. In other words, when more precision is sought with respect to one characteristic, it must be achieved at the expense of others.

For example, the MODIS instrument can obtain a nearly daily image of the Earth in 36 spectral bands at the expense of the spatial resolution being relatively coarse. Among the seven MODIS land bands, bands 1 and 2 (i.e., red and NIR centred on 645 nm and 858 nm, respectively) are collected with a nominal spatial sampling of 250m at nadir, while bands 3 to 7 have a 500m pixel size. ASTER can image the Earth at 15, 30, and 90m in the visible, SWIR, and thermal infrared, respectively. But such a spatial resolution is obtained at the expense of a 16-day repeat time. Sensors such as QuickBird, or recently GeoEye-1, acquire images with unprecedented spatial resolution, but with less spectral bands and for a limited geographical extent. The causes for such tradeoffs are multiple, ranging from the sensitivity of detectors that operate in spectral domain with low energy fluxes, to the inherent limitation of the bandwidth available to download data, as well as that associated with the computing power required to manage and process images.

The near daily global coverage and multispectral capability of MODIS makes it a powerful tool for the operational monitoring of the snow cover extent and properties. However, as explained in Section 2.4.1.2, the Normalized Difference Snow Index (NDSI) remains the prime indicator of the presence of snow, by taking advantage of its spectral contrast between the green and the short wave infrared parts of the spectrum (Crane and Anderson, 1984; Dozier, 1989; Hall *et al.*, 2002). Thus, it

¹The content of this section is partially published in: Sirguey, P., Mathieu, R. and Arnaud, Y. (2008). Improving MODIS spatial resolution for snow mapping using wavelet fusion and ARSIS concept. *IEEE Geoscience and Remote Sensing Letters*, 5(1), 78–82, doi:10.1109/LGRS.2007.908884.

relies on MODIS bands 4 and 6 (centred at 555 and 1640 nm, respectively) and constrains the mapping of the snow cover at a spatial resolution of 500m. However, the resolution does not satisfy the recommendation of 100m established by the Global Climate Observing System (GCOS) with regard to the scale of satellite observations of snow areal extent (GCOS, 2006, pg. 46). Clearly, such a relatively coarse pixel size also complicates the accurate mapping of the snow cover when slopes become steep. In the context of the Southern Alps of New Zealand, this is readily illustrated in Figure 3.8 that depicts the footprints of MODIS MOD10 pixels, compared to the simultaneous ASTER image draped over the DEM in the upper Pukaki region. It demonstrates that 500m resolution pixels potentially fail to resolve the snow cover in this environment, and may introduce large uncertainties with regard to the position and elevation of the snowline.

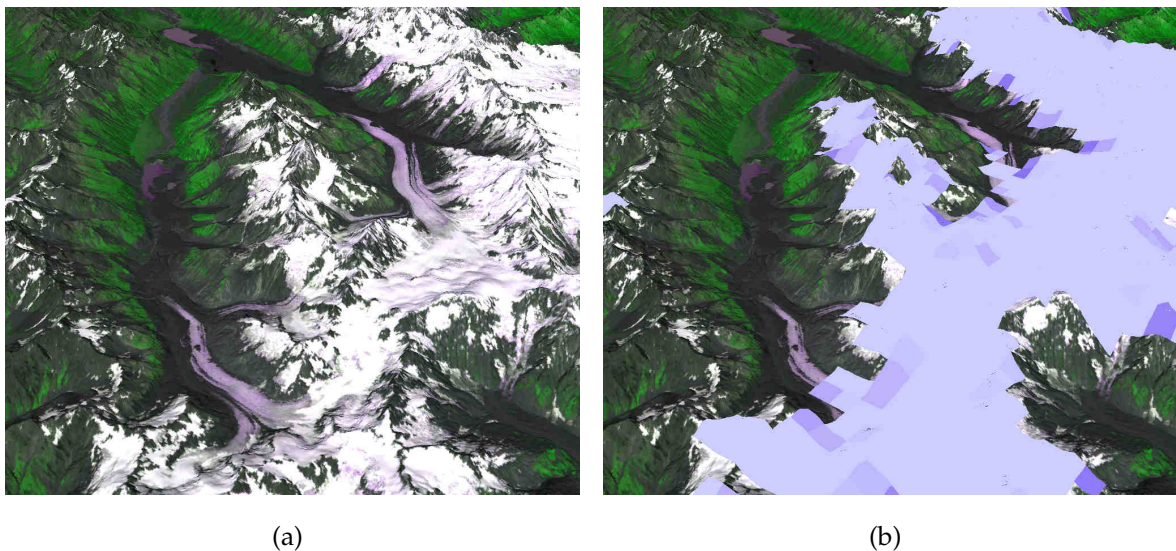


Figure 3.8 (a) ASTER image of the upper Pukaki basin (29 January 2002, 22:35 GMT) draped over the DEM (looking south, note from left to right Murchison and Tasman glaciers). (b) The MOD10 snow product of the corresponding MODIS acquisition illustrating the footprint of 500m pixels and its limited resolution in very rugged terrain.

It is evident that obtaining the highest possible amount of spatial detail is desirable, especially when dealing with such a rugged terrain. The potential of taking advantage of the two MODIS spectral bands at 250m spatial resolution has not yet been explored by many researchers. In their early work Hall *et al.* (1995) simply suggested that these bands could be used to produce more detailed maps of snow cover. Recently, Luo *et al.* (2008) developed a method to produce all MODIS land

bands at 250m by means of a regression and normalization approach between the radiometric information supported by MODIS bands 3-7 with respect to that from bands 1-2. Such a technique belongs to the domain of research referred to as *image fusion*. It involves merging images from different sources, which hold information of a different nature, to create a synthesized image that retains the most desirable characteristics of each input (Pohl and Genderen, 1998; Wald, 2002; Zhang, 2004; Amolins *et al.*, 2007).

Image fusion has proved to be efficient at merging bands from separate sensors (Chavez *et al.*, 1991; Li *et al.*, 2002). Alternatively, many optical sensors (e.g., Landsat, SPOT, Ikonos, QuickBird) routinely acquire one panchromatic image (PAN), covering a wide part of the electromagnetic spectrum, simultaneously with one multispectral image (MS) that accounts for several bands (Figure 3.9). By collecting energy over a wider spectral range, PAN detectors are exposed to a larger radiative flux (in $W.m^{-2}$) than those of individual multispectral channels. Thus, all other things being equal, an acceptable signal-to-noise ratio can still be met based on a smaller spatial sampling. The ability to identify finer features is thus considerably improved by the gain in spatial resolution, at the expense of the spectral resolution.¹ Image processing techniques known as *multispectral image fusion* or *pan sharpening* have been developed specifically to merge the rich spatial content of a high spatial resolution image (i.e., PAN band) with the rich spectral content of a low spatial resolution image (i.e., MS bands) (Garguet-Duport *et al.*, 1996; Ranchin *et al.*, 2003; González-Audicana *et al.*, 2004; Tu *et al.*, 2004; Garzelli and Nencini, 2006; Zhang and Kang, 2006). Today, such methods are routinely applied by some image suppliers who provide pan-sharpened multispectral images as upper level products. These images are becoming increasingly popular in various field due to their ability to improve the detection and extraction of ground targets (Robinson *et al.*, 2000; Nichol and Wong, 2005; Lasaponara and Masini, 2005; Malpica, 2007), or the spatial resolution of post-classified products (Gross and Schott, 1998; Pasqualini *et al.*, 2005; Jin and Davis, 2005).

MODIS does not use PAN bands, therefore, existing techniques of pan-sharpening cannot be readily implemented and an appropriate method of image

¹For instance, SPOT 5 holds a PAN channel at 5m spatial sampling versus five MS bands being provided at 10m in the visible to NIR wavelength, and 20m in the SWIR domain. Alternatively, the PAN channel of Ikonos and Quickbird has a spatial resolution that is fourfold finer than that of the MS bands.

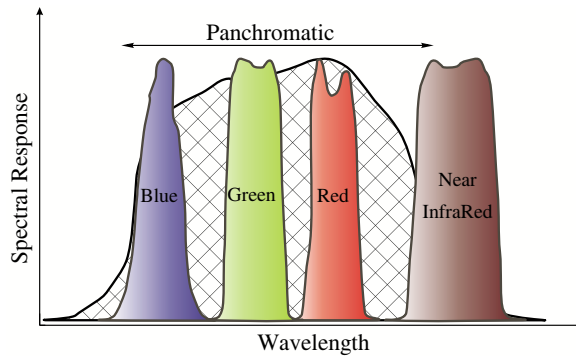


Figure 3.9 Example of spectral coverage of multispectral and panchromatic channels in modern sensors (e.g., IKONOS, QuickBird).

fusion remains to be designed and assessed. However, working with L1B data towards the design of a customized classification technique of snow with MODIS provides a unique opportunity to investigate the potential of image fusion to enable the determination of snow at 250m. In addition, the proposed method can provide an objective improvement compared to the mapping of snow at 500m. This section reports on the design of a fusion technique to increase the spatial resolution of MODIS Land bands 3-7. A first assessment of the fusion performance, both qualitatively (i.e., visual assessment) and quantitatively (i.e., metrics such as RMSE between reference images and fused images) is provided. However, the performance of the method was assessed more thoroughly as part of the evaluation of the snow classification algorithm (see Chapter 5), by investigating the differences of accuracies of snow maps obtained on the basis of fused and non-fused bands.

3.4.2 Principle and methods

When dealing with remotely sensed imagery, fusion methods usually aim to merge the rich spatial content of a high resolution image (HR) with the rich spectral content of a low spatial resolution image (LR), as illustrated in Figure 3.10 (e.g., typically, the HR and the LR are respectively the PAN and MS channels for sensors such as Landsat, Ikonos or Quickbird). As noted above, image fusion is a relatively new and active domain of research with instruments that specifically implement PAN bands to enable post-processing of MS image fusion (Alparone *et al.*, 2007). Several methods have been designed, falling within two main categories known as *substitution* and *multi resolution* techniques (an extensive discussion about the principle and methods of image fusion can be found in Wald, 2002).

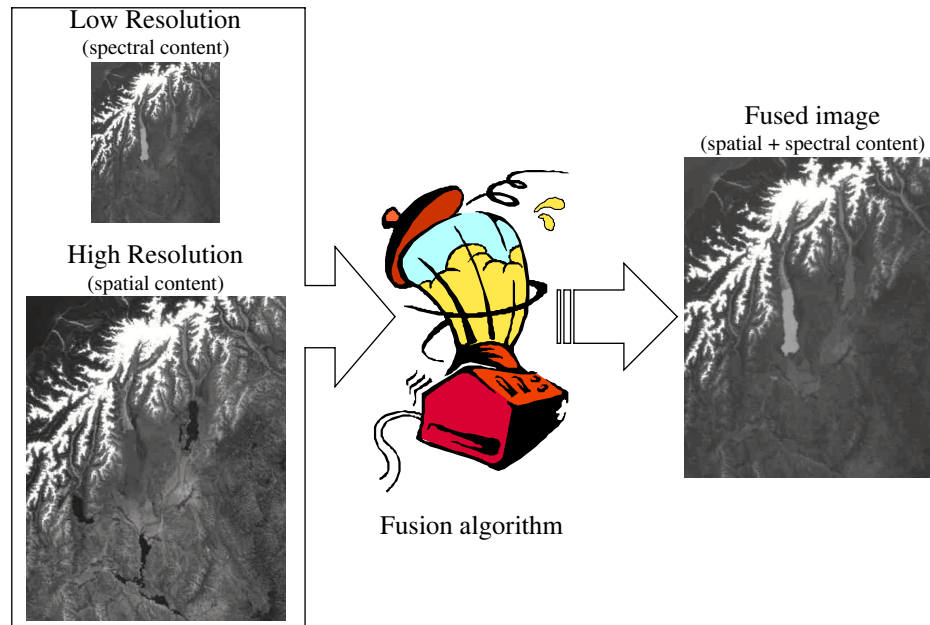


Figure 3.10 Concept of image fusion.

3.4.2.1 Substitution methods

Substitution involves the transformation of a three band composite (RGB) into another colour space using methods such as Intensity Hue Saturation (IHS) or principal components by means of a Principal Component Analysis (PCA). In the new colour space, the intensity image (I) or the first principal component (PC1), respectively, holds intensity information. The HR band (e.g., PAN channel) is then used as a substitute for I or PC1, while the inverse transformation allows merging the finer spatial information and creating the pan-sharpened spectral bands (Figure 3.11).

Such transformations are based on the proposition that a spectral equivalent of the HR bands can be formed by a linear combination of the MS bands provided by the colour space transformation. However, it is rare that the spectral response of the PAN channel overlaps that of contiguous spectral bands (see a typical configuration of MS and PAN spectral response in Figure 3.9). Nevertheless, these methods remain adequate when the HR band remains well correlated with I or PC1 (González-Audicana *et al.*, 2004). Digressions in the spectral domain may otherwise result in noticeable radiometric distortions (Tu *et al.*, 2004). In addition, it is often required that the histograms of the HR band and the Intensity or PC1 be matched to mitigate such distortions. For some sensors, specific models have been designed to optimize the weighting of each spectral band in the colour space transformation, to create a

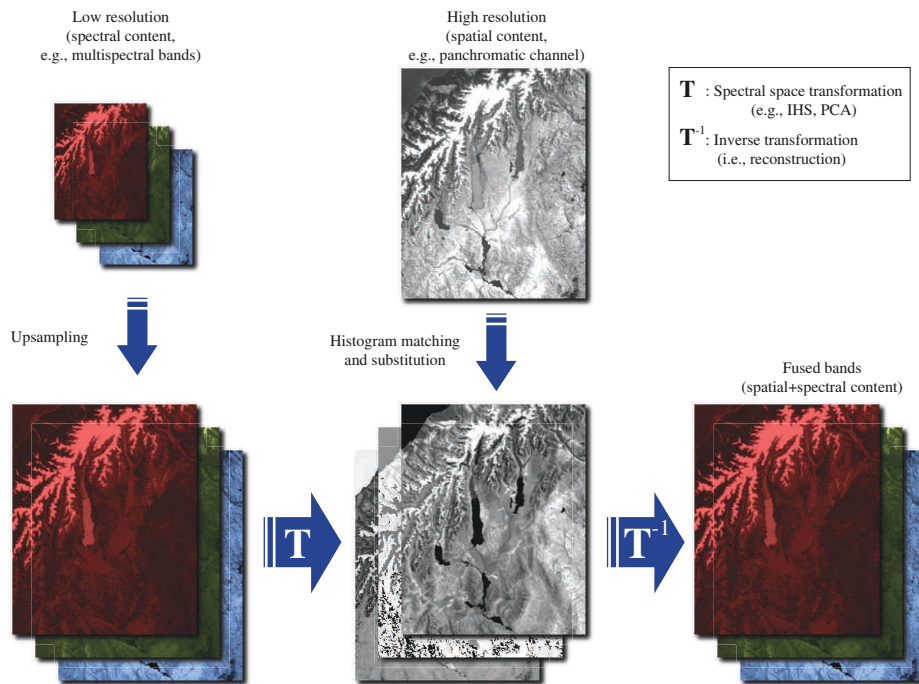


Figure 3.11 Principle of fusion by band substitution method.

synthetic band that spectrally approaches the PAN channels as closely as possible. This enables the computation of a substitution with little radiometric distortion (Tu *et al.*, 2004; González-Audicana *et al.*, 2006; Malpica, 2007).

MODIS only holds MS bands, among which the HR bands (i.e., MODIS land bands 1 or 2) cannot truly play the part of a PAN channel. The correlation between bands is generally high and significant in the visible wavelength, but is generally limited, or not significant, in the SWIR domain (Figure 3.12). Therefore, it is believed that the signal supported by the HR bands is too small with regard to the SWIR bands to permit a traditional colour space substitution method. Alternatively, Trishchenko *et al.* (2006) attempted a more sophisticated approach of spectral transformation, in which MODIS bands 3 to 7 were expressed as a function of bands 1 and 2, and a quadratic function of the NDVI. A non-linear regression model was established on the basis of aggregated HR bands 1 and 2 for different types of land cover. The resulting coefficients were then applied to the original HR bands to form the fused bands 3-7. Although this approach can perform well in the visible bands 3 and 4 due to the generally good correlation with bands 1 and 2, it was found that large radiometric distortions can still be created with regard to the fused bands 5-7 in the SWIR domain.

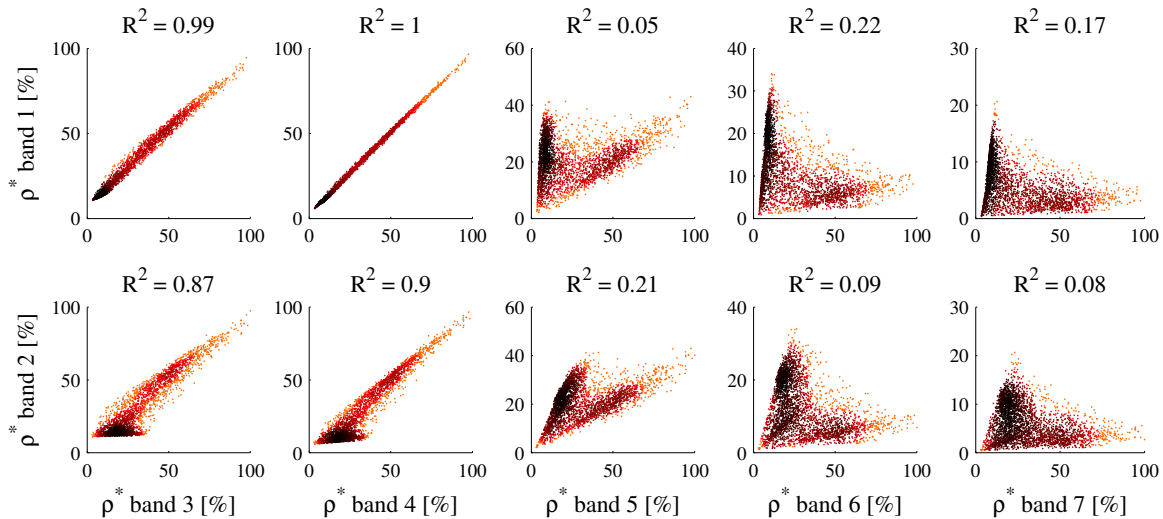


Figure 3.12 Correlations between the reflectance in MODIS Low Resolution bands 3-7 and the reflectance in the High Resolution bands 1-2 for a scene acquired on May, 16th 2006. The colour indicates the point density. Note the good correlation in the visible bands and large scatters in the SWIR domain.

3.4.2.2 Multi-resolution methods

Multi-resolution methods have been designed to resolve this problem. They aim at extracting the spatial detail contained in the HR band, and subsequently “inject” this detail into the LR image. The extraction of spatial information refers to the analysis of the spatial frequency within the image. This can be achieved by different methods such as High Pass Filtering (HPF, [Chavez *et al.*, 1991](#)), Laplacian Pyramid (LP, [Aiazzi *et al.*, 1999](#)), Wavelet Transform (WT, [Ranchin and Wald, 1993](#); [Garguet-Duport *et al.*, 1996](#); [Amolins *et al.*, 2007](#)), and more recently a curvelet transform ([Nencini *et al.*, 2007](#)). Processing the HR band with such a filtering technique (known as the multi-resolution decomposition scheme) permits additional spatial content to be obtained that can be used along with the LR band to reconstruct a fused image. Such methods have the advantage of permitting band-to-band fusion as opposed to traditional transformation of the colour space that requires a multi-band’s feature space to be processed.

3.4.2.3 A brief description of 2-D wavelet transform

In this thesis, an approach based on wavelet transform was adopted as the multi-resolution decomposition scheme ([Ranchin *et al.*, 2003](#)). Wavelet analysis arose from signal processing theory as an alternative to the Fourier transform to

analyse frequency content in non-stationary signals (Mallat, 1989a; Daubechies, 1990, 1992). It was generalized to two-dimensional signals such as remotely sensed images (Mallat, 1989b), whereby a band is decomposed into a low frequency approximation that describes the trend (i.e., the radiometry), and a series of zero-mean coefficients that account for the high frequency information in the vertical, horizontal, and diagonal directions. In the wavelet-based fusion schemes, the spatial details are represented by the wavelet coefficient (Figure 3.13), and incorporated into the LR image using the inverse wavelet transform acting as a reconstruction method. In addition to the efficiency of wavelet methods to extract spatial detail, merging zero-mean wavelet coefficients during the reconstruction has the advantage of preserving the radiometry of the original image and avoiding the large radiometric bias that can occur with substitution techniques (Li *et al.*, 2002).

It is beyond the scope of this thesis to describe in detail the wavelet decomposition algorithm, for which excellent reviews can be found in Mallat (1989b), Daubechies (1992), Shensa (1992), or Amolins *et al.* (2007). However, it is worth mentioning that two main algorithms exist for processing 2-D wavelet transforms, namely continuous and discrete, which are abbreviated by CWT and DWT, respectively. The predilection for computers to process binary or discrete instructions generally enforces the use of DWT. The latter can be processed on images using a decimated algorithm (Mallat, 1989b), that acts as a bank of convolving wavelet filters applied to the rows and columns of the original image. Despite its computational efficiency, the decimated DWT has the drawback of implementing a subsampling (i.e., decimation) of the wavelet coefficients, causing the coefficients to be translated in space. The undecimated “à trous” algorithm [also known as the stationary wavelet transform (Shensa, 1992)] was designed to overcome this issue and makes the wavelet transform translation invariant. It modifies the decimated DWT decomposition algorithm by up-sampling the signal before entering the convolution filters, in order to retain the same sample size at each level of the decomposition. This up-sampling is done by including zeros between samples, thus justifying its French name “à trous”.¹

The undecimated “à trous” wavelet transform algorithm, combined with Daubechies D12 wavelets, was used as the multi-resolution decomposition approach. In order to avoid the possible impact of the up-sampling operator, which aims to match the size of the LR and HR images, the LR bands to be fused (i.e.,

¹English: “with holes”.

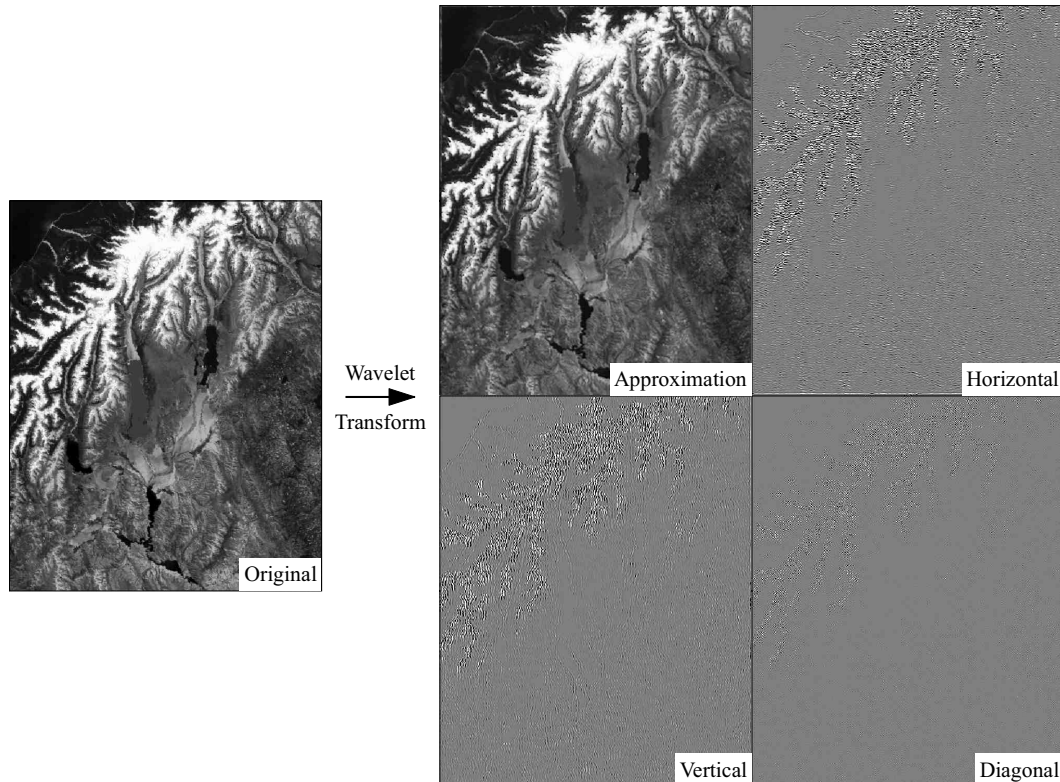


Figure 3.13 Single level 2-D wavelet decomposition illustrating the approximation and coefficients of detail.

MODIS bands 3-7) were projected from the MODIS L1B swath product at 250m pixel size. A preliminary wavelet decomposition of these images (gridded at 250m) provided an approximation that still accounted for the genuine spatial content of the original LR band. However, this approximation had the advantage of retaining the size and the co-registration of the wavelet coefficients obtained from the decomposition of the HR band.

3.4.3 The ARSIS concept

3.4.3.1 Implementation

Developed by [Ranchin and Wald \(2000\)](#), the ARSIS model (from its French name “Amélioration de la Résolution Spatiale par Injection de Structures”) is a multi-resolution concept of image fusion. The first decomposition of the HR image produced coefficients of spatial detail C at a scale that is not resolved in the LR image (Figure 3.14). In its simplest form, ARSIS can be applied by injecting unchanged coefficients, which represent the fine spatial structures, into the LR image

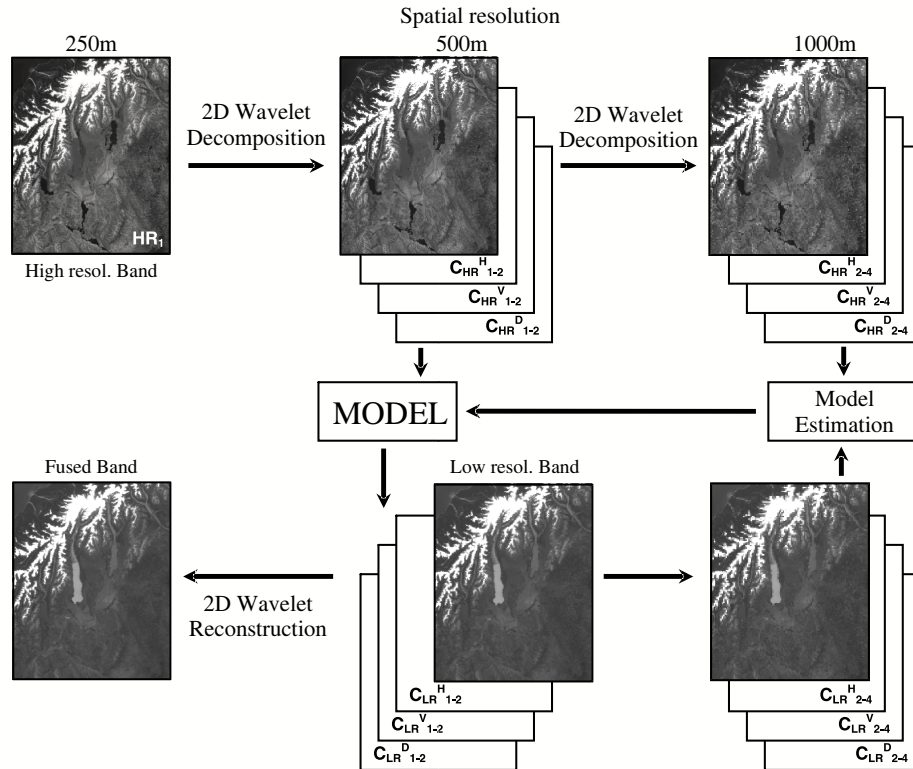


Figure 3.14 ARSIS concept as implemented in the case of MODIS using the undecimated wavelet transform, adapted from Ranchin and Wald (2000)

by means of an inverse wavelet transform. It is referred as the M1 identity model, whereby

$$C_{LR1-2}^Z = C_{HR1-2}^Z, \quad (3.8)$$

with $Z = H, V, \text{ or } D$ accounting for the type of coefficient, namely Horizontal, Vertical, or Diagonal, respectively. However, such a direct injection is not always suitable because it ignores the spectral differences in high-frequency information between the HR and the LR images (Ranchin and Wald, 2000). In order to improve the quality of the synthesized image, it is therefore desirable to model the coefficients to approach those that would have been obtained if the band to fuse was available at high resolution. Specifically, this involves a second level of 2-D wavelet decomposition permitting the ready comparison of the wavelet coefficients from both images. The model M2, proposed by Mangolini *et al.* (1992), aims at adjusting the variance and mean of the wavelet coefficients to be injected at the first level of decomposition, according to image-dependent factors derived from the second level of decomposi-

tion as follows:

$$\begin{aligned}
 C_{LR1-2}^Z &= a^Z C_{HR1-2}^Z + b^Z \\
 a^Z &= \sigma^Z(LR) / \sigma^Z(HR) \\
 b^Z &= \mu^Z(LR) - a^Z \mu^Z(HR),
 \end{aligned} \tag{3.9}$$

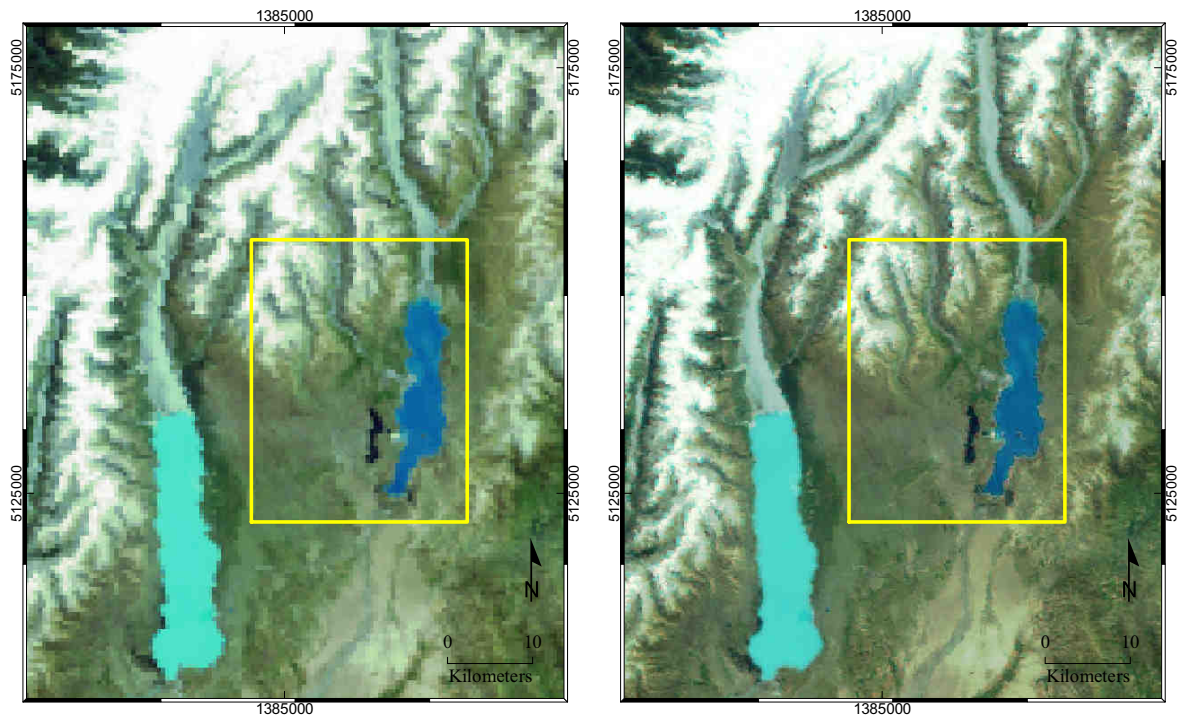
where $\mu^Z(LR)$ and $\sigma^Z(LR)$ are the mean and the standard deviation of C_{LR2-4}^Z , respectively. Clearly, the M2 model corresponds to stretching the histogram of the HR wavelet coefficients to match those of the LR image.

Since MODIS disposes of two HR bands and five LR bands, spread over the reflective part of the spectrum, it was decided to use the HR band that is spectrally the closest to the LR band to be fused. Consequently, spatial details of band 1 were merged into bands 3 and 4, while the spatial details of band 2 were merged into bands 5, 6, and 7. This choice remains subjective and disputable and no sensitivity analyses were yet carried out to assess whether an alternate use of bands might produce better results.

3.4.3.2 Assessing the quality of the fused images

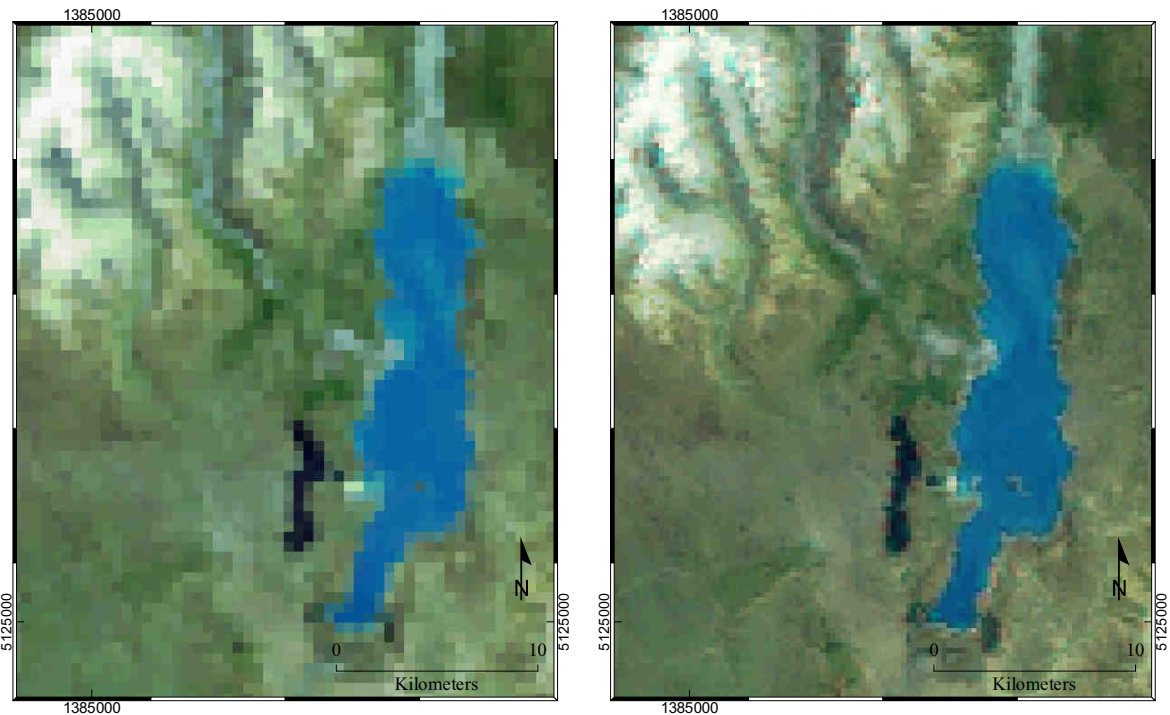
Image fusion algorithms often create radiometric distortions and/or artefacts in the fused spectral bands (Wald *et al.*, 1997; Du *et al.*, 2003; Tu *et al.*, 2004; González-Audicana *et al.*, 2006) that may have an impact on the quality of higher resolution products. Therefore, the quality of the fusion process must be investigated thoroughly, in order to assess its performance and robustness, as well as the relevance of the fused product. The assessment of the quality of the fusion process usually relies on the investigation of both subjective and objective approaches (Aiazzi *et al.*, 1999; Shi *et al.*, 2005; Laporterie-Déjean *et al.*, 2005; Alparone *et al.*, 2007; Petrovic, 2007).

Qualitative analysis: Subjective methods are based on a visual analysis of the fused image (i.e., a three-band composite of a selection of spectral bands). They aim to provide a judgment (e.g., an opinion score) on the quality of the fusion according to a set of criteria, defined with regard to the needs of the users (Petrovic, 2007; Laporterie-Déjean *et al.*, 2005). An example of a fused image is shown in Figure 3.15. The true colour RGB composite at 500m spatial resolution formed by bands 1 (degraded), 4, and 3 (originals), and compared with its equivalent formed by the 250m resolution bands 1 (original), 4, and 3 (obtained from the fusion algorithm).



(a) Without fusion

(b) With fusion



(c) Subset without fusion

(d) Subset with fusion

Figure 3.15 Example of multispectral fusion (12 December 2002, 22:35 GMT). (Left column) RGB composite with MODIS bands 1, 4, and 3 at 500m spatial resolution (i.e., without fusion); (right column) the same composite with bands 3 and 4 at 250m spatial resolution obtained by fusion with band 1, originally at 250m spatial resolution.

Despite the finer spatial information genuinely provided by band 1, it is evident from this example that spatial details are better resolved in the fused image. The improvement provided by the fusion algorithm is further demonstrated by comparing the fused image with that obtained from a pure interpolation. Figure 3.16 shows RGB composites formed by MODIS bands 5, 6, and 3, all originally acquired at 500m spatial resolution and upsampled at 250m using (a) the fusion algorithm and (b) a cubic convolution interpolator (CC). The CC tends to blur the image as no additional spatial content is added. It contrasts with the image obtained from the fused bands that exhibits sharper patterns and a more desirable visual product.

Quantitative analysis: Visual analysis is a powerful means to assess improvement resulting from a fusion exercise because of the human ability to evaluate the increase in spatial detail as the resolution of the image increases. However, it is not appropriate to account accurately for the preservation of the radiometry in the fused image. In addition, since it involves subjective human visual perception, such qualitative assessment is inevitably biased by the observer's experience and appreciation (Toet and Franken, 2003; Chen and Varshney, 2007) and lacks consistency and scientific rigor.

Therefore, numerous researchers have designed and assessed metrics to quantify objectively the quality of fused images (Wald *et al.*, 1997; Ranchin and Wald, 2000; Xydeas and Petrovic, 2000; Wald, 2002; Wang and Bovik, 2002; Alparone *et al.*, 2004). The metrics are usually based on and/or derived from standard descriptive statistics computed on a per pixel basis. They aim to measure the discrepancy between the fused image and a reference image to quantify both the gain of information generated by an increase of spatial resolution and its spectral integrity with regard to the original radiometry. The reference image must be the same spatial resolution as the fused products. Since obviously no reference image is available at this resolution (otherwise the fusion exercise would not be necessary), a popular protocol is to assess the method at a coarser resolution (Wald *et al.*, 1997; Wald, 2002, Chap. 8). The HR images are degraded relative to their original resolution so that the pixel size of the degraded HR matches that of the original LR. The fusion process is computed with the degraded HR images. The original LR can then be used as the reference in the process of accuracy assessment. If the latter is satisfying, the method is assumed to perform similarly at the finer scale.

A sample of ten scenes was randomly selected for applying the above men-

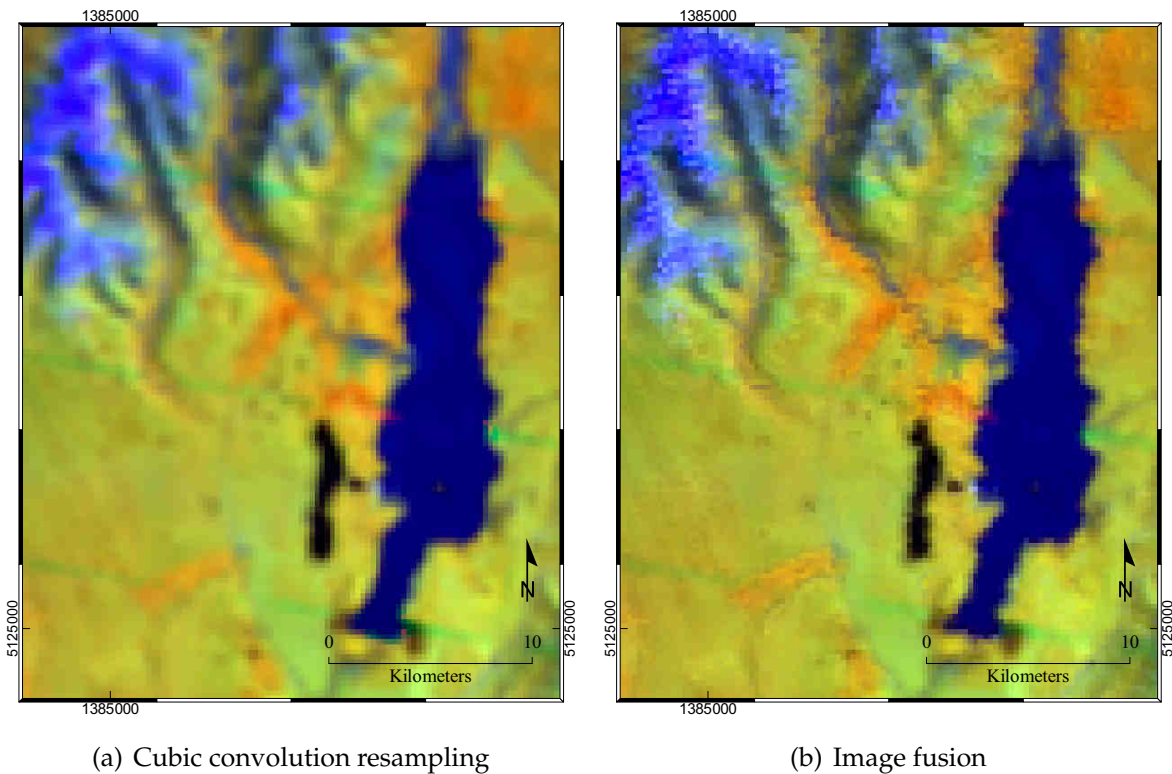


Figure 3.16 Comparison between the multispectral image fusion and the cubic convolution resampling (12 December 2002, 22:35 GMT). (a) RGB composite with MODIS bands 5, 6, and 3 at 250m spatial resolution using a cubic convolution interpolation; (b) the same colour composite with bands resampled at 250m spatial resolution using the image fusion algorithm.

tioned accuracy assessment protocol. All MODIS bands 1-7 are available at 500m and 1000m spatial resolution in the MODIS MxD02HKM and MxD021KM products, respectively. Bands 1 and 2 from the MxD02HKM were projected at 500m pixel size and used as the HR image, while bands 3-7 at 500m resolution were used as reference images. Bands 3-7 from the MxD021KM files (i.e., aggregated at 1000m) were projected at 500m using a NN technique and used as LR bands for the fusion algorithm. An additional set of bands 3-7 was obtained from the MxD021KM files and projected at 500m using a CC algorithm for the purpose of comparison. Both sets of fused and interpolated bands 3-7 at 500m spatial resolution could then be compared readily with the genuine bands 3-7 obtained from the MxD02HKM files.

The comparison was done on the basis of the RMSE between the predicted bands and the reference bands. Table 3.2 gives the results of this comparison. In terms of radiometric consistency, the fusion algorithm exhibits a RMSE 20% less

than that obtained with the cubic convolution interpolation. In addition to the better visual appearance of the fused image (see Figure 3.16) it demonstrates that the fusion outperforms a simple interpolation by better preserving the radiometry as compared to the reference images. The CC obtained slightly better scores in only three instances out of 50, thus revealing a good consistency of the fusion approach. Although this simple protocol permitted an assessment of the performance of the fusion algorithm at increasing the spatial resolution of MODIS bands 3-7, additional efforts were made to achieve a more comprehensive assessment of the benefit of the fusion. In particular, since the MODIS images were primarily intended to be used for the creation of snow distribution maps, the quality of this post-processed product was considered whether the fusion was processed or not. This comparison is provided in greater detail in Chapter 6.

Table 3.2 RMSE values [% reflectance] as compared to the reference images for the images obtained from the fusion and those obtained by a resampling with cubic convolution (CC). The values in bold correspond to the cases where CC achieved better than the fusion.

Scene	Fusion						Cubic convolution					
	b3	b4	b5	b6	b7	Overall	b3	b4	b5	b6	b7	Overall
A2000129.2245	1.7	2.0	1.6	1.4	0.9	1.5	2.4	2.8	2.0	1.5	1.0	2.0
A2001003.2240	2.3	2.4	2.3	2.4	1.8	2.2	3.0	3.2	2.5	2.4	1.7	2.6
A2001346.2240	3.4	3.5	3.4	3.0	2.4	3.2	4.4	4.6	4.0	3.5	2.6	3.9
A2002365.2235	1.8	2.0	2.0	2.0	1.6	1.9	2.3	2.6	2.1	1.8	1.3	2.1
A2003336.2235	2.9	3.1	3.4	2.7	2.1	2.8	3.8	4.1	3.8	3.0	2.2	3.5
A2004042.2240	1.7	1.8	2.6	2.0	1.6	2.0	2.3	2.4	3.0	2.4	1.7	2.4
A2004291.2235	3.5	3.7	3.8	2.8	2.0	3.2	4.6	4.9	4.4	3.1	2.1	4.0
A2005163.2245	1.5	1.8	1.4	0.9	1.0	1.4	2.1	2.6	1.8	1.0	1.0	1.8
A2006024.2235	2.4	2.5	3.6	2.5	2.0	2.6	3.2	3.5	4.1	3.0	2.2	3.2
A2007002.2240	2.5	2.7	3.5	2.5	2.1	2.7	3.3	3.6	3.9	2.8	2.2	3.2
Overall	2.5	2.6	2.9	2.3	1.8	2.4	3.3	3.5	3.3	2.5	1.9	3.0

Given the number of samples in each image, the 95% confidence interval on RMSE values are of the order of 0.01% reflectance. All differences of RMSE in the table are therefore significant at the .05 significance level.

3.5 Cloud detection and masking

In Section 2.4.3, it was explained that the MxD10 MODIS snow product (Riggs *et al.*, 2006) relies on the MxD35 cloud mask, so the snow detection algorithm could be applied only to clear sky pixels. Several researchers pointed out the overly conservative tests used in collection 4 of the cloud product and the fact that snow was often classified as cloud (Stroeve *et al.*, 2006; Lopez *et al.*, 2008; Liang *et al.*, 2008; Luo *et al.*, 2008). Despite the large improvements in cloud commission errors made recently to collection 5 of the MxD35 product, it was observed in the previous chapter that snow and cloud discrimination problems persist (Riggs *et al.*, 2006) and affect the quality of the MxD10 snow product in collection 5. This required the implementation of a cloud masking processing chain specifically designed for research in this environment.

3.5.1 Discrimination of snow and clouds

3.5.1.1 In the reflective domain

When using remote sensing to study the snow cover, the discrimination of snow from clouds is essential. The latter encompasses a variety of types, from haze to thick clouds and from ice clouds to water clouds. Because of their optical thickness and scattering properties, snow and thick clouds are highly reflective targets across the visible and near infrared wavelengths, resulting in a similarly white appearance. Nevertheless, ice features an increased absorption coefficient compared to liquid water in the short-wave infrared (SWIR, MODIS band 6 at 1.640 μm) as shown in Figure 3.17 (a) (Dozier, 1989). This spectral contrast is apparent in Figure 3.17 (b) that shows the scatter plot of MODIS band 4 (Green at 555 nm) *vs.* band 6 for ten scenes featuring snow and various types of clouds. Unlike snow, the reflectance of most thick water clouds in MODIS band 6 remains high as illustrated in Figure 3.18. This contrasted spectral behaviour often permits clouds to be distinguished from snow by means of spectral tests and thresholding techniques.

The strong difference of reflectance in MODIS band 6 between thick water clouds and snow explains the generally good performance of the NDSI at discriminating snow from clouds. With a higher SWIR reflectance, clouds exhibit low or slightly negative NDSI values compared to snow. This multispectral enhancement reveals the strong contrast between both targets [see Figure 3.19 (a)], and often form the basis of cloud masking techniques in snowy environments (König *et al.*, 2001).

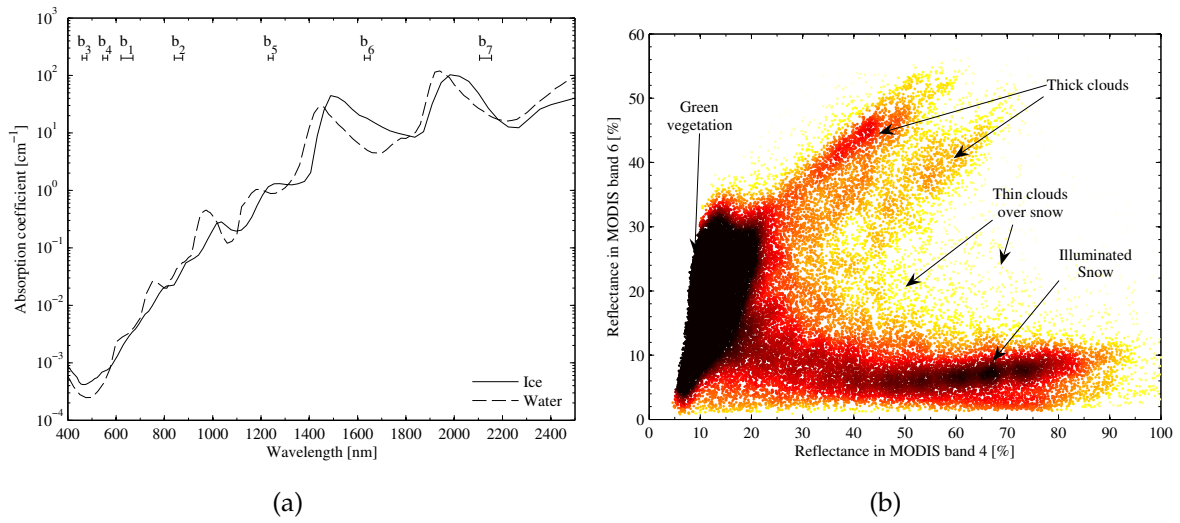


Figure 3.17 (a) Absorption coefficient of water and ice with data from [Warren \(1984, revised in 1995\)](#) and [Hale and Querry \(1973\)](#), respectively. (b) Bivariate distribution of MODIS band 4 (Green at 555 nm) vs. band 6 (SWIR at 1.640 μm) for ten scenes featuring snow and various types of clouds (adapted for MODIS from [Khlopenkov and Trishchenko, 2007](#), the colour coding indicates the point density).

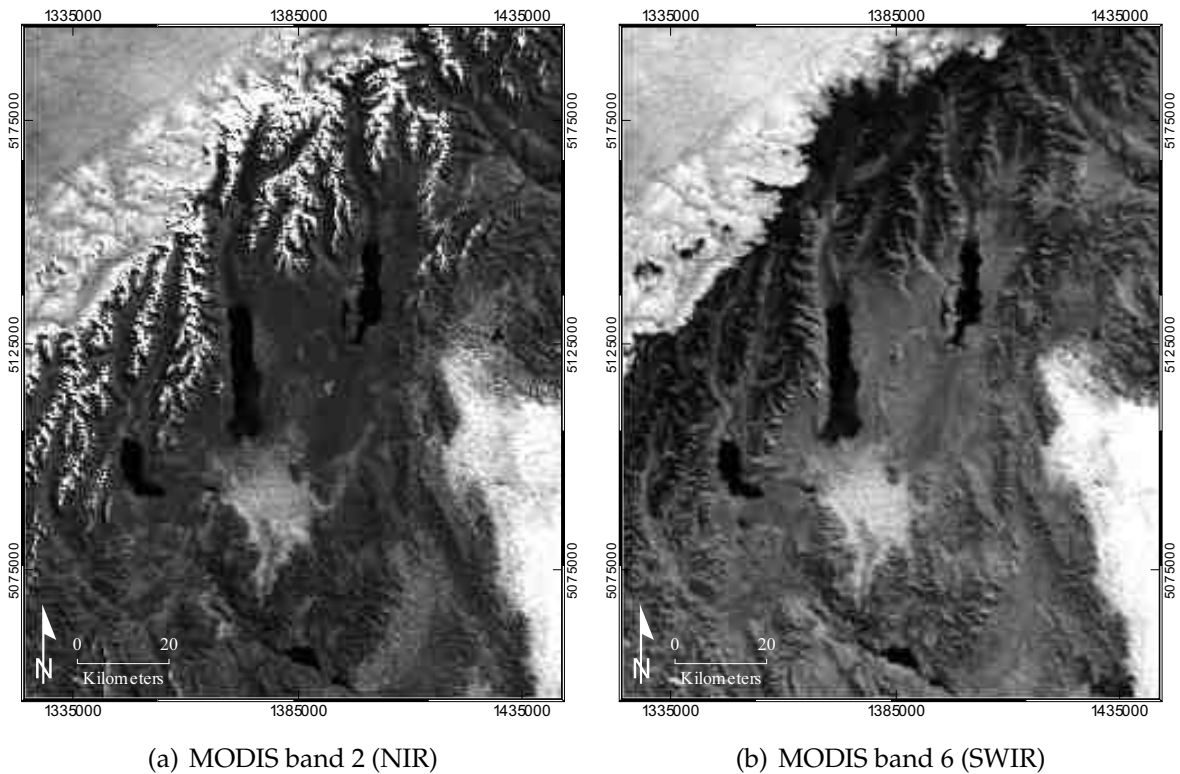


Figure 3.18 Example of MODIS band 2 (NIR) and 6 (SWIR) of a snowy scene (9 September 2005, 22:40 GMT).

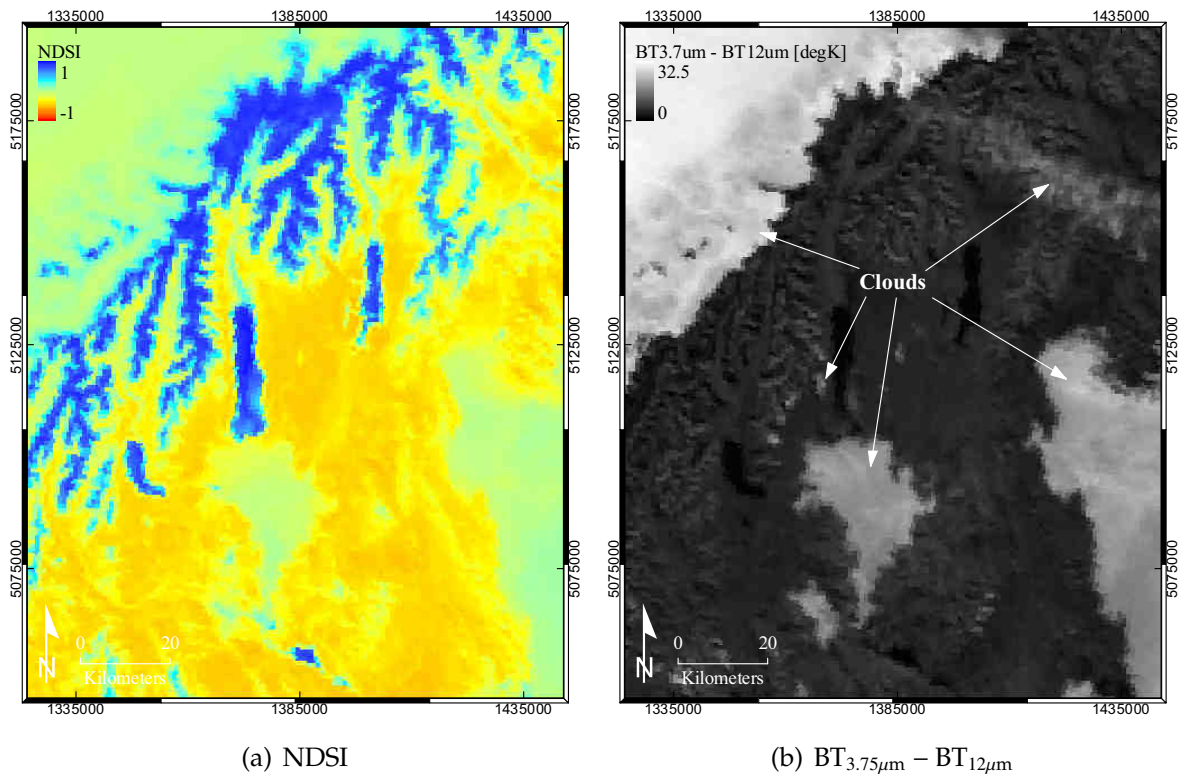


Figure 3.19 Example of NDSI and infrared brightness temperature difference for the image shown in Figure 3.18 (9 September 2005, 22:40 GMT).

3.5.1.2 In the emissive domain

Despite the relatively good spectral separation of snow and clouds [Figure 3.17 (b)], the spectral variability of both targets (including the variability due to the different properties of the various cloud types), as well as mixed pixel issues still create spectral overlaps that complicate a robust discrimination (König *et al.*, 2001). For instance, the spectral signature of ice clouds can exhibit a very close resemblance to that of snow, including in the SWIR region. On the other hand, mixed cloud and snow pixels, as well as optically thin clouds over snow, can substantially distort the radiometric signal, making a reliable identification challenging. In order to improve the performance and reliability of cloud detection, masking techniques often take advantage of the thermal properties of clouds that are generally colder than the background, and associate spectral tests in the reflective domain with thermal tests on emissive bands when available (see for example Khlopenkov and Trishchenko (2007) for cloud detection with AVHRR, Frey *et al.* (2008) or Luo *et al.* (2008) for MODIS).

A lot of effort has been invested in determining the presence of clouds in MODIS images. This led to the creation of the MODIS MxD35 cloud mask product (Ackerman *et al.*, 1998; Platnick *et al.*, 2003; Ackerman *et al.*, 2006; Frey *et al.*, 2008) that identifies clouds by means of a series of tests and thresholds on both the reflective and the emissive bands of MODIS. For instance, in order to detect clouds over snow or ice, the MxD35 cloud mask uses the infrared brightness temperature difference $BTD_1 = BT_{3.9\mu\text{m}} - BT_{11\mu\text{m}}$ that is large and positive in daylight due to the reflection of solar energy at $3.96\ \mu\text{m}$. At night, $BTD_2 = BT_{3.7\mu\text{m}} - BT_{12\mu\text{m}}$ also is used because of its ability to separate thin cirrus and cloud free conditions (Ackerman *et al.*, 1998).

Figure 3.19 (b) shows BTD_2 for the image shown in Figure 3.18. It illustrates the good thermal contrast between clouds and unobstructed land. In particular, Figure 3.19 (b) reveals isolated clouds on the slope of the mountain range near lake Pukaki, that were not readily visible in the NDSI image. It also suggests the presence of a thin layer of clouds north-east from lake Tekapo that could not be seen in the reflective bands. This simple example demonstrates how useful thermal criteria can be and how they can efficiently supplement the tests implemented in the reflective bands. Despite the recommended use of BTD_1 for detecting clouds over snow in daylight (Ackerman *et al.*, 2006), the investigation of several MODIS images with various sorts of clouds at different times of the year revealed that BTD_2 generally provided a better contrast than BTD_1 between clouds and clear sky surfaces. This is illustrated for the image shown in Figure 3.18 by the comparative dynamic of each BTD image revealed by their histograms in Figure 3.20.

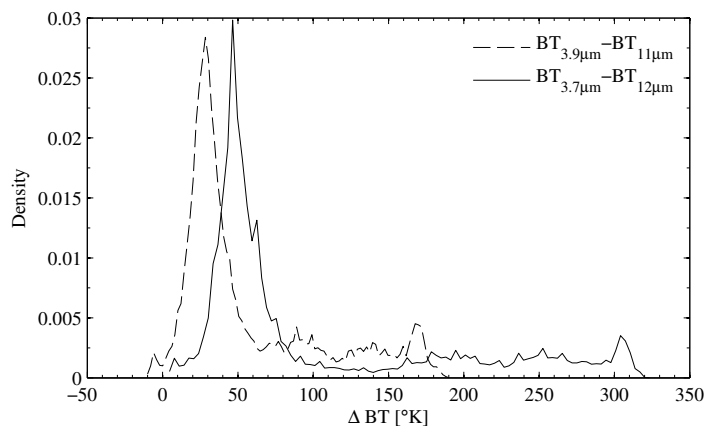


Figure 3.20 Histograms of the infrared brightness temperature difference of the image shown in Figure 3.18.

3.5.1.3 Alternative technique

Alternative strategies have been tested for screening out clouds in optical remote sensing. With respect to MODIS imagery, it is worth mentioning the recent and original method of [Lyapustin *et al.* \(2009\)](#) over Greenland. The latter implemented the dynamic building of a reference clear sky image of the surface through successive observations. The likelihood of cloud obscuration in any individual scene is measured by the loss of correlation with the clear sky image, rather than by using any spectral tests. Despite its originality, this technique is restricted to non- or slowly-changing environments. In the context of seasonal snow monitoring, the definition of a clear sky reference image is problematic as any new snow episode would result in a loss of correlation that would be identified as clouds by [Lyapustin *et al.*'s](#) technique.

3.5.2 Cloud detection and masking design

A cloud mask that considers only visible clouds was implemented. Clouds were detected using a selection of tests applied on the MODIS reflective and emissive bands, largely inspired from the MxD35 product ([Ackerman *et al.*, 2006](#)). All bands used for the detection of clouds were obtained from MODIS L1B MxD01KM products at 1km spatial resolution and projected at both 250 and 500m spatial resolution using NN resampling. The inputs were processed identically to produce a cloud mask at both spatial resolutions that would apply to the fused and non-fused images, respectively.

The quantification of the performance of the cloud mask is difficult because of the lack of references in terms of the actual presence of clouds. Thus, the assessment of cloud masking algorithms generally relies on visual image interpretation ([Ackerman *et al.*, 1998](#)). In this instance, the correct masking of clouds was assessed based on the inspection of nearly 40 MODIS images for various times of year and cloud cover, and the comparison with simultaneous ASTER images when available. The tests of the cloud mask algorithm were defined and adapted to the local environment, and the thresholds were tuned progressively until the mask detected satisfactorily the various visible cloud types, while minimizing misclassifications with snow targets. Five groups of tests were defined that accommodated different situations observed in the images. The final cloud mask was set as the Boolean logical disjunction ('OR' operation) of the mask corresponding to each group.

3.5.2.1 Group 1, thick water clouds

This mask was designed to identify thick water clouds using their relatively high reflectance across the visible and infrared spectra. As a first criterion, an envelope of cloud membership was defined in the feature space formed by the reflectance at the top of the atmosphere ρ^* in MODIS reflective land bands 1-7. Then, in order to avoid obvious commission errors with snow targets, only pixels whose NDSI value was less than 0.5 were retained. An additional threshold on the infrared brightness temperature $BT_{12\mu\text{m}}$ was found to be efficient for removing commission errors often encountered at the boundary with water bodies. This criterion produced a first guess for the set \mathfrak{M}_{1g} of potentially cloudy pixels defined as the Boolean logical conjunction ('AND' operation)

$$\begin{aligned} \mathfrak{M}_{1g} = \{p : & \rho_{0.47}^* > 0.18 \wedge \rho_{0.56}^* > 0.15 \wedge \rho_{0.65}^* > 0.15 \wedge \rho_{0.86}^* > 0.25 \wedge \\ & \rho_{1.24}^* > 0.25 \wedge \rho_{1.64}^* > 0.15 \wedge \rho_{2.13}^* > 0.10 \wedge \\ & \text{NDSI} < 0.5 \wedge \text{BT}_{12} < 289\}, \end{aligned} \quad (3.10)$$

where p represents the pixels of the image to be processed. Finally, the infrared brightness temperature difference $\text{BTD}_2 = \text{BT}_{3.7\mu\text{m}} - \text{BT}_{12\mu\text{m}}$ was used to constrain \mathfrak{M}_{1g} based on the observation that clouds have a relatively high BTD_2 in comparison with background surfaces. However, despite the good contrast observed between clouds and unobstructed terrain, no clear threshold could be found that allowed the BTD_2 image to be segmented consistently in all conditions. Thus, a two-step statistical approach was designed to estimate the threshold to be used for this mask. The BTD_2 value of the pixels that belonged to the first guess \mathfrak{M}_{1g} provided a distribution of BTD_2 values for potentially cloudy pixels. The BTD_2 threshold was defined as the 10th percentile of this distribution. Finally, by denoting $P_\alpha(\mathfrak{A})$ the α -th percentile of a countable set of real numbers \mathfrak{A} , the set \mathfrak{M}_1 of pixels identified as clouds for this group of criteria was defined as follows:

$$\mathfrak{M}_1 = \mathfrak{M}_{1g} \cap \{p : \text{BTD}_2 > P_{10\%}[\text{BTD}_2(\mathfrak{M}_{1g})]\}. \quad (3.11)$$

3.5.2.2 Group 2 & 3, thick water clouds

The previous mask did not detect all the thick water clouds. Two additional masks were designed empirically to reduce omission errors. The set \mathfrak{M}_2 of pixels identified clouds characterized by a high visible reflectance in MODIS band 3 (Blue at 645 nm), a small or slightly negative NDSI, and a relatively large BTD_2 . For this

mask, a suitable threshold for BTD_2 was found to vary depending on the time of year expressed as the Julian day j . Although the reason for such variations was not rigorously investigated, the thermal contrast between clouds and the ground was found to weaken in winter. The day-dependent threshold aimed at capturing this variation. Pixels identified as clouds for this group of criteria was defined as follows:

$$\mathfrak{M}_2 = \{p : \rho_{0.47}^* > 0.25 \wedge -0.25 < NDSI < 0.15 \\ \wedge BT_{12} < 289 \wedge BTD_2 > 1.5 \cos(j + 30) + 7.5\}. \quad (3.12)$$

The mask \mathfrak{M}_3 permitted to detect obvious clouds characterized by a medium to small NDSI value, but a relatively high visible, NIR, and very high SWIR reflectances:

$$\mathfrak{M}_3 = \{p : \rho_{0.65}^* > 0.21 \wedge \rho_{0.86}^* > 0.25 \wedge \rho_{1.64}^* > 0.35 \wedge -0.25 < NDSI < 0.2\}. \quad (3.13)$$

3.5.2.3 Group 4, cirrus clouds

MODIS reflective band 26 at 1.375 μm was designed to take advantage of the strong absorption of water vapour to detect the presence of thin cirrus clouds. A water vapour column amount as low as 1 cm is sufficient to absorb all of the energy reflected from the ground (Ackerman *et al.*, 2006). Thus, the concentration of water vapour at high altitude in the upper troposphere can contrast with the dark background at this wavelength. This channel was used here with a more restrictive threshold than that recommended by the MxD35 algorithm, and under the condition that NDSI did not suggest the presence of snow. Finally, \mathfrak{M}_4 was defined as follows:

$$\mathfrak{M}_4 = \{p : \rho_{1.38}^* > 0.05 \wedge NDSI < 0.6\}. \quad (3.14)$$

3.5.2.4 Group 5, strong Brightness Temperature Difference

An additional test directly inherited from the MxD35 algorithm (Bit 17 in Ackerman *et al.*, 2006) was applied to the brightness temperature contrast between $BT_{3.7\mu\text{m}}$ and $BT_{12\mu\text{m}}$ (i.e., BTD_2). A relatively high threshold was used to ensure a high confidence with regard to cloud presence. Moreover, the test was used under the condition that the target did not have a sufficient NDSI value to suggest the presence of snow:

$$\mathfrak{M}_5 = \{p : BTD_2 > 15 \wedge NDSI < 0.4 \wedge BT_{12} < 289\}. \quad (3.15)$$

3.5.2.5 Final mask

The final cloud mask \mathfrak{M}_c was formed as the Boolean logical disjunction of all masks \mathfrak{M}_i as

$$\mathfrak{M}_c = \bigcup_{i=1}^5 \mathfrak{M}_i. \quad (3.16)$$

Due to the considerable size of each MODIS Level-1B Swath products (500 Mbytes) and repeated cloud cover in the area, only potentially good images were selected from preview and downloaded. Among the 935 granules initially selected to cover the period from 27th February 2000 to 1st May 2007 (i.e., seven whole hydrological years in New Zealand), only 679 appeared to be usable with regard to monitoring the snow cover in the upper Waitaki catchments. According to the size of the study area, 281 images had less than 10% snow cover, 362 had between 10% and 50% snow cover and 36 had more than 50% snow cover.

A Few misclassifications still occurred, especially commission errors on the north-facing slopes at the edges of the snow cover. At the time of MODIS/TERRA image acquisition (i.e., 10:30am local time), north-facing slopes are illuminated, resulting in a configuration that artificially increases the amount of SWIR radiation reflected back to the sensor. At the edges of the snow cover, vegetation and rocks mixed with snow also contribute to an increase in the reflected SWIR radiation. However, these mixed pixels generally have a relatively high reflectance in the visible spectrum due to the presence of snow. Therefore, they can exhibit a spectral signature that is very similar to clouds, resulting in misclassifications that are very difficult to avoid. No rigorous analysis was conducted to assess quantitatively the accuracy of the cloud mask \mathfrak{M}_c . Nevertheless, all MODIS images used in the thesis and processed through the cloud masking algorithm were inspected visually and revealed satisfying performances overall. Eight images processed with various conditions of snow and clouds are provided in Appendix F to illustrate the performance of this cloud mask.

3.6 Summary

This chapter has detailed the initial steps that were undertaken to prepare the data required for the remainder of the thesis. It accounts for the creation and assessment of a DEM that would be used for various purposes as detailed in the

subsequent chapters. The SRTM3 DEM was tested, as well as several methods of interpolation of contour lines and other vector-based topographic data. A thorough assessment of the accuracy demonstrated that the interpolation of 20m contours from the national topographic database outperforms the SRTM in terms of accuracy. However, despite obvious dissimilarities between interpolators, standard statistics failed to reveal significant differences. Additional criteria, both qualitative (e.g., the visual interpretation of DEM derivatives such as slopes, aspect, and curvature) and quantitative (e.g., through the computation of the contour bias), permitted the enhancement and identification of artefacts resulting from the interpolations. They demonstrated that the thin plate smoothing spline method ANUDEM is the most capable to represent the terrain as far as the study area is concerned.

MODIS L1B data provided in swath format were projected using the MRT Swath Reprojection Tool v2.1. A multi-resolution analysis identified a severe pit-fall of MRT with respect to the geocoding of the output images. Depending on the output cell size requested, the MRT software does not project images consistently in terms of co-registration. A spatial correlation method demonstrated that a shift of half the specified pixel size is artificially introduced towards the south-east direction, possibly due to the misuse of the GeoTiff tags in the output file format. A correction was implemented in the processing chain in order to achieve the best co-registration possible between images of different spatial resolution.

Such co-registration is all the more important since an innovative fusion technique is introduced in the thesis. It aims at enabling the mapping of the snow distribution at 250m spatial resolution to achieve a better depiction of the snow in rough terrain. A multispectral wavelet fusion technique based on the ARSIS multi-resolution concept of [Ranchin and Wald \(2000\)](#) was implemented to merge the high spatial content of MODIS bands 1 and 2 at 250m spatial sampling into the coarser spectral bands 3-7 at 500m. Although the benefit of the fusion for the mapping of snow is addressed in detail in [Chapter 6](#), a preliminary assessment of the relevance of the fusion algorithm was conducted. The wavelet-based multi-resolution algorithm allows the introduction of radiometric bias in the fused image to be minimized. Moreover, the implementation of [Wald's protocol \(2002, Chap. 8\)](#) for assessing image fusion demonstrates that the fused bands are more accurate in terms of radiometry than a pure interpolation.

Finally, a cloud masking algorithm was created using a combination of spectral tests in the reflective and emissive domains. Although no quantitative assessment of

the quality of the cloud mask was undertaken due to the lack of suitable references, a visual inspection of 40 images showed that this mask performs well at identifying clouds in most cases, while it minimizes commission errors whereby snow is wrongly classified as clouds. As a result of this initial step, maps of radiance at the top of the atmosphere for the seven land bands were projected at 250 and 500m spatial resolution. The following chapter details how these data are corrected further to account for atmospheric and topographic illumination effects in order to create a consistent time series of ground reflectance images. The DEM as well as the cloud mask provide necessary ancillary layers towards this goal.

Chapter 4

Atmospheric and TOPOgraphic CORrection (ATOPCOR)¹

4.1 Introduction

As explained in the previous chapter, the imagery available in the MODIS Level-1B (L1B) product provides measurements of radiance at the top of the atmosphere (L_{TOA}). In rugged terrain and in the case of a multi-temporal dataset these measurements are affected strongly by changes of atmospheric and topographic conditions. Topographic effects are readily visible in a satellite image because they enable the interpreter to distinguish slopes, whether they are facing the direct source of illumination or not, thus providing the sensation of relief. Although atmospheric effects can sometimes be clearly identified in an image, for example due to large concentrations of aerosols such as dust and ashes caused by fires, they are generally more subtle and can be qualitatively assessed by the presence of haze and the loss of contrast.

Quantitatively, both of these effects are the source of potentially large radiometric distortions (Leprieur *et al.*, 1988; Chavez, 1996). They increase the variance of L_{TOA} measured over similar targets that are subject to various conditions of irradiance (including shadow effects) and contaminated by environmental and atmospheric path radiance. Such spatial and temporal variability complicates the classi-

¹The content of this chapter is largely published in: Sirguey, P., Mathieu, R. and Arnaud, Y. (2009). Subpixel monitoring of the seasonal snow cover with MODIS at 250m spatial resolution in the Southern Alps of New Zealand: Methodology and accuracy assessment. *Remote Sensing of Environment*, 113(1), 160–181, doi:10.1016/j.rse.2008.09.008

fication of surfaces because similar targets can appear with very different spectral signatures. In addition, it can reduce the robustness of routine algorithms that are aimed at dealing with multi-temporal datasets, as well as prevent the user from estimating accurately the physical parameters of the ground such as the surface reflectance. In the context of mapping snow automatically in the Southern Alps based on MODIS L1B data, correcting the imagery beforehand for both atmospheric and topographic effects is critical. Converting the radiometric measurements into ground spectral reflectance allows the multiple images forming the time series to be standardized with respect to time. This has the potential to improve the robustness of the classification process described in the next chapter.

Thus, this chapter describes the physically-based three-dimensional topographic and atmospheric correction model that was implemented, inspired by the iterative approach suggested by Richter (1998). In the first section, the equations that govern the radiative transfer in mountainous terrain are presented and the use of an iterative correction method is justified. The following section describes more specifically how to account for topographic effects. In particular, it includes a novel approach to model multiple reflections between adjacent slopes (Sirguey, 2009). This leads to a comprehensive description of an atmospheric model that is adapted from the simple SPECTRAL2 model of Bird and Riordan (1986). The performance of the SPECTRAL2 model is carefully assessed by means of a comparison with the rigorous solution of the radiative transfer provided by the 6S model (Verote *et al.*, 1997). Finally, the performance of the joint atmospheric and topographic correction is discussed.

4.2 Radiative transfer

4.2.1 Generalities

In the context of optical remote sensing, the radiance measured at the top of the atmosphere $L_{TOA}(\lambda)$ at the centre wavelength λ can be formulated as the sum of:

- the radiance $L_g(\lambda)$ reflected by the ground in the direction of the detector and affected by the ground-to-sensor atmospheric transmittance $T_v(\lambda)$;
- the atmospheric intrinsic radiance $L_p(\lambda)$ (or path radiance), which represents the radiance scattered by the atmosphere within the detector field of view; and

- the background radiance $L_k(\lambda)$, which is the radiance reflected by neighbouring surfaces (i.e., outside the detector field of view) and scattered by the atmosphere within the detector field of view.

These three components of the measured radiance are illustrated in Figure 4.1 and described by

$$L_{\text{TOA}}(\lambda) = T_v(\lambda)L_g(\lambda) + L_p(\lambda) + L_k(\lambda). \quad (4.1)$$

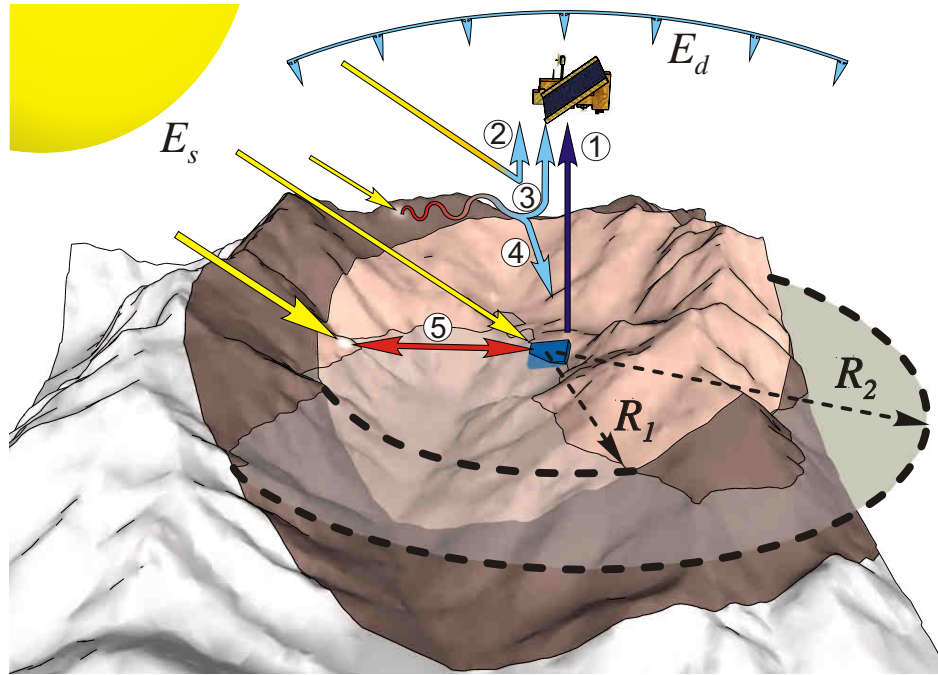


Figure 4.1 Radiation components in rugged terrain. E_s and E_d are respectively the direct solar and diffuse solar irradiance. (1) Target radiance L_g , (2) atmospheric intrinsic radiance L_p (path radiance), (3) background radiance L_k , (4) diffuse environmental irradiance E_m (5) reflected terrain irradiance E_t . R_1 and R_2 define the neighbourhoods from where pixels are assumed to contribute either to (5), or (3) and (4), respectively.

Equation 4.1 and Figure 4.1 illustrate how the ground radiance L_g that relates to the reflectance of the surface is considerably affected by topographic and atmospheric effects. When dealing with imagery in rugged terrain, many authors have advocated mitigation of such radiometric distortions in order to improve image analysis and classification of land cover (e.g., Civco, 1989; Itten and Meyer, 1993; Tokola *et al.*, 2001; Dorren *et al.*, 2003; Shepherd and Dymond, 2003; Hale and Rock, 2003; Blesius and Weirich, 2005). A range of methods exists to achieve this goal. For instance, in the context of multispectral remote sensing, band ratioing is a common way to reduce the effects of varying illumination due to the topography (Lillesand

and Kiefer, 2000, chap. 7.6). This relies on the assumption that the change of illumination is a multiplicative factor that affects similarly the spectral bands that form the ratio. Thus, equal multiplicative factors are discarded when two spectral bands are divided, resulting in a ratio image for which the dependence on topography is generally reduced. Nevertheless, the strict linearity of the relationship between the measured radiance and the varying illumination caused by the topography is a disputable assumption because of the presence of additional sources of irradiance to the surface (e.g., diffuse sky and reflected terrain irradiance), as well as additional radiance components (e.g., environmental and atmospheric path radiance). Eventually, this assumption loses most of its relevance when considering shaded surfaces that are illuminated mostly by diffuse sky irradiance, which is strongly dependent on the wavelength for Rayleigh scattering and, to a lesser extent, Mie scattering. Thus, when considering similar targets, the ratio between spectral bands can be greatly different whether it is computed over a surface that is shaded or not. Finally, ratioing is performed at the expense of the spectral resolution (i.e., two spectral bands are needed to compute one ratio image) and penalizes multispectral classification.

On the other hand, the increasing availability of precise DEMs has enabled the design of correction methods that minimize the impact of topography by modelling the local condition of illumination (Teillet, 1986; Riaño *et al.*, 2003). In general, the methods are empirical or semi-empirical and designed to account for the effect of the topography depending on the nature of the reflective surface. For instance, the cosine correction (Civco, 1989; Lopez *et al.*, 2008) and C-correction (Teillet *et al.*, 1982; Riaño *et al.*, 2003) have been used when a Lambertian assumption can reasonably be made. Alternatively, the Minnaert correction is sometimes preferred (Minnaert, 1941; Colby, 1991; Blesius and Weirich, 2005). Other non-Lambertian models have also been designed specifically to address the correction of satellite images of forested slopes, such as the Sun-Canopy-Sensor model (SCS) (Gu and Gillespie, 1998) or the WAK model proposed by Dymond and Shepherd (1999) and Dymond *et al.* (2001).

Despite their generally acknowledged performance, none of these methods attempts to address comprehensively the radiative transfer that occurs between the source, the target, and the sensor. They solely address topographic effects due to the varying local illumination and ignore atmospheric perturbations. In this context, the radiometric correction is better referred to as a topographic normalization and the

retrieved values can still depart noticeably from the ground reflectance. Thus, the normalization with respect to time is not ensured, nor is the physical meaning of the corrected value. This potentially compromises the processing of time series of satellite images in an automated and consistent way. [Ekstrand \(1996\)](#) and [Blesius and Weirich \(2005\)](#) advocated the use of an atmospheric correction prior to the topographic normalization although they were satisfied by an empirical haze removal procedure ([Chavez, 1988](#)). Over rugged terrain reaching high elevations it is preferable to consider a more rigorous atmospheric correction ([Dozier and Frew, 1981](#); [Vermote et al., 1997](#)) to account better for the decrease of diffuse irradiance with increasing altitude, as well as other environmental factors affecting the measured radiance (e.g., aerosols, ozone absorption, atmospheric path radiance).

The methods noted above can only mitigate topographic effects for slopes that receive direct illumination, but none is designed to account for shaded areas ([Meyer et al., 1993](#)). This can be problematic when snow is the main type of surface to be detected in alpine terrain. Since winter time corresponds to low solar elevation, a very steep environment such as the Southern Alps often experiences dramatic shadowing. Shaded areas are also more prone to hold snow cover due to a lower energy input, thus preserving the snowpack. On this basis, they should receive specific attention. It is believed that none of the previous methods is suitable to normalize correctly the images in extreme configurations of illumination. Consequently, the strategy followed in this thesis is aimed at correcting for both topographic and atmospheric effects concurrently, as recommended by [Sandmeier and Itten \(1997\)](#), [Richter \(1998\)](#), and [Shepherd and Dymond \(2003\)](#), by modelling comprehensively the radiative transfer in mountainous terrain.

Ultimately, the outcome of a physically-based correction is the conversion of the maps of radiance measured at the top of the atmosphere into ground spectral reflectance $\rho(\lambda)$. This type of correction algorithm is readily available in commercial packages (i.e., ATCOR3) for images from selected sensors (e.g., ASTER, Quickbird, IKONOS). However, this algorithm has not yet been adapted to MODIS data. Despite its potential complexity, this task offers several advantages. Not only does this approach facilitate the classification of areas that are more or less illuminated including shadows, but it also makes all images comparable throughout the year. Thus it enables the design of a robust classification scheme that can deal efficiently with multi-temporal datasets. Moreover, it is possible to take advantage of the fact that the ground spectral reflectance is a parameter of the surface that can theoret-

ically be measured *in situ*. Hence, its magnitude can be monitored through time to depict changes of the physical properties of the target. Finally, the implementation of a comprehensive physical model capable of managing both atmospheric and topographic effects including shadows is desirable because it is a necessary step towards the estimation of snow albedo in further work. It can also be used to monitor the properties of other types of targets.

4.2.2 Bidirectional Reflectance Distribution Function

The ground spectral albedo $\alpha(\lambda)$ is the fraction of incident flux that is reflected by a surface as a function of the wavelength. It is the intrinsic property of the ground that is ideally aimed at being retrieved to identify the nature of the surface from remotely sensed data in the reflective part of the spectrum (i.e., 300–2500 nm). The ability of a target to reflect the incident flux varies according to both the incident direction of the illumination source (measured by the zenith and azimuth angles: θ_s and φ_s , respectively) and the viewing perspective (θ_v, φ_v) (Tanré *et al.*, 1979; Thomas, 1997). The relative geometry of the source, the target, and the sensor is illustrated in Figure 4.2. Anisotropic reflection also is referred to as a non-Lambertian behaviour of the surface. It is formulated using the Bidirectional Reflectance Distribution Function $f_p(\theta_s, \theta_v, \varphi_s, \varphi_v, \lambda)$ (BRDF) which is defined as the ratio between the radiance reflected upward in the direction of the sensor (L_g) and a collimated incident flux (Hudson *et al.*, 2006). In general, the BRDF does not depend separately on φ_s and φ_v , but only on the relative azimuth $\varphi = \varphi_s - \varphi_v$ as follows:

$$f_p(\theta_s, \theta_v, \varphi, \lambda) = \frac{L_g(\theta_s, \theta_v, \varphi, \lambda)}{E_{\text{incident}}(\theta_s, \theta_v, \varphi, \lambda)}. \quad (4.2)$$

Thus, multiple measures of the radiance reflected by the surface, in all directions of the overlying hemisphere and according to all possible directions of the illumination, are required to estimate the total upwelling flux and accurately retrieve the spectral albedo by integration of the BRDF over the hemisphere enclosing the surface:

$$\alpha(\lambda) = \int_0^{2\pi} \int_0^{\frac{\pi}{2}} f_p(\theta_s, \theta_v, \varphi, \lambda) \cos \theta_v \sin \theta_v d\theta_v d\varphi. \quad (4.3)$$

In practice, a direct measurement of the spectral albedo [Equation (4.3)] by satellite sensors is difficult to achieve because the diffuse irradiance compromises the hypothesis of a well collimated flux and satellite measurements are rarely made in multiple geometric configurations. Instead, the satellite measurement allows

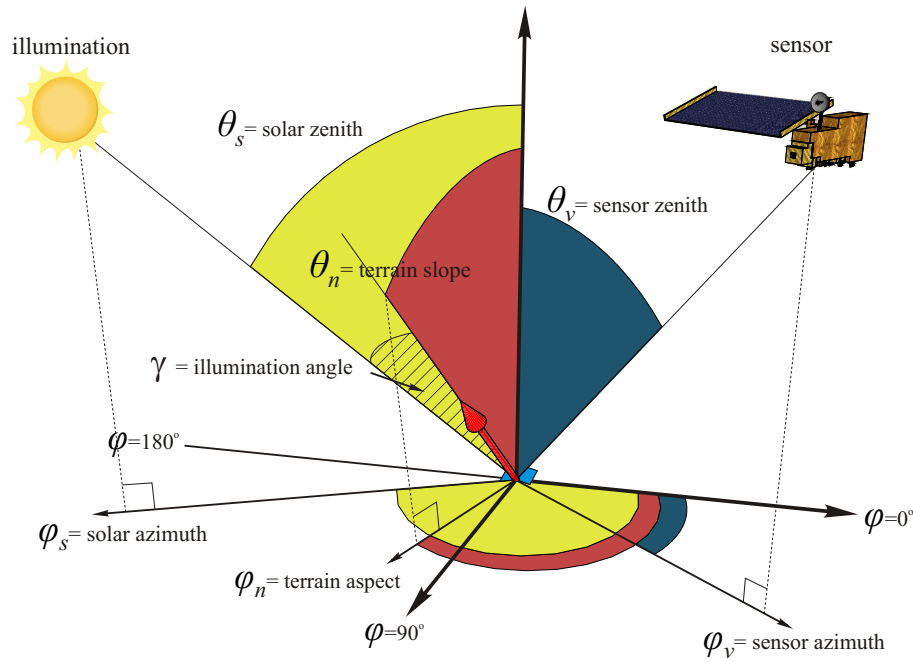


Figure 4.2 Relative geometry of the sun, the sensor, and the target.

merely a single value of the Hemispherical Reflectance Distribution Factor (HRDF) to be measured. It corresponds to the ratio between L_g and the total flux received by the surface from the entire hemisphere (i.e., including both the collimated and the diffuse incident flux) according to the relative geometry between the illumination (i.e., the Sun), the surface, and the sensor at the time of acquisition (Hudson *et al.*, 2006). In these conditions, an *a priori* knowledge of the ground target and its anisotropic reflectance properties is needed to estimate the ground spectral albedo from a single measurement.

Numerous papers have characterized and eventually modelled the BRDF of snow generally characterized by a strong forward scattering and an anisotropy that varies with wavelength, grain size and shape, and surface rugosity (e.g., Wiscombe and Warren, 1980; Winther, 1994; Leroux *et al.*, 1998; Aoki *et al.*, 2000; Painter and Dozier, 2004; Hudson *et al.*, 2006). However, in alpine terrain snow transforms constantly, as does the grain size. Thus, it is inadequate and hazardous to select a model of BRDF (or HRDF) prior to any form of surface classification. It is also believed that the benefit of such a correction compared to the cost of its implementation is disputable for the sole purpose of snow detection. The BRDF of snow should be considered only subsequently to the classification if the purpose is, for example, to estimate the broadband albedo of the surface in order to compute rigorously the en-

ergy budget of the snow pack. Alternatively, in a first approximation, the surfaces can be assumed to be Lambertian and the ground spectral reflectance $\rho(\lambda)$ denomination is used instead of spectral albedo to avoid confusion.

4.2.3 Model equations

The previous approximation allows formulation of the ground radiance of a pixel on a slope, so that

$$L_g(\lambda) = \frac{\rho(\lambda) [bE_s(\lambda) \cos \gamma + E_d^*(\lambda) + E_t(\lambda)]}{\pi}, \quad (4.4)$$

where b is the coefficient that accounts for the shading of the direct sunlight (see Section 4.3.3); E_s is the direct solar irradiance; γ is the relative angle between the solar ray and the normal to the surface; E_d^* is the total diffuse irradiance on the slope that accounts for its orientation and both the diffuse solar irradiance E_d and the diffuse environmental irradiance E_m ; and E_t is the radiation reflected by the adjacent slopes (Figure 4.1). E_s is calculated by

$$E_s(\lambda) = \frac{T_s(\lambda)E_0(\lambda)}{d^2}, \quad (4.5)$$

where T_s is the sun-to-ground atmospheric transmittance, d is the Earth-Sun distance, and E_0 is the extraterrestrial solar irradiance. The last two parameters are provided for each image within the corresponding MxD03 data product. Alternatively, the extraterrestrial solar spectrum can be obtained from the World Radiation Center¹. A simple formula for the calculation of the Earth-Sun distance given by Spencer (1971) can also be used:

$$d = (1.00011 + 0.034221 \cos \phi + 0.00128 \sin \phi + 0.000719 \cos 2\phi + 0.000077 \sin 2\phi)^{-\frac{1}{2}}, \quad (4.6)$$

where ϕ is the day angle given by $\phi = \frac{2\pi(\text{julian day}-1)}{365}$. A review of Spencer's and other algorithms has been recently published by Grena (2008), as well as a more sophisticated formulation.

In Equation (4.1), the components L_k , E_m (included in E_d^*), and E_t represent the influence of the surrounding terrain on the radiance of the pixel under consideration, as seen by the sensor. Achieving an accurate and deterministic estimation

¹http://ftp.pmodwrc.ch/pub/data/irradiance/spectral_irradiance, last retrieved in October 2008.

of these neighbouring effects is a formidable calculation challenge. Most operational correction models usually address the neighbouring effects using simplified approaches (Dubayah and Loechel, 1997; Sandmeier and Itten, 1997; Richter, 1998; Shepherd and Dymond, 2003; Wang *et al.*, 2006). They assume that each component can be estimated through the average reflectance of a suitable contributing area that receives the global irradiance (sum of direct solar, diffuse solar, and environmental irradiance). Such contributing neighbourhoods are illustrated by the radii R_1 and R_2 in Figure 4.1 and are assumed to be of the order of 500m for E_t and 1–2 km for E_m and L_k (Richter, 1998).

The fact that these components are dependent themselves on the ground reflectance constitutes a closed-loop system that complicates the resolution of the radiative transfer equation. Among the authors who developed algorithms for the radiometric correction of satellite imagery in rugged terrain and cited in the previous paragraph, only Richter's (1998) model (i.e., ATCOR3) is based on an iterative approach that potentially can address this feedback. At each new step it updates individual pixel reflectance according to the surrounding effects that are estimated from the reflectance computed for their respective contributing area at the previous step. Finally, when combining Equations (4.1), (4.4), and (4.5), the ground reflectance at iteration i can be formulated as

$$\rho^{(i)} = \frac{\pi(L_{\text{TOA}} - L_p - L_k^{(i)})}{T_v [bT_s E_0 d^{-2} \cos \gamma + E_d^{*(i)} + E_t^{(i)}]}, \quad (4.7)$$

where wavelength λ is omitted for clarity. The two following sub-sections provide details with regard to the estimation of the topographic and atmospheric parameters required to solve Equation (4.7). The last sub-section discusses the stability of the iterative process.

4.3 Topographic considerations

In rugged terrain, measurements from optical satellite sensor imagery are greatly affected by a combination of topographic effects. Changes in slope and aspect modify the local illumination as a function of the relative geometry between the Sun and the target. The neighbouring configuration has an impact on the portion of the diffuse sky irradiance that reaches the target, as well as on the occurrence of cast shadows. Finally, in mountainous environments, the multiple reflections of

radiation between a surface and the surrounding slopes tend to complicate the radiative transfer, by increasing the global irradiance that reaches a target (Duguay, 1993) (Figure 4.1). Thus, it is necessary to address all these effects to retrieve realistic values of ground reflectance (Proy *et al.*, 1989; Richter, 1998), or estimate accurately the energy budget (Duguay, 1993).

4.3.1 Illumination angle

Changes in slope and aspect modify the amount of energy received by a pixel. The geometric expansion of the irradiance beam, for angles other than normal incidence to the surface, must be accounted for with regard to the relative geometry of the target, the sensor, and the illumination source (i.e., the Sun) as shown in Figure 4.2. The illumination angle γ is the relative angle between the solar ray and the normal to the surface. It can be obtained using Euler's rotation theorem¹ and is given by

$$\cos \gamma = \cos \theta_n \cos \theta_s + \sin \theta_n \sin \theta_s \cos(\varphi_n - \varphi_s), \quad (4.8)$$

where terrain slope (θ_n) and terrain azimuth (φ_n) are derived from the analysis of the DEM; solar zenith (θ_s) and solar azimuth (φ_s) are retrieved for every pixel from the MODIS MxD03 product.

4.3.2 Sky-view factor and terrain configuration factor

4.3.2.1 Sky-view factor

The sky obstruction by surrounding slopes reduces the amount of diffuse solar irradiance that reaches a pixel (see Section 4.4.2.1 and Figure 4.3). The use of the sky-view factor V_d is an effective way to address this effect. It is defined as the fraction of the hemispherical diffuse sky irradiance that is incident on the surface. Dozier and Frew (1990, pg. 964) rephrased equivalently this definition as:

“The sky-view factor V_d is the ratio of the diffuse sky irradiance at a point to that on an unobstructed horizontal surface.”

Thus, V_d ranges from 0 for a totally obscured sky to 1 for an unobstructed horizontal surface. Various approaches have been designed to estimate this parameter. They usually involve different simplifications with regard to the topography and

¹The detail of this calculation is provided in Appendix C.

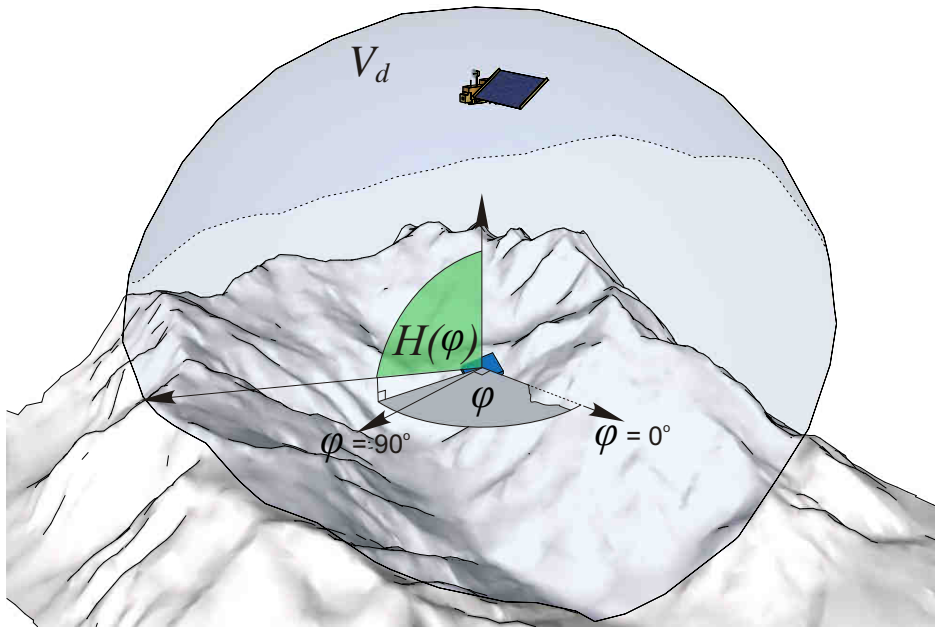


Figure 4.3 Sky obstruction by surrounding slopes. It is measured by horizon lines H_φ of the point under consideration in all azimuth angles φ . The Sky-view factor V_d is defined as the fraction of the hemispherical diffuse sky irradiance that is incident on the surface.

assume the diffuse sky radiance to be isotropic. It is of interest to review the principal methods because some have led to alternative, and sometimes inappropriate or confusing ways to define the sky-view factor.

In the first place, it is important to note that the sky-view factor is a ratio of radiation quantities. Under the assumption of an isotropic skylight, the radiance emitted by a portion dS of the sky is constant and equal to L_d . Thus, a flat unobstructed surface dA receives from this elementary surface a radiant flux $d^2\Phi$ given by

$$d^2\Phi = L_d \cos \theta d\Omega dA, \quad (4.9)$$

where the parameterization in spherical coordinates of the solid angle $d\Omega$ is illustrated in Figure 4.4 (a). The diffuse sky irradiance \overline{E}_d received on a horizontal unobstructed surface is obtained by integration of $d\overline{E}_d = \frac{d^2\Phi}{dA}$ obtained from Equation (4.9) over the hemisphere:

$$\overline{E}_d = \iint_{\text{Hem.}} \frac{d^2\Phi}{dA}. \quad (4.10)$$

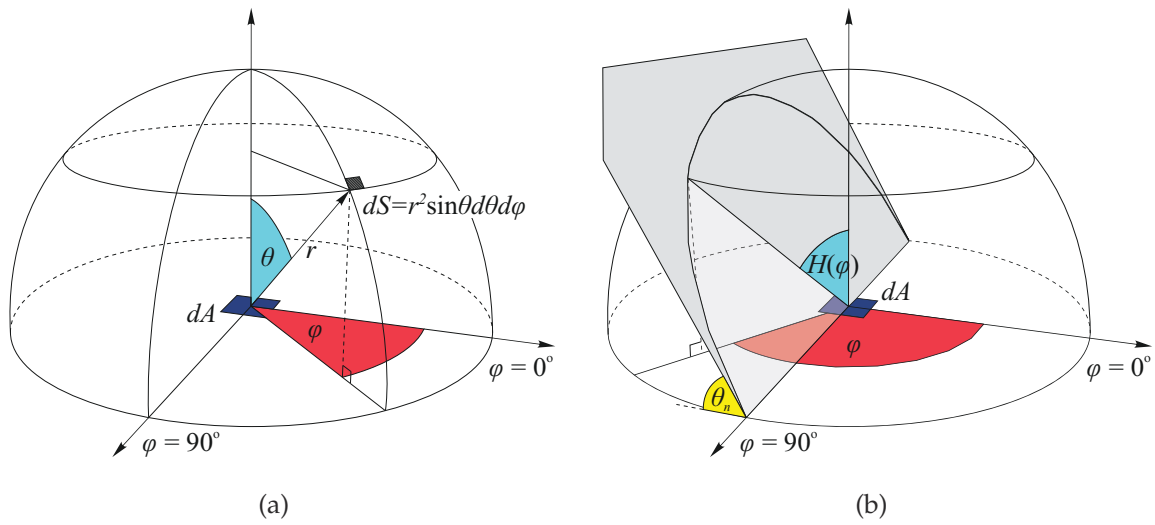


Figure 4.4 (a) Parameterization in spherical coordinates. (b) The trigonometric approach for determining V_d .

It comes that

$$\overline{E}_d = L_d \int_0^{2\pi} \int_0^{\frac{\pi}{2}} \cos \theta \sin \theta d\theta d\varphi \quad (4.11a)$$

$$= \pi L_d. \quad (4.11b)$$

The trigonometric approach. Early literature (e.g., Kondratyev, 1969; Iqbal, 1983) studied a simple case to formulate V_d . In this case, a surface was considered in which an obstruction to diffuse sky irradiance is only due to an adjacent and infinite slope as illustrated in Figure 4.4 (b). Although this approximation has the advantage to rely only on the local slope which can be estimated from the DEM, it ignores the obstruction caused by a more complex surrounding topography. Under this assumption, the integral used in Equation 4.10 should be limited to the portion of sky that is visible. It requires the parameterization of the horizon angle $H(\varphi)$ which is the zenith angle of the horizon line in the direction of the azimuth φ . In spherical coordinates, the equation of the adjacent plane (P) shown in Figure 4.4 (b) can be written

$$(P) : r(\sin \theta \cos \varphi \sin \theta_n + \cos \theta \cos \theta_n) = 0. \quad (4.12)$$

This allows the horizon angle to be obtained as a function of the azimuth angle as follows:

$$\tan H(\varphi) = \frac{-1}{\cos \varphi \tan \theta_n}. \quad (4.13)$$

Thus, the downward irradiance coming from the visible portion of the sky incident on the surface becomes

$$E_d = L_d \left[\int_0^{\frac{\pi}{2}} \int_0^{\frac{\pi}{2}} \cos \theta \sin \theta d\theta d\varphi + \int_{\frac{\pi}{2}}^{\frac{3\pi}{2}} \int_0^{\arctan\left(\frac{-1}{\cos \varphi \tan \theta_n}\right)} \cos \theta \sin \theta d\theta d\varphi + \int_{\frac{3\pi}{2}}^{2\pi} \int_0^{\frac{\pi}{2}} \cos \theta \sin \theta d\theta d\varphi \right] \quad (4.14a)$$

$$= L_d \left[\frac{\pi}{2} + \frac{1}{2} \int_{\frac{\pi}{2}}^{\frac{3\pi}{2}} \left[\sin^2 \theta \right]_0^{\arctan\left(\frac{-1}{\cos \varphi \tan \theta_n}\right)} d\varphi \right]. \quad (4.14b)$$

It yields¹

$$E_d = \pi L_d \underbrace{\frac{1}{2} \left(1 + \frac{1}{\sqrt{1 + \tan^2 \theta_n}} \right)}_{V_d}, \quad (4.15)$$

where V_d simplifies to the formula largely found in the literature (Kondratyev, 1969; Iqbal, 1983; Sjoberg and Horn, 1983; Hay and McKay, 1985; Perez *et al.*, 1986; Bird and Riordan, 1986; Proy *et al.*, 1989; Bonan, 2002) and is sometimes referred to as the trigonometric approach (Sandmeier and Itten, 1997; Richter, 1998; Shepherd and Dymond, 2003) given by

$$V_d = \frac{1 + \cos \theta_n}{2}. \quad (4.16)$$

From Equation (4.16) it is apparent that the sky-view factor is equivalent to the ratio of the surface defined by the projection onto the horizontal plane of the solid angle subtended by the horizon lines, to that of a unit disk (Figure 4.5). This approach to estimate V_d is called the *unit-sphere method* by Iqbal (1983, pg. 297).

It is suggested here that the interpretation of this method by other authors has led to alternative and sometimes confusing and inappropriate definitions of the sky-view factor. For instance, Corripio (2003, pg. 13) defines the sky view factor as:

“(...) the hemispherical fraction of unobstructed sky visible from any point.”

Sandmeier and Itten (1997, pg. 710) cite Dozier and Marks (1987) and state:

¹This is achieved using:

$$\sin(\arctan a) = \frac{a}{\sqrt{1 + a^2}}$$

$$\int \frac{dx}{a^2 + b^2 \cos^2 x} = \frac{1}{a \sqrt{a^2 + b^2}} \arctan \left(\frac{a \tan x}{\sqrt{a^2 + b^2}} \right), \quad [a > 0]$$

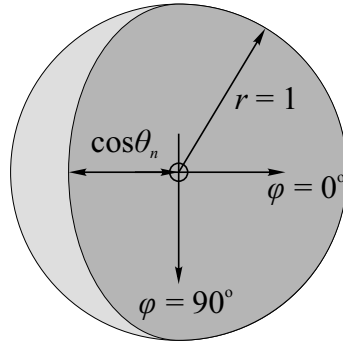


Figure 4.5 V_d computed from the unit-sphere method as the horizontal projection of the portion of sky visible from the point to that of a unit disk (Iqbal, 1983, pg. 297). The ratio between the dark and the light areas is equal to V_d given in 4.16

“(..) V_d defined as the ratio of the sky portion seen from a specific surface to that on an unobstructed horizontal surface (..)”.

Shepherd and Dymond (2003, pg. 3504) loosely define V_d as:

“(..) the fraction of sky seen (..)”.

Finally, Duguay (1993, pg. 342) states more appropriately but without being specific that the sky-view factor is:

“(..) a measure of the portion of the overlying hemisphere visible to a grid point.”

Horizon line approach. To add to the confusion, when Dozier *et al.* (1981) described an efficient horizon algorithm, based on the analysis of a DEM to determine the horizon angle $H(\varphi)$ (Figure 4.3) while accounting for the surrounding topography, they refer specifically to the reduction of diffuse solar irradiance by adjacent slopes. Thus, they suggest the sky-view factor although they define only its complementary part (Dozier *et al.*, 1981, pg. 145):

“(..) the portion of the overlying hemisphere which is obscured by terrain”

as being the ratio of the solid angle comprised between the horizon lines and the horizontal plane, to that of the entire upper hemisphere ($\Omega = 2\pi$):

$$\frac{1}{2\pi} \int_0^{2\pi} \cos H(\varphi) d\varphi. \quad (4.17)$$

When this formulation¹ and its semantic justification is put into perspective with the definitions given above by some authors, it can lead to a false estimation of the sky-view factor as a ratio of the solid angle defined by the horizon lines and that of the upper hemisphere ($\Omega = 2\pi$). Mislead by these unspecific definitions, [Sirguyev et al. \(2009\)](#) wrongly computed the sky-view factor using

$$\begin{aligned} V_d &= \frac{1}{2\pi} \int_0^{2\pi} \int_0^{H(\varphi)} \sin \theta d\theta d\varphi \\ &= \frac{1}{2\pi} \int_0^{2\pi} [1 - \cos H(\varphi)] d\varphi. \end{aligned} \quad (4.18)$$

Instead, when the horizon angles have been determined, to comply with the definition of V_d being the ratio between the diffuse sky irradiance received by the surface (i.e., affected by the topography) to that received by an unobstructed horizontal surface ($\overline{E_d}$), Equation 4.18 must, at least, be modified as follows

$$V_d = \frac{1}{2\pi} \int_0^{2\pi} [1 - \cos^2 H(\varphi)] d\varphi. \quad (4.19)$$

It corresponds to the projection of the potentially complex viewing geometry onto the horizontal plane as illustrated in Figure 4.6 (a). This approach is used by [Corripio \(2003\)](#), although he considerably simplified the calculation by using an average of the horizon angles $[\overline{H(\varphi)}]$ yielding $V_d = \sin^2 \overline{H(\varphi)}$.

Accounting for the local slope and aspect. The determination of horizon angles, using for instance the algorithm of [Dozier et al. \(1981\)](#) or other ray tracing algorithms borrowed from computer graphics (e.g., [Woo et al., 1990](#); [Shirley and Morley, 2003](#); [Policarpo et al., 2005](#)), considerably helped to obtain a more realistic value of V_d because it permitted the skyline to be considered truly, unlike the trigonometric approach that only accounted for the local slope. However, calculating the sky-view factor by projecting horizontally the solid angle subtended by the horizon lines ([Corripio, 2003](#)) is not entirely rigorous since it is equivalent to making the assumption that the surface is horizontal ($\theta_n = 0$).

In a more rigorous manner, the calculation of V_d should account for the local slope (θ_n) and aspect (φ_n) of the elementary surface under consideration (see Figure 4.2). This approach was proposed by [Dozier and Frew \(1990\)](#) and subsequently

¹Note the use of a *cosine* in Equation (4.17) instead of a *sine* given in [Dozier et al. \(1981, pg. 145\)](#) due to the parameterization of the horizon line using zenith angle as shown in Figure 4.3 instead of elevation angle in [Dozier et al. \(1981\)](#).

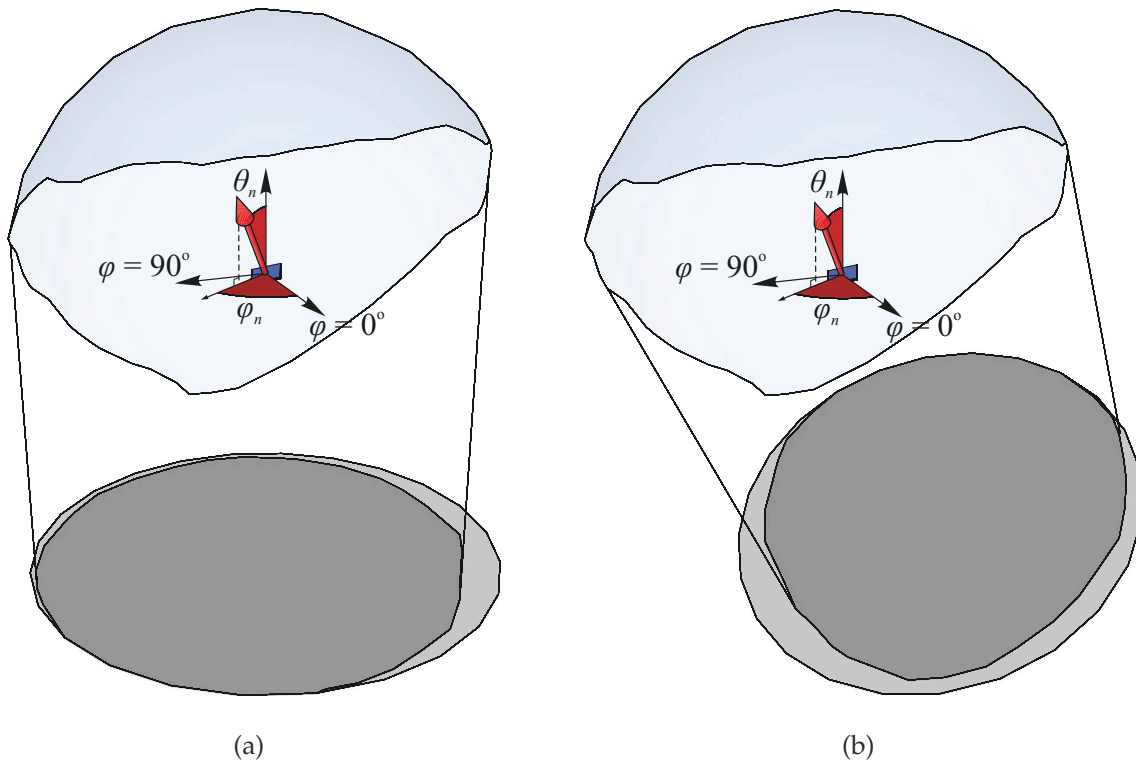


Figure 4.6 Computation of the sky-view factor: (a) ratio of surfaces projected onto the horizontal plane as proposed by [Iqbal \(1983, chap. 10\)](#) and used by [Corripio \(2003\)](#) ($V_d = 0.11$); (b) ratio of surfaces projected onto a plane parallel to the slope as proposed by [Dozier and Frew \(1990\)](#) ($V_d = 0.14$).

used for a more accurate modelling of diffuse radiation in rugged terrain ([Dubayah et al., 1990](#); [Duguay, 1993](#); [Sandmeier and Itten, 1997](#); [Dubayah and Loechel, 1997](#); [Richter, 1998](#); [Garen and Marks, 2005](#); [Chen et al., 2006](#); [Wang et al., 2006](#)). It consists of the modification of Equation (4.9) so that it accounts for the relative orientation between the surfaces dA and dS . Similarly to the illumination angle defined in Equation (4.8), the relative angle Γ between dA and dS is given by

$$\cos \Gamma = \cos \theta_n \cos \theta + \sin \theta_n \sin \theta \cos(\varphi_n - \varphi). \quad (4.20)$$

As for Equation (4.10), it yields an expression of the diffuse irradiance received by the orientated slope which is given by

$$E_d = L_d \int_0^{2\pi} \int_0^{H(\varphi)} \cos \Gamma \sin \theta d\theta d\varphi. \quad (4.21)$$

Substituting Equation (4.11b) into Equation (4.21) yields

$$E_d = \overline{E_d} \frac{1}{2\pi} \int_0^{2\pi} \underbrace{\left[\cos \theta_n \sin^2 H_\varphi + \sin \theta_n \cos(\varphi - \varphi_n) (H_\varphi - \sin H_\varphi \cos H_\varphi) \right]}_{V_d} d\varphi.$$

Again, the sky-view factor can be computed by the ratio of two projected surfaces, namely the projection of the solid angle subtended by the viewing geometry and the area of a disk of radius 1 (π). Unlike the earlier approach that corresponded to a projection onto the horizontal plane, this approach is equivalent to a projection onto the plane that is parallel to the slope, as shown in Figure 4.6 (b). In this illustration, the same viewing geometry as depicted in Figure 4.3 is used to compute V_d using the two approaches (i.e., ignoring and accounting for the local slope and aspect, respectively). It shows a variation of V_d of more than 20% as would be the variation of estimation of E_d . Therefore, it stresses the importance of estimating this parameter by accounting for the local slope and aspect using Equation (4.22).

4.3.2.2 Terrain configuration factor

The terrain configuration factor C_t ($0 \leq C_t < 1$) is the counterpart of the sky-view factor V_d . As the sky-view factor measures the fraction of the sky that is visible from the point, the terrain configuration factor measures the fraction of the surrounding terrain that is within the field of view of a target. It is used to estimate the reflected terrain irradiance E_t (see Section 4.3.4) and can be defined as the ratio of the irradiance at a point that originates from surfaces that are visible from it, to the exitance reflected effectively by these surfaces under the assumption that they are Lambertian with reflectance ρ_t and exposed to the same global irradiance E_g . This yields

$$E_t = \rho_t C_t E_g. \quad (4.22)$$

Since the assumption of the surrounding terrain being lambertian and having the same reflectance wherever it is visible from the point is unlikely to be met, and since all surfaces are clearly exposed to varying global irradiance, this formulation is a great simplification of reality. Nevertheless, it is a useful way to accommodate the geometry and the complexity of the nearby slopes, but keeping the computation manageable.

In these conditions, the radiance emitted by all elementary surface of the terrain is $\frac{\rho_t E_g}{\pi}$. The irradiance originating from the terrain received by a point is the integral of the radiance over all angles that correspond to a line of sight between the

point and the terrain. When accounting for the local slope and aspect at the point, the limits of the inner integral [Equation (4.24)] are from the horizon angle [$H(\varphi)$] downwards to where a ray is parallel to the slope (Dozier and Frew, 1990). This cutting angle $\Psi(\varphi)$ is smaller than $\frac{\pi}{2}$ in the upslope direction and greater in the down slope direction. Using Euler's decomposition of angles it can be shown that

$$\Psi(\varphi) = \arctan [\tan \theta_n \cos(\varphi - \varphi_n)] + \frac{\pi}{2}. \quad (4.23)$$

Thus, the irradiance received from the surrounding terrain is

$$E_t = \rho_t E_g \underbrace{\frac{1}{\pi} \int_0^{2\pi} \int_{H(\varphi)}^{\Psi(\varphi)} \cos \Gamma \sin \theta d\theta d\varphi}_{C_t}. \quad (4.24)$$

Using Equations (4.20) and (4.23) in (4.24) yields

$$\begin{aligned} C_t = & \frac{1}{2\pi} \int_0^{2\pi} \left[\cos \theta_n \left(\frac{1}{1 + \tan^2 \theta_n \cos^2(\varphi - \varphi_n)} - \sin^2 H_\varphi \right) + \right. \\ & \cos(\varphi - \varphi_n) \sin \theta_n \left[\arctan [\tan \theta_n \cos(\varphi - \varphi_n)] + \frac{\pi}{2} - H_\varphi \right. \\ & \left. \left. + \frac{\tan \theta_n \cos(\varphi - \varphi_n)}{1 + \tan^2 \theta_n \cos^2(\varphi - \varphi_n)} + \sin H_\varphi \cos H_\varphi \right] \right] d\varphi. \end{aligned} \quad (4.25)$$

Dozier and Frew (1990) did not carry out the calculation of this integral and suggested that C_t may be written as

$$C_t \approx \frac{1 + \cos \theta_n}{2} - V_d. \quad (4.26)$$

They justified this approximation without providing more explanation than:

“We therefore note that V_d for an infinitely long slope is¹ $\frac{1 + \cos \theta_n}{2}$, which leads to the approximation (...)” (Dozier and Frew, 1990, pg. 965).

However, this formula contradicts Iqbal (1983, pg. 297) who demonstrated that configuration factors are additive and if an elementary surface is totally enclosed by mutually exclusive surfaces, the sum of the configuration factors between each surface and the one under consideration is equal to 1. This is the enclosure equation (Iqbal, 1983, Equation 10.2.8). Clearly, when considering a point and a line of sight that is not drawn towards the sky, then it must intercept the terrain, and reciprocally, proving that both surfaces of the upper dome are exclusive (i.e., the surface associated with the portion of the sky and the portion of the surrounding terrain

¹This is demonstrated in Equation (4.16).

visible from the point, respectively). Therefore, according to [Iqbal \(1983\)](#), C_t and V_d must be complementary to 1:

$$C_t = 1 - V_d. \quad (4.27)$$

An analytical integration of Equation (4.25) is provided in Appendix D which confirms Equation (4.27) in the sense of [Dozier and Frew's \(1990\)](#) method of calculation. Thus, it is shown that there is no serious basis for using Equation (4.26), and hence Equation (4.27) must be always preferred to it.

4.3.2.3 Computation

Horizon lines must be computed in a discrete number of azimuths. Although [Dozier et al. \(1981\)](#) suggested that 32 directions were sufficient to obtain a good estimation of the sky-view factor, 64 directions are preferred as this provides a more detailed representation of obstructions. In particular, this larger number of directions is desirable to achieve a more accurate representation of shadows (see Section 4.3.3). In order to limit the artefacts that may occur due to the spatial resolution of the DEM ([Richter, 1998](#)), the horizon angles, maps of sky-view factor, and terrain configuration factors can be first computed with the 125m spatial resolution DEM and aggregated at 250m and 500m spatial resolution using a mean operator. Figure 4.7 illustrates these two parameters and their range of magnitude in the area.

4.3.3 Shadows

4.3.3.1 Self and cast shadows

Self shadows and cast shadows affect the radiation budget in mountainous terrain by blocking the direct solar irradiance (Figure 4.8). Self-shadows account for slopes facing away from the solar rays. They are readily identified by the negative cosine of their illumination angle ($\cos \gamma \leq 0$). Cast shadows are areas where the direct sun illumination is blocked by surrounding ridges or clouds. Shadows induced by clouds are complicated to correct because they create total or partial shadowing that is difficult to identify in the image and complicated to model ([Richter and Müller, 2005](#); [Khlopenkov and Trishchenko, 2007](#)). Nevertheless, cast shadows due to surrounding terrain can be modelled deterministically through the analysis of the DEM with the horizon line algorithm used in Section 4.3.2.1, and the local sun elevation and azimuth provided in the MODIS MxD03 product. Simply, a pixel is cast

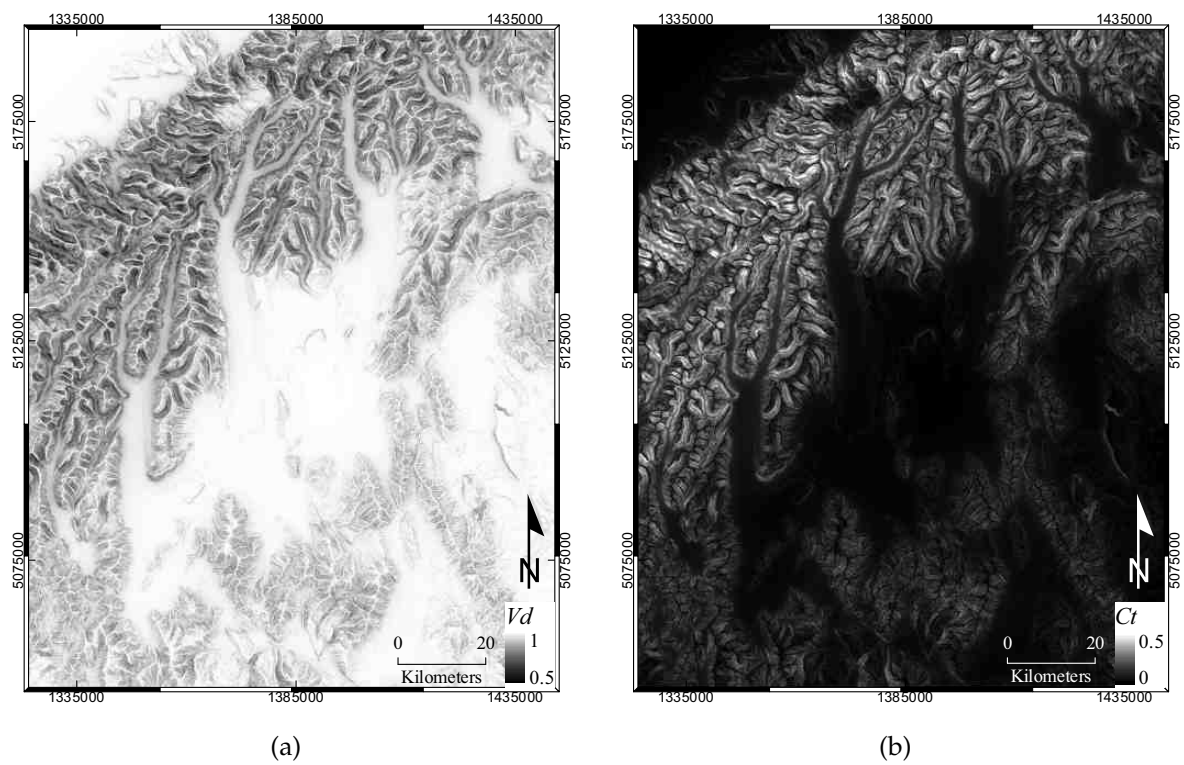


Figure 4.7 Topographic parameters in the study area: (a) sky-view factor V_d and (b) Terrain configuration factor C_t .

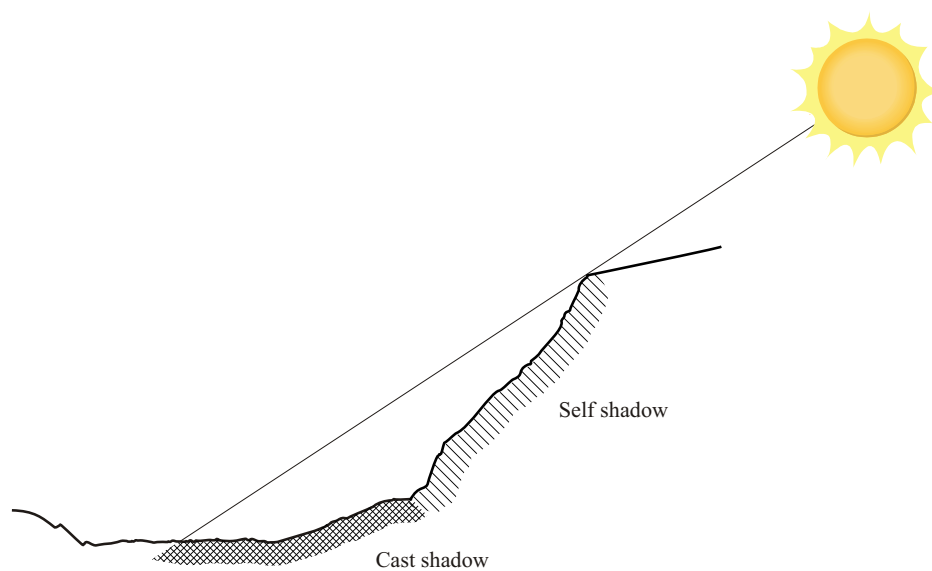


Figure 4.8 Self and cast shadowing in rugged terrain.

shadowed when the horizon angle in the direction of the solar azimuth is smaller than the solar zenith angle [$H(\varphi_s) < \theta_s$].

Ten MODIS images acquired at different times of the year were investigated to assess the binary mapping of shadows by comparing their position and extent depicted in the corresponding orthorectified ASTER images. Visual analysis showed that the shadow maps are affected by numerous misclassifications that would lead to unacceptable over- and under-corrected pixels. Indeed, shadows strongly rely on the DEM and its first-order derivatives (i.e., slope and aspect), which are affected in turn by its spatial resolution (Kienzle, 2004). Thus, slight variations of the slope and aspect of the terrain tend to introduce noise in the representation of cast shadows when the horizon line in the direction of the solar azimuth runs close to the slope. Two such examples of noisy maps of cast shadow computed in a relatively difficult configuration are illustrated in Figures 4.9 & 4.10 (b). This issue is easily addressed by computing a slightly larger map of cast shadow (i.e., assuming the sun to be slightly lower) followed by a binary erosion. The filtering effect of this morphological operation (Pratt, 1991) results in the removal of spurious isolated pixels as shown in Figures 4.9 & 4.10 (c). The union of both maps of cast and self shadow [Figures 4.9 & 4.10 (c) & (e), respectively] provides the total shadow mask.

4.3.3.2 Fractional shadow map

Usually ‘shadowed’ and ‘non-shadowed’ pixels are binary classified at the same spatial resolution relative to the image to be corrected (Sjoberg and Horn, 1983; Duguay, 1993; Sandmeier and Itten, 1997; Dubayah and Loechel, 1997; Richter, 1998; Shepherd and Dymond, 2003; Chen *et al.*, 2006). Thus, the coefficient b [in Equations (4.4) and (4.7)] is either 1 or 0, with 1 corresponding to a pixel free of shadow and 0 to a pixel fully shadowed. However, the accurate representation of shadows is strongly compromised when the spatial resolution of the DEM becomes comparable with the range of elevations found in the image. For instance, a coarse DEM tends to erode peaks and ridges and smooth slopes, leading to possible misrepresentations of shadows. Moreover, the spatial resolution of MODIS (250m) facilitates mixtures of shadowed and non-shadowed targets within a single pixel.

Ideally, the computation of shadows should take advantage of a DEM provided at a much finer spatial resolution to achieve a highly detailed representation of shadows. Thus, it becomes feasible to account better for possibly mixed shadowed and non-shadowed targets within MODIS pixels by calculating the fraction of

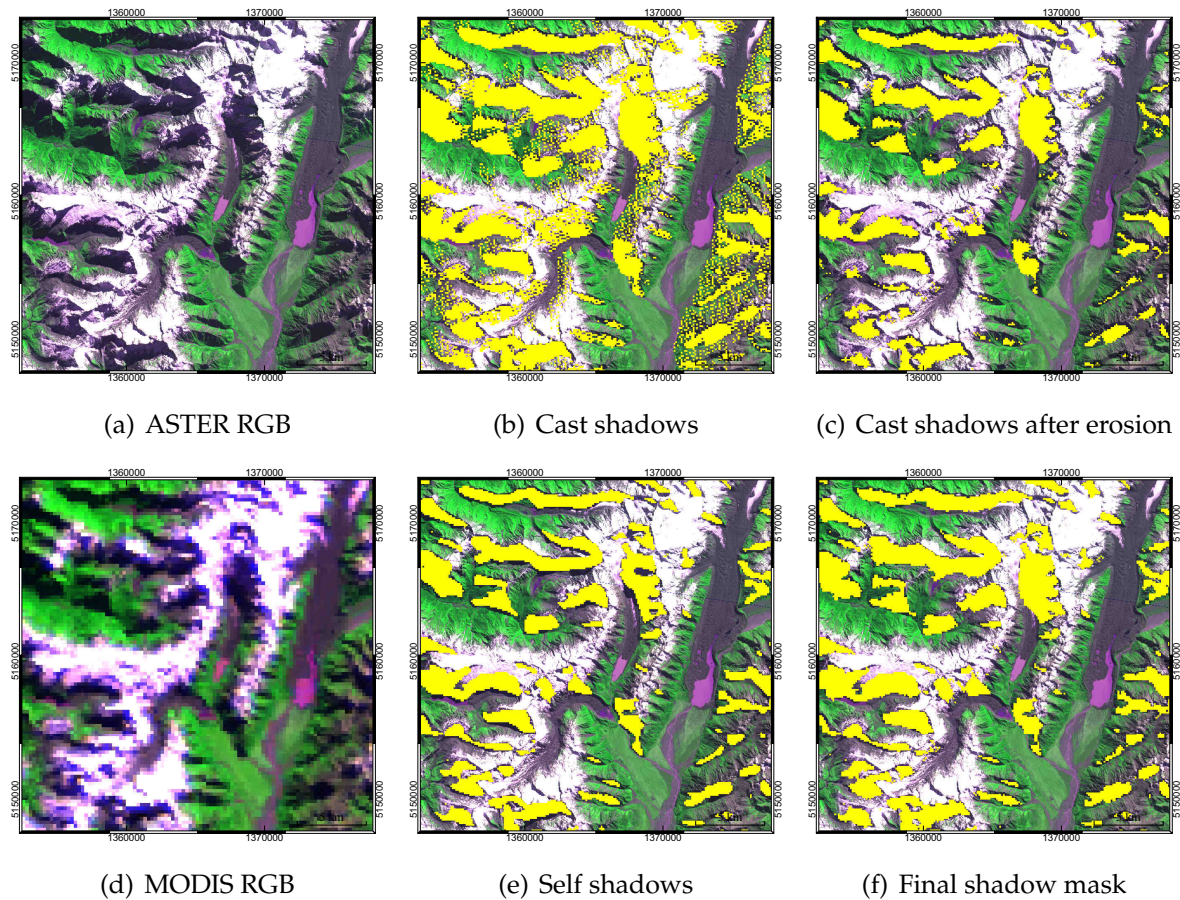


Figure 4.9 Example of computation of shadows (7 April 2001, 22:53 GMT): (a) False colour RGB composite from ASTER bands 2, 3, and 1; (b) Cast shadow computed at 125m spatial resolution; (c) Removing of spurious pixels by erosion; (d) False colour RGB composite from MODIS bands 1, 2 and 3; (e) Self shadow computed at 125m spatial resolution; (f) Final binary shadow mask.

the pixel that is really shaded. This is easily done by aggregation using a mean operator of the binary shadow mask computed at a finer spatial resolution relative to the pixel size of MODIS. In practice, the computation of horizon lines for all elements of the terrain becomes quickly resource consuming and a compromise must be found in terms of the finest spatial resolution that can be achieved for the binary shadow mask with regard to the size of the image. Here, a finer representation of shadows at 125m spatial resolution could be achieved. Aggregated maps of subpixel fraction of shadow were obtained from this at 250m and 500m spatial resolution by averaging the 125m pixels (e.g., at 250m spatial resolution, $b \in \{0, 0.25, 0.5, 0.75, 1\}$ from a pixel fully shadowed to a pixel free of shadow).

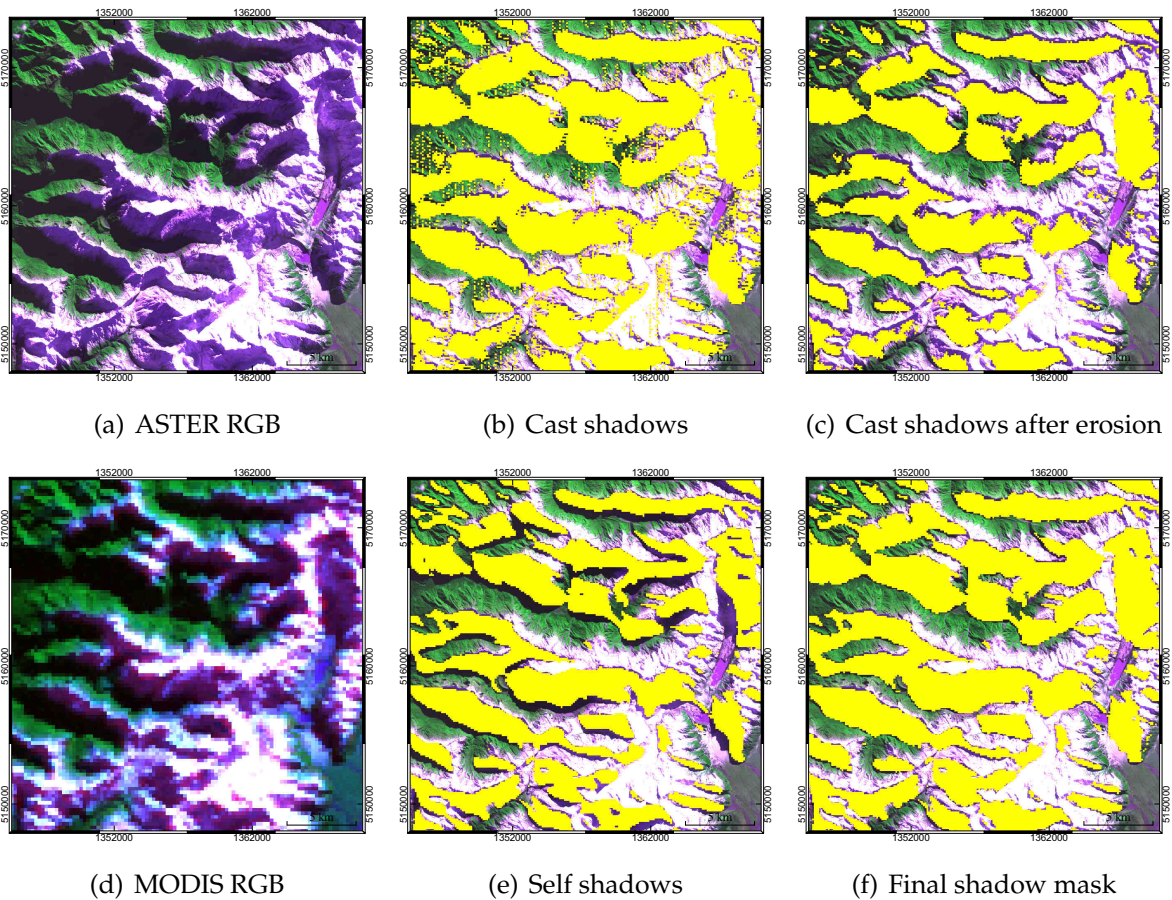


Figure 4.10 Example of computation of shadows (5 May 2006, 22:35 GMT): (a) False colour RGB composite from ASTER bands 2, 3, and 1; (b) Cast shadow computed at 125m spatial resolution; (c) Removing of spurious pixels by erosion; (d) False colour RGB composite from MODIS bands 1, 2 and 3; (e) Self shadow computed at 125m spatial resolution; (f) Final binary shadow mask.

4.3.3.3 Final cleaning

Despite all efforts to represent shadows satisfactorily, misclassifications remained due to the coarseness and inaccuracies of the DEM. Omission errors (false negative, i.e., a pixel wrongly classified as non-shadowed) result in severely underestimated ground reflectance but are difficult to address. In such a case, the failure of the deterministic geometric approach should be addressed by a fundamentally different strategy, most likely based on spectral considerations (Simpson and Stitt, 1998; Ackerman *et al.*, 1998; Luo *et al.*, 2008). It is argued that a spectral approach for detecting shadows in mountainous terrain covered by snow is impracticable due to the large variation of spectral signatures that can potentially be encountered in shad-

ows whether the terrain is snowy or free of snow. Indeed, the apparent reflectance of shaded snow can sometimes be similar or larger than the apparent reflectance of some types of land cover in the sunlight (e.g., coniferous forest, dark rock debris). Such overlaps would doubtless create confusion if the shadows were to be detected using spectral tests based on ratios and/or thresholds, therefore jeopardizing the efficiency of such a strategy.

Commission errors (false positive or false alarm, i.e., a pixel classified as shaded while sunlit) lead to over-estimated ground reflectance that is problematic because over-corrected pixels may be confused with snow in the subsequent classification. Nevertheless, such confusions are practically addressed using an empirical threshold applied to the reflectance at the top of the atmosphere. This simply aims to reclassify pixels mapped as ‘shadowed’, but more likely to be ‘non-shadowed’ due to their relatively high reflectance. MODIS band 2 ($\lambda = 858$ nm) is a relevant candidate to use for this strategy because the relatively high reflectance of most natural targets (except water) in the Near Infrared (NIR), and the weakness of the diffuse irradiance, provides a good contrast between shadowed and non-shadowed areas. The threshold was weighted according to the NDSI to account for the possible presence of snow in shadow which would provide a substantial radiance. Finally, a pixel originally classified as ‘shadow’ was reclassified as ‘non-shadow’ if

$$\begin{cases} \rho_{0.86}^* \geq 0.05 + 0.2 \times \text{NDSI} & \text{if } \text{NDSI} \geq 0 \\ \rho_{0.86}^* \geq 0.05 & \text{if } \text{NDSI} < 0. \end{cases} \quad (4.28)$$

4.3.4 Reflected terrain irradiance¹

The multiple reflexions of radiation between a target and the surrounding slopes increases the total irradiance that reaches a location, and therefore the upwelling radiance received by the sensor (Shoshany, 1989; Chen *et al.*, 2006). By being related to the reflective properties of the surrounding terrain and the configuration of the local topography, it is widely acknowledged that this extra radiation may become significant in the case of steep terrain and highly reflective targets such as in a snowy environment. For instance, Dozier (1980) estimated the terrain reflected radiation to contribute on average 17% of global radiation with a maximum of 66% for a partly snow-covered study site. In alpine areas covered by snow, Proy *et al.* (1989)

¹The content of this sub-section is published in: Sirguey, P. (2009). Simple correction of multiple reflection effects in rugged terrain. *International Journal of Remote Sensing*, 30(4), 1075–1081, doi: 10.1080/01431160802348101

estimated that the effects of terrain reflected irradiance can reach 24% of the total irradiance received by a surface. In his review of radiation modelling in mountainous terrain, [Duguay \(1993, pg. 344\)](#) also stated that:

“(.. .) failure to account for terrain-reflected irradiance in snow-covered mountain areas could result in serious computational errors of global solar irradiance estimates.”

The use of a 3-D radiative transfer and a DEM could theoretically achieve an accurate and deterministic estimation of the reflected terrain radiation reaching a pixel by considering the multiple scattering between a target and its environment ([Chen et al., 2006](#)). Such exact computation must consider the irradiance that originates from all surfaces that are visible from the pixel, along with their respective relative geometry, distance, and eventually BRDF. This is a formidable calculation challenge that is largely out of reach of the computing power available to most users of satellite imagery. Hence, in order to be tractable, operational algorithms usually implement an empirical first-order reflection model, along with neighbourhood simplifications ([Dubayah and Loechel, 1997](#); [Sandmeier and Itten, 1997](#); [Richter, 1998](#); [Shepherd and Dymond, 2003](#); [Wang et al., 2006](#)).

4.3.4.1 First-order approximation

The first-order approximation assumes that, at iteration i , a fraction of the global irradiance over a horizontal surface $E_g^{(i)} = E_s \cos \theta_s + E_d + E_m^{(i)}$ (direct beam plus diffuse sky irradiance) is only reflected once by the surrounding terrain of mean reflectance $\bar{\rho}_t^{(i-1)}$ (computed from the reflectance values obtained from the previous iteration), in the direction of the pixel under consideration, and modulated by its terrain configuration factor C_t . This leads to the expression of the reflected terrain irradiance $E_t^{(i)}$ given by

$$E_t^{(i)} = \bar{\rho}_t^{(i-1)} C_t E_g^{(i)}, \quad (4.29)$$

where $\bar{\rho}_t^{(i)}$ is updated at each iteration i from the map of pixel reflectance [i.e., computed using Equation (4.7)], by means of a moving window average with size set arbitrarily according to the expected influence of the adjacency effect, and represents 0.5–1 km in ATCOR3 ([Richter, 1998](#)). Here R_1 is set to 1 km (see Figure 4.1).

4.3.4.2 Multiple reflections model

Higher-order reflections between adjacent slopes are usually neglected, as they are assumed to be a small contribution relative to direct and diffuse flux ([Proy et al.,](#)

1989; Dubayah and Loechel, 1997). In flat terrain, however, the mechanisms of multiple reflections of radiation between the Earth's surface and the atmosphere are commonly addressed (Tanré *et al.*, 1979; Vermote *et al.*, 1997). This leads to the formulation of the diffuse environmental irradiance E_m addressed later in Section 4.4.2.1. In cases of very rugged terrain (high values of C_t) with highly reflective targets (high values of $\bar{\rho}_t$), it is reasonable to expect that this effect will play a similar role by successively adding the reflected radiation up to a significant contribution. The first-order approximation given in Equation (4.29) may thus become insufficient to represent accurately the whole part of the reflected terrain radiation, and can lead to overestimation of the ground reflectance.

Thus, in mountainous terrain, the trapping mechanism of radiation, within the neighbourhood of a pixel, consists of the neighbourhood receiving a portion of its own reflected radiation. The simplified approach based on the terrain configuration factor C_t can still be used to account for this mechanism. The radiation can be formulated as being successively reflected by the terrain of mean reflectance $\bar{\rho}_t^{(i-1)}$, and modulated by the mean configuration factor \bar{C}_t . Radiation having interacted n times between adjacent slopes and the pixel under consideration can then be written as

$$E_{t,n} = \left(\bar{\rho}_t^{(i-1)}\right)^n \bar{C}_t^{n-1} E_g^{(i)}. \quad (4.30)$$

The pixel under consideration thus receives only a fraction of all this radiation due to its own C_t , and the total contribution of the multiple reflections of radiation between the pixel and its surrounding can be written as the geometric series

$$E_t^{(i)} = \bar{\rho}_t^{(i-1)} C_t E_g^{(i)} \sum_{k=0}^{\infty} \left(\bar{\rho}_t^{(i-1)} \bar{C}_t\right)^k, \quad (4.31)$$

which converges to

$$E_t^{(i)} = \frac{\bar{\rho}_t^{(i-1)} C_t}{1 - \bar{\rho}_t^{(i-1)} \bar{C}_t} E_g^{(i)}. \quad (4.32)$$

Both the first-order model and the multiple reflections model are critically assessed in Section 4.5.3.

4.4 Atmospheric model

Atmospheric effects such as Rayleigh and aerosol scattering as well as gaseous and aerosol absorption must be accounted for to compute Equation (4.7) [e.g.,

sun-to-ground transmittance $T_s = T(z, \lambda, \theta_s)$, ground-to-sensor transmittance $T_v = T(z, \lambda, \theta_v)$, diffuse solar irradiance on a horizontal surface E_d , diffuse environmental irradiance E_m , and atmospheric intrinsic radiance L_p]. The use of an atmospheric radiative model is also justified by the very rugged nature of the terrain in the study area and the dramatic effects of the topography on the imagery. In such an environment, shadowing probably is the biggest issue when seeking to normalize reflectance values, because of the much lower level of the diffuse sky irradiance compared to the direct sunlight, as well as the great difference in terms of spectral distribution. Atmospheric models with various degrees of sophistication exist that are able to provide estimations of the required quantities. These can be grouped into two categories, namely radiative transfer models and atmospheric transmittance model.

- *Radiative transfer codes* are “exact” or “rigorous” approaches in the sense that they use computational methods to solve the integro-differential transfer equation of the radiation field in a heterogeneous atmosphere (Chandrasekhar, 1960; Lenoble, 1985, chap. 1 in both), generally divided into a discrete number of layers, while accounting for the coupling between absorption and scattering of light by its constituents (i.e., molecules and aerosols). For example, in the context of the correction of remotely sensed imagery, MODTRAN (Berk *et al.*, 1998) has been largely used for the correction of the Airborne Visible/Infrared Imaging Spectrometer (AVIRIS) and implements the method of Discrete Ordinates ascribed to Chandrasekhar (1960, Chap. 2) and made computationally effective by Stamnes *et al.* (1988) (Discrete Ordinates Radiative Transfer Program for a Multi-Layered Plane-Parallel Medium, or DISORT). Alternatively, 6S (Vermote *et al.*, 1997) provides the method of Successive Orders of Scattering (Lenoble, 1985, chap. 2), and has found an operational application for the atmospheric correction of MODIS data (Vermote *et al.*, 1997, 2002).
- *Transmittance models* aim for more simplicity by assuming that gaseous absorption can be de-coupled from scattering as if all absorbing constituents were above the atmosphere. Thus, the atmosphere is considered as a homogenous single layer medium whose transmittance is commonly expressed as the product of the transmittances attributed to Rayleigh scattering T_r , water vapour absorption T_w , ozone absorption T_o , uniformly mixed gas absorption T_u , and aerosol absorption and scattering $T_a = T_{aa}T_{as}$ (see subsequent sections for a

description of each component). This relation is expressed as follows:

$$T(z, \lambda, \theta) = T_r T_w T_o T_u T_a. \quad (4.33)$$

Each transmittance is calculated by means of Bouguer-Lambert-Beer's law¹ which states that the intensity of light transmitted through a layer decays exponentially with respect to the distance traversed in the medium l :

$$T = e^{-\sigma_e l}, \quad (4.34)$$

where σ_e is the extinction coefficient that accounts for the concentration of the absorbing species. $\tau = \sigma_e l$ is called the optical depth when it refers to a vertical path. Under oblique illumination ($\theta_s > 0$), the optical depth is multiplied by the airmass factor to account for the longer path caused by the solar zenith angle and the atmospheric refraction. The practical use of transmittance models is achieved by the mean of parameterization such as that of [Leckner \(1978\)](#) or developed by other authors for which a useful comparison is given in [Iqbal \(1983, Chap. 7\)](#). Parameterization models have the advantage over the rigorous radiation transfer approach in that they permit a rapid estimation of the incident radiation under specified atmospheric conditions.

Despite their availability, rigorous codes such as 6S² can be difficult to implement into a routine process because they require detailed inputs and a relatively long execution time. For example, interfacing 6S into the MATLAB[®] environment required close to 0.1 s for the computation of a single solution of the radiative transfer with an AMD Athlon™64 at 3.2GHz equipped with 2GB RAM. Under these conditions, the correction of all pixels of a MODIS image at 250m spatial resolution (for an area of 600 rows and 480 columns, and 7 spectral bands) would need 56 h of computing time. This is a limiting factor to its operational use from the perspective of a near daily dataset. Such difficulty of implementation is often overcome by the

¹The law was empirically determined by [Bouguer \(1729, 1760\)](#), theoretically modelled by [Lambert \(1760\)](#), and extended to include the concentration of absorbing species in the layer by [Beer \(1852\)](#). Some controversy still exists with regard to whom the law should be ascribed to and relevant material to elucidate this debate can be found in [Middleton \(1964\)](#), [Iqbal \(1983, pg. 164\)](#), and [Tagirov and Tagirov \(1997\)](#).

²The scalar version of 6S is freely available on <ftp://kratmos.gsfc.nasa.gov/pub/6S/>; its recently released vector version can be found on <ftp://kratmos.gsfc.nasa.gov/pub/eric/6S/>. MODTRAN is not free and can be ordered from <http://www.kirtland.af.mil/library/factsheets/factsheet.asp?id=7915>, last retrieved in November 2008.

preliminary computation of large Look Up Tables (LUT) using the radiative transfer code, with pre-defined conditions of water vapour content, aerosol types and loading, ground elevation, source and sensor geometry (Nunes *et al.*, 2008). In ATCOR3 for instance, Richter (1998) used MODTRAN to compile the LUT, while the routine calculation of MODIS ground reflectance product (MxD09) was performed using a LUT compiled with 6S (Vermeulen and Vermote, 1999; Kotchenova *et al.*, 2008). The subsequent correction was processed by determining the adequate value for the pixel by interpolation from the multidimensional LUT. This achieves an operation which can be performed much faster than by computing individual spectra.

The acceptable performance of simple parameterization methods compared to the exact solution from radiative transfer code (de La Casinière *et al.*, 1997) probably explains the success of this approach, whether it is used for the estimation of the total quantity of radiant energy integrated over a wide spectrum (Alados-Arboledas *et al.*, 2000; Wang *et al.*, 2006) or for the correction of optical sensor spectral bands in the reflective part of the spectrum (Wu *et al.*, 2005; Kobayashi and Sanga-Ngoie, 2008). In the context of implementing a routine algorithm into MATLAB[®], the use of a transmittance model is justified as it allows computation of the required radiative quantities, as well as transmittance values, for each pixel of the image using simple matrix operations within a reasonable time. Thus, the SPECTRAL2 model (Bird and Riordan, 1986) was considered and is described in the subsequent sections. Nevertheless, a careful evaluation of the quality of the model outputs was conducted with regard to the 6S code to assess its correct implementation, general performances, and necessary adaptation.

4.4.1 SPECTRAL2 constituents

4.4.1.1 Rayleigh scattering

Rayleigh scattering is due to particles whose size is small compared to the wavelength (diameter $\ll 0.2\lambda$). Thus, in the reflective part of the electromagnetic spectrum, Rayleigh scattering can be attributed to the interaction of photons with gaseous molecules constituting the medium. It is selective (i.e., wavelength dependent) and symmetrical (i.e., the amount of light scattered in the backward direction is equal to that in the forward direction, as shown in Figure 4.11).

The extinction coefficient due to Rayleigh scattering is approximately inversely proportional to the fourth power of the wavelength and directly proportional to the

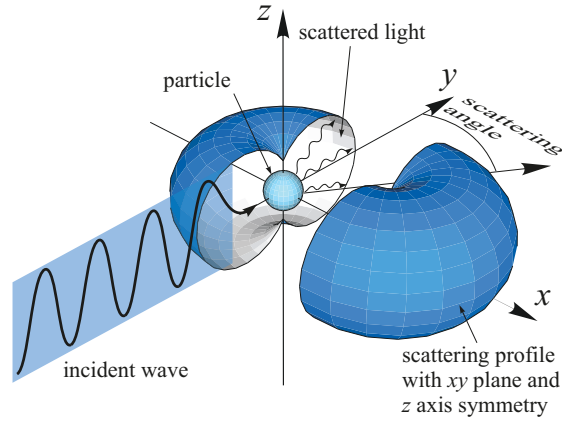


Figure 4.11 Phase function for Rayleigh scattering.

density of atmospheric molecules (Iqbal, 1983). The atmospheric transmission due to Rayleigh scattering is modelled more accurately by Bird and Riordan (1986) who suggested an expression of the form

$$T_r(z, \lambda, \theta) = e^{-\frac{M'(z, \theta)}{\lambda^4(115.6406 - 1.335/\lambda^2)}}. \quad (4.35)$$

This accounts for the pressure-corrected optical air mass $M'(z, \theta) = M(\theta)p(z)/p_0$, where $M(\theta)$ is the relative optical air mass, $p_0 = 1013$ mb and $p(z)$ is the surface pressure in [mb] at the elevation z . The empirical expression of Kasten and Young (1989) was used to estimate the relative optical air mass as follows

$$M(\theta) = \frac{1}{\cos \theta + 0.50572(96.07995 - \theta)^{-1.6364}}, \quad (4.36)$$

where θ is either the solar zenith angle θ_s , when accounting for the sun-to-ground transmittance or the sensor zenith angle θ_v , when accounting for the ground-to-sensor transmittance. The decline of the surface pressure with increasing elevation is efficiently computed using the DEM and the following barometric formula (NASA, 1976):

$$p(z) = p(z_0) \left[1 - \frac{0.0065 \cdot (z - z_0)}{t(z_0) + 273.15} \right]^{5.256}, \quad (4.37)$$

where $p(z_0)$ and $t(z_0)$ are the pressure [mb] and temperature [$^{\circ}\text{C}$], respectively, measured by an automatic weather station managed by NIWA at Mount Cook Village (43.736 S, 170.096 E, $z_0 = 765\text{m}$, see location in Figure 2.1) at the time of the image acquisition.

4.4.1.2 Water vapour absorption

Water vapour is one of the main gases affecting the transmission of radiation through the atmosphere and can reduce the signal measured by the sensor by more than 10% in the NIR and shortwave infrared (SWIR) (Vermote *et al.*, 1997). It is possible to estimate the spatial distribution of the water vapour column directly from MODIS images. Thus, maps of water vapour are distributed as Level 2 data in MxD05 Water Vapour products (Gao and Kaufman, 2003). Nevertheless, since the routine algorithm developed for this thesis relied on MODIS L1B data, it permitted the water vapour retrieval algorithm to be implemented.

The two-channel ratio method described in Gao and Kaufman (2003) was selected. It relies on the difference between the reflectance in the water vapour transmission band (band 2 centred at 865 nm) and that in water absorption bands (band 17, 18, and 19 at 905, 935, and 940 nm, respectively). The correct implementation of this algorithm was assessed by comparing maps of water vapour derived in this thesis to the MxD05_L2.V004 Water Vapour data product at four different dates, with total water vapour column in the range of 0–3 cm. The analysis of the relative error resulted in an overall bias of -0.5% and RMSE of 9.7% compared to the original MODIS product. The discrepancies could be attributed to the use of the two-channel ratio method over clear sky targets, instead of the three-channel ratio used in the original MODIS product. Nevertheless, the magnitude of the discrepancies remained within the expected error of 13% predicted for the MxD5 product. This demonstrated that acceptable performances were achieved by the algorithm.

The water vapour transmittance was estimated using the expression of Leckner (1978) and absorption coefficients¹ $a_w(\lambda)$ adapted by Bird and Riordan (1986):

$$T_w(\lambda, \theta) = e^{-\frac{0.2385a_w(\lambda)WM(\theta)}{[1+20.07a_w(\lambda)WM(\theta)]^{0.45}}}, \quad (4.38)$$

where W is the precipitable water vapour [cm] derived for each MODIS pixel. Note that the optical air mass used in Equation (4.38) is not pressure-corrected because W is directly estimated at the ground surface.

4.4.1.3 Ozone absorption

Ozone absorption was estimated with Leckner's (1978) ozone transmittance equation and absorption coefficients¹ $a_o(\lambda)$:

$$T_o(\lambda, \theta) = e^{-a_o(\lambda)O_3M_o(\theta)}, \quad (4.39)$$

¹The table of absorption coefficients is provided in Appendix E.

where O_3 is the total ozone amount [atm-cm], and M_o the ozone optical air mass given by [Staelin *et al.* \(1995\)](#):

$$M_o(\theta) = \frac{R + h_o}{[(R + h_o)^2 - (R \sin \theta)^2]^{1/2}}, \quad (4.40)$$

where R is the mean radius of earth, and h_o is the altitude of the maximum ozone concentration ($h_o = 22$ km). Daily measurements of the total ozone column that potentially affect MODIS bands 1, 3–4 were obtained from Lauder station, New Zealand (LDR), which operates a Dobson Ozone spectrophotometer and is situated very near to the study area (45.0 S, 169.7 E). A near complete record from February 1987 to December 2005 is available from the Ozone & Water Vapour Group (OZVW¹). This dataset was incomplete for 2006, but missing data were obtained from the daily estimations of the tropospheric ozone measured by the Ozone Monitoring Instrument (OMI²) since August 2004. Simultaneous measurements from both OMI and LDR were available for 300 days. The mean difference between both estimates was found to be 1.1 DU (1 Dobson Unit = 0.001 atm-cm), while the standard deviation was 7.2 DU. This corresponded to only 1 to 2 percent of the total ozone amount generally found in the region. In consequence, the ozone measurements were retrieved at LDR and both measurements were averaged when available. It was assumed that this unique value was suitable to be applied for the entire study area due to its limited size and relative proximity to the measurement site.

4.4.1.4 Uniformly mixed gas absorption

Among the various species of gases that constitute the atmosphere and have not yet been accounted for, dioxygen (O_2), carbon dioxide (CO_2), methane (CH_4), and nitrous oxide (N_2O) are the principal remaining absorbers in the solar spectrum ([Vermote *et al.*, 1997](#)). Nevertheless, their concentration in the atmosphere is not as variable as water vapour and ozone. Thus, they are commonly dealt with by atmospheric models as if they were of constant concentration and uniformly mixed in the atmospheric layer ([Vermote *et al.*, 1997](#); [Iqbal, 1983](#), pg. 128). With regard to parametric models, [Leckner \(1978\)](#) empirically determined tabulated coefficients³ $a_u(\lambda)$ that combined both the gaseous amount and absorption properties and suggested that the transmission for uniformly mixed gas may be written as follows:

$$T_u(z, \lambda, \theta) = e^{-\frac{1.41a_u(\lambda)M'(z,\theta)}{[1+118.93a_u(\lambda)M'(z,\theta)]^{0.45}}}. \quad (4.41)$$

¹<http://www.esrl.noaa.gov/gmd/ozwv/>, last retrieved in November 2008.

²http://toms.gsfc.nasa.gov/teacher/ozone_overhead_v8.html, last retrieved in November 2009.

³The table of absorption coefficients is provided in Appendix E.

4.4.1.5 Aerosol absorption and scattering

Unlike Rayleigh scattering, Mie scattering occurs when electromagnetic waves interact with particles whose size is of the order of the wavelength. In the reflective part of the solar spectrum, such particles are typically aerosols such as smoke, dust, or ocean sprays. This type of scattering is strongly anisotropic and characterized by a dominating forward component. It means that the incident radiation is scattered mostly in the direction of propagation within a relatively closed angle. In reality, scattering may occur in all directions with more or less probability. It is measured by the phase function $p(\vec{r}, \vec{\Omega}, \vec{\Omega}')$, which is defined as the probability density function for an incoming radiation received from direction $\vec{\Omega}$ to be scattered in direction $\vec{\Omega}'$ at the location identified by the coordinate vector \vec{r} . p is often normalized so that its integration over the enclosing sphere is either 1 or 4π (Liu, 1994; Lenoble, 1985, pg. 6). It varies with the particle size and shape so that bigger particles will generally result in stronger forward component, while smaller and smaller particles will have their phase function progressively approach that of Rayleigh scattering (Figure 4.11).

Figure 4.12 (a) illustrates an extreme case of Mie scattering where the phase function would be mostly reduced to a condensed forward envelope (e.g., such as the scattering of an incoming wave at 550 nm by a particle of 3 μm in diameter), but in general, phase functions are complicated by numbers of additional lobes which make them difficult to handle mathematically [Figure 4.12 (b)]. Thus, the variability of particle size, shape, and distribution finally make aerosols the constituent of the atmosphere that is the most difficult to grasp and model.

Parameterization models also seek to simplify the estimation of the attenuation of light by aerosols using Bouguer-Lambert-Beer's law so that

$$T_a(z, \lambda, \theta) = e^{-\tau_a(z, \lambda)M(\theta)}. \quad (4.42)$$

One way to estimate the aerosol optical depth τ_a is to rely on Ångström's (1961) formulation which empirically established that τ_a can be modelled by

$$\tau_a(z, \lambda) = \beta(z)\lambda^{-\alpha}, \quad (4.43)$$

where β and α are the Ångström turbidity coefficient and Ångström turbidity exponent, respectively. The dependence of the Ångström turbidity coefficient to the elevation z is used to model the main concentration of aerosol close to the ground in the lowest 2000m (Dozier, 1981) by means of a decreasing exponential function as follows:

$$\beta(z) = \beta(0)e^{-z/2000}. \quad (4.44)$$

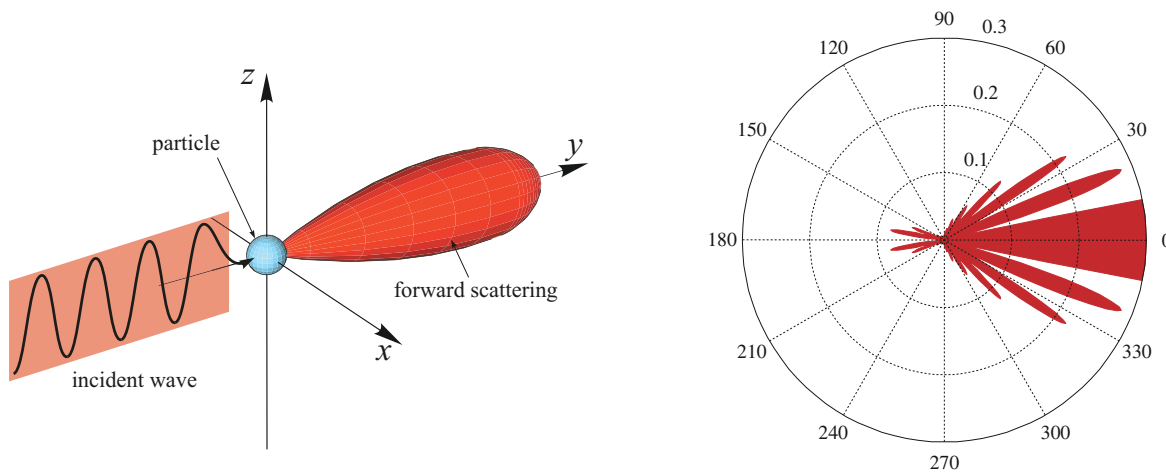


Figure 4.12 Phase function for Mie type of scattering: (a) general representation; (b) close-up view for a specific emphasis on possible configuration of additional scattering lobes.

Although α and β could theoretically be determined simultaneously with a dual-wavelength sun photometer (Iqbal, 1983, pg. 118), such measurements are at best only rarely available in the study site. Alternatively, the Ångström turbidity exponent α can be specified to depict a specific type of aerosol model (i.e., distribution of size and shape. e.g., rural, maritime, desert, urban) so that Equation (4.43) can be solved with a single measurement. For instance, Bird and Riordan (1986) proposed a rural aerosol model for which $\alpha = 1.0274$ for $\lambda < 500$ nm, and $\alpha = 1.2060$ for $\lambda \geq 500$ nm. This is assumed to be relevant for most of the study site although it may not be as suitable towards the West coast, by the Tasman Sea. In this area, a maritime aerosol model may intuitively be more suitable (Gregg and Carder, 1990).

A measurement of the aerosol optical depth is required to invert Equation (4.43). It was obtained from near hourly visibility observations at the nearby Mount Cook Airport (43.769 S, 170.133 E, $z = 656$ m asl). Although visibility observations account for the aerosol extinction coefficient in a horizontal column, while aerosol optical depth is related to the aerosol's extinction through a vertical column in the atmosphere, $\tau_a(656\text{m}, 550\text{ nm})$ can be estimated from visibility provided in [km] using a subroutine described in 6S (Vermote *et al.*, 1997, subroutine ODA550). The observed aerosol optical depth at 550 nm and at mean seal level was estimated using Equation (4.43) and the exponential decay given in Equation (4.44), then exponentially lapsed to compute maps of aerosol optical depth according to the local elevations provided by the DEM.

Aerosol transmittance can be separated into its scattering component T_{as} and absorption component T_{aa} so that

$$T_{as}(z, \lambda, \theta) = e^{-\omega(\lambda)\tau_a(z, \lambda)M(\theta)} \quad (4.45)$$

$$T_{aa}(z, \lambda, \theta) = e^{-[1-\omega(\lambda)]\tau_a(z, \lambda)M(\theta)}, \quad (4.46)$$

where $\omega(\lambda)$ is the aerosol single scattering albedo. It is computed using

$$\omega(\lambda) = \omega_{0.4} e^{-\omega' \left[\ln \frac{\lambda}{0.4} \right]^2}, \quad (4.47)$$

where $\omega_{0.4}$ is the aerosol single scattering albedo at 0.4 μm and ω' is the wavelength variation factor. In the case of the rural aerosol model $\omega_{0.4} = 0.945$ and $\omega' = 0.095$ (Bird and Riordan, 1986).

4.4.2 Radiation quantities

4.4.2.1 Diffuse irradiance

On horizontal surface. Diffuse irradiance on a horizontal surface can be divided into two parts.

1. The *diffuse solar irradiance* incident upon a horizontal surface E_d accounts for the Rayleigh and aerosol scattering of light. E_d was calculated as in Bird and Riordan's (1986) model using modifications of Justus and Paris's (1985) expressions. It implements a two-stream approximation assuming that the downward irradiance associated with Rayleigh scattering $E_r \downarrow$ and aerosol scattering $E_a \downarrow$, respectively, are independent of each other and can be linearly separated. Hence, E_d can be written as follows:

$$E_d = E_r \downarrow + E_a \downarrow. \quad (4.48)$$

Since Rayleigh scattering is symmetric, half of the radiation that is not absorbed is scattered downward so that

$$E_r \downarrow = \frac{1}{2} E_0 d^{-2} \cos \theta_s T_w T_o T_u T_{aa} (1 - T_r^{0.95}), \text{ and} \quad (4.49a)$$

$$E_a \downarrow = f_s(\cos \theta_s) E_0 d^{-2} \cos \theta_s T_w T_o T_u T_{aa} T_r^{1.5} (1 - T_{as}), \quad (4.49b)$$

where all transmittance terms are computed for a relative air mass that accounts for the sun elevation θ_s , but omitted for clarity purposes. $f_s(\cos \theta_s)$ is

the fraction of radiation scattered forward by aerosols. It varies with the solar zenith angle and is modelled using

$$f_s(\cos \theta) = 1 - \frac{1}{2} e^{\cos \theta (A f_s + B f_s \cos \theta)} \quad (4.50a)$$

$$A f_s = Lng \cdot [1.459 + Lng \cdot (0.1595 + Lng \cdot 0.4129)] \quad (4.50b)$$

$$B f_s = Lng \cdot [0.0783 + Lng \cdot (-0.3824 - Lng \cdot 0.5874)] \quad (4.50c)$$

$$Lng = \ln(1 - g), \quad (4.50d)$$

where g is the aerosol asymmetry factor that measures the preferred scattering direction. It is rigorously obtained by integration of the aerosol scattering phase function p weighted by the angular scattering over the enclosing sphere. It approaches 1 for strong scattering mostly in forward direction, and -1 in the backward direction. It is fixed to $g = 0.65$ by [Bird and Riordan \(1986\)](#) for the rural aerosol model.

2. The *diffuse environmental irradiance* $E_m^{(i)}$ accounts for the multiple reflections of direct solar irradiance E_s and diffuse solar irradiance E_d between the ground and the atmosphere. The trapping of radiation between the ground, of environmental reflectance $\bar{\rho}_e^{(i)}$, and the sky, of atmosphere spherical albedo ρ_s , results in a geometric series that converges to

$$E_m^{(i)} = (E_s \cos \theta_s + E_d) \frac{\bar{\rho}_e^{(i-1)} \rho_s}{1 - \bar{\rho}_e^{(i-1)} \rho_s}. \quad (4.51)$$

The atmosphere spherical albedo is adapted from [Justus and Paris \(1985\)](#) as follows:

$$\rho_s = T_w'' T_u'' T_{aa}'' \left[\frac{1}{2} (1 - T_r'') + [1 - f_s(\cos 56.25)] T_r' (1 - T_{as}') \right]. \quad (4.52)$$

The first term on the left hand side in ρ_s corresponds to the albedo of clean air solely due to Rayleigh scattering, while the second term on the right hand side is the albedo due to the presence of aerosols. It must be noted that [Justus and Paris \(1985\)](#) and [Bird and Riordan \(1986\)](#) considered the sky reflectivity at sea level. Therefore, the prime and double prime over the transmittance terms mean that these are evaluated at a constant effective relative air mass of $M = \sqrt{3}$ for [Justus and Paris \(1985\)](#) and $M = 1.8$ for [Bird and Riordan \(1986\)](#) using the equations of transmittance provided earlier. However, the spherical albedo is expected to reduce as the altitude increases due to the decaying air

mass (Iqbal, 1983, pg. 178). Since the term due to aerosols already accounts for the altitude in the calculation of the aerosol optical depth [see Equation (4.44)], only the term corresponding to clear sky albedo must be corrected to account for a standard barometric decay. Thus, in the present implementation of the model, the double prime means that the transmittances are computed at an effective relative air mass of $M = 1.8e^{-z/8574}$. A comparison with the 6S model for altitude within the range [0, 10 km] (Figure 4.13) showed that the spherical albedo was estimated with no more than 7% mean relative error depending on the MODIS spectral band.

The environmental diffuse irradiance¹ is a local effect with a range of influence of a few kilometres (Tanré *et al.*, 1981; Richter, 1998). Thus, the ground environmental reflectance $\bar{\rho}_e^{(i)}$ depends on the pixel under consideration and is updated at each iteration i . It can be calculated as a spatial average of each pixel's reflectance within a neighbourhood of an arbitrary specified size as illustrated by the radius R_2 in Figure 4.1. The spatial average can be weighted according to the distance of each contributing point within the neighbourhood to the pixel under consideration through an environmental weighting function (Vermote *et al.*, 1997). Although such sophistication for the calculation of the environmental reflectance can lead to better estimates of the environmental irradiance, it requires considerably more computation resources. Since the environmental irradiance is a second-order effect, only a range-independent moving window average was implemented with a $R_2 = 1500\text{m}$ radius to estimate $\bar{\rho}_e^{(i)}$ as recommended by Richter (1998).

On slope. The model described in the previous section assumes the diffuse irradiance to be isotropic and on a flat terrain. However, it is well known that the diffuse irradiance coming from the sky has two zones of strong anisotropy (Hay and McKay, 1985; Perez *et al.*, 1986; Rich *et al.*, 1994; Vartiainen, 2000; Igawa *et al.*, 2004; Torres *et al.*, 2006; Cucumo *et al.*, 2007):

1. Near the sun direction, the higher circumsolar diffuse irradiance is explained by the strong forward-scattering of aerosols (Perez *et al.*, 1986; Li and Cheung, 2005).

¹Sometimes called adjacency effect (Richter, 1998).

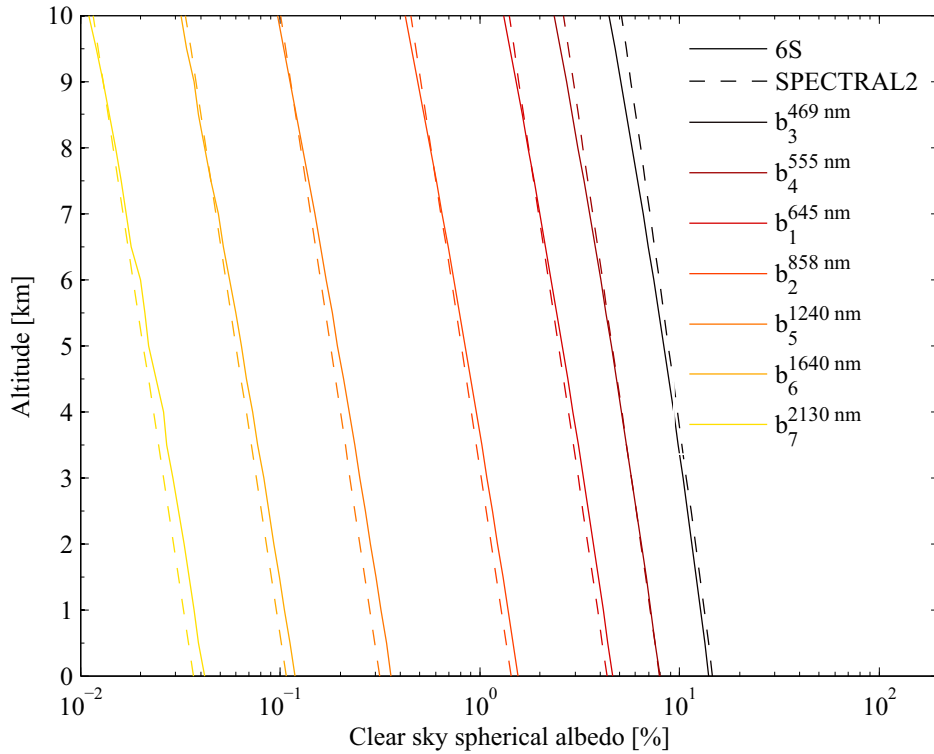


Figure 4.13 Decay of the atmosphere spherical albedo with elevation as computed by 6S and the adapted version of the SPECTRAL2 model for MODIS spectral bands.

2. Near the horizon, the horizon brightening is attributed to multiple Rayleigh scattering (Perez *et al.*, 1986).

Thus, in mountainous terrain, the geometry of the target has an impact on the amount of diffuse irradiance that it receives. The anisotropic model proposed by Hay and McKay (1985) to estimate the diffuse irradiance on a tilted plane $E_d^{*(i)}$ is used here. It accounts for the isotropic contribution of the sky dome and the circum-solar component depending on the fraction of shadowing in the pixel as follows:

$$E_d^{*(i)} = (E_d + E_m^{(i)}) \left[bT_s \frac{\cos \gamma}{\cos \theta_s} + (1 - bT_s)V_d \right]. \quad (4.53)$$

The fact that Hay and McKay's (1985) model does not account for the horizon brightening is an acceptable simplification because the horizon is generally obstructed by adjacent slopes in the mountainous study area.

4.4.2.2 Atmosphere intrinsic radiance

The atmosphere intrinsic radiance L_p can be approximated by the fraction of the light scattered upwards by the atmosphere. Similarly to the downward diffuse solar irradiance E_d , L_p is the sum of the Rayleigh ($E_r \uparrow$) and aerosol ($E_a \uparrow$)

upward scattering components. Both are the counterpart of $E_r \downarrow$ and $E_a \downarrow$ [Equation (4.49b) & (4.49b)] and are given by

$$E_r \uparrow = \frac{1}{2} E_0 d^{-2} \cos \theta_s T_w T_o T_u T_{aa} (1 - T_r^{0.95}) \quad (4.54a)$$

$$E_a \uparrow = [1 - f_s(\cos \theta_s)] E_0 d^{-2} \cos \theta_s T_w T_o T_u T_{aa} T_r^{1.5} (1 - T_{as}). \quad (4.54b)$$

A fraction of the scattered radiation is absorbed by gas and aerosols while moving in the direction of the sensor. It leads to an expression of L_p as follows:

$$L_p = \frac{(E_r \uparrow + E_a \uparrow) T_w T_o T_u T_{aa}}{\pi}, \quad (4.55)$$

where, unlike Equation (4.54b) & (4.54b), the transmittance terms are calculated to account for a relative air mass in the direction of the sensor [i.e., $T = T(\theta_v)$].

4.4.2.3 Background radiance

The background radiance $L_k^{(i)}$ is the contribution, at the sensor level, of the radiation reflected by the surrounding environment of the pixel under consideration (illustrated by the radius R_2 in Figure 4.1). The environment of average reflectance $\bar{\rho}_e^{(i-1)}$ reflects a fraction of the total irradiance $E_g^{(i)}$. A fraction of this radiation is scattered into the field of view of the sensor and decreased according to the ground to sensor diffuse transmittance $t_d(\theta_v)$ (Vermote *et al.*, 1997):

$$t_d(\theta_v) = \frac{E_d(\theta_v)}{E_0 d^{-2} \cos \theta_v}. \quad (4.56)$$

It yields the following expression of the background radiance

$$L_k^{(i)} = \frac{t_d(\theta_v) \bar{\rho}_e^{(i-1)} E_g^{(i)}}{\pi}. \quad (4.57)$$

4.4.3 Accuracy assessment of the atmospheric model

4.4.3.1 Comparison with 6S

In order to assess the implementation and quality of the previously described single layer atmospheric model, estimations of E_s , E_d , E_m , T_s , T_v , and L_p were compared to corresponding estimations obtained from the 6S model (Vermote *et al.*, 1997). It is assumed that the sophistication of 6S makes it a relevant candidate to assess the performance of the SPECTRAL2 model. The purpose was not to assess the sensitivity of Bird and Riordan's model to these parameters taken individually, but to ensure that the model outputs are of sufficient reliability for all MODIS bands

1 to 7. Such a comparison would require that the various parameters potentially affecting the output quantities should be changed independently [i.e., Ozone (O_3), water vapour column (W), height (h), solar zenith angle (θ_s), sensor zenith angle (θ_v), environmental ground reflectance (ρ_e), and aerosol optical depth (τ_a)]. In addition, the quantities must be retrieved for each of the seven MODIS spectral bands.

As mentioned earlier, the implementation of 6S in the MATLAB[®] environment required a relatively long time to return the result of a single computation. Thus, if each parameter was to take ten different values within their respective range, then 7×10^7 computations would be needed, requiring over a hundred days of processing time with the computer configuration available. Thus, only a limited number of runs could be made and an alternative strategy inspired from a Monte-Carlo statistical analysis was conducted. A number of combinations of parameters ($n = 5000$) were selected. For each combination, the parameters were randomly selected within their respective range of values (Table 4.1).

Table 4.1 Range of values for the parameters used in the comparison between atmospheric models 6S and SPECTRAL2.

Parameter	Range of values
Ozone (O_3)	270–340 Dobson Unit
Water vapour column (W)	0–3 cm
Height (h)	0–3500m
Solar zenith angle (θ_s)	0–70 deg
Sensor zenith angle (θ_v)	0–30 deg
Environmental ground reflectance (ρ_e)	0–60 %
Aerosol optical depth (τ_a)	0.1–0.6

The radiation quantities can vary over several orders of magnitude depending on the spectral bands and, to a lesser extent, on the parameter's values within a single spectral band. Thus, a normalized indicator was needed to measure the goodness of fit between both models, while keeping discrepancies comparable. In these conditions, the Relative Error ($\epsilon\%$) and associated measures [e.g., Mean Relative Error (MRE), Mean Relative Square Error (MRSE), and Root Mean Relative Square Error (RMRSE)] computed between the inferred value (i.e., computed from SPECTRAL2) and the reference value (i.e., computed from 6S) of a quantity x were

regarded as appropriate metrics:

$$\epsilon_{\%} = 100 \cdot \frac{x_{\text{SPECTRAL2}} - x_{6\text{S}}}{x_{6\text{S}}} \quad (4.58a)$$

$$\text{MRE} = \frac{\sum_{i=1}^n \epsilon_{\%}}{n} \quad (4.58b)$$

$$\text{MRSE} = \frac{\sum_{i=1}^n \epsilon_{\%}^2}{n} \quad (4.58c)$$

$$\text{RMRSE} = \sqrt{\text{MRSE}}. \quad (4.58d)$$

Among all metrics, the RMRSE was considered as a good measure of quality because, similarly to its counterpart the Root Mean Square Error (RMSE), it accounts simultaneously for both the bias (accuracy) and the standard deviation (precision) of the digression between both models (Willmott *et al.*, 1985). Additionally, the coefficient of determination R^2 and an ordinary least squares linear regression between the inferred and the reference values were considered. Figure 4.14 shows the scatter plots of each quantities estimated by the SPECTRAL2 model compared to the values from 6S used as a reference.

4.4.3.2 Correction for the atmosphere intrinsic radiance

Figure 4.14 reveals that, unlike all other quantities, L_p exhibits a substantial dispersion. The estimation of L_p , as computed using Equation (4.55), exhibited strong discrepancies as the wavelength increased, eventually reaching up to 200% MRE for band seven. Although L_p decreases rapidly as the wavelength increases and therefore is not critical in the correction process, an investigation of the relative error revealed that it could be attributed mostly to the solar zenith angle θ_s . This is illustrated in Figure 4.15 which shows that, while no correlation exists between the relative error and most parameters, there is an obvious non-linear relationship with θ_s . This dependency is believed to be due to the anisotropic nature of L_p (Dozier, 1981). Empirically, the relative error could be successfully linearized when plotted against $\cos^{3/2} \theta_s$ [Figure 4.16 (a)]. It suggested a relationship of the form

$$\epsilon_{\%} = 100 \cdot \frac{L_p^{\text{SPECTRAL2}} - L_p^{6\text{S}}}{L_p^{6\text{S}}} = a(\lambda) \cos^{3/2} \theta_s + b(\lambda). \quad (4.59)$$

In addition, Figure 4.16 (b) shows that the coefficients a and b were significantly correlated to the wavelength (p-value lower than 10^{-4}). Thus, it led to an improved expression of L_p as follows:

$$L_p = \frac{(E_r \uparrow + E_a \uparrow) T_w T_o T_u T_{aa}}{\pi(-1.86\lambda \cos^{3/2} \theta_s + 2.27\lambda + 0.84)}. \quad (4.60)$$

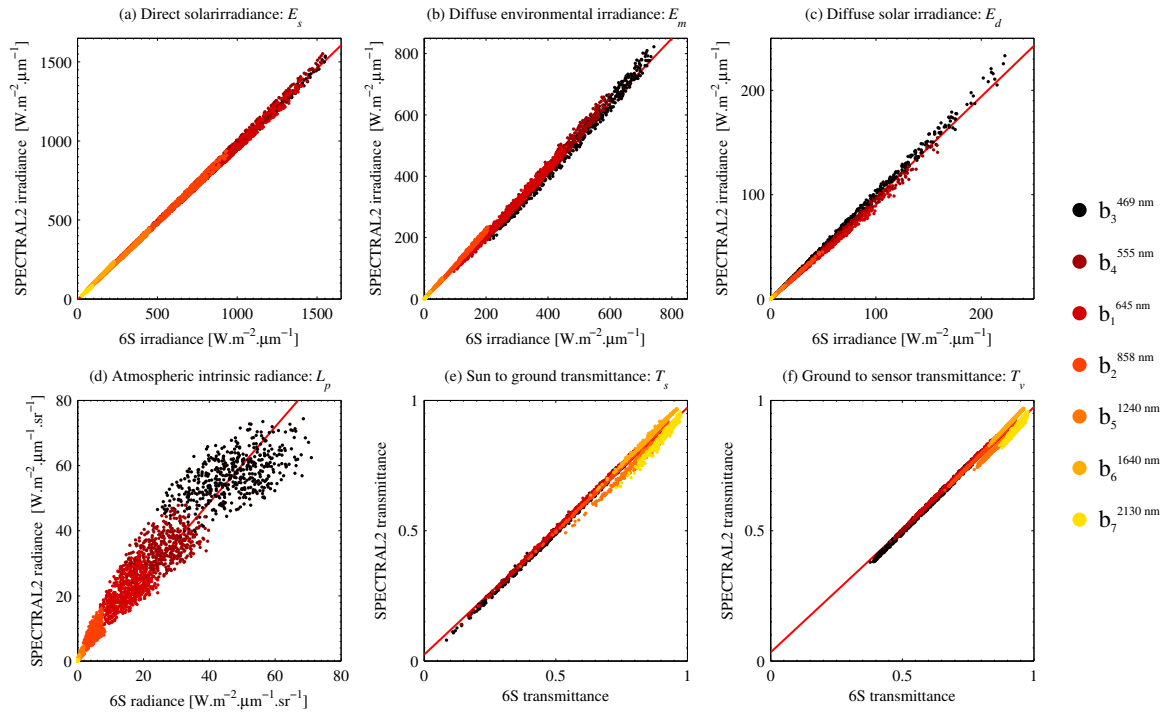


Figure 4.14 Scatter plot of the predicted values retrieved from the SPECTRAL2 model versus the value obtained from the 6S model for MODIS bands 1–7. 500 combinations of atmospheric parameters were randomly selected within appropriate ranges. Each MODIS band is colour coded.

4.4.3.3 Performance of SPECTRAL2 in the seven MODIS land bands

Table 4.2 provides the results of the comparison between both models based on a new set of 5000 combinations. For all MODIS spectral bands, the RMRSE for atmospheric transmittance (i.e., T_s and T_v) was generally within 5%. It suggested an appropriate estimation of the absorption coefficients associated with each atmospheric component. With regard to E_{s_i} , a good agreement was obtained for all spectral bands except band seven, where the RMRSE reached 14.7%. This discrepancy in the SWIR range can be explained by the differences in the extraterrestrial solar spectrum used in each model (Table 4.3)¹. The discrepancies regarding E_d and E_m are more difficult to grasp and no clear relationship between these differences and any of the parameters could be established. Despite the fact that the RMRSE sometimes exceeded 10% for two spectral bands, overall it was within an acceptable range of

¹For this comparison, the quantities estimated with the SPECTRAL2 model are computed using the solar spectrum used at the World Radiation Center (WRC), Meteorologisches Observatorium Davos, Publication 615, 1985.

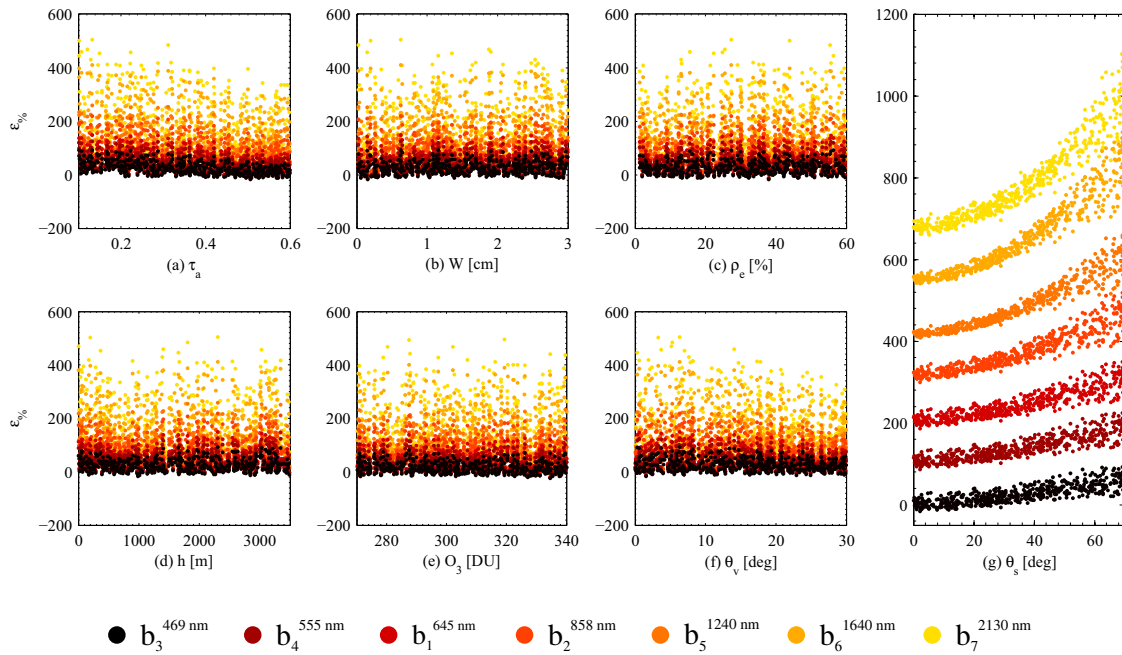


Figure 4.15 Dependence of the relative error $\epsilon_{\%}$ of L_p to parameters (a) aerosol optical depth, (b) water vapour column, (c) environmental ground reflectance, (d) height, (e) ozone, (f) sensor zenith angle, and (g) solar zenith angle. Each MODIS band is colour coded as for Figure 4.14. In the case of θ_s , the relative error for each spectral band is offset by 100% relatively to the previous one for clarity.

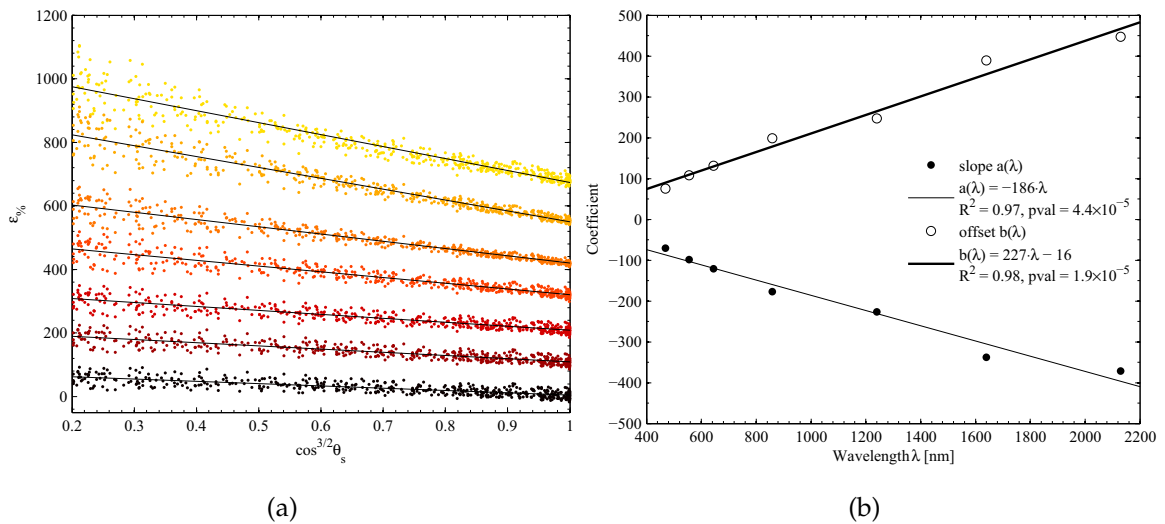


Figure 4.16 Linearization of the relative error of L_p : (a) Linearization per spectral band, each spectral band is offset by 100% relative to the previous one for clarity; (b) Slope and offset of the linearization as a function of the wavelength.

Table 4.2 Comparison of E_s , E_d , E_m , T_s , T_v , and L_p estimated from SPECTRAL2 and 6S.

Spectral band		E_s			E_d			E_m		
Nº	Wavelength [nm]	R ²	Regression	RMRSE [%]	R ²	Regression	RMRSE [%]	R ²	Regression	RMRSE [%]
3	459-479	1.00	y=0.97x-4.32	4.1	0.99	y=1.15x-48.47	5.8	1.00	y=1.00x-0.02	2.4
4	545-565	1.00	y=0.98x+1.25	2.3	0.99	y=1.15x-29.98	7.1	1.00	y=0.93x+0.26	6.6
1	620-670	1.00	y=0.96x+2.92	3.9	0.99	y=1.11x-16.15	5.6	1.00	y=0.88x+0.23	11.1
2	841-876	1.00	y=0.98x-1.95	3.5	0.99	y=1.14x-5.46	9.8	1.00	y=0.93x-0.07	8.5
5	1230-1250	0.99	y=0.97x-6.60	5.5	1.00	y=1.13x-0.58	11.7	1.00	y=0.92x-0.09	12.5
6	1628-1652	0.99	y=1.00x+0.37	2.4	1.00	y=1.17x-0.20	15.0	1.00	y=1.01x-0.02	4.0
7	2105-2155	0.99	y=0.88x-1.62	14.7	0.99	y=0.98x-0.03	4.6	1.00	y=0.99x	4.7
Overall		1.00	y=0.97x-2.68	6.6	1.00	y=0.97x-0.53	9.2	1.00	y=1.06x-0.54	7.9

Spectral band		L_p			T_s			T_v		
Nº	Wavelength [nm]	R ²	Regression	RMRSE [%]	R ²	Regression	RMRSE [%]	R ²	Regression	RMRSE [%]
3	459-479	0.76	y=0.81x+7.42	10.4	1.00	y=1.00x	2.1	0.99	y=1.01x-0.01	1.5
4	545-565	0.84	y=0.78x+5.54	9.9	1.00	y=1.00x	1.0	1.00	y=1.00x	0.6
1	620-670	0.90	y=0.75x+3.50	9.5	1.00	y=0.99x+0.01	1.0	1.00	y=1.00x+0.01	0.6
2	841-876	0.95	y=0.83x+0.91	9.9	1.00	y=1x-0.01	0.9	1.00	y=1.00x-0.01	0.7
5	1230-1250	0.97	y=0.81x+0.11	10.4	0.99	y=1.01x-0.05	5.3	0.99	y=0.98x-0.02	4.4
6	1628-1652	0.97	y=0.91x+0.03	8.2	1.00	y=1.02x-0.01	0.7	1.00	y=1.06x-0.05	0.5
7	2105-2155	0.96	y=0.89x+0.01	7.9	0.97	y=1.17x-0.20	5.4	0.93	y=1.15x-0.18	4.5
Overall		0.98	y=0.96x+0.27	9.5	0.99	y=0.95x+0.02	3.0	0.99	y=0.94x+0.03	2.5

Table 4.3 Mean extraterrestrial solar irradiance values for MODIS spectral bands.

Spectral band Nº	3	4	1	2	5	6	7
Spectral range [μm]	0.459–0.479	0.545–0.565	0.620–0.670	0.841–0.876	1.230–1.250	1.628–1.652	2.105–2.155
E_0 used in 6S [$\text{W}\cdot\text{m}^{-2}\cdot\mu\text{m}^{-1}$]	1660	1018	2081	1917	475	239	96
E_0 used in SPECTRAL2 from [$\text{W}\cdot\text{m}^{-2}\cdot\mu\text{m}^{-1}$]	1611	984	2016	1859	476	237	87
$\epsilon\%$	-3.0	-3.3	-3.1	-3.0	0.3	-1.0	-9.1

10%. The empirical correction of L_p permitted its estimation generally within 10% of the reference value computed with 6S. This comprehensive comparison stressed the good performance of this simple model and its relevance for the correction of atmospheric effects affecting MODIS spectral bands 1–7 is confirmed.

4.5 Performance of ATOPCOR

4.5.1 Stability and convergence of the iterative process

The convergence of the iterative process described in Equation (4.7) is essential to ensure that the final values of reflectance are reliable. This must be investigated to determine the number of iterations required to obtain stable reflectance values, as well as minimizing the computing time. Richter (1998) found that three iterations were sufficient to ensure a suitable convergence in ATCOR3. However, Richter's investigation was based on targets having less than 25% reflectance on average (coniferous and deciduous forests, grassland), and is therefore biased by the absence of highly reflective targets such as snow. This experiment showed that the convergence tends to be slower in the presence of very bright targets such as snow, with ten iterations not always sufficient to ensure the convergence (Figure 4.17). The fluctuations were also more important in shadowed areas, because the absence of direct solar irradiance artificially increases the relative contribution of E_t and E_m in the total downward irradiance. In shadowed areas, these two components form the denominator of Equation (4.7), which in turn becomes much more sensitive to the iterative process, thus causing the slow convergence. Figure 4.17 shows that substantial fluctuations can also occur when shadowed areas are part of the neighbourhood of a non-shaded pixel. The estimation of environmental and reflected terrain radiation for an illuminated pixel can be affected by fluctuations in a partially shaded neighbourhood, which in turn lengthens the convergence to a stable reflectance value.

In order to mitigate these fluctuations and increase the processing speed, a simple damping strategy was implemented. At each new iteration (i), the average terrain reflectance $\bar{\rho}_t^{(i)}$ and the average environmental reflectance $\bar{\rho}_e^{(i)}$ were averaged with their previous value at iterations ($i - 1$):

$$\bar{\rho}_t^{(i)*} = 0.5(\bar{\rho}_t^{(i)} + \bar{\rho}_t^{(i-1)}) \quad (4.61a)$$

$$\bar{\rho}_e^{(i)*} = 0.5(\bar{\rho}_e^{(i)} + \bar{\rho}_e^{(i-1)}), \quad (4.61b)$$

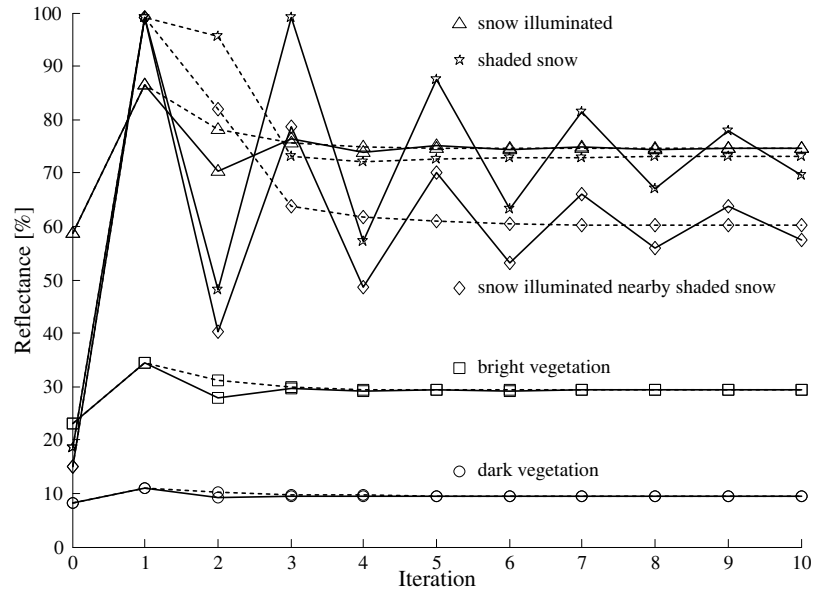


Figure 4.17 Convergence of reflectance values (MODIS band 2) for various targets. Solid line represents the convergence without damping; dashed line is the convergence with damping.

where the superscript * denotes the updated value. This damping mechanism limited the magnitude of the fluctuations due to the feedback. Therefore, it enabled the iterative process to converge faster without affecting the final value. Figure 4.17 illustrates the positive effect of the damping mechanism on the convergence speed.

4.5.2 Assessment of the correction

Assessing the accuracy of the estimated ground reflectance is a very difficult task. The best approach would require the collection of many ground spectral measurements for various targets, distributed in multiple locations to account for the various configurations of illumination and at different times of the year simultaneously with the acquisition of satellite data (Vermote *et al.*, 1997). Simulating 250m pixel size reflectance with ground reflectance data would be another challenge. This would involve a significant investment in terms of time, cost, and logistics that were not available for this thesis. In a similar context of correction of satellite imagery in mountainous terrain, Sjoberg and Horn (1983) acknowledged this difficulty and proposed that such assessment could be made by the subjective evaluation of the map of ground reflectance based on three qualitative criteria:

1. the loss of relief perception;

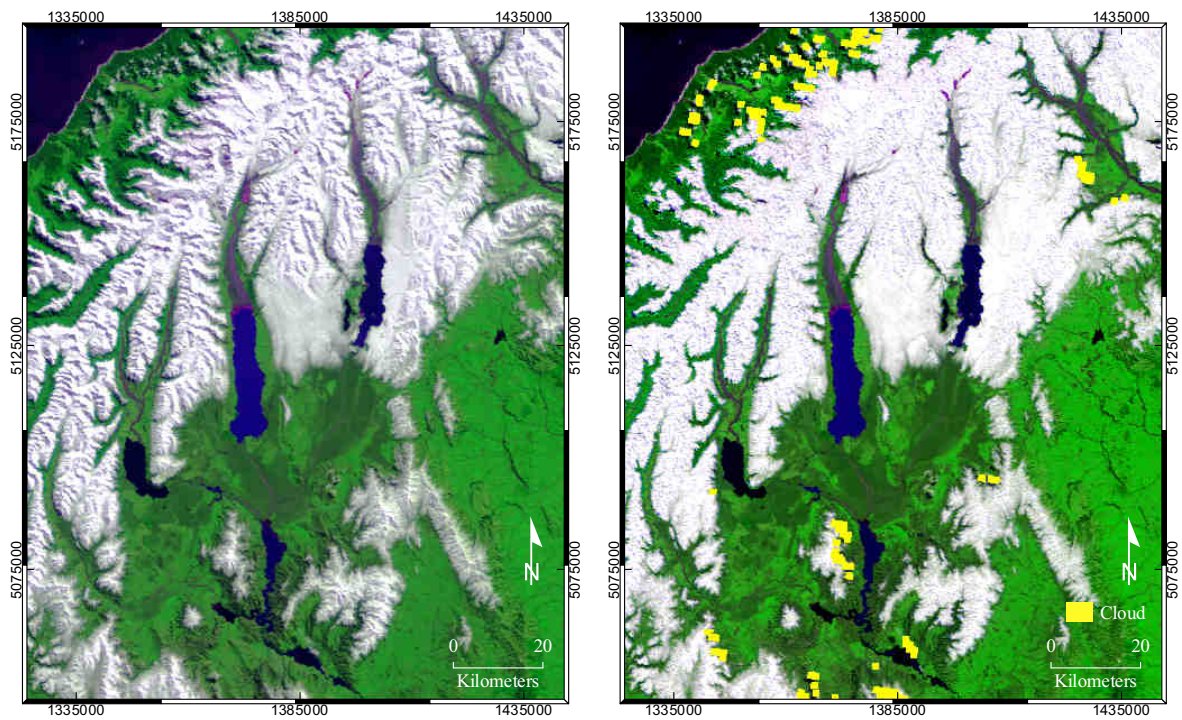
2. the similar reflectance of homogeneous targets whether sunlit or shadowed;
3. reflectance values within the acceptable range (i.e., [0, 1]).

While these criteria are relevant to such an evaluation, it is suggested that the assessment of the quality of the atmospheric model and the careful consideration of most of the effects encountered in mountainous terrain using a comprehensive 3-D radiative model has the potential to ensure a realistic estimation of the ground reflectance.

In addition, based on [Sjoberg and Horn's](#) recommendations, the visual inspection of numerous images with various configurations of illumination and snow cover proved to be a useful step to assess, if not quantitatively at least qualitatively, whether there were any obvious flaws in the correction process. The aim in this instance is to ensure that the ground reflectance is realistic with respect to the interpreted land cover. For instance, in a mountainous environment, the unbalanced irradiation that reaches slopes having different aspect often results in a large variance with respect to the values of apparent reflectance for similar targets on each side of ridges. It is in fact these variations that largely control the interpreter's sensation of relief from an image by emphasizing the ridges and valleys. After correction, it is expected to find comparable values of reflectance on each side of ridges for similar targets.

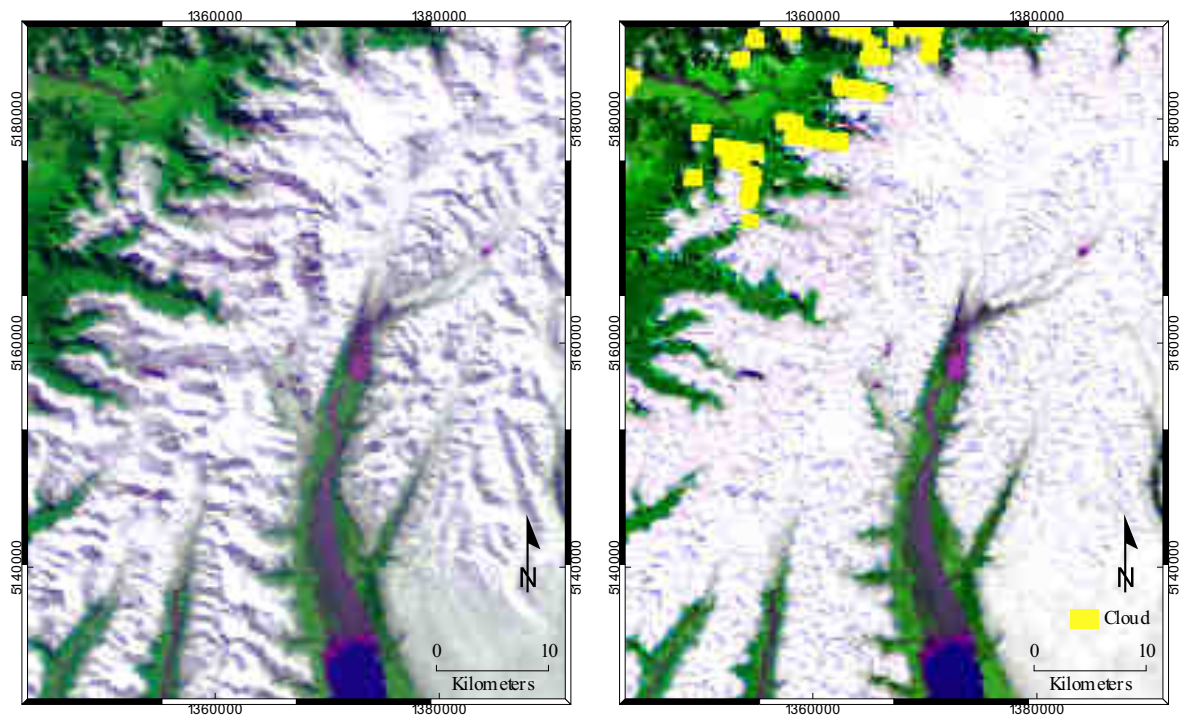
Differences in aspect are still likely to have a noticeable impact on the land cover due to the effect of a variable total irradiance received by a target. For instance, it is well known that the metamorphism of snow occurs at a different rate between North and South faces. In the Southern Hemisphere, South faces are less exposed to sunlight than North faces, resulting in a generally more preserved snowpack, concurring with an increased reflectance. Nevertheless, if the correction is conducted successfully, then such variations are expected to be of a reasonably small magnitude compared to the apparent reflectance. This was satisfactorily assessed from the inspection of numerous images such as those illustrated in [Figure 4.18](#) showing a RGB composite of a corrected image in a relatively difficult configuration with many shadows and large snow cover. The loss of visual sensation of relief in the corrected image and the general improvement of the contrast are indicative of the correct normalisation process.

[Richter \(1998\)](#), who also mentioned the difficulty of assessing the correction process in rugged terrain, limited his strategy of assessment to the investigation



(a) False colour RGB composite from original MODIS bands 1, 2, and 3

(b) False colour RGB composite from corrected MODIS bands 1, 2, and 3



(c) Subset of (a)

(d) Subset of (b)

Figure 4.18 Example of the atmospheric and topographic correction (20 September 2003, 22:40 GMT).

of the correlation between Landsat TM reflectance and illumination angle, before and after correction. He concluded that the loss of correlation after correction was indicative of a correct normalisation of the reflectance. The same approach has also been used by many authors concerned with this problem (e.g., Meyer *et al.*, 1993; Ekstrand, 1996; Bishop *et al.*, 2003; Kobayashi and Sanga-Ngoie, 2008) and is also used here.

This is illustrated in Figure 4.19 where the NIR reflectance of the MODIS image shown in Figure 4.18 is plotted against the illumination angle, before and after the correction process. Without correction, the correlation between the reflectance and the illumination angle is evident [Figure 4.19 (a)]. The correlation is complicated by the presence of various types of targets and the image is segmented into two main clusters. Snow targets with relatively high apparent reflectance values show the greatest magnitude of reflectance variation while snow free targets, mostly covered by vegetation, show a much reduced reflectance. As the illumination angle increases (i.e., $\cos \gamma$ decreases), the reflectance decreases due to the larger expansion of the irradiance beam. A large number of pixels with relatively low reflectance cluster around $\gamma = 51$ deg (i.e., $\cos \gamma \approx 0.63$). They correspond to the flat vegetated areas for which the illumination angle is the solar zenith angle at the time of the acquisition. After correction, both main clusters are still identifiable. The general loss of correlation indicated by reflectance values that are more evenly balanced across all illumination angles confirms the correct behaviour of the correction process.

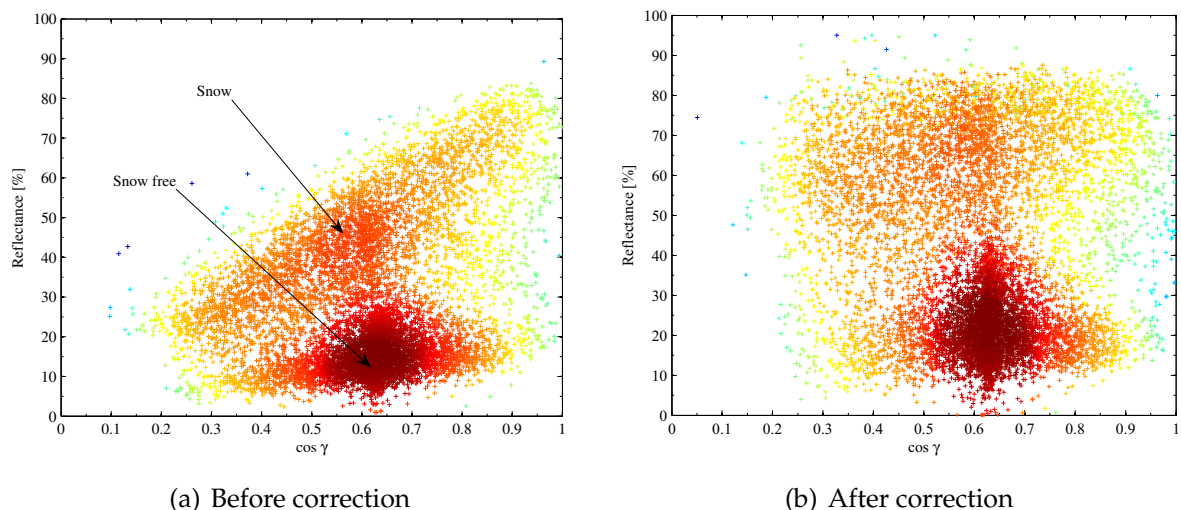


Figure 4.19 Scatter plot of MODIS band 2 (NIR, image of the 20 September 2003, 22:40 GMT) and $\cos \gamma$. The dots are colour coded according to their density.

4.5.3 Critical assessment of the model of multiple reflections¹

4.5.3.1 Theoretical considerations

To demonstrate the impact of rugged topography and ground reflectance on the terrain reflected radiation, the theoretical relative error between the reflectance computed with the first-order approximation ρ_1 and the reflectance estimated using the multiple reflections model ρ_∞ were calculated. A simple case was considered with Lambertian surfaces and homogeneous reflectance and topography in the whole surroundings ($\rho = \bar{\rho}$ and $C_t = \bar{C}_t$). Using Equations (4.29) & (4.32) and calling f_1 and f_∞ the ratio between E_t and E_g , respectively for the first-order reflection model and the multiple reflections model, two simple functions are compared, namely

$$f_1(\rho, C_t) = \rho C_t \quad (4.62a)$$

$$f_\infty(\rho, C_t) = \frac{\rho C_t}{1 - \rho C_t}. \quad (4.62b)$$

Using Equation (4.4) the reflectance ρ of a flat Lambertian surface that receives direct solar irradiance can be written as

$$\rho = \frac{\pi L_g}{E_g + E_t}, \quad (4.63)$$

where L_g is the upward surface reflected radiance. Thus, the relative error is

$$\begin{aligned} \epsilon_{\%} &= \frac{\rho_1 - \rho_\infty}{\rho_\infty} \\ &= \frac{f_\infty - f_1}{1 + f_1} \\ &= \frac{\rho^2 C_t^2}{1 - \rho^2 C_t^2}. \end{aligned} \quad (4.64)$$

Figure 4.20 shows that, when the average terrain configuration factor lies between 0.4 and 0.5, as is common in very steep alpine environments, the reflectance of highly reflective targets such as snow (i.e., reflectance between 75% and 90% in the visible spectrum) could be overestimated by 10% to 25% when neglecting multiple terrain reflections. In the context of assumed Lambertian surfaces, the area of impossible values indicates the range of targets for which the reflectance would be estimated higher than 100% if considering only the first-order reflection. This reveals the potential for underestimating the incoming irradiance, and suggests that

¹ The content of this sub-section is published in: Sirguey, P. (2009). Simple correction of multiple reflection effects in rugged terrain. *International Journal of Remote Sensing*, 30(4), 1075–1081, doi: 10.1080/01431160802348101

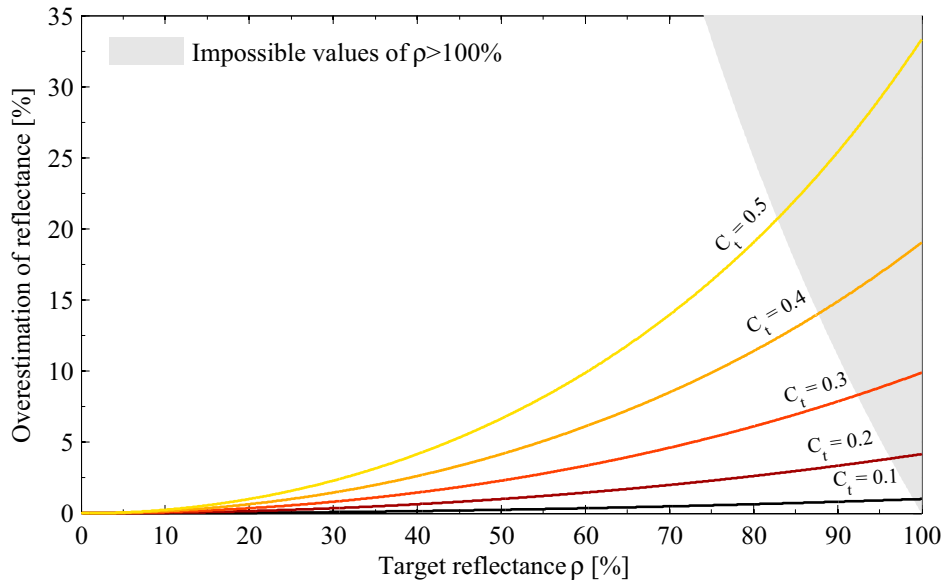


Figure 4.20 Theoretical overestimation of ground reflectance if assuming Lambertian surfaces and neglecting multiple terrain reflections, for varying terrain configuration factor (C_t).

extra radiation from multiple scattering must be accounted for to avoid unrealistic saturated ground reflectance. This effect will be stronger in shaded areas, where the relative contribution of terrain induced irradiance is greater.

4.5.3.2 Practical application

A challenging subset of an ASTER image of rugged terrain largely covered by snow was used to assess the benefit of the multiple reflections model over the first-order approximation (Figure 4.21). The close-up view of a shaded area in Figure 4.21 illustrates the additional contribution that can be attributed to terrain reflected radiation. The shaded area accounts for both cast (①) and self (②) shadow situated on nearby facing slopes at the bottom of the cirque illustrated in the Figure. Contextual photo-interpretation suggests that both are similarly covered by snow. While the self shaded slope faces a terrain that is largely illuminated and covered by snow, the cast shaded slope belongs to the illuminated wall, and is therefore facing a shaded terrain. Clearly, the self shaded slope (②) appears brighter than its neighbouring cast shaded slope (①). Since both areas lack direct solar irradiance and are exposed to a comparable amount of diffuse irradiance due to a similar sky-view factor, the observed difference of brightness can only be explained by a substantial difference of terrain reflected radiation received by each surface. Clearly, the self shaded por-

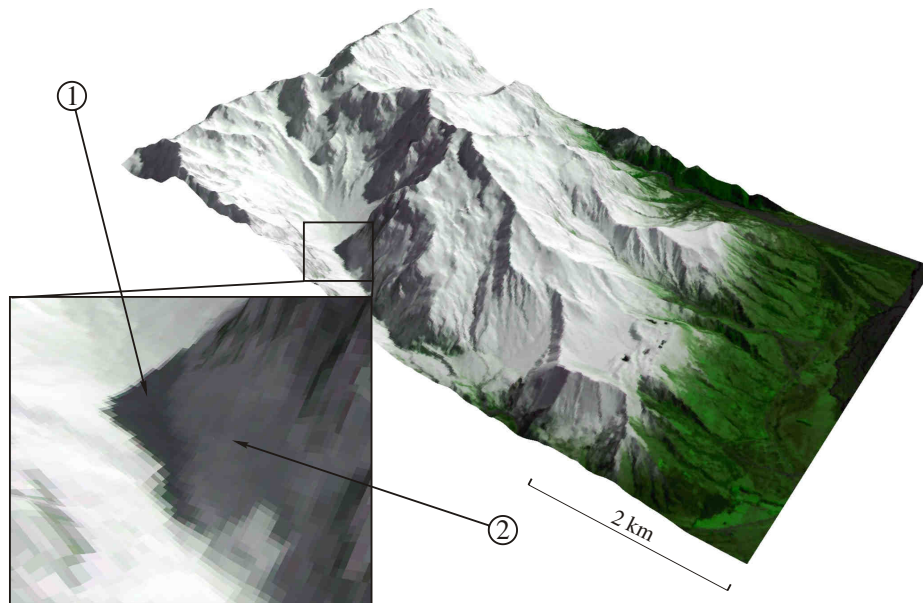


Figure 4.21 RGB composite from ASTER bands 2, 3, and 1 of the test image of a rugged terrain covered with snow draped over a Digital Elevation Model. The close-up view on a shaded area illustrates the additional contribution that can be attributed to terrain reflected radiation: (1) A shaded area facing a shaded slope; (2) a shaded area facing a largely illuminated slope.

tion (②) receives a higher amount of reflected radiation than the cast shaded portion (①) for it is facing a fully illuminated and snowy counterpart. Yet this example only points out the potentially significant contribution of the terrain reflected radiation to the upwelling radiance and confirms the remark made by [Duguay \(1993\)](#) quoted earlier in Section 4.3.4.

ASTER bands 1–4 of the subset were processed using the previously described atmospheric and topographic correction model (ATOPCOR). As explained in Section 4.5.1, 10 iterations along with the damping strategy were required for the process to converge in the case of such highly reflective targets. Typically, as shown for ASTER band 1 (520–600 nm) in Figure 4.22, the reflectance of illuminated and shaded snow targets were unbalanced when using the first-order reflected terrain correction, with higher reflectance values and saturation in the shade. The same observation was made for bands 2–4. Although this difference could be explained by the underestimation of diffuse sky irradiance and/or snow that is preserved and more reflective in the shade, a substantially higher proportion of saturated pixels was found in the shade (Table 4.4). More realistic and much less saturated values

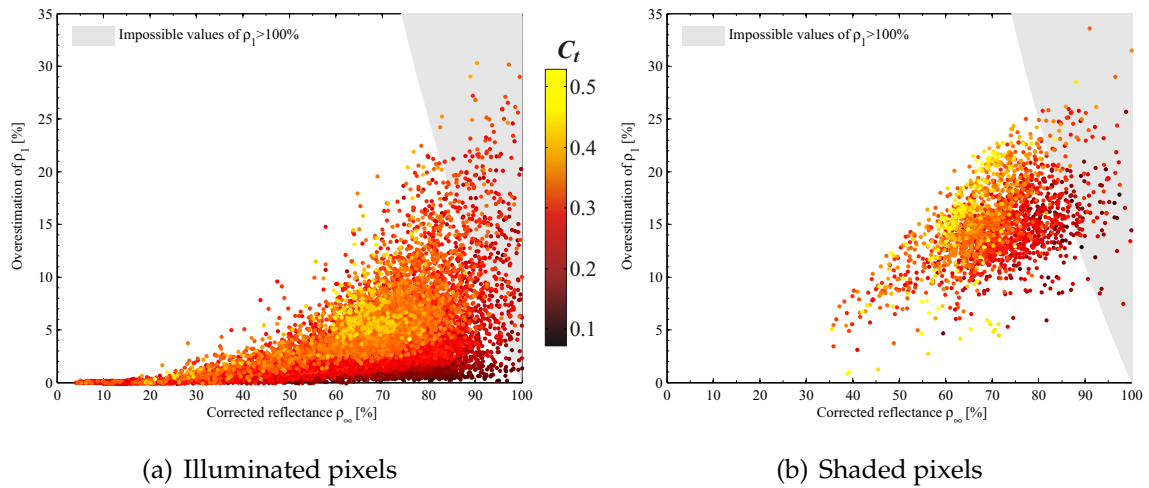


Figure 4.22 Overestimation of reflectance ρ_1 corrected using ATOPCOR and the first-order model, according to the reflectance ρ_∞ obtained using the multiple reflections correction for ASTER band 1. Targets are assumed Lambertian and separated whether they are (a) illuminated, or (b) shaded. The colour indicates the value of C_t .

Table 4.4 Proportion of saturated pixels for ASTER bands 1–4. Pixels are accounted whether they are illuminated or shaded.

Spectral band № (Spectral range [nm])	Shaded pixels [%] ($n = 14470$)		Illuminated pixels [%] ($n = 166022$)	
	First-order	Higher-order	First-order	Higher-order
1 (520–600)	8.7	1.5	2.2	0.9
2 (630–690)	8.7	1.7	1.4	0.5
3 (780–860)	21.6	3.6	1.8	0.7
4 (1600–1700)	6.9	2.2	0.0	0.0

were obtained experimentally when using the multiple reflections correction. The number of saturated pixels greatly dropped for all bands especially when considering shaded pixels. Similar targets either illuminated or shaded also obtained more consistent reflectance values within the admissible range [0, 100%].

4.6 Summary

This chapter has described in detail the implementation of a comprehensive three-dimensional physical model to transform calibrated radiance values measured at the top of the atmosphere (MODIS L1B products) into ground reflectance. The model is inspired largely from the ATCOR3 model described by Richter (1998) that

addresses atmospheric and topographic effects concurrently. The specific interest in snowy targets when implementing this model to correct MODIS and ASTER imagery allowed identification and correction of some shortcomings of the original formulation. Specifically:

1. It is shown that three iterations, as presently used in commercially available ATCOR3, are not sufficient to allow the convergence of the reflectance in the presence of highly reflective surfaces. In such cases, more iterations should be used and a damping strategy is proposed to speed up the convergence without affecting the final value.
2. In rugged terrain and snowy environments, the trapping of radiation between adjacent slopes can make the first-order approximation for reflected terrain radiation inadequate because it does not account for the trapping of radiation between adjacent slopes. The reflectance of snowy targets, in very rugged terrain, may be overestimated by up to 30% if multiple reflections are ignored. This potentially explains the high number of saturated values obtained when the topographic correction only implements a first-order terrain function. Thus, the correction for multiple reflections is desirable in specific environments. In order to mitigate these effects, a simple correction of multiple reflection effects is proposed that rely on the same neighbourhood simplifications.

With regard to the atmospheric correction, a simple transmission atmospheric model is preferred to rigorous radiation transfer code, despite the availability and supposedly better accuracy of the latter. This choice was justified by the ease of implementation into a computing environment as well as its shorter processing time. A careful assessment with 6S demonstrated the good performance of the parametric approach inspired from the SPECTRAL2 model of [Bird and Riordan \(1986\)](#) for the retrieval of transmittance and radiation quantities that are required for the correction. Nevertheless, it was shown that the atmosphere's intrinsic radiance is significantly correlated with the solar zenith angle. Thus, an empirical correction was proposed that resulted in L_p being estimated within 10% of the value calculated by 6S.

Chapter 5

Snow classification

5.1 Introduction

The previous chapter explained how the MODIS images were standardized and processed to compute ground spectral reflectance values. This chapter describes the method implemented to map snow cover from the satellite images. Traditionally, the mapping of snow is addressed in a binary fashion and pixels are categorized as being completely snow covered or snow free (Hall *et al.*, 2002). It is obvious that in very steep terrain such as the Southern Alps of New Zealand, the spatial resolution of the sensor has an effect on the accuracy of the snow maps. For example, large pixel size and steep slopes have the potential to introduce substantial uncertainties with regard to the positional accuracy of the transient snowline. Moreover, the criterion used to classify pixels as being ‘snow’ or ‘not snow’ is often based upon the area occupied by snow within the pixel. Thus, a subjective judgement is made and a pixel is considered to be snowy when it includes more than 50% snow.

However, such a criterion raises several issues. First, it requires the snow cover to be a measurable object.¹ This implies specific considerations with regard to the topology of the snow cover. In particular, it raises the issue of the fractal nature of the set, and thus the relevance of the measures used for its characterization. Second, it is often considered that the 50% threshold is optimal to estimate accurately the

¹Here the term *object* is used in its mathematical sense, i.e., something on which it is possible to use mathematics. In geometry as a branch of mathematics, objects encompass, but are not limited to, points, lines, surface, volumes, etc. More generally, in mathematics, the term *set* is often used to designate a collection of definite and separate objects (Cantor, 1955, pg. 85). The objects are called the *elements* of the set, with the *set* itself being a mathematical object. In the following, the terms *set* and *object* are used interchangeably and mostly refer to geometrical objects.

total snow covered area (SCA) in the image. This threshold relies on the intuition that over-estimations due to pixels considered fully covered when they are not are balanced by under-estimations due to pixels with less than 50% snow but classified as ‘snow free’.

This chapter first examines the issues raised by the fractal nature of the snow cover and its implications with regard to the mathematical measures used to characterize it. It then clarifies the basis and justification of binary mapping by revealing the intimate relationship between the statistical distribution of sub-pixel snow fractions, the spatial structure of the snowpack, and the pixel size. Finally, an alternative strategy used to map the snow cover is described. This relies on the use of a linear unmixing technique to create maps of sub-pixel snow fractions. Such an approach maximizes the amount of detail, while avoiding the pitfalls associated with binary mapping. By taking full advantage of the topographic and atmospheric correction of images described in the previous chapter, the method has the potential to be robust and well suited to the local environment. It was applied to both the 500m and 250m spatial resolution multispectral datasets, obtained without and with the fusion algorithm (see Section 3.4), respectively. This yielded two maps of sub-pixel snow fractions that enabled a comparative accuracy assessment to be conducted in Chapter 6 with regard to the performance and relevance of the fusion technique.

5.2 A matter of scale

5.2.1 The raster representation

Imaging sensors provide a discrete representation of the Earth’s surface by means of picture elements (pixels). This generates a raster data structure that is characterised, among other things, by its spatial resolution [e.g., the size of the pixels that is defined by the detector instantaneous field of view (IFOV)]. As a first approximation, the footprint of the pixel on the ground determines the limits from where the energy reflected or emitted by the surface is collected and integrated by the detector to obtain a single radiative measure. Such a measurement is repeated for a number of spectral bands, thus providing a multispectral raster dataset whose dimension characterizes the sensor’s spectral resolution.

However, it is evident that the materials forming the surface of the Earth and contributing to the signal vary spatially in a non-crisp or continuous manner (Bur-

rough, 1996, Chap. 1). Thus, the boundary between classes or objects is very unlikely to match the footprint of the pixels.¹ Instead, pixels are prone to account for an inhomogeneous mixture of materials. For instance, Fisher (1997) categorized mixed pixels as being caused by:

- small sub-pixel objects that cannot be resolved by the spatial resolution of the detector;
- the boundary between mapping units;
- linear objects such as roads whose width cannot be resolved;
- the continuous transition area between adjacent ecological entities (ecotone).

Inevitably, the raster structure of the data is an abstraction and a generalization of a geographic context, whose systematic sampling determines the spatial scale of the observation (Woodcock and Strahler, 1987; Blaschke and Strobl, 2001). The scaling nature of remotely sensed images caused by the dependence on spatial resolution (Gabriel *et al.*, 1988) eventually eludes the potentially complex geometry of natural geographical phenomena, and particularly the fact that they often exhibit fractal characteristics that can be difficult to grasp and model (Mandelbrot, 1983; Goodchild and Mark, 1987; Lam and Quattrochi, 1992; Blöschl, 1999).

5.2.2 Fractal considerations

Traditional Euclidean geometry has long been the framework to describe geometrical objects observed in nature. Thus, it is common to characterize spatial pattern and/or natural objects by their length, surface, or volume. However, it is now recognized that geographic phenomena may possess characteristics that fail to be

¹Note that in reality, the measure attributed to a nominal pixel location can depart from the actual region of the Earth that is sensed due to the Point Spread Function (PSF) and, eventually, to the response weighting function of the system. For instance, in the case of across-track scanners such as the MODIS instruments, the scan mirror rotates at constant speed. Thus, the detectors do not face the nominal footprint of a pixel sequentially, but instead, they sweep continuously across the terrain. Hence, the nominal location of a pixel is within the field of view of the detectors as it sweeps over a distance that is twice as large as the width of the pixel itself. In order to accommodate the surplus energy, the detectors implement a triangular response weighting function. Thus, there is still the potential for part of the radiometry attributed to one pixel to originate from the neighbouring pixels (Nishihama *et al.*, 1997).

measured by the Euclidean geometric language. Probably the most revealing example of the possible irrelevance of such measures has been brought to public attention by Mandelbrot (1967), who highlighted the inherent impossibility to approach the length of the coast of Britain with a classical measure of Euclidean geometry. Thus, Mandelbrot demonstrated that the length of the coastline is dependent on the size of the elementary segments used to depict it (i.e., the gauge). A power-law relationship forces the length of the boundary to increase indefinitely as the gauge to measure it gets smaller. This is caused by the fact that the coastline reveals infinite details as the scale of observation gets larger. In other words, the coastline is an object whose geometry is so rough and fragmented that any attempt to describe it by its length is irrelevant, as the latter is dependent on the scale of observation and does not converge to a finite quantity as the gauge's length tends to 0.

Mandelbrot (1975) coined the term *fractal*¹ to categorize sets that exhibit fine and irregular structures at arbitrary scales, and fractal geometry to encompass the tools and characteristics to describe them. The fractal manifestation of an object is not limited to its boundary and can account for multiple scenarios. For example, the set could be a connected set whose boundary is fractal such as the coastline of England. Alternatively, the set could be a countable infinite set of disjoint subsets whose distribution of size, pattern, and location comes under the concept of fractal geometry. A typical example used by Mandelbrot (1983, Chap. 13) involves the fractal nature of a cluster of islands. Even if the boundary of each island were rectifiable (i.e., non fractal), the relationship between their size and frequency can exhibit a fractal dimension that measures the fragmentation of the set rather than the irregularity of its boundary.

One of the properties that is often encountered with fractal objects is known as *self-similarity*, when any part of an object is exactly or approximately similar to the whole object in terms of shape or statistical properties (if the object is the outcome of a random process). Self-similarity is referred to as *scale invariance* when at any scale there is a part of the object that exactly matches the object as a whole. Among the tools used to characterize fractal objects, the notion of *dimension* is a central concept. Generally speaking, it is a real number assigned to the set and designed to measure its size and complexity. Two types of dimensions are distinguished (Mandelbrot, 1983, Chap. 3):

¹From the Latin *fractus* meaning “broken”.

- the *topological dimension*¹ of a set derived from the work of mathematicians Lebesgue, Menger, Brouwer, and Urysohn is a positive integer that corresponds to the “naïve” idea of dimension where points, lines, surfaces, and volumes have dimension 0, 1, 2, and 3, respectively.²
- the *fractal dimension* is a positive real number, not necessarily an integer, that measures how completely a set S fills the Euclidean space E in which it is embedded. Several specific definitions exist for the fractal dimension, with the most important probably being the *Hausdorff–Besicovitch dimension* (Falconer, 2003, Chap. 2). Alternative dimensions exist such as the *box-counting dimension*, *packing dimension*, or *correlation dimension* (Falconer, 2003, Chap. 3).

For example, consider the set S defined by Great Britain. The coastline of Britain is the boundary of S noted ∂S . Since ∂S has an empty interior, its topological dimension is less than 2, and thus is 1. However, Mandelbrot (1967) showed that the coastline has a Hausdorff–Besicovitch dimension of 1.25. This non-integer dimension, in between the topological dimension of the set and the next, indicates the fragmented and complex nature of the coastline. More specifically, it measures the ability of the line to fill up the plane in which it is embedded. It also highlights the departure of this line from a smooth and rectifiable Euclidean line whose fractal dimension would equal its topological dimension. In other words, a Euclidean line corresponds to the naïve idea of a set that has a length but no area. A fractal line accounts for a more complex scenario whereby, in a way, the line “occupies” the plane and its length is not a measurable quantity. This example can easily be extended to the next dimension by considering a rough surface in the 3-D space. The surface of natural terrain is the boundary of a volume in 3-D space, thus, it has a topological dimension of 2. However, its fractal dimension is often more than 2 (and less than 3) depending on the smoothness of the terrain (Polidori *et al.*, 1991), thus characterizing its fractal manifestation. In such a case, any attempt to approach the area covered by the terrain in the 3-D Euclidean space is as irrelevant as trying to estimate the length of a fractal line in a 2-D space.

Later, Mandelbrot (1983, Chap. 3) proposed a definition of fractal sets as being

¹Also called *Lebesgue covering dimension*.

²More rigorously, a set in a metric space has a topological dimension 0 if every point has arbitrarily small neighbourhoods whose boundaries do not intersect the set. A set S has a topological dimension D if each point in S has arbitrarily small neighbourhoods whose boundaries intercept S in a set of dimension $D - 1$, and D is the least non-negative integer for which this holds.

those which fractal dimension strictly exceeds the topological dimension. Nevertheless, this definition is considered too strict by some theorists who, rather than a hard definition, prefer to categorize fractal sets as being geometric objects that have most of the following properties (Falconer, 2003, pg. xxv):

1. the set has a fine structure, i.e., details on arbitrarily small scales;
2. the set is too irregular to be described in traditional geometrical language, both locally and globally;
3. often the set has some form of self-similarity, perhaps approximate or statistical;
4. usually, the fractal dimension of the set is greater than its topological dimension;
5. in most cases, the set has a simple and recursive definition.

It is beyond the scope of this thesis to provide a comprehensive review of fractal geometry or to discuss its framework of definitions, but only to draw attention to the potential complexity of the geometric objects found in nature, in particular the snow cover on which this thesis focuses. The two simple examples given above stress the need for precaution when using a measure to describe and quantify a geographic phenomenon that has continuous properties. In other words, the set or part of the set (e.g., its boundary) may be immeasurable. Therefore, when characterizing a set, the choice of a measure must be carefully considered to account for its potential fractal manifestation. The use of a measure potentially affected by the fractal nature of the phenomenon may severely jeopardize the validity of the conclusions that it suggests. Examples of such misuse exist such as the Gravelius compactness coefficient that is largely used in hydrological sciences to characterize drainage basins, but has been found irrelevant by Bendjoudi (2002).

Nevertheless, the possible fractal manifestation of the set (e.g., the fractal coastline of Britain) does not necessarily mean that the set is not measurable. Clearly Britain as a whole is a bounded set having interior points, so its Lebesgue measure is well-defined, positive, and finite. In simple words, despite the fractal manifestation of Britain with regard to its coastline whose exact length is not measurable, the set as a whole is a surface which is embedded in a 2-D Euclidean space. Its topological dimension is exactly two and the area is a relevant measure to characterize it.

Measuring the projection of the set onto a metric space of the same topological dimension is another way to characterize it. Indeed, the projection of a set of topological dimension D and fractal dimension k ($D < k < D + 1$) onto a metric space of dimension D is a set whose fractal dimension inherits the integral topological dimension D of the metric space in which it is embedded (Falconer, 2003, Chap. 6). The projection is thus a measurable set. As an illustration, although it has been explained above that the area of a natural terrain may be immeasurable due to the likely fractal nature of the surface in three dimensions, its orthogonal projection (or “shadow”) onto a plane inherits the dimension of the plane (i.e., 2) as both its topological and fractal dimensions. Thus, the projection can be measured and characterized by its area, although such a projection may still possess a fractal manifestation through its boundary.

5.2.3 The fractal nature of the snowpack

Since it is a surface embedded in a three dimensional space, snow cover can inherit a fractal behaviour from the underlying terrain (Lehning, 2005). Estimating the area covered by snow in three dimensions only makes sense if reasonable assumptions can be made with regard to the rectification of the underlying bare ground and/or eventually the smoothing effect of the snowpack. In addition, a phenomenon can inherit fractal properties from an underlying fractal pattern of the causal phenomena (Halley *et al.*, 2004). The spatial distribution of the snow in alpine terrain results from the combination of multiple causes associated with the competing processes of accumulation and ablation. These are summarized by Elder *et al.* (1991) and reviewed here in the light of their potential, although not exhaustive, fractal inheritance.

- **Accumulation**

- The *variability of snowfall fields*, both spatial and temporal, whose chaotic and fractal nature can be inferred from the space-time multi-fractal character often observed in rain fields (Lovejoy and Mandelbrot, 1985; Peters and Christensen, 2002).
- The *transport and re-distribution of snow by wind*, whose profiles have been shown to exhibit spatial self-similarity over several orders of magnitude (Tabler, 1980). Kavasseri and Nagarajan (2005) also presented evidence

of multifractal behaviour in wind speed with respect to time. Tchiguirinskaia *et al.* (2006) obtained a similar conclusion when considering wind extremes. In addition, complex processes such as cohesion and sublimation affect the blowing of snow (Schmidt, 1982). For instance, cohesion determines the threshold wind speed at which snow can be redistributed, resulting in potentially strong non-linearities with regard to the transport of snow particles by wind. The complex interactions of turbulent wind fields with features such as bowls and gullies, as well as vegetation, complicates the spatial distribution and re-distribution of snow by wind, by favouring the interception and/or the greater exposure of the snow pack. Given that the fractal nature of both the terrain (Mandelbrot, 1983, pg. 256; Polidori *et al.*, 1991) and the vegetation distribution (Kunin, 1998) are generally recognized, it yields a potentially highly variable pattern of snow in terms of depth and/or density, both likely being inherited from the fractal characteristics of the causal processes.

- The *transport of snow by avalanches* also changes considerably the spatial pattern of snow depth and snow water equivalent (SWE). In terms of fractal behaviour, Birkeland and Landry (2002) presented evidence that the frequency of avalanches follows power laws with respect to avalanche size. They also observed that the fractal dimension of the frequency-size relationship of snow avalanches was similar whether avalanches were of natural or artificial causes. Similarly, Rosenthal and Elder (2003) studied the number-size relationship of slab avalanches and also observed a fractal behaviour in most cases. Although they acknowledged the fractal nature of topography in general, they assessed the terrain of their experiment as being not scale-independent (i.e., non-fractal). Hence they rejected the topography as the cause of the scaling nature of avalanches. Similarly, they did not identify any fractal characteristic in new snow falls over the time frame of their investigation. Hence, they also rejected new snow layering as a potential source of chaos in the slab avalanche process.
- **Ablation** The ablation of snow is governed by the energy fluxes associated with several processes of heat transfer that occur to and/or from the snow-pack.
 - *Shortwave and longwave radiation* are received from the sun, the atmo-

sphere, and reflected by adjacent slopes, while the snowpack itself emits longwave radiation due to its own kinetic temperature. Shadowing obviously affects the energy budget by reducing the amount of shortwave radiation received from the sun and longwave radiation received from surrounding materials. [Klinkenberg \(1994\)](#) showed that the distribution of shadows and sunlit areas inherits fractal behaviour from the terrain surface. [Barsky and Petrou \(2005\)](#) eventually proposed a theoretical method to compute such a fractal shadowing.

- The *sensible heat flux* results from the convective exchange of heat between the snowpack and the surrounding air, while the *latent heat flux* corresponds to the processes of sublimation and condensation at the surface of the snowpack. Both are turbulent energy components that are affected by wind velocity ([Etchevers et al., 2004](#)), whose fractal nature was briefly discussed above.
- The *advective heat flux* is induced by new precipitation events (rain or snow) occurring on the existing snowpack. Its potential spatio-temporal pattern may also be inherited from the fractal nature of precipitations.
- The *conduction* of heat at the interface between the ground and the snowpack.
- The *rate of change of internal energy* corresponds to the energy that is used to change the temperature of the snowpack or freeze the liquid water that it contains.

As noted above, the spatial distribution of snow with regard to its depth and density (and by consequence SWE) has multiple reasons for inheriting fractal characteristics from the combination of complex processes that govern its formation and depletion. Experimentally, [Shook and Gray \(1996\)](#) studied the spatial distribution of snow depth based on data collected along 1000m transects. This gave rise to a pronounced fractal nature of this parameter within ranges less than 20m. The fractality (i.e., amount of self-similarity) progressively decreased until a range of approximately 100m. At a larger range, the variance of the snow depth reached a maximum, thus showing the loss of self-similarity in the spatial distribution at smaller scale. Later, in their attempt to model snow cover, [Shook and Gray \(1997\)](#) went into more detail by exploring snow depth, snow density, and SWE. All parameters proved to possess fractal characteristics. SWE and snow depth revealed similar

fractal characteristics, while they departed from that of snow density. It suggested that the spatial structure of snow density has a marginal impact relative to that of the SWE. Hence, the fractal geometry of the latter seemed more directly inherited from that of snow depth.

Kuchment and Gelfan (2001) also observed a fractal behaviour of the SWE field in various locations, despite a relatively small number of data points to construct their variograms. A deeper insight was provided by Deems *et al.* (2006) who used airborne light detection and ranging (LIDAR) altimetry to study the spatial distribution of snow depth in a variety of environments, from low to high relief and with different vegetation cover. The snow depth was obtained after processing the difference of surface elevation based on two LIDAR datasets obtained from snow free and subsequently snow covered terrain. The high number of data points allowed the multifractal nature of the spatial distribution of snow depth to be detected and confirmed the variation of the fractal dimension from short- to long-range. The fractality of the spatial distribution of snow depth was revealed by a power-law relationship of its semi-variogram as illustrated in Figure 5.1 at short-range. The break of slope at approximately 20m accounts for a change of fractal characteristics (e.g., a potentially multifractal behaviour). The fractal nature of the spatial variable is much less pronounced at long-range (i.e., scale greater than 100m), and confirms the progressive loss of self-similarity in snow depth spatial patterns at small scales.

As the snowpack depletes during the ablation season, the fractal behaviour of the spatial distribution of SWE potentially induces a fractal manifestation to the set of snow patches resulting from the break-up of the snow cover. Aerial or satellite imagery is a practical way to observe, investigate, and characterize this set. Thus, using air photos in two different catchments (i.e., Alpine and prairie regions) over different timeframes of snow depletion, Shook *et al.* (1993) showed that both the area-frequency and perimeter-area distribution of patches follow power-law relationships. It revealed the fractal nature of the set of snow patches as well as the consistency between the two catchments over the different timeframes. Granger *et al.* (2002) repeated the experiment and also obtained a fractal dimension for the perimeter-area relationship.

In this respect, any measure used to characterize the snow cover from images whose pixel size defines the scale of observation must be chosen in the perspective of their relevance for describing a potentially fractal phenomenon. For instance, measuring the perimeter of the snow cover (or any patches forming it) has the po-

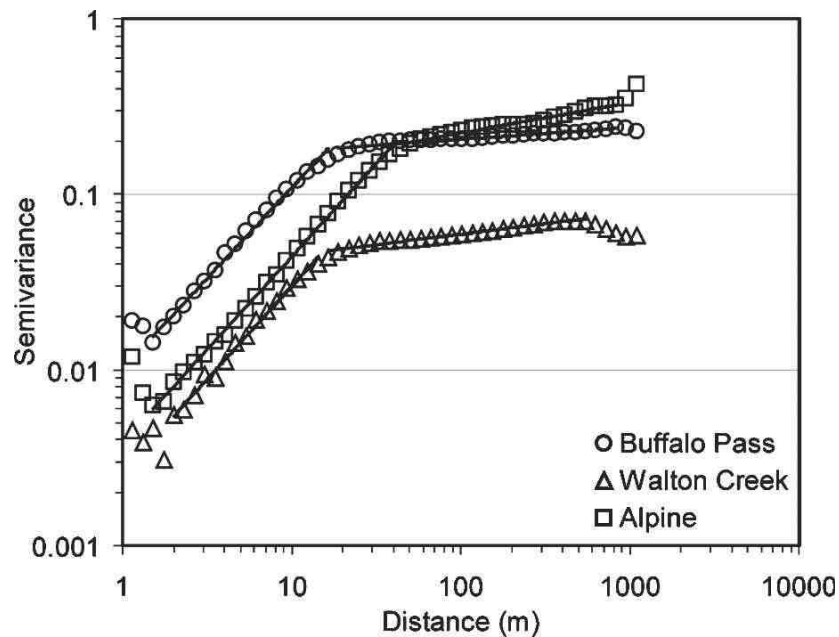


Figure 5.1 Characterization of the fractal behaviour of snow depth in three locations, reproduced from Deems *et al.* (2006). The fractal nature of the spatial distribution of snow depth is revealed in the variogram by a power-law relationship between the semivariance and the lag (i.e., distance) at short-range. The break of slope at approximately 20m accounts for a change of fractal characteristics. A null slope would correspond to a randomly distributed field that does not exhibit self-similarity properties (i.e., not fractal).

tential to be a vain exercise that should be considered very carefully. Alternatively, the projected surface of the snow cover onto the 2-D plane of the image is a bounded set with interior points. Thus, it is measurable in the sense of the 2-D Lebesgue measure (i.e., the area).¹ Despite the discretization of the plane induced by the pixels, the estimation of the area of the snow cover tends to its true area as the pixel size gets smaller. Of course, this estimation supposes that pixels can be identified according to whether they account for snow or not.

¹This holds even if the snow cover is discontinuous, regardless of the distribution of snow patches and its potential fractal behaviour, because individual snow patches form a countable (infinite or not) set of disjoint subsets, all of them measurable.

5.3 Binary and sub-pixel classification

5.3.1 Pixel-wise binary classification

Pixel-wise classification techniques aim at recognising spectral patterns in the multispectral dataset so that individual pixels are assigned to a limited number of land cover classes. Thus, these methods increase even more the level of generalization by categorizing entire pixels into the class whose spectral signature they most closely resemble. Although the spectral similitude to a class can generally be attributed to its prevalence within the pixel, such a crisp classification fails to provide an insight with regard to the presence of other materials that may contribute to the pixel radiometry.

In most cases, the results of pixel-wise classifications are simply regarded as binary for they ultimately aim at categorizing pixels whether they belong either to the 'snow' or the 'no snow' classes. In general, the threshold on the NDSI is designed so that a pixel is classified as 'snow' if it accounts for more than 50% snow, and 'no snow' otherwise (Robinson *et al.*, 1993; Hall *et al.*, 2002). This threshold can eventually be customized in order to fit specific conditions, such as detecting snow in forested areas. In these locations, the threshold can be reduced to ensure the detection of pixels that account for more than 50% snow but whose reflectance is decreased by the vegetation canopy (Klein *et al.*, 1998). Alternatively, the threshold may be set higher to favour the detection of pixels more fully covered by snow or avoid misclassification of bright, non-snow targets (Hall *et al.*, 1995).

5.3.2 Intuitive justification of binary mapping

It has been shown that the snow cover possesses a fractal geometry that requires care with regard to the choice of appropriate measures to characterize it. In this respect, the area covered by the snow cover surface projected onto the Euclidean plane is a relevant measure because it inherits the integral topological dimension of the two-dimensional Euclidean space (Falconer, 2003, Chap. 6). Despite its abstraction, the binary representation of snow by pixels is meaningful given that the criteria for classification into the 'snow' or 'no snow' classes is based on the projected surface fraction of 'snow' relative to 'no snow' (e.g., 50% threshold).

However, binary classifications that are designed to map pixels more than half covered by snow rely on the assumption that, overall, overestimates will balance

underestimates. This is justified by the fact that, intuitively, the process of rasterization of the irregular boundary between snowy and snow-free targets into sub-pixel fractions of snow shall provide pixels whose values will distribute evenly whether they account for more or less than 50% snow. Authors such as [Elder *et al.* \(1998\)](#) investigated various thresholds (i.e., 40, 50, and 60%) and experimentally confirmed that 50% was the most appropriate to approach the total snow covered area (SCA) in general. Nevertheless, this assumption deserves further clarification.

5.3.3 Distribution of sub-pixel snow fractions

Consider a random patch of snow, such as that illustrated by the simple case shown in Figure 5.2 (a). Figure 5.2 (b) shows the rasterization of the patch at an arbitrarily fine scale so that the pixels accounting for fractional snow cover are identified and the proportion of the pixel's area that they represent is calculated. Figure 5.2 (c) provides the experimental distribution of area proportion along the boundary. As expected, the distribution of values is shown to be symmetrical with respect to the midpoint value (50%). By symmetry each mixed pixel with a fractional cover x shall have a counter part of fractional cover $(100\% - x)$. Hence, in such a case, accounting for all pixels more than half covered as being totally covered, would be balanced by ignoring all pixels less than half covered in the estimation of the total area of the patch.

Assuming a rasterization independent of a random connected set of the plane (i.e., the intersection between pixels and the set boundaries does not follow any preferred path) that is fine enough to resolve its boundaries (i.e., the pixel size provides a relatively large number of mixed pixels), it would be intuitive to expect the distribution of sub-pixel fractions to be uniform. In other words, the fractional cover within pixels would have as many chances to take any value in the interval $]0, 1[= \{x \in \mathbb{R} : 0 < x < 1\}$. However, Figure 5.2 (c) clearly contradicts this intuition. Although it provides only a single example, the experiment was repeated a number of times with random shapes, as well as with deterministic shapes such as circles and polygons. All revealed an increased probability for mixed pixels to have fraction closer to 0 or 100% than to 50%.

[Key \(1994\)](#) investigated the problem of the distribution of area proportion in mixed pixels. He also observed U-shaped distributions such as that shown in Figure 5.2 (c) and suggested that it can be modelled by a beta distribution $\text{Beta}(\alpha, \beta)$. The latter has a density function defined on the interval $[0, 1]$ and is parameterised

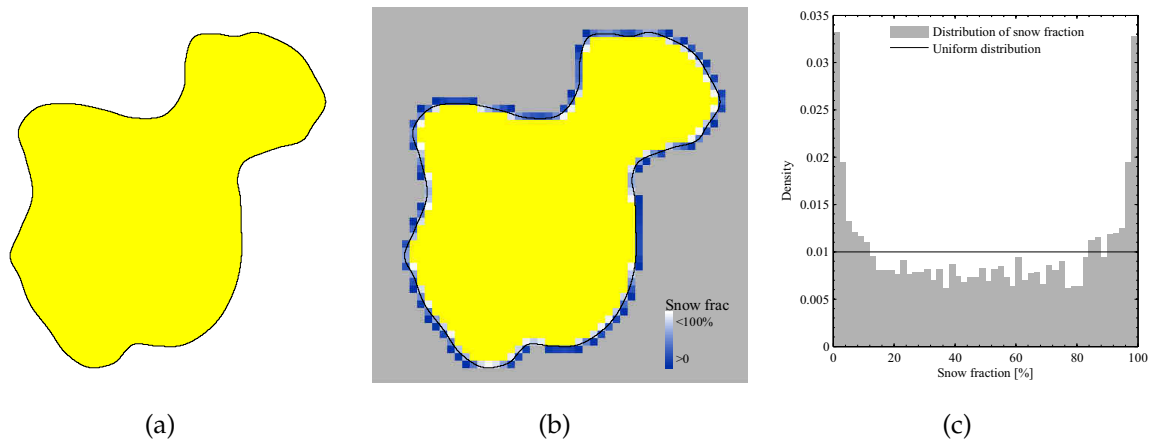


Figure 5.2 Empirical distribution of fractional snow cover at the edge of a “toy” snow patch: (a) Snow patch of random shape; (b) fractional snow cover after rasterization (pixels fully covered and free of snow are yellow and gray, respectively); (c) density of probability of sub-pixel snow fraction [note that the histogram was obtained from a rasterization at a much smaller pixel size than shown in (b)].

by two positive parameters α and β that control its shape. The density function of a Beta distribution is given by

$$f_{\alpha,\beta}(x) = \begin{cases} \frac{\Gamma(\alpha+\beta)}{\Gamma(\alpha)\Gamma(\beta)} x^{\alpha-1} (1-x)^{\beta-1}, & \alpha, \beta > 0, 0 < x < 1, \\ 0 & \text{elsewhere,} \end{cases} \quad (5.1)$$

where $\Gamma(a)$ is the gamma function defined by the integral $\Gamma(a) = \int_0^\infty e^{-t} t^{a-1} dt$. Beta distributions can be unimodal when $\alpha, \beta > 1$ (e.g., L-, J-, or bell-shapes), or bimodal when $\alpha, \beta < 1$ (e.g., U-shapes). With $\alpha = \beta = 1$, the beta distribution identifies to a uniform distribution. Examples of possible shapes for different values of the parameters are shown in Figure 5.3. Such a large range of shapes makes this theoretical distribution highly versatile to accommodate various scenarios and often used for modelling proportions (Falls, 1974; Ferrari and Cribari-Neto, 2004; Ozdogan and Woodcock, 2006). Kitamoto and Takagi (2000) also identified the beta distribution as a relevant candidate to approach the area proportion distribution of mixed pixels. However no theoretical background, and/or physical explanation, was found to support the choice of the beta distribution in the problem of mixed pixels. Furthermore, no clear reason could be identified to explain the U-shaped distribution and the appearance of two modes near 0 and 100% in many cases.

The two parameters of $\text{Beta}(\alpha, \beta)$ can be estimated by the mean μ_X and the variance σ_X of the random variable X associated with the sub-pixel fraction as follows:

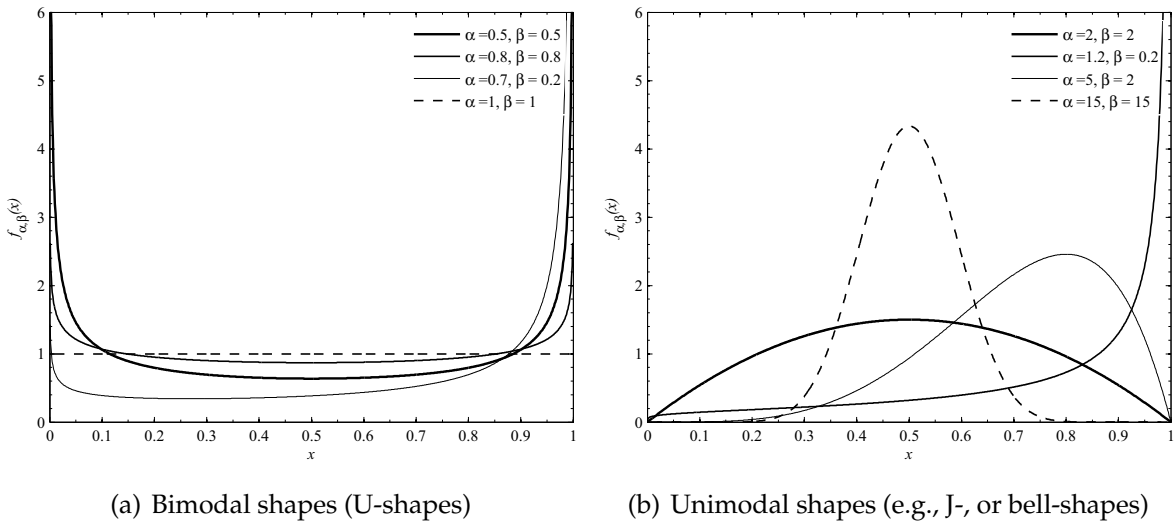


Figure 5.3 Example of beta distributions for various shape parameters.

$$\alpha = \mu_X \left(\frac{\mu_X(1 - \mu_X)}{\sigma_X^2} - 1 \right), \quad (5.2a)$$

$$\beta = \frac{1 - \mu_X}{\mu_X} \alpha. \quad (5.2b)$$

Key (1994) explained that the shape of the distribution is controlled by the size of the pixel relative to the spatial structure of the object (i.e., the distribution of size and positions of the connected components of the object). For example, Figure 5.4 (a) depicts a nearly continuous snowfield with small bare patches relative to the pixel size. None of the connected components of this set can be resolved by the pixel size. Snow is the dominant target in the image and most pixels account for more than 50% snow. This yields that $\mu_X > 50\%$ hence $\alpha > \beta$ according to Equation (5.2b). Thus, the distribution of sub-pixel snow fractions could be modelled by an asymmetric bell-shaped [e.g., Figure 5.3 (b) with $\alpha = 5$, $\beta = 2$], J-shaped [e.g., Figure 5.3 (b) with $\alpha = 1.2$, $\beta = 0.2$], or an asymmetric U-shaped [e.g., Figure 5.3 (a) with $\alpha = 0.7$, $\beta = 0.2$] beta distribution, for small to large values of σ_X , respectively. Reciprocally, a bare field with small snow patches relative to the pixel size [Figure 5.4 (b)] would yield distributions of area proportion with a reverse shape with respect to the 50% midpoint (i.e., inversion of α and β). A symmetric distribution corresponds to shape parameters $\alpha = \beta$. It is achieved when:

1. Pixels are small enough to resolve patch boundaries, and the intersections between the boundaries and the pixels do not follow any preferred path. It yields

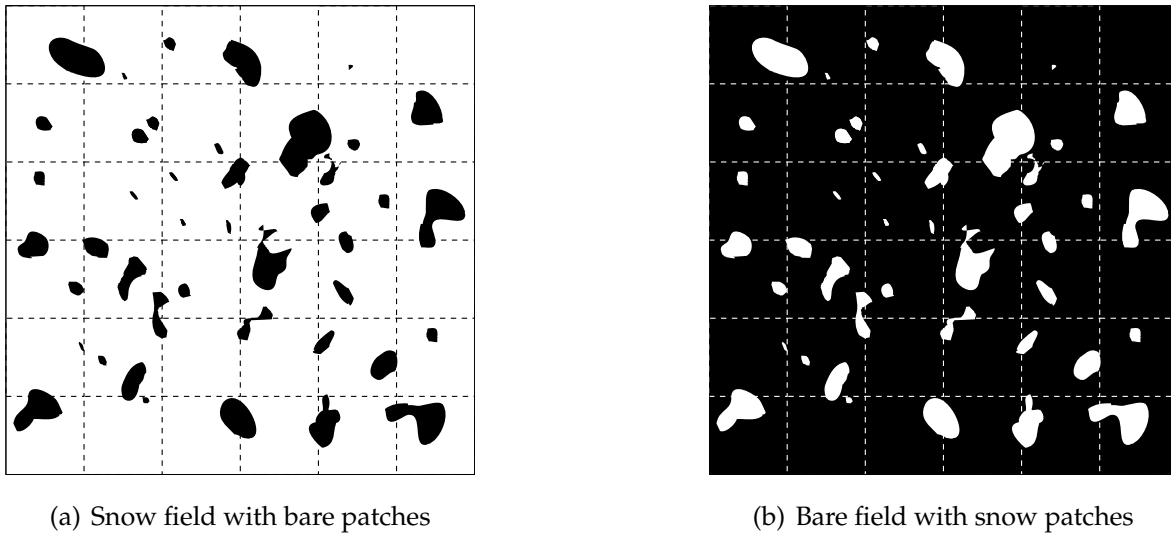


Figure 5.4 Conceptualization of (a) a snow field with bare patches, and (b) a bare field with snow patches. Dotted lines represent the pixel footprint. A binary representation of the subset based on a threshold of 50% snow cover within pixels would lead to (a) an overestimation, and (b) an underestimation of the SCA.

a symmetric U-shaped distribution such as that shown in Figure 5.2 (c)].

2. Pixels are too large to resolve patch boundaries but the structure of the set of patches enables the population of mixed pixels to account equally for both types of scenarios shown in Figure 5.4 (a) and (b). It yields a symmetric U-shaped or bell-shaped distribution.
3. A combination of both configurations above, where the snow cover accounts for large objects relative to the pixel size whose boundaries can be resolved, as well as areas with bare and snow patches relatively large compared to the pixel size but evenly represented.

The thresholding approach corresponds to setting the pixels having $x < t$ as 0 and 1 otherwise, where $0 < t < 1$ is the threshold. Such an approach is considered optimal if the estimation of the total area from the pixels retained as fully covered equals the true area of the object. The threshold t that satisfies this criterion is a solution of $\text{Prob}(X \leq t) = \text{Prob}(X \geq t)$. If $X \sim \text{Beta}(\alpha, \beta)$, then t is solution of

$$\int_0^t x f_{\alpha, \beta}(x) dx = \int_t^1 x f_{\alpha, \beta}(x) dx. \quad (5.3)$$

Thus, it is solution of¹

$$t^{\alpha+1} {}_2F_1(\alpha + 1, 1 - \beta; \alpha + 2; t) = \frac{\Gamma(\alpha + 2)\Gamma(\beta)}{2\Gamma(1 + \alpha + \beta)}, \quad (5.4)$$

where ${}_2F_1(a, b; c; z) = \sum_{n=0}^{\infty} \frac{(a)_n(b)_n}{(c)_n} \frac{z^n}{n!}$ is the standard hypergeometric series and $(a)_k = \frac{\Gamma(a+k)}{\Gamma(a)}$ is the Pochhammer symbol. It essentially demonstrates that the choice of the optimal threshold is a function of the parameters of the distribution. Consequently, it depends on the relationship between the pixel size and the spatial structure of the snow patches.

5.3.4 Limitations of the binary representation and need for sub-pixel mapping

If the shape parameters of the distribution of sub-pixel fractions are known, solving Equation (5.4) analytically remains a challenge but can be addressed efficiently with numerical techniques. However, it is problematic to determine such a shape *a priori*, because the relationship between the object structure and the pixel size that governs the shape parameters is not explicit and difficult to grasp. This is especially true when the set is fractal, yielding a geometrical structure that is difficult to formalize. The appropriate threshold that provides a reliable SCA cannot be predicted when the distribution is not an achievable outcome. It highlights the paradox of a thresholding strategy, whose purpose is often to avoid the complication of retrieving sub-pixel fractions, although it possesses an intimate relationship with it.

Kitamoto and Takagi (2000), who investigated synthetic images with fractal boundaries, have shown that the sub-pixel fractions are identically and symmetrically distributed regardless of the fractal dimension of the boundary. This experimental result is important here because it suggests that even fractal boundaries, such as those of the snow cover, at least can be reasonably expected to provide a symmetrical area proportion distribution when the pixels are small enough. It justifies that the assumption of a symmetrical distribution is the only alternative in the general case, and the use of the 50% threshold can be considered optimum.

However, it is now clear that the relationship between the spatial structure of the snow cover and the pixel size governs the validity of this assumption in specific contexts. An inappropriate pixel size, relative to the spatial structure of the snow

¹This is achieved using $\int x^\alpha(1-x)^{\beta-1} dx = \frac{x^{1+\alpha} {}_2F_1(\alpha+1, 1-\beta; \alpha+2; x)}{1+\alpha}$ and ${}_2F_1(a, b; c; 1) = \frac{\Gamma(c)\Gamma(c-b-a)}{\Gamma(c-a)\Gamma(c-b)}$.

cover, can yield a departure from the symmetric distribution that compromises a reliable estimation of the total SCA. If the investigation is applied to an image (or a subset of an image) that depicts unevenly a snow field with bare patches [i.e., more than 50% SCA for the image, Figure 5.4 (a)], or a bare field with snow patches [i.e., less than 50% SCA, Figure 5.4 (b)], so that the pixel size does not permit to resolve the boundaries of individual patches, then large errors can be expected.

Such a limitation of the binary representation is sometimes associated with its potential for overestimation (Xiao *et al.*, 2004). Hall *et al.* (2002) mentioned this drawback of binary classification by referring merely to a patchy but nearly continuous snowpack whereby the areal extent of the snow cover would be overestimated. It is evident that this issue is symmetric. The SCA of a nearly-continuous snow field with bare patches would be overestimated, while a bare field with snow patches would be underestimated. More generally, Dozier and Painter (2004) demonstrated the larger inaccuracy of binary classification algorithms, when applied to spatially highly-variable or patchy snow cover as the pixel size gets larger. Thus, they stressed the need for mapping snow cover at sub-pixel resolution.

As introduced in the example shown in Section 5.3.3, sub-pixel resolution refers to the estimation of the projected fraction of specific land cover types, or *end-members*, within individual pixels. This approach avoids the pitfall of binary classification schemes. Being computed as the sum of the fractions in all pixels, the SCA can be estimated realistically regardless of the continuity of the snow cover. It does not require a population of binary pixels to balance over- and underestimates. Thus, it does not depend on the spatial resolution and it is appropriate to depict a discontinuous snowpack even if the latter exhibits fractal geometry.

In the context of pixel-wise classifications based on classical clustering techniques (whether trained or not, i.e., supervised or unsupervised, respectively), the classifier has the potential to distinguish several types of snow classes. This is due to the variability of the pixels' spectral signature which depends on the prevalence (i.e., more or less) and type of snow (e.g., fine to coarse granular, dry to melting). In general, it corresponds to the transient zone between the snow covered and the snow free area. For instance, Swamy and Brivio (1997) trained a maximum likelihood classifier (MLC) to identify the snow transition zone in alpine terrain and assumed that the pixels belonging to such a class were half covered by snow, while pixels belonging to the class of pure snow were assumed to be fully covered. In the case of the unsupervised ISODATA classifier, Slater *et al.* (1999) identified class

spectra that corresponded to partially snow covered pixels. They then estimated the fractional snow cover for pixels belonging to such classes using the Normalized Difference Vegetation Index (NDVI) as a surrogate. To some extent, these two latter examples can be considered as sub-pixel methods, although they correspond more to hybrid solutions that rely on pixel-wise classifications in association with an arguable appreciation of mixed classes. In this regard, they do not truly attempt to model the underlying physics that govern the radiometric quantities originating from a mixed pixel.

5.4 Spectral mixture analysis¹

5.4.1 Mixing models description

Spectral mixture analysis is aimed at modelling the relative contribution of selected materials on pixel radiometry (Horowitz *et al.*, 1971). Several approaches exist that can be grouped into two categories:

1. *Linear Mixing Models (LMM)* approach the physics of multi- and hyper-spectral radiometric mixing based on the assumptions that: (1) each individual pixel of the remotely sensed image can be represented by a mixture of discrete *end-members* (i.e., pure pixels corresponding to land cover classes such as snow, vegetation, forest, rock), and (2) the measured radiance is the sum of the contribution of each end-member as a linear function of its respective fraction in the pixel (Keshava, 2003). These assumptions are generally considered valid when the materials at the surface are organized so that multiple scattering of energy between the different substances forming the pixel are negligible (Singer and McCord, 1979; Keshava, 2003; Dozier and Painter, 2004). In the reflective domain, it corresponds typically to planar surfaces upon which the incident radiation is expected to bounce only once [Figure 5.5 (a)].
2. *Non-linear Mixing Models* are generally designed to account for more complicated scenarios with regard to the interaction of incident energy with the surface. Multiple scattering of the incident radiation between the substances

¹The content of this section is largely published in: Sirguey, P., Mathieu, R. and Arnaud, Y. (2009). Subpixel monitoring of the seasonal snow cover with MODIS at 250m spatial resolution in the Southern Alps of New Zealand: Methodology and accuracy assessment. *Remote Sensing of Environment*, 113(1), 160–181, doi:10.1016/j.rse.2008.09.008

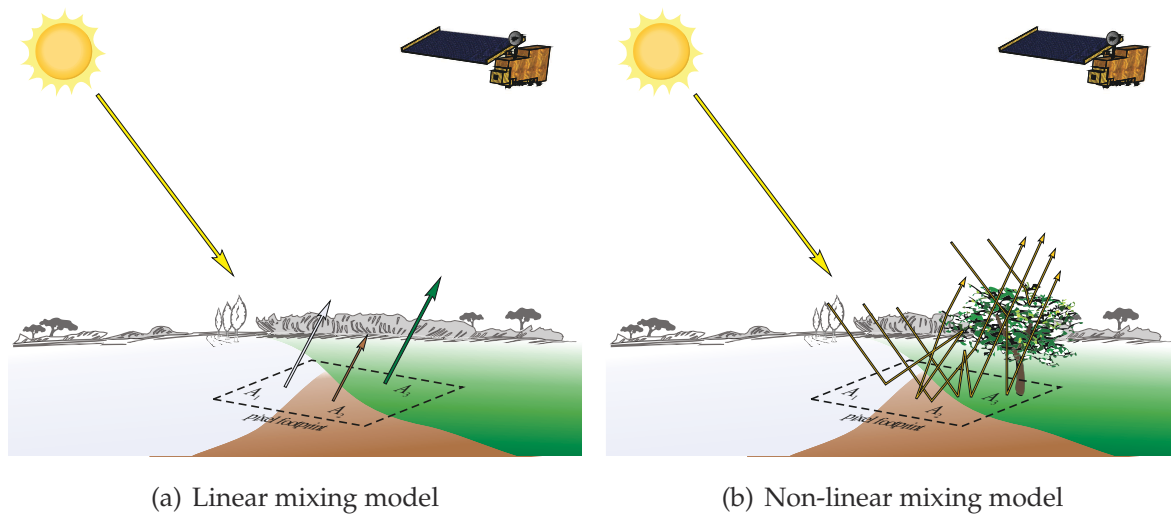


Figure 5.5 Two mixing models: (a) the linear mixing model is applicable when the illumination can be assumed to reflect only once onto the surface; (b) the non-linear mixing model attempts to describe a more complex scenario of reflexion between the substances present within the pixel footprint, such as volume scattering within forest canopy.

that form the surface may jeopardize the assumption of linear mixing. For instance, by reflecting and transmitting NIR wavelengths, green vegetation creates volume scattering within canopy and potential multiple reflection from the ground substrate [Figure 5.5 (b)]. It complicates the radiometric mixture which may depart consequently from the linear approximation (Roberts *et al.*, 1993).

Spectral unmixing is an image classification technique that corresponds to the process of inverting the spectral mixture model to estimate the *abundance* (i.e., percentage) of each possible end-member in a pixel (van der Meer, 2002). Numerous unmixing methods exist that are designed for the resolution of the linear or the non-linear problem and for which a comprehensive taxonomy can be found in Keshava (2003). Non-linear inversion techniques include for example fuzzy classification, neural network, support vector machine, regression and decision trees. These methods rarely rely on a physically-based model of the radiometric mixture. Instead, they are statistical or empirical methods sometimes based on the principles of learning theory (Vapnik, 2000) and often require a careful design and training before yielding acceptable results. Despite the acknowledged performance of some of these techniques (Brown *et al.*, 1999; Liu and Wu, 2005) non-linear mixing models

were not considered in this thesis due to their lack of physical meaning, and because, as explained in the next section, relevant assumptions could be used to justify the framework of the linear mixture model.

The spectral resolution of the sensor is crucial to spectral unmixing because it sets the dimensionality of the feature space, and hence the number of independent points available to invert the mixture model. This dimension determines the number of end-members that can possibly be resolved, and therefore, the complexity of the scene that can be analysed (Boardman, 1994; Small, 2001). Such a dependence on the spectral sampling limited the application of unmixing techniques in remote sensing until progress in multi- and especially hyper-spectral technologies provided a spectral dimension suitable to analyse complex scenes and identify unique materials (Goetz *et al.*, 1985; Sabol *et al.*, 1992).

Hyper-spectral imagery acquired by instruments such as the NASA's Airborne Visible/Infrared Imaging Spectrometer (AVIRIS) or space-borne EO-1 Hyperion is ideally suited to spectral unmixing because measurements are made for a high number of spectral bands in the visible range to shortwave infrared (e.g., AVIRIS and Hyperion are capable of resolving 224 and 220 contiguous spectral bands, respectively). Very complex scenes can be analyzed for which end-members are often chosen from a spectral library of pure materials (e.g., type of rock, crop species, etc.) and their abundance retrieved. Such techniques have found many applications in geology (van der Meer *et al.*, 2001), agriculture (Fitzgerald *et al.*, 2005; Bannari *et al.*, 2006), vegetation mapping (Roberts *et al.*, 1993, 1998), or environmental monitoring (Shrestha *et al.*, 2005; Miao *et al.*, 2006).

Despite a much lower spectral resolution, multispectral instruments such as Landsat TM, NOAA AVHRR, ASTER, or MODIS have also proven to be suitable for spectral unmixing in a wide range of domains including urban mapping (Wu and Murray, 2003; Lu and Weng, 2004; Pu *et al.*, 2008), forestry (Shimabukuro *et al.*, 1994; Adams *et al.*, 1995; Souza *et al.*, 2003), terrestrial and extraterrestrial geology (Adams *et al.*, 1986; Ballantine *et al.*, 2005), ecology and agriculture (Graetz and Gentle, 1982; Quarmby *et al.*, 1992), or glaciology (Klein and Isacks, 1999). Multispectral applications generally differ from hyper-spectral by the fact that end-members are chosen to be representative of a class of land cover rather than pure materials due to the much lower dimensionality of the feature space, and the integration of upwelling radiance over a wider spectral range.

5.4.2 Spectral unmixing of snow

In the context of sub-pixel snow mapping, [Nolin *et al.* \(1993\)](#) and [Painter *et al.* \(1995\)](#) demonstrated the potential of linear unmixing to produce maps of sub-pixel snow fractions from a selection of AVIRIS spectral bands. [Rosenthal and Dozier \(1996\)](#) developed a snow mapping algorithm for Landsat TM imagery based on both linear and non-linear approaches. First, they used a linear unmixing algorithm to produce maps of sub-pixel snow fractions for two reference scenes acquired in winter and spring. Then, in order to reduce the computation time of Landsat TM images from the same region, [Rosenthal and Dozier \(1996\)](#) developed a decision tree based on the two preliminary classifications and the sensor spectral bands. However, this method was designed for a local environment with few images and was not proven to be applicable globally ([König *et al.*, 2001](#)), or for a large temporal dataset. [Painter *et al.* \(2003\)](#) developed further the linear unmixing of AVIRIS images and this approach has become increasingly popular for mapping snow at the sub-pixel level with other multispectral sensors such as MODIS ([Vikhamar and Solberg, 2003](#); [Painter *et al.*, 2009](#)), or AVHRR ([Foppa *et al.*, 2004](#)).

Alternatively, some researchers took advantage of the sensitivity of spectral ratios such as the NDSI to map snow abundance within pixels. It allowed the development of statistical regressions that enabled the retrieval of sub-pixel snow fractions from the index or specifically designed band combinations. Thus, [Barton *et al.* \(2000\)](#) used data from [Rosenthal and Dozier \(1996\)](#) and established a quadratic polynomial regression between the NDSI and the snow fraction. They also considered the NDVI as an additional variable in a bivariate third-order polynomial regression. Although this relationship was developed on the basis of a single Landsat TM scene, [Barton *et al.* \(2000\)](#) applied this model to MODIS images but did not provide any rigorous assessment of its accuracy. With regard to MODIS data, a simple linear regression between the NDSI and the sub-pixel snow fraction was preferred by [Salomonson and Appel \(2004, 2006\)](#). It was considered to be a robust and fast approach to map snow on the sub-pixel basis at the global scale and became a component of the collection 5 of the MODIS MOD10 snow product ([Riggs *et al.*, 2006](#)). Other forms of combinations between spectral bands have been considered which are examples of statistical linear or non-linear mixture analysis depending on the formula implemented ([Kaufman *et al.*, 2002](#); [Metsämäki *et al.*, 2002](#); [Romanov *et al.*, 2003](#)).

In their comparison of both linear and non-linear mixing algorithms for sub-pixel snow mapping, [Zhang *et al.* \(2005\)](#) concluded that a linear mixture model and

support vector machine achieved comparable performance and supplanted fuzzy classification and neural network approaches. However, the computing requirements of linear unmixing limit its use at the global scale (Dozier and Painter, 2004). The same issue applies to large temporal datasets and this thesis is among the first to attempt the implementation of linear unmixing on hyper-temporal imagery.

In this chapter, radiation is assumed to interact only once with the surface. This is justified by the fact that, in the optical range (i.e., visible, NIR, and SWIR wavelength), a snow layer of no more than a few centimetres thickness is sufficient to reach almost semi-infinite albedo (Warren, 1982; Armstrong and Brun, 2008, pg. 54), and prevent the underlying substrate to contribute to the radiometry. In addition, considerable effort has been invested to address multiple scattering between adjacent slopes and retrieve ground reflectance (see Chapter 4). Finally, the area of interest is mostly composed of low vegetation and bare ground covered by snow during winter. Tall vegetation only includes small and scattered patches of pine trees and native forests at low elevations that are rarely covered by short-lived snow fall. Consequently, the complications that would require the use of a non-linear unmixing approach are not an obstacle in this case. The implementation of a linear mixing strategy is preferred and assumed to be reasonable in such a context.

5.4.3 Linear mixing model

The spectral signature of each pixel is modelled as a linear combination of the spectral signatures of selected end-members with regard to their respective fractions. The abundance of each end-member can be estimated by the inversion of the following linear system:

$$\begin{pmatrix} \rho_1 \\ \vdots \\ \rho_7 \end{pmatrix} = \begin{bmatrix} r_{11} & \cdots & r_{1N} \\ \vdots & \ddots & \vdots \\ r_{71} & \cdots & r_{7N} \end{bmatrix} \cdot \begin{pmatrix} f_1 \\ \vdots \\ f_N \end{pmatrix} + \begin{pmatrix} \epsilon_1 \\ \vdots \\ \epsilon_7 \end{pmatrix}, \text{ or } \boldsymbol{\rho} = \mathbf{R}\mathbf{f} + \boldsymbol{\epsilon}, \quad (5.5)$$

where $\boldsymbol{\rho}$ is the vector of ground reflectance (i.e., ρ_i is the reflectance in band i), \mathbf{R} is the matrix containing the spectral signature of the N end-members (i.e., r_{ij} is the reflectance of end members j in band i), \mathbf{f} is the vector of abundance (i.e., f_j is the fractional cover of end-member j), and $\boldsymbol{\epsilon}$ is the vector of residuals of the linear unmixing (i.e., ϵ_i is the residual for band i). Thus, by accounting for snow end-members, it is possible to estimate sub-pixel snow fraction, i.e., the estimate of percent snow cover within each individual pixel.

If the number of end-members equals the number of bands, the linear system is likely to be determined and have a unique solution. This solution may seem attractive but it is not desirable since it cannot accommodate the uncertainties related to the choice of end-members (i.e., $\epsilon = 0$). It is preferable to over-determine the system by providing less end-members than spectral bands. The system then can be resolved with a least-squares approach that produces a vector of residuals ϵ ; the latter can be used as an indication of the correctness of the fit (Nolin *et al.*, 1993; Adams *et al.*, 1995; Dennison and Roberts, 2003). In the case of sensors such as MODIS that have a relatively small number of spectral bands for the classification of land cover (i.e., seven bands), this requirement with regard to end-members limits the use of linear unmixing techniques to local studies where the land cover generally can be categorized with a limited number of classes.

The resolution of Equation (5.5) for \mathbf{f} in the least-squares sense is referred to as the unconstrained least squares (ULS) and is obtained as

$$\hat{\mathbf{f}}_{\text{ULS}} = (\mathbf{R}^T \mathbf{R})^{-1} \mathbf{R}^T \boldsymbol{\rho}. \quad (5.6)$$

Additionally, when unmixing remotely sensed data, additional constraints can be used to ensure realistic estimations of fractions of end-members. Each fraction must be in the $[0, 1]$ range (i.e., *non-negativity* and *purity* constraints, respectively) and the sum of fractions must equal 1 (i.e., *full additivity* constraint):¹

$$\sum_{i=1}^N f_i = 1, \text{ or } \mathbf{1}^T \mathbf{f} = 1 \quad (5.7a)$$

$$\forall j \in \{1, \dots, N\}, 0 \leq f_j \leq 1, \quad (5.7b)$$

where $\mathbf{1}^T = [1, 1, \dots, 1]$ is a $1 \times N$ vector. If only the full additivity constraint is enabled [Equation (5.7a)], the system is said to be partially constrained and the least squares solution of Equation (5.5) (denoted PCLS) can still be obtained analytically from simple matrix operations (Settle and Drake, 1993). It is given by

$$\hat{\mathbf{f}}_{\text{PCLS}} = \hat{\mathbf{f}}_{\text{ULS}} + (\mathbf{R}^T \mathbf{R})^{-1} \mathbf{1} \left[\mathbf{1}^T (\mathbf{R}^T \mathbf{R})^{-1} \mathbf{1} \right]^{-1} (1 - \mathbf{1}^T \hat{\mathbf{f}}_{\text{ULS}}). \quad (5.8)$$

The fully constrained problem (FCLS) accounts simultaneously for both the full additivity and the non-negativity constraints. Nevertheless, the use of inequality constraints complicates the resolution for which no analytical form exists (Lawson and

¹Together, the additivity and non-negativity constraints ensure the purity constraint.

Hanson, 1974, Chap. 23). The inversion algorithm must be addressed as an optimization process in the framework of quadratic programming and solved with numerical and iterative techniques (Shimabukuro and Smith, 1991; Heinz and Chang, 2001; Keshava, 2003). In this thesis, the fully constrained problem is solved using MATLAB[®]'s function `lsqlin.m` which implements an optimization algorithm similar to that described in Gill *et al.* (1981).

In this application, it is logical not to permit any end-member abundance to be negative or greater than one (van der Meer and De Jong, 2000). When this constraint is not enforced, impractical values are typically interpreted as a result of the poor performance of the model (Adams *et al.*, 1995; Painter *et al.*, 1998; Duran and Petrou, 2007). However, negative and largely over-estimated contributions to the radiometry generally are the result of poorly defined end-members that cannot accommodate the radiometry of the pixel (Sabot *et al.*, 1992). Small digressions from the bounds can be ascribed to the system's noise and to the fact that the end-member's spectra are generally obtained from an "average" material response (Robinson *et al.*, 2000). Not enforcing the full additivity constraint corresponds to relaxing the system and provides a form of "acknowledgement" that other end-members may exist in the scene without having been defined. However, the full additivity constraint [Equation (5.7a)] permits the definition of an additional end-member, while preserving the over-determination of the system. The next section explains why some authors prefer not to implement the non-negativity and purity constraints in the system's inversion, but instead use them as criteria for determining the suitable candidate end-members. Nevertheless, a fully constrained linear unmixing method has been shown to outperform the unconstrained method by providing better estimates of the sub-pixel abundance of materials (Chang *et al.*, 2004). This approach is preferred here.

5.4.4 End-members

5.4.4.1 Different approaches of selection

The choice of end-members corresponds to finding a non-orthogonal basis of the feature space. It is complicated by the fact that end-members should represent realistic classes of materials and account adequately for the ones to be found in the scene and to be extracted from the pixel. One difficulty is that natural land covers are continuous rather than categorized into a discrete number of classes. For

instance, snow optical properties greatly vary according to grain size and presence of impurities (Warren, 1982; Dozier, 1989). Various strategies exist to define appropriate end-members and these can be considered as supervised or non-supervised approaches.

- Like supervised classification, a *supervised selection* of end-members refers to the input of an *a priori* knowledge to the spectral pattern recognition process. Thus, the operator must provide reference spectra of materials or classes of land cover that are known or expected to be present in the scene. For example, Nolin *et al.* (1993) identified spectra of end-members to process two AVIRIS images by using 3-band colour composites and expert photo-interpretation. Depending on the image, they extracted three or four spectra from pixels that were considered to be pure and representative of the classes to be extracted. However, they eventually failed to discriminate classes such as shade and rocks or water due to irresolvable spectral similarity.

Although laboratory spectra of materials can be used as references when ground spectral reflectance is computed from the images, Rosenthal and Dozier (1996) estimated that the atmospheric and topographic correction of their two test images were not suitable to allow this strategy. Consequently, they selected four end-members spectra from the image to unmix five Landsat TM bands. They treated separately a winter and a spring image to accommodate various states of snow. Thus, two types of snow spectra were extracted and attributed to fine and coarse granular snow, respectively. Rosenthal and Dozier (1996) also split the end-member of snow for both seasons to account for sunlit and shaded snow in order to retrieve snow fractions under different conditions of illumination.

Finally, Vikhamar and Solberg (2003) used a selection of spectra obtained from a preliminary classification of the images, and on the basis of a local land-cover map. They selected up to five end-members to unmix seven MODIS bands for each of the two images tested. Shaded snow was addressed by enabling the spectrum of the snow end-member to vary within ± 1 standard deviation of the mean snow spectrum obtained from the preliminary classification.

- The *unsupervised selection* of end-members corresponds to an image-dependent process whereby the determination of pure pixels is autonomous and based solely on the information contained in the image itself. Several techniques ex-

ist for which a review and references can be found in [Martínez *et al.* \(2006\)](#) and [Nascimento and Bioucas-Dias \(2007\)](#). They are generally based on a geometric approach whereby pure pixels representing end-members are assumed to be the vertices of the convex hull formed by the scatter plot of the data points in the feature space, following a dimension reduction such as a Principal Component Analysis (PCA) ([Settle and Drake, 1993](#)). For example, [Foppa *et al.* \(2004\)](#) were able to unmix routinely three spectral bands of AVHRR images by constructing a pair of end-members from the vertices of the first two principal components. The limited number of bands drastically narrows the choice of end-members. Consequently, [Foppa *et al.* \(2004\)](#) calculated a single snow end-member from all spectra that were assumed to be representative of snow. The second end-member was selected as the one that provided the smallest model residual, regardless of its real meaning. Issues raised by shaded pixels were ignored by [Foppa *et al.* \(2004\)](#) since no topographic correction was implemented and because of the impossibility to accommodate an additional end-member. It is evident, however, that the 1-km spatial resolution of AVHRR and its application in alpine terrains make pixels prone to mixture of shaded and sunlit surfaces. [Foppa *et al.* \(2007\)](#) later explained that this issue compromises the accuracy of this strategy.

- The *multiple end-member spectral mixture analysis* (MESMA) developed by [Roberts *et al.* \(1998\)](#) can be regarded as a hybrid method. It relies on a large collection of spectra of real materials, from which the combination that produces the smallest residual in terms of the ULS or PCLS models is assumed to represent the materials contributing to the pixel's radiometry. The non-negativity and purity constraints are not enforced but they become, in addition to the residuals, a criterion for assessing fitness of the model. MESMA is supervised in the sense that known spectral signatures are provided, while it is unsupervised because it is designed to retain automatically the signatures that best accommodate the pixel's radiometry under the linear mixing model. The advantage of the MESMA approach is that it allows end-members to vary on a per pixel basis, and thus to account for the variance of the main classes' signature across the scene (e.g., vegetation, rocks, soils, snow). The drawback lies in the computational load required to process all the permutations of end-members until appropriate candidates are found. Thus, the method is rarely considered for processing global datasets or large time series.

Painter *et al.* (2003) implemented this strategy in the context of sub-pixel snow mapping with AVIRIS. With regard to the snow class, they considered a range of snow spectra for various grain sizes. The spectrum of snow that satisfied the criteria of least residual and practical fractions not only provided the sub-pixel snow fraction, but also an estimate of the snow grain size in the pixel. Hence, the acronym MEMSCAG was used for *multiple end-member snow-covered area and grain size*. More recently, Painter *et al.* (2009) extended the MEMSCAG concept to MODIS (MODSCAG). As for MEMSCAG, MODSCAG requires the image to be converted to ground reflectance and, therefore, relies on the MODIS MxD09GA ground reflectance product provided at 500m spatial resolution.¹ Since topographic effects, and especially shadowing, are not addressed in the MOD09 product, a photometric shade end-member is systematically considered in the mixture. The final estimate of sub-pixel snow-covered area in the pixel is obtained by normalizing the sunlit fraction of snow to that of all sunlit materials. Painter *et al.* (2009) acknowledged the high requirement of computer resources of their algorithm. They proposed to mitigate the computational load by selecting a single end-member candidate appropriately (e.g., obtained from a land cover map) in addition to the snow and shade end-members, and reducing the snow spectral library.

5.4.4.2 Strategy of selection

The considerable efforts conducted to convert MODIS reflectance data at the top of the atmosphere into ground reflectance values has allowed standardization of the images and mapping of physical values that are theoretically measurable *in situ*. Shadow effects are also addressed so that end-members do not need to be split into sunlit and shade types. Moreover, since the purpose is to map fractions of snow in a local environment, a supervised approach for the definition of the end-members becomes relevant. The strategy implemented here relies on the definition of a fixed set of end-members that includes the types of land cover potentially mixed with snow such as vegetation and rocks. Candidate reference spectra were either measured on the ground, photo-interpreted from pure targets in corrected MODIS images, or selected from unsupervised classifications of selected corrected MODIS images. Several maps of sub-pixel snow fractions were created for various combinations of

¹Available from the Land Processes Distributed Active Archive Center: <https://lpdaac.usgs.gov/>, last retrieved in November 2009.

end-members representing snow, vegetation, and rocks. The accuracy of the maps was assessed with four reference maps of snow fractions according to the methodology described in Chapter 6. This continued until a set was determined that provided satisfactorily robust results for the four images.

Up to eight end-members (Figure 5.6) were defined to over-determine the model and to produce a best fit solution with a residual [seven equations from Equation (5.5), plus Equation (5.7a) and Equation (5.7b)]. Since glacier debris appeared significantly darker than most of the rocks, both end-members were used and retrieved by averaging the spectra of photo-interpreted pixels in a selection of corrected MODIS images. Bright and dark vegetation classes were obtained from the analysis of several unsupervised classifications of corrected MODIS images. The spectra were the mean spectral signature of the selected classes. Bright vegetation generally was associated with pasture and dark vegetation was associated with either rain forest on the West Coast or native bush and patches of coniferous forest in the catchment. It was assumed that having both dark and bright vegetation spectra potentially would accommodate any type of active vegetation which would be approached by a linear combination of both classes.

The steep slopes in the Southern Alps introduce a difference of altitude within a pixel of the same order of magnitude than the spatial resolution. The vertical gradient of temperature in addition with the fact that air mass temperature fluctuates rapidly in the region can result in the coexistence of snow at various level of metamorphism within a single MODIS pixel. In this context, the uniqueness of a snow end-member is not guaranteed and multiple snow end-members were considered. Four end-members were used to represent snow at various states of transformation, namely medium granular, transformed, coarse granular snow, and ice. The spectrum for ice was obtained by averaging the spectra of photo-interpreted pixels in corrected MODIS images. All other spectra, apart from the coarse granular spectrum obtained from measured ground reflectance, were mean spectra from unsupervised classifications of corrected MODIS images. Fine granular snow that is more reflective in the visible wavelengths was considered in the set of snow end-members but failed to provide robust results and was discarded.

Finally, water was not considered as an end-member as it seemed preferable to mask this land cover class. Moreover, glacial lakes such as Lakes Tasman and Pukaki are so loaded in sediments that their spectral signature was practically indistinguishable from ice and created too many misclassifications. The fractions of

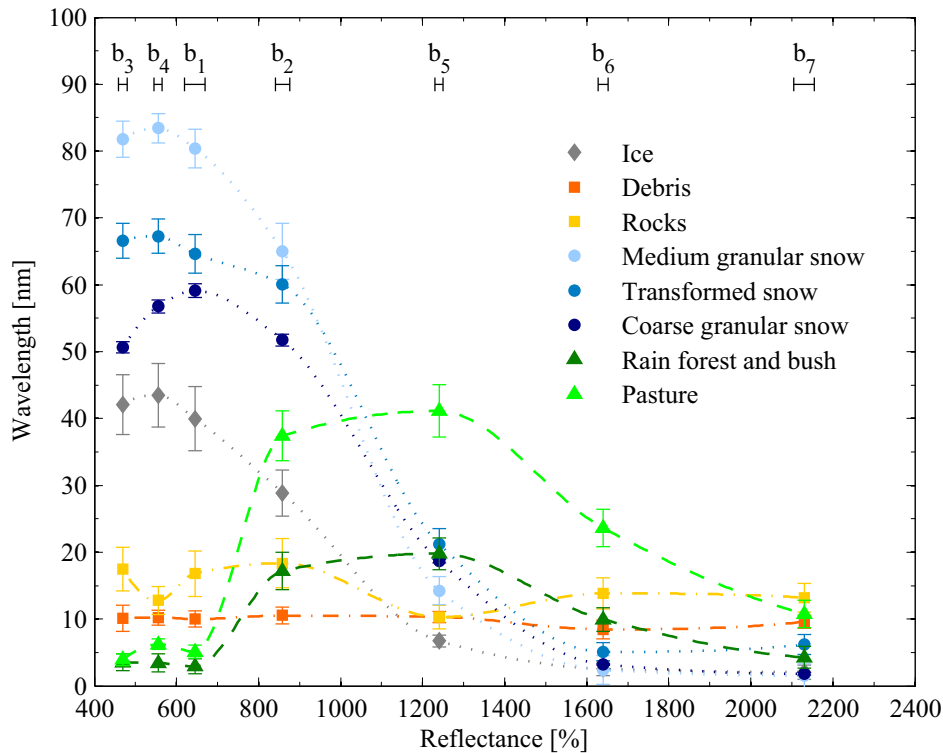


Figure 5.6 Spectral signature of the end-members used in the linear unmixing. The latter are plotted at MODIS bands 1–7, whose spectral range is indicated. The error bar corresponds to $\pm 1\sigma$ of the values retained to compute the spectra.

the end-members representing ice and snow were then summed to produce the map of sub-pixel snow fractions.

5.4.4.3 Additional criterion

The fully constrained linear unmixing is a computationally expensive process. The processing time increases linearly with the number of pixels to unmix. Since the purpose was only to retrieve information about snow within pixels, an additional criterion was considered to screen out pixels that were unlikely to contain snow at all. It relied on the fact that little snow is required within a pixel to ensure a positive NDSI. Simulations of mixture between snow and vegetation or rocks made by [Painter *et al.* \(2003\)](#) showed that as little as 10% snow is sufficient to guarantee a positive NDSI value. Similarly, the linear regression between sub-pixel snow fraction and NDSI established by [Salomonson and Appel \(2006\)](#) provides a positive fraction only for positive NDSI values as follows:

$$fra = -0.1 + 1.45 \times \text{NDSI}. \quad (5.9)$$

The creation of the ASTER snow cover reference maps for eight concurrently observed ASTER and MODIS scenes is explained later in Section 6.4.2. However, the relationship between the ASTER aggregated sub-pixel snow fraction and the MODIS NDSI values is examined here to support the choice of the NDSI as a restrictive criterion for unmixing pixels. Figure 5.7 confirms that the presence of snow is mostly associated with positive NDSI values. Over the eight images, only 5.5% of all pixels with snow had a negative NDSI and accounted for a mean snow fraction of $2.6\% \pm 3$. Hence, discarding these pixels from the analysis potentially induces only a marginal underestimation. Consequently, in order to reduce the processing time, only pixels having a positive NDSI were processed by the unmixing algorithm.

Figure 5.7 shows the universal regression determined by Salomonson and Appel (2006). It demonstrates that this regression it is not performing for the test images selected for this thesis as it would tend to overestimate largely the snow fraction. The NDSI thresholds used to create the references from ASTER were greater than those used by Salomonson and Appel (2006) for Landsat ETM+ images, thus mapping potentially less snow. However the magnitude of the discrepancy between the scatter plot and the ‘universal’ regression is considered too large to be explained by this difference only and therefore is attributed to the intrinsic variability of such a relationship.

A different regression between the NDSI of MODIS and the sub-pixel snow fraction was also observed by Lina *et al.* (2005). Salomonson and Appel (2006) themselves experienced this variability from one image to an other and it is noted that the ‘universal’ relationship is in fact a refinement of a previously supposed ‘universal’ regression from the same authors but obtained from different data (Salomonson and Appel, 2004). Such variability of the regression shows that, although the ‘universal’ linear regression is now recognized to perform at a global scale, and used on an operational basis in the MxD10 Snow product, it still should be regarded carefully for local analysis.

5.5 Post processing of the snow maps

5.5.1 Cleaning of the snow maps

A final filtering of the snow maps was processed to remove spurious pixels unlikely to contain any snow. The vector of residuals measures the discrepancy be-

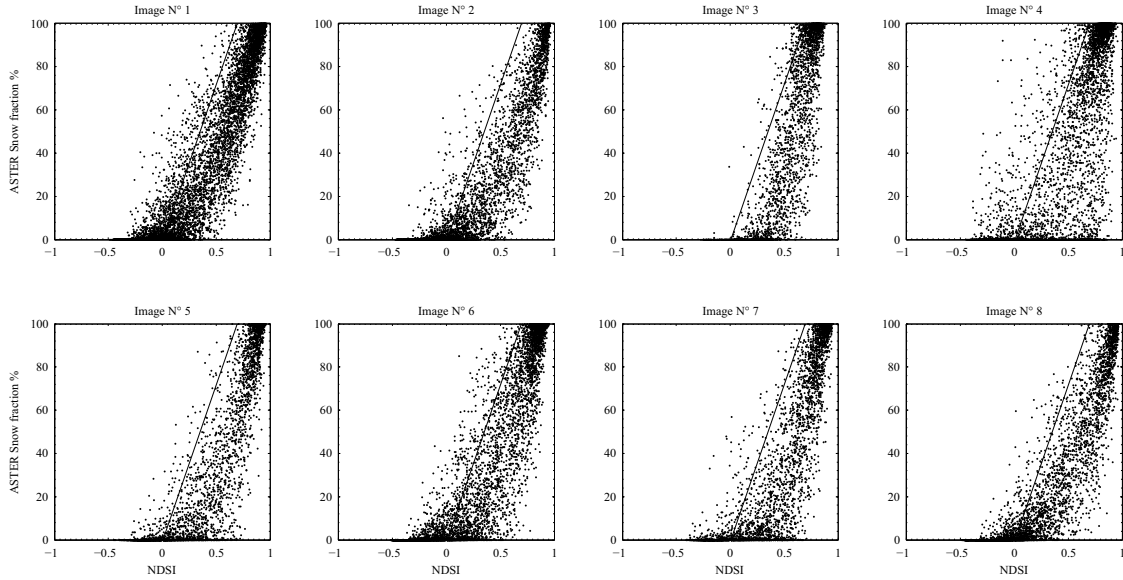


Figure 5.7 Relationship between the sub-pixel snow fractions and the NDSI value for the eight test images. The solid lines is the linear regression determined by (Salomonson and Appel, 2006): $fra = -0.1 + 1.45 \times NDSI$ and implemented in the MxD10 Snow product.

tween the vector of reflectance ρ and the reflectance modelled from the estimated fractions of end-members. This residual is often inspected spectrum-wide by computing its Root Mean Square Error (RMSE) as follows:

$$RMSE = \sqrt{\frac{1}{7} \sum_{i=1}^7 \epsilon_i^2}. \tag{5.10}$$

The RMSE is an indicator of the goodness-of-fit of the model. It measures its ability to accommodate the observations of reflectance with the set of end-members. For example, Painter *et al.* (2003, 2009) reject the model if the RMSE or more than three spectrally consecutive residuals exceed 2.5% in reflectance units. However, Dennison *et al.* (2004) pointed out that the RMSE is dependent on the reflectance so that dark targets tend to have smaller RMSE values than bright targets. In order to account for this dependence of the residual on target reflectance, a new criterion named the Normalized Error of Modelling (NEM) was formed as the ratio between the norm of the vector of residuals and that of the vector of reflectance:

$$NEM = \frac{\|\epsilon\|}{\|\rho\|} = \sqrt{\frac{\sum_{i=1}^7 \epsilon_i^2}{\sum_{i=1}^7 \rho_i^2}}. \tag{5.11}$$

Figure 5.8 (a) & (b) show the map of RMSE and NEM values for the subset of

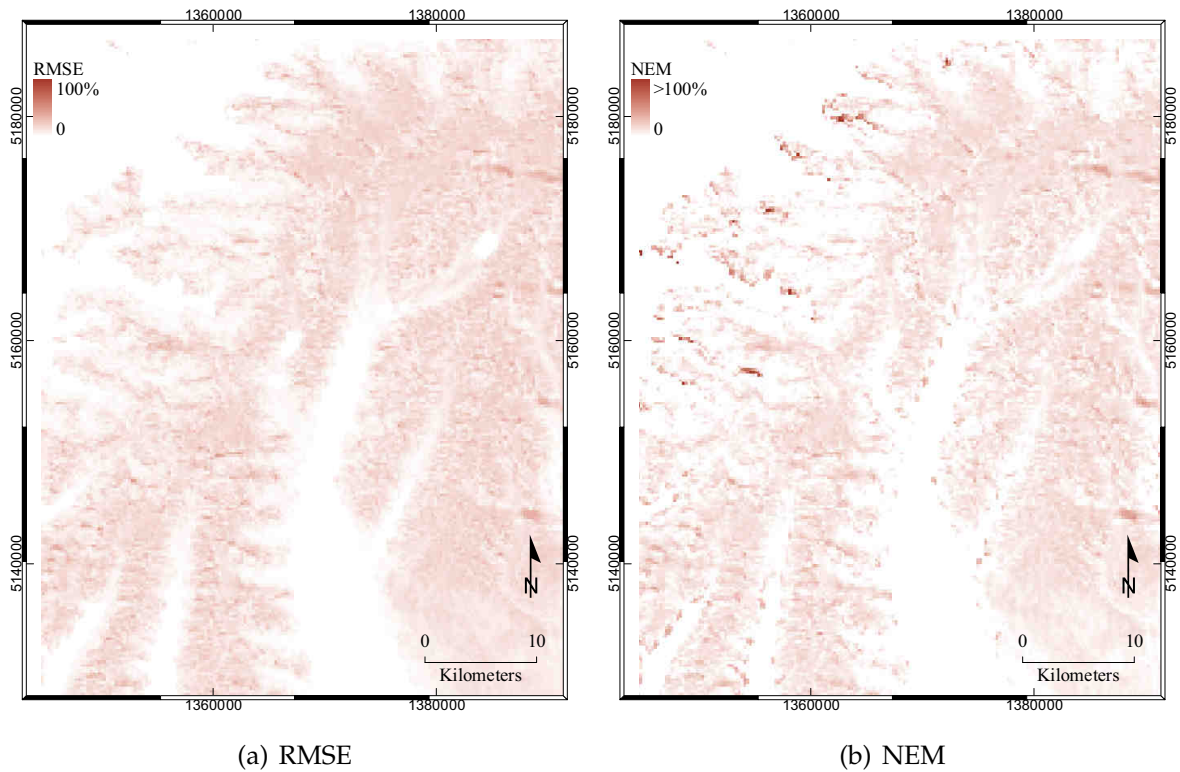


Figure 5.8 Error of modelling of the linear unmixing for image shown in Figure 4.18 (c). (a) Root mean square error (RMSE), (b) normalize error of modelling (NEM). Note the differences in the north-west part of the image where increased NEM reveals regions of poor modelling due to inaccurate atmospheric and topographic correction in strongly shaded slopes. The same pixels are not highlighted by the RMSE.

the image previously shown in Figure 4.18 (d). Large NEM values occur for pixels in the north-west part of the image corresponding to very steep and shaded slopes on the West Coast [see image before correction in Figure 4.18 (c)]. An inaccurate extraction of shadows is generally the cause of large NEM values and this was visually assessed on a number of images. Such pixels have a positive NDSI value but are too dark to be accommodated appropriately by any end-member. However, the low level of reflectance yielded small RMSE values that were less than 5% and smaller than the mean RMSE for the image, which reached 8%. Nevertheless, the NEM indicated that the norm of this residual was always more than 100% of the norm of the reflectance. Thus, it highlighted more readily the regions of poor modelling than the RMSE and was found appropriate to reveal obvious errors in pixels whose corrected spectra could not be correctly accommodated by the end-members.

Consequently, pixels that were predicted to contain snow were reset as ‘snow-

free' when the NEM was greater than one. This operation was successful at removing most of the badly modelled pixels that were clearly free of snow, although sparse, isolated spurious pixels remained and needed to be filtered out. They corresponded to pixels that were over-corrected possibly due to BRDF effects or for being wrongly flagged as shaded. It also created sparsely distributed holes in the snow cover for a limited number of images associated with extreme winter sun geometry. The shadow mask cannot possibly depict exactly all pixels in shadow and, although marginal, misclassified pixels systematically yield poor unmixing performances. A visual inspection showed that small patches of pixels set as snow-free because $NEM > 1$ should generally be retained as snowy when they were within a large snowy entity. Both removing spurious snowy pixels outside the main snow entity and retaining small snow-free patches within the snow entity were achieved using a series of morphological and logical operations. The operations are illustrated in Figure 5.9 on a 'toy' snow map that depicts sparse pixels outside, those that need to be filtered out, and small patches inside that must be identified and retained. The operations were conducted as follows:

1. The map of sub-pixel snow fraction is binary classified and denoted A (1 if snow fraction > 0 , 0 otherwise).
2. A 3×3 majority filter is applied on A to remove spurious misclassified snow pixels. It produces B where bare patches inside the snow entity have expanded and the boundaries have been altered.
3. A dilatation is applied on B to create C.
4. The intersection of A and C denoted D permits the identification of the pixels that form the main entity and restore the correct boundaries, but it still contains bare patches.
5. E is obtained from a closing operation on D to fill the bare patches.
6. Finally, pixels belonging to bare patches inside the main snow entity are identified by exclusive disjunction between D and E with the condition that they do not belong to A.

This series of operations was successful at removing sparse isolated pixels, preserving the integrity of the main snow entities, and keeping their boundaries intact. Finally, a mask covering the sea and the main lakes was manually developed and

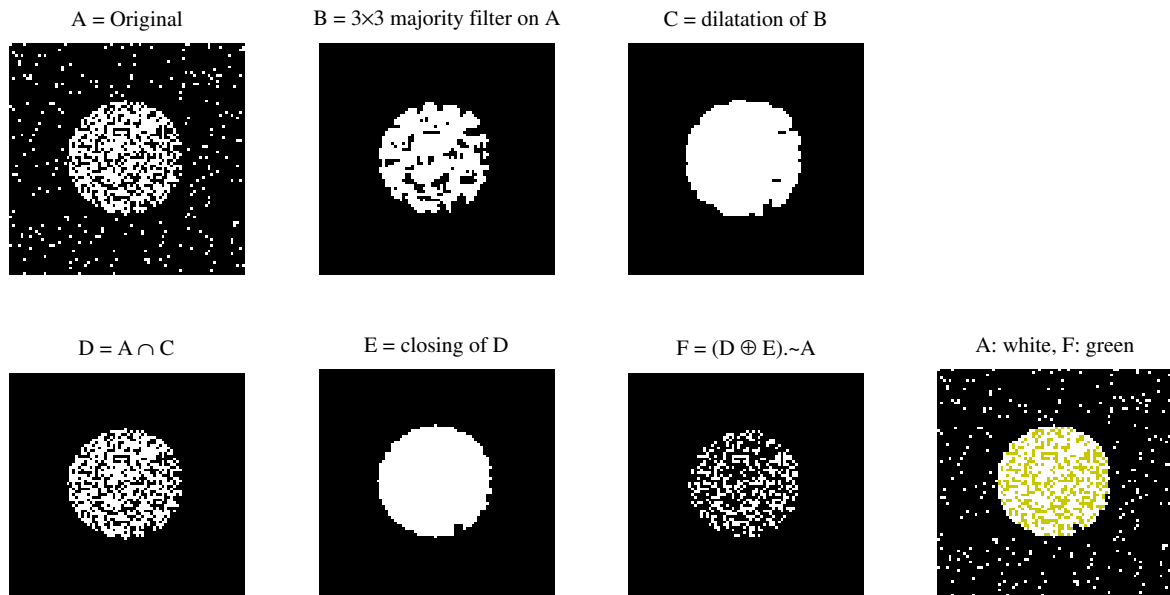


Figure 5.9 Series of morphological and logical operations to remove spurious ‘snow’ pixels outside a snow entity, while retaining small ‘snow-free’ patches inside. Spurious ‘snow’ pixels are readily filtered out by the initial ‘majority’ filter (B). The subsequent operations allow the identification of small patches of ‘snow-free’ pixels inside the main snow entity (i.e., mask F). Snow covered pixels that were excluded because of a large NEM criterion are restored when they belong to the set F.

applied to all images. Two examples of maps representing the spatial distribution of snow end-members in winter and summer are shown in Figure 5.10. The images are computed as weighted sums of the fractions of each snow end-member to enhance the mixture of different types of snow: $3 \times fra_{\text{medium grain}} + 2 \times fra_{\text{transformed}} + fra_{\text{coarse grain}}$. Both examples depict a realistic configuration of the snowpack. The medium granular snow end-member is principally found at high elevations, while the fraction of transformed and coarse granular snow progressively increases toward lower elevations. Only coarse granular snow is found near the transient snowline. A similar pattern was generally observed with other images.

5.5.2 Completing snow maps under clouds

As explained in Section 3.5.2, entirely cloud free images are rare in the region. However, complete snow maps are needed in the next chapter to estimate snow depletion curves. In this context, a strategy of multi-date aggregation is often used to mitigate cloud effects and provide a complete snow coverage. Cloudy pixels on

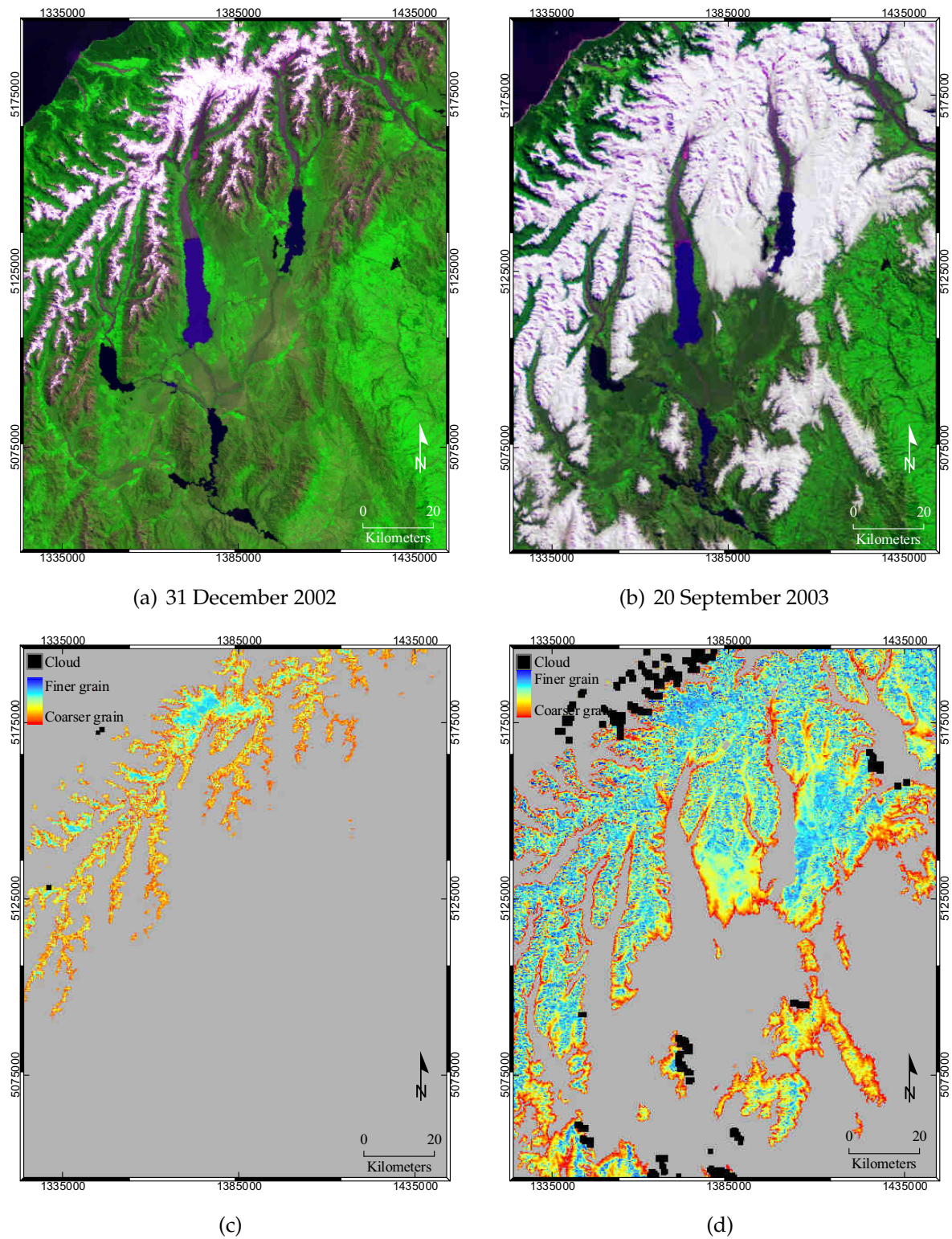


Figure 5.10 Examples of spatial distribution of the three snow end-members. (a) and (b) are RGB composite of images acquired on 31 December 2002 and 20 September 2003, respectively. (c) and (d) are composite images of snow end-member fractions computed as $3 \times fra_{\text{medium grain}} + 2 \times fra_{\text{transformed}} + fra_{\text{coarse grain}}$ and colour coded.

one date are usually given the maximum cloud-free value measured over several days (Riggs *et al.*, 2006). Alternatively, Dozier *et al.* (2008) proposed to estimate snow fractions under clouds and complete time-series of observations by means of an interpolation in space and time of the initial maps of fractional snow cover. Although such methods are appropriate for global studies, it may have prejudicial effects for local and specific environments. In New Zealand, the snowpack is highly dynamic. Snowfall at low elevations rarely stays longer than one or two days and quickly depletes upslope until reaching the typical seasonal equilibrium. In such situations and frequent cloud cover, a multi-date strategy may over-represent short-lived snowfall. Both effects compromise the accurate depiction of the snow cover depletion dynamic.

An alternative strategy is preferred in this thesis, because suitable MODIS images were initially selected by visual inspection. Images were considered acceptable and processed depending on the extent and location of cloud cover relative to the catchments of interest. Images were considered useable when the snow pack in the catchments was mostly cloud free and only marginal clouds remained and obstructed some pixels. Using the DEM and its first derivatives (i.e., slope and aspect), all pixels were classified depending on altitude (every 250m), slope (every 15°), and aspect (every 45°). Sub-pixel snow fractions under cloudy pixels were estimated by the mean snow fraction of all cloud-free pixels in the same topographical configuration. This method relies on the assumption that snow coverage is correlated with elevation, slope, and orientation. It is also justified by the fact that the subjective selection of largely cloud-free images provided a large number of measurements to estimate missing values. Visually, it provided more realistic results than a multi-date aggregation. It also had the advantage to ensure that the observations remained snapshots of the situation at a precise time.

5.6 Summary

This chapter has reviewed the problem of mapping the snow cover using binary and sub-pixel approaches. Although the binary method is generally considered to be robust and simple, it relies on underlying assumptions that are often disregarded. This strategy is based on a measure (i.e., the area) applied to a geographical object that has potentially a fractal nature. The relevance of this measure in this case was clarified. The projection of the snow cover onto the Euclidean space

of the image makes it inherit the integer dimension of the plane and justifies the use of the surface to characterize it. The fractal consideration also provides a contextual framework against which other measures used to characterize the phenomenon must be considered.

In addition, it was shown that binary mapping strategies rely on a thresholding approach that is intimately related to the distribution of area proportion of snow within pixels. The latter depends on the spatial structure of the object relative to the pixel size. The beta distribution is a relevant candidate to model the density function of sub-pixel fractions. However, it is believed that this remains to be justified theoretically. Although binary mapping can provide reasonable results when it comes to estimating the total SCA, this estimation can only be accurate when the distribution of sub-pixel snow fractions is symmetrical. The conditions enabling such symmetry would benefit from a more theoretical context. Relating explicitly the spatial structure of the set and the pixel size to the shape parameters of the theoretical distribution would be useful but is potentially very difficult. This relationship is the pitfall of binary approaches when the conditions are not fulfilled to achieve a symmetric distribution. It demonstrates that finding the optimum threshold to be used in binary mapping is an ill-posed problem since it depends on a statistical distribution of mixed pixels that binary mapping is unable to reveal.

This drawback was addressed in the chapter by implementing a fully constrained linear unmixing technique. Along with the fusion method that reduced the pixel size, the unmixing method allows the amount of details of the snow maps to be increased by providing estimates of sub-pixel snow fractions. The unmixing technique also has constraints with regard to the number of end-members, which limit its use to relatively small areas where a limited number of land cover types coexist. Nevertheless, the normalization of images and the correction of shadows allows a unique set of end-members to be determined that was suitable to accommodate most configurations of radiometric mixture. Such a fixed set yielded an acceptable computational load, as it was desirable for processing routinely hyper-temporal series of images.

Chapter 6

Accuracy assessment of the snow maps¹

6.1 Introduction

The previous chapter explained how maps of sub-pixel snow fractions were created from MODIS images converted to ground spectral reflectance by means of a constrained linear unmixing technique. The use of the multispectral fusion method described in Section 3.4 allowed these maps to be produced at both 250 and 500m spatial resolution, with and without applying the fusion algorithm, respectively. This chapter is devoted to the assessment of the accuracy of the snow maps and encompasses two main objectives. First, it aims at quantifying the statistical error of estimation of the sub-pixel snow fraction in the MODIS-derived snow maps, and thus to judge the usability of the MODIS-derived output. Second, it aims at assessing objectively the gain of information that is provided by the fusion algorithm.

Although the fusion method enables mapping of the spatial distribution of snow with half the pixel size (250m) of the nominal images (500m), the potential improvement needs to be quantified and its significance proven. The relevance and pitfalls of common statistical measures computed on a per-pixel basis to score such multi-resolution datasets are investigated and discussed. An alternative feature-

¹The content of this chapter is largely published in: Sirguey, P., Mathieu, R. and Arnaud, Y. (2009). Subpixel monitoring of the seasonal snow cover with MODIS at 250m spatial resolution in the Southern Alps of New Zealand: Methodology and accuracy assessment. *Remote Sensing of Environment*, 113(1), 160–181, doi:10.1016/j.rse.2008.09.008, as well as in: Sirguey, P., Mathieu, R. and Arnaud, Y. (2008). Improving MODIS spatial resolution for snow mapping using wavelet fusion and ARSIS concept. *IEEE Geoscience and Remote Sensing Letters*, 5(1), 78–82, doi:10.1109/LGRS.2007.908884.

based metric that is itself based on an object-level representation of the geographic phenomenon (i.e., the snow cover) is proposed.

This leads to the creation of the reference dataset that was used to assess the snow mapping algorithm described in the previous chapter. The spectral and spatial characteristics of ASTER (see Section 2.4.2.2 for more detail about the ASTER instrument), as well as its simultaneous acquisition with MODIS, make it a unique candidate to map the snow at fine spatial resolution and provide reference material. Thus, after highlighting the strategy implemented to assess the performance of the sub-pixel snow mapping algorithm, the validation dataset that was obtained from eight concurrent pairs of ASTER and MODIS images is described.

In order to ensure the robustness of the conclusions, the strategy of assessment relied on a combination of several pixel- and feature-based measures that are described and applied in the next two sections, respectively. The pixel-based measures accounted for common statistics such as the mean error, the mean absolute error, or the root mean square error. Additional pixel-based indicators originating from image fusion research and signal processing science were also considered in order to investigate their behaviour and strengthen the assessment of the MODIS outputs. The next section focuses on the Modified Directed Hausdorff Distance (MDHD) as a feature-based measure to score the depiction of the snowline. Its ability is demonstrated to address the limitations of standard statistical measures based on pixel representation in a multi-resolution framework. Finally, despite the considerable effort invested to assess the quality of the snow mapping process, the last section discusses qualitatively the sources of errors and potential limitations of the mapping method.

6.2 Context

6.2.1 The need for references

The accuracy assessment of maps of sub-pixel snow fractions retrieved from remotely sensed data has been addressed in different ways. For example, [Romanov *et al.* \(2003\)](#) estimated the accuracy of their algorithm by propagating the magnitude of known errors without using any reference data. They concluded that value of the snow fraction was retrieved with accuracy of around 10%. [Metsämäki *et al.* \(2002\)](#) used references of snow fraction obtained during snow courses and daily observa-

tions from weather stations. Reference observations were grouped into categorical classes (e.g., observed fractional snow cover within 0–5% > 5%–20% > 20%–40% > ...). The observations were then analysed in terms of omission and commission errors only, thus failing to address comprehensively the statistical error of the retrieval process.

Alternatively, it is efficient to assess the accuracy of maps of sub-pixel snow fraction by taking advantage of simultaneous co-registered imagery with a finer spatial resolution when available. The use of higher resolution imagery permits a synoptic view of the area and a potentially high number of samples to assess the estimation of the sub-pixel snow fraction. This is desirable in complex terrain when there is a lack of ground-based observing stations and/or specific snow surveys to provide adequate field reference data. Specifically, a number of selected areas or the whole reference image is binary classified into ‘snow’ and ‘no snow’ pixels using either photo-interpretation, or the classical method of rationing and thresholding based on the NDSI, for example. The binary maps are then aggregated with a mean operator to the spatial resolution of the map to assess, thus providing the reference material relative to the sub-pixel snow fractions. Typical statistics (e.g., bias or difference of means, RMSE, coefficient of determination R^2 , standard deviation σ) are then used on a per-pixel basis to quantify objectively the discrepancies between the test and the reference snow maps. This method relies on the robustness of the binary classification which ensures generally a satisfying accuracy. In addition, the statistical effect of the aggregation process makes the variance of the sub-pixel snow fraction inversely proportional to the number of samples used to compute it. This effect can be demonstrated as follows:

Let n be the number of pixels forming an area A whose fraction covered by snow is denoted f . Let p_k be the probability of success associated with the discrete random variable X_k that measures the correct classification of a pixel k as being ‘snow’ or ‘no snow’.¹ The classification of each pixel is assumed to be pairwise independent with the same probability of success. Thus, $\forall k \in \{1, \dots, n\}$, X_k obeys the Bernoulli distribution $\mathcal{B}(1, p)$. Assume that $\forall k \in \{1 \dots fn\}$ and $\forall k \in \{fn + 1 \dots n\}$ the pixel k is snowy and snow free, respectively. Let Y_k be a discrete random variable that takes the value 1 if the pixel k

¹The probability of success corresponds to the accuracy of the classification, i.e., the ratio between the number of correctly classified pixels and the total number of pixels in the image.

is classified as snow, and 0 otherwise. Let $F = \frac{1}{n} \sum_{k=1}^n Y_k$ be the discrete random variable that measures the fraction of snow in A . F is proportional to the sum of two independent random variables N_1 and N_2 that measure the number of pixels classified as snow whether they belong to the snowy or snow free sets of pixels, respectively:

$$\begin{aligned} F &= \frac{1}{n}(N_1 + N_2) \\ &= \frac{1}{n} \left(\sum_{k=1}^{fn} Y_k + \sum_{k=fn+1}^n Y_k \right). \end{aligned}$$

A pixel contributes to the snow cover in A if it is covered by snow and correctly classified, or if it is not covered by snow and incorrectly classified. Thus,

$$F = \frac{1}{n} \left(\sum_{k=1}^{fn} X_k + \sum_{k=fn+1}^n (1 - X_k) \right).$$

Clearly, N_1 and N_2 obey the binomial distributions $\mathcal{B}(fn, p)$ and $\mathcal{B}((1-f)n, 1-p)$, respectively. Hence, the expected value of F is

$$E[F] = fp + (1-f)(1-p). \quad (6.1)$$

The variance of F is obtained as

$$\begin{aligned} \text{Var}[F] &= \frac{1}{n^2} (\text{Var}[N_1] + \text{Var}[N_2]) \\ &= \frac{1}{n^2} [fnp(1-p) + (1-f)n(1-p)p] \\ &= \frac{p(1-p)}{n}. \end{aligned} \quad (6.2)$$

From Equation (6.1) it appears that the expected value of the sub-pixel snow fraction is biased depending on the fraction of the area that is really covered by snow. The fraction is expected to be overestimated when less than half of A is covered by snow, and underestimated otherwise. If the accuracy p of the binary classification process is known,

$$\hat{f} = \frac{\frac{1}{n} \sum_{k=1}^n Y_k + p - 1}{2p - 1} \quad (6.3)$$

may be regarded as a better estimator of the sub-pixel snow fraction in the aggregation process. Although the bias reduces the accuracy of

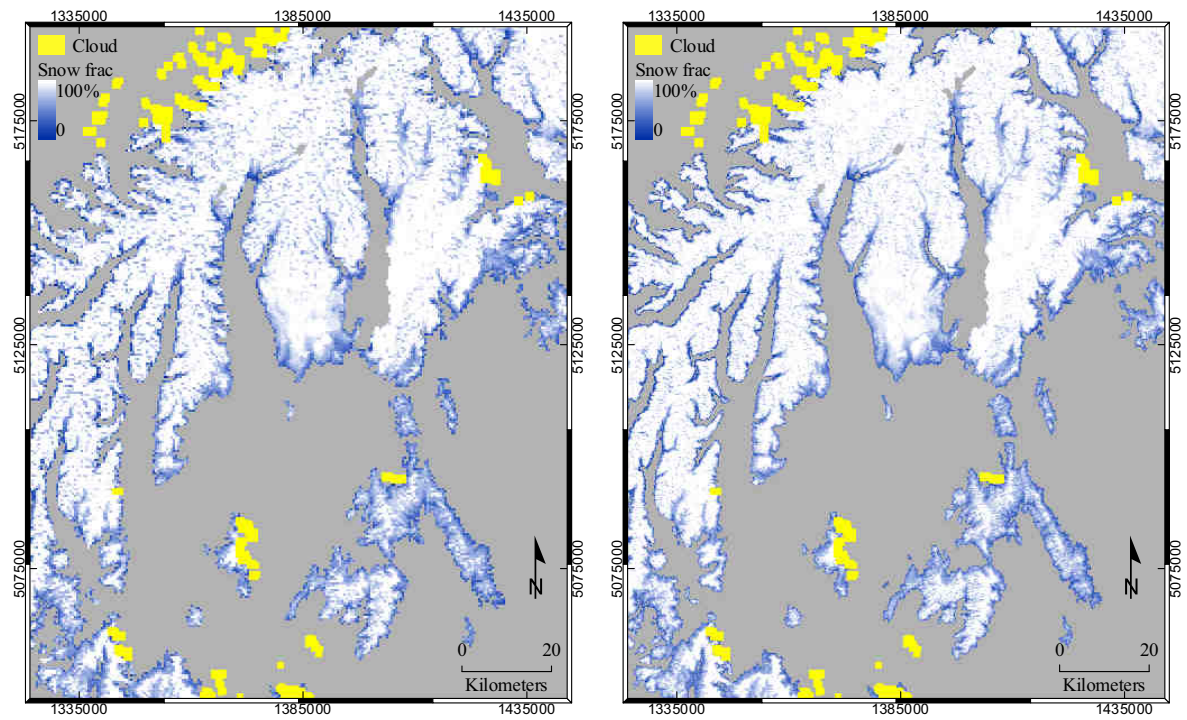
the abundance estimate in the aggregated area, Equation (6.2) demonstrates that the precision of that estimate improves as the number of pixels increases.

Rosenthal and Dozier (1996) and Painter *et al.* (2003) used selected test sites mapped from aerial photography at 1m resolution to assess the maps of sub-pixel snow fractions derived from Landsat TM (30m spatial resolution) or AVIRIS (17m spatial resolution), respectively. Vikhamar and Solberg (2003) and Salomonson and Appel (2004, 2006) took advantage of Landsat ETM+ imagery (30m spatial resolution) to assess MODIS derived snow maps (500m spatial resolution). Foppa *et al.* (2007) used ASTER (15m spatial resolution) as a reference to assess the maps of sub-pixel snow fraction derived from AVHRR (1km spatial resolution). Finally, Painter *et al.* (2009) used references obtained from Landsat ETM+ and TM to assess the mapping of sub-pixel snow fractions with MODIS, but they did not rely directly on a binary classification. Instead, their reference images were initially processed into maps of sub-pixel snow fraction based on the method of Rosenthal and Dozier (1996).

6.2.2 Assessment of the performance of the fusion

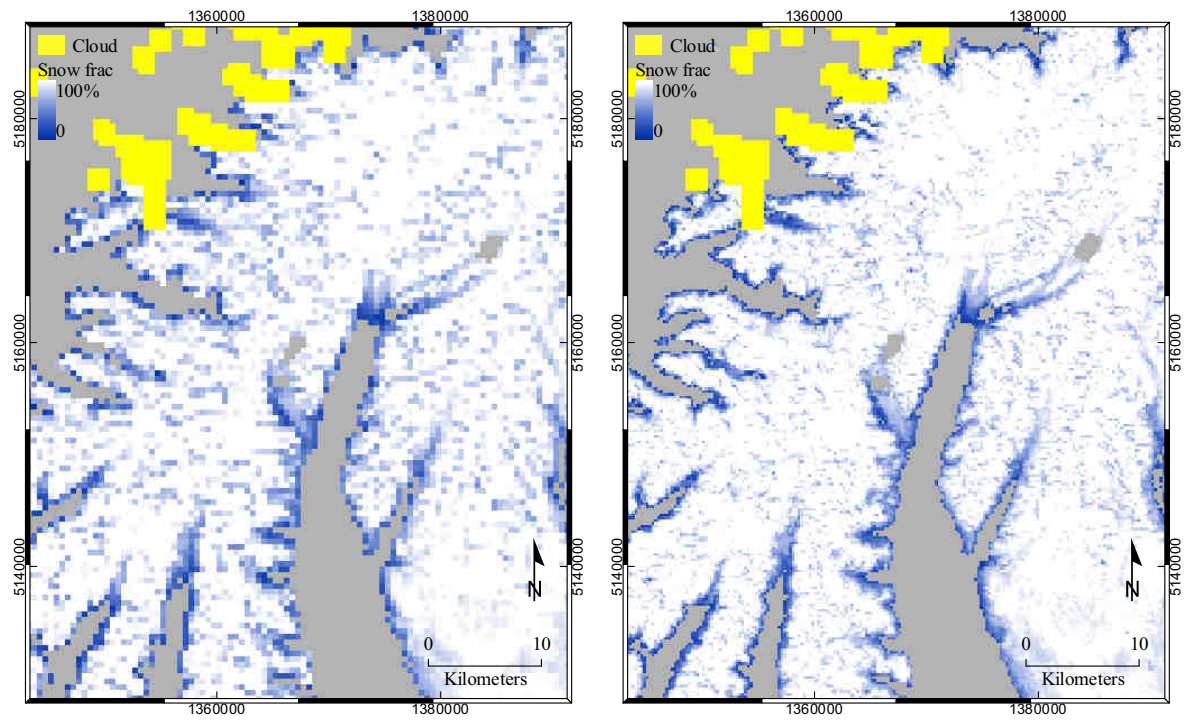
Assessing the accuracy of the mapping process is a crucial step to ensure the usability of the derived snow covered surface. In this thesis, the assessment of the quality of the snow maps involves an additional aspect. As explained in Section 3.4 the rich spatial content of the 250m resolution MODIS high resolution (HR) bands was fused into the 500m resolution MODIS low resolution (LR) bands in order to enable the mapping of snow at a higher spatial resolution and improve the level of detail in mountainous terrain. Maps of sub-pixel snow fraction were created at both 500 and 250m spatial resolution by unmixing the set of spectral bands without and with the fusion, respectively. In the rest of the thesis, these maps are referred to as M500 and M250, respectively. An example of each of these outputs is shown in Figure 6.1 corresponding to the image previously shown in Figure 4.18.

Section 3.4 explained that the performance of the fusion can be assessed both qualitatively and quantitatively. This was conducted, by visually inspecting the fused image, as well as qualitatively, by implementing the protocol of assessment of Wald *et al.* (1997) (see Section 3.4.3.2). However, these types of assessment are limited to the investigation of the fused image itself. They aim to score the quality of the image that is obtained from the fusion, in relation with the theoretical image that



(a) Map of sub-pixel snow fractions computed from MODIS bands at 500m (M500)

(b) Map of sub-pixel snow fractions computed from MODIS bands at 250m (M250)



(c) Subset of (a)

(d) Subset of (b)

Figure 6.1 Example of map of sub-pixel snow fractions created from MODIS imagery (20 September 2003, 22:40 GMT, see RGB composite of the image in Figure 4.18).

would have been acquired if the sensor had the desired spatial resolution. Sometimes, however, the images obtained from the fusion are to be post-processed, such as in the present case to create maps of sub-pixel snow fractions with an increased spatial resolution. In this context, the relevance and performance of the fusion can be measured in terms of the quality of the post-processed output, rather than the quality of the fused image only. Indicators of quality can be computed for both outputs whether they implement the fusion algorithm or not. The performance obtained for each output not only enables quantification of their respective accuracy, but also permits measurement of the gain of information that can be attributed to an increase in spatial resolution, thus assessing objectively the benefit of the fusion process.

6.3 Assessment metrics and multi-scale issues

A visual interpretation of M250 maps compared to M500 [Figure 6.1 (d) & (c) and other test images provided in appendix F] can subjectively demonstrate an improvement in the ability to map snow with the fused images. A higher amount of detail is seen and the richer spatial information generally achieved a realistic depiction of the snow cover. However, from a quantitative point of view, comparing images of different spatial resolutions raises issues that are related to multi-scale analysis, so that not all measures are suitable to assess the gain of information generated by an increase in spatial resolution. This issue is a form of the *modifiable areal unit problem* (MAUP) whereby, in geography, the statistics of point-based measures of spatial phenomena can be radically affected by the area on which they are computed (Openshaw, 1984).

6.3.1 Snow cover area (SCA)

For instance, assume having only one pixel for the whole area for which the unmixing method is applied. If the linear unmixing model is accurate, the fraction of snow will be close to the true value. In this case, the performance, in terms of the estimation of the total snow cover area (SCA), would be perceived as high. However, no information would exist with regard to the spatial distribution of the snow cover. On the other hand, when unmixing smaller but more abundant pixels with a slightly less accurate model (e.g., larger bias), a larger digression of the total

SCA is expected, despite the fact that the determination of snow presence on a pixel basis would be dramatically improved. Although SCA is a fundamental variable frequently used in climate research, its investigation only reveals the overall bias of the unmixing process and is of limited benefit to assess the correct distribution of snow. It integrates all pixels regardless to their individual representation of reality and, therefore, is irrelevant for quantifying the improvement of snow cover mapping gained by the fusion.

6.3.2 Pixel-based statistics

Alternatively, the spatial sampling provided by the pixelization allows the error between the estimated abundance and a reference dataset to be localized geographically. It not only enables assessment of the total amount of snow being mapped, but also the fact that it is mapped appropriately in space. A problem remains if maps of different spatial resolution need to be compared with statistics established pixel-wise. To illustrate this issue, consider only one pixel in which the real snow cover is depicted, as in Figure 6.2 (a). Assume that the unmixing process is able to retrieve sub-pixel snow fractions with a mean error μ_{M500} and standard deviation σ_{M500} from the set of spectral bands at the larger resolution (i.e., without fusion). The fusion process can, at best, achieve an intermediate result between a hypothetical set of seven HR bands, which would be resampled and interpolated from the LR bands (i.e., no genuine spatial information added), and a genuine set of seven measured HR bands, which obviously is not available. Consequently, it is logical to expect worst performances from the unmixing process when it is based on the set of fused spectral bands (i.e., pixels at 250m spatial resolution) because the real spatial information originally exists in only two spectral bands (i.e., MODIS band 1 & 2) rather than seven. Standard descriptive statistics of the modelling error for M250 can be $|\mu_{M250}| > |\mu_{M500}|$ (i.e., less accurate) and/or $\sigma_{M250} > \sigma_{M500}$ (i.e., less precise). However, μ_{M250} and σ_{M250} do not account for the fact that M250 is mapped with a finer spatial resolution and depicts four times more pixels than M500.

Assume that the errors of both unmixing processes leading to M500 and M250 are normally distributed with no bias (i.e., $\mu_{M500} = \mu_{M250} = 0$) but $\sigma_{M250} > \sigma_{M500}$. In Figure 6.2 (b), the estimated fraction of snow in a 500m pixel has 68% probability to be within σ_{M500} . The probability for each pixel of the M250 map [Figure 6.2 (b)] to be within the same range is smaller, but it does not allow the conclusion that M250 achieves worse results than M500. In fact, it is reasonable to assume

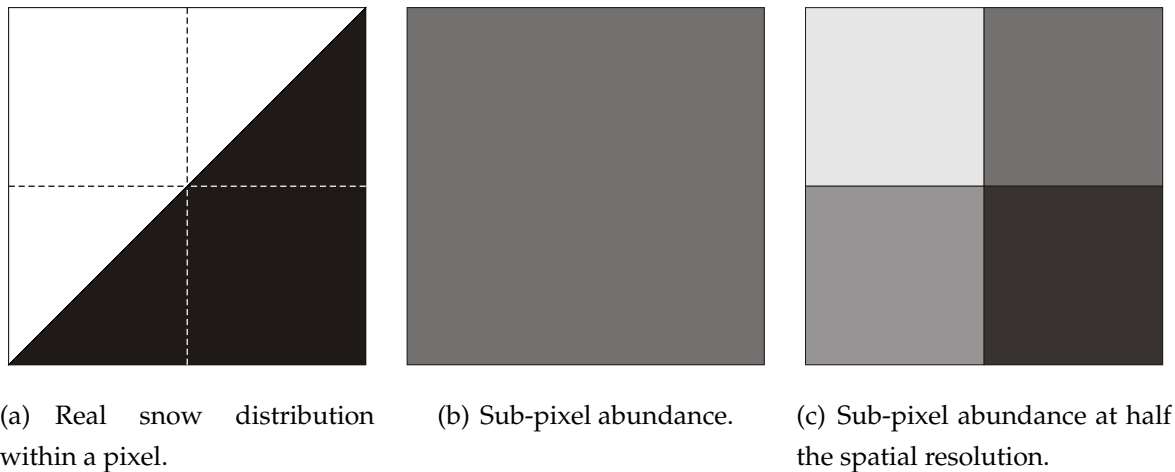


Figure 6.2 Sub-pixel abundance mapping at two spatial resolutions.

that Figure 6.2 (c) may provide a more desirable result than Figure 6.2 (b) despite a worse precision. For proper comparison, the statistics must represent the same phenomenon. In other words, they must be established on maps having the same spatial resolution. Thus, M250 must be aggregated at 500m spatial resolution and such an aggregation will be denoted G500 from now on. In the ideal case of errors being independent, the statistical effect of the aggregation yields $\sigma_{G500} = \frac{\sigma_{M250}}{2}$ and only σ_{G500} can be compared directly to σ_{M500} . If $\sigma_{G500} < \sigma_{M500}$ then the information available in M250 is of better quality than that of M500.

Above, it was explained why worse statistics do not necessarily mean that information is lost in the process of fusion, or that the fusion is irrelevant. In fact spatial information may be added but not depicted in the raw statistics of M250 compared to M500. Both sets are not strictly comparable or must be interpreted along with the qualitative knowledge that one set relates to pixels whose size is smaller. The aggregation enables standardization of the measures so they can be compared. However, doing this makes the statistics of G500 relate to a map with a coarser spatial resolution, and better statistics merely indicate a better determination of snow within larger pixels. Although this approach has the potential to demonstrate objectively whether the fusion is capable of adding information or not, it fails to measure the change of spatial resolution objectively. Therefore, in the context of a multi-scale assessment, pixel-based metrics are also limited and a metric that can score the snow maps objectively regardless of the difference of spatial resolution is desirable. Such a metric is proposed in the following section.

6.3.3 Feature-based metric: the Hausdorff Distance

6.3.3.1 Object representation

Edges and contours are essential in understanding natural scenes. Mapping a geographic phenomenon at a higher spatial resolution is motivated by the ability to enhance the representation of the boundaries between objects and identify smaller features more clearly. It also permits reduction of the planimetric uncertainties associated with the location of the boundaries between objects. Thus, an image with better depiction of such boundaries is generally perceived as having a higher quality (Guangtao *et al.*, 2005). A feature-based metric is a measure that is designed to score the accuracy of object boundaries. For example, in an object-based environment, Zhan *et al.* (2005) proposed several measures based on intersections of sets to account for the correct classification, size, and position of spatial objects. They suggested that such an approach can be used along with per-pixel measures to provide a more comprehensive assessment of the quality of classified objects. Sophisticated metrics based on multi-scale wavelet analysis have also been designed to assess objectively the quality of contour and edges in an image (Guangtao *et al.*, 2005).

In this thesis, the snowline, which stands for the boundary between snowy and bare patches, is the relevant representative object. It is expected that mapping the snow cover with a higher spatial resolution allows identification of a snowline that better depicts reality than otherwise. Assessing the quality of the image comes down to the design of a measure which is able to quantify the match between the estimated snowline and a reference. Moreover, in a multi-resolution context, a candidate metric must be capable of measuring the match regardless of the fact that boundaries are mapped from images of different pixel sizes, so that the measures can be compared across multi-resolution datasets. In addition, it is desirable that the metric will provide a score that is linearly related to the pixel size. In other words, the score must be optimally twice as good when the snowline is mapped from pixels that are half the size. In this way the potential improvement of a map produced with a higher spatial resolution can be directly assessed without the need for aggregation. More specifically, a function $D(X, R)$ that would score a set X according to a reference R must satisfy the following conditions:

1. D is non-negative: $D(X, R) \geq 0$;
2. $D(X, R) = 0$ iff $X = R$;

3. the set X matches the reference R better than the set Y iff $D(X, R) \leq D(Y, R)$;
4. D can be applied on sets retrieved from images of different spatial resolution and can be compared;
5. the magnitude of change of the D must match the magnitude of change in spatial resolution.

Note that the purpose is only to score a candidate set X compared to a fixed set R assumed to be the reference or ground truth. R is not supposed to be scored according to X , thus D is not required to be symmetric.

6.3.3.2 The Hausdorff Distance

The scoring process described above essentially corresponds to measuring the distance between two nonempty paths X (i.e., the test snowline either depicted from low or high resolution images) and R (i.e., the reference snowline) in the Euclidean plane E . In topology, paths are closed and bounded sets, hence X and R are compact. The *Hausdorff distance* is a classical metric defined on the space of compact subsets of E denoted C (Gromov, 2007, pg. 72). It is specifically defined on pairs of elements $\{X, Y\} \in C^2$ as

$$d_H(X, Y) = \max\left\{ \sup_{x \in X} \inf_{y \in Y} d(x, y), \sup_{y \in Y} \inf_{x \in X} d(x, y) \right\}, \quad (6.4)$$

where d is the metric associated with the metric space, presently the Euclidean distance. The quantity $\inf_{y \in Y} d(x, y) = d(x, Y)$ is the distance between the point x and the set Y . Note that d_H is constructed from the quasimetric¹ $h: X, Y \mapsto h(X, Y) = \sup_{x \in X} d(x, Y): C^2 \rightarrow \mathbb{R}$ to ensure the symmetry condition. Huttenlocher *et al.* (1993) refer to the quasimetric h as the *directed Hausdorff distance*. Figure 6.3 illustrates both directed Hausdorff distances computed between two paths.

The Hausdorff distance has found practical applications in the domain of visual recognition where it is used to identify patterns in images such as faces (Huttenlocher *et al.*, 1993; Riucklidge, 1996). Beauchemin *et al.* (1998) also used d_H as a criterion to assess the segmentation of remotely sensed images. A simple application can be illustrated based on the trivial image shown in Figure 6.2 (a). The intrinsic information aimed to be retrieved is illustrated by the diagonal of the image whose length is denoted $\delta \sqrt{2}$. From a low resolution pixel such as that shown in Figure 6.2 (b), the boundary is either the whole square or an empty set, whether the

¹A quasimetric is a metric that is not necessarily symmetric.

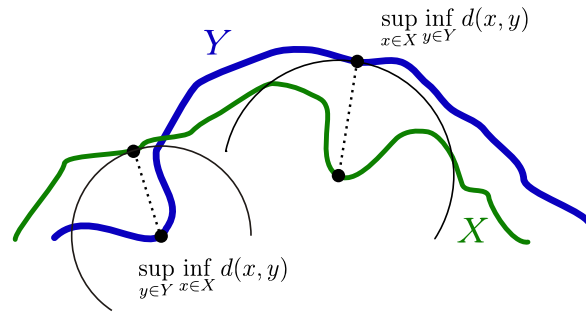


Figure 6.3 Computation of the Hausdorff distance as the largest of both directed Hausdorff distances.

abundance is estimated to be more or less than 50% as explained in Section 5.3.3. The empty set is not of interest and is not considered here. However, in Figure 6.2 (c), the upper left and lower right pixels are most likely to be considered snowy and bare, respectively, even with a relatively inaccurate model.¹ Only the lower left and upper right pixels may be mapped randomly in one class or the other. All configurations yield a boundary that includes the edges of the smaller pixels inside the square. The general case corresponds to boundaries that are set up as shown in Figure 6.4. For the lower resolution image it comes that $h(Y, R) = \sup_{y \in Y} d(y, R) = \delta \frac{\sqrt{2}}{2}$ and $h(R, Y) = \sup_{r \in R} d(r, Y) = \frac{\delta}{2}$. Thus, $d_H(Y, R) = \delta \frac{\sqrt{2}}{2}$. The higher resolution image yields $h(X, R) = \sup_{x \in X} d(x, R) = \delta \frac{\sqrt{2}}{4}$ and $h(R, X) = \sup_{r \in R} d(r, X) = \frac{\delta}{4}$, yielding $d_H(X, R) = \delta \frac{\sqrt{2}}{4}$. From this $d_H(X, R) = \frac{1}{2}d_H(Y, R)$ and d_H satisfies all conditions given above, with all other conditions being trivial.

6.3.3.3 Modified Hausdorff Distance (MDHD)

However, Dubuisson and Jain (1994) pointed out that d_H was sensitive to the noise in the image. Line features and points sparsely distributed in the image perturb the distance d_H since it is set as the maximum distance between points belonging to the sets. A single point in the test set far from the reference path has the potential to radically affect d_H , so that d_H quickly saturates and loses all discriminative power even with the slightest amount of noise. Dubuisson and Jain (1994) investigated a number of variations of the Hausdorff distance in terms of its response to noise. They proposed a *modified directed Hausdorff distance* (MDHD) m defined on

¹Note that if the model is inaccurate as to confuse systematically fully covered and bare pixels, it does not perform better than guessing, so it must be discarded.

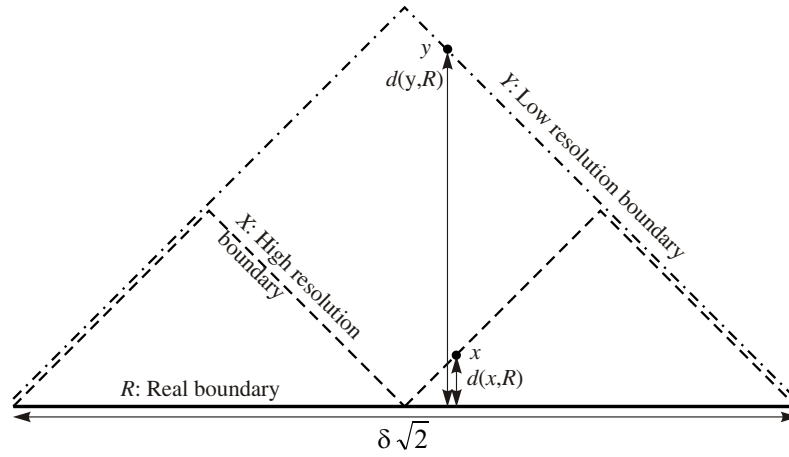


Figure 6.4 Mapping of boundaries extracted from low and high resolution imagery.

pairs of sets of points $A = \{a_1, \dots, a_{n_A}\}$ and $B = \{b_1, \dots, b_{n_B}\}$ as follows:

$$m(A, B) = \frac{1}{n_A} \sum_{a \in A} d(a, B). \quad (6.5)$$

In this formulation, m is neither symmetric nor does it satisfy the triangular inequality. Additionally, m is designed to operate on point sets rather than compacts, and thus requires a sampling process if continuous curves are to be measured. Both properties jeopardize the behaviour of m . However, [Dubuisson and Jain \(1994\)](#) showed that, for similar patterns, m tends to be small with low noise and increases progressively with the level of noise. In fact, m is more robust to noise than d_H because it better accommodates the outlier points possibly resulting from segmentation errors. [Dubuisson and Jain \(1994\)](#) also demonstrated that m possesses a stronger discriminative power for discerning or identifying patterns. This approach was then successfully used for face recognition by [Takács \(1998\)](#) with minor adjustments.

In the example shown in [Figure 6.4](#), consider that the real boundary R is sampled into $n + 1$ equally spaced points referenced by their abscissa r_k along the orientated diagonal so that $r_k = \frac{k\delta\sqrt{2}}{n}$, $k \in \{0, \dots, n\}$. Let $\{x_1, \dots, x_n\} \subset X$ and $\{y_1, \dots, y_n\} \subset Y$ be the sets of points of X and Y , respectively, whose abscissa match r_k , $\forall k \in \{1, \dots, n\}$. Then $m(Y, R) = \frac{1}{n} \left(\frac{\delta\sqrt{2}}{2} + 2 \sum_{k=0}^{n/2-1} \frac{k\delta\sqrt{2}}{n} \right) = \frac{\delta\sqrt{2}}{4}$. Similarly, $m(X, R) = \frac{\delta\sqrt{2}}{8}$. Again $m(X, R) = \frac{1}{2}m(Y, R)$ and m satisfies the conditions given above.

When computed for a number of samples n along the tested snowline X , the distribution of $d(x_k, R)$, $\forall k \in \{0, \dots, n-1\}$ provides a statistical distribution of ‘how far’ X lies from reality. The modified directed Hausdorff distance that scores the match between X and R corresponds to the mean of this distribution. Along with

other descriptive statistics such as the standard deviation of $d(x, R)$, it provides a quantitative insight with regard to the planimetric accuracy of the snowline position.

A last property that needs attention relates to the potential behaviour of the MDHD to fractal sets. As explained in Section 5.2.2, a metric aimed at measuring spatial objects is potentially affected by fractal manifestations and must be designed so as to ensure that the objects being addressed are measurable. Although there is, of course, uncertainty in the measurement of the Euclidean distance between points of a test snowline to the reference snowline, it is always possible to determine lower and upper bounds at all resolutions. In fact, the distance always ranges between 0 and the maximum length of the image diagonal and so does m . Thus, the MDHD only requires sets to be closed and bounded which is always the case when considering a real phenomenon such as a snowline even if it possesses a fractal nature.

6.4 Assessment strategy

6.4.1 Initial argument

It has been shown that a number of approaches can be used to assess the quality of the maps of snow fractions. Whether they are based on global representations such as the SCA, raster representation such as pixel-based statistics, or object-based representation such as the MDHD, different indicators have both merits and disadvantages. SCA is a global measure that provides only little insight on the quality of the map but no indication about the correct spatial depiction of the snow cover. In addition, it fails at assessing objectively the improvement that can be attributed to the fusion process. Pixel-based indicators carry more information and are the basis for the statistical assessment of the parameter to be retrieved (i.e., the sub-pixel snow fraction). However, their dependence on spatial resolution limits their usefulness at assessing multi-resolution datasets. Finally, a feature-based measure such as the MDHD has the potential to quantify objectively the gain that can be attributed to an increase in spatial resolution. It has also the advantage of measuring the correct depiction of representative objects in terms of their geographical position. However, unlike pixel-based statistics, the MDHD requires a crisp segmentation and fails at assessing the accuracy of the estimation of continuous quantities.

In order to provide the most comprehensive assessment of the quality of

MODIS-derived maps of snow fractions, as well as demonstrating objectively the benefit of the fusion, a variety of indicators were considered based on the three strategies described above. The next sub-section describes the creation of reference datasets from concurrent pairs of MODIS and ASTER images. ASTER and MODIS snow maps were compared using the measures enumerated below and described in detail in the subsequent sections.

1. *Global and pixel-based indicators*

- The total mapped Snow Cover Area error (SCA error) which is the mean of the error.
- The pixel-based statistics considered were Mean Absolute Error (MAE), Root Mean Square Error (RMSE), coefficient of determination R^2 , linear regression.
- Two additional measures used in image processing were also considered. The universal quality index, or Q index (Wang and Bovik, 2002), was designed to quantify the quality of images and has found applications in the assessment of fusion algorithms. Receivers Operating Characteristics (ROC) curves (Fawcett, 2006) provide a graphical and comprehensive interpretation of confusion matrices. Despite being applicable in a pixel-based framework, both indicators were examined as to their potential merit for assessing multi-resolution datasets.

2. *Feature-based indicators*

- The distribution of the Euclidean distance between ASTER and MODIS-based snowlines was considered and its potential to be an objective measure for the multi-resolution dataset was investigated. The mean of this distribution [the modified directed Hausdorff distance (MDHD)] and its standard deviation were used to score the match between the reference and estimated snowlines.

6.4.2 Reference images

In the study area of the Waitaki catchment, there are only two ground-based stations that have recorded snow height (i.e., Panorama Ridge since 1997 and Rose Ridge since 2005, see Figure 2.1 for location). Neither of these two locations can

seriously be assumed to be representative of the whole study area. Moreover, the parameter required to assess (i.e., the sub-pixel snow fraction) this is not monitored by these stations. Thus, the number of sites is insufficient and inadequate for providing suitable reference material to assess the mapping process. To address this issue, the simultaneity of acquisition between the ASTER and MODIS sensors on the TERRA platform was used. ASTER spatial resolution (15m) compared to the 250m and 500m MODIS spatial resolution provides a ratio of 277 and 1111 ASTER pixels, respectively, for each MODIS pixel. Thus, it is argued that a binary classification of snow from ASTER provides a suitable ground truth to assess the snow cover distribution retrieved from MODIS.

Four pairs of simultaneous ASTER/MODIS images initially were selected to assess the accuracy of the snow maps (№ 1–4 in Table 6.1). The pairs were chosen on the basis of the availability of ASTER images and as to include images taken at different times of the year and with various extents of snow cover. As explained in Section 5.4.4, these four images were used to determine a robust selection of end-members. However, tuning the set of end-members until finding a reasonably good agreement potentially biased the results that could be inferred from these pairs only. Thus, four additional pairs were chosen to assess independently the accuracy and robustness of the retrieval process (№ 5–8 in Table 6.1). The PCI Geomatica v9.1 physical model was used with the 15m resolution DEM to orthorectify the eight ASTER images with Ground Control Points collected both on the ground and from the New Zealand digital topographic database. Approximately 25 ground control points were used to compute the bundle block models and independent set of about 30 Check Points were used to assess the accuracy of the orthorectification. For all of the ASTER images, the root mean square error did not exceed 1.5 pixels. Therefore, all ASTER images were considered to match the MODIS images geographically. Three-band colour composites of all pairs are provided in appendix F.

6.4.2.1 Snow classification from ASTER

The ASTER snow maps were produced at 15m spatial resolution based on a binary classification using the NDSI computed from top of atmosphere apparent reflectance following

$$\text{NDSI} = \frac{\rho_{560 \text{ nm}}^* - \rho_{1650 \text{ nm}}^*}{\rho_{560 \text{ nm}}^* + \rho_{1650 \text{ nm}}^*}. \quad (6.6)$$

Cloud-free acquisitions in the area are exceptional, especially in winter. Therefore, the images were selected despite the presence of some clouds, but only when a large

Table 6.1 Pairs of simultaneous ASTER/MODIS acquisitions used for the accuracy assessment of the snow maps.

Image №	Day [mm/dd/yyyy]	Time ASTER (UTC)	Sun elevation [deg]	Sun azimuth [deg]	
Used for the selection of end-members	1	12/31/2002	22:38:37	57.4	61.4
	2	01/29/2002	22:39:55	52.0	57.6
	3	09/11/2000	22:58:41	37.2	31.4
	4	05/16/2006	22:36:55	21.2	30.3
Used for independent assessment	5	04/07/2001	22:53:48	33.9	32.8
	6	09/09/2005	22:42:46	34.7	35.6
	7	04/03/2002	22:38:58	33.4	38.6
	8	01/24/2006	22:36:04	52.8	59.8

cloud-free portion existed and provided a high number of samples accounting for snowy and snow free pixels. Clouds and most water targets were masked manually so that the samples only accounted for land targets. Similarly to [Foppa et al. \(2007\)](#), the histograms of the NDSI images were used in addition to visual inspection to determine the adequate threshold that subjectively depicted the snow appropriately while minimizing obvious misclassifications. Most thresholds were set to 0.6 but three images needed a threshold of 0.5 to represent the snow cover boundaries with satisfaction (Table 6.2). The histograms of the NDSI for all sample pixels retained in the reference ASTER images are shown in Figure 6.5. The variability of the threshold to depict snow targets was attributed to the possible presence of optically thin cirrus cloud which could have affected differently the ASTER bands 1 and 4 resulting in a decrease of the NDSI ([Barton et al., 2000](#)). An additional threshold was used based on the green spectral band (ASTER band 1 at 560 nm) to remove dark pixels whose NDSI values can be large because of detector noise, or because of shade due to the greater amount of incoming radiation with short wavelength relative to longer wavelength. Thus, only pixels having

$$\rho_{560 \text{ nm}}^* \geq 13\% \quad (6.7)$$

were retained as potentially snow covered. The latter test was particularly efficient for image № 4, which accounted for a relatively large portion of shadow with high NDSI values due to a very low sun elevation. The effect of these pixels is visible on the histogram of the NDSI where they yield an additional mode in the distribution for relatively high values (Figure 6.5, upper right).

Table 6.2 Value of NDSI thresholds used for each image.

Image N ^o	1	2	3	4	5	6	7	8
NDSI	0.5	0.6	0.5	0.6	0.6	0.5	0.6	0.6

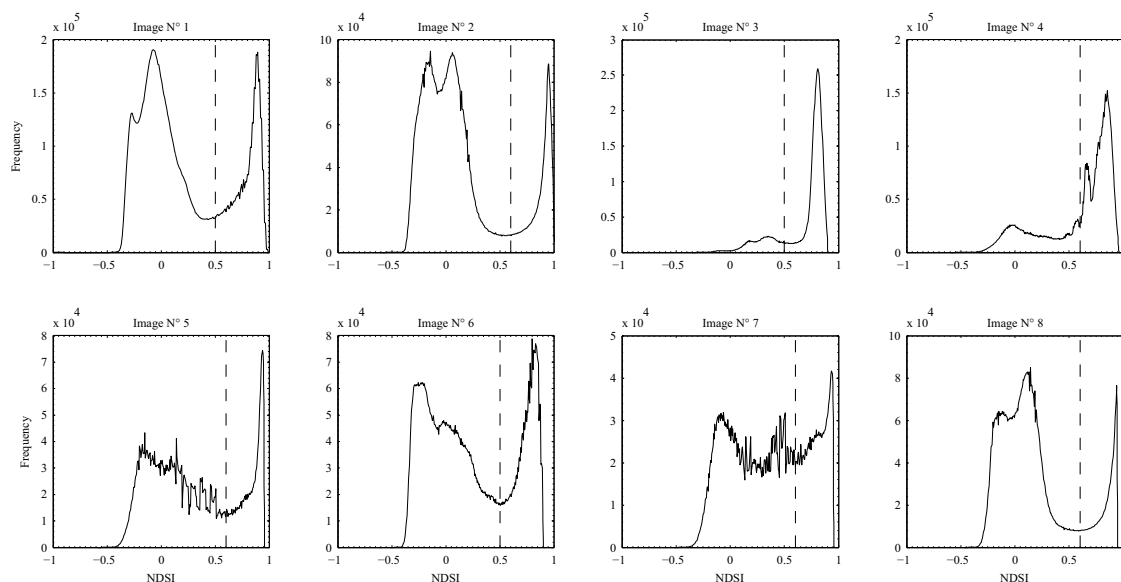


Figure 6.5 Histogram of the NDSI values for all sample pixels retained in the reference ASTER images. The dotted lines represent the threshold chosen to classify the pixels into the ‘snow’ and ‘no snow’ classes.

6.4.2.2 Aggregation

The aggregation process uses a spatial filter to decrease the spatial resolution of the input image. It applies a mathematical operator to the pixel values that are within the footprint of a coarser pixel to populate the coarser resolution output image (Figure 6.6). A mean operator is used as the kernel to produce the reference map of sub-pixel snow fractions from the ASTER binary snow map (i.e., 1 if snowy and 0 otherwise). It is obvious that the aggregated map has a spatial resolution that is a multiple of that of the input image. Since 15 is not a divisor of 250 nor 500, the binary snow maps obtained from ASTER had to be resampled at a resolution close to a common divisor of 250 and 500. 12.5m was considered to be the most appropriate resolution (it is the common divisor of 250 and 500 that is the closest from 15), while only a nearest neighbour method was relevant due to the binary nature of the map. Although some pixels may disappear or be duplicated during the resampling process, the effect on the snow fraction within much larger pixels was considered to

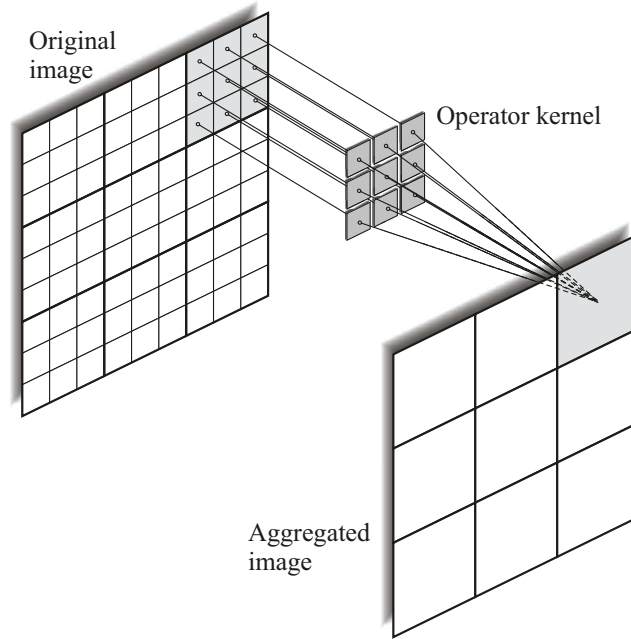


Figure 6.6 Schematic illustration of the aggregation process.

be negligible. The 12.5m resolution binary maps were then aggregated to 250m and 500m spatial resolution to match the MODIS-derived maps of sub-pixel snow fractions M250, M500, and G500 (see Section 6.2.2 and 6.3.2 for the definition of the three outputs). Figure 6.7(a)–(c) shows an example of the simultaneous ASTER/MODIS pair № 1, the binary classification of snow at 15m spatial resolution and the aggregation at 250m spatial resolution, respectively. Figure 6.8 shows a subscene identified by the yellow square in Figure 6.7 to illustrate the difference of spatial resolution between MODIS and ASTER. The 250m or 500m aggregated ASTER images used as references had from 30% to 90% of pixels partially or fully covered by snow with a snow cover area varying from 20% to 80% (Table 6.4). Overall for the eight images, around 50% of the pixels contained snow according to ASTER, and the snow cover represented around 35%.

6.4.2.3 Mapping of the snowline

From the binary classification at 15m spatial resolution, the reference snowline, which stands for the boundary between the group of pixels classified as ‘snow’ or ‘no snow’, was extracted. The ESRI shapefile made of polygons provided the reference layer for the feature-based assessment.

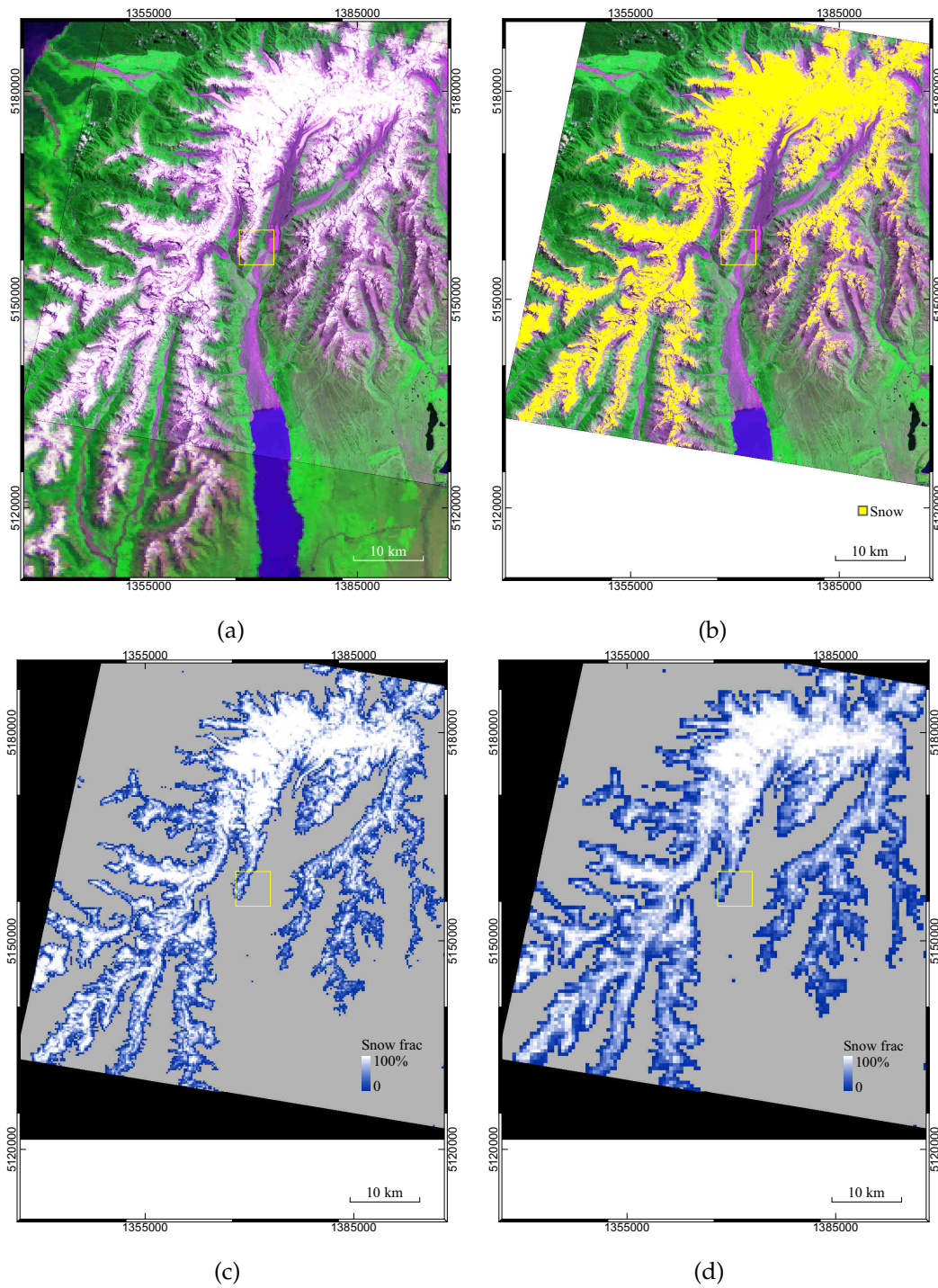


Figure 6.7 Example of simultaneous ASTER and MODIS imagery (31 December 2002 22:35 GMT). (a) False colour RGB composite from ASTER bands 2, 3, and 1 (15m) overlaid onto MODIS bands 1, 2 (250m), and 3 (fused to 250m); (b) Binary classification of snow from ASTER (snow pixels are drawn in yellow); (c) & (d) Reference maps of sub-pixel snow fractions at 250m and 500m resolution, respectively, aggregated from the 15m resolution binary classification shown in (b). The difference of spatial resolution is clearly visible in Figure 6.8 and when zooming into the pdf version of this thesis.

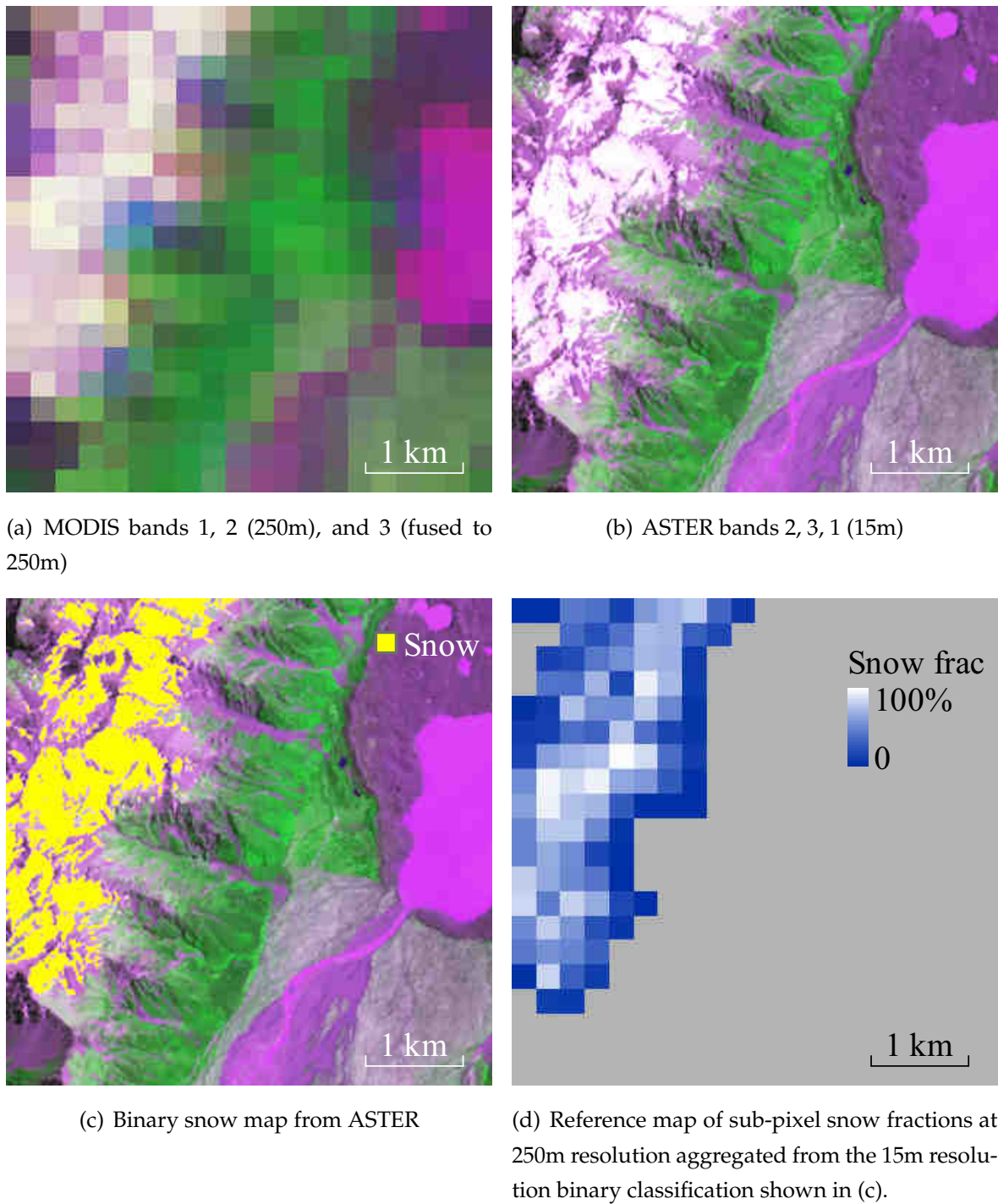


Figure 6.8 Subset of Figure 6.7.

6.5 Pixel-based measures

6.5.1 Statistical and spatial structure of the error

$e_i = fra_{MODIS,i} - fra_{ASTER,i}$ is the error between MODIS- and ASTER-derived sub-pixel snow fraction for sample i . The distribution of e is shown for each individual image in Figure 6.9, as well as for the combination of all samples in Figure 6.10. Pixels that were completely covered by snow or totally bare according to ASTER were not accounted for in computing the histograms. Such pixels do not correspond to a mixture of snow with other materials and are generally correctly estimated. Their disproportionately large number yields an excessive peak at $e = 0$ that complicates the investigation of the statistical distribution of e . Once these are removed, the histograms of errors depict the modelling performance for mixed pixels only.

All distributions of e failed the Kolmogorov-Smirnov test of normality (KS-test). A t location-scale distribution was found to be a better candidate for evaluating the histograms.¹ Despite the fact that the fitted $t(\mu, \sigma, \nu)$ better matched the histograms than normal distributions, the KS-test between the fitted $t(\mu, \sigma, \nu)$ and e also rejected the hypothesis of identical distributions. However, no other theoretical distribution was found that approximated better the statistical structure of the error.

The histograms show that errors from M250 maps have generally a larger dispersion than M500, while G500 maps account for the smallest. Overall, the standard deviation of the distribution of errors when excluding pixels full or free of snow were $\sigma_{e,M500} = 19.8\%$, $\sigma_{e,M250} = 23.4\%$, and $\sigma_{e,G500} = 15.1\%$ for M500, M250, and G500, respectively. As mentioned earlier in Section 6.3.2, the aggregation of M250 to G500 has a statistical effect that reduces the dispersion. In this case, $\sigma_{e,G500}$ would be half of $\sigma_{e,M250}$ if errors were independent pixel-wise. The fact that this magnitude of change is not achieved reveals covariance between errors within groups of four pixels.

Figure 6.11 (a) shows that there is a weak ($R^2 = 9\%$) but statistically significant relationship (p-value ≈ 0) between e and fra_{ASTER} . Sub-pixel snow fractions

¹The t location-scale distribution is a translated and scaled version of the Student's t -distribution. It accounts for the location μ , scale $\sigma > 0$, and shape $\nu > 0$ parameters. If X obeys a $t(\mu, \sigma, \nu)$ location-scale distribution, then $\frac{X-\mu}{\sigma}$ has a Student's t -distribution with ν degrees of freedom. The variance of $X \sim t(\mu, \sigma, \nu)$ is $\text{Var}[X] = \frac{\sigma^2\nu}{\nu-2}$. Note that σ identifies with the standard deviation of X only when $\nu \rightarrow \infty$. Only in such a case does $\frac{X-\mu}{\sigma}$ become a Z-statistics following the standard normal distribution.

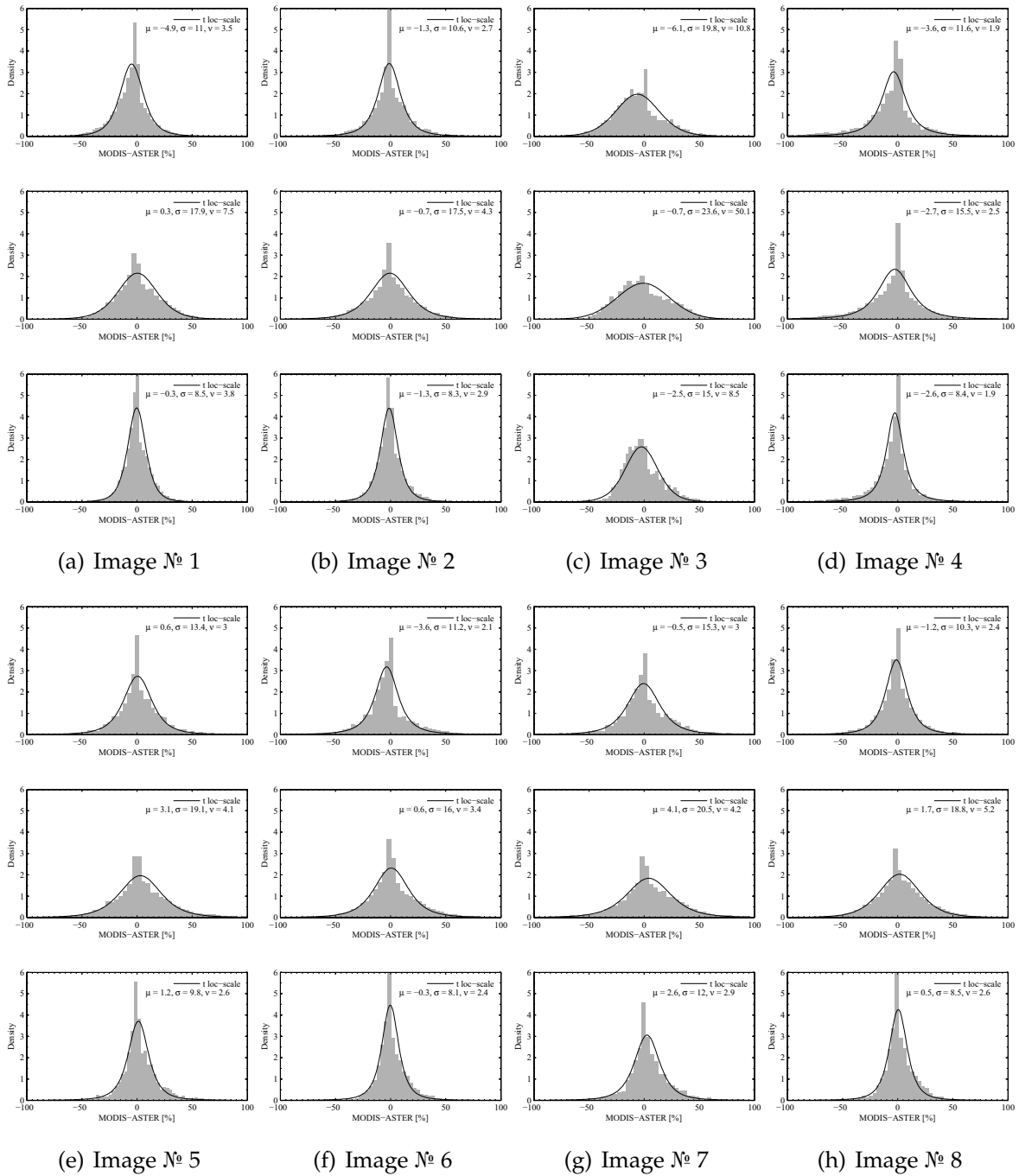


Figure 6.9 Distribution of the error between MODIS-derived and ASTER sub-pixel snow fractions for each date. From each image, the histogram for M500 (top), M250 (Middle), and G500 (Bottom) are provided. The parameters indicated on the graph refer to the t -location-scale distribution.

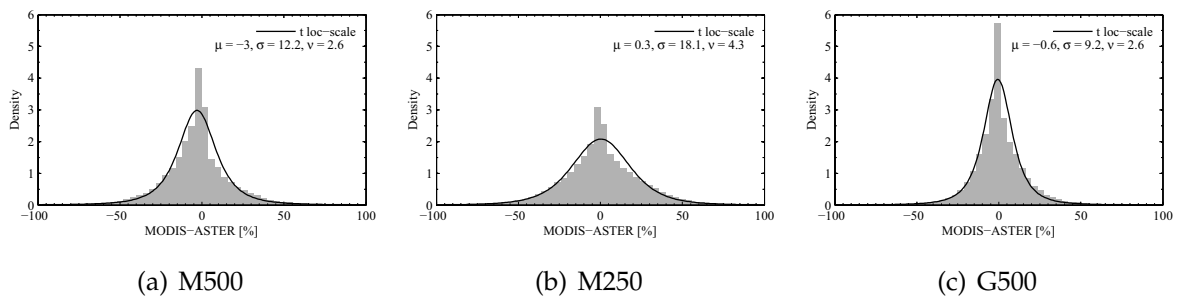


Figure 6.10 Distribution of the error between MODIS-derived and ASTER sub-pixel snow fractions for all samples from the eight images combined.

are slightly overestimated when less than half the pixel is covered by snow, and underestimated otherwise. Figure 6.11 (b) shows the variogram of fra_{ASTER} for a subset of image № 1. This reveals that the sub-pixel fraction of snow exhibits spatial autocorrelation up to 2km. The same range was observed from variograms produced from other subsets of the same images as well as other images. It means that the fra is spatially autocorrelated within the distance of the aggregation kernel. Since the error is also correlated with fra , the errors of estimation from contiguous 250m MODIS pixels are autocorrelated, thus explaining the covariance between aggregated pixels. Nevertheless, the reduced dispersion between G500 and M500 demonstrates that the estimation of snow fractions in 500m spatial resolution pixels is more precise when it is based on the unmixing of the fused spectral bands at 250m spatial resolution followed by an aggregation.

Figure 6.12 (a) shows the distribution of fca_{ASTER} that belongs to $]0, 100\%[= \{fra \in \mathbb{R} : 0 < fra < 1 \text{ for all samples at 500m resolution. It has a U-shape as expected from the distribution of area proportion in mixed pixels discussed in Section 5.3.3. Visually, a beta distribution could be fitted to the sample distribution, although a KS-test failed to assess equal distributions. Nevertheless, it provided parameters that are nearly equal, thus describing a nearly symmetrical distribution. In fact the means of mixed pixels area proportion were 51.2% and 52.1% at 500 and 250m, respectively. This symmetry suggests that, overall, 500 and 250m spatial resolution pixels were suitable to resolve the internal structure of mixed pixels without dominance of relatively bare patches over relatively snowy patches, or reciprocally. In this case, a 50% threshold is optimal to classify pixels into binary 'snow' or 'no snow' classes. Table 6.3 provides the mean of the area proportion distribution per image for the reference ASTER- and the estimated MODIS-derived$

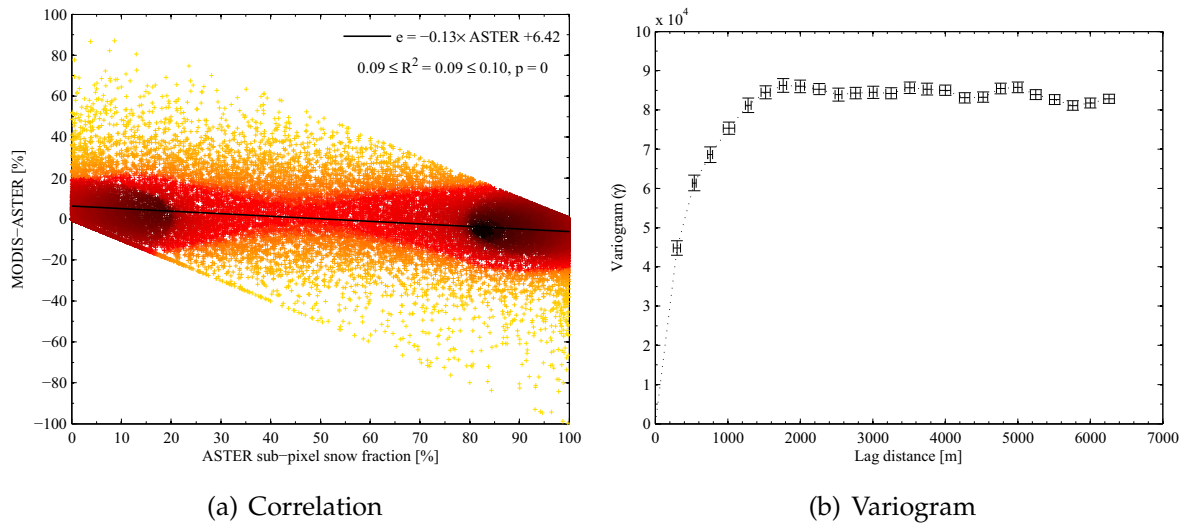


Figure 6.11 (a) Relationship between the error of sub-pixel snow fractions and ASTER reference value for all eight images combined. Points are colour coded to depict density. The confidence interval for R^2 is given at the 95% level. (b) Variogram of ASTER reference value for a subset of image № 1. Vertical error bars indicate the standard error for the variogram, horizontal bars indicate the standard deviation of the lag.

snow maps. It highlights the potential asymmetry with respect to the 50% midpoint. This digression can be related to the different configurations of snow cover shown in appendix F. Mixed pixels from Images № 3 & 4 have a mean proportion greater than 50%. They depict a large and nearly continuous snow cover (i.e., winter images) for which the spatial resolution is not capable of resolving equally pixels that are mostly free or mostly covered by snow. The structure of the snowpack makes the latter over-represented compared to the former at this spatial resolution. Images № 2 & 8 are summer images that exhibit the opposite scenario with a more patchy and discontinuous snow cover. Mixed pixels are more likely to account for small patches whose area is less than half the area of the pixel, resulting in an unbalanced distribution of area proportion towards 0. Finally, Images № 1 & 5–7 account for a structure of the snowpack that is close to being optimally resolved by the 250 and 500m resolution pixels.

In Figure 6.12 (b), the distribution of the corresponding fra_{MODIS} depicts a somewhat more complicated scenario. The progressively increasing probability of having fra_{ASTER} as it gets nearer to 0 mostly corresponds to $fra_{MODIS} = 0$. This is revealed by a lower density of $fra_{MODIS} < 10\%$ and a large bar for $fra_{MODIS} = 0$. The conclusion drawn previously about the overall overestimation of the sub-pixel

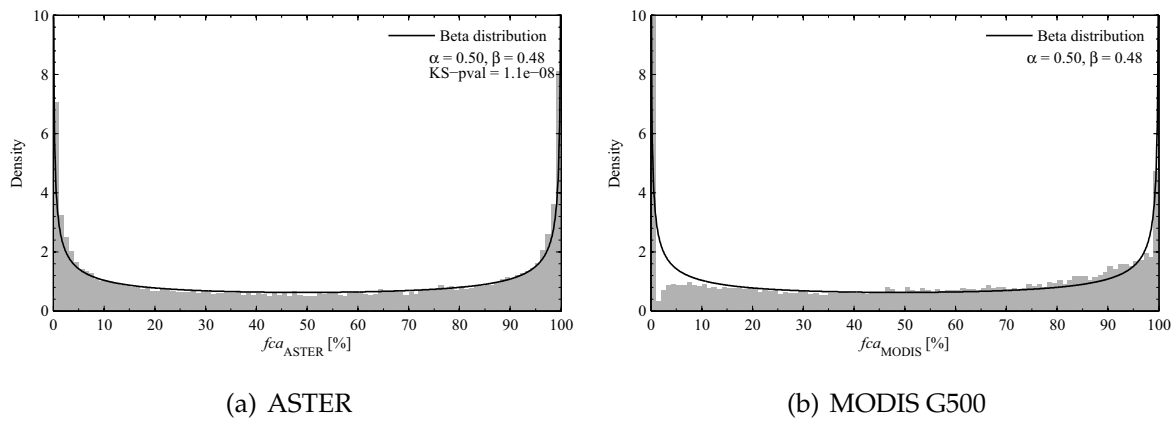


Figure 6.12 (a) Distribution of ASTER sub-pixel snow fractions belonging to $]0, 100\%[$ for all samples combined computed at 500m spatial resolution. The solid line is the fitter beta distribution. (b) Distribution of the corresponding MODIS sub-pixel snow fractions.

Table 6.3 Mean of the sub-pixel snow fraction fra for strictly mixed pixels (i.e., $fra_{\text{ASTER}} \in]0, 100\%[$) at both 500 and 250m spatial resolution.

Image N°	1	2	3	4	5	6	7	8	Overall
$E[fra_{\text{ASTER}}] [\%]$									
500m	48.9	39.2	63.3	65.7	50.4	52.0	49.0	41.6	51.2
250m	51.8	42.5	58.5	64.9	51.0	52.8	50.8	44.6	52.1
$E[fra_{\text{MODIS}}] [\%]$									
M500	43.4	38.5	57.8	59.2	51.6	49.7	49.4	40.3	48.2
G500	48.9	38.7	61.9	60.6	53.2	53.0	52.5	43.0	51.2
M250	52.4	42.2	57.9	59.4	55.2	54.7	55.5	47.0	52.9

snow fraction in MODIS outputs when $fra \leq 50\%$ can be refined from this observation. The fact that the unmixing is processed only on pixels having a positive NDSI is likely to contribute to this effect. Pixels accounting for less than 10% snow with positive NDSI tend to be overestimated [see Figure 6.11 (a)], while they are set to a null fraction if the NDSI is negative (see Section 5.5.1). This explains why the unmixing algorithm has difficulties to detect snow in pixels that account for less than 10%. Nevertheless, Table 6.3 shows that the expected value of fra_{MODIS} is very close to that of fra_{ASTER} . It suggests that the underestimation attributed to pixels that are discarded from the unmixing is balanced by the slight overestimation of pixels with low abundance.

6.5.2 Common statistical measures

6.5.2.1 Description

In the pixel-based representation, the mean error (μ_e), the mean absolute error (MAE), and the root mean square error (RMSE) were initially used to describe the ability of the model to produce reliable observations. These measures were described in Section 3.2.2.1, as along with the method to estimate their confidence interval (see Appendix B for more detail about confidence intervals for MAE and RMSE). Consider μ_e be the mean error between the snow fractions retrieved from MODIS images relative to ASTER references computed over n samples (i.e., pixels). From this, the total SCA error is $n\delta^2\mu_e$, with δ being the pixel size. μ_e is more readily interpretable as it provides the error of estimated SCA relative to the total area of the image. However, it gives relatively little information about the errors, as they can cancel out in the estimation of the total SCA.¹ This justifies the use of the MAE and the RMSE, as these measures account for errors regardless of whether it is positive or negative.

The match between fra_{MODIS} and fra_{ASTER} was examined using the coefficient of determination R^2 and linear regression between both quantities. R^2 indicates the portion of variance in the ASTER-derived reference snow map that is accounted for in the MODIS-derived snow map. This dimensionless measure can be used along with dimensioned ones as a goodness-of-fit indicator. CI for R^2 are calculated using Fisher's z -transformation given by $R = \tanh z_R \Rightarrow z_R = \frac{1}{2} \ln \frac{1+R}{1-R}$. z has an asymptotic normal distribution, with an approximate variance equal to $\frac{1}{n-3}$, where n is the number of samples (Fisher, 1921). Hence,

$$\text{Prob}\left(\hat{z}_R - z_{\alpha/2} \sqrt{\frac{1}{n-3}} \leq z_R \leq \hat{z}_R + z_{\alpha/2} \sqrt{\frac{1}{n-3}}\right) = 1 - \alpha. \quad (6.8)$$

The relation between z_R and R enables computation of the CI for the Pearson correlation coefficient R , and subsequently R^2 .

Despite the fact that ASTER-derived snow fractions are considered as the reference layer, ASTER snow maps still have some degree of uncertainties, mostly due to the arbitrary choice of the NDSI threshold. *Ordinary least squares linear regression* (OLS) of fra_{MODIS} with respect to fra_{ASTER} is equivalent to assuming that the reference dataset is error-free. The linear model is established so that only residuals of the independent variable fra_{MODIS} are minimized with respect to the explanatory

¹Note that G500 is obtained from M250 via a mean operation. Hence μ_e is identical for both maps.

variable [Figure 6.13 (a)]. When this assumption cannot be satisfied, it raises the issue of “error-in-variable” which can jeopardize the quality of the linear model.

Salomonson and Appel (2004) addressed this problem by comparing two distinct OLS regressions using either one or the other variable as the explanatory one. Alternatively, a single *standard weighted least squares linear regression* can be used to estimate a more robust linear model when both variables potentially account for errors that are either equal or unknown (Borcherds and Sheth, 1995). Figure 6.13 (b) shows that it corresponds to minimizing simultaneously the residual of the pairs of data $\{fra_{MODIS,i}, fra_{ASTER,i}\}$ to the linear model. This method is preferred here, and ideally the linear regression should fit the 1:1 ratio line.

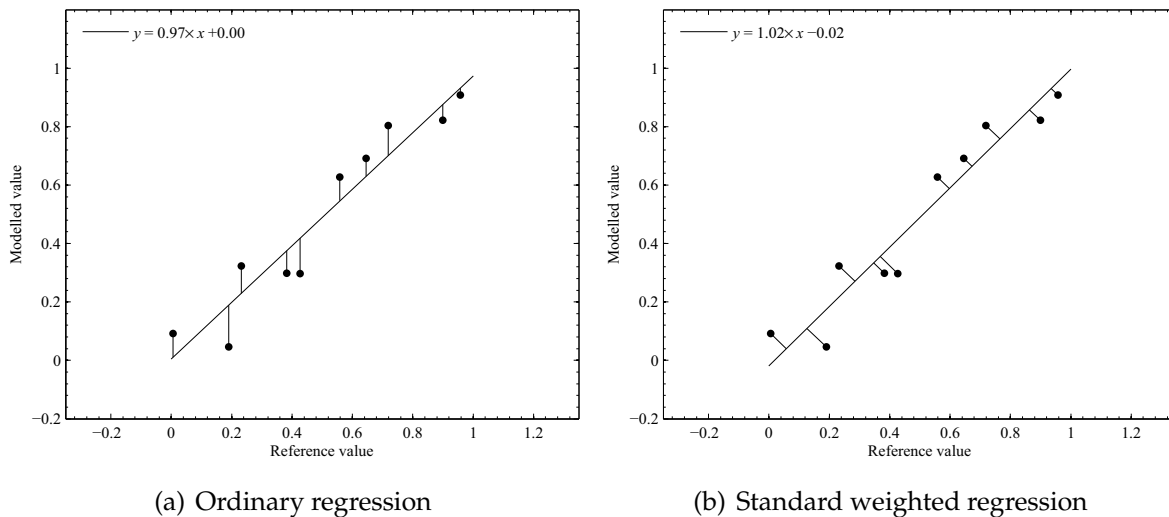


Figure 6.13 Illustration of ordinary (a) and standard weighted (b) least squares linear regression. Note the different residuals used for the least squares fit.

6.5.2.2 Overall measures

The calculation of confidence intervals is primarily achieved pixel-wise. In other words, pixels are considered to be independent samples drawn from a population. Statistical significance can be established when confidence intervals of statistics computed on different samples do not overlap. The estimation of the overall performance can be achieved in two ways. First, all pixels from each image are combined. The newly formed vector is then treated *pixel-wise* as if it were drawn from a new population. For example, the mean error, MAE, or RMSE are computed on the basis of the combination of all pixels from each image, regardless of their date. Alternatively, it is possible to consider images as individual samples. In such a case,

the overall performance is investigated *image-wise* by considering the distribution of the measures across different images viewed as independent events. The variability of the indicators and the limited number of image pairs available potentially affect the confidence interval computed image-wise. However, both types of overall performance were considered in order to assess the method as comprehensively as possible.

6.5.2.3 Results of the statistical measures

For each MODIS image shown in appendix F, and their corresponding ASTER reference, M500 and M250 illustrate the resolution improvement obtained with the fusion. The visual interpretation of the snow maps for each granule led to the subjective judgement that the fused output (M250) was “significantly better” than the non fused one (M500) because more detail could be seen in the 250m maps. This richer spatial information generally matched quite well features depicted in the ASTER reference image.

Quantitative results provided in Table 6.4 show that the total SCA sometimes is estimated well with the M500 map and deteriorates with the M250 map and reciprocally. No clear relationship was found between the SCA error and any attributes of the image (e.g., percent of snow cover, time of year) that could explain this erratic performance. It must be noted, however, that when accounting for all samples, the SCA error was reduced by 1.5% (i.e., from -1.8% error with M500 to -0.3% error with M250) compared to the true SCA value retrieved from ASTER. However, there is no evidence that this improvement would be consistent with other test images. Image-wise, the error of estimation of SCA from MODIS-derived snow maps was generally within 5% of the true SCA value retrieved from ASTER.

Generally, the performance in terms of RMSE, MAE, and R^2 was similar between the M500 and M250 maps. It suggests that the implementation of the fusion technique permits retrieval of snow fractions within 250m resolution pixels with a comparable level of accuracy than when retrieved from the original 500m resolution pixels. The improved statistics obtained for G500 maps compared to M500 maps illustrate that when aggregating the M250 maps at 500m spatial resolution, a better determination of snow can be achieved than with the original 500m resolution bands. It indicates the improvement of snow mapping performance that is enabled by the use of the fusion algorithm.

Overall, the RMSE and MAE for the G500 maps showed a 25% improvement

Table 6.4 Comparison of ASTER- and MODIS-derived snow maps.

Image №	ASTER reference snow maps			SCA error [%]		RMSE [%]		MAE [%]		R ²		Linear regression ^c	
	Pixels (n) (% <i>snowy pixels</i>) ^a		SCA ^b	M500	M250	M500	M250	M500	M250	M500	M250	M500	M250
	500m	250m	[%]				G500		G500		G500		G500
1	12048 (50%)	48192 (43%)	27.1%	-2.6%	0.0%	11.2	12.7	5.5	5.9	0.92	0.90	y=0.96x-0.01	y=0.98x+0.01
							7.9		3.9		0.96		y=1.00x+0.00
2	7915 (40%)	31660 (33%)	17.8%	-0.3%	-0.3%	10.5	12.8	4.5	5.2	0.90	0.86	y=1.04x-0.01	y=0.97x+0.00
							8.1		3.6		0.93		y=0.98x-0.00
3	7310 (91%)	29240 (88%)	79.7%	-4.0%	-1.9%	14.9	14.3	8.7	7.7	0.84	0.86	y=0.91x+0.03	y=0.87x+0.08
							11.2		6.6		0.91		y=0.88x+0.08
4	6668 (70%)	26672 (63%)	50.8%	-5.0%	-3.9%	18.9	18.6	10.1	9.0	0.83	0.85	y=0.96x-0.03	y=0.95x-0.01
							14.4		7.6		0.90		y=0.94x-0.01
5	4854 (51%)	19416 (45%)	29.0%	0.3%	1.2%	14.1	15.9	6.8	7.2	0.88	0.85	y=1.00x+0.00	y=0.98x+0.02
							11.1		5.3		0.92		y=0.99x+0.02
6	8185 (53%)	32740 (46%)	30.3%	-1.4%	0.4%	14.4	14.4	7.2	6.5	0.87	0.88	y=0.97x-0.01	y=0.98x+0.01
							9.9		4.8		0.94		y=0.98x+0.01
7	4679 (59%)	18716 (51%)	31.3%	0.1%	1.9%	17.6	19.1	9.4	9.6	0.80	0.79	y=0.98x+0.01	y=0.98x+0.03
							14.2		7.6		0.87		y=0.97x+0.03
8	7587 (40%)	30348 (34%)	18.9%	-0.4%	0.7%	11.1	13.2	4.7	5.5	0.89	0.86	y=1.02x-0.01	y=1.00x+0.01
							8.9		3.8		0.93		y=1.02x+0.01
Overall	59246 (56%)	236984 (50%)	34.9%	-1.8%	-0.3%	13.9	14.8	6.8	6.8	0.89	0.88	y=0.97x-0.01	y=0.96x+0.01
							10.5		5.1		0.94		y=0.97x+0.01

M500 refers to the maps of sub-pixel snow fractions at 500m spatial resolution derived from MODIS 500m resolution bands (i.e., without using the fusion method). M250 refers to the maps of sub-pixel snow fractions at 250m spatial resolution derived from MODIS 250m resolution bands (i.e., using the fusion method). G500 refers to the M250 maps aggregated at 500m spatial resolution using a mean operator.

^a Number of pixels containing a non null fraction of snow according to the reference snow map, expressed as a percentage.

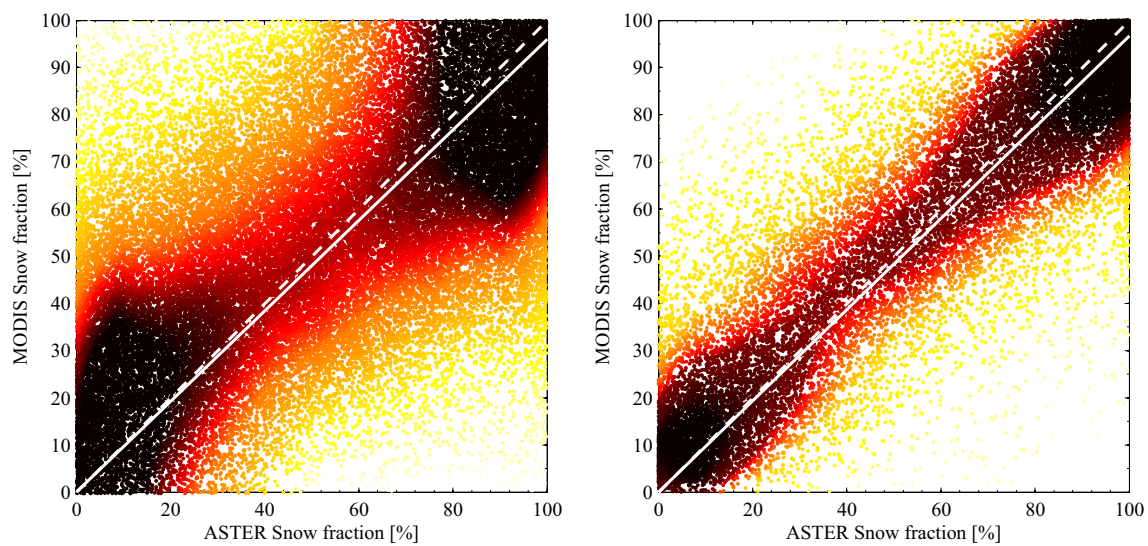
^b Snow Cover Area, i.e., the area of the scene covered by snow in the reference ASTER image, expressed as a percentage.

^c Standard weighted linear regression where x represents the sub-pixel fraction of snow from ASTER (fra_{ASTER}) reference and y is the tested sub-pixel fraction of snow from MODIS (fra_{MODIS}).

compared to the M500 maps, while R^2 increased 5.6%. The values of MAE and R^2 for the images № 1–4, presented in Table 6.4, are slightly different from what was published in [Sirguey et al. \(2008\)](#) because NDSI thresholds were refined for the classification of snow from ASTER. The four test images selected independently from the determination of end-members (i.e., images № 5–8) exhibit similar performances as the dependent set, thus demonstrating the robustness of the mapping process.

Figure 6.14 provides the scatter plot of the snow fraction retrieved from all MODIS pixels versus the reference snow fraction obtained from ASTER for all eight images. Figure 6.14 (a) is the distribution of all pixels accounted for in the M250 maps ($n = 236984$) and Figure 6.14 (b) is the scatter plot of all pixels available in the G500 maps ($n = 59246$). The scatter plots are colour coded according to pixel density because of the high number of pixels and to represent better the pixel distribution. The linear regressions are generally good and the reduced dispersion in Figure 6.14 (b) accounts for the positive effect of aggregation on the determination of snow within a 500m resolution pixel. The values of the linear regressions, R^2 , MAE, and RMSE obtained for M250 and G500 were substantially better than what was obtained from AVHRR by [Foppa et al. \(2007\)](#) ($R^2 = 0.78$, MAE = 10.4%) and competitive with the sub-pixel snow fraction available in the Collection 5 of the MODIS MxD10 Snow product ([Salomonson and Appel, 2006](#), $R^2 = 0.9$, RMSE = 10%).

Confidence intervals for the mean error were so small that there is no need to report them. Figure 6.15 displays the performance in terms of MAE, RMSE, and R^2 for each image, as well as pixel-wise and image-wise overall results. Pixel-wise, the confidence intervals demonstrate that for each image, as well as when combining all pixels, the results reported above are statistically significant and G500 is significantly better than M500. The differences between M500 and M250 are more confusing. For example, M500 scored consistently better than M250 for images № 1, 2, & 8. For images № 3, 4, & 6, M250 maps obtain significantly better MAE than M500, while RMSE values are not distinguishable. Images № 5 & 7 also show confusing results, rating M500 either better or not significantly better than M250. Overall, MAE from M500 and M250 are not significantly different, unlike RMSE and R^2 that score M500 slightly better than M250. It confirms that different measures sometimes suggest different and confusing conclusions. Only their association has the potential to reveal a consistent pattern. It is interesting to note that RMSE has more discriminative power than MAE and, hence, it is not disregarded, thus disputing the point raised by [Willmott and Matsuura \(2005\)](#). Without doubt, G500 achieves significantly better



(a) Scatter plot according to 250m spatial resolution snow maps (M250). (b) Scatter plot according to 500m spatial resolution snow maps after aggregation of all 250m spatial resolution snow maps (G500).

Figure 6.14 Scatter plots of the fractional snow cover retrieved from MODIS versus the reference snow fractions obtained from ASTER, for all pixels of the eight test images. The dots are colour coded according to pixel density to better represent the pixel distribution. The dashed lines are the 1:1 ratio line, the solid line is the standard weighted linear regression.

results than M500, while M250 may be regarded as slightly less precise than M500. However, as explained in Section 6.3.2, the difference of scores between both maps does not account for the fact that M250 contains pixels half the size of M500. Only a subjective judgement allows the difference of performance to be appreciated, and a conclusion that the fusion method objectively created more detailed snow maps.

Image-wise overall performances are illustrated in boxplots in Figure 6.15. They depict the median, quartile, and extent of the measures considering each image as a single realisation. The notches represent the 95% CI for the median (McGill *et al.*, 1978). From this, it is clear that the median values of MAE for the eight images are not significantly better for any type of map; the median of the RMSE for the set of G500 maps is close to being significantly lower than both M500 and M250. Only the median of the R^2 values is significantly larger for G500 than those of the other maps. The image-wise overall results never allow discrimination of M500 and M250.

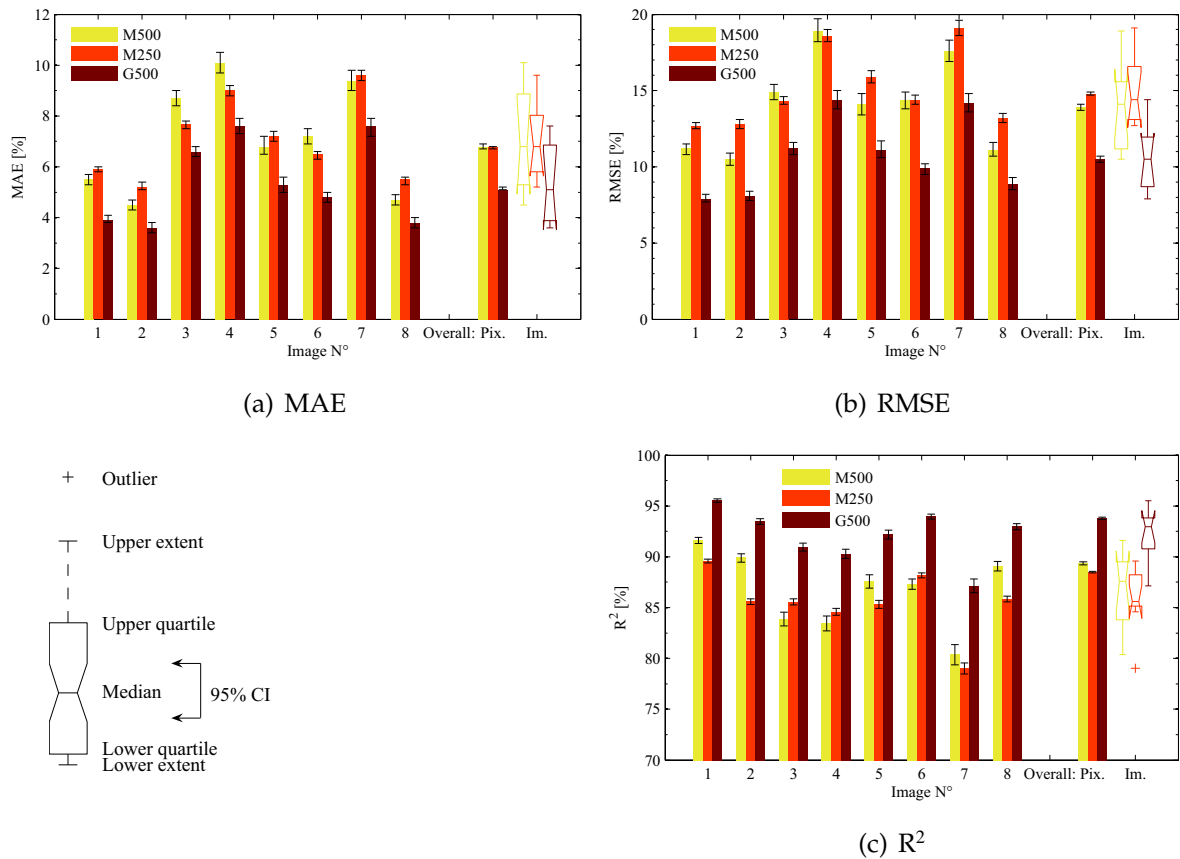


Figure 6.15 Results of pixel-based metrics: (a) MAE, (b) RMSE, and (c) R^2 . The scores are given for each image and when combining all samples (i.e., pixel-wise overall results). The box plots illustrate the distribution of scores when considering all images (i.e., image-wise overall results). The notches depict the 95% confidence interval around the median value.

Clearly, this assessment strategy would benefit from being computed with more images. It is reasonable to expect that the relative difference between medians will not change much, while the confidence interval on the median would narrow. It is reasonable to expect the same conclusions as those drawn from the pixel-wise overall assessment. G500 would be assessed as achieving significantly better performance than any other in terms of determination of snow within pixels. M250 and M500 achieve similar accuracy although slightly better for M500, but given the fact that M250 is twice better resolved.

6.5.3 Global quality or Q Index

6.5.3.1 Description

MODIS snow fraction maps are grayscale raster datasets. Their similarity to the corresponding ASTER reference maps can be evaluated using a global image quality index such as the Q index designed by Wang and Bovik (2002) and later generalized for the assessment of multispectral image fusion methods by Alparone *et al.* (2004). Since the Q index has been widely used to assess image fusion performance (Garzelli and Nencini, 2006; Pardo-Igúzquiza *et al.*, 2006; Alparone *et al.*, 2007), it was relevant to investigate its results when applied to the present outputs. For monochrome images, the Q index is defined by

$$Q_{xy} = \frac{\sigma_{xy}}{\sigma_x \sigma_y} \frac{2\bar{x}\bar{y}}{\bar{x}^2 + \bar{y}^2} \frac{2\sigma_x \sigma_y}{\sigma_x^2 + \sigma_y^2}, \quad (6.9)$$

where x and y are the values from the test and the reference images (here, these are the sub-pixel snow fractions fra_{ASTER} and fra_{MODIS}). σ_{xy} is the covariance between x and y ; \bar{x} and \bar{y} are the means, and σ_x^2 and σ_y^2 are the variances of x and y respectively. This index incorporates the Pearson correlation coefficient R and is sensitive to the bias and the change in contrast between the images tested. It provides a unique score that ranges between -1 and 1 making it appropriate for ranking processing strategies according to their performance.

Since the signal from images is generally non-stationary and the quality may be variable in space, Wang and Bovik (2002) advocated computing Q as the average of a series of Q_j estimated from subsets of the image using a sliding window approach. In their experiment, Alparone *et al.* (2004) established that Q had the best discriminative power for a block of size 32×32 pixels. It must be noted that the sliding window approach can only apply to individual images, thus it is irrelevant to combine all pixels to compute a pixel-wise overall estimation of the index. With regard to the CI of the Q index, its distribution is potentially complicated. However, making the assumption that Q_j are pairwise independent and obey the same distribution, the CI for the mean Q can be estimated similarly to Equation (3.4).

6.5.3.2 Results of the Q index

Figure 6.16 shows the scores obtained from the Q index. G500 ranks significantly better than both M500 and M250 for all images taken independently. Overall (image-wise), the Q Index increased nearly 6% between M500 and G500 and both

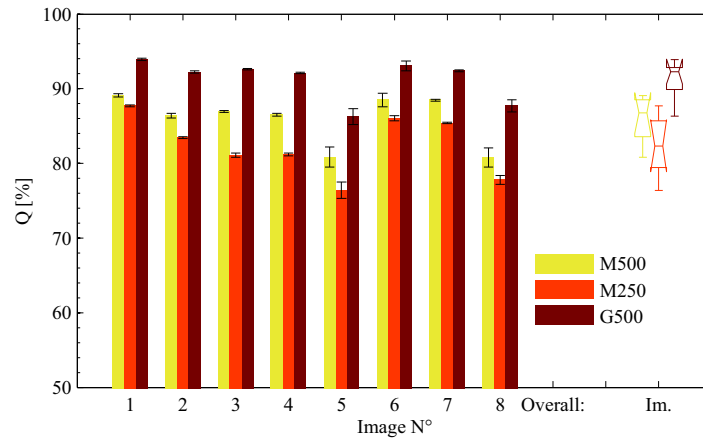


Figure 6.16 Results of Q index.

medians are significantly different. The main difference with other pixel-based measures is that it systematically discriminates M500 and M250, the latter being of less quality than the former. No clear explanation could be found as to the reason for this distinction when all other metrics lead to more confusing results between both of these maps. One reason could be the use of the sliding window approach that may enable local discrepancies to impact on the final results. Nevertheless, it does not alter fundamentally the conclusion that the fusion objectively improves the mapping performance. It must be added that, as for other pixel-based metrics, the Q index fails to account for the change in spatial resolution. Thus, the lower performance of M250 maps must be interpreted, again, with respect to the smaller pixel size.

6.5.4 Receiver Operating Characteristics curves

6.5.4.1 Description

The process of mapping snow in a binary fashion (i.e., pixels are ‘snow’ or ‘no snow’) is analogous to a thematic classifier. In such a framework, the performance of the classification process is often assessed using measures obtained from the confusion matrix (Congalton, 1991). When the classifier is binary, the confusion matrix has the simplest form, shown in Figure 6.17 (a). The common binary performance measures that can be derived from this representation are given in Equation (6.17). The *hit rate* (also called *recall*) is the *producer’s accuracy* of the positive class (here the ‘snow’ class). It corresponds to the probability of correctly detecting a ‘snow’ pixel. The *precision* is the *user’s accuracy* of the positive class. It corresponds to the probability of a pixel classified as snow to truly belong to the ‘snow’ class. The *false alarm*

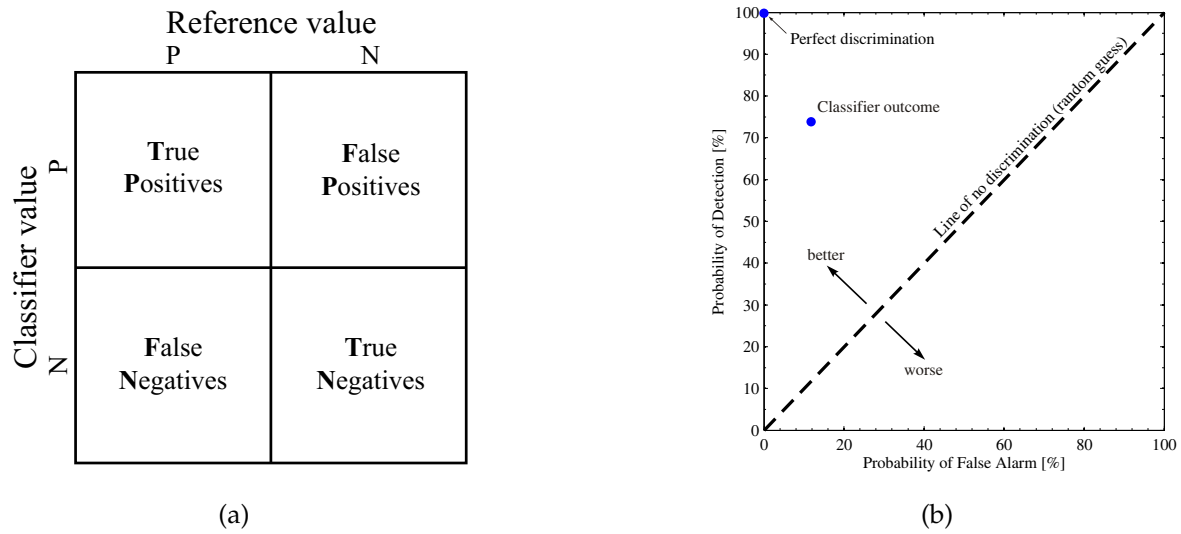


Figure 6.17 (a) Confusion matrix for a binary classifier. (b) Representation of the classifier performance in the ROC space.

$$\text{Hit rate} = \frac{TP}{P} \quad (6.10a)$$

$$\text{False alarm rate} = \frac{FP}{N} \quad (6.10b)$$

$$\text{Precision} = \frac{TP}{TP + FP} \quad (6.10c)$$

$$\text{Accuracy} = \frac{TP + TN}{P + N} \quad (6.10d)$$

rate is one minus the producer's accuracy of the negative class. It corresponds to the probability of wrongly classifying a pixel as snow when it is not (i.e., commission error). Finally, the *average accuracy* measures the probability of correctly classifying pixels regardless if they are 'snow' or 'not snow'. For example, [Hall et al. \(2001\)](#) measured the accuracy of MODIS MxD10 Snow product based on the confusion matrix and the *accuracy* measure. This was justified by the binary nature of the outputs. In the framework of snow abundance mapping, [Painter et al. \(2009\)](#) segmented the modelled and reference snow maps of sub-pixel snow fractions using a 15% threshold to categorize pixels as being snow or not. The maps were then assessed using precision, hit rate, and accuracy.

The hit rate and false alarm rate computed from the confusion matrix [Figure 6.17 (a)] of a discrete classifier define a single point in the *receiver operating characteristics* (ROC) space formed by the axis corresponding to both probabilities [Figure 6.17 (b)]. The 1:1 ratio line depicts the positions of classifiers that have the same probability to detect correctly a 'snow' pixel, as to flag it inappropriately as

‘no snow’. In other words, such classifiers are equivalent to a fair binomial random guess. The lower triangle of the ROC graph is worse than the random guess and any classifier whose *ROC point* falls in this region must be discarded. In the upper triangle, the position of a classifier’s outcome can be interpreted as better or worse as it gets nearer to or further away from the perfect discrimination (i.e., 100% probability of detection while no false alarm).

Clearly, the performance of crisp classifiers can be compared readily without the need for a graphical representation. In fact, the ROC graph is designed to depict the performance of binary classifiers whose outcome is associated with a membership function that measures the probability for the pixel to belong in one or the other class [Figure 6.18 (a)]. In this case, hit rate and false alarm rate can be computed for any value of the classifier outcome and plotted in the ROC space. The curve formed by these points for increasing thresholds is the ROC curve. The performance of the classifier can then be assessed with regard to its position relative to the lines of perfect and no discrimination [Figure 6.18 (b)].

ROC curves provide a graphical interpretation of confusion matrices in the case of fuzzy classifiers and have become very popular in signal detection theory and medical diagnostic testing [see [Fawcett \(2006\)](#) and references therein]. Clearly, they can also be used to represent the separation of the two membership functions (or two histograms). Perfectly separated or matching histograms correspond to a perfect discrimination and a random guess, respectively. In between, the ROC curve depicts graphically the structure of the overlap between both histograms. To assess the performance of a classifier, a single score can be retrieved from the area under the ROC curve (AUC). It corresponds to the probability of correctly classifying a random pair of pixels belonging to distinct classes ([Hanley and Mcneil, 1982](#)). Alternatively, the area between the curve and the no discrimination line (AUCD) can be used to rank classifiers.¹

This approach cannot be applied directly in this application since the classifier is continuous. Indeed, the snow fraction within a pixel can take any value in the range [0, 1]. To tackle this issue, the reference snow maps aggregated at 250 and 500m spatial resolution were segmented into eleven classes (ten thresholds applied to fra_{ASTER} : {0.5, 0.15, ..., 0.95%}). To accommodate for the non-uniform pixel distribution in each class, pixels fully or not covered by snow were removed and an equal number of pixels were randomly selected in each class, based on the smallest class.

¹Note that $AUC = AUCD + \frac{1}{2}$.

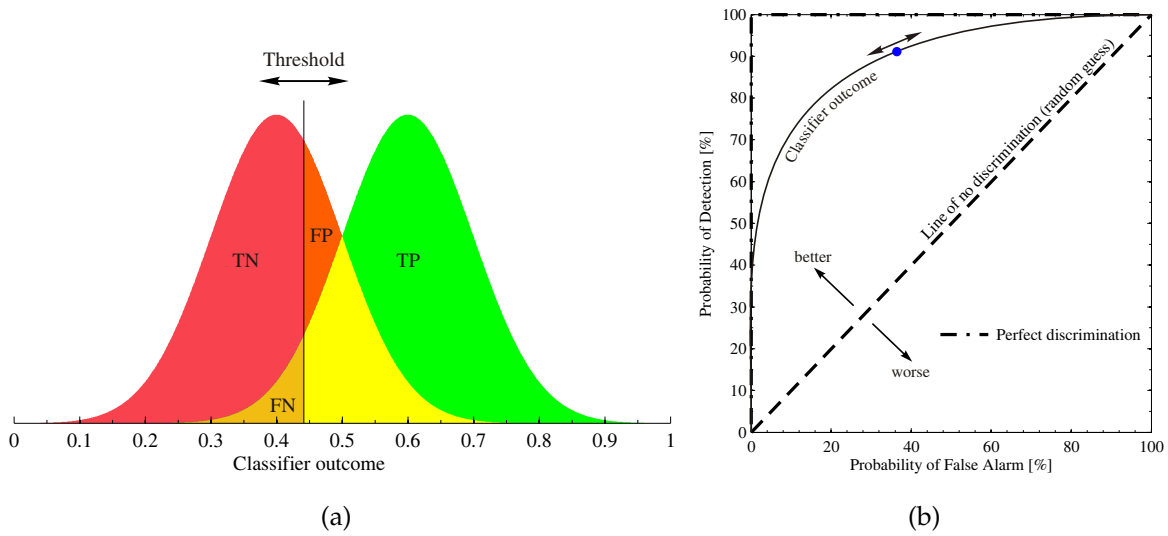


Figure 6.18 (a) Membership to class according to classifier continuous outcome value. (b) Representation of the classifier performance in the ROC space.

For each threshold, the corresponding pixels in MODIS-derived maps were combined into two distinct sets whether their true abundance (i.e., fra_{ASTER}) was lower or greater than the given threshold. Both sets account for pixels whose fra_{MODIS} does not match the classes of reference.

An example of the distribution of both sets for all thresholds is shown in Figure 6.19. A parallel can be drawn here with the work of Painter *et al.* (2009) who measured the accuracy of their process based on a single segmentation of the reference and modelled snow maps using a 15% threshold on both maps. It corresponds to computing the binary performance measures only once at the position highlighted by the arrow in Figure 6.19. However the spread of the distribution across the reference can be more comprehensively assessed using a ROC curve computed for increasing value of fra_{MODIS} . This depicts the ability for the classifier to discriminate pixels covered by more or less snow than the threshold applied on the reference. Such ROC curves were processed for M500, M250, and G500 for all images. AUCD relative to the total area of the ROC space were computed for each threshold and averaged to provide a single scalar value. Confidence intervals for ROC curves (and thus AUCD) are challenging to determine and were not estimated here, but methods to compute these are proposed by Fawcett (2006) and Kerekes (2008).

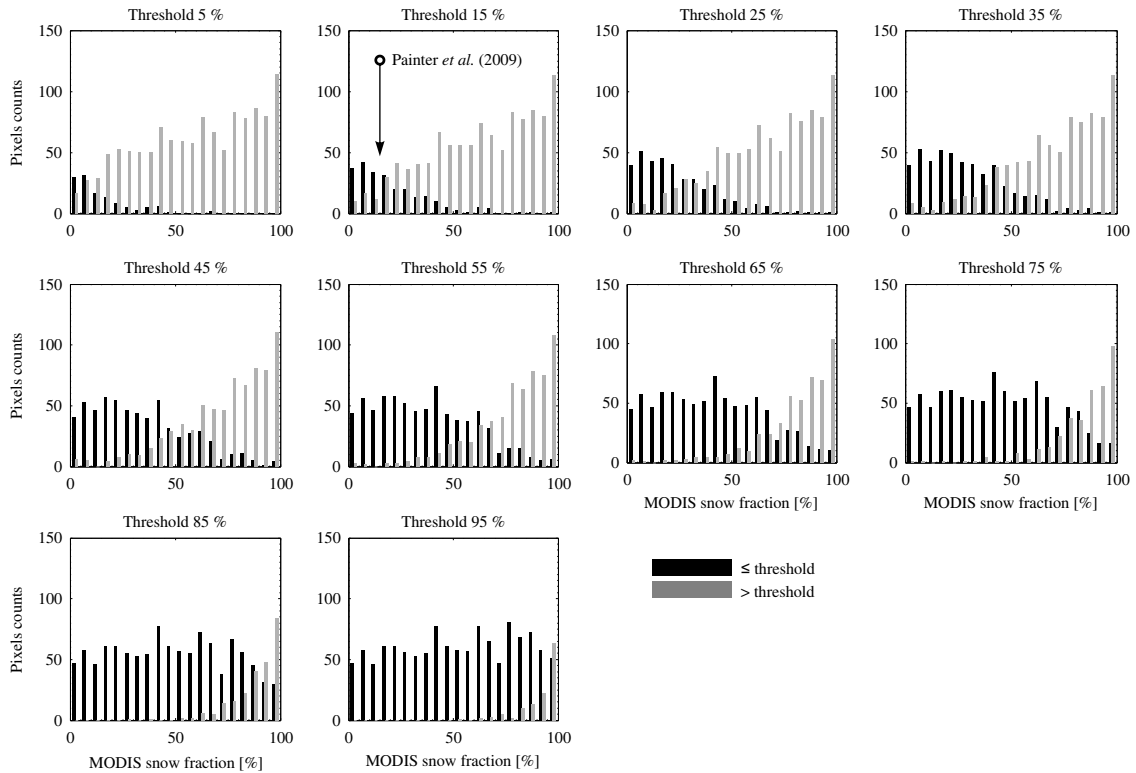


Figure 6.19 Distribution of MODIS sub-pixel snow fractions relative to thresholds defined on ASTER reference snow map (G500 maps for image N° 7: April 3rd, 2002). The arrow indicates the threshold used by [Painter et al. \(2009\)](#) to compute binary performance measures.

6.5.4.2 Results of ROC curve analysis

An example of the set of ROC curves is shown in Figure 6.20 as well as the AUCD according to the threshold on fra_{ASTER} . Only curves corresponding to image N° 7 are given but these results are typical of all images. The ROC curve of M500 is always (i.e., for all threshold and for all images) between that of G500 and M250, G500 being the nearest from the perfect determination line. Like previous methods, this strategy of assessment indicates that the ROC curves of the aggregated snow maps benefit from the fusion process and tend towards a better determination of the snow classes than M500. Figure 6.21 provides the mean AUCD values for all maps. G500 maps are ranked consistently better than both other outputs, thus confirming the pattern observed with other measures. Like the Q index, the AUCD scores of the M500 maps is better than M250 in all cases. Interestingly, the magnitude of the differences departs from that of Q (Figure 6.16). For example, M250 and M500 for images N° 1 & 2 had relatively close Q values but very different AUCD, while

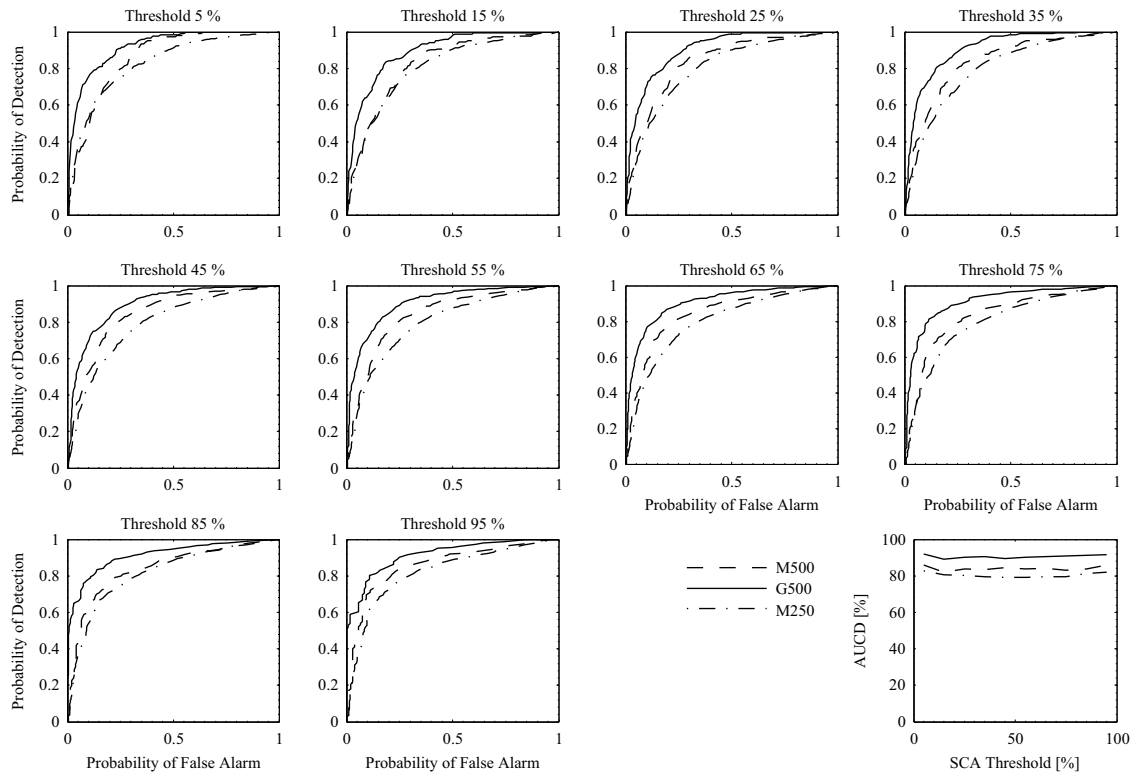


Figure 6.20 Receiver Operating Characteristics (ROC) curves and Area Under (ROC) Curve and non-Discrimination line (AUCD) obtained for snow maps M500, M250, and G500 (image № 7: April 3rd, 2002).

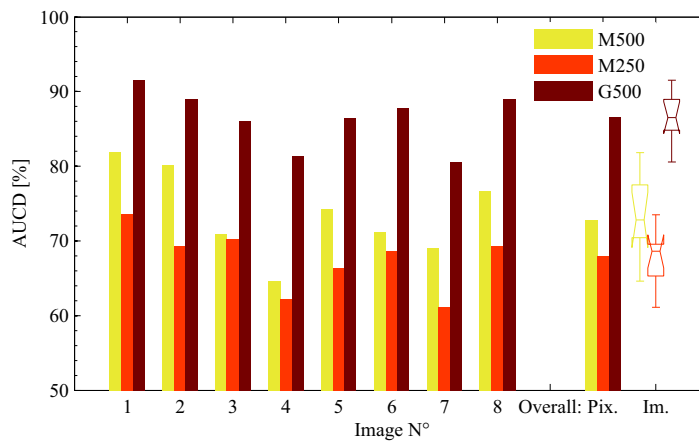


Figure 6.21 Results of AUCD.

the reverse is true for images № 3 & 4. Overall, the AUCD increased nearly 20% between M500 and G500 and both medians were significantly different.

As for other pixel-based measures, the ROC analysis was not appropriate to score objectively maps with respect to their spatial resolution. The general pattern of performance is clearly identified. It assessed that a gain can be attributed to the use of the fusion algorithm. This is supported by the multiple measures based on various approaches that guarantee the reliability of this conclusion. However, pixel-based measures do not agree with the magnitude of the improvement. SCA error was reduced by 1.5%, RMSE and MAE decreased by 25%, the dimensionless measures R^2 and Q increased by around 6%, finally AUCD increased by 20%. In addition, all such improvements refer to maps compared at the same spatial resolution (M500 and G500), while the map with the finest detail (M250) was consistently ranked as the worst. It highlights the difficulty of interpreting the results of pixel-based indicators in the context of image fusion and justifies the effort presented in the following section towards a measure that is better suited to assess multi-resolution datasets.

6.6 Feature-based measure¹

This section investigates the use of the modified directed Hausdorff distance (MDHD, see Section 6.3.3) as an alternative or complementary measure of the snow mapping performance. First the methodology implemented to retrieve the MDHD is described. Then, the behaviour and sensitivity of the MDHD is investigated based on synthetic maps created from ASTER data only. Finally, the method is applied to the MODIS-derived M500 and M250 snow maps obtained ‘without’ or ‘with’ implementing the fusion method, respectively, to assess the potential improvement.

¹The content of this section has been largely published in: Sirguey, P., Oltmer, S., and Mathieu, R. (2007). Assessment of the performance of image fusion for the mapping of snow using Euclidean distance. In P. A. Whigham (Ed.), *19th Annual Colloquium of the Spatial Information Research Centre*, Dunedin, New Zealand, 13–24. The University of Otago.

6.6.1 Methodology

6.6.1.1 Calculation of Euclidean distance

Section 6.3.3 explained how the MDHD, calculated in a two-dimensional Euclidean space, between the path T extracted from the classifier or ‘test line’, and the ‘reference snowline’ S extracted from 15m ASTER imagery, can be used to score the match between both sets. For any given point $p \in T$, the distance between p and the set S , denoted $d(p, S)$, is the minimum Euclidean distance between p and any point $x \in S$, as shown on Figure 6.22. It is formulated as

$$\forall p \in T, d(p, S) = \min_{x \in S} d(p, x). \quad (6.11)$$

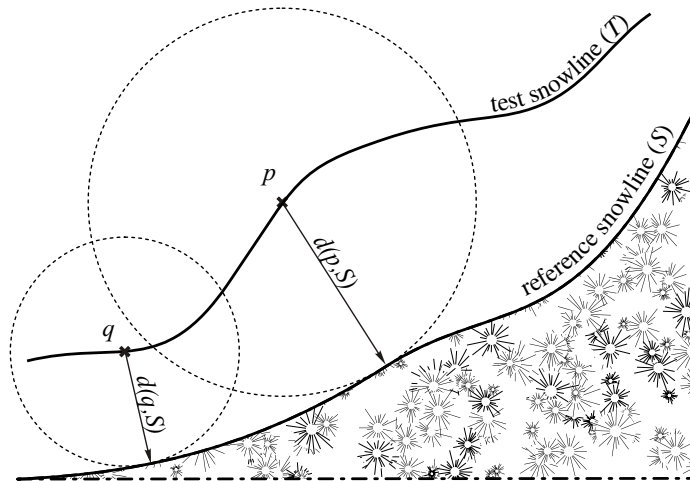


Figure 6.22 Minimum Euclidean distance $d(p, S)$ between a point p on the ‘test snowline’ and the ‘reference snowline’ S .

From a computational point of view, the Euclidean distance cannot be computed for all points on continuous line, but it can be estimated according to a set of samples. This is supported by the method of [Dubuisson and Jain \(1994\)](#) who suggested to extract finite sets of points from the paths. All combinations of distances between points from T and S can be computed and the shortest for each point of T retained. The MDHD is then defined as the average distance considering the set of points of T . This result can be achieved by computing a raster image, using a function widely available in GIS packages, which contains the distance from every cell to its closest point of S . The pixel size of this ‘distance raster’ must be smaller than, or equal to, the pixel size at which the reference snowline S was mapped. A

subset of an ASTER image with the mapped snowline and the corresponding ‘distance raster’ is shown in Figure 6.23. The cells of this raster, that are intersected by the snowline to test T , account for the distribution of Euclidean distance. The mean of this distribution is the MDHD and its standard deviation σ_{ED} provides valuable information with regard to the dispersion of Euclidean distances between S and T .

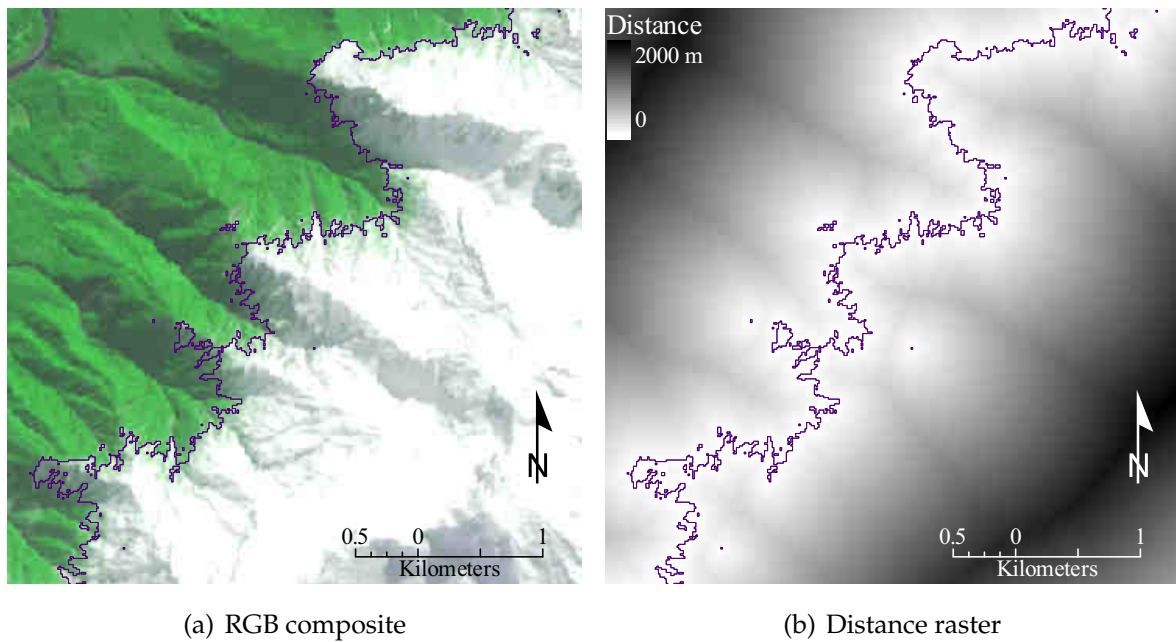


Figure 6.23 Example of reference snowline and corresponding Euclidean distance raster image created at 12.5m pixel size and computed from the ASTER-derived (15m) reference snowline.

6.6.1.2 Theoretical behaviour of the MDHD based on ASTER reference data

To assess the relevance of the MDHD as an indicator capable of scoring binary classifications independently of their spatial resolution, its theoretical behaviour was investigated on the basis of reference material only, simulated at various pixel sizes. From the original ASTER binary snow map, reference maps of sub-pixel snow fraction were created. The four ASTER binary snow maps from image N° 1 & 4 were first resampled at 12.5m, then aggregated to 50m, 125m, 250m, 500m, and 1000m to create a multi-resolution reference dataset of maps of snow abundance, all originating from the same ground truth. The computation of MDHD requires binary classes (e.g., ‘snow’ or ‘no snow’), thus, a threshold must be defined to extract the snowline from each map of sub-pixel snow fraction. Section 5.3.3 explained that the

50% threshold is the optimum in the general case, that is to say when the spatial resolution allows the spatial structure of the snow cover to be resolved, so that the sub-pixel abundance follows a symmetrical distribution.

Although Table 6.3 shows that the selected images do not always exhibit this property individually, mapping pixels as 'snow' when they are more than half covered still appears as the most versatile and relevant criterion overall. Based on this threshold, Figure 6.24 illustrates how the match between the snowlines extracted from various spatial resolutions and the original 15m 'reference snowline' degrades as the pixel size increases. The sensitivity of the MDHD to this threshold can be investigated to assess its expected behaviour. In order to determine the most appropriate threshold, for all dates, the 250m resolution maps of sub-pixel snow fractions were binary classified, with increasing thresholds.

By definition, aggregated maps of ASTER sub-pixel snow fractions integrate, in one pixel, all the information in terms of distribution that can be found in the original 15m resolution binary map. This information accounts for numerous small snow patches that can be found, usually, nearby the main snow-covered entity. Snow patches larger than half the area of an aggregated pixel contribute positively to map the pixel as 'snow'. Smaller patches are problematic because they act as 'islands' where the 'distance raster' has small values (Figure 6.23). These 'islands' of small distances can bias the estimation of the MDHD. Indeed, as the pixel size increases, the aggregated snow map tends to map bigger objects. Retaining all the small features to create the distance raster image, will increase the probability of intercepting small distances, thus depressing the MDHD. However, a fraction of these small values would come from patches that could no longer be accounted for in the main object.

Similar bias can occur for small 'no snow' patches, inside the snow cover, near the main snowline. Such patches are illustrated in Figure 6.25. To address this issue, a 'cleaning' strategy was implemented, dependent on the resolution for which the MDHD is computed. For a given resolution, all patches smaller than half the area of the pixel are removed prior to computing the 'distance raster'. Later, 'cleaning' and 'no cleaning' refer to values of MDHD that are computed with and without implementing this strategy, respectively.

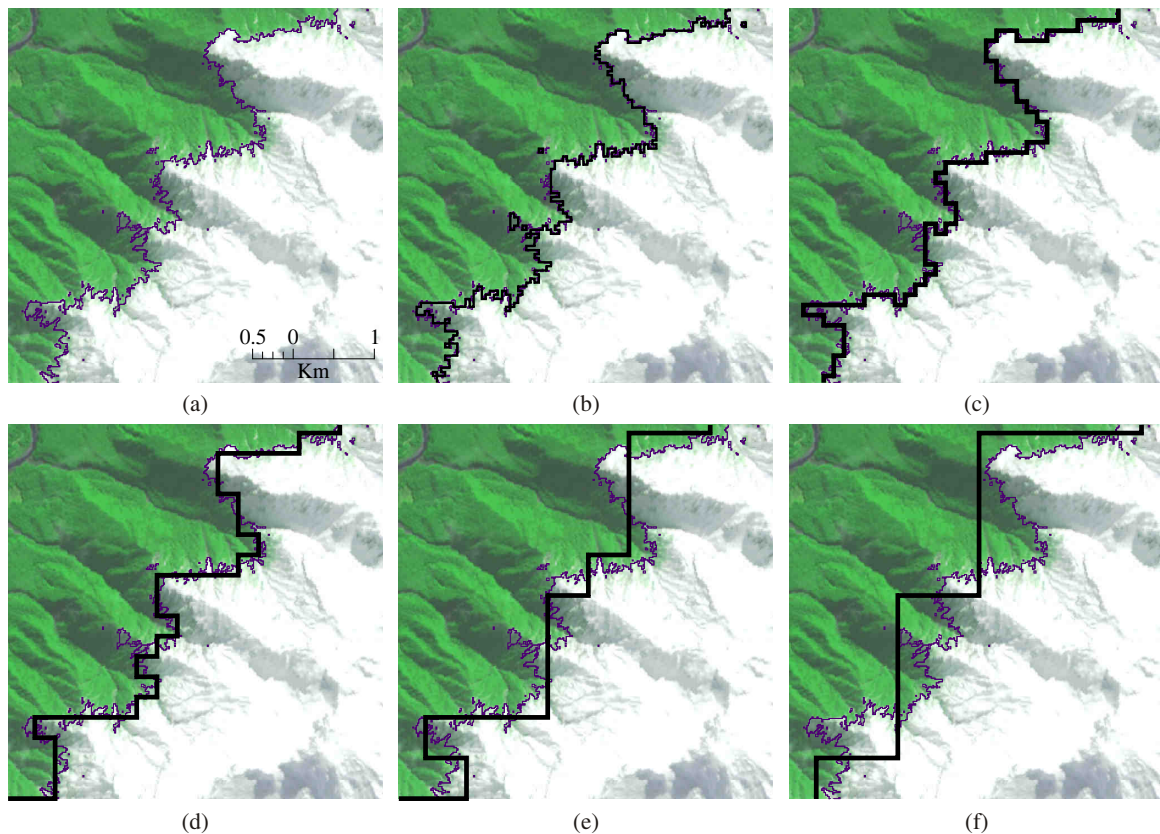


Figure 6.24 Example of snowlines extracted from an ASTER image at different spatial resolutions. (a) 15m resolution snowline used as reference extracted from the binary snow classification of the ASTER image (ground truth); (b), (c), (d), (e) and (f) show the snowlines extracted after aggregation of the ASTER binary snow map at 50, 125, 250, 500, and 1000m spatial resolution, respectively.

6.6.1.3 Empirical application of the MDHD to fused and non fused MODIS snow maps

Once the theoretical behaviour of the MDHD was assessed using ASTER-derived reference material, the MDHD was applied to the actual MODIS images. The snowlines were extracted from both the M250 and M500 maps, obtained ‘with’ and ‘without’ the fusion method, respectively. These are referred to as SL-M500 and SL-M250. Moreover, in order to ensure that the supposed additional information truly originates from the implementation of the fusion algorithm, additional 250m resolution maps of snow fractions were produced by resampling M500 maps using a simple bicubic interpolator. This is justified by the fact that spatial autocorrelation of snow fractions was proven to exist at short range (see Section 6.5.1). The snowlines extracted from the interpolated maps are referred to as SL-I250. Euclidean distances

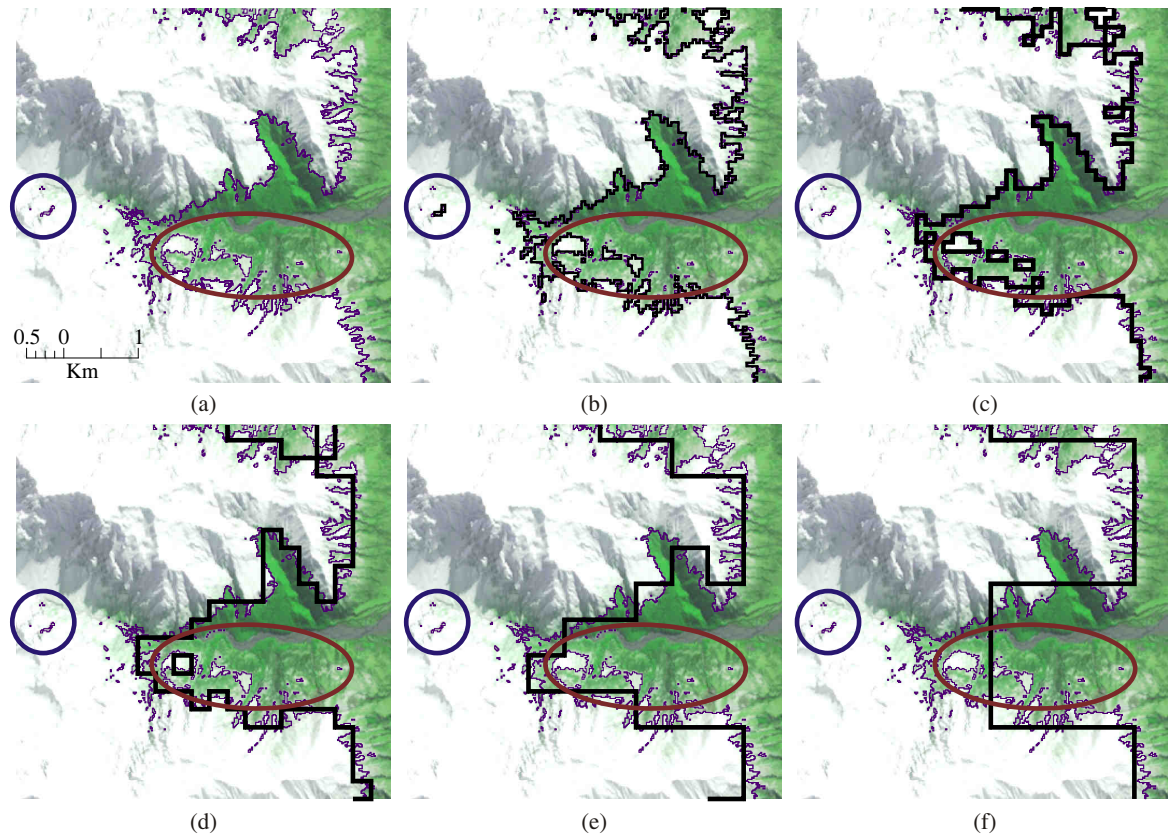


Figure 6.25 Illustration of the influence of small patches on the determination of snowlines at various spatial resolutions. (a) The 15m resolution snowline used as reference extracted from the binary snow classification of the ASTER image (ground truth); (b), (c), (d), (e) and (f) show the snowlines extracted after aggregation of the ASTER binary snow map at 50m, 125m, 250m, 500m, and 1000m spatial resolution, respectively. The ellipses show snow patches of different sizes, the circles show “snow voids” within the main snow entity that can alter the value of the Euclidean distance.

from the test snowlines to the ASTER 15m reference snowline were computed on regular intervals using the ‘distance raster’.

The mean (i.e., MDHD) and standard deviation of the distributions of Euclidean distance were used to quantify the match between both features. However, from each distribution of Euclidean distances, only the lower 90% of the observations smaller than 2000m were used to avoid an inappropriate influence of misclassified pixels far from any snow entity on the MDHD statistics. This was relevant since the MDHD was aimed at measuring the correct depiction of the snowline rather than the presence of isolated misclassified pixels. Furthermore, such misclassifications were already measured by the pixel-based metrics.

6.6.2 Results and discussion

6.6.2.1 Metric behaviour

Figure 6.26 (a) shows the behaviour of the MDHD as a function of the threshold used to segment the ASTER-derived map of sub-pixel snow fractions aggregated at 250m spatial resolution. It demonstrates that, as expected, the smallest MDHD is achieved for a snowline created from pixels having more than 50% snow, confirming the relevance of the measure. Consequently, all MDHD were computed after classification of the sub-pixel snow fractions using this threshold.

Since they are all derived from the same 15m reference, the ASTER-derived maps of sub-pixel snow fractions, successively aggregated at 50, 125, 250, 500, and 1000m, provided the reference dataset with which the sensitivity of the MDHD relative to pixel size could be estimated. Figure 6.26 (b) shows that the MDHD increases monotonically with the pixel size, both when trimming or retaining the smallest snow patches. It confirms that the snowline is generally depicted closer to the reference as the resolution increases, meaning a better match. When computing the MDHD without the ‘trimming’ strategy, the relationship between the MDHD and the pixel size was non-linear. In this case, the dispersion of the MDHD according to the different dates (see error bars on Figure 6.26) (b), was larger, suggesting that the metric may be sensitive to the area covered by snow, and possibly the number and spatial distribution of snow patches. However, when applying the ‘trimming’ strategy, the MDHD becomes linear with respect to the pixel size. The dispersion of the MDHD between the different dates is also greatly reduced. This highlights the impact of small patches in this type of multi-scale analysis. Further, when applying the ‘cleaning’ strategy the MDHD consistently drops by 50% when pixel size is reduced by a factor of two. This matches the magnitude of theoretical change that is desirable from a metric that assesses the quality of a feature as the resolution increases.

6.6.2.2 Application to MODIS-derived snow maps

Figure 6.27 illustrates the distribution of Euclidean distances and Table 6.5 provides the results of MDHD and standard deviation for all images taken individually and as a whole. From the box plot shown in Figure 6.27 it is apparent that 90% of the SL-M500 snowline is generally within 300m of the true snowline, 90% of SL-I250 is within 250m, and 90% of SL-M250 is generally within 200m. Distributions of Euclidean distances are positively skewed and depart largely from a normal distribu-

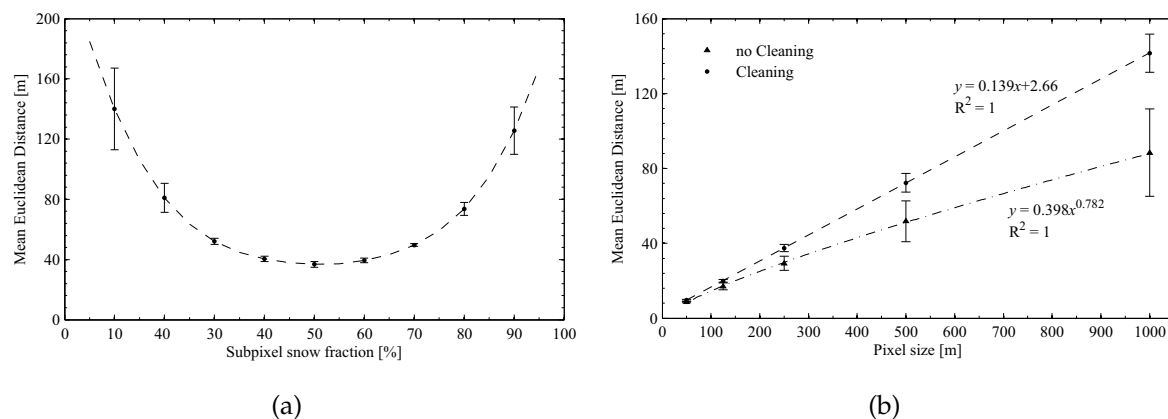


Figure 6.26 (a) Sensitivity of the MDHD to the sub-pixel snow fractions used to classify the snow cover map. For all dates, the ASTER-derived 250m resolution maps of sub-pixel snow fractions were binary classified, with increasing thresholds. The error bars indicate the standard deviation of the MDHD for the four images. (b) Sensitivity of the Mean Euclidean Distance (MED) to the aggregation of the binary ASTER-derived snow cover map. The error bars indicate the standard deviation of the MED for the four images.

tion. Nevertheless, the very high number of realisations allows the construction of confidence intervals for MDHD in accordance with the central limit theorem using Equation (3.4). At the 95% confidence level, these CI were negligible compared to the difference between MDHD of the three outputs. Similarly, the notches depicting the CI of the median in the boxplot are barely visible. For all dates, the MDHD values of SL-M250 are consistently and significantly smaller than SL-I250 and SL-M500. The MDHD dropped about 33% on average (min 20%, max 41%). This magnitude of improvement must be compared to the 50% improvement that would be expected in an ideal case when reducing the pixel size by a factor of two. However, in this case theoretical improvement is not achieved. It suggests that, as expected, the fusion does not fully replace all the extra spatial information that would be available if all MODIS bands were provided at 250m spatial resolution.

In contrast, the MDHD of SL-I250 obtained from the interpolated map improved 15%. It shows that the interpolation process moves the snowline closer to the reference. This result can be explained by the spatial autocorrelation of the sub-pixel snow fraction shown in Section 6.5.1. Nevertheless, the range of improvement is only half of that which was achieved with the fusion. Therefore, this measure directly indicates what can be attributed to the fusion process and whether it is suc-

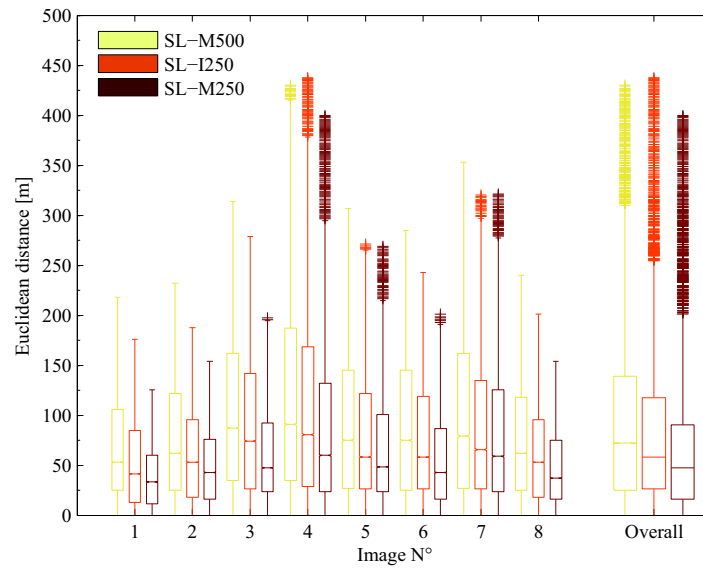


Figure 6.27 Comparison of the distributions of Euclidean distances for the test snowline retrieved from MODIS-derived maps of sub-pixel snow fractions and the reference snowline obtained from the binary classification of snow at 15m spatial resolution with ASTER. Box plots for individual images № 1–8 and overall are shown.

Table 6.5 Descriptive statistics of the distribution of Euclidean distances between the test snowlines derived from MODIS and the reference snowline obtained from ASTER.

Image №	SL-M500		SL-I250		SL-M250		(% decrease)	
	MDHD ^a	σ_{ED} ^b	MDHD	σ_{ED}	MDHD	σ_{ED}	MDHD	σ_{ED}
1	69	58	56 (-19%)	46 (-20%)	43 (-38%)	35 (-40%)		
2	78	62	63 (-19%)	50 (-19%)	52 (-32%)	42 (-33%)		
3	104	84	91 (-12%)	74 (-12%)	61 (-41%)	50 (-40%)		
4	122	105	112 (-9%)	102 (-4%)	85 (-30%)	78 (-26%)		
5	94	79	79 (-16%)	68 (-14%)	71 (-25%)	65 (-17%)		
6	92	76	76 (-17%)	64 (-15%)	60 (-35%)	53 (-31%)		
7	104	91	89 (-15%)	80 (-12%)	83 (-20%)	76 (-16%)		
8	77	63	63 (-19%)	51 (-18%)	50 (-35%)	40 (-36%)		
Overall	93	81	79 (-15%)	72(-11%)	62 (-33%)	59 (-28%)		

SL-M500, SL-I500, and SL-M250 refer to the distribution of Euclidean distances for the snowline extracted from binary snow maps derived from M500 (i.e., without using the fusion method), I250 (i.e., M500 resampled at 250m resolution), and M250 (i.e., using the fusion method), respectively.

^a Modified Directed Hausdorff Distance [m].

^b Standard deviation of the distribution of Euclidean distances [m].

cessful or not. It proves that the fusion adds significantly more information, with regard to the accuracy of snow distribution, than a simple interpolation.

6.7 Error sources and method limitations

Each step of the method described above is associated with potential uncertainties that propagate into the final estimation of the sub-pixel snow fractions. For instance, the projection of the MODIS Level-1B Swath data potentially affects the locational accuracy due to the resampling method. The fusion algorithm can create radiometric distortions and artefacts. The topographic correction strongly relies on the accuracy of the DEM for the representation of shadows, terrain derivatives (e.g., slope and aspect), and terrain parameters such as V_d and C_t . The atmospheric model is empirical and relies on atmospheric parameters that are difficult to estimate. Among the parameters, the aerosol type and optical depth probably are the most critical as they greatly affect the diffused irradiance and are quite variable both in space and time. Nevertheless, it is reasonable to consider that their potential effects are limited in mountainous areas since aerosols usually concentrate in the lower part of the atmosphere.

The detection of clouds is problematic and experience showed that despite considerable effort to design a global and robust cloud masking algorithm, misclassifications still occur. The estimation of ground reflectance in very rugged terrain is probably one of the most difficult tasks and is not easy to assess as it requires costly field validation data. In shadowed areas the signal is weak and its correction requires an accurate determination of the irradiance components that are generally associated with the highest levels of uncertainty (diffuse irradiance and reflected terrain irradiance).

The neighbourhood simplifications used in the topographic correction are also an approximation of reality that hardly describes the real processes of radiation transfer in mountainous terrain. Additionally in rugged terrain, complicated geometry and varying BRDF of snow, as well as changes of snow properties, also can create over- or under-corrections that are difficult to address and model before a preliminary classification of ground targets. Finally, the unmixing technique models the land cover diversity with an unrealistic number of classes and relies on the disputable assumption that radiance behaves linearly in terms of class proportions.

It would be desirable to obtain quantitative estimates or even approximates of

errors or uncertainties associated with each effect individually and how they propagate into the final estimation of sub-pixel snow fraction. However, it must be noted that all these uncertainties are of a very different nature and affect the final output in very different ways. For example, the uncertainty of spatial location may eventually lead to inadequate correction of pixels due to mis-registration with the DEM and subsequent terrain derivatives. Artifacts from the fusion algorithm are difficult to quantify, as are their corresponding effects on the estimation of snow fractions. The DEM interpolation and spatial resolution affects terrain derivatives that strongly impact on the correct computation of shadows and parameters such as the sky-view factor and terrain configuration factor. How a known uncertainty of the DEM translates into an uncertainty in the final snow map is rather difficult to grasp. It can be due to the production of an unreliable shadow mask, to uncertainties in computing the illumination angle, or to uncertainties in estimating the radiation components that are dependent on elevation.

Providing relevant estimates of uncertainties due to each effect would require specific reference materials for each intermediate step that are simply non-existent. Therefore, it is believed that relating uncertainties of snow mapping to the uncertainty of one of the inputs or steps of the process would only be a rather disputable wild guess. It is the reason why a careful assessment of the final output was preferred instead, based on a multitude of accuracy indicators, and computed for different areas, times and configurations of illumination. Although some of these issues and related uncertainties have been addressed, it must be reiterated that the primary objective of this aspect of the research was to map snow targets, generally well contrasted with other natural targets, in rugged terrain and with a high level of spatial detail. The careful investigation of the accuracy of the final output was a necessary task to assess the performance, robustness, and benefit of the chosen approach.

6.8 Summary

The chapter has addressed two distinct points: (1) to quantify the error of estimation of sub-pixel snow fractions, and thus to benchmark the quality of the snow maps, and (2) to quantify objectively the improvement that can be achieved by using a wavelet fusion algorithm between MODIS spectral bands. ASTER imagery was shown to be a highly valuable reference source due to its much finer spatial resolu-

tion as well as its strict simultaneity with MODIS acquisitions. Several pixel-based statistics were used to investigate the consistency of the results. They included standard statistical approaches (bias, MAE, RMSE, R^2) as well as more sophisticated assessment techniques used in image and signal processing sciences (Q index and ROC curves).

All techniques showed a consistent pattern towards improvement. This demonstrates that the snow fraction can be estimated significantly better with the aggregated version of the fused 250m MODIS-derived snow maps (G500) than with the original 500m one (M500). The range of improvements was found to be highly variable between measures, from +1.5% for the bias to +25% for the RMSE and MAE. Results were sometimes confusing between M250 and M500 and not all measures were able to discriminate both maps with regard to their quality. This stresses the importance of considering several assessment methods to ensure reliable conclusions. The Q index and AUCD had the maximum discriminatory power and both ranked G500, M500, and M250 maps, from the best to the worst results, respectively. However, none of these measures was able to account appropriately for the fact that M250 maps had a better spatial resolution than M500. This demonstrates the inherent difficulty of assessing the performance of image fusion methods.

To quantify objectively the gain of information that can be attributed to an increase in spatial resolution, the distribution of Euclidean distances between the snowline obtained from the binary classification of maps of snow fractions, and a reference snowline (or a ground truth line), was proven to be a relevant approach. The mean of this distribution is referred to as the modified directed Hausdorff distance (MDHD). The MDHD measures both the discrepancy between datasets at different spatial resolutions, and the accuracy of the mapping process in an object-based framework. The theoretical approach based on aggregating detailed reference images from ASTER shows that the MDHD possesses a linear relationship with the pixel size that makes it suitable to assess images of different resolutions. Applied to the MODIS-derived snow maps, the MDHD identifies a significant value added, in terms of mapping accuracy, which can be attributed to the fusion process. Over the eight pairs of test images, the MDHD overall decreased by 33%, while purely interpolated images only show a 15% decrease. This improvement should be related to the 50% maximum improvement that is achievable if MODIS had all spectral bands provided at 250m spatial resolution. It demonstrates that the fusion achieved 66% of the maximum achievable result. Although a significant improvement in terms of

MDHD could be achieved by a simple interpolation of M500 maps to 250m resolution, the interpolation clearly fails to depict as much information as the fusion.

Based on these results, the snow mapping algorithm was used to compute 679 maps of seasonal snow cover in the upper Waitaki catchments for the 2000–2007 period. Figure 6.28 illustrates the dynamic of the SCA in each catchment of interest (i.e., Tekapo, Pukaki, and Ohau). It merely shows an aggregated version of the time series (an animation that better reveals the spatial dynamic of the snow cover is playable in the .pdf version of this thesis and available in the DVD enclosed at \\Animations\07.06.20_Animation_ts_cplg_250_RGB143_qual75_v2-0.avi). These time series will be used in the following chapters to provide the reference for assessing the performance of the SnowSim snowmelt model currently used in the Pukaki catchment (Fitzharris and Garr, 1995; Kerr, 2005). It will also provide the snow depletion curves required for input into the Snowmelt Runoff Model (SRM) (Dewalle and Rango, 2008, Chap. 11).

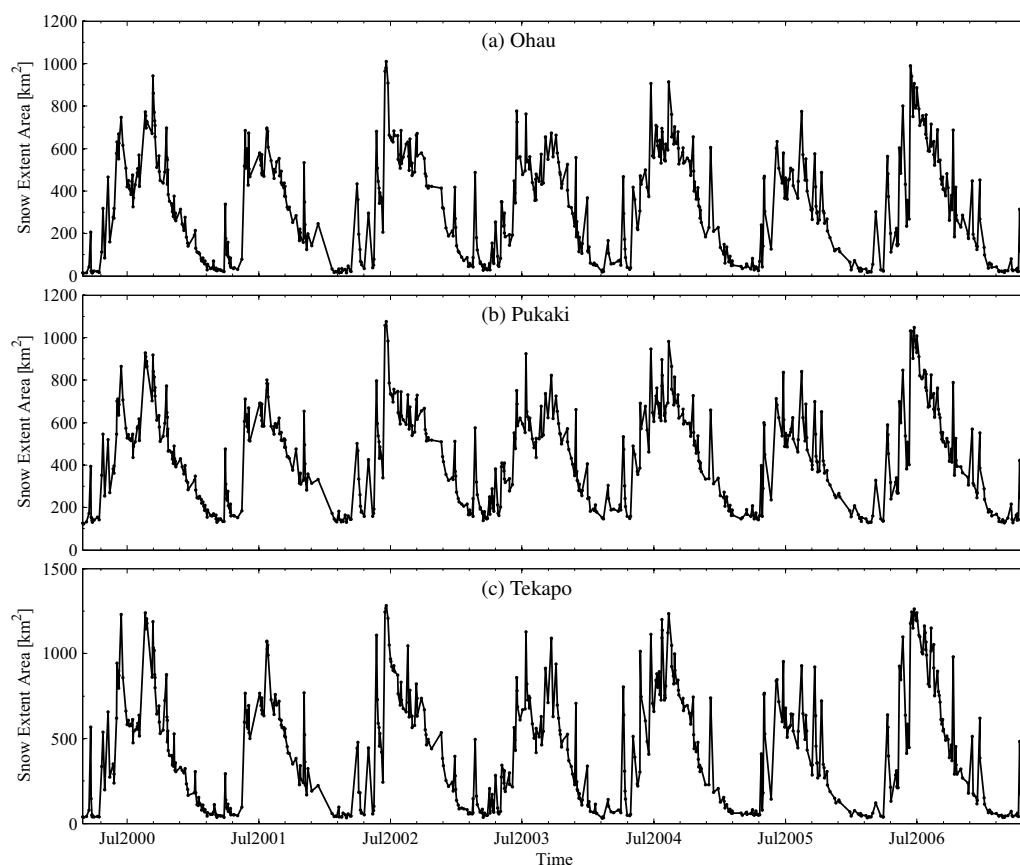


Figure 6.28 Time series of MODIS-derived snow cover area.

Chapter 7

Modelling the snowpack

7.1 Introduction

The previous chapters have demonstrated how optical remote sensing can be used to support the frequent mapping of the snow cover in the Southern Alps. Advanced and original remote sensing techniques were applied to MODIS imagery to achieve snow maps of sufficient quality to monitor the dynamics of the snow cover in the upper Waitaki basin. Seven years of data, covering the hydrological years 2000 to 2006, were processed, representing 679 maps of sub-pixel snow fractions at 250m spatial resolution.

Such a detailed time series of the spatial distribution of snow is unprecedented in the region and it allowed the cycles of accumulation and depletion of the snowpack to be resolved with a relatively high temporal resolution (i.e., one map every four days on average). Nevertheless, the images from optical instruments cannot directly provide spatial estimates of the Snow Water Equivalent (SWE). Thus, a modelling approach of the snowpack is required to make the most of this new dataset. The snow maps obtained from MODIS provide observations of the snow cover distribution that can be used indirectly to assess the performance of snow models.

This chapter describes a first application of the multi-temporal observations of the snow cover distribution within a modelling environment. The first section provides a brief review of snowpack modelling. It outlines the components of the energy budget that control the melting of snow. It also discusses their relative importance and governing factors in the context of New Zealand. Then, specific emphasis is given to the degree-day approach for modelling snow melt. This method has been used successfully worldwide due to its simplicity and useful performance

(Hock, 2003). It forms the basis of the two modelling strategies that are examined in this chapter and the next.

The second section is devoted to the SnowSim model that represents the most recent operational snow model developed for New Zealand conditions. It is a distributed degree-day model that simulates the accumulation and ablation of snow using only precipitation and temperature data. Several versions of SnowSim have been created since its original design by Fitzharris and Garr (1995). Only the latest version produced by Kerr (2005), and optimized for the Pukaki catchment, is considered in this research. Daily maps of SWE produced by SnowSim-Pukaki are indirectly compared with snow maps obtained from MODIS to assess the performance of the model.

7.2 The energy budget of the snowpack

7.2.1 The energy balance equation

The melt of snow or ice is controlled by energy fluxes associated with several processes of heat transfer to and from the snowpack (Figure 7.1). The heat flux ϕ_m that controls the melting of snow (i.e., flow of energy per unit area per unit time, measured in $\text{W}\cdot\text{m}^{-2}$) can be written as the sum of heat fluxes corresponding to each process in a global energy budget equation (Male and Gray, 1981, Chap 9; U.S. Army Corps of Engineers, 1998, pg. 2-1; Armstrong and Brun, 2008, Chap 3):

$$\phi_m = \phi_s + \phi_l + \phi_h + \phi_e + \phi_g + \phi_p - \frac{\partial U_i}{\partial t}. \quad (7.1)$$

Each of these quantities is either positive or negative, whether it increases or decreases the total net heat energy available for melting.

- Radiative fluxes

ϕ_s corresponds to the net *shortwave radiation*. It accounts for the direct illumination from the sun, the diffuse scattering by the atmosphere, and the reflection by adjacent slopes. The proportion of shortwave radiation effectively absorbed by the snowpack is controlled by the albedo of the snow surface.

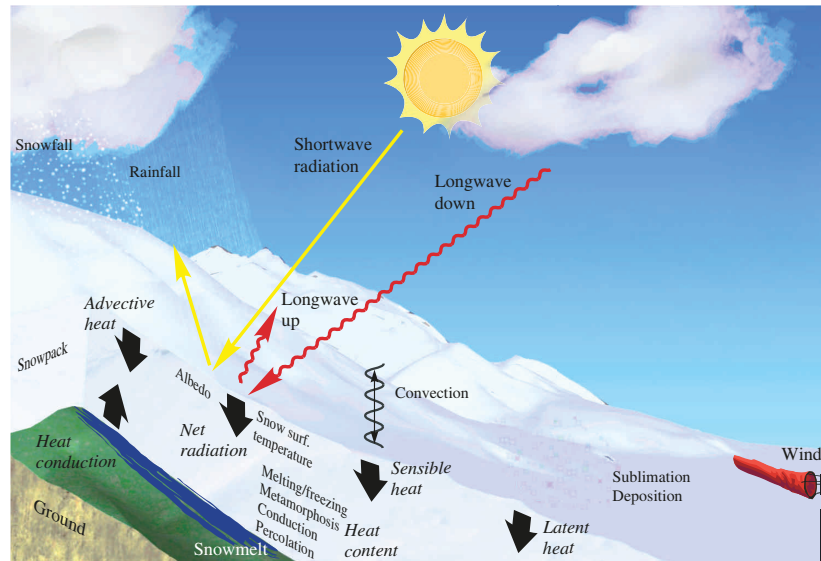


Figure 7.1 Processes contributing to the global energy budget of the snowpack.

ϕ_l accounts for the net *longwave radiation*. It is the sum of two processes producing a loss and a gain of energy. The outgoing longwave radiation ($\phi_l \uparrow$, counted negatively) emitted by the snowpack obeys Stefan-Boltzmann's blackbody theory and is a function of the snow emissivity ($\epsilon_{\text{snow}} \approx 1$) and kinetic surface temperature. The incoming longwave radiation ($\phi_l \downarrow$, counted positively) originates from the emission by the atmosphere, clouds, and by adjacent surfaces.

- Turbulent fluxes

ϕ_h is the *sensible heat flux* resulting from the convective exchange of heat between the snowpack and the surrounding air.

ϕ_e is the *latent heat flux* imputable to the processes of sublimation and condensation at the surface of the snowpack.

- Other energy exchange processes

ϕ_g is the heat flux caused by the *conduction* of heat at the interface between the ground and the snowpack.

ϕ_p is the *advective heat flux* induced by precipitation occurring on snow.

$\frac{\partial U_i}{\partial t}$ is the rate of change of the *internal energy* of the snowpack. It accounts for the energy required to change its temperature.

Melt occurs when the snowpack reaches 0°C and ϕ_M is positive. The amount of snowmelt W_s [mm] produced over a period of time can then be expressed as

$$W_s = \frac{Q_m}{\rho L_f B}, \quad (7.2)$$

where Q_m [J.m⁻²] is the heat energy corresponding to the heat flux received over a period of time, ρ is the density of water (1000 kg.m⁻³), L_f is the enthalpy of fusion of water (335.10³ J.kg⁻¹), and B is the thermal quality of the snow defined as the ratio of heat required to melt a unit mass of snow to that of ice at 0°C. The latter is explained by the presence of free water percolating through the snow matrix once the melt has begun. It slightly reduces the amount of energy further required to melt additional snow (Male and Gray, 1981, pg. 363). It ranges between 0.95 and 0.97 for a snowpack in thermal equilibrium at 0°C and accounting for 3–5% liquid water.

7.2.2 General considerations

Net radiation ($\phi^* = \phi_s + \phi_l \downarrow + \phi_l \uparrow$) is often regarded as the dominant contributor of heat energy available for melt (Ferguson, 1999; Hock, 2003; Lehning, 2005). Micro-climatic measurements over ice and snow often identified the net longwave radiation as a sink of energy (Brun *et al.*, 1989; Prowse and Owens, 1982; Plüss and Mazzoni, 1994; Ohmura, 2001; Etchevers *et al.*, 2004; Armstrong and Brun, 2008, Chap. 3.5). This is caused by the fact that the snowpack generally emits more longwave radiation than it effectively receives from the environment, thus resulting in a net loss of heat (U.S. Army Corps of Engineers, 1998, Chap. 5). This is particularly true under a cloudless sky which causes the snowpack to cool and refreeze at night. Net shortwave radiation absorbed by the snowpack during clear days generally outweighs the net loss due to longwave radiation (Ferguson, 1999), thus leading some authors to stress specifically the major role played by shortwave radiation (Plüss and Mazzoni, 1994; Braithwaite, 1995; Slaymaker and Kelly, 2007, pg. 57).

However, such considerations remain general and the relative importance of the terms of the energy budget equation [Equation (7.1)] can exhibit large temporal and spatial variations depending on cloud cover, air mass temperature and relative humidity, wind velocity, adjacent land surfaces (e.g., snow, forest, rock), topography, condition of the snowpack (e.g., albedo, age, liquid water content). For example, Olyphant (1986) pointed out the importance of adjacent surfaces in alpine terrain on the net longwave radiation. He showed that surrounding rock walls can reduce by half the longwave losses in cirque glaciers and snowfields compared to an unobstructed horizontal surface. This effect was observed on a deeply embanked part of Franz Josef glacier (West coast of New Zealand) by Ishikawa *et al.* (1992). In summer, more incoming than outgoing longwave radiation was measured and the surplus was ascribed to the heated rocks of the surrounding terrain. Treidl (1970) gave early evidences of the importance of the sensible heat flux on snowmelt. Plüss and Mazzoni (1994) showed that its magnitude can be of the same order than net radiation in some climatic conditions, such as on warm and windy days (Ferguson, 1999). This was corroborated in mid-latitude regions by measurements on glaciers and snowfields (Hay and Fitzharris, 1988; Brun *et al.*, 1989; Schneider *et al.*, 2007).

Advected heat from rainfall and conduction at the snow-ground interface is often found to be small in comparison with the radiative and sensible heat fluxes (Prowse and Owens, 1982; Kuusisto, 1986; Neale and Fitzharris, 1997; Slaymaker and Kelly, 2007, pg. 58). By the use of controlled experiments, Singh *et al.* (1997) revealed that rain-on-snow generates only little snowmelt due to the direct supply of heat by liquid water. Instead, the percolation of rain water into the snow enables the mass transport and redistribution of heat uniformly throughout the snowpack. Although rain-on-snow events can occasionally play a significant role in accelerating the melting process and lead to the fast release of water (Moore and Prowse, 1988; Sui and Koehler, 2001), most of the energy supplied to the snowpack can be ascribed to larger turbulent fluxes caused by higher winds and warmer temperatures during rainfall events (Marks *et al.*, 2001).

7.2.3 Energy balance measurements in New Zealand

In the Southern Alps of New Zealand, energy balance measurements of the snowpack by Prowse and Owens (1982) in the Craigieburn Ranges (East of the main divide) during melting season (i.e., October, November) showed that the major source of heat was the sensible heat flux was (57%), followed by net radiation

(30%) and latent heat (13%). The relative share of the latent heat even overwhelmed that of the net radiation during the days with the greatest overall heat supply or rain. Additional measurements on snow by Moore (1983) in Ski Basin (Craigieburn Ranges) and in Temple Basin (closer to the main divide) confirmed that the sensible heat flux was the major component of the energy budget for the alpine snowpack in this region. The dominance of the sensible heat over net radiation and latent heat was also observed by Ishikawa *et al.* (1992) on the lower parts of Franz Josef glacier, with a single exception in October when the net radiation provided the major contribution. In this case, however, the deeply embanked location often covered by clouds could explain that less shortwave radiation are received. Besides, Kelliher *et al.* (1996) made measurements on the open sky névé of the Franz Josef glacier after fresh snowfall in late summer (March) and observed that the net radiation provided about 60% of the energy for surface melt. In contradiction with Prowse and Owens (1982) and Moore (1983), Clark (1993) ascribed a major role to net radiation in the Craigieburn Ranges. Closer to the main divide at Muller hut Neale and Fitzharris (1997) also showed that net radiation dominated the energy budget of the snowpack, but the sensible heat remained a large contributor.

Neale and Fitzharris (1997) compiled various research efforts conducted on snowfields and glaciers in New Zealand. They suggested a pattern of energy flux distributions across the Southern Alps from the West coast (Franz Josef glacier) eastwards to the Craigieburn Ranges. The net radiation dominates the energy budget of the snowpack on the West coast and near the main divide, while the sensible heat prevails at the eastern sites. Neale and Fitzharris (1997) attributed this contrast to the influence of the north-west Föhn winds that develop in the lee of the Southern Alps (Moore and Prowse, 1988). In addition, they revealed a relationship between large-scale synoptic weather patterns and energy inputs. Neale and Fitzharris (1997) provided evidence that north-westerly flows have a great impact on snowmelt. Warmer air mass and high wind speed considerably increase the sensible heat in comparison to southerly flow. Anticyclonic conditions over the Alps generally yield clear weather and increased net radiation that also favours snowmelt. Troughs of low pressure or fronts generally bring overcast weather and cooler air temperatures that greatly reduce both the net radiation and the sensible heat, thus resulting in the weakest energy input. Both the latent heat and the advected energy from rain corresponded to minor contributions in all cases.

7.3 Modelling the snow pack

7.3.1 Energy balance models

Many models have been developed to address comprehensively the energy budget equation of the snowpack [Equation (7.1)] for snowmelt-runoff prediction, glacier mass balance simulation, and/or avalanche risk prediction (e.g., Brun *et al.*, 1989; Jordan, 1991; Fernandez, 1998; Bartelt and Lehning, 2002; Fierz *et al.*, 2003; Garen and Marks, 2005; Assaf, 2007). An extensive review can be found in Armstrong and Brun (2008, Chap 4) and a comparison of models is reported in Etchevers *et al.* (2004). Although they address each of the energy terms with varying levels of complexity, they have in common their requirement for a high number of meteorological variables.

The net shortwave radiation absorbed by the snowpack relies on the snow surface albedo which varies temporally and spatially in large alpine catchments, due to the coexistence of snow at various stages of metamorphosis. An accurate estimation of the albedo is crucial to limit the uncertainties about the net shortwave radiation absorbed by the snowpack. In energy balance models, the albedo is often parameterized empirically on the basis of the age of the snow surface (Armstrong and Brun, 2008, pg. 137). However, this parameter can be monitored effectively using remote sensing (Klein and Stroeve, 2002; Schaaf *et al.*, 2002; Greuell and Oerlemans, 2004; Painter *et al.*, 2009; Liu *et al.*, 2009). The use of albedo observations in distributed snowmelt models has been shown to provide substantial improvements when and where radiation contribute the most to the energy budget (Molotch *et al.*, 2004).

Estimating the net longwave radiation is more complicated and a dense network of sensors in a large mountainous area is rarely available. $\phi_l \uparrow$ requires knowledge about the snow surface temperature (SST). Optical remote sensing has the potential to provide spatial estimates of this parameter (Key *et al.*, 1997; König *et al.*, 2001; Wan *et al.*, 2002), but is limited by the sensor's temporal and spatial resolutions. The daily variations of SST can only be resolved by sensors capable of multiple acquisitions per day at the expense of the spatial resolution. The mixtures of snow and rocks within pixels complicate the accurate retrieval of the SST. Large errors about $\phi_l \uparrow$ can be introduced because of the dependence of Stefan-Boltzmann's law on the forth power of the temperature. The incoming longwave radiation $\phi_l \downarrow$ is also hard to model. The emissivity of the atmosphere varies spatially and temporally, due to its dependence on air humidity and temperature. In addition, the

cloud cover and nearby slopes can strongly affect $\phi_l \downarrow$. Their uncertain emissivity, surface temperature, and relative configuration to the surface complicate the spatial modelling of incoming longwave radiation in mountainous terrain.

Turbulent fluxes in mountainous terrain are also particularly difficult to estimate because they depend on variables that are impractical to monitor over large areas such as wind, surface roughness, and air temperature and humidity profiles. It is evident that, in alpine terrain, the spatial variability of these quantities makes the representativeness of local measurements, as well as the applicability of extrapolations over large areas, questionable. The direct measurement of turbulent fluxes based on the Eddy correlation technique requires specific instrumentation, such as a 3-dimensional sonic anemometer, that is rarely available over a dense network. Similarly, estimating the variations of internal energy requires data on the temperature profile, as well as water movements in the snowpack, which are difficult to obtain.

7.3.2 The degree-day approach

In an attempt to estimate melt water from snow cover and glaciers, early research pointed out the connection between air temperature and the persistence of solid water, whether in the state of ice or snow. For example, [von Hann \(1897, Chap. 17\)](#) compiled data about the elevation of snowlines and glacier terminus along with mean annual and/or mean summer temperature from worldwide locations. He concluded that the heavier the snowfall the higher must be the temperature at the temporary snow-line in the spring ([von Hann, 1897, pg. 316](#)). The first use of air temperature as an index to explain and estimate melt rates is ascribed to [Finsterwalder and Schunk \(1887\)](#) in their research on the ablation of Alpine glaciers. Later, [Horton \(1915\)](#) and [Clyde \(1931\)](#) conducted laboratory experiments on snow samples and obtained melt rates for each degree above freezing point maintained during 24 hours. More evidence of the influence of the mean positive temperature on melt was given for glaciers (e.g., [Ahlmann, 1924](#); [Krenke and Khodakov, 1966](#)) and for snow (e.g., [Collins, 1934](#); [Church, 1941](#); [Archer, 1970](#)). High correlations between melt and air temperature have also been shown by [Zuzel and Cox \(1975\)](#), [Braithwaite and Olesen \(1989\)](#), or [Kirkbride \(1995\)](#). These studies provided an empirical basis for using the positive degree-day as an index to estimate runoff originating from snow and/or ice-melt ([U.S. Army Corps of Engineers, 1956, Chap. 6](#)).

The *degree-day method*¹ is a considerable simplification of the energy budget equation [Equation (7.1)]. It relates linearly the total heat energy received by the snowpack during a day to the number of positive degrees to which it was exposed (ΔT). Thus, the snowmelt W_s is assumed to be proportional to ΔT by means of the *melt factor*² a as follows:

$$W_s = a\Delta T. \quad (7.3)$$

ΔT is generally approached by the mean daily temperature. Singh *et al.* (2000) showed that the mean of the maximum and minimum daily temperature was as good as the mean hourly temperature for computing the number of degree-days. The success of this approach over the energy balance to model snowmelt or glacier ablation can be explained by the fact that data about air temperature are widely available, relatively easy to interpolate, and because the model performs relatively well despite a very simplistic formulation (Rango and Martinec, 1995; Hock, 2003, 2005). Widely used hydrological models, such as the Snowmelt Runoff Model (SRM) (Martinec, 1975) and the Hydrologiska Byråns Vattenbalansmodell (HBV) (Bergström, 1976), implement a degree-day approach to address snowmelt.

The good performance of the degree-day method finds a justification in the fact that air temperature is more or less connected to most of the components of the energy budget (Chap. 5, U.S. Army Corps of Engineers, 1998; Sicart *et al.*, 2008). Shortwave radiation is the only substantial source of heat energy that is not directly affected by air temperature. Thus, Ambach (1988) and Plüss and Mazzoni (1994), who considered that net shortwave was the largest energy source for melt questioned the performance of the degree-day method, because they considered that only the sensible heat could be explained by air temperature. On the other hand, Lang and Braun (1990) pointed out the importance of incoming atmospheric long-wave radiation. Under clear skies, this source of heat is proportional to the fourth power of air temperature in accordance with Stefan-Boltzmann's law.³ Despite such a strong dependency and sensitivity of $\phi_l \downarrow$ to air temperature, the fact that $\phi_l \uparrow$ generally overwhelms $\phi_l \downarrow$ enhances the importance of the shortwave radiation.

Ohmura (2001) demonstrated that discriminating $\phi_l \downarrow$ and $\phi_l \uparrow$ as a source and a sink of heat, respectively, was more appropriate to interpret the energy balance of the snowpack. It showed that $\phi_l \downarrow$ in fact represents by far the largest source

¹Also called *temperature-index method*.

²Also called *degree-day factor*.

³Under clouds or canopy, the temperature of the cloud base or forest canopy shall be considered.

of heat energy effectively absorbed by the snowpack and accounts for 60 to 80% of all energy sources. [Ohmura \(2001\)](#) also showed that most of the atmospheric longwave radiation originates from the first 100m of the atmosphere and can reasonably be estimated by the standard screen-level air temperature (i.e., measured at 2m above the ground). Thus, [Ohmura](#) concluded that air temperature in fact largely controls the energy absorbed by the snowpack, thus providing a physical basis for the temperature-index approach.

Recently, [Sicart *et al.* \(2008\)](#) investigated this explanation by studying the daily surface energy balance (SEB) of three glaciers in very distinct climates. They obtained only poor correlations between $\phi_l \downarrow$ and the air temperature. The variability of $\phi_l \downarrow$ was mostly controlled by cloud emission, but was found to be very small compared to that of the other energy fluxes. Larger $\phi_l \downarrow$ was generally observed because of cloud cover rather than periods of warmer temperatures. In such cases, much less shortwave radiation was available but with a larger impact on the net energy absorbed by the snowpack. It revealed that $\phi_l \downarrow$ was not or negatively correlated with the SEB, thus disputing the explanation of [Ohmura \(2001\)](#). In fact [Sicart *et al.* \(2008\)](#) provided evidence that the correlation between the SEB and air temperature was governed by micro climatic conditions rather than the atmospheric longwave radiation. For example, the very poor correlation observed over a tropical glacier at very high-altitude (i.e., the Zongo glacier, Bolivia) was due to the prevailing role of shortwave radiation on the SEB.

Although shortwave radiation also dominated the SEB of a temperate alpine glacier (i.e., the St Sorlin glacier, France), a good correlation between the air temperature and the SEB was observed. It was ascribed to the diurnal advection of warm air from the valley floor. In this case, the correlation could not be interpreted as a cause and effect relationship (i.e., a controlling process), but rather measured two concurrent effects of the same cause (i.e., the diurnal cycle). Finally, a moderate correlation was found for a sub-arctic glacier (i.e., the Storglaciären glacier, Sweden). It could be explained by the high share of sensible fluxes, and thus indicated the forcing of melt by air temperature. In conclusion, it seems that a single physical process such as proposed by [Ohmura \(2001\)](#) is not enough to explain the good correlations often observed between the snow- and ice-melt and air temperature. It appears that the temperature is not necessarily a forcing process that controls the melt. The often good correlations between the SEB and air temperature can also be the result of the simultaneous effects generated by common causes.

7.3.3 The degree-day factor

The melt factor a [$\text{mm} \cdot ^\circ\text{C}^{-1} \cdot \text{day}^{-1}$] is the parameter that relates the melt to positive degree-days, and thus encompasses all the terms of the energy balance. Since the latter are affected differently by air temperature, the value of the melt factor is expected to vary spatially and temporally depending on the relative share of each type of heat source. [Ambach \(1988\)](#) stressed the role of sensible heat in controlling the variation of the melt factor. He suggested that a higher share of sensible heat causes necessarily a decrease of the melt factor. However, [Ambach \(1988\)](#) only considered the effect of warmer temperatures and ignored that a similar share of the sensible heat relative to the other heat components could be achieved with a larger wind velocity ([U.S. Army Corps of Engineers, 1998](#), Equation 5-10). In this case, using the same reasoning of [Ambach \(1988\)](#), it is easy to show that the melt factor would increase rather than decrease under stronger winds, as it is generally well documented ([U.S. Army Corps of Engineers, 1998](#), pg. 6-2). Thus, the melt factor does not necessarily decrease as the fraction of sensible heat fraction increases, but remains dependent on the prevailing role of temperature or wind. Based on this biased analysis, [Ambach](#) concluded that lower melt factors are generally encountered at lower elevations due to warmer temperatures, and can explain the observations obtained on the Greenland ice sheet. In her review, [Hock \(2003\)](#) proposed this conclusion as a general rule regarding the sensitivity of the melt factor. However, measurements on snow by [Arendt and Sharp \(1999\)](#) and on ice by [Kirkbride \(1995\)](#) contradict this hypothesis and showed that the melt factor is often found to be larger at lower elevations.

A strong seasonal variation of the melt factor is often observed. Melt rates increase during the ablation season for both snow ([Martinec, 1960; Male and Gray, 1981](#), pg. 419) and ice ([Kirkbride, 1995](#)). [Lang and Braun \(1990\)](#) explained that variations of the melt-factor are predictable at various times and spatial scales.

- The diurnal and seasonal cycles of solar radiation, as well as the effect of topography clearly affect the shortwave fluxes, since the lack of a direct relationship between ϕ_s and air temperature causes the melt factor to vary accordingly. In addition, the metamorphic evolution of an ageing snowpack yields a coalescence of snow grains whose increasing size causes a decrease of the albedo, resulting in more absorption of solar radiation and increasing melt rates ([Warren, 1982; Armstrong and Brun, 2008](#), Chap. 2.5). The concurrent evolution of

the snow density changes the thermal quality of the snowpack and increases its water content with the effect of facilitating snowmelt as well. Thus, [Martinec \(1960\)](#) and [Kuusisto \(1980\)](#) observed a good correlation between the melt factor and snow density, and advocated the use of the latter to parameterize the former ([Rango and Martinec, 1995](#)). Alternatively, [Arendt and Sharp \(1999\)](#) suggested that the melt factor could be approached by the surface albedo due to a good inverse correlation. It is therefore evident that the melt factor inherits the spatial and temporal variability of the snow's physical properties.

- The relative share of the energy components is also affected by large-scale synoptic meteorological conditions, local climatic effects such as Föhn winds, and/or micro-climatic perturbations due to the influence of the topography on the turbulent exchanges ([Plüss and Mazzoni, 1994](#)). For example, [Cutler and Fitzharris \(2005\)](#) measured the summer melt factor of the snowpack on the névé of the Tasman glacier. They noted a very large increase associated with a change of the regional synoptic situation (i.e., from 3.4 to 9.1 mm.°C⁻¹.day⁻¹ on average). Melt rates three to four times the usual value occurred when north-west flux of air mass prevailed. Although the mechanism was not studied in depth, such events generally corresponded to warm and moist air advected onto the snowpack from the Tasman Sea, resulting in a larger contribution of the sensible heat ([Neale and Fitzharris, 1997](#)). The condensation of humid air onto the snowpack is also likely to play a role in such events by enhancing the contribution of latent heat and possibly increasing the melt factor.
- Forest and cloud cover generally increase the amount of incoming longwave radiation locally but at the expense of the shortwave radiation. It generally results in a decrease of the melt factor ([Kuusisto, 1980](#); [U.S. Army Corps of Engineers, 1998](#), pg. 6-2). Rain-on-snow also favours snowmelt. However, as discussed earlier, the amount of heat advected by liquid precipitation is generally negligible except for very intense and warm rainfall. Thus, the variation of the melt factor can be attributed to the larger share of the turbulent fluxes associated with the relatively warm air temperature and stronger winds during rain events.

Because of such potentially variable melt rates, many values of a have been found and used to estimate snow- and ice-melt at different locations or time ([Singh *et al.*, 2000](#); [Hock, 2003](#); [Cutler and Fitzharris, 2005](#)). For example, the [U.S. Army Corps](#)

of Engineers (1998, pg. 6-2) suggested that, for snow, a typically ranges from 1.8 to 3.7 mm. $^{\circ}\text{C}^{-1}\cdot\text{day}^{-1}$ in rain-free conditions and can be as high as 8 mm. $^{\circ}\text{C}^{-1}\cdot\text{day}^{-1}$ with heavy rain and windy conditions. Martinec (1960) measured melt rates of snow with a radioactive snow-gauge (Singh and Singh, 2001, Chap. 4.2) and reported a daily melt factor ranging from as low as 0.8 to as high as 15.8 mm. $^{\circ}\text{C}^{-1}\cdot\text{day}^{-1}$. This range was limited to 1.9–8.9 mm. $^{\circ}\text{C}^{-1}\cdot\text{day}^{-1}$ when the melt was averaged over a six-day period. The melt factor generally tends to be larger for ice than for snow. Hock (2003) attributed this difference to the lower albedo of ice that favours absorption of shortwave radiation, and thus produces more melt for a given temperature. As mentioned earlier, Rango and Martinec (1995) preferred to relate the degree-day factor to the snow density. Their observations are consistent with the differences of melt factor often observed between ice and snow. It can also explain the increasing trend of a toward the ablation season as the snowpack gets more compact.

The large variability of this parameter suggests that a universal relationship is not achievable in practice. Hock (2003) even questioned the relevance of point observations and subsequent generalization to a wide basin. Rather, she advocated that the melt factor should be set within an acceptable range based on an optimization procedure of the model outcomes with regard to historical observations. The spatial and temporal change of the melt factor in large basins and/or for study over long periods must also be addressed. The melt factor must be allowed to vary according to independent relationships or qualitative settings (Martinec and Rango, 1986; U.S. Army Corps of Engineers, 1998, pg. 6-2).

7.3.4 Modelling the snowpack in the Southern Alps of New Zealand

Previous attempts on modelling the snowpack and/or the hydrology of catchments dominated by snowmelt in New Zealand were reviewed in Chapter 2 (see Section 2.3.2). Most of this work is based on the degree-day approach.

Moore and Owens (1984a) developed a simple snow accumulation and ablation model for the Craigieburn Range in the Waimakariri River catchment, East of the main divide. The daily precipitation levels from a single rain gauge were extrapolated to the elevation of a snow course using an empirical multiplying factor. The mean daily temperatures were extrapolated using a constant lapse rate of 6.5 $^{\circ}\text{C}\cdot\text{km}^{-1}$. The snow storage was augmented when the mean temperature was be-

low a critical threshold, so that precipitation could be assumed to be snow. As noted above, the snow ablation procedure implemented the positive degree-day approach. The temperature records from two locations were considered and yielded substantially different calibration parameters. Optimal results were obtained with the melt factor ranging from 4 to 8 $\text{mm}\cdot^{\circ}\text{C}^{-1}\cdot\text{day}^{-1}$, the critical temperature from 1.2 to 2.2 $^{\circ}\text{C}$, and the precipitation factor from 1.1 to 1.3, depending on the station used to provide the temperature data. The large variation of the degree day factor to model the SWE at a same location from different data stresses the lack of representativeness of this parameter and its potential departure from a measurable quantity. [Moore and Owens \(1984a\)](#) also identified the variability of the lapse rate as a critical source of errors.

[Barringer \(1989\)](#) introduced a variable melt factor that implemented a one-year period harmonic to capture the seasonal change discussed in the previous section. Two optimization procedures yielded the melt factor to range from 1.45 (1.8, respectively) in winter to 4.35 $\text{mm}\cdot^{\circ}\text{C}^{-1}\cdot\text{day}^{-1}$ (5.4, respectively) in summer. [Barringer](#) did not consider the storage of snow but investigated the variability of the temperature lapse rate and its impact on the accurate modelling of the elevation of the snowline. Despite a detailed categorization of lapse rate profiles, the determination of the snowline elevation from valley-floor temperature records was not accurate. Nevertheless, this approach stressed one important problem of snow models that rely solely on sparse climatic data. The use of an extrapolated mean temperature and a crisp level for discriminating rain from snow runs the risk to propagate and build up errors. For example, if the snowline was consistently estimated too low, then the model would tend to accumulate snow at low elevations that does not exist in reality. When it comes to ablation, warmer temperatures would yield the release of a non-existent storage that can compromise the accuracy of the simulated runoff. Clearly, the reverse situation (i.e., when snowline tends to be estimated too high) would have an inverse but equally problematic effect.

In its original design, the SnowSim model ([Fitzharris and Garr, 1995](#)) was semi-distributed to estimate the SWE in elevation bands of 300m over the whole southern Alps with data from only five climate stations. A variable melt factor ranging from 3 to 8 $\text{mm}\cdot^{\circ}\text{C}^{-1}\cdot\text{day}^{-1}$ was used and snow storage was reconstructed over the 1930–93 period. The mean snow storage provided a quantitative benchmark against which the yearly departure could be compared to facilitate operational decisions by water managers. The distributed version of SnowSim for the whole country developed

by McAlevey (1998) took advantage of 41 automatic climate stations that supplied the temperature and precipitation data. In addition McAlevey (1998) used an empirically determined parameterization of the snow albedo from Woo and Dubreuil (1985) as a surrogate for the melt factor. Kerr (2005) retained this approach but refined its parameters in the Pukaki catchment. Kerr also implemented a new interpolation method for the precipitation. It is the performance of this last version that is assessed in the following section (see Section 7.4), based on the regular observations obtained from MODIS.

7.4 SnowSim

7.4.1 Principle

The SnowSim-Pukaki model is a distributed degree-day model that simulates the accumulation and ablation of snow in the Pukaki catchment with forcing solely from precipitation and temperature data. Only a brief outline of the model principles is provided below and a more comprehensive description can be found in Kerr (2005).

1. The daily mean temperature from climate stations are adjusted to sea level using a constant lapse rate of $5^{\circ}\text{C.km}^{-1}$. The local field of temperature at sea level is spatialized over a gridded network using an Inverse Distance Weighted (IDW) interpolation. The field of temperature is finally estimated on the basis of the lapse rate according to each point elevation in the DEM.
2. As explained in Section 2.2.2, the pattern of precipitation in the Waitaki region exhibits a very strong northwest–southeast gradient due to the orographic forcing of the prevailing north-westerly flow. McAlevey (1998) interpolated the precipitation using IDW with an additional enhancement based on a locally variable exponential function of elevation. Kerr (2005) questioned the relevance of the precipitation-elevation relationship in this area. This was confirmed by Tait *et al.* (2006), who did not find statistically significant correlations between daily rainfall and elevation in New Zealand. Similarly, Kerr *et al.* (2007) only observed a very poor correlation in the Pukaki catchment. Alternatively, Kerr (2005) suggested that the precipitation was better explained by distance from the topographic barrier. Thus, the spatial interpolation of

daily precipitation measurements could benefit from the use of a regional annual average precipitation surface as an additional independent variable in the interpolation process.

This surface was created for the whole country by the New Zealand Meteorological Service (NZMS) based on the total annual rainfall measured over the 1951–80 period (Thompson, 1985). Limited measurement in the Southern Alps required manual adjustment of the surface in the Alpine regions based on expert judgment (Tait *et al.*, 2006). Kerr (2005) pointed out the inaccuracy of the NZMS rain surface in the upper part of the Pukaki catchment. Instead, he proposed a new relationship between the long term annual precipitation and the distance from a reference baseline situated on the 1200m contour on the western side of the main divide [see Figure 7.2 (a)] (McSaveney *et al.*, 1978). This approach was justified by the near-normal incidence of the flux with respect to the mountain range. It explains why transects perpendicular to the alpine fault were often used to reveal the distribution of rainfall (Griffiths and McSaveney, 1983; Sinclair *et al.*, 1997; Henderson and Thompson, 1999; Weingartner and Pearson, 2001). Thus, in SnowSim-Pukaki, the long term mean annual precipitation $P_{\text{mean}}(x)$ [mm] at a distance x from the 1200m western contour was modelled, in the northern part of the catchment ($x < 33$ km), by an exponential decay as follows:

$$P_{\text{mean}}(x) = 28500e^{-x/12.5}. \quad (7.4)$$

At larger distances ($x \geq 33$ km), the national NZMS 1951–80 rain surface was retained. Figure 7.2 (b) shows the profile of precipitation established by Kerr (2005) (dotted line) based on limited measured and estimated data (circles). Additional measurements of mean total rainfall computed over the whole period of record from selected climate stations [see Figure 7.2 (a)] are indicated. Kerr's profile slightly overestimates the observed values although it can potentially accommodate rain undercatch due to wind and/or snow. The annual total precipitation at Rose Ridge (climate station ID: 30531) was estimated rather than measured due to the frequent snow at this high elevation site. The profile of the NZMS surface in the Pukaki catchment exhibits a much larger overestimation compared to the observations [Figure 7.2 (b)]. Kerr (2005) showed that the proposed precipitation profile upheld better the long term water balance of the basin. In the SnowSim-Pukaki model, in order to account for the long term rain surface into the spatialization of the daily rain field, the daily proportions

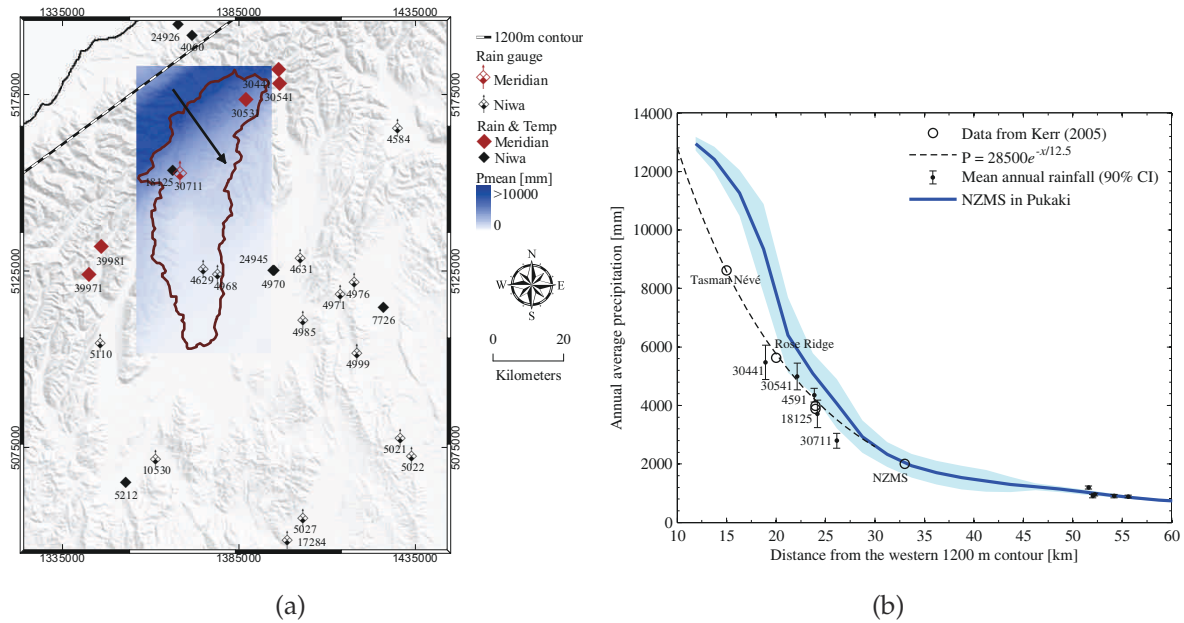


Figure 7.2 (a) The long term annual rain surface used in SnowSim-Pukaki and the situation of climate stations. (b) Comparison of the mean precipitation profile suggested by Kerr (2005) and the NZMS rain surface in a transect perpendicular to the 1200m western contour [identified by the arrow in (a)]. The solid line and the envelope relate to the mean and the standard deviation of the NZMS surface, respectively.

of the mean annual rain accounted for by individual stations are extrapolated to the entire catchment using IDW. The distributed daily rain field is obtained by reverting the extrapolated proportions into actual precipitation using the rain surface.

- From the daily fields of rain and mean temperature, SnowSim simply associates two routines of snow accumulation and ablation (Figure 7.3). When precipitation occurs for a mean temperature colder than a constant critical temperature T_c , then the snow storage (S_{stor}) is incremented. Otherwise, the precipitation is assumed to be rainfall and directly contributes to the free water W in the catchment. The ablation is addressed with the degree-day approach. When the mean daily temperature is positive, the snow storage in the corresponding grid cell is decreased by aT_{mean} and this snowmelt is added to the free water. The originality of SnowSim relies on the use of a dynamic melt factor designed to accommodate the spatial and temporal variability of the snowpack conditions. For each grid cell, the melt factor a is parameterized

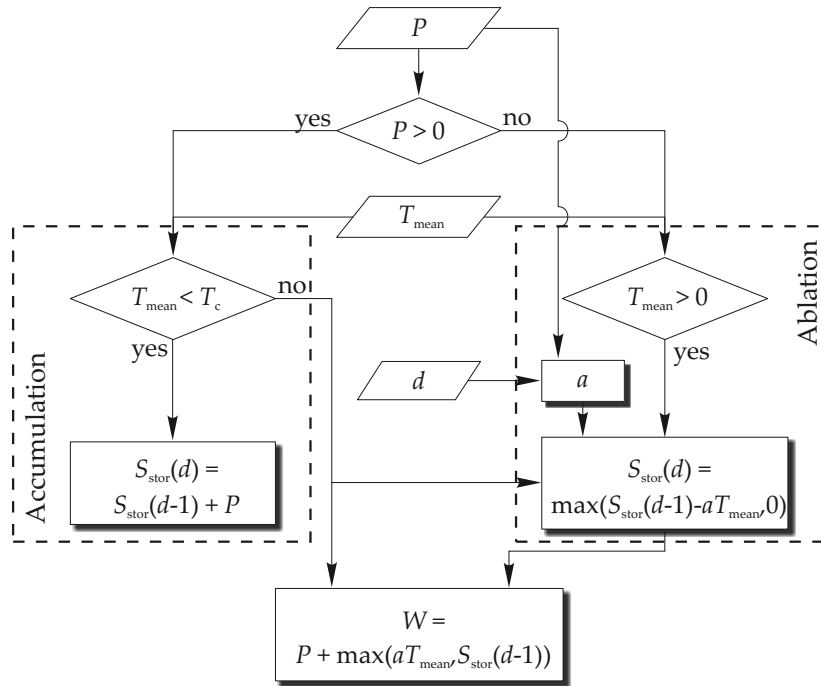


Figure 7.3 Flowchart of the SnowSim model. P is the daily precipitation per cell of the grid, T_{mean} is the mean daily temperature, T_c is the critical temperature at which precipitation is assumed to fall as snow, a is the degree-day factor, and d is the day. Note that the computation of a depends on the number of days that passed since the last snowfall.

based on an empirical formulation of albedo from [Woo and Dubreuil \(1985\)](#). It is modelled as

$$a = a_{\min} + \frac{a_{\max} - a_{\min}}{e^{(2.5-0.2pn)} + 1}, \quad (7.5)$$

where a_{\min} and a_{\max} correspond to the possible range of the melt factor, p is 1 or 2 for dry and rainy days, respectively, and n is the number of days since the last snowfall. Thus, fresh snowfalls yield a sharp reduction of the melt factor, while rain is supposed to enhance it. The seasonal increase of a is modelled by incrementing progressively a_{\max} during the ablation season (i.e., from December to March).

7.4.2 SnowSim outputs and performance

At any given day the output of the SnowSim model depicts the spatial distribution of the Snow Water Equivalent (SWE) stored in the snowpack (Figure 7.4).

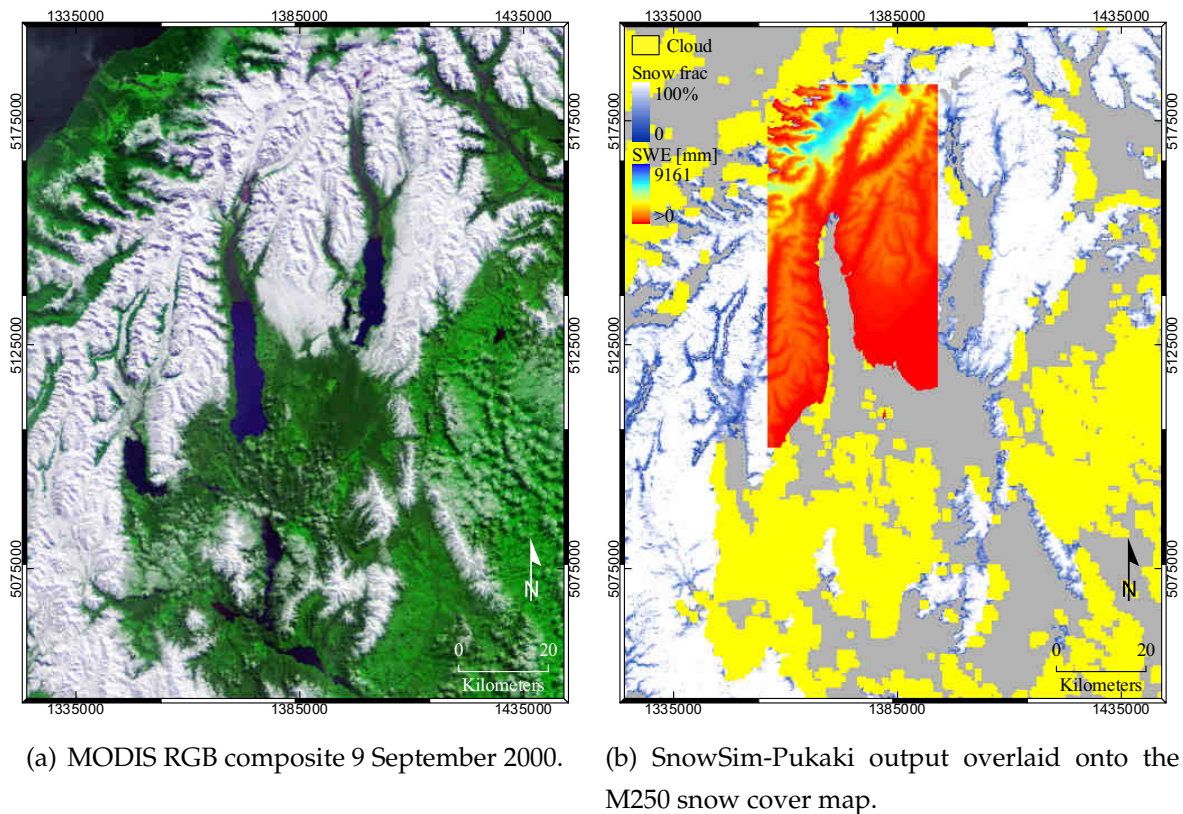


Figure 7.4 Example of an output from SnowSim compared with the simultaneous observation from MODIS.

This amount is reset at the beginning of each hydrological year (i.e., 1st of April), and any snow left is assumed to contribute to the mass balance of the glaciers in the area. SnowSim-Pukaki was calibrated by Kerr (2005) on the basis of the 2003 hydrological year by varying the parameters of SnowSim (e.g., a_{\min} , a_{\max} , rain-snow temperature threshold). Kerr retained the parameters that achieved the maximum modelling performance. The model was then assessed by two means over the period from April 2000 to March 2004.

1. The modelled SWE was compared with point observations from a snow pillow at the Rose Ridge climate station [ID: 30531 in Figure 7.2 (a)].
2. The modelled free water was compared to the observed inflow into Lake Pukaki.

The goodness of fit between the modelled values y_i and the observed values x_i (i.e., the SWE or the discharge Q at day i) was measured by Kerr (2005) using the

Nash-Sutcliffe efficiency coefficient (Nash and Sutcliffe, 1970, see Section 8.4.1 for more details about the Nash-Sutcliffe criterion). The latter measures the percentage of variance of the observed data that is accounted for by the model as follows

$$R^2 = 1 - \frac{\sum_i (x_i - y_i)^2}{\sum_i (x_i - \bar{x})^2}. \quad (7.6)$$

The SnowSim model is not a hydrological model in the sense that the production of free water for a given day (i.e., the water originating from liquid rain and snowmelt that is available for runoff in the catchment) is not linked to a transformation routine to simulate the delayed streamflow. In consequence, Kerr (2005) applied a 14-day moving average on both the modelled and the observed discharge to mitigate the discrepancies between the daily net production and the delayed response of the hydrograph. The calibration and assessment of the model at the catchment scale was achieved by computing the Nash-Sutcliffe coefficient on the basis of the filtered signals (R_{14d}^2). Kerr (2005) reported contradictory performance from the two assessment strategies, resulting in different sets of calibration parameters to perform satisfactorily at the point observation (i.e., the SWE at Rose Ridge) or at the catchment scale (i.e., the free water available in the catchment). Due to an uncertain calibration of the snow pillow that questioned the validity of SWE observations at Rose Ridge (Kerr, 2008, pers. com.) the results of this latter assessment are ignored here and only the performance in terms of the modelled discharge is considered. Kerr (2005) obtained the best results during the calibration year by using a critical temperature $T_c = 2.5^\circ\text{C}$ and a melt factor ranging from 1 to 6 $\text{mm}\cdot^\circ\text{C}^{-1}\cdot\text{day}^{-1}$. This yielded $R_{14d}^2 = 76\%$ for the calibration year (i.e., the hydrological year 2003–2004), while $R_{14d}^2 = 61\%$ was achieved on average over the verification period from April 2000 to March 2004. These indicators provided a benchmark that could be compared with the results of the SRM model used in this thesis (see Chapter 8).

7.5 Assessment of SnowSim

The maps of snow cover obtained from optical satellites cannot provide spatial estimates of the SWE. Nevertheless, they depict the spatial distribution of the snowpack and can be used to assess the correct representation of reality by the model. The performance of snow models has often been addressed on the basis of frequent observations of the snowpack provided by aerial photography (Blöschl *et al.*, 1991) or maps derived from space borne sensors (Turpin *et al.*, 1997, 1999; Barrett *et al.*, 2001;

Holzmann *et al.*, 2007; Brown *et al.*, 2008). McAlevey (1998) used maps of snow cover derived from AVHRR to assess the total snow cover area (SCA) predicted by the country-wide version of SnowSim during the 1992–93 hydrological year. Although the extent of the snowpack modelled by SnowSim approached relatively well the satellite observations, large overestimations occurred during the winter and spring 1993. The accuracy of the model was not questioned. Instead, the discrepancies between the modelled and the observed SCA were attributed to an inadequate classification of snow from the AVHRR images (Fitzharris and McAlevey, 1999). This experiment was repeated in this thesis to assess the correctness of SnowSim-Pukaki, on the basis of the time series of MODIS-derived snow maps.

7.5.1 Method and data

The 679 MODIS-derived maps of sub-pixel snow fractions at 250m spatial resolution (M250) covering the period 2000–2007 were used to assess the corresponding outputs from the SnowSim-Pukaki model produced at the same pixel size. Both the snow maps derived from MODIS and the outputs obtained with SnowSim cannot be readily compared. SnowSim provides maps of SWE with a lower limit of 5 mm, and assumes that the pixels are evenly covered by snow. However, when the SWE is small and translates into a very thin layer of snow, it is likely that the SWE indicates a depleted snowpack. Thus, the maps of SWE needed to be reinterpreted to generate SnowSim-based maps of total SCA by means of a threshold to categorize pixels as being snow or not. The total SCA predicted by the model can be defined for different amounts of SWE. In this thesis, thresholds in the range 5–200 mm SWE were selected to assess the performance of SnowSim at estimating the total SCA in the catchment. The maximum threshold of 200 mm was considered to be a sufficient SWE amount to ensure that a pixel was fully covered by snow. At any given time SnowSim- and MODIS-derived total SCA were compared. Although this strategy can easily point out whether the snow cover extent was over- or under-estimated by the model at the catchment scale, it provided only a limited insight with regard to the behaviour of the model.

As a complementary assessment strategy, it is possible to take advantage of the fact that the M250 maps provide observations about the spatial distribution of snow on a per pixel basis. Thus, a classical technique of classification assessment was investigated to elucidate specific pitfalls of SnowSim. In order to achieve such a comparison, it was necessary to segment each corresponding map in a binary fash-

ion and to categorize pixels as being snow or not. The maps of SWE from SnowSim and the maps of sub-pixel snow fractions from MODIS (M250) were binary classified and compared on the basis of a confusion matrix (Figure 7.5). As discussed in the previous chapter (see Section 6.5.4), *hit rate* and *precision* of a binary classification are equivalent to the *producer's* and *user's accuracy*, respectively. On the other hand, the total accuracy measures the overall rate of correct classification. Reference pixels from the M250 maps were categorized as 'snow' when they accounted for more than 50% snow, and 'no snow' otherwise. The maps of SWE were binary classified with various thresholds of SWE within the range 5–200 mm in order to determine which provided the highest accuracy. Pixel-to-pixel comparison of the binary maps was then used to create the time series of hit rate, false alarm rate, and precision.

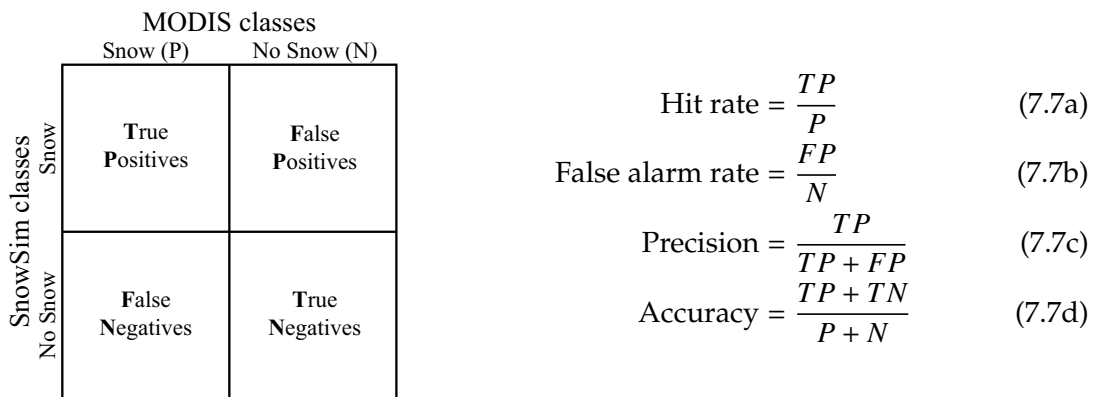


Figure 7.5 Confusion matrix for a binary classification with associated performance measures.

7.5.2 Results and discussion

An animation of the snow cover dynamics as modelled by SnowSim and observed by MODIS is embedded in Figure 7.6 (the animation is playable in the .pdf version of the thesis or available from the DVD enclosed \\Animations\snowsim_modis_640x480_qual75_v1-0.avi). Figure 7.7 (a) reveals the overall performance achieved by SnowSim-Pukaki in terms of representing the total SCA over the period 2000–2007. There are large discrepancies between the total extent of the snow cover predicted by the model and that observed from MODIS. Despite the fact that the MODIS SCA data integrates some errors associated with the mapping process, it is evident that SnowSim largely overestimates the area cov-



Figure 7.6 Animation of the dynamic of the snow cover distribution as modelled by SnowSim (left) and observed by MODIS (right) in the Pukaki catchment over the period 2000-2007 (the animation is playable in the .pdf version of the thesis or available from the DVD enclosed \\Animations\snowsimsim_modis_640x480_qual75_v1-0.avi).

ered by snow during the ablation season, regardless of the SWE threshold that is used to represent snowy pixels. Large over-estimations of total SCA by SnowSim at the end of the accumulation season are more pronounced with low thresholds. It reinforces that a small SWE modelled by SnowSim over a specific area is more likely to represent fragmented snow patches rather than evenly covered pixels. During the ablation season, the depletion of the snow cover was depicted similarly by all thresholds. It indicates that SnowSim modelled the transition between snowy and snow free areas with a steep gradient of SWE. Only few pixels at the boundary of the snow cover account for low SWE. One or a combination of the following reasons can cause such digressions:

- SnowSim progressively accumulates too much snow due to an overestimation of the amounts of snowfall;
- the melt factor is generally underestimated;
- the critical temperature is overestimated; and/or
- the field of temperature is underestimated.

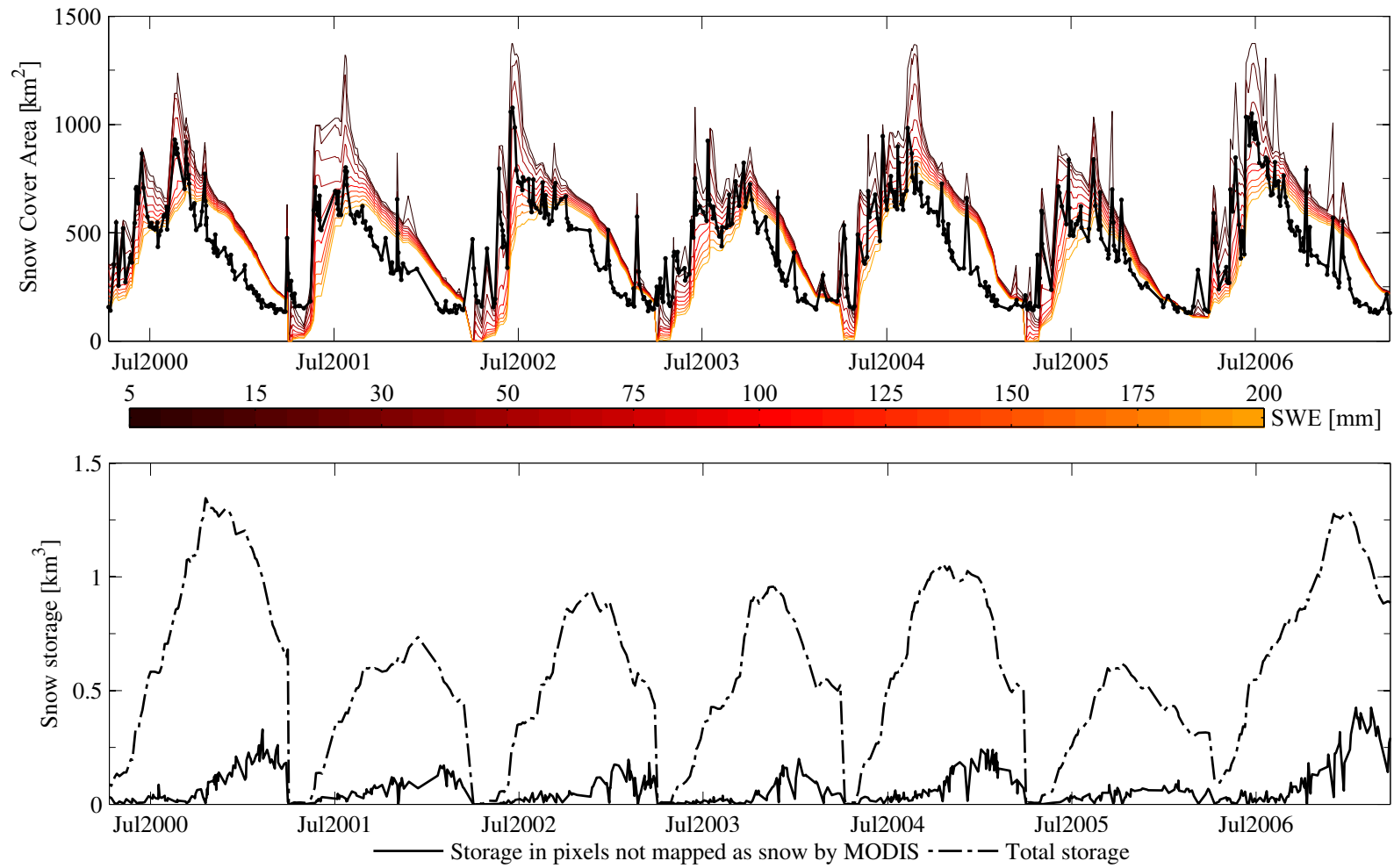


Figure 7.7 (top) MODIS- and SnowSim-derived snow cover area in the Pukaki catchment depending on the SWE threshold indicated by the colour bar. (bottom) Total storage in the modelled snowpack and in pixels not mapped as snow by MODIS.

While it is evident that a lower threshold results in more snow being mapped, the associated variability of the snow cover extent is exacerbated during the accumulation season (i.e., April to August). During accumulation, the pixels with low SWE represent a much larger surface than observed by MODIS. This consistent bias may be explained by an inadequate value of the critical temperature T_c and inaccuracies of the interpolated temperature field. The value of 2.5°C used in SnowSim is potentially set too high, resulting in snow being constantly mapped inappropriately at lower altitudes, thus representing a total extent much greater than reality. It also prevents the ablation when precipitation occurs (see Figure 7.3), thus resulting in the propagation and accumulation of substantial water storage in pixels free of snow according to the satellite observations. Figure 7.7 (b) shows that only limited storage is modelled in such pixels during the accumulation season. It further demonstrates that during this period the overestimated area accounts principally for pixels with low SWE whose contribution is negligible compared to the total storage. However, the amount of water being stored in pixels free of snow increases progressively during the ablation season, reaching 25–30% of the total storage modelled by SnowSim in summer. This suggests that a large quantity of water is falsely accumulated and prevents SnowSim from depicting the ablation accurately.

The deficiencies of SnowSim to depict reality were explored in more detail on a per pixel basis. Figure 7.8 shows that the mean of the accuracy time series reached a maximum when a threshold of 50 mm was used to segment the maps of SWE modelled by SnowSim. Thus, the time series of the other binary measures (i.e., hit rate, false alarm rate, and precision) were computed on the basis of this threshold. They are shown in Figure 7.9. During the accumulation/ablation seasons, the following four key phases were identified:

1. The snow storage is reset in SnowSim at the start of the hydrological year (i.e., 1st of April). Ice and perennial snow are identified by MODIS. Therefore, the number of True Positives (TP) and False Positives (FP) are zero. This results in a null Hit Rate (HR) and a null False Alarm Rate (FAR).
2. Then precipitation occurs and snow is being mapped by SnowSim. The FAR rises quickly to reach approximately 25% of pixels wrongly classified as snow by SnowSim. The HR simultaneously reaches 100%, indicating that pixels truly covered by snow are correctly modelled by SnowSim. Interpreted together, these two measures corroborate that SnowSim tends to build up the

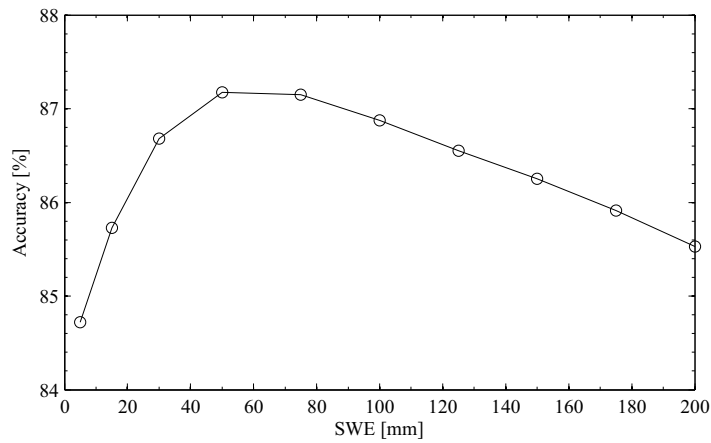


Figure 7.8 Mean accuracy of the classification of snowy pixels by SnowSim depending on the threshold of SWE.

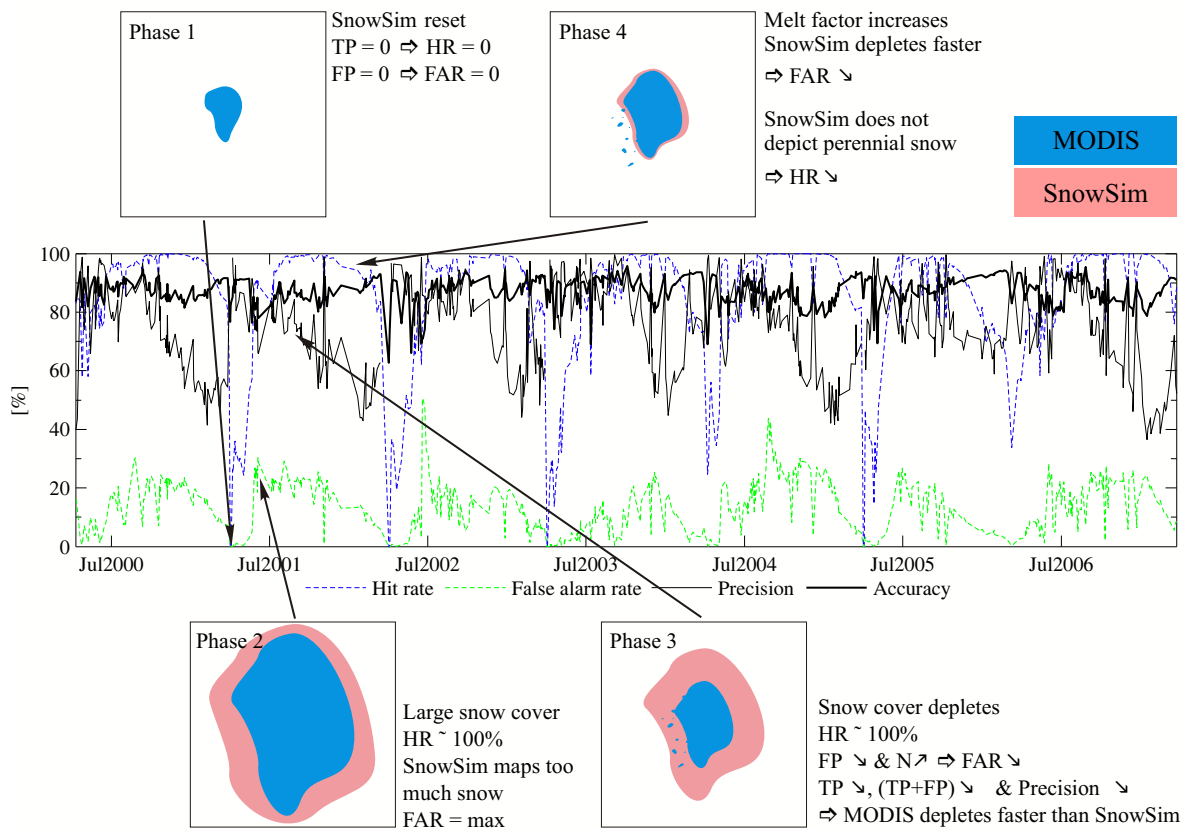


Figure 7.9 Classification performances of SnowSim. The map of SWE was segmented using a threshold of 50 mm.

snow cover at lower elevations where it does not exist, probably due to a critical temperature set too high, or a field of temperature estimated too cold.

3. During the ablation, the snow cover area reduces, resulting in an increasing number of 'no snow' pixels [N in Equation (7.7c)]. SnowSim depicts the depletion as well, thus the number of FP decreases. It explains the reduction of the FAR. In the meantime, the number of TP also decreases. The drop of the precision indicates that the number of TP decreases faster than that of FP. It demonstrates that the snow cover modelled by SnowSim depletes slower than in reality. The lower rate of depletion suggests that SnowSim accumulated too much SWE and/or the ablation procedure is inappropriate to deplete the snowpack fast enough (e.g., the melt factor is set too small, and/or the temperature is generally underestimated).
4. In February, by the end of the ablation season, the precision rises. It corresponds to the last but largest seasonal increase of the varying melt factor. It enables the snow cover modelled by SnowSim to catch up with the observations from MODIS, thus reducing the FAR. However, localized perennial snow and ice is observed by MODIS but not modelled by SnowSim, thus resulting in a decrease of the HR.

The total accuracy of the classification remains relatively constant, indicating that both the hit rate and the false alarm rate balance each other. Although it is difficult to identify the precise causes of the inaccurate behaviour of SnowSim, this comparison stressed the main pitfalls of a model that relies solely on precipitation and temperature data to simulate the accumulation and subsequent melting of the snowpack. Despite the fact that the comparison with optical images cannot assess the correctness with regard to the total storage of SWE, it is clear that the model is prone to the propagation of errors and it fails to represent the reality of the distribution of snow in the catchment.

7.6 Summary

This chapter has examined an application of the time series of MODIS-derived snow maps over the period from April 2000 to March 2007. The dataset was used to assess the SnowSim-Pukaki model (Kerr, 2005) with regard to its capacity to model

adequately the variability of the snow cover extent. Comparison of 679 observations of the snow spatial distribution with predictions of SWE from SnowSim revealed that the model achieves an overall classification accuracy of 87%. However, SnowSim consistently overestimates the extent of the snow cover and models snowfalls at too low elevations. In addition, the rate of depletion of the snowpack is generally lower than that observed from MODIS. It indicates that too much snow is wrongly accumulated and/or the ablation procedure underestimates snow melt. It is evident that a field of temperature set to be too cold could partially explain both effects. However, a misrepresentation of T_c and the melt factor cannot be discarded. This comparison cannot elucidate with certainty whether too much snow is accumulated and delays the ablation, or if the parameters governing the ablation lead to an underestimation of snow melt. It was suggested that both phenomena contribute to the model discrepancies.

SnowSim-Pukaki failed to model the dynamic nature of the snowpack accurately and hence propagates errors that increase to an important level. Thus, every year by the end of the ablation season, SnowSim falsely stores nearly 0.25 km³ of water in locations that are free of snow according to MODIS. This represents a quarter of the total storage modelled in summer. The progressive increase of this error reveals the pitfall of models that rely solely on precipitation and temperature measured at lowland climate stations to model the accumulation and ablation of snow over an entire year. Any bias in interpolation of temperature and/or precipitation, or a misrepresentation of model parameters, such as the critical temperature or the melt factor, can accumulate significant errors after six months of free run. This strongly jeopardizes the reliability of the model output. Thus, it is recommended that when such a modelling strategy is implemented, it must be supported with timely observations of the snowpack. Alternatively, a specific modelling strategy that uses observed SCA information can be considered. This is examined in the next chapter by implementing the Snowmelt Runoff Model (Martinec, 1975) to simulate discharge from the three catchments of Lakes Ohau, Pukaki, and Tekapo.

Chapter 8

Snowmelt Runoff Model (SRM)¹

8.1 Introduction

The previous chapter described some aspects of modelling the snowpack evolution. In particular, the use of a time series of MODIS-derived snow maps demonstrated that the SnowSim model (Fitzharris and Garr, 1995) is prone to the propagation of errors. In order to address this issue, this chapter puts together the frequent mapping of the snowcover described in the previous chapters and the Snowmelt Runoff Model (SRM, Martinec, 1975; Dewalle and Rango, 2008, Chap. 3) to propose a novel approach for modelling the hydrology of the three catchments of this study. The SRM model is a semi-distributed hydrological model whose snow component is based on the degree-day approach. Unlike classic accumulation-ablation models, there is no attempt to simulate the daily storage of seasonal snow *a priori*. Instead, along with climatic data (i.e., temperature and precipitation), the model is designed to take advantage of the observed distribution of snow (Martinec, 1982) as an additional forcing in order to simulate daily streamflow.

Although the SRM has been successfully applied in many parts of the world (Martinec *et al.*, 2005), it was only investigated once in the Pukaki catchment to simulate runoff, and that was for a single and incomplete hydrological year (Bowden, 1994). No support from satellite observations was used and a relatively poor performance was reported. The new dataset of MODIS-derived snow maps developed

¹The content of this chapter is largely published in: Sirguey, P., Mathieu, R., Arnaud, Y., and Fitzharris, B. B. (2009). Seven years of snow cover monitoring with MODIS to model catchment discharge in New Zealand. *Proceedings of the IEEE International Geoscience and Remote Sensing Symposium*, Cape Town, South Africa, II, 863–866, doi:10.1109/IGARSS.2009.5418232.

in this thesis enables the SRM to be revisited as an alternative to SnowSim to estimate snow melt. It also provides a potential framework to simulate lake inflows. A successful implementation of this model could support decision making and management of hydro lakes, and provide new insights about the hydrology of these catchments.

The first section introduces the concept and formulation of the SRM, as well as its practical implementation in the Ohau, Pukaki, and Tekapo catchments. Next, the creation and assessment of the forcing data are presented. This accounts for the interpolation of the fields of temperature and precipitation over the area, based on locally distributed daily observations. A novel approach based on a Savitzky-Golay filtering technique is proposed to create the snow cover area curves that are needed to compute snow melt in SRM. In addition, the temporal and spatial variations of the melt factor are addressed through the monitoring of the ground spectral reflectance of snow, following the atmospheric and topographic correction presented in Chapter 4.

The third section describes the calibration of SRM in the three catchments (i.e., Ohau, Pukaki, and Tekapo) based on three hydrological years from April 2000 to March 2003. The last section presents the results of the hydrological simulations. The performance and robustness of the calibrated models are assessed using the remaining four hydrological years from April 2003 to March 2007. Differences between the simulated and observed lake inflows during the ablation season are examined and interpreted. A final adjustment of the models provides new estimates of the contribution of melt water from seasonal snow and from glacier melt over the seven year study period. Finally, a statistical model of the errors calculates confidence intervals for the predictions of lake inflow. This should aid decision making for electricity managers in operational use of the models.

8.2 General principle of SRM

8.2.1 Main assumption

To simplify, the foundation of SRM can be summarized as *“where there is snow, it can melt, and the amount of melt is determined by the degree-day method.”* The free water released from liquid rain and snowmelt is linked to a transformation routine to simulate daily streamflow based on a simplified hydrological response of the

catchment. The general formulation of the SRM model is based upon the assumption that, in absence of supply, the runoff Q from a catchment exposed to an initial production Π_0 (i.e., the water available for runoff originating from liquid precipitation, snowmelt, and/or icemelt) obeys an exponential decay characterized by the recession coefficient k and the geometric progression (Martinec, 1975)

$$k = \frac{Q_{n+1}}{Q_n}, \quad (8.1)$$

where n is the index corresponding to the time step (e.g., days). If k can be assumed to be constant, then this recurrence relation yields the *recession law*

$$Q_n = Q_0 k^n. \quad (8.2)$$

The recession law describes the falling limb of the hydrograph, while the discharge is formed by the superposition of single hydrographs corresponding to distinct recession events (Figure 8.1). This approach corresponds to a conceptualization of the catchment by a single linear reservoir (additional details about the recession law are provided in Appendix G). In practice, the recession coefficient can be empirically determined from the analysis of the historical discharge of a basin in the absence of recharge, by plotting $\ln(Q_{t+\Delta t})$ versus $\ln(Q_t)$ for an arbitrary time difference Δt (e.g., 1 day). If the recession model is valid, then such a plot should reveal a linear relationship of slope 1 and intercept $\ln k \Delta t$ (de Zeeuw, 1973).

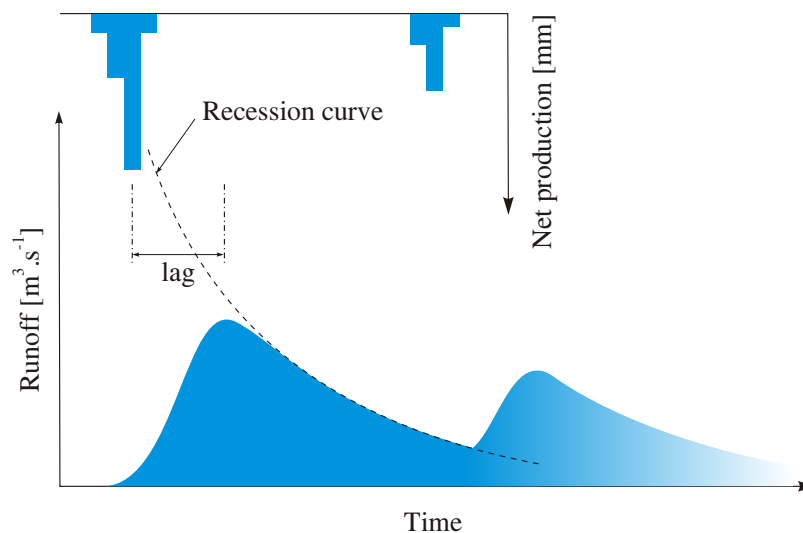


Figure 8.1 The basin hydrograph, recession, and lag.

8.2.2 The SRM formulation

8.2.2.1 Foundation

Based upon the linear reservoir assumption, equalizing the net production (in $[\text{m}^3]$) and the total discharge Q (in $[\text{m}^3 \cdot \text{s}^{-1}]$) using Equation 8.2, while noting that $0 < k < 1$, yields

$$\begin{aligned}\Pi_0 &= 86400 \sum_{i=0}^{\infty} Q_i \\ &= 86400 \frac{Q_0}{1-k} \\ \Rightarrow Q_0 &= \frac{\Pi_0}{86400} (1-k).\end{aligned}\quad (8.3)$$

Equation (8.3) allows estimation of the initial discharge, and thus the discharge for all subsequent days, from the amount of water available for runoff. By generalizing, it is possible to obtain an expression for the discharge at day n as the sum of the recessed discharge from the previous day, augmented by the flow associated by the production of the day (Π_n), namely

$$Q_{n+1} = kQ_n + \frac{\Pi_n}{86400} (1-k).\quad (8.4)$$

The net production Π_n is given by the sum of snowmelt water W_s [see Equation (7.3)] and liquid rainfall W_r , each being reduced by a *runoff coefficient* c_s and c_r , respectively, to account for the losses between the total amount of water produced by each component and their net contribution to runoff (e.g., evapo-transpiration, ground recharge). From this,

$$Q_{n+1} = (c_{s,n} a_n \Delta T_n \text{SCA}_n + c_{r,n} W_{r,n}) \frac{A}{86400} (1-k) + Q_n k,\quad (8.5)$$

where ΔT_n is the number of positive degree-day for day n , a_n is the melt factor (see Section 7.3.3), A is the area of the catchment and SCA_n is the fraction of this area covered by snow. Such a use of the fractional snow cover enables the direct input of remotely sensed observations. SRM differs largely from most snow models, in the sense that it does not attempt to model the progressive accumulation and subsequent melting of snow throughout the season. Instead, the contribution of snowmelt is estimated for each day based upon knowledge of the spatial distribution of snow and its exposition to climatic forcing. Thus, unlike classical accumulation-ablation snow models, SRM is not capable of providing estimates of the amount of snow

that is stored at any given instant, but it is designed to achieve a correct estimation of the snowmelt and its contribution to the catchment's hydrograph. The additional forcing, enabled by the monitoring of the snow cover mitigates the propagation of errors in the computation of the daily snowmelt. Nevertheless the total storage can only be estimated *a posteriori*.

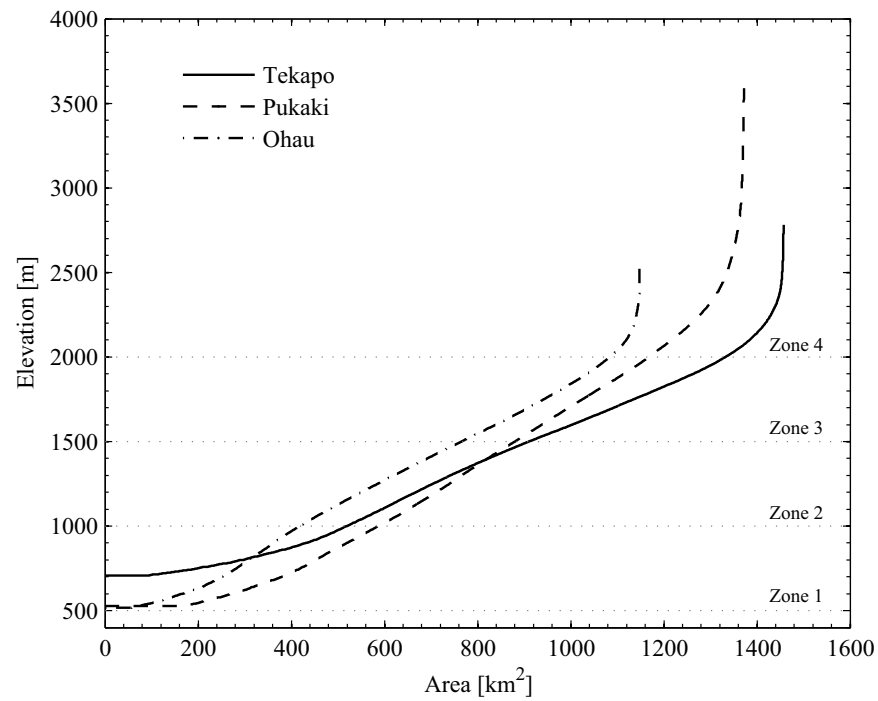
8.2.2.2 Zonal definition

In mountainous terrain it is evident that the spatial distribution of temperature, precipitation, and snow cover is variable. In order to address this effect, SRM implements a semi-distributed approach that relies on the segmentation of the basin into zones exposed to similar meteorological conditions. The production for the whole basin is the sum of the production originating from each zone and Equation 8.5 is modified as follows:

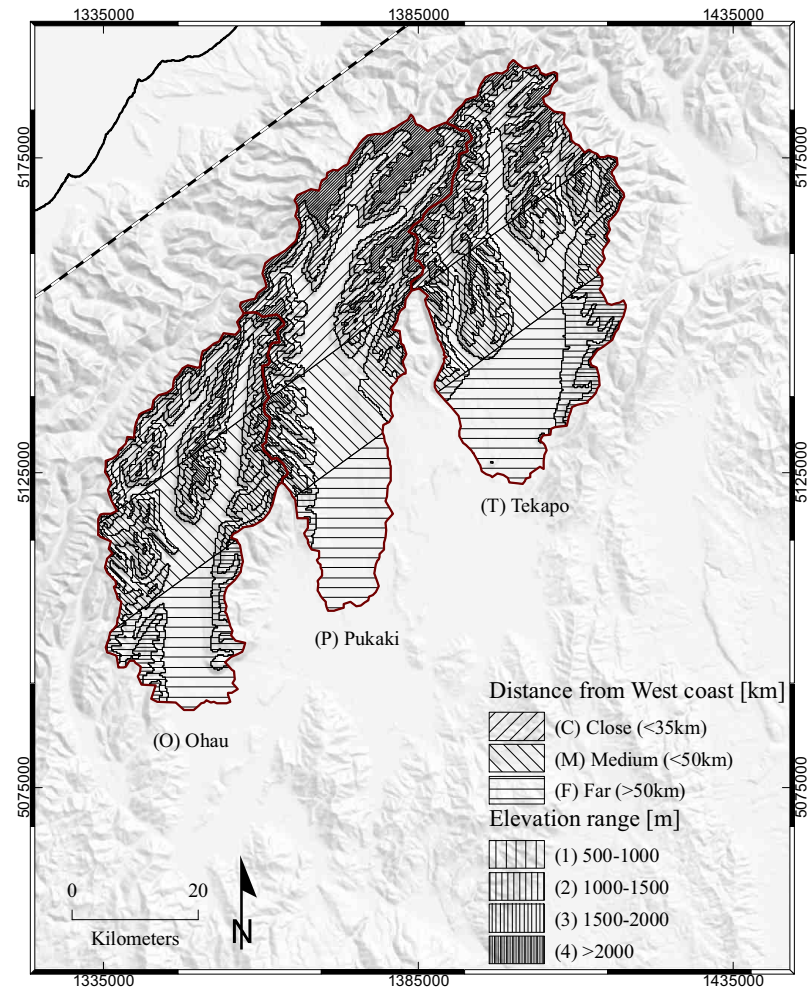
$$Q_{n+1} = \left[\sum_{i=1}^p (c_{s,n,i} a_{n,i} \Delta T_{n,i} S_{n,i} + c_{r,n,i} W_{r,n,i}) \frac{A_i}{86400} \right] (1 - k) + Q_n k, \quad (8.6)$$

where p is the number of zones, each identified by the index i . Since temperature, precipitation, and snow cover are often considered to vary with altitude, this segmentation is usually done for a range of elevations based on the hypsometric curve of the catchment (Martinec *et al.*, 2005). Such a segmentation originally enabled the use of a limited number of climate stations assumed to be representative of altitude bands, and whose records are extrapolated to other zones by means of a temperature lapse rate and a precipitation factor. It must be noted that some authors define zones as Hydrological Response Units (HRU) based on elevation, land cover, and sub-catchment boundaries (e.g., Nagler *et al.*, 2008; Holzmann *et al.*, 2007)

In order to apply the SRM in the upper Waitaki catchments (i.e., Ohau, Pukaki, and Tekapo), the zones were first defined according to the hypsometry of each watershed by a segmentation into elevation bands of 500m intervals. Given the limited surface covered by the terrain at high elevations, a single zone accounted for all pixels above 2000m. The relative distribution of the elevation bands in each catchment can be read from the hypsometric curves shown in Figure 8.2 (a). It was explained and illustrated in Section 7.4 that the distribution of precipitation in the Waitaki basin depends more on the distance from the main divide than on elevation. Therefore, in order to accommodate the gradient of precipitation in these catchments, an additional segmentation was introduced with respect to the distance from the 1200m western contour. Three rain zones were defined whether pixels were at



(a) Hypsometric curves of the catchments.



(b) Segmentation by catchment, range of elevation, and rain zones. Note the position of the 1200m western contour (dotted line).

Figure 8.2 Zonal definition of the upper Waitaki catchments in SRM.

close (< 35 km), medium (≥ 35 and < 50 km), or far (> 50 km) range from the topographic barrier. The combination of both segmentations provided 12 zones in Tekapo, and 11 zones in both the Pukaki and Ohau catchments. The final zonal definition is shown in Figure 8.2 (b).

8.3 Forcing data

8.3.1 Source of climatic data

The SRM model is generally used with a limited number of climate stations in a semi-distributed manner. Daily precipitation and mean temperature from representative climate stations were extrapolated to the mean elevation of each zone to compute Equation (8.6). In this thesis, a fully distributed approach of the climatic fields is associated with the semi-distributed design of SRM. The daily fields of temperature and precipitation were spatially distributed to match the 250m resolution grid, using the complete network of climate stations available in and around the area during the seven-year study period. A map showing the distribution of the climate stations available is shown in Figure 8.3.

Most climate stations are owned and operated by NIWA and data can be freely retrieved from the national climate database (CliFlo, <http://cliflo.niwa.co.nz/>). Five additional automatic weather stations (AWS) were installed in the catchments by Meridian Energy Ltd following the 1992 national energy crisis (such stations are identified by a larger symbol in Figure 8.3). All stations but three are below 1000m altitude, and thus only occasionally affected by snow. The remaining stations identified in Table 8.1 are more likely to be affected by snow in winter due to the altitude of the sites and their proximity to the main divide. Most problems occurred with the stations at Rose Ridge (ID: 30531) and Panorama Ridge (ID: 30441) whose precipitation records exhibit an unusual deficit due to snowfall from June to September. In order to reduce interpolation issues, rainfall data collected during this period at the three high elevation stations were ignored.

Min and max daily temperature and total rainfall, both read at 09:00am local time, were retrieved from the stations available in the CliFlo database. Scripts were written using MATLAB[®] software to transform the hourly records from the AWS of Meridian Energy into min-max daily temperature and total precipitation in accordance with the specifications of NIWA [i.e., the daily min and max temperatures

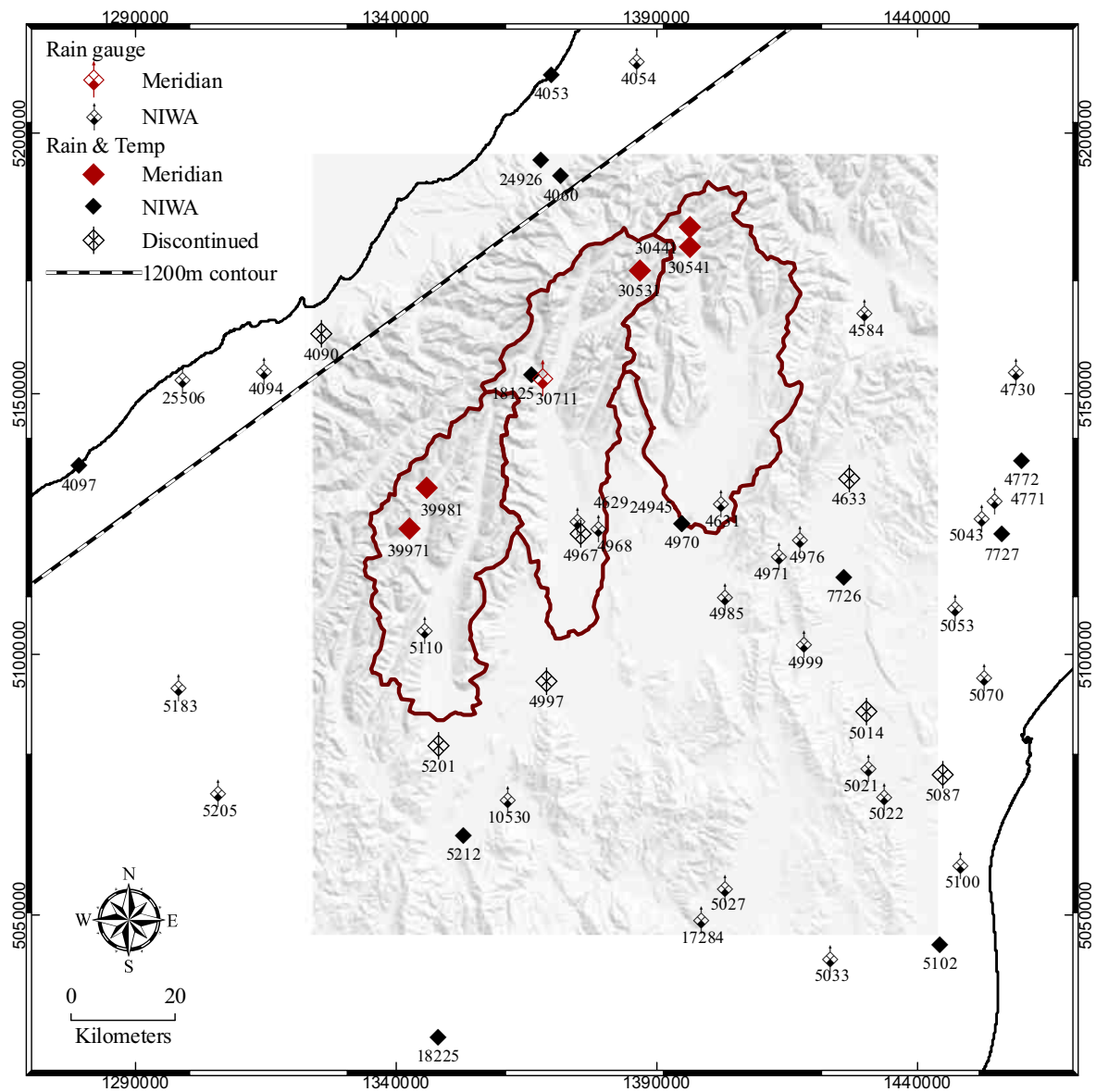


Figure 8.3 Situation of climate stations used to spatially distribute temperature and precipitation in the upper Waitaki catchment. The area of interest corresponds to the hillshaded DEM. The stations decommissioned before the 1st of January 2008 are shown, except when upgraded by a new one at the same location.

Table 8.1 Climate stations at high elevation (see location in Figure 8.3).

Name	ID	Altitude	Data available from
Hopkins at Boanerges Ridge	39971	1402	December 1993
Godley at Panorama Ridge	30441	1509	December 1993
Rose Ridge	30531	1980	October 2002

were retrieved from the hourly record on the basis of a 10:00am (previous day) to 09:00am (current day) interval and total rainfall was computed over the same period]. In order to accommodate the time of reading, the daily maximum temperature (T_{\max}) and precipitation for a given day were considered from the record of the following day, while the minimum temperature (T_{\min}) was obtained from the day of measurement.

8.3.2 Distributed temperature field

8.3.2.1 Review of techniques

A number of interpolation techniques have been used to interpolate sparsely distributed temperature data (Dodson and Marks, 1997; Jarvis and Stuart, 2001a,b; Xia *et al.*, 2001). Methods include but are not limited to IDW (DeGaetano and Belcher, 2007), trend surface analysis, polynomial regression (Stahl *et al.*, 2006), thin plate spline (TPS) Luo *et al.* (1998), or kriging (Garen and Marks, 2005). Dodson and Marks (1997) stressed the difficulty of interpolating temperature data at high elevations due to the limited access to data and the variable effect of adiabatic cooling. They also reviewed various strategies that have been developed to account for the effect of the elevation.

The most common approach relies on the use of a specified lapse rate to standardize the temperature observations to sea level according to the station elevation. The interpolation is processed on the adjusted data to determine the regional trend. The final field of temperature is obtained by applying the opposed lapse rate to the gridded trend using the DEM created for this thesis and discussed in Section 3.2. This method cannot address the spatial and temporal variability of the lapse rate, unless the latter is specified by the user. For example, Stahl *et al.* (2006) noted a marked seasonal pattern of the temperature gradient in British Columbia (Canada) with a lapse rate for T_{\max} ranging from $3^{\circ}\text{C.km}^{-1}$ in summer to $9^{\circ}\text{C.km}^{-1}$ in winter, and from 3 to $5^{\circ}\text{C.km}^{-1}$ for T_{\min} . Moore and Owens (1984a) also observed a seasonal pattern of the lapse rate in the Craigieburn Range, although it followed the opposite trend and was larger in summer than in winter. Stahl *et al.* (2006) compared several interpolation techniques and implemented either a seasonally variable lapse rate specified *a priori*, or a dynamic lapse rate calculated daily between stations by a weighted regression. The performance of the latter method depended strongly on the availability of data from high elevation stations to support an accurate estimate

of the lapse rate. In such a case, it outperformed the methods based on a specified lapse rate. For SnowSim-Pukaki, [Kerr \(2005\)](#) did not obtain better performance by implementing a daily lapse rate inferred from the data and preferred instead to use a constant value of $5^{\circ}\text{C.km}^{-1}$.

Nevertheless, the relevance of the constant lapse rate itself can be questioned given the multiple profiles upheld by the air temperature with respect to the elevation. [Barringer \(1989\)](#) showed that a constant gradient of $5^{\circ}\text{C.km}^{-1}$ was only one of the eight types of lapse rate profiles that occur in the Remarkables (Central Otago, New Zealand). Although it represented one of the most common profiles along with a simple temperature inversion, this stresses the need for an alternative method of interpolation. Techniques of spatial interpolation exist that can take advantage of an additional covariable to the geographical coordinates. [Wahba and Wendelberger \(1980\)](#) were the first to suggest the use of thin plate (smoothing) splines [TP(S)S] in a multivariate approach to spatially distribute meteorological fields. [Hutchinson \(1989\)](#) successfully incorporated the elevation in a trivariate (TV) TPSS to interpolate temperature in rugged terrain. [Boer \(2001\)](#) showed that TV-TPSS performed similarly to TV regression-kriging and was an attractive alternative to the time-consuming co-kriging technique.

8.3.2.2 Temperature interpolation method

In this thesis, the thin plate spline interpolation method was chosen because of its physical basis, mathematical elegance, and ease of implementation. Appendix A provides the mathematical background and the solution of the thin plate problem. The thin plate spline can be implemented either as a pure interpolator (TPS) or with smoothing or regularization (TPSS) (see Appendix A). The smoothing spline is generally preferred when a dense network of noisy data is available ([Wahba, 1990](#), pg. 65). In this case, a smoothing parameter permits the trend of the data to be approached while accommodating the noise. Due to the sparsity of the network, not enough information was available to separate the signal from the noise. Consequently, the data were considered free of error and no optimal smoothing was sought. Consequently, the TPS interpolator was preferred and three strategies were tested:

1. The traditional approach detailed in the previous paragraph was implemented, based upon a specified lapse rate of $5^{\circ}\text{C.km}^{-1}$. The trend of the adjusted sea-level temperature was interpolated using a bivariate TPS and re-

verted for each cell according to the DEM heights. This technique is referred to as the *bivariate lapse rate* (BVLRL).

2. A trivariate TPS (here referred to as TV) was investigated. The elevation covariable was scaled by a factor 10^4 to match the order of magnitude of the Easting and Northing coordinates.
3. Finally, a composite method (BVLRL-TV) averaging both fields obtained from the aforementioned techniques was tested. The BVLRL relies on a rigid lapse rate that can introduce substantial errors given the potentially large spatial and temporal variability of this parameter. On the other hand, despite its ability to incorporate elevation information, the TV method requires a good distribution of input data over the altitude range as to determine the local variation of temperature with elevation. In this area, only three stations are above 1000m, while the remaining 17 stations concentrate around a mean elevation of 425m (standard deviation $\sigma = 313$ m). In the trivariate strategy, this dataset may be affected by a marked regional trend that can conceal the variance associated with the elevation. This could potentially yield errors as problematic and uncontrolled relative to those associated with the BVLRL technique. Nonetheless, if the errors from each technique have some degree of independence, then the mean of their respective output can be expected to be more accurate than each single output.

This last point is illustrated in Figure 8.4 where the field of minimum temperature was interpolated with each technique at two dates. The BVLRL and TV exhibit similar outputs for the first date. This demonstrates that the TV method can successfully accommodate a vertical gradient on the basis of the elevation covariable. However, the second date depicted large discrepancies that indicate a more complicated scenario. The BVLRL integrates the specified lapse rate into the field of temperature. Thus, it always enhances the topography in a similar manner, regardless of the regional trend and local atmospheric conditions. For the same date, the TV method suggested a much reduced lapse rate and revealed the regional northwest-southeast gradient. Despite the local conditions, it remained surprising that high mountains have warmer or approximately similar minimum temperatures than inland locations at much lower elevations. It is possible that, when exposed to a specific regional trend, the distribution of stations according to elevation may not be sufficient to resolve a realistic vertical gradient of the temperature field. Neverthe-

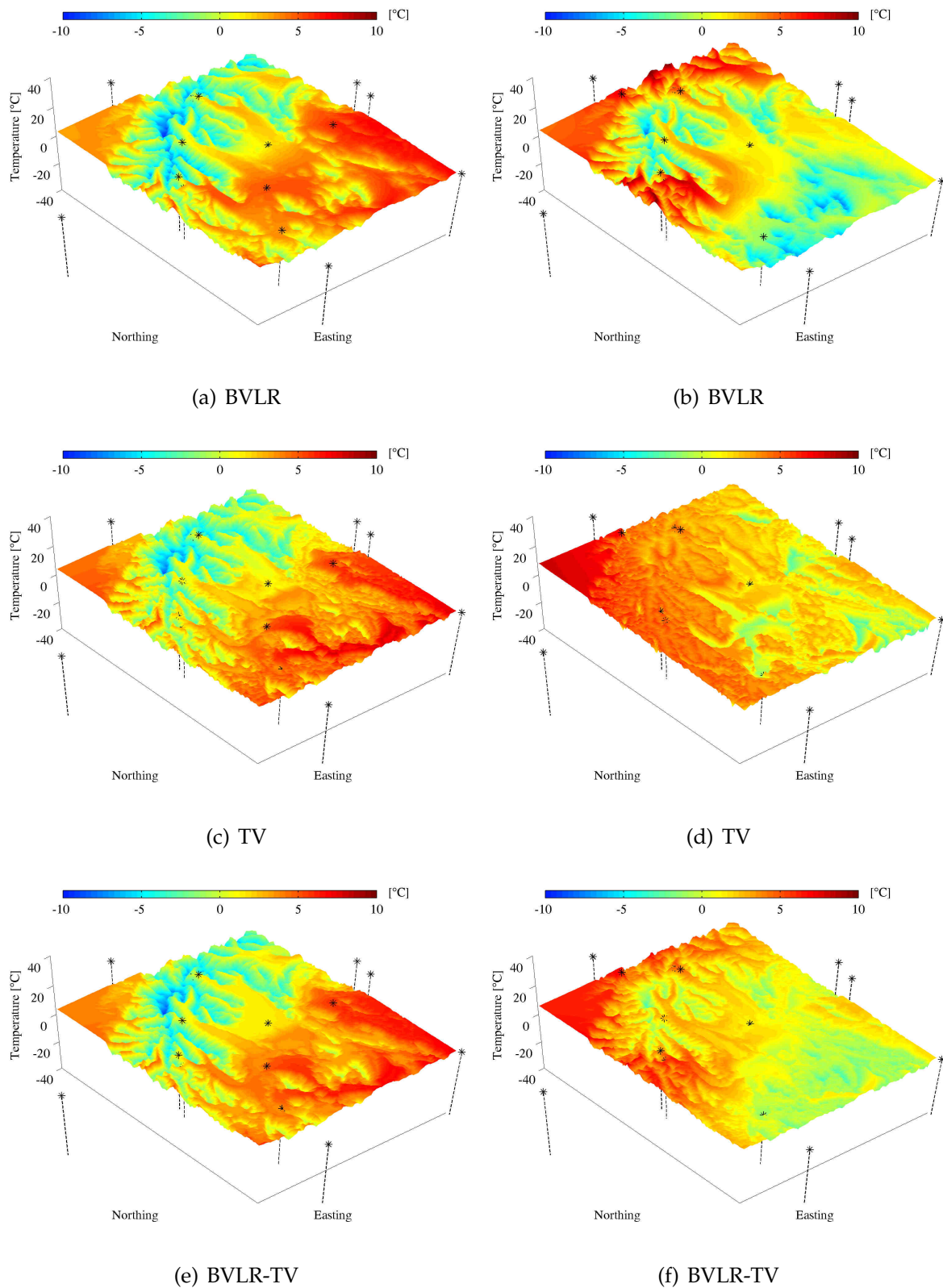


Figure 8.4 Examples of temperature interpolation (T_{\min}) for 1st January 2001 (left) and 3rd April 2003 (right). The fields are only shown for the area of study; the asterisks (*) indicate the data points available for the interpolation.

less, each method has a potential pitfall and it remains uncertain which of them is more accurate for the second date. For this reason it is believed that the mean of both fields may provide a reasonable tradeoff that has the potential to mitigate the errors from both techniques.

The performance of each method was examined on the basis of the *leaving-one-out cross validation* (CV). For every day from 2001 to 2007, each interpolation was carried out several times, by ignoring one of the climate stations successively. The errors between the interpolated field and the left out data were summarized into bias, Mean Absolute Error (MAE), and Root Mean Squared Error (RMSE) [see Section 6.5.2 for a description of the measures and the computation of their confidence interval (CI)]. The thin plate interpolation can yield unreasonable errors near the edges due to the lack of constraints. The use of data from climate stations outside the area of interest helped to limit the degrees of freedom of the interpolation near the edges. Only the errors from the stations inside the study area (see Figure 8.3) were considered in the final statistics.

8.3.2.3 Assessment of the accuracy of the temperature field

The results of the CV calculated over seven years are given in Table 8.2. 95% confidence intervals (CI) were calculated, but are not shown as they only affected the second decimal. The BVLR had a weaker predictive power for T_{\min} than T_{\max} . This could be explained by a differential lapse rate for both variables, as observed by [Stahl et al. \(2006\)](#). TV achieved similar performance for both types of temperature with comparable results to BVLR for T_{\max} . However, TV appeared to be significantly better than BVLR at estimating T_{\min} . Both methods had generally a small bias but the RMSE values revealed a relatively large dispersion. Overall, the results of the cross validation from both techniques compared well with the performance obtained from other experiments in extensive mountainous areas ([Xia et al., 2001](#); [Stahl et al., 2006](#)). The combination of methods significantly improved the interpolation accuracy for both types of temperature with a near null bias, a MAE of 1.2°C, and a RMSE of 1.9°C.¹ This suggests that the errors associated with both methods have some degree of independence and tend to cancel each other out.

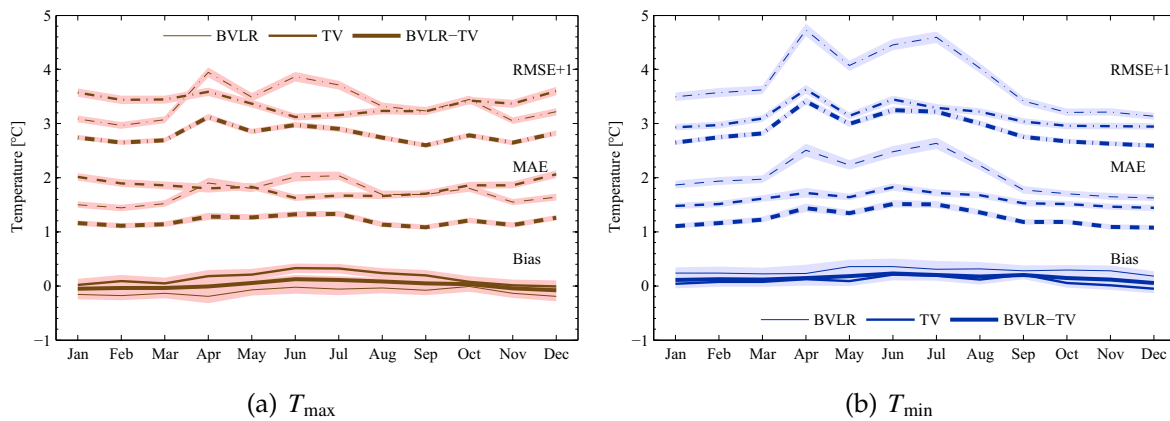
The CV errors were plotted into monthly values in order to identify any seasonal pattern. Although the bias did not exhibit any marked seasonal variation, Figure 8.5 shows that BVLR performed generally worse in winter than in summer

¹Note that in this case the RMSE identifies to the standard deviation.

Table 8.2 Results of the cross validation from the interpolation of the daily temperature over the period 2001–2007.

Method	T_{\max} °C			T_{\min} °C		
	bias	MAE	RMSE	bias	MAE	RMSE
BVLR	-0.1	1.7	2.4	0.3	2.1	2.8
TV	-0.1	1.8	2.4	0.1	1.6	2.1
BVLR-TV	0.0	1.2	1.8	0.1	1.3	1.9

The 95% CI for each measure are not reported because they only affected the second decimal. All differences are thus statistically significant at the .05 significance level.

**Figure 8.5** Monthly variation of the cross validation errors for the temperature. Note that RMSE values are shifted on the graph (RMSE+1) for clarity purposes. The envelopes indicate the 95% CI.

for both types of temperature. Larger MAE and RMSE values indicated a larger dispersion of the error and was more pronounced for T_{\min} than for T_{\max} . Although the possible correlation between the error and the temperature was not explored further, it seems that BVLR predicted lower temperatures with less precision. This would suggest that a seasonally varying lapse rate should be preferred to a constant lapse rate. The TV method achieved a more consistent performance, thus suggesting that it can accommodate the conditions prevailing on any given day, regardless of the season. The combination of both methods benefited from the TV approach since a seasonal variation can hardly be detected. Better results were obtained with a significant reduction of the dispersion of errors. In consequence, the BVLR-TV method proved to be the best candidate to interpolate the field of temperature and was therefore selected.

8.3.3 Distributed precipitation field

The estimation of precipitation in the Southern Alps is complicated by the effect of the strong orographic lift on the prevailing northwesterly flow. Figure 8.6 shows the long term mean annual rainfall surface prepared by the New Zealand Meteorological Service based on data from the period 1951–80 and expert interpretation in areas with few or no observations. Sinclair *et al.* (1997) and Henderson and Thompson (1999) showed that this surface compares well with the individual profile of rainfall induced by northwesterly storms. However, rain gauges remain sparsely distributed in the catchments, and measurements near the precipitation barrier and at high elevation are limited (see Figure 8.3 and 8.6). Therefore, the network generally fails to resolve the extreme pattern of rainfall with sufficient detail to enable a simple interpolation of the precipitation field.

8.3.3.1 Review of techniques

Similarly to the temperature lapse rate, a correction factor can be designed to accommodate the gradient of precipitation often observed with respect to altitude (Weingartner and Pearson, 2001). For instance, Fitzharris and Garr (1995) implemented a simple exponential increase of precipitation with elevation in the first version of SnowSim. This approach was retained by McAlevey (1998) for the country-wide version of the model, but was refined to depict the marked northwest–southeast gradient featured on the NZMS rain surface. Kerr (2005) believed that the elevation was not a relevant covariable and suggested that the long term annual average precipitation should be used instead (see Section 7.4.1). He also amended the NZMS 1951–80 surface to satisfy better the observations and the long term water balance of the Pukaki catchment. Although this approach may become weak when the spatial distribution of unusual rainfall events departs from that of the long term rainfall surface, it remains justified by the fact that most significant rainfall events generally approach the mean annual profile.

McAlevey (1998) and Kerr (2005) used the IDW technique. Kerr (2005) incorporated the annual average precipitation by the mean of a climatologically aided IDW interpolation, related to the anomaly approach. Instead of spatially distributing the daily measurements from climate stations, Kerr (2005) interpolated the proportion of the long term mean annual precipitation value represented on a given date. The gridded proportions were then reverted into rainfall using the long term rainfall surface. As explained in the previous section, interpolation methods exist that can take

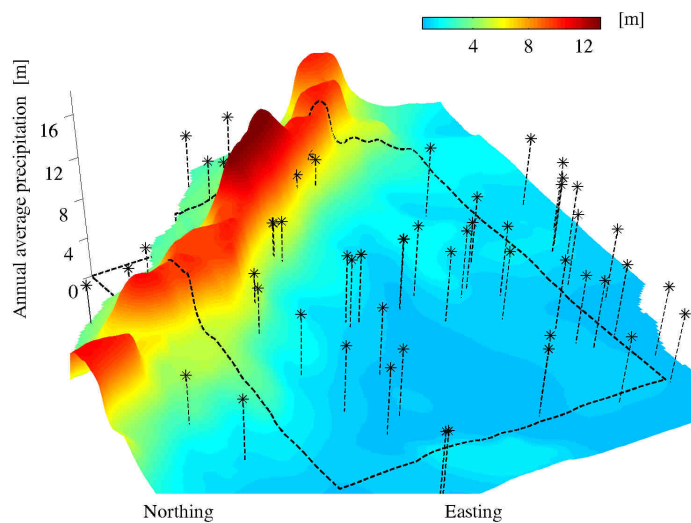


Figure 8.6 New Zealand Meteorological Service (NZMS) normal rain surface 1951–80. The dotted line indicates the extent of the area of interest; the asterisks (*) indicate the position of the rain gauges.

advantage of additional covariables in a more elegant way, such as co-kriging or thin plate spline. [Hutchinson \(1989\)](#) showed that the elevation can be incorporated in a trivariate TPSS to improve the accuracy of the interpolated rain field across Australia, and repeated the experiment with success in Switzerland ([Hutchinson, 1998b](#)). The same approach was tested in New Zealand by [Tait and Turner \(2005\)](#) who showed that rainfall events required an additional scaling at high-elevation to achieve acceptable interpolation results. Subsequently, [Tait et al. \(2006\)](#) demonstrated that the field of daily rainfall could be improved by using the long term rain surface rather than the elevation in a trivariate TPSS.

8.3.3.2 Precipitation interpolation method

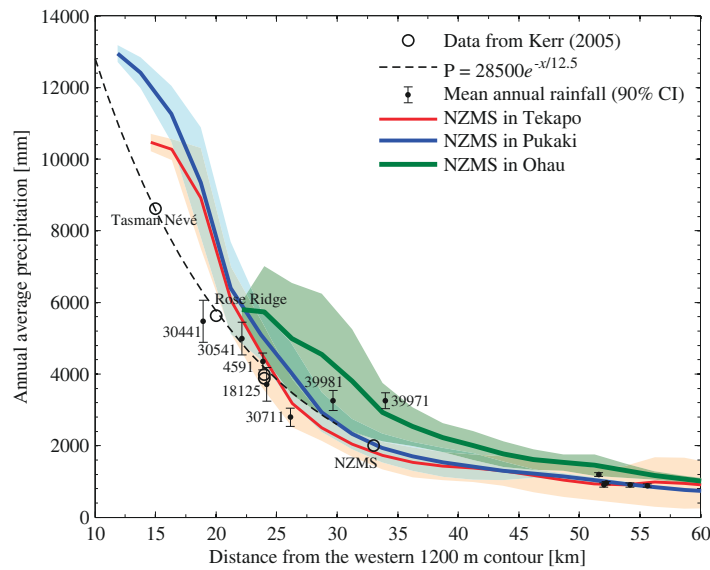
A similar approach to that used by [Tait et al. \(2006\)](#) was implemented in this thesis apart from the fact that the thin plate spline interpolator is preferred to the smoothing spline. Climate stations are too sparse and cannot support enough information to separate the signal from the noise, thus making irrelevant the smoothing approach. Following the recommendations of [Hutchinson \(1998a\)](#) and [Tait et al. \(2006\)](#), a square root transformation was applied to the rainfall data before the interpolation in order to reduce the skewness of the rainfall distribution. The interpolated values were then squared to provide the field of precipitation. In addition,

data from high elevation sites (see Table 8.1) were ignored during winter (i.e., from June to September) when they were likely to be affected by snowfall. The bivariate TPS (BV) (i.e., based on northing and easting coordinates) and trivariate TPS (TV) (i.e., with addition of the long term annual precipitation surface) were compared, as well as the average between both methods (BV-TV). The mean error (bias), MAE, and RMSE for the climate stations inside the area of interest were obtained from the cross-validation and used to measure the performance of each approach over the 2001–2007 period. In addition, the mean annual amount of precipitation modelled by the different techniques over the hydrological years 1994 to 2006 was compared to the annual average lake inflow from each catchment.

8.3.3.3 The long term annual precipitation surface

The NZMS 1951–80 mean annual average precipitation surface was modified in the Pukaki basin to incorporate the exponential relationship established by Kerr (2005) [see Section 7.4.1 and Figure 8.7]. Too few data were available to address the rain surface in the Tekapo and Ohau catchments in a similar way. Consequently, the original NZMS surface was used for both watersheds. Figure 8.7 shows the mean (tick lines) and 90% CI (the coloured envelope represents 1.6 times the standard deviation) of the annual average precipitation according to the NZMS surface along a transect perpendicular to the alpine fault for each individual catchment. The thin envelopes for the Tekapo and Pukaki basins illustrate that annual precipitation is expected to be consistent within a given distance from the main divide. This supports as a reasonable option the use of a single profile such as the exponential function proposed by Kerr (2005) for the Pukaki basin. In the Ohau catchment, the envelope shows a much larger dispersion of the annual precipitation parallel to the main divide indicating more complex precipitation patterns.

The values of mean annual precipitation measured by the climate stations are plotted in Figure 8.7. The observations match quite well the values retrieved from the NZMS surface at a distance larger than 40 km from the main divide. The station situated at Panorama ridge (ID: 30441) exhibited a large deficit compared to the NZMS surface. Its climate graph (see Figure 2.2) strongly suggests that precipitation values are largely underestimated during winter due to snowfalls. The measurements in the Pukaki and Tekapo basins at close range (see Figure 8.3 for locations) fit the exponential and the NZMS profiles reasonably well, respectively. In the Ohau catchment, the mean annual precipitation at Boanerges Ridge (ID: 39971) compares



(a)

Figure 8.7 Rain profiles along a transect normal to the main divide. The thick lines are the mean precipitation obtained from the NZMS 1950–81 surface, the corresponding envelopes indicate the 90% CI for the precipitation; the dotted line is the profile established by Kerr (2005) for the Pukaki catchment based on observed and estimated data (circled dots); the mean precipitation from selected rain gauges are indicated along with their 90% CI (plain dots).

to that of the NZMS surface (i.e., 3256 mm.y^{-1} measured compared to an estimated 3222 mm.y^{-1}), thus suggesting a marginal effect of snowfall on the rain gauge. However, the station at Elcho Flats (ID: 39981) reveals a severe discrepancy (i.e., 3260 mm.y^{-1} measured compared to an estimated 5077 mm.y^{-1}). At 761m elevation, the mean temperature at the station stays above freezing most of the time and its climate graph shows that mean monthly rainfalls are nearly constant throughout the year. Only a slight deficit in winter suggests a limited impact of snowfall. It was believed that the ratio of 1.6 between the measured and estimated mean annual rainfall can be attributed to a location exposed to wind that could result in a severe and consistent undercatch. Retaining this station was desirable because it allowed the rain field in the Ohau catchment to be resolved. Therefore, an additional trivariate interpolation was processed by applying a correction factor of 1.6 to the records from Elcho Flats. The relevance of this modification was investigated with regard to the long term water balance.

8.3.3.4 Assessment of the accuracy of the precipitation field

Figure 8.8 illustrates the difference between the BV and the TV methods for three dates in April 2003. The BV method provided surfaces that differed substantially from those produced by the TV spline. The addition of the normal rain surface as a covariable clearly enhanced the precipitation over the main divide. Table 8.3 gives the overall results of the cross validation during the 2001–2007 period for all climate stations inside the area of interest. All methods had a very small bias and the BV method had the largest dispersion of errors. The TV and BV-TV methods provided a significant improvement to the BV spline by decreasing the RMSE 33%. Although the MAE from BV-TV was less than that from TV, the RMSE values were not different at the .05 significance level.

The monthly values of the cross validation errors [Figure 8.9 (a)] revealed that the BV approach yielded larger errors in winter, when high elevation stations were ignored. It contrasted with the TV method whose errors were relatively consistent throughout the year. This demonstrates that the TV method better accommodates the removal of data points than the BV method. Therefore, it suggests that the use of the rain surface covariable permitted achievement of a more realistic representation of the rain field. The errors of the BV-TV method are slightly smaller than that of the TV spline when all stations were retained (i.e., outside the winter period). Although a limited degree of independence between the errors of both methods was expected and could benefit the interpolation of the rainfield, the BV-TV approach was considerably penalized in winter by the poor performance of the BV spline.

Table 8.3 Results of the cross validation for the interpolation of daily precipitation over the period 2001–2007.

Method	P [mm] ^a		
	bias	MAE	RMSE
BV	0.3±0.1	3.2±0.1	13.0±0.1
TV	-0.5±0.1	2.7±0.1	8.7±0.1
BV-TV	-0.1±0.1	2.3±0.1	8.8±0.1

^aThe intervals for each measure correspond to the 95% confidence.

Figure 8.9 (b) shows the RMSE from individual climate stations according to the mean annual precipitation. Errors are erratic but generally larger in areas exposed to more precipitation. It illustrates the difficulty for the interpolation to depict accurately the extreme pattern caused by the topography. As opposed to the TV

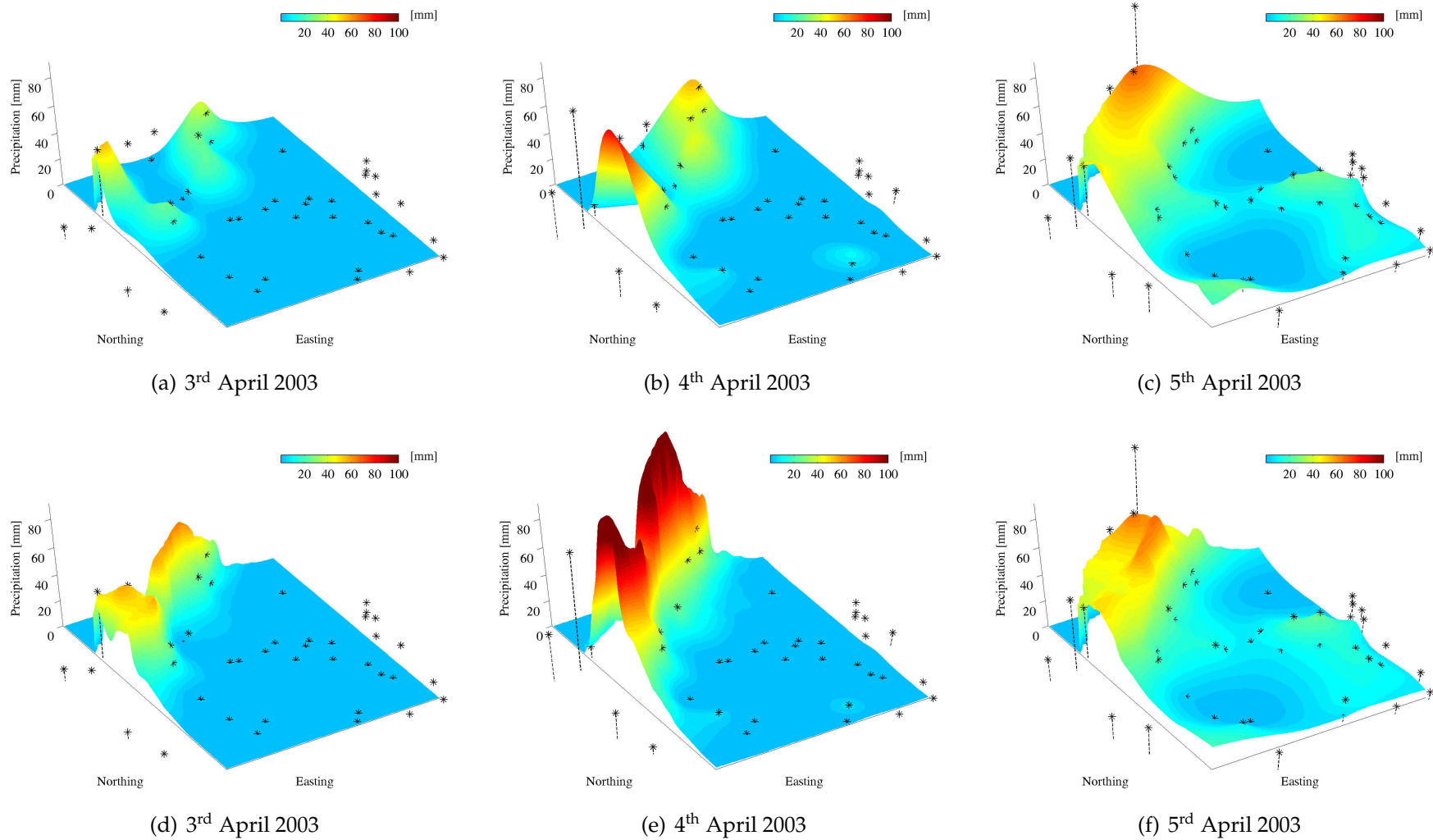


Figure 8.8 Examples of interpolation of the precipitation field with the BV (top) and TV (bottom) methods. The fields are only shown for the area of study; the stars (*) depict the data points available for the interpolation.

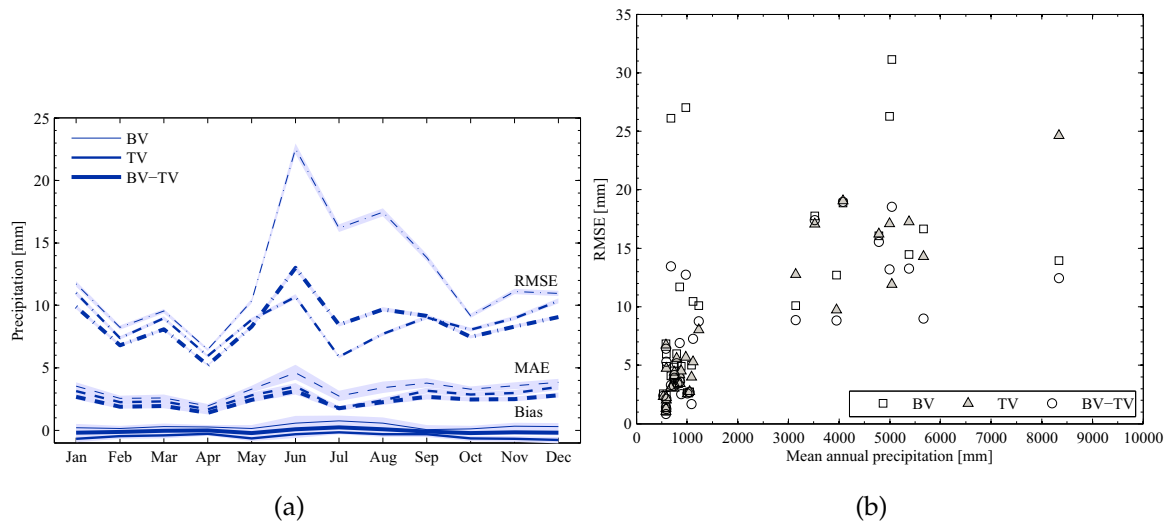


Figure 8.9 (a) Monthly variation of the cross validation errors for the precipitation. (b) RMSE error versus mean annual precipitation.

method, the BV spline yielded very large errors for stations with relatively low annual rainfall. Stations ID 5110, 4629, 4968, 4631, and 4584 obtained an average RMSE of 17 mm with the BV technique, while it reduced to only 5 mm with the TV spline. These stations are situated along a line 50 km south of the main divide (see Figure 8.3). It confirmed that the BV interpolation had difficulties to resolve the extreme decay of precipitation in the lee of the alpine range, while the use of the normal rain surface in the trivariate approach was better capable of accommodating it. Closer to the main divide, where the mean annual precipitation exceeds 3000 mm.y^{-1} , the RMSE values were more dispersed but generally larger than 10 mm for all methods. Again, the BV spline produced very large errors for stations ID 4090 and 39981, but eventually performed better at Rose Ridge (ID: 30531) with a precipitation above 8000 mm.y^{-1} .

The methods were also assessed by simulating the components of the water balance and comparing the predicted and observed lake inflows. The catchments were assumed to have negligible groundwater recharge (McKerchar and Pearson, 1997), thus the water balance equation reduced to

$$P = R + ET + \Delta I, \quad (8.7)$$

where R is the total runoff measured by the lake inflow, ET is the evapotranspiration, and ΔI is the long term ice storage. Kerr (2005) compiled several estimations of ET

in the alpine catchments ranging from 400 to 700 mm.y⁻¹ (Anderton, 1974a; Fitzharris and Garr, 1995; McKerchar and Pearson, 1997). An average value of 540 mm.y⁻¹ is used in this thesis and is assumed not to vary significantly from year to year. Purdie and Fitzharris (1999) estimated the long term ice melt in the Pukaki catchment to represent 6% of the annual lake inflow, thus corresponding to 0.23 km³ of water per year on average. Due to the lack of data in the Ohau and Tekapo basins, this value was simply extrapolated proportionally to the area covered by ice and perennial snow. The average annual inflow was calculated over the 1994–2006 hydrological years when data from the climate stations installed by Meridian energy became available. Table 8.4 shows the components of the water balance. As reported by Kerr (2005), the NZMS surface is not always accurate. The mean annual precipitation provided by the NZMS surface is substantially overestimated in the Pukaki catchment (i.e., 5.46 km³ compared to a target of 4.32 km³), and justified the design of the exponential adjustment applied by Kerr (2005). In addition, despite the uncertainties associated with *ET* and ΔI , it is possible that the NZMS surface underestimates the mean annual precipitation in the Ohau and Tekapo basins. However, it is unclear how the surface should be modified, unless more detailed precipitation data become available for both basins.

Table 8.4 Mean annual values of the components of the water balance computed over the hydrological years 1994–2006.

Catchment	Ohau	Pukaki	Tekapo
Area [km ²]	1148	1372	1457
% perennial Snow and Ice cover	2.9	15.7	4.4
Estimated ice volume [km ³] ^a	542	6650	2584
Lake inflow (<i>R</i>) [km ³]	2.54	3.81	2.65
Evapotranspiration (<i>ET</i>) [km ³]	0.62	0.74	0.79
Long term ice storage (ΔI) [km ³]	-0.02	-0.23	-0.09
Targeted precipitations (<i>P</i>) [km ³]	3.14	4.32	3.35
Annual average precipitation surface [km ³]	NZMS: 2.79	NZMS: 5.46 Kerr (2005): 4.44	NZMS: 3.04
BV [km ³]	2.30	3.69	3.09
TV [km ³]	2.34	4.23	3.09
BV-TV [km ³]	2.32	3.96	3.09
TV (1.6× ID: 39981) [km ³]	2.81	4.44	3.09
Error [%]	-10.5	2.8	-7.8

^a Data from the New Zealand glaciers inventory (Chinn, 2001).

In the Ohau and Pukaki catchments, the BV interpolation method did not model enough precipitation to match the inflow, regardless of the other components of the water balance. It provides more evidence that the BV method was not capable of predicting the rain field accurately. The TV spline had a substantial impact on the water balance in the Pukaki basin and permitted the target value to be approached (Table 8.4). However, it provided only little change to the mean annual precipitation in the Ohau and Tekapo basins, with a poor performance for the Ohau basin. As mentioned in the previous section, the rain gauge installed at Elcho Flats (ID: 39981) in the Ohau catchment may underestimate the precipitation by a factor 1.6, and possibly more if the NZMS surface was itself underestimated. The obvious digression of annual precipitation based on the uncorrected record further suggests that the measurements from the gauge are not representative of its location. The TV spline processed with the correction factor still produced nearly 11% less than the target precipitation amount in Ohau. However, it was considered a more realistic result since it allowed the lake inflow to be exceeded. The correction had an impact on the precipitation field and annual amounts in the Pukaki catchment due to the proximity of the gauge, but barely affected the rain field in the Tekapo basin.

Overall, the cross-validation experiment demonstrated that the trivariate TPS provided a significant improvement and a more robust estimation of the daily rain field than the bivariate approach. Although the combination of both methods was capable of producing a slightly more precise estimation due to the averaging effect, it was compromised by the large errors of the bivariate approach. With respect to the annual water balance, the use of the rain surface as a covariable permitted a more realistic amount of precipitation to be obtained in the Pukaki catchment but improved only marginally the results in the Ohau and Tekapo basins. Finally, this analysis confirmed that the climate station at Elcho Flats does not provide measurements of rainfall representative of the location. The underestimation of precipitation is unlikely to be accounted for by the effect of snowfall during winter months, but can rather be attributed to a consistent undercatch due to a location which is exposed to wind. In consequence, the trivariate spline along with the correction of the record at Elcho Flats was considered to be the most accurate method and was used to interpolate the precipitation field in the area of interest.

8.3.4 Snow cover area curves

In order to estimate snowmelt, SRM requires the fraction of each zone covered by snow daily. The contribution of snowmelt is often considered only during the ablation season. Thus, the change of fractional snow cover generally follows a monotonic decrease according to time. The frequent observations of the snow cover enable the construction of functions often referred to as *snow cover depletion curves* (SDC) (Tekeli *et al.*, 2005; Li *et al.*, 2008; Dewalle and Rango, 2008, Chap. 11). In New Zealand, the mild and fast changing temperatures can make snowmelt contribute substantially to the runoff at all times, including during the accumulation season (Fitzharris *et al.*, 1999). Hence, for the purpose of this thesis, SRM is used to model the discharge from each catchment throughout the year on a daily basis. Given this, the time series of fractional snow cover in each zone must encompass both the accumulation and the ablation seasons and are simply referred to as the *snow cover area curves* (SCA curves).

Despite the frequent observations permitted by MODIS, many gaps remain in the time series of snow maps because of persistent cloud cover and/or strongly off-nadir satellite configurations. Although the sensor can achieve a daily repeat time, the number of suitable images over the period from February 2000 to May 2007 was limited to 679, so in average one image every 3.85 days. Only 205 granules were acquired on consecutive days, and 90%, 95%, and 99% of the images were acquired within 8, 11, and 18 days from the previous image, respectively. The largest gap totaled 39 days and occurred between the 13th of December 2001 and the 21st of January 2002. Such discontinuities are problematic because they prevent satisfactory depiction of the SCA curves. For instance, images obtained on day following a short-lived snowfall can affect the correct representation of the SCA time series if they are not followed immediately by a sequence that reveals the fast depletion of the snowy event. Such episodes distort the SCA curves. They complicate the determination of the persisting snowpack and its gradual depletion during spring and summer. Consequently, simply connecting all observations would yield a severe overestimation of snowmelt by SRM (Martinec *et al.*, 2005, pg. 18). In order to mitigate this effect, short-lived snow fall must be ignored from the construction of the SCA curves, while SRM addresses the extra snow fall by means of an additional reservoir (Martinec *et al.*, 2005, pg. 13, see also Section 8.4.5 of this thesis).

The construction of the SCA curves from the time series requires a specific interpolation capable of extracting the persistent snow cover, while removing the

sharp peaks corresponding to the short-lived snow falls. In order to achieve this goal, data points are often interpreted subjectively and connected manually (Hall and Martinec, 1985, pg. 47). Methods have been developed to address the subjectivity of a manual interpretation, and to provide an automatic and repeatable alternative to construct these curves. Li *et al.* (2008) proposed constructing the curve based on an analysis of pixel trajectories (i.e., the sequence of changes of pixel class between ‘cloud’, ‘snow’, and ‘no snow’ over a series of successive images) and defining a set of classification rules to determine whether pixels should be accounted for as belonging to the seasonal or the short-lived snow cover. Li and Williams (2008) developed a temporal filter that considered pixels as belonging to the persistent snowpack when they were classified as snow for more than 3 weeks per month.

Alternatively, it can be noted that the raw SCA curves are simply time series of irregularly spaced observations, in which the persistent snow cover forms the lower envelope. It contrasts with the short-lived snow fall events that correspond to sharp increases with respect to the underlying trend. Techniques of signal processing exist to complete such series while adapting only to its envelope. A valuable example was provided by Jönsson and Eklundh (2004) who designed the TIMESAT algorithm based on a Savitzky-Golay filtering technique to extract the seasonality from time series of the normalized difference vegetation index (NDVI). As opposed to Jönsson and Eklundh (2004), who needed to accommodate the negatively biased noise of the NDVI data by fitting a curve to the upper envelope of the observations, the short-lived snow fall can be considered as positively biased noise that must be removed from the underlying persistent snow cover.

Savitzky-Golay filtering. Similarly to TIMESAT, filtering the raw SCA curves with an adaptation to the lower envelope was achieved by means of a two-steps Savitzky-Golay filter (Savitzky and Golay, 1964). The smoothing was obtained by a convolution of the observed signal with the following model function:

$$f(t) = \sum_{k=0}^M c_k \phi_k(t), \quad (8.8)$$

where $\phi_k(t)$ are arbitrary basis functions. Here the model function was simply a quadratic polynomial, i.e., the basis functions were $\phi_k(t) = t^k$, $M \leq 2$. The size of the convolution window determines the degree of smoothing and controls how the variations of the signal can be captured according to different time scales. A sliding window of $N = 60$ days was chosen because it could accommodate the largest

gaps in the time series and was capable of resolving sub-seasonal variations of the snow cover extent. Thus, it could depict the bimodal formation and depletion of a persistent snow pack, instead of a single monotonic depletion per year. Such a phenomenon is often observed in New Zealand [see for example the SCA curve of the Pukaki catchment during winter 2000 and 2003 in Figure 7.7 (a)].

8.3.4.1 Least-squares fitting and adaptation to the lower envelope

The time series of SCA in each zone were completed by connecting linearly the irregularly spaced observations. Then, the Savitzky-Golay filter was applied to find the best values for c_k within the sliding window positioned around the time step t_i , and retrieve the filtered value $f(t_i)$. This was done in the least-squares sense by solving the system of normal equations

$$\mathbf{A}^T \mathbf{A} \mathbf{c} = \mathbf{A}^T \mathbf{b}, \quad (8.9)$$

where $A_{ij} = w_i \phi_j(t_i)$ and $b(i) = w_i \text{SCA}_i$. w_i accounts for the weight of the i^{th} data point and it was set to 1 for all points during the first step. The adaptation to the lower envelope was obtained by comparing this first fit to the observations. The importance of data points that were above the curve, as well as the points created by the linear gap-filling, was reduced by applying a weight of 0.1, while a weight of 1 was retained for all actual observations that were below the first fit. The Savitzky-Golay filter was then repeated with the new weights and provided the continuous, gap-filled SCA curve that captured the lower envelope of the observations.

Examples of such curves in three zones of the Pukaki catchment are shown in Figure 8.10 to illustrate the performance of the technique. The PC4 zone (i.e., the 4th elevation band, close to the western 1200m contour, see Figure 8.2) accounts for most perennial snow and glacier surfaces. The fractional coverage exceeds 50% at all times. Figure 8.10 (PC4) demonstrates how the Savitsky-Golay filter allowed the data to be smoothed after the first fit, and adapted to the lower envelope after the second step, by successfully removing sharp peaks of short-lived snow falls in summer. In addition, using variable weights and retaining all observations enables the filter to accommodate the noise due to errors from the retrieval of the sub-pixel snow fraction (see Section 6.5.2).

For example, the SCA fluctuates during winter because of both the short-lived snowy episodes and errors of classification. The second fit does not necessarily match the smallest SCA observations, and thus it potentially mitigates the introduction of a negative bias to the SCA curve. The zones PM3 (i.e., the 3rd elevation

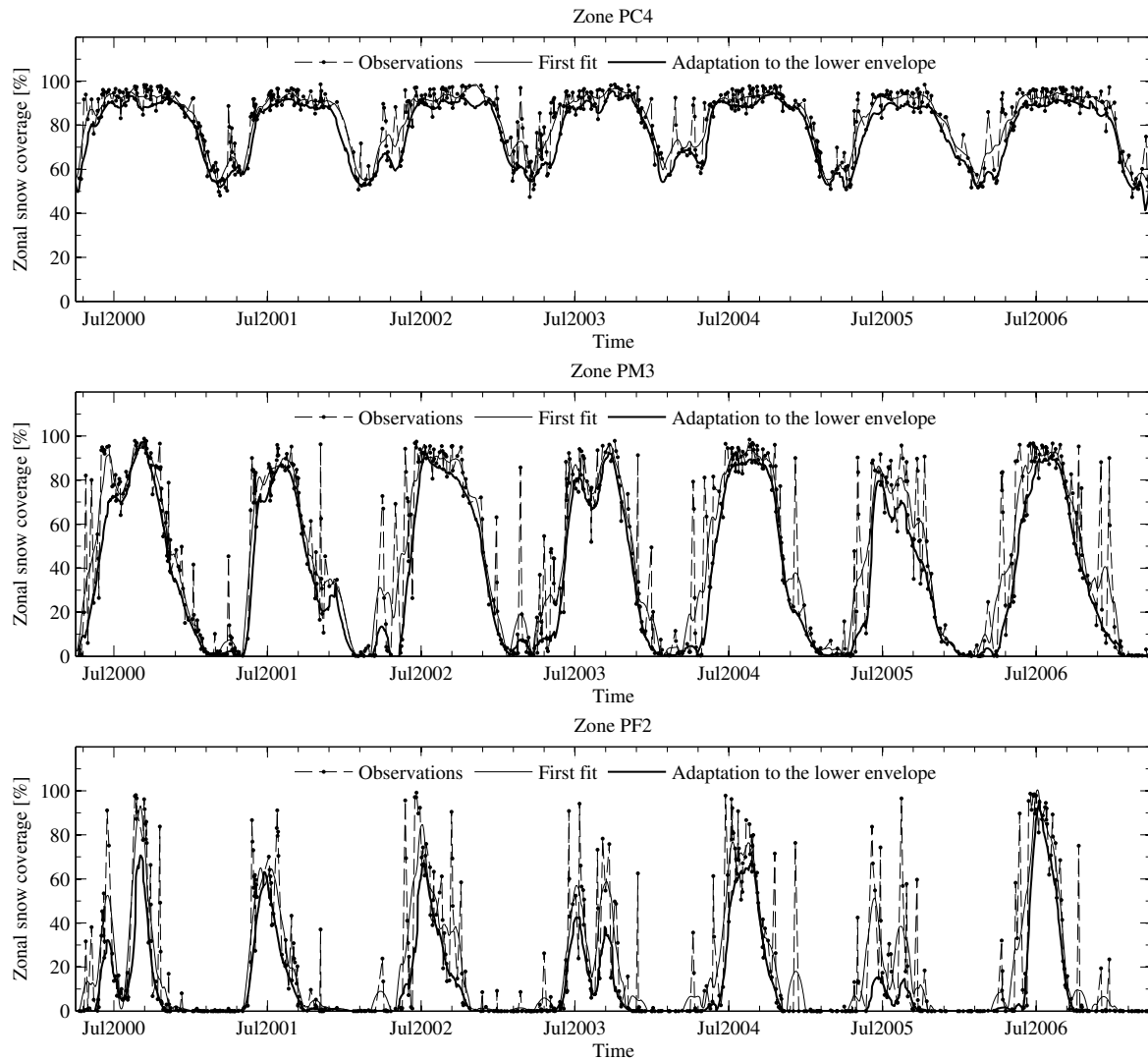


Figure 8.10 Interpolation of the snow cover area from MODIS using Savitzky-Golay filtering with adaptation to the lower envelope. Examples are given for three zones in the Pukaki catchment at various elevations and proximity to the main divide.

band at medium range from the western 1200m contour) and PF2 (i.e., the 2nd elevation band, far from the western 1200m contour) are clearly exposed to more frequent short-lived snow episodes. Again the two-step Savitzky-Golay filter performed well at removing the rapid changes, while retaining the underlying trend. Finally, the 60 day sliding window clearly permitted capture of sub-seasonal accumulation and depletion events. At high elevations, early snowfalls and cold temperatures often yielded a persistent snowpack at the start of the accumulation season. This early accumulation was often depleted within the next month, probably due to a temporary

mild spell. Only the subsequent snowfalls associated with a substantial decrease of the average temperature then accumulated into what could be considered as the seasonal snow pack.

The sub-seasonal variations of the snowpack are more readily visible at lower elevations, further away from the main divide. In particular, Figure 8.10 (PF2) captured the rapid depletion of the snow cover during the winters of 2000 and 2003, followed by a new accumulation episode. Figure 8.10 not only reveals how variable the pattern of snow cover accumulation and depletion can be from year to year, but it also demonstrates that the build up and subsequent depletion of snow cover is not necessarily monotonic in these catchments. This can compromise the use of a single depletion curve as it is often the case in applications of SRM elsewhere, and also confirms the need to model the snowpack throughout the year.

8.3.5 Forcing the melt factor

It was explained in Section 7.3.3 why and how the melt factor is expected to vary spatially and temporally. It generally decreases after a fresh snowfall, while it increases as the snow metamorphoses during the ablation season, because of the increase of water content and snow density, as well as the decrease of the albedo of the snowpack. Although it is now well established that melt models perform better when the melt factor is allowed to vary (Martinec and Rango, 1986; Rango and Martinec, 1995; Hock, 2005), the potential departure from a true physical property complicates its estimation. The seasonal variation of the melt factor is sometimes captured by means of a one-year period sinusoidal curve that oscillates between two extreme values (Hock, 2003). Additional but subjective adjustments may be introduced, such as a dependence with regard to the elevation (Fitzharris and Garr, 1995). More sophisticated approaches have tried to relate the melt factor to a physical property of the surface such as the albedo (Arendt and Sharp, 1999; Li and Williams, 2008). For example, it has been described how the SnowSim model implements a dynamic melt factor based on an empirical model of the snow albedo (Woo and Dubreuil, 1985) modified by punctual and seasonal adjustments (Kerr, 2005, see Section 7.4.1 of this thesis). Although the latter technique was designed to capture the short- and long-term variations due to the ageing of snow, rainfall, and seasonal compaction, it remains limited by the validity of the empirical model and the correct discrimination of snow versus rainfall episodes.

In this thesis, it is believed that linking the melt factor to an observed prop-

erty of the snow surface is more desirable than an uncertain and empirical parameterization of a dynamic degree-day. In particular, considerable efforts have been made towards the retrieval of the ground spectral reflectance from the MODIS images (see Chapter 4). Such standardized physical values observed at frequent intervals provided a new insight that could reveal changing within the snowpack. It is well established that the near-infrared (NIR) reflectance of snow is sensitive to the snow grain size and plays an important role in snowmelt (Warren, 1982). This was illustrated recently by Gupta *et al.* (2007) who established a clear relationship between the NIR reflectance and the elevation of melting snow. The decrease of the reflectance of melting snow with elevation could be explained by the increase in moisture and grain size in the melting zone. It is hypothesized that the relationship between the melt factor and the albedo can identically be applied to the NIR reflectance because of its similar capacity to reveal the ageing of snow and increase in water content, both generally corresponding to an increase in melt factor. Thus, the signal obtained from the corrected NIR band of MODIS (i.e., band 2 centred on 858 nm) was thought to be a relevant candidate to be used as a surrogate for the melt factor.

In order to assess the relevance of this hypothesis, the NIR reflectance of snow was explored with regard to its relationship with elevation and its evolution through time. First, the average reflectance of fully snow covered pixels was computed for selected dates in 2003 within 200m elevation bands. Figure 8.11 shows that the snow is generally more reflective at higher altitude, thus confirming the observations of Gupta *et al.* (2007). Although the relationship varies from day to day, it is consistent with the fact that the snowpack is expected to be dryer, and snow to have a finer grain size at higher altitudes. This would logically correspond to a melt factor being higher at lower elevations, where the snowpack tends to be denser, wetter, and whose lower albedo favours the absorption of shortwave radiation.

Second, the time series of the corrected NIR reflectance is plotted in Figure 8.12 for two ranges of elevation, from 1000m to 2000m, and above. Again, the greater reflectance of snow above 2000m is consistent with a more preserved snowpack. Moreover, the NIR signal depicts clearly a lowering trend of the snow reflectance during the ablation season, which reveals the progressive metamorphosis and compaction of the snowpack. Overall, the signal was consistent over the seven years. It indicates the ability of the atmospheric and topographic correction to retrieve consistent ground reflectance values.

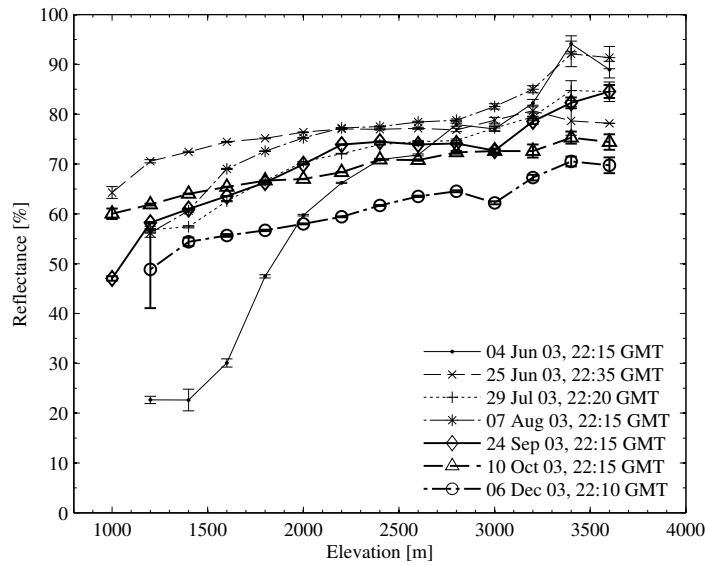


Figure 8.11 Average ground NIR reflectance (MODIS band 2, 858 nm) of not shaded, fully snow covered pixels versus altitude for selected dates. The error bars correspond to the 95% CI on the mean of the samples.

Figure 8.12 also reveals sharp increases of the NIR reflectance of snow. Among the 273 observations that indicated an increase of the SCA, 207 (75%) corresponded to an increase of the NIR reflectance. Conversely, 286 (71%) out of the 405 observations showing a decrease of the SCA revealed a decrease of the NIR reflectance. In other words, for more than 70% of the images, fresh snowfall yielded a larger NIR reflectance, while the depletion of the snow cover resulted in a lowered reflectance. This correlation demonstrates that the sudden rises of the NIR reflectance are unlikely to be artefacts of the correction process. Instead, it demonstrates the ability of the signal to capture new snow episodes as well as the seasonal evolution of the snowpack. It is believed that the consistency of the corrected NIR reflectance in space and time, and the fact that it accounts for most of the characteristics expected from the melt factor, justifies its use as a surrogate despite the lack of field experiments to confirm such a relationship. There could be scope for further investigation to determine the correlation. Without additional data, an arbitrary scaling to compute the melt factor in each zone was used as follows:

$$a = -0.75\bar{\rho}_{858 \text{ nm}} + 0.975, \quad (8.10)$$

where $\bar{\rho}_{858 \text{ nm}}$ is the mean of the corrected NIR reflectance of fully snow covered pixels in the corresponding zone. The scaling was chosen as to provide a reasonable

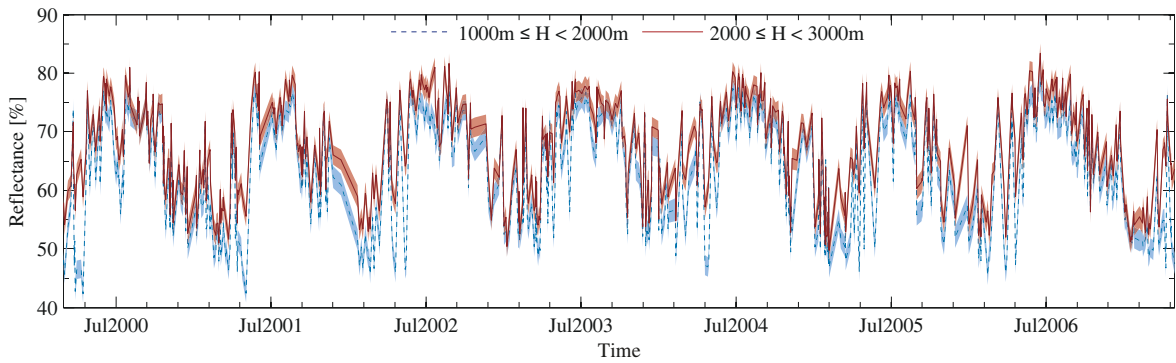


Figure 8.12 Time series of ground NIR reflectance (MODIS band 2, 858 nm) of not shaded, fully snow covered pixels. The dotted and solid lines represent the mean reflectance of pixels within $1500\text{m} \pm 500\text{m}$ and $2500\text{m} \pm 500\text{m}$, respectively. The coloured envelop represents $\pm 1\sigma$ of the samples.

range of melt factors from $3 \text{ mm} \cdot \text{C}^{-1} \cdot \text{day}^{-1}$ when $\rho_{858 \text{ nm}} = 90\%$, to $6 \text{ mm} \cdot \text{C}^{-1} \cdot \text{day}^{-1}$ when $\rho_{858 \text{ nm}} = 50\%$.

8.4 Estimation of model parameters

8.4.1 Goodness of fit measures

As introduced in Section 7.4.2, the *coefficient of determination* measures the goodness of fit between the predicted outcomes of a model and the real observations as follows

$$R^2 = 1 - \frac{\sum_i (x_i - y_i)^2}{\sum_i (x_i - \bar{x})^2}, \quad (8.11)$$

where x_i and y_i are the observed and the modelled values of a variable at the time step i , respectively. R^2 measures the fraction of the variance of the observed data that is explained by the model.¹ The latter is widely used in hydrological modelling with x_i and y_i being the observed and modelled discharge values, respectively. In this context, the criterion is known as the *Nash-Sutcliffe efficiency coefficient* (Nash and Sutcliffe, 1970; Martinec *et al.*, 2005, pg. 32). R^2 takes values ranging from $-\infty$ to 1, the latter meaning a perfectly fitted model. A negative value indicates that the variance of the errors is larger than the variance of the signal itself and the model

¹Note that since y_i is the outcome of a model, the coefficient of determination R^2 shall not be computed on the basis of a linear fit between y_i and x_i . Therefore, R^2 can be close but is not equal to the square value of the Pearson correlation coefficient, also referred to as the coefficient of determination.

is not achieving better predictions than the mean of the observations. It is generally considered that a hydrological model performs satisfactorily when R^2 exceeds 60% and well if it exceeds 80% (Duckstein *et al.*, 1985). In order to compare the results achieved in this thesis with the results obtained by Kerr (2005), the R^2 criterion was also computed on the observed and modelled discharge filtered with a 14-days running average and noted R^2_{14d} .

In addition to the Nash-Sutcliffe criterion, the normalized deviation between the predicted and observed runoff volume was used. It is defined as

$$D_v = 1 - \frac{\sum_i y_i}{\sum_i x_i}. \quad (8.12)$$

D_v provides an indication about the bias of the model, expressed as a fraction of the mean observed inflow. The criteria are generally computed for a single year but overall performances from several years can be measured:

- by averaging the criteria from each year; and
- by computing a single criterion on the basis of the combined outputs from all years under consideration.

In addition, the total modelled runoff volume combined from the three catchments over multi-year periods was computed and the normalized deviation with the observed total volume over the same period was considered as an additional overall indicator of the modelling performance.

8.4.2 Time lag

The *time lag* of a watershed measures the delay between the production of water in the basin (i.e., rainfall, snow and ice melt available for runoff) and the corresponding signal in the hydrograph. It is generally defined as the time elapsed between the centre of the area of the production time series, and the peak discharge, or the centre of the area of the resulting graph of direct runoff (Singh and Singh, 2001, pg. 285). The delayed response of a catchment is due to the time required by overland flow to travel from the most remote part of the basin to its outlet, the effect of channel storage, and the response time associated with the release of groundwater that is caused by water infiltrations and the rise of the water table.

The time lag of each basin was investigated by studying the cross-correlation between the daily precipitation and the mean daily inflow into the lakes. Fig-

ure 8.13 (a), (c), and (e) show the Pearson correlation coefficients between the precipitation received in each zone and the estimated inflow, calculated over the period 2000–2007. In the Pukaki and Tekapo catchments, the maximum correlation indicated a lag of two to three days depending on the proximity of the zones to the lake. The lag was only one to two days in the Ohau catchment. A clear example of the delayed response of the lake inflows compared to the precipitation received in the zone C4 (i.e., close to the main divide and above 2000m, see Figure 8.2) is illustrated in March 2003 in Figure 8.13 (b), (d), and (f).

These lags are considerably longer than what could be expected from watersheds of this size. For example, [Martinec and Rango \(1986\)](#) suggested that the time lag for a catchment whose area comprises between 680 and 2000 km² should be in the order of 10 to 12 hours. A conservative estimate of the time lag in the Pukaki catchment based on the equation provided by the Natural Resources Conservation Service ([Kent, 1972](#))

$$t_L = 0.342 \frac{L^{0.8}}{w_s^{0.5}} \left(\frac{1000}{CN} - 9 \right)^{0.7}, \quad (8.13)$$

with a hydraulic length $L = 120$ km, a curve number $CN = 50$, and a average slope $w_s = 20\%$ yields a time lag of only 19 hours. A large contribution of the ground-water input and the retention of rain by snow could partly explain the longer delay obtained from the cross-correlation. Moreover, since inflows are estimated on the basis of the water balance by monitoring lake levels, part of the delay can also be explained by the integrator effect of the storage reservoir.

Such a characteristic was observed by [Chikita *et al.* \(2004\)](#) in lake Kussharo (Japan) where the peak of the lake level rise occurs five hours later than the peak of the inflows from tributary rivers. Under the simplest assumptions, the lake level obeys an inhomogeneous first order linear differential equation whose time constant depends on the volume of the reservoir and the outflow resistance. It makes the lake behave as a transfer function that introduces a time response between the input (i.e., the inflow) and the output (i.e., the lake level). The forced response of the lake level to the dynamic signals of inflow and outflow prevents the system from reaching a steady state, in which case the lake level would be a direct measure of the inflow. Instead, a phase angle between the input and the lake level is introduced that can explain part of the lag. Lake Ohau is the smallest of the three reservoirs and exhibits the shortest lag, thus supporting this interpretation. Despite the differences of delay between zones and catchments, a lag of two days for all catchments was found to achieve the best synchronization between the modelled and observed discharge.

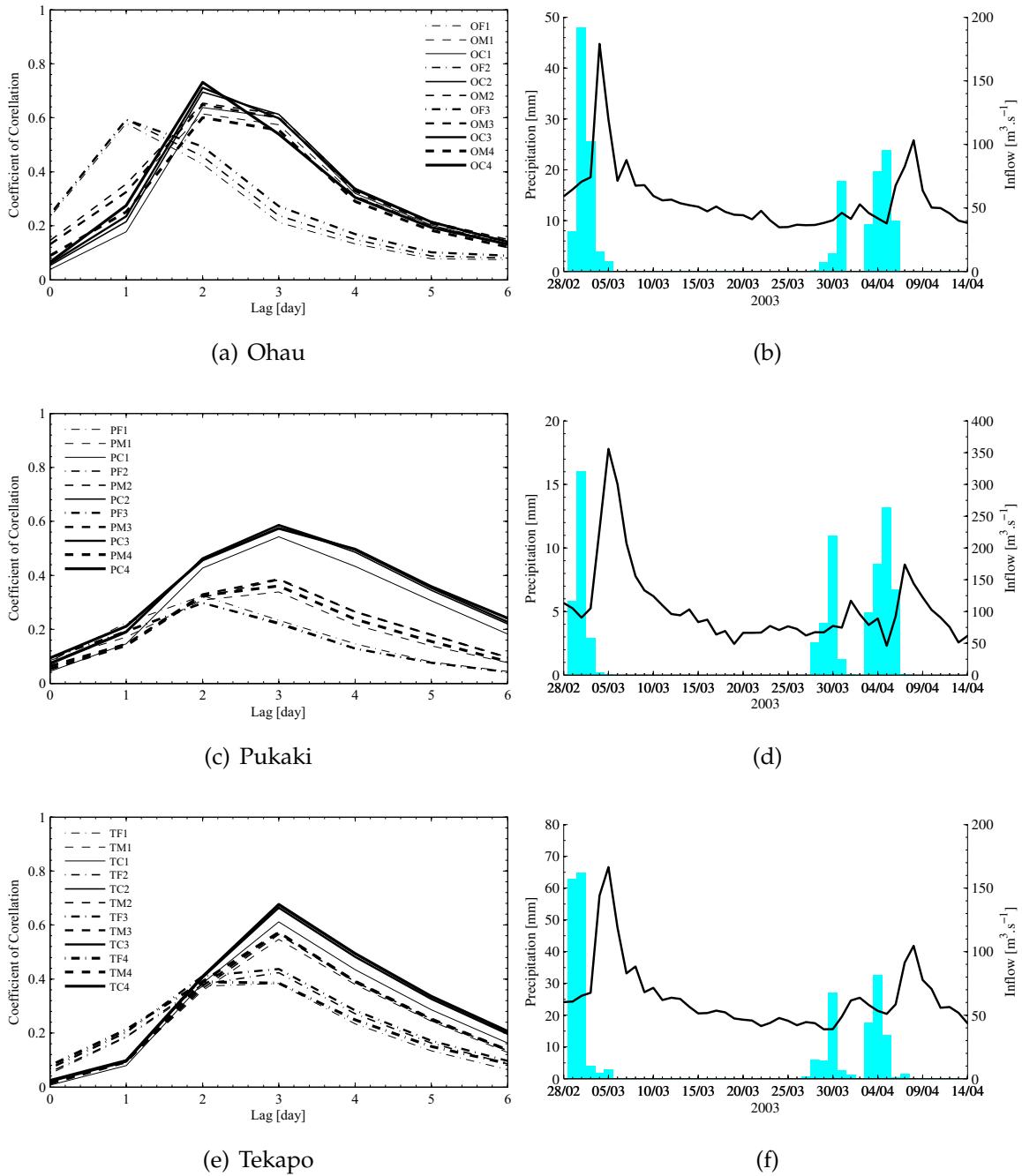


Figure 8.13 Left: Pearson correlation coefficient between the precipitation from each zone and the lagged discharge computed over the hydrological years 2000–2006. Right: example of the precipitation in zone C4 (i.e., close to the main divide and above 2000m) and corresponding lake inflow in March 2003.

8.4.3 Recession coefficient

The recession coefficient k is defined as the ratio between the discharge measured at day $n + 1$ and day n in the absence of new precipitation, snowmelt, or ice melt. It describes how the water produced in the catchment is released progressively. In a gauged basin, the recession phenomenon can be studied from the analysis of the hydrograph. A constant recession coefficient indicates that the catchment behaves as a linear reservoir. However, this hypothesis is rarely valid (Appendix G) and the recession coefficient often depends on the discharge itself as it is the case in the three catchments under consideration. Thus, in SRM, the recession coefficient is modelled by a function of the form

$$k_{n+1} = xQ_n^{-y}, \quad (8.14)$$

where x , and y are constants retrieved from the analysis of the historical hydrograph. Noise in the observed inflow complicated the estimation of x and y for each catchment. Preliminary values of the parameters were obtained based on the method given in [Martinec et al. \(2005, pg. 23\)](#) and described in Appendix G. They were refined on the basis of SRM simulations until the profile of the modelled recessions approached satisfactorily that of the observed discharge. More details are provided in Appendix G and the optimal parameters are given in Table 8.5.

Table 8.5 Parameters of the recession coefficient, k .

Catchment	Ohau	Pukaki	Tekapo
$k_{n+1} =$	$1.96Q_n^{-0.21}$	$1.50Q_n^{-0.13}$	$1.60Q_n^{-0.14}$

8.4.4 Estimation of the runoff coefficient c_r and c_s

The calibration of SRM is achieved primarily by adjusting the rainfall and snowmelt runoff coefficients [i.e., the parameters c_r and c_s in Equation (8.5)]. Both parameters have a physical meaning since they theoretically account for the losses between the actual precipitation or snowmelt and the water available for runoff ([Martinec and Rango, 1986](#)). As general rules, losses are expected to be small during winter and increase during the ablation season, due to a larger evapotranspiration and interception by growing canopies. On the other hand, [Martinec and Rango](#)

(1986) explained that the snow runoff coefficient is expected to increase by the end of the snowmelt period due to the direct channelling of melt water from the remaining snowpack.

In SRM, the runoff coefficients can be tuned daily and be addressed differently in each zone. Although a better fit for one year can then potentially be achieved, it complicates the calibration when the number of zones is large. Moreover, the multiplication of degrees of freedom can introduce an adverse effect on the performance of the model outside the calibration period. The purpose of this research was to achieve a robust calibration, so that discharge could be modelled satisfactorily over several years with only minor adjustments. Therefore, in the interest of simplification and robustness, the runoff coefficients were only allowed to vary on a monthly basis and irrespective of the zone or the year. The three hydrological years 2000, 2001, and 2002 (i.e., from the 1st of April until the 31st of March of the following year) were used for the calibration.

As a preliminary stage, the daily fields of precipitation were segmented into rainfall and snowfall by using a critical temperature T_c of 1.5°C. For each zone, the rainfall and the filtered SCA curves were used to determine a suitable set of runoff coefficients within the possible range (i.e., $\{c_r, c_s\} \in [0, 1]^2$). The fit of the model was assessed using the R^2 and D_v criteria. A Monte-Carlo approach was tested to find optimal monthly values for c_r and c_s in each catchment. Good simulations could be obtained with this method but the parameters were not consistent between years. The mean parameter values yielded poor modelling performances, thus suggesting that the parameters found by the statistical approach only corresponded to local minima and failed to provide a robust calibration. Alternatively, the coefficients were manually adjusted on the basis of the indications provided by [Martinec et al. \(2005\)](#) outlined above. Multiple runs were processed and assessed using the R^2 and D_v criteria, as well as visual judgment until acceptable performances were achieved simultaneously for the three calibration years.

Figure 8.14 shows the runoff coefficients determined for each catchment. The rainfall runoff coefficient c_r required only little change over the year and followed a similar pattern in each catchment. Only a moderate reduction of c_r in spring (i.e., September to December) was needed. An increase of evapotranspiration and vegetation growth could explain larger losses in spring and summer. Nevertheless, increasing c_r back to its original level as early as January was required to capture rainfall events better in the hydrograph. The snow runoff coefficient c_s was found

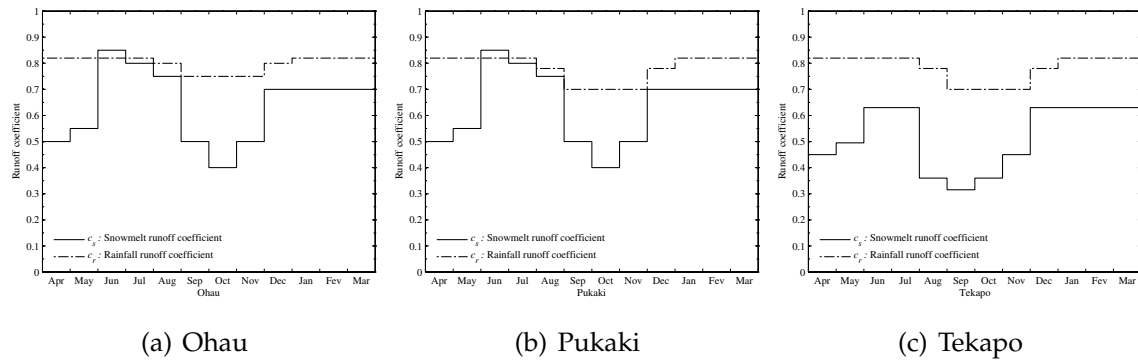


Figure 8.14 Runoff coefficients.

to be relatively low at the start of the accumulation season (i.e., April and May). It was increased to its maximum in winter but was decreased rapidly in spring to accommodate the observed runoff signals. Toward the summer, c_s was increased following an earlier pattern than suggested by [Martinec *et al.* \(2005, pg. 20\)](#).

Although the runoff coefficients are physically designed to represent losses, they remain the primary candidates to adjust the modelled discharge. The interpretation of the variation of c_r and c_s remains complicated because both parameters accommodate errors in the forcing data, as well as the limitations inherent to the modelling strategy. For example, summer is the ablation period for glaciers but SRM does not include a routine to estimate ice melt. Some contribution from glacier melt is accounted for through the mapping of ice surfaces in the SCA curves. However, ablation from the debris-covered parts of glaciers and from calving in the terminal lake, cannot be addressed. It is therefore reasonable to expect the discharge from January to March to be underestimated by the model.

The increase in runoff coefficients as early as January is not necessarily due to a reduction of losses only, but can also indicate a contribution of ice melt that is underestimated by SRM. It is evident from Equation (8.5) that part of the variation of c_s can accommodate some changes of the melt factor. Larger values of c_s in summer may indicate that the melt factor was larger than expected. The melt factor estimated by scaling the NIR reflectance (see Section 8.3.5) rarely exceeded $6 \text{ mm} \cdot ^\circ\text{C}^{-1} \cdot \text{day}^{-1}$ although values of $7 \text{ mm} \cdot ^\circ\text{C}^{-1} \cdot \text{day}^{-1}$ and over are often encountered for glacier surfaces ([Kirkbride, 1995](#); [Hock, 2003](#)). During summer, when ice becomes exposed, an underestimation of the melt factor by 15% requires an overestimation of c_s by nearly 18% to achieve the same amount of melt. In other words, if the melt factor

was adjusted to reach $7 \text{ mm} \cdot \text{C}^{-1} \cdot \text{day}^{-1}$ instead of $6 \text{ mm} \cdot \text{C}^{-1} \cdot \text{day}^{-1}$ over this period, then the value of c_s estimated to be 70% from December to March in the Ohau and Pukaki catchments, and 63% in the Tekapo catchment, should be reduced to 60% and 53%, respectively. Nevertheless, the runoff coefficients did not depart enough from the recommendations given by [Martinec *et al.* \(2005\)](#) as to provide a solid basis for reviewing the melt factor. It was believed to be more desirable to keep the forcing data unchanged, and to consider the runoff coefficients as the primary variables of adjustment, despite the difficulties introduced with regard to the interpretation of their variations.

Table 8.6 summarizes the outputs obtained with these coefficients, and Figure 8.15 illustrates the simulation results compared to the observed discharge over the calibration period. This set of coefficients achieved simulations in all catchments with average R^2 criteria of 76%, 81%, and 80% in Ohau, Pukaki, and Tekapo catchments, respectively. R^2_{14d} in the Pukaki catchment from April 2002 until March 2003 reached 87% compared favourably with 74% obtained by [Kerr \(2005\)](#) with SnowSim-Pukaki. This illustrates the substantial improvement provided by the SRM approach. The overall R^2 values calculated from the combination of the three annual hydrographs slightly exceeded the arithmetic mean and confirmed that the discharges were satisfactorily modelled over the three year period (see Figure 8.15).

The best R^2 values were obtained during the hydrological year 2001. This year was characterized by less intense rainfall events in winter compared to 2000 and 2002 (Figure 8.15, centre column), and two major rainstorms in December and January (i.e., the peak discharge in Lake Pukaki reached 900 and 1500 $\text{m}^3 \cdot \text{s}^{-1}$). The extreme variance of the observed discharge in 2001 had an artificially positive effect on the R^2 criteria in all basins. Nearly 90% of the variance of the observed signals was accounted for by the simulations. Conversely, the worst R^2 values corresponded to the 2002 hydrological year when the observed inflow had the least variance. The total runoff volume was generally underestimated (i.e., $D_v > 0$) with an overall bias for all catchments combined that reached 2.5% of the observed volume.

8.4.5 SRM, the critical temperature and the “new snow reservoir”

Despite the near-daily repeat time of MODIS, the frequent cloud coverage prevents the identification of short-lived snowfalls with sufficient detail to enable the use of the raw SCA curves. It was explained in Section 8.3.4 how the signal was processed to filter out such events while retaining only the long-lived snow cover, i.e.,

Table 8.6 Performance criteria obtained from the calibration of the runoff coefficients.

	Year	Ohau			Pukaki			Tekapo			All
		D_v [%]	R^2	R^2_{14d}	D_v [%]	R^2	R^2_{14d}	D_v [%]	R^2	R^2_{14d}	D_v [%]
Calibration	2000	5.1	0.78	0.83	-4.0	0.84	0.87	4.0	0.70	0.69	-0.3
	2001	8.6	0.86	0.96	6.0	0.89	0.95	1.9	0.89	0.96	3.1
	2002	4.2	0.65	0.80	-2.5	0.71	0.87	3.4	0.80	0.86	5.8
	2000–2002 ^a	6.0	0.76	0.86	-0.2	0.81	0.90	3.1	0.80	0.84	3.1
		5.8	0.78	0.88	-0.3	0.85	0.92	3.1	0.82	0.89	2.5

^a For overall results, the first line provides the mean of the measures from each year; the second line is the measure computed from the combination of the hydrological years into a single signal.

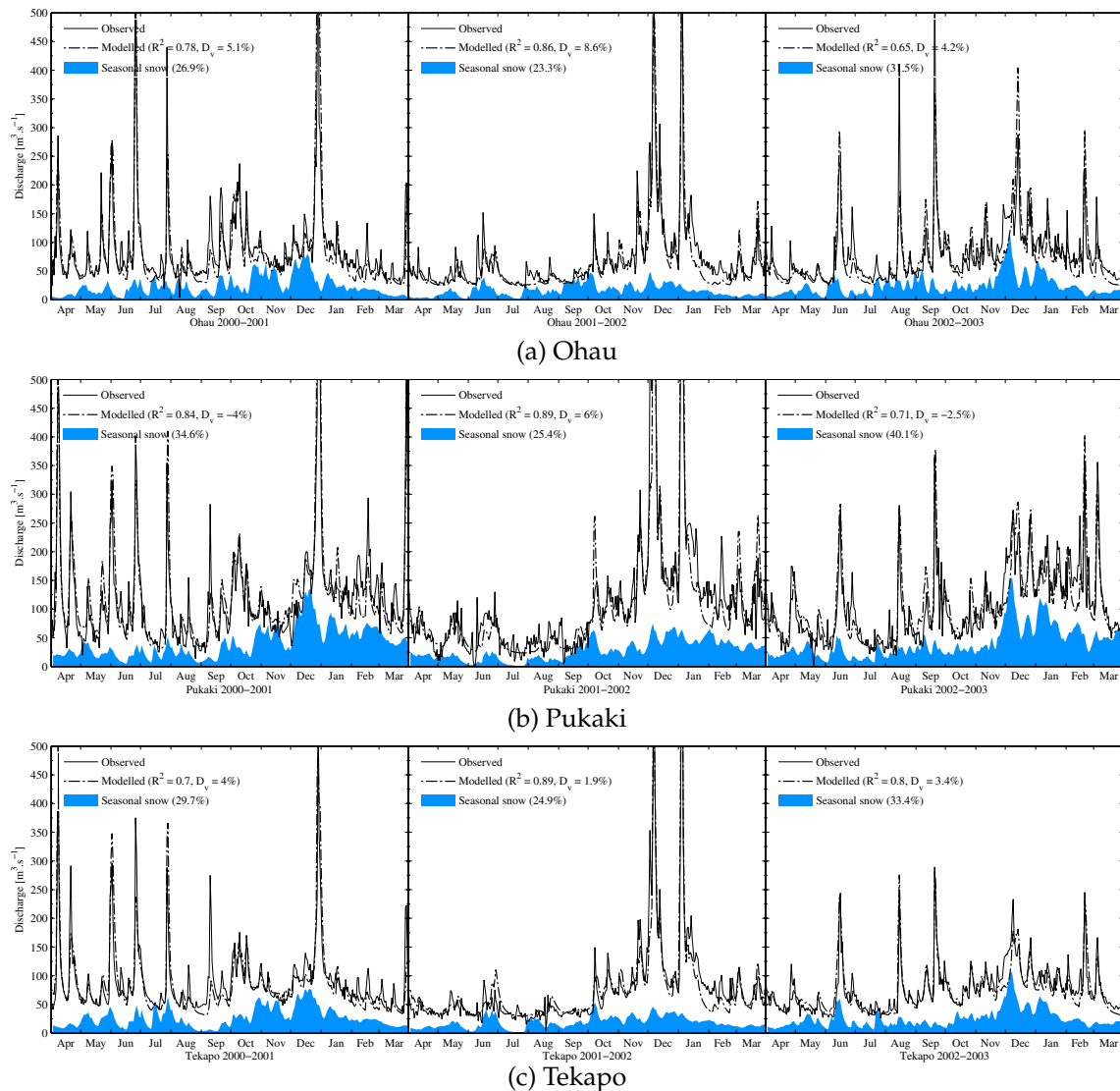


Figure 8.15 Observed and modelled hydrographs over the calibration period. Note that the plots are limited to a maximum runoff of $500 \text{ m}^3 \cdot \text{s}^{-1}$ for clarity.

the snow that last for more than a month, and thus contributes to the seasonal and potentially long-term storage. Nevertheless, the short-lived snow cover can store a substantial amount of water that can be rapidly released in the catchment. SRM accounts for the snow falling in addition to that represented by the filtered SCA curve by means of a *new snow reservoir* whose storage is governed by a classic routine of snow accumulation and ablation.

A critical temperature T_c is applied to the field of mean temperature T_{mean} to determine whether the zonal precipitation must be treated as snow or rain. When snow is inferred (i.e., $T_{\text{mean}} < T_c$), then the amount of precipitation in the zone is treated in two ways:

1. the fraction of the precipitation that corresponds to the relative share of snow cover area determined by the SCA curve of the zone is ignored;
2. the complement is stored temporarily in the new snow reservoir, whose delayed release is controlled by the degree day method.

As for SnowSim and other accumulation-ablation snow models, this additional snow routine is prone to the propagation and accumulation of errors. However, it only deals with a relatively low amount of water compared to models that rely exclusively on the accumulation-ablation strategy. Thus, it is reasonable to expect the magnitude of such errors to have a lesser impact on the modelling performance. In SRM, critical temperatures can be changed daily during the model calibration. It permits mitigation of the uncertainties associated with the interpolation of the temperature field and the inherent variability of the critical temperature itself (Braun, 1991). However, as mentioned in the previous section, it is believed that a single and robust value of T_c is preferable so that SRM can be run over several years with only minimum adjustments. Several runs of SRM were processed for each catchment during the three calibration years (i.e., 2000, 2001, and 2002) using the runoff coefficients determined in the previous section and values of T_c ranging from 0.5°C to 4°C. D_v and R^2 values were averaged and plotted as a function of T_c in Figure 8.16.

Clearly, a critical temperature too low yields overestimations of the total runoff volume (i.e., $D_v < 0$). Indeed, some precipitation can be falsely considered as direct rainfall although it is more likely to be snowfall. However, part of the snow is already counted for by the SCA curve, thus resulting in a fraction of the precipitation that is accounted twice. Conversely, when T_c is set too high, direct rainfall is stored

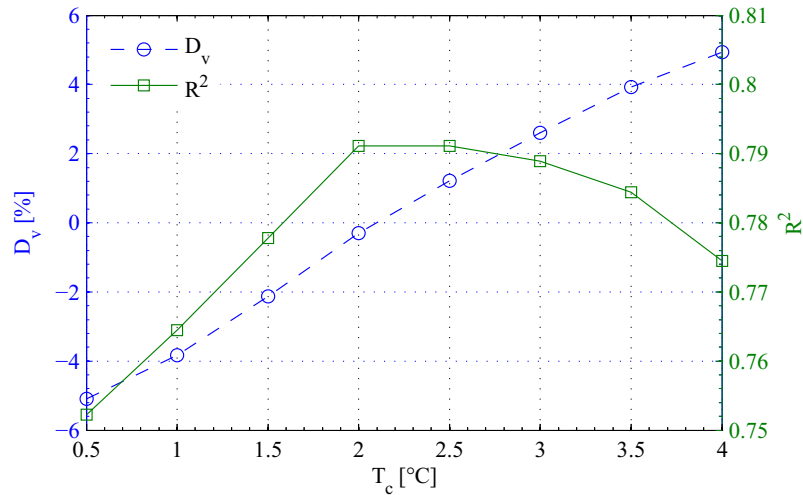


Figure 8.16 Goodness of fit criteria averaged over all catchments and calibration years depending on the critical temperature T_c .

by SRM. The fraction corresponding to the extent covered by the SCA curve is ignored, thus resulting in an underestimation of the total runoff.

A critical temperature set to 2°C was found to be optimum since it yielded only a little bias overall and corresponded to a maximum of the averaged Nash-Sutcliffe criteria. This threshold is meaningful because snow is expected to fall at slightly positive temperatures. However, it must be noted that the mean daily temperature obtained from the average of maximum and minimum temperature is generally an overestimation of the true daily mean temperature due to the shorter duration of high than of low temperatures (Aslyng and Stendal, 1965; Ca'zorzi and Fontana, 1986; Kerr, 2005). Kerr (2005) reported overestimation of 0.4°C on average. This suggests that the value of T_c determined above would correspond to a critical temperature of 1.6°C if a better estimate of the mean daily temperature were available from more frequent observations.

8.5 Simulation Results

8.5.1 Verification of the model performance

The performance achieved by the models over the calibration period is shown in Table 8.7. The final calibration of the critical temperature achieved average R^2 values of 77%, 81%, and 78%, and average D_v values of 3.4%, -1.7%, and 1.6% in the

Table 8.7 Performances obtained over the calibration and verification periods.

	Year	Ohau			Pukaki			Tekapo			All
		D _v [%]	R ²	R ² _{14d}	D _v [%]	R ²	R ² _{14d}	D _v [%]	R ²	R ² _{14d}	D _v [%]
Calibration	2000	2.4	0.76	0.83	-5.4	0.83	0.85	1.1	0.73	0.74	-1.3
	2001	6.2	0.86	0.94	3.4	0.88	0.95	1.5	0.89	0.96	3.4
	2002	1.6	0.69	0.81	-3.1	0.71	0.87	2.1	0.72	0.82	0.0
	2000–2002 ^a	3.4	0.77	0.86	-1.7	0.81	0.89	1.6	0.78	0.84	0.7
		3.3	0.78	0.87	-1.9	0.85	0.91	-1.5	0.82	0.89	0.6
Verification	2003	-1.1	0.73	0.89	0.7	0.80	0.90	-3.8	0.78	0.85	-1.1
	2004	7.4	0.65	0.87	5.4	0.79	0.89	6.4	0.73	0.84	6.3
	2005	1.2	0.65	0.76	16.8	0.75	0.84	8.8	0.73	0.77	10.3
	2006	-4.1	0.64	0.74	12.5	0.78	0.84	12.1	0.79	0.89	7.5
	2003–2006	0.8	0.67	0.82	8.8	0.78	0.87	5.9	0.76	0.84	5.7
		0.7	0.67	0.83	8.4	0.79	0.88	5.6	0.78	0.86	5.3
	2000–2006	1.9	0.71	0.83	4.3	0.79	0.88	4.0	0.77	0.84	3.6
		1.9	0.74	0.85	3.9	0.82	0.89	3.8	0.80	0.88	3.2

^a For overall results, the first line provides the mean of the measures obtained from each year; the second line corresponds to the measure computed into a single signal from the combination of the hydrological years.

Ohau, Pukaki, and Tekapo catchments, respectively. As a result, the models were considered to be satisfactorily calibrated for each catchment.

The three models were then run with the same parameters over the hydrological years 2003–2006 to assess their performance and robustness. The goodness of fit obtained from the annual and overall simulations is provided in Table 8.7. The simulated and observed hydrographs from each catchment are shown in Appendix H and reveal the contribution of the snow components (i.e., the seasonal and the short-lived snow). Over the verification period, the averaged R² criteria were 2% and 3% less than those obtained during the calibration period in the Tekapo and the Pukaki basins, respectively, but dropped 10% in the Ohau catchment. The worst R² value was 64% and was obtained from April 2006 until March 2007 in the Ohau basin. On average the R² coefficient over the verification period in the Pukaki basin was 78%, thus outperforming by 8% the simulation of Bowden (1994) made on a single calibration year.

R²_{14d} values were computed to enable a comparison with Kerr (2005). The 14-day running average filter applied on both the modelled and observed discharges artificially reduced the variance of each signal. This statistical effect improved the

Nash-Sutcliffe efficiency coefficient generally by 10%. Over the verification period, the mean R^2_{14d} criteria obtained in the Pukaki basin reached 87% and compares to 61% obtained by Kerr (2005) with SnowSim-Pukaki. When the seven years were combined into a single signal, the models obtained overall R^2 values of 74%, 82%, and 80%. In all cases, this overall R^2 was 3% more than the averages of the yearly R^2 values (see Table 8.7). The latter compared well with successful implementations of SRM compiled by Martinec *et al.* (2005) (i.e., the mean R^2 from 87 applications worldwide is 80%). Given the extreme climate in the region and the complex discharge signals (see Appendix H), these modelling performances demonstrated the success and robustness of the modelling strategy. With respect to the Pukaki catchment, the modelling performance provided undeniable improvements over the previous attempts conducted by Bowden (1994) and Kerr (2005).

Although the R^2 criterion assessed that most of the variance of the discharge signals was modelled accordingly, the total inflow estimated during the verification period was substantially underestimated in the Pukaki and the Tekapo catchments ($D_v = 8.8\%$ and 5.9% , respectively). The most severe underestimations occurred from April 2005 until March 2007 and reached 16.8% in 2005 in the Pukaki basin. The corresponding hydrographs (see Figures H.2 & H.3 in Appendix H) revealed that the modelled discharge exhibited a nearly homothetic translation compared to the observation from December to March. This underestimation during the ablation seasons was confirmed by the cumulative discharge of both catchments shown in Figure 8.17. Although the total runoff volume was correctly estimated from April to October by the models, the latter departed progressively from the observations during the summer.

8.5.2 Interpretation of the model performance

The worst performances obtained in the Ohau basin with respect to the R^2 criterion can be imputed to several factors. First, it was discussed in Section 8.3.3 that the pattern of rainfall in Ohau is more complicated than in Pukaki and Tekapo. The NZMS long term annual rainfall surface clearly suggests that the distribution of rainfall in Ohau departs substantially from a simple profile [see Figure 8.7]. Moreover, the accuracy of the rain field interpolation can be compromised by the fact that the climate station in the northern part of Ohau (ID: 39981) does not record representative amounts of rainfall. The multiplying factor that was applied to this station is merely empirical, and remains an unsatisfactory correction that may ultimately

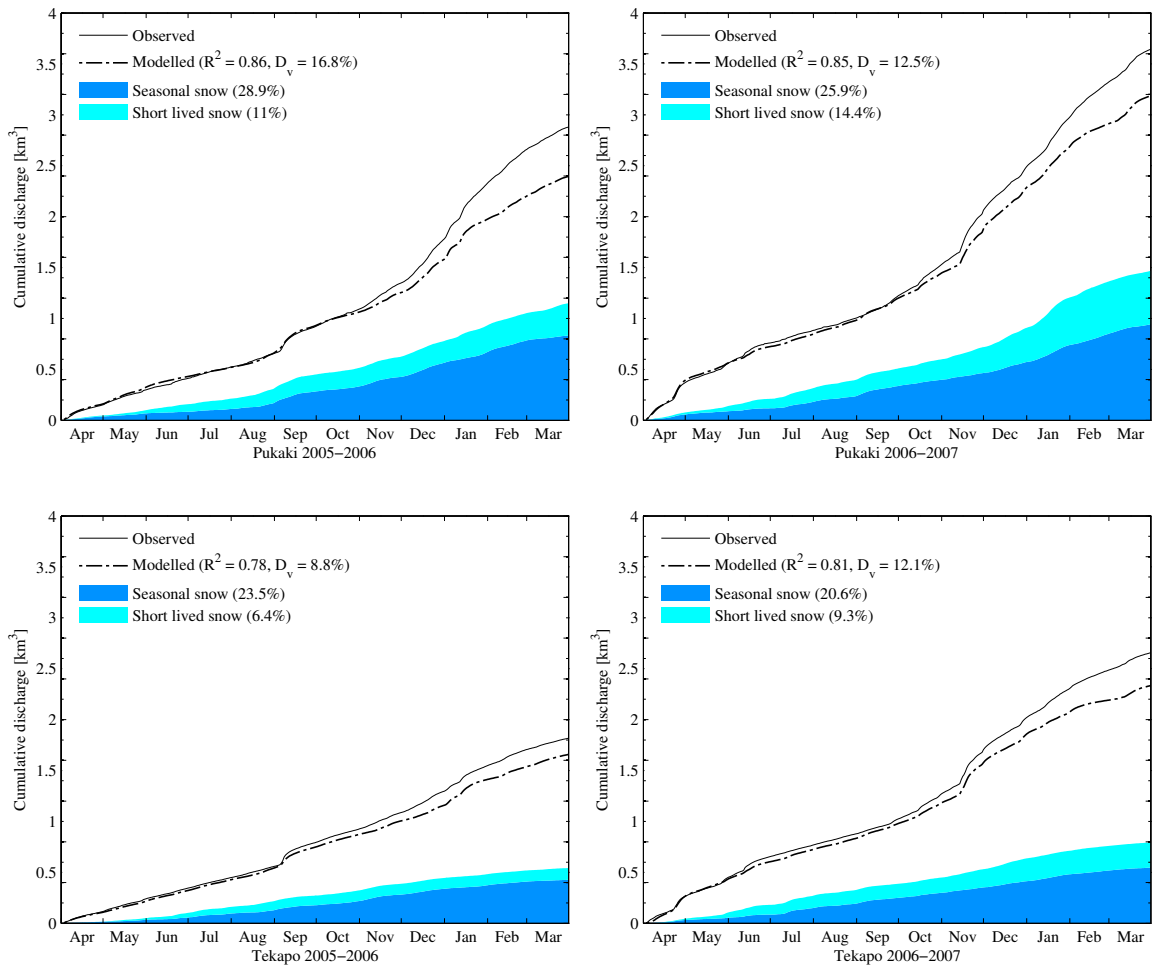


Figure 8.17 Cumulative discharge in the Pukaki (top) and the Tekapo (bottom) catchments for hydrological year 2005 and 2006.

affect the correct depiction of rainfall events in this region. Finally, the observed daily discharge of the Ohau basin exhibits the smallest variance. This alone tends to generate lower R^2 values than in Tekapo and Pukaki catchments.

Despite the lower R^2 values, the SRM performance in Ohau contrasted with Pukaki and Tekapo as it achieved a better D_v . In fact, the underestimation of the total runoff exhibited several patterns. Over the verification period, the total runoff was underestimated by 8.8% in Pukaki, 5.9% in Tekapo, and 0.8% in Ohau (see Table 8.7). On an annual basis, the hydrological years 2005 and 2006 were the most affected. Finally, on a monthly basis, the underestimation generally occurred during the ablation season. From the latter aspect, and given that SRM does not specifically address glacier melt (apart from the fraction of the ice surface accounted for by the

SCA curves), it is reasonable to venture the hypothesis that the contribution of ice melt is undervalued and caused the model's underestimation.

This interpretation is supported by the comparison between the annual total runoff volume and total precipitation received in each catchment. The regulating role of glaciers on river flow and especially their capacity to release water during warm/dry periods is now largely recognized (Anderton, 1973; Jansson *et al.*, 2003; Casassa *et al.*, 2009). Studies have also highlighted the effect of the ratio of basin ice-cover on the variation of runoff (Koboltschnig *et al.*, 2007). Fountain and Tangborn (1985) and Chen and Ohmura (1990) have shown that the variability of the annual runoff from a catchment decreases as the share of ice cover increases from 0 up to around 40%.

Figure 8.18 reveals that the Ohau, Pukaki, and Tekapo catchments accommodated differently the variations of precipitation over the study period. The variations of total runoff in the Ohau basin followed closely those of the precipitation, whereas the latter appeared to be mitigated in the Tekapo and Pukaki catchments. This was especially true during the severe drought in 2005, when the Ohau, Pukaki, and Tekapo catchments received 24.9%, 34.5%, and 31.5% less precipitation, respectively, than the average computed over the seven year study period. This deficit of precipitation only corresponded to 21.8%, 16.7%, and 25.6% decrease of total runoff, respectively. In other words, in 2005, the reduced precipitation was largely, substantially, and poorly mitigated in the Pukaki, Tekapo, and Ohau basins, respectively.

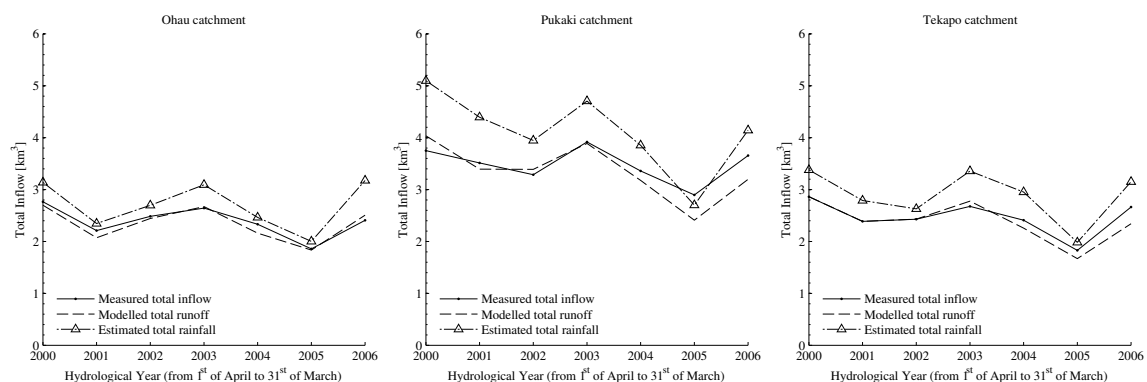


Figure 8.18 Total precipitation and discharge in each catchment during the study period.

Although not enough data were available to support a statistical relationship,

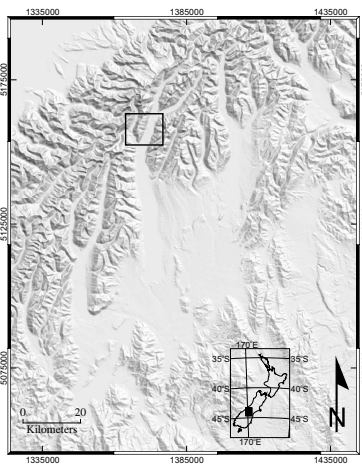
this pattern agreed with the glacierized fraction of the catchment area (see Table 8.4), the glacierized area being the largest for Pukaki and the smallest for Ohau. In the Pukaki basin, the total runoff volume exceeded the total precipitation in 2005, further suggesting that a release of long term stored water occurred. The overall D_v values, as well as the annual pattern of D_v with respect to that of the precipitation, were consistent with the proportion of glacier and perennial snow area of the catchments.

A time series of annual satellite observations of the main glacier terminal lakes in the Pukaki catchments gave additional evidence to strengthen this interpretation. Using Landsat and ASTER images processed for the purpose of this thesis, Strong (2008) documented the retreat of the Tasman glacier over nearly two decades. Figure 8.19 illustrates the combination of calving and merging of supraglacial ponds that drove the expansion of Lake Tasman over the study period. Figure 8.20 reveals clearly that the rate of lake growth significantly increased between 2004 and 2007 as the lake margin collapsed, showing that the drought was concurrent with a period of fast retreat of the glacier. Although no rigorous mass balance measurements were available for the glaciers in the area to confirm an increase of glacier melt water, this specific event matched well the timing of the modelling discrepancies. In addition to the fact that larger underestimations were observed during the ablation season, this forms a consistent body of clues supporting the interpretation that the underestimation of SRM is likely to be related to the misrepresentation of glacier ablation during this period.

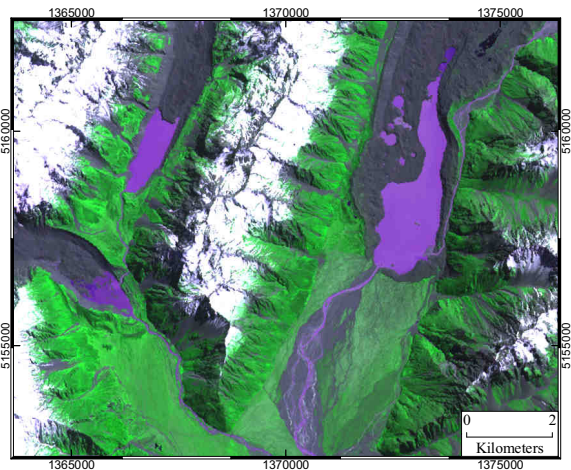
8.5.3 Final adjustment of SRM and determination of the stored water component

8.5.3.1 Model adjustments

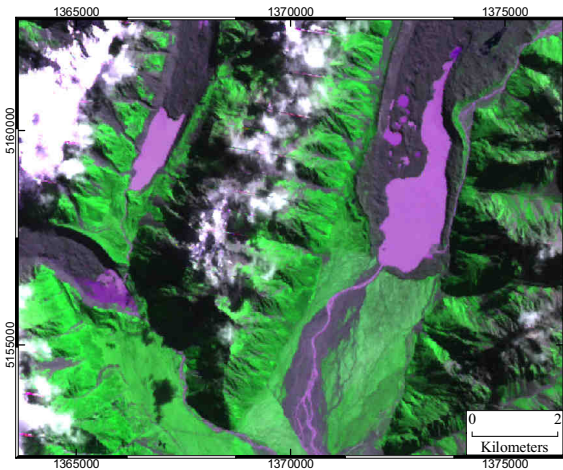
Convincing and consistent evidence strongly suggests that the large discrepancies between the observed and modelled volume discharge could reasonably be attributed, at least for its major fraction, to the contribution of glacier melt. Since SRM does not account specifically for this component of the water balance, the models were manually adjusted until they achieved a better agreement with regard to D_v . This was done by increasing the monthly value of the snow runoff coefficient c_s independently for each year and during the ablation season only, until both the modelled and the observed hydrographs matched reasonably well. This operation



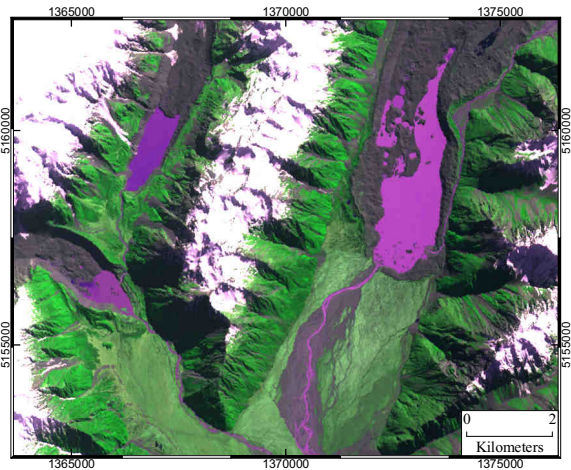
(a) Map of situation



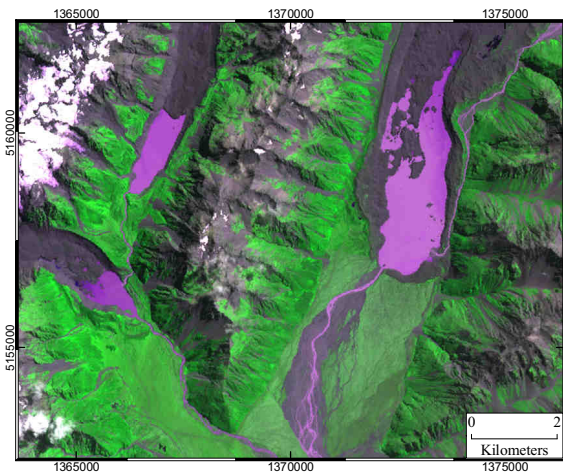
(b) 24/02/2003 ASTER



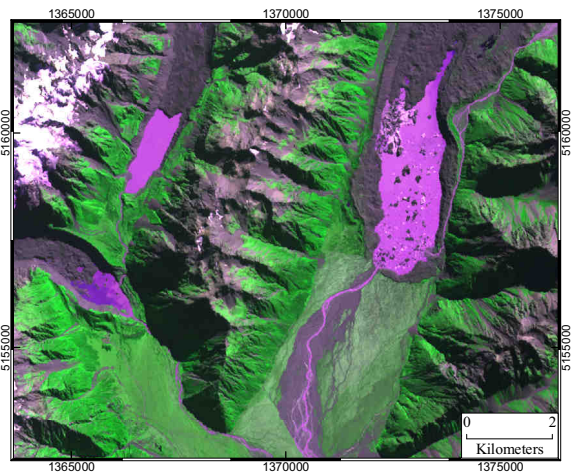
(c) 23/03/2004 ETM+



(d) 09/09/2005 ASTER



(e) 09/02/2006 ASTER



(f) 08/04/2007 ASTER

Figure 8.19 Growth of the glacier terminal lakes in the Pukaki catchment between 2003 and 2007.

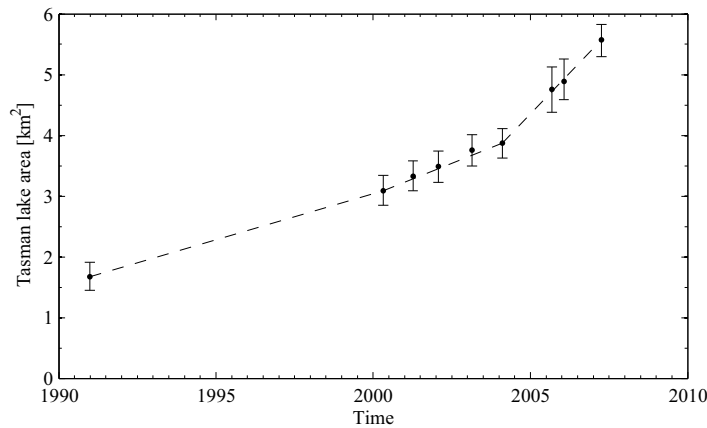


Figure 8.20 Growth of Tasman Lake as interpreted from ASTER and Landsat imagery.

was equivalent to introducing a larger melt factor than the one modelled using the near infrared ground reflectance. This resulted in increasing the melt water from the area of seasonal snow and exposed ice represented by the SCA curves. It could also accommodate the release of melt water by the glaciers from areas that are ignored by the SCA curves, such as melt occurring under the debris cover and calving into the terminal lakes (see [Purdie and Fitzharris, 1999](#)).

The hydrographs from the adjusted models are provided in Appendix I, while the final performance of the simulations are given in Table 8.8. The additional runoff introduced by these manual adjustments was attributed to long term water storage (i.e., ice), and thus completed the water storage associated with seasonal and short-lived snow. It must be pointed out that the subjective approach used for calibration and adjustment of the models introduced necessarily some degree of uncertainty with regard to the boundary between the melt water attributed to the seasonal snow or the long term storage. For instance, if the calibrated values of c_s determined in Section 8.4.4 were set lower during the ablation season (as they may well be), then the relative proportion of the seasonal snow would appear reduced in favour of the melt water considered to originate from the glaciers. Unfortunately, without data or models available to assess more accurately the contribution of glaciers to the inflow during the calibration period, there was no solid basis to review the calibrated values of c_s . Thus, it is possible that the relative proportion of the long term storage estimated from the models (i.e., provided by the adjustment of c_s) is offset relative to that of the seasonal snow (i.e., provided by the calibrated value of c_s). One can only assume that the loss associated to the seasonal snow during the ablation season

Table 8.8 Performances obtained after manually adjusting the snow runoff coefficient during the ablation season.

	Year	Ohau			Pukaki			Tekapo			All
		D _v [%]	R ²	R ² _{14d}	D _v [%]	R ²	R ² _{14d}	D _v [%]	R ²	R ² _{14d}	D _v [%]
Calibration	2000	0.6	0.77	0.84	-7.6	0.83	0.85	-2.6	0.75	0.81	-3.9
	2001	5.2	0.85	0.94	-0.9	0.88	0.95	-1.6	0.88	0.95	1.1
	2002	-0.5	0.70	0.82	-5.7	0.72	0.89	-0.4	0.73	0.85	-2.5
	2000–2002 ^a	1.8	0.77	0.87	-4.1	0.81	0.90	-1.5	0.79	0.87	-1.8
		1.6	0.78	0.88	-4.3	0.85	0.91	-1.7	0.82	0.91	-1.8
Verification	2003	-1.8	0.73	0.90	-0.8	0.79	0.89	-5.5	0.78	0.85	-2.5
	2004	5.6	0.65	0.86	-0.1	0.82	0.94	2.0	0.76	0.91	-2.3
	2005	-0.5	0.64	0.74	-3.4	0.86	0.96	0.9	0.78	0.90	-1.8
	2006	-6.3	0.64	0.73	-2.4	0.85	0.94	5.0	0.81	0.93	-0.4
	2003–2006	-0.7	0.67	0.81	1.2	0.83	0.93	0.6	0.78	0.90	0.5
-0.9		0.69	0.82	1.1	0.82	0.93	0.5	0.80	0.90	0.3	
2000–2006	0.3	0.71	0.83	-1.1	0.82	0.92	-0.3	0.78	0.89	-0.5	
	0.2	0.74	0.85	-1.2	0.84	0.92	-0.4	0.81	0.90	-0.6	

^a For overall results, the first line provides the mean of the measures obtained from each year; the second line corresponds to the measure computed from the combination of the hydrological years into a single signal.

does not vary too much from year to year. In such a case, all years can be considered to be similarly affected by this limitation. Thus, the annual variation of the relative proportion of both components could still be reasonably interpreted.

The hydrographs presented in Appendix I demonstrate the satisfying performance achieved by the models, as well as a realistic partitioning of the stored water components. The adjustments were mostly limited to January, February, and March, but the hydrological years 2005 and 2006 required an increase of c_s as early as October or November, depending on the catchment. The R^2 values slightly increased as the result of reducing the modelling error during the ablation season. Of course, the subjectivity of this manual approach prevented consideration of the D_v values as a representative measure of the modelling performance. At the most, it demonstrates that good simulation (i.e., simultaneously acceptable R^2 and D_v values) could be obtained using the calibrated models along with limited but subjective adjustments during the ablation season.

8.5.3.2 The long term storage

Figures I.2 & I.3 in Appendix I picture how the contribution of ice melt increased in 2004, 2005, and 2006 compared to the previous years, in the Tekapo and in the Pukaki basins. It suggests that, as the dry period developed from 2004 and peaked in 2005 (see Figure 8.18), the ablation started as early as mid spring. As a consequence, this research provides some evidence supporting the intuition of [Anderton \(1973\)](#), who suggested that the melt water contribution from glaciers is likely to extend over a greater period of time during dry periods. From April 2004 to March 2007, the release of long term storage was 17%, 81%, and 50% larger than the average over the seven year period in the Ohau, Pukaki, and Tekapo basins, respectively. This latter aspect is readily visible in Figure 8.21 which represents the relative proportion of each water component to the annual discharge volume.

Over the seven year study period, ice melt in the Pukaki basin accounted for 5.4% of the mean annual inflow. This compares to 6% of the long term annual inflow estimated by [Purdie and Fitzharris \(1999\)](#) as originating from glacier melt. On average over the four hydrological years from 2000 to 2003, this contribution represented 7.2% of the summer inflow, slightly less than the estimation of 10% given by [Anderton \(1973\)](#). In Ohau, Pukaki, and Tekapo, the melt water attributed to glaciers accounted for 11.5%, 21.0%, and 15.1% of the summer inflow, respectively, during the dry period from April 2004 to March 2007. In the Ohau and the Tekapo catchments, the contribution of ice melt was estimated to be 1.6% and 4.3% of the mean annual inflow, respectively (Figure 8.21). In the Tekapo basin, it represented 9.1% of the summer inflow until March 2004 and rose to 11.8%, 15.2%, and 17.8% of the summer inflow in 2005, 2006, and 2007, respectively. In the Ohau catchment, the average contribution of ice melt to the summer inflow was 7.6% over the seven year study period, but did not reveal such an obvious increase during the dry period.

The SRM simulations in three neighbouring catchments over seven years including a severe drought revealed a pattern of hydrological behaviour that can be related to the glacierized portion of each basin. It generally suggests that the glaciers contributed more than usual to the inflow during the dry period. As a consequence, this modelling exercise supports the theory that glacier melt has a greater contribution to runoff during dry years, and thus maintains and regulates river inflows. It also supports observations suggesting that this mitigating effect depends on the relative extent of glacier area ([Chen and Ohmura, 1990](#)). Nevertheless, too few years and not enough catchments were considered to assess rigorously the validity of both

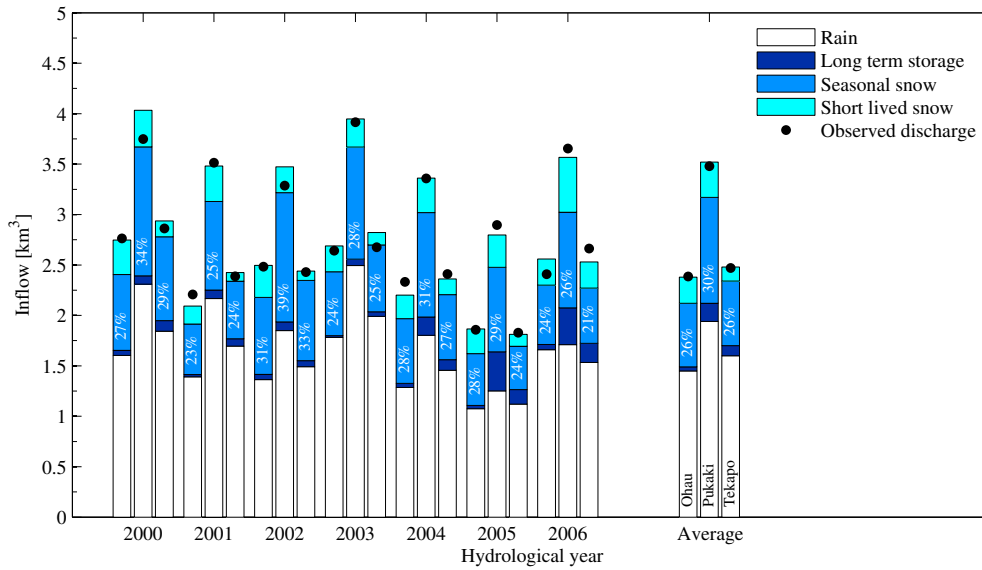


Figure 8.21 Modelled and observed annual discharge showing the relative proportion of stored water components. Only the percentage representing the seasonal snow is indicated for clarity purposes.

hypotheses in the upper Waitaki basin. In other words, despite the consistency and unprecedented detail of the hydrological modelling of the three alpine catchments over seven years, the observed signal is not believed to be yet sufficient to demonstrate that the drought necessarily caused the increase of ice melt. Although this research potentially provides a striking example of the positive effect of glaciers on inflow during a severe drought, more years must be simulated to elucidate the possible relationships between both aspects in the Alpine catchments of New Zealand.

It is shown that a large calving episode of the most prominent glaciers of the Pukaki catchment occurred simultaneously to a dry period. However, it would remain pure speculation to conclude, at this stage, that the former was caused by the drought. It cannot be excluded that it corresponded to a mere coincidence resulting from the uncontrolled retreat of glaciers that are considered to be not always in phase with the climate (Purdie and Fitzharris, 1999). It remains also unclear what proportion of the ice melt actually originated from the retreat of the terminus during this event. Further simulations with a concurrent monitoring of the glacier terminus and mass balance may help to elucidate the relationship between dry periods and glacier retreat in the Waitaki basin in order to confirm or invalidate a cause to effect relationship.

This modelling strategy clearly suffers from the inherent uncertainty associated with the accurate partitioning of the seasonal snow relative to the long term storage. If the calibrated values of c_s were set smaller, it would simply result in an increase of the estimated share of glacier melt indicated above, while it would reduce the share of the seasonal snow discussed in the next sub-section. Nevertheless, the signal revealed by the empirical adjustment of the hydrographs would retain its shape overall and seems strong enough to accommodate some degree of uncertainty without jeopardizing the interpretation given above. In the future, however, it will be necessary to address the contribution from the long term storage in a more deterministic way. This could be done within the model formulation by discriminating glacierized area from the snowy area, associating different runoff coefficients and melt factors with each type of surface (see for example [Schaper *et al.*, 1999](#); [Seidel and Martinec, 2003](#)). This strategy could be improved by adding a routine capable of estimating the melt originating under the debris as well as from the calving processes.

8.5.3.3 The seasonal snow

The hydrographs in Appendix I reveal unprecedented detail about the daily distribution of melt water originating from the snowpack. Unsurprisingly, the variability of the snow melt on a daily and yearly basis is large in all catchments and can reasonably be explained by the variability of the climatic conditions in the area. Figure 8.21 shows that the annual proportion of seasonal snow melt with respect to the total runoff volume is also highly variable in each catchment. No significant correlation was found to relate this proportion to the total annual inflow. Over the seven year study period, the seasonal snow was estimated to contribute 26.3%, 30.2%, and 26% to the total discharge in the Ohau, Pukaki, and Tekapo catchments, respectively. This is substantially more than the long term estimates (1947 to 1995) proposed by [McKerchar *et al.* \(1998\)](#) of 18%, 24%, and 19% of the inflow originating from the seasonal snowpack. Several factors can explain such a difference.

- First, the estimates of [McKerchar *et al.* \(1998\)](#) related to a much longer and distinct period than those those examined in this thesis. Given the annual variability of the seasonal snow, it cannot be excluded that there has been an increase of snowfall relative to rainfall during the period of study, compared to the long term average.
- On the other hand, [McKerchar *et al.* \(1998\)](#) used SnowSim ([Fitzharris and Garr,](#)

1995) to simulate monthly changes of snow accumulation for various altitude bands. Their model relied on rainfall estimates produced from only five precipitation gauges. Given the extreme pattern of rainfall in the region and the inherent limitations of SnowSim, this may have led to potentially large uncertainties associated with their model and concept, as it was acknowledged by the authors themselves.

- Finally, the first version of SnowSim, ignored the contribution of snow melt originating from areas above 2350m. This assumption may have introduced a negative bias to the estimates of [McKerchar *et al.*](#)

As explained in the previous paragraph, the SRM simulation also has limitations and uncertainties. Nevertheless, the methodology implemented in this thesis relied on far more data whose quality has been carefully assessed and criticised. Given the generally good and realistic performances obtained from the simulations, it is reasonable to consider that the simulations conducted in this thesis produced more reliable estimates. It stresses even more the importance of the seasonal snow-pack to the water balance of the basins.

Figure 8.22 details how the seasonal snow melt water was distributed on a monthly basis. In all three catchments, the release of seasonal snow melt water generally peaks in December although this varies from year to year. Although the contribution to the lake inflows fell rapidly in the Ohau and Tekapo basins, it remained important over the summer in the Pukaki catchment. In fact, the seasonal snow melt in Pukaki revealed a disproportionate contribution from zones PC3 & PC4 (i.e., the zones close to the main divide and above 1500m asl.) compared to the other zones. This can be explained by the much larger area of the Pukaki basin close to the main divide, exposed to prevailing precipitation [see Figure 8.2 (b)]. Thus, it results in a relatively larger accumulation of snow over the winter, with a longer period seen as snow covered. In all catchments, the contribution of the seasonal snow melt water reached a minimum in April-May.

The daily patterns shown in Appendix I also demonstrate that intense melt episodes can occur at any time and contribute significantly to the discharge, even in winter. The seasonal variability is much more pronounced in the Pukaki catchment (see Figure I.2 in Appendix I) where the melt of seasonal snow contributed from 25% up to 45% (mean 33%) of the summer inflow (i.e., December, January, February). In the Ohau and the Tekapo basins, most contributions from seasonal snow relative

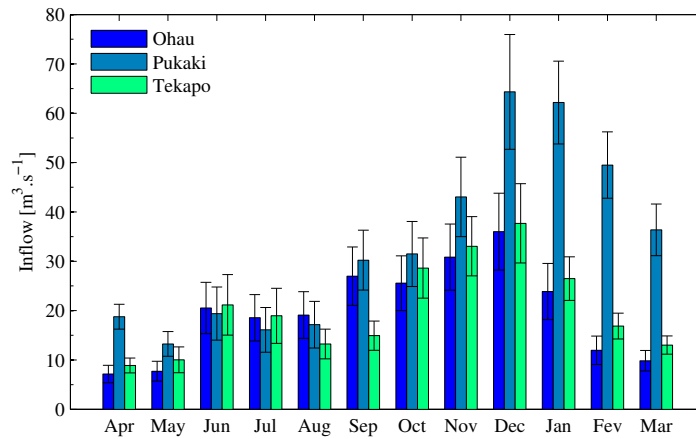


Figure 8.22 Monthly distribution of the inflow from the seasonal snow cover in the catchments of the upper Waitaki. The bars represent the mean computed over the seven year study period, while the error bars indicate ± 1 standard error.

to the inflow generally occurred earlier, from as early as October until January, but also reached up to 45% (mean 30%) of the monthly discharge. These estimates are less than those of [McKerchar *et al.* \(1998\)](#) by nearly 15%. Whether the discrepancies originated from the inherent variability of the snowpack and/or the reliability of the uncertainties associated with each methodology remains unclear.

8.5.3.4 The short-lived snow

The definition of the short-lived snow depends strongly on the duration of the time window used to filter the SCA curves (see Section 8.3.4). The latter was defined to accommodate the repeat time of the imagery available in this thesis. Thus, the short-lived snow component corresponded to the snow that does not last more than 30 days on the ground, and thus was filtered out from the SCA curves. With more frequent images, this window could potentially be shortened. As a consequence, a fraction of what is defined here as short-lived snow would be merged with the seasonal snow. Ideally, with a much higher temporal resolution (e.g., several snow maps per day), the dynamic of the snowpack could be monitored in near real time and short-lived snow fall would not be discriminated from what is defined here as the seasonal snowpack. On the basis of the definition of short-lived snow used in this thesis, the figures in Appendix I show that such events can contribute to the runoff all year. Figure 8.21 reveals that the short-lived snow accounted for a substantial fraction of the water released from the catchments.

Overall, the contribution of all snow, whether it lasted or not, is found to have represented on average 37.3% (min 30.8%, max 43.5%), 40.3% (min 35.0%, max 46.8%), and 31.6% (min 27.5%, max 36.5%) of the runoff into lakes Ohau, Pukaki, and Tekapo, respectively. The relative proportion of all snow melt components did not reveal any significant correlation with the inflow. Nevertheless, Figure 8.23 illustrates that there was a significant contribution ($R^2 = 0.82$, $p = 1.7 \times 10^{-8}$) from the total melt water from the snow to the lake inflow. It simply confirms that the snow accumulation varies in accordance with the precipitation. The largest amount of snow melt occurred over the hydrological year 2000 when there was the most precipitation, while the drought in 2005 logically corresponded to the minimum amount of snow melt.

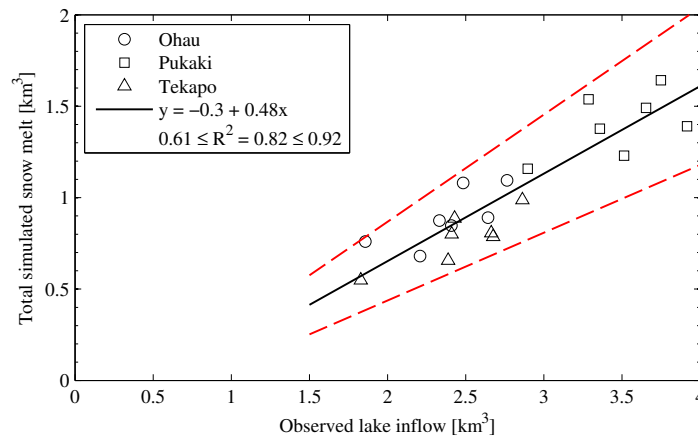


Figure 8.23 Correlation between the total snow melt simulated by SRM and the observed runoff volume. The dotted line and the confidence interval on R^2 correspond to the .05 significance level.

8.5.4 Study of the errors of modelling

8.5.4.1 Error *vs.* discharge

Although the robustness of the models was assessed by the Nash-Sutcliffe efficiency coefficient, the error of modelling (i.e., the difference between the observed and the computed daily inflow: Q_o and Q_c , respectively) was also examined in order to provide more detailed knowledge of the modelling performance and identify possible pitfalls. Figure 8.24 illustrates the relationship between the errors and the observed inflow. Although the dispersion of the error increased in accordance with

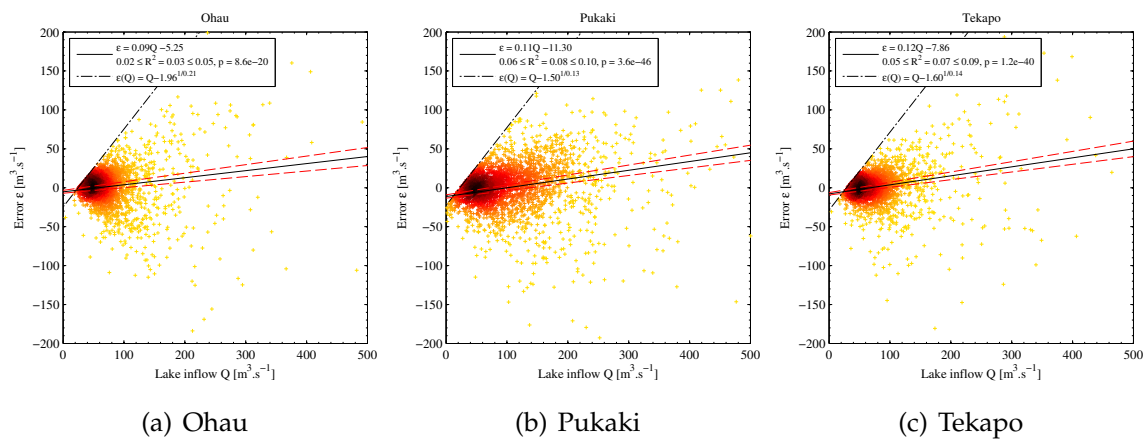


Figure 8.24 Scatter plot of the errors of modelling. The plot is colour coded to indicate the density of points; the confidence interval on R^2 is provided at the 5% risk level. Note that Q_c is bounded by $x^{\frac{1}{y}}$ as its lower limit because of the non linear recession law used in SRM (see Appendix G). It yields that the error $\epsilon = Q_o - Q_c$ is bounded by the linear function of the observed discharge $\epsilon(Q) = Q - x^{\frac{1}{y}}$.

the discharge, it revealed that the error itself was very poorly associated with the inflow. R^2 ranged from 3% to 8%, while the significance of the correlation at the .05 significance level was mostly due to the sample size. As a consequence, the models appeared to achieve similar performance at predicting the peak inflows and the low flow periods. This is readily visible in the hydrographs in Appendix I, which clearly show that the peaks of discharge due to large rainfall events are generally well captured by the model, while the modelled recession correctly matches the experimental hydrographs. This result contrasts with Bowden (1994) who concluded that SRM was not able to model low flow accurately in this region. It suggests that Bowden's calibration was not good enough and/or the data used were not of sufficient quality to achieve such performance. Thus, the modelling approach proposed in this thesis is also an improvement in that regard.

8.5.4.2 The statistical structure of the error

Figure 8.25 shows the histogram of the modelling errors for each hydrological year in each catchment, as well as the histogram of errors from all years combined. "t location-scale" distributions (see Section 6.5.1) can be fitted to each histogram. All the empirically fitted distributions matched the experimental distributions at the 95% confidence level according to the Kolmogorov-Smirnov test. Table 8.9 provides

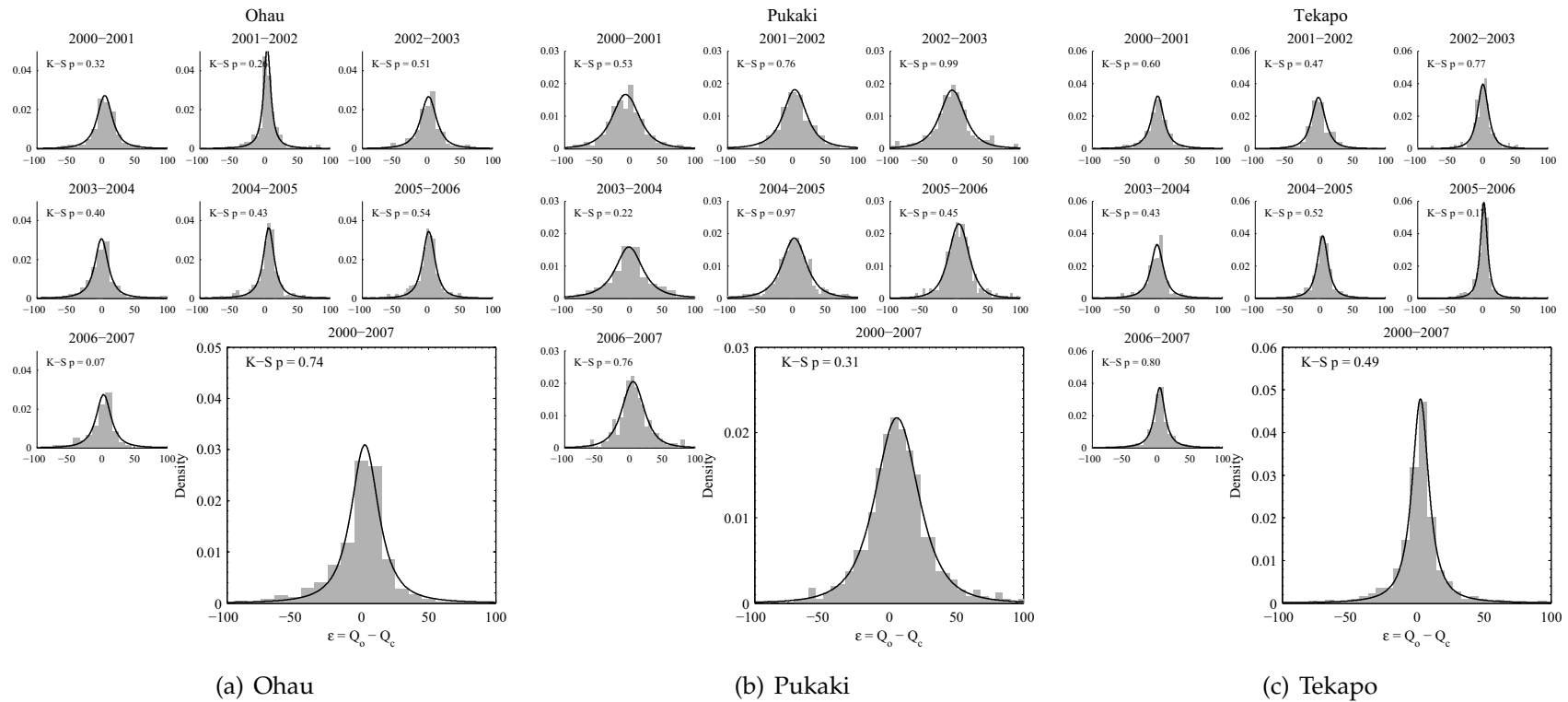


Figure 8.25 Density of probability of the modelling error. The gray bars are the empirical density distributions, the solid lines are the fitted t location-scale distributions. The $K-S p$ value in each subplot indicates the significance of the Kolmogorov-Smirnov test; if $K-S p > 0.05$, then one cannot reject the null hypothesis that both samples (i.e., the experimental and modelled error) are drawn from the same distribution at the .05 significance level.

Table 8.9 Parameters of the t location-scale distributions^a fitted to the experimental distribution of modelling errors.

	Year	Ohau			Pukaki			Tekapo		
		μ^b	σ^b	ν	μ	σ	ν	μ	σ	ν
Calib.	2000	2.7	13.4	1.8	-8.0	22.8	3.0	0.1	9.3	1.4
	2001	3.2	10.4	1.7	1.6	20.9	2.1	-2.4	12.2	2.2
	2002	1.2	12.9	1.9	-4.9	18.3	2.3	0.2	8.5	1.8
Verif.	2003	-2.4	12.4	1.8	-2.9	20.2	2.0	-1.7	10.3	1.6
	2004	3.3	11.1	1.9	-0.8	20.9	2.9	1.4	10.4	2.2
	2005	0.7	12.1	2.5	2.7	16.7	3.7	0.4	6.0	1.8
	2006	-1.1	16.4	2.2	2.2	20.0	2.6	1.3	11.5	2.2
	2003–2006 ^c	1.1	12.7	2.0	-1.4	20.0	2.8	-0.1	9.8	1.9
		1.3	12.6	1.9	-1.3	20.2	2.6	-0.2	9.6	1.8

^a The t location-scale distribution is a translated and scaled version of the Student's t -distribution. It accounts for the location μ , scale $\sigma > 0$, and shape $\nu > 0$ parameters. If X obeys a $t(\mu, \sigma, \nu)$ location-scale distribution, then $\frac{X-\mu}{\sigma}$ has a Student's t -distribution with ν degrees of freedom. Hence, the variance of $X \sim t(\mu, \sigma, \nu)$ is $\text{Var}[X] = \frac{\sigma^2\nu}{\nu-2}$.

^b μ and σ are in $[\text{m}^3 \cdot \text{s}^{-1}]$.

^c For overall results, the first line provides the mean of the measures obtained from each year; the second line corresponds to the measure computed from the combination of the hydrological years into a single signal.

the parameters of all the fitted distributions. Among all parameters of the t location-scale distribution, μ measures the bias of the error, while its spread is measured by the scaling parameter σ and the number of degrees of freedom ν .

Over the seven years and for each catchment, μ is the only parameter that has a standard deviation much larger than its mean. It indicates that the bias of the model cannot be anticipated. This is coherent with the fact that no deterministic method is yet available to predict the adjustments required during the ablation season. Nevertheless, σ and ν were less variable from one year to the next. Furthermore, the mean parameter values for each individual year matched quite closely the parameters obtained from the t location-scale distributions fitted to all errors combined (Table 8.9). Although it illustrates that the variance of the error does vary each year, it allows the mean of these parameters to be used as a reasonable trade-off in the attempt to model empirically the uncertainty of the model predictions. Therefore, this set of parameters seemed robust enough to provide an empirical and fair estimation of the confidence of the prediction.

8.5.4.3 Towards providing confidence intervals with the predicted discharge

The proposed approach of error modelling is disputable and largely weakened by its empiricism. It is evident that a more legitimate method should rather rely on an approach based on error propagation. For example, a Monte-Carlo scheme could be designed whereby the daily value of each variable is set randomly within its realm of possibility based on its own error structure (see, for instance, the errors associated with the mapping of the snow covered area, the temperature, or the precipitation). Such an ensemble modelling approach could practically provide the range of output that would be obtained given a level of uncertainty applied to the forcing data. Clearly, it is desirable to achieve such an implementation in the future. Nonetheless, it is a computational challenge that will require a specific modelling environment, interfaced with SRM, and capable to provide the set of random input data.

Such a design is beyond the scope of this research. As a first approximation, the empirical “middle of the road” model of error seemed capable of accommodating the statistical structure of the error for all years. Therefore, it is suggested that it can still provide valuable information about the reliability of the model predictions. Examples of model outputs displayed along with confidence intervals are shown in Figure 8.26. Such outputs can surely facilitate the operational use of the models presented above in the context of decision making.

8.6 Summary

This chapter applied the Snowmelt Runoff Model (SRM) to the three catchments of this study. This approach was chosen because it is specifically designed to take advantage of SCA observations as forcing data. Thus, it allowed the use of the time series of MODIS-derived snow maps developed in earlier parts of this thesis. The fields of temperature and precipitation were spatially interpolated in order to accommodate the strong spatial gradients of the region. Several interpolation strategies based on the thin plate spline method were tested and assessed using cross-validation.

- The bivariate interpolation of temperature data using a specified lapse rate was shown to produce the largest overall errors. The trivariate thin plate spline approach provided only a limited improvement over the bivariate approach,

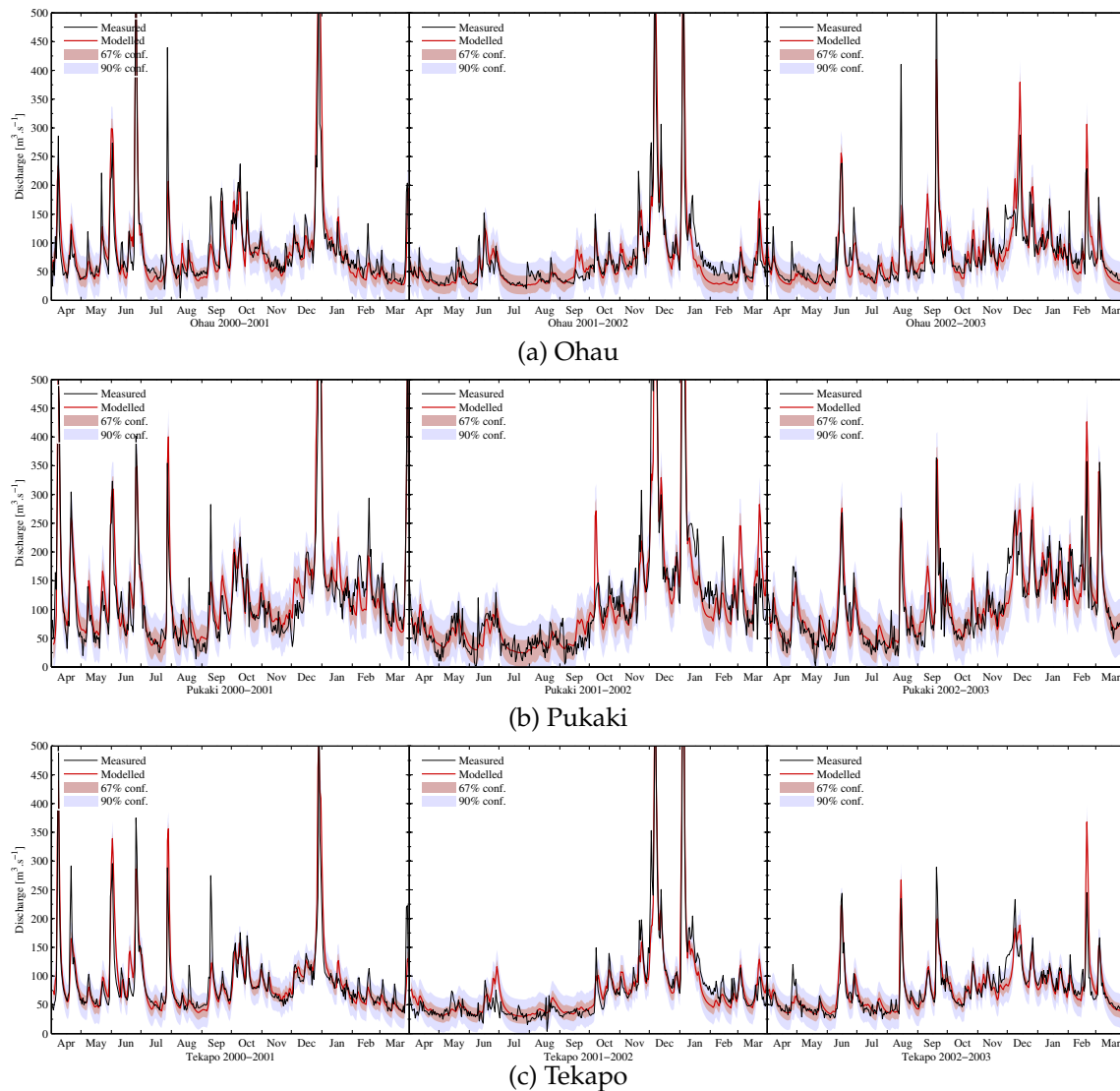


Figure 8.26 Modelled discharge with confidence intervals for the hydrological years 2000–2002.

but is more robust and better accommodates the spatial and temporal variability of lapse rate. Errors from both methods were sufficiently independent that best estimates of the temperature were provided by averaging the surfaces modelled by each technique.

- Trivariate thin plate interpolation based on the long term rain surface was shown to yield smaller errors than a bivariate interpolation. The former method was also found to be more robust with respect to the removal of data from climatic stations affected by snowfall during winter. As long as the spatial distribution of significant rainfall events is similar to that of long term pre-

precipitation, this interpolation technique was shown to provide a good representation of the steep gradient of precipitation over and east of the Main Divide.

An innovative technique based on Savitsky-Golay filtering with adaptation to the lower envelope was found to be an efficient and repeatable method to filter short-lived snow events and create the SCA curves used by SRM. The technique was able to remove transient snow events that could not be resolved entirely by the available imagery. A dynamic melt factor was implemented based on repeated measurement by MODIS of the snow reflectance in the near-infrared.

Based on three calibration years (i.e., from April 2000 to March 2003), a robust set of parameters was determined to produce the best models of inflow for each catchment. Verification of model performance over the four following years gave Nash-Sutcliffe efficiency coefficients of 67%, 79%, and 78% in the Ohau, Pukaki, and Tekapo catchments, respectively. Despite the complexity of the lake inflows, model performance compared well with other hydrological modelling experiments elsewhere in the world. Moreover, this performance is a noticeable improvement over previous simulations for the catchments. It therefore provides a new benchmark.

The hydrological simulations showed that the contribution of snow melt over the study period is substantially larger (see brackets for differences) than the long term estimates reported by previous studies. Together, short-lived and seasonal snow was shown to account for 37% (+19), 40% (+16), and 31% (+12) of the discharge in the Ohau, Pukaki, and Tekapo catchments, respectively. There is evidence to suggest a large melting of the long term water resource stored in glaciers.

For example there are large differences between modelled and observed lake inflows for the the severe drought of the 2005 hydrological year. Only a contribution of glacier melt much larger than normal (i.e., at least double the 6% of the total annual inflow that is attributed to long term ice melt) could have sustained the inflow into Lake Pukaki within 17% of the mean annual inflow over the seven years period, even though precipitation was reduced by 34%. This glacier melt is less marked in Tekapo and not readily apparent in the Ohau basins, in accordance with the relative proportion of glacierized areas in the catchments.

Chapter 9

Conclusion, and future work

This thesis fills a considerable void in research about snow in New Zealand. A first achievement is the implementation of a routine monitoring of the snow cover dynamics with the MODerate Imaging Spectro-radiometer (MODIS). The monitoring of snow with this sensor is not, strictly speaking, an original topic. However, this research integrated several advanced remote sensing techniques that are novel to MODIS to create a single operational algorithm to better address the snow cover mapping requirements in the local environment.

An image fusion algorithm enabled the mapping of snow with MODIS at 250m spatial resolution instead of the 500m resolution currently possible. In the context of processing time series of images in mountainous terrain, the thesis is the first of its kind to propose a standardization of MODIS data by means of a physically based atmospheric and topographic correction (ATOPCOR). In addition, the radiometric normalization of the MODIS time series permitted the design of a robust spectral unmixing technique. This allowed further enhancement of the spatial details of the snow maps through the determination of sub-pixel snow fractions.

The combination of these techniques forms an unprecedented processing chain that is well suited to mountainous environments so that snow is mapped with the highest possible amount of spatial detail. The quality of maps of snow fractions was assessed by means of comparison with high resolution reference snow maps obtained from the Advanced Spaceborne Thermal Emission and Reflection Radiometer (ASTER). The processing of seven years of MODIS observations covering the period from February 2000 to April 2007 provided a unique time series depicting the changing spatial distribution of snow. It revealed the dynamics of the seasonal snow cover in the important hydro catchments of Lakes Ohau, Pukaki, and Tekapo.

Two applications based on this new dataset illustrate the usefulness of satellite observations. They give a better understanding of and an improved tool for management of water resources in New Zealand. The first shows that the current modelling approach of the snowpack by the accumulation-ablation model SnowSim fails to represent seasonal accumulation and melt accurately and propagates increasing errors. The second applies snow cover area data to hydrological modelling. The Snowmelt Runoff Model (SRM) is used with maps of snow cover distribution and daily climatic data to simulate daily discharge of the Ohau, Pukaki, and Tekapo catchments for seven hydrological years from April 2000 until March 2006. These are the three largest hydroelectric water reservoirs in New Zealand. New light is shed on the relative contribution of seasonal snowmelt and ice melt to the river discharge.

9.1 Methodological contributions

9.1.1 Multispectral fusion of MODIS bands

A first achievement is the fusion of MODIS land bands using the ARSIS concept (Ranchin *et al.*, 2003) and a wavelet-based multi-resolution approach. This is an original contribution to remote sensing research. Producing a full set of land bands (i.e., MODIS bands 1-7) at 250m spatial resolution is a desirable enhancement of the MODIS data, and enables the mapping of snow cover boundaries with more spatial detail.

The assessment of the fusion technique by means of Wald's protocol (2002, Chap. 8) demonstrated that the radiometry of the fused bands is generally well preserved and significantly more accurate than a simple interpolation.

The thesis has revealed the difficulty of comparing datasets in a multi-resolution framework. When using quantitative measures computed on a per pixel basis [e.g., mean absolute error (MAE), root mean square error (RMSE) between a reference snow map and the snow maps obtained from MODIS data], the non-fused 500m resolution snow maps obtained generally better scores than the fused 250m resolution snow maps. This observation was consistent for all the "pixel-based" statistics used to assess the results. They included standard statistical approaches (e.g., bias, mean absolute error, root mean square error, coefficient of determination), as well as more sophisticated metrics used in image and signal processing sciences

(e.g., the Q index of Wang and Bovik, 2002 and the analysis of Receiver Operating Curves).

Although a subjective judgement allows the difference of performance to be appreciated, the potential provided by the fusion technique could only be quantified following an aggregation of the snow maps obtained with image fusion (i.e., at 250m) to the coarser resolution of the non-fused images (i.e., at 500m). After this step, all pixel-based measures showed that the determination of snow fractions within 500m resolution pixels can be significantly improved when the fusion is implemented. Nevertheless, the range of improvements was highly variable between measures, from +1.5% for the bias to +25% for the RMSE and MAE. These results stress the importance of considering several assessment methods to ensure reliable conclusions.

To address the pitfalls of the pixel-based approach and quantify objectively the gain of information that can be attributed to an increase in spatial resolution, the thesis investigated the potential of the modified directed Hausdorff distance (MDHD). This “feature-based” measure, inspired from the domain of feature recognition, is aimed at scoring the match between a reference and a test geometrical shape (here the snowline as depicted by the ASTER images, i.e., reference, and the fused and non-fused MODIS images, i.e., test). A theoretical investigation illustrated the suitable behaviour of this metric in the context of multi-resolution datasets. It demonstrated that the MDHD is capable of scoring the representation of the snowline irrespectively of the spatial resolution of the snow map. Furthermore, the MDHD varies linearly with the pixel size, making it suitable to assess images of different resolutions. When applying the MDHD to snow maps from fused MODIS images, the MDHD decreased 33%, while only a 15% decrease was achieved when the fusion was replaced by a simple interpolation. This improvement should be put into perspective with the 50% maximum improvement that is achievable, if snow was mapped from a set of seven land bands with a genuine spatial resolution of 250m. In other words, the fusion achieves 66% of the maximum achievable result, while a simple interpolation achieves only 30%.

9.1.2 Atmospheric and topographic correction of MODIS data

Adapting the ATCOR3 algorithm (Richter, 1998) to MODIS data is a second methodological contribution of this thesis. In remote sensing, the conversion of radiance measured at the top of the atmosphere to ground reflectance is a desirable

feature to monitor ground properties. In the context of this research, the combined atmospheric and topographic correction proposed by ATCOR3 is implemented as a means to standardize the time series of MODIS data and to enable a more robust detection of snow.

The specific interest in snowy targets in very rugged terrain identified several shortcomings of the iterative formulation of ATCOR3. It was shown that the three iterations presently used in commercially available ATCOR3 are not sufficient to allow the convergence of reflectance in the presence of highly reflective surfaces. Results from this thesis suggest that more iterations should be used. A damping strategy was also proposed to speed up the convergence of the iterative process without affecting the final value of ground reflectance.

Furthermore, the operational correction of optical satellite sensor imagery usually models radiation reflected from surrounding terrain with a first order reflection function. This thesis showed that, in rugged areas and snowy environments, the trapping of radiation between adjacent slopes can make such an approximation inadequate. It potentially leads to underestimation of the amount of irradiance, and overestimation of the ground reflectance. A multiple reflection model was proposed that converges to a simple correction factor. A theoretical comparison between the first order and the multiple reflection models suggested that the reflectance of snow targets, in very rugged terrain, may be overestimated by up to 30%, if multiple reflections are disregarded.

The proposed correction provides only limited fundamental understanding of the terrain reflected radiation process. Nevertheless, it remains competitive in terms of computing efficiency, and is easy to implement in algorithms that addresses topographic correction. It also relies on the same assumptions and empirical approach as the first order reflection model that is currently used in operational algorithms such as ATCOR3. The proposed correction allows better correction of illumination in mountainous terrain.

9.1.3 Snow mapping

In revisiting the mapping of snow from MODIS data, this thesis discussed the intimate relationship between the sub-pixel snow fractions, the spatial structure of the snowpack, and the pixel size. Unexpectedly, the distribution of sub-pixel snow fractions is not uniform. Although this conclusion arises from empirical experiments on simple geometrical shapes, it is confirmed by the experimental distribu-

tions of sub-pixel snow fractions derived from ASTER data. This special case is in line with the wider problem discussed by [Key \(1994\)](#) and [Kitamoto and Takagi \(2000\)](#) of the distribution of area proportion in mixed pixels. It implies that the shape of this distribution is controlled by the size of the pixel relative to the spatial structure of the snow cover (i.e., the distribution of size and position of the snow patches).

This raises issues with respect to binary approaches of classification. The latter are often designed to label pixels as “snowy” if they are more than half covered by snow. This design leads to an ill-posed problem. No deterministic method was identified to estimate the shape of this distribution *a priori*. This is further complicated by the fractal nature of the snowpack. Thus, the conditions of symmetrical distributions are not necessarily satisfied in the general case. In other words, the binary approach to map snow is inherently compromised by the difficulty of estimating the mean of the distribution of snow fractions *a priori*. This necessarily introduces a bias in the estimation of the snow covered area from any strategy relying on binary mapping.

The mapping of snow fractions at a sub-pixel resolution is an effective way to tackle this issue. This thesis has clarified the validity of this approach in the framework of fractal geometry. Towards this goal, a fully constrained linear unmixing technique was considered. The approach implemented in this thesis contrasts with the strategies of unmixing proposed by [Painter *et al.* \(2009\)](#) or [Vikhamar and Solberg \(2003\)](#). The standardization of the MODIS images to ground reflectance allowed a fixed set of end-members to be selected, while shaded end-members could be ignored. The fixed set of end-members means that the computational load is acceptable. This is desirable when routinely processing hyper-temporal series of images.

Eight simultaneous ASTER images at high spatial resolution were successfully used to assess the competitive performance, and the robustness of the method. The sub-pixel snow fractions were estimated at 250m spatial resolution with a RMSE of 14.8% on average. The RMSE dropped to 10.5% when the maps of snow fractions were aggregated at 500m spatial resolution, thus benefiting from the statistical effect of the spatial aggregation. In addition, the results from the MDHD measure showed that 90% of the snowlines extracted from the maps of sub-pixel snow fractions at 250m spatial resolution were within 200m of the reference snowline extracted from ASTER data. These results, as well as those from the other metrics tested, establish based parameters for further investigations of snow mapping strategies.

9.1.4 MODImLab

For the purpose of this thesis, all image processing steps were implemented in the MATLAB[®] software. This led to the development of a suite of data analysis tools that together comprise the MODImLab toolbox (“MODIS Imagery Laboratory”). The graphical user interface (GUI) and flowchart of MODImLab are provided in Appendix J. This toolbox comprised a general management program that handles the automatic processing of multiple MODIS images. It is linked to several functions that implement tasks such as the projection of MODIS level-1B data on a user-defined coordinate system, the creation of RGB composites, the detection of clouds, the retrieval of water vapour, the image fusion algorithm, the atmospheric and topographic correction, and the computation of maps of snow fractions.

The potential of MODImLab extends far beyond the mere creation of maps of snow fractions. Its implementation in MATLAB[®] software provides access to specialized mathematical functions and a programming environment that offers great potential for experimentations with image processing techniques. The implementation of existing algorithms aimed at retrieving physical variables (e.g., aerosol optical depth) and the development of new processing schemes is thus facilitated and can be developed easily for the processing of time series of MODIS images. For instance, an additional capability of the MODImLab toolbox not discussed in this thesis is the implementation of the split-window algorithm of [Wan and Dozier \(1996\)](#) that allows computation of ground surface temperature. MODImLab also provides additional tools for the processing of Digital Elevation Models, such as the computation of shadows and topographic parameters. This makes MODImLab a very versatile and flexible platform for the creation of hyper-temporal datasets of physical variables from MODIS.¹

9.2 Hydrological contributions

9.2.1 Performance and pitfalls of the SnowSim model

Observations of snow cover distribution provide a dataset to assess the quality of snow models like SnowSim but there are limitations. Indeed, such snow models attempt not only to simulate the spatial distribution of snow, but, more importantly, the snow water equivalent (SWE), while maps of snow from MODIS cannot readily

¹The source code of MODImLab is made available to the scientific community upon request.

provide this variable. Thus, comparison between the model outputs and the snow observations cannot directly involve the SWE.

In the simplest approach, such a comparison can only reveal whether the snow model over- or under-estimates the snow coverage. This thesis showed that SnowSim tends to over-estimate the snow extent consistently. In investigating metrics inherited from classification accuracy techniques (such as hit rate, false alarm rate, or precision), more subtle behaviours of SnowSim were identified. For example, SnowSim tends to represent snow at lower altitudes than is found in reality. Furthermore, SnowSim has a tendency to build up snow storage in areas which are free of snow according to MODIS. Finally, the depletion of the snow cover as modelled by SnowSim is slower than in reality.

However, this assessment cannot elucidate with certainty the causes of inaccuracies of SnowSim. Whether too much snow is accumulated or the processes of ablation are not well parameterized remains unclear. A combination of both is likely. It demonstrates that models that rely solely on precipitation and temperature data to simulate the accumulation and melting of the snowpack tend to propagate errors. This appears to be the main pitfall of this approach. In the case of SnowSim, it is shown that error propagation leads to a wrong but consistent representation of about 25% of the SWE in summer in areas that are free of snow according to MODIS.

It should be noted that this issue could be revealed only because of the tendency of SnowSim to over-estimate the snow cover extent. The alternative (i.e., under-estimation of the snow cover extent) would have prevented such a conclusion to be reached. Indeed, MODIS could not have supported any indication with respect to the SWE potentially missed by SnowSim. However, it is believed that such a situation would have simply concealed a similarly severe pitfall.

Snow models like SnowSim are aimed at representing reality as closely as possible. The snow extent is part of this reality. Thus, a convergence between the outputs of SnowSim and the frequent observations of snow cover extent must be sought. Ways to enforce such a convergence exist. For instance, a data assimilation strategy, such as that proposed by [Clark *et al.* \(2006\)](#), can benefit from observations of the snow cover area so as to reduce the model uncertainties. This approach was recently investigated in New Zealand by [Hreinsson \(2008\)](#) on the basis of the frequent snow maps provided by this thesis. Alternatively, it is believed that a modelling approach whereby the parameterization of SnowSim is adapted on the basis of regular observations of the snow cover (by MODIS or other sensors) should be considered.

9.2.2 Hydrological simulations with SRM

Fifteen years after [Bowden \(1994\)](#) and more than twenty years after [Grimmond \(1980\)](#) and [Turner \(1986\)](#), this thesis has demonstrated the potential of the SRM model to simulate daily lake inflows in New Zealand. This thesis makes two original contributions to the implementation of the SRM model. SRM relies on snow cover depletion curves (SDC) that depict a monotonic decrease of the snow cover extent, from its maximum at the end of the accumulation season down to its minimum at the end of the ablation season. Monitoring of the snow cover dynamics by MODIS is insufficiently frequent in New Zealand due to the very rapid evolution of snow pack and frequent cloud cover. Thus, the rapid depletion of short-lived snow events remains difficult to resolve and can introduce bias to the model outputs. As the first original contribution, this issue was successfully addressed by implementing a new approach for constructing the SDC through the use of a Savitzky-Golay filter with adaptation to the lower envelope. This technique permits short-lived snow falls to be efficiently filtered out.

The second original contribution to implementation of the SRM model is the introduction of a dynamic melt factor linked to an observed parameter of the snow cover. ATOPCOR enables time series of the ground reflectance of snow to be retrieved. Thus, the signal of near infrared reflectance provides a valuable insight into the dynamic of the snowpack. This property which is sensitive to the grain size exhibits a pattern consistent with the behaviour of the melt factor. Its use in the SRM to force the melt factor parameter allows the degrees of freedom of the model to be reduced, thus facilitating its calibration.

The SRM model was successfully calibrated for the three catchments on the basis of three consecutive hydrological years (i.e., 2000–2002). The modelling performance in the following four years were measured by the Nash-Sutcliffe efficiency coefficient R^2 . With R^2 reaching 67%, 79%, and 78% over the four years in the Ohau, Pukaki, and Tekapo basins, respectively, this implementation of SRM has achieved unprecedented performance in New Zealand in terms of daily hydrological modelling of snow fed catchments. It assesses the robustness of the model and provides base parameter values and benchmarks for further investigation.

In revealing the large daily variability of the snowmelt contribution to the lake inflows, the thesis has shown that this contribution over the study period was substantially larger than the long-term estimations reported by previous researchers ([McKerchar *et al.*, 1998](#)). Over the 2000–2006 hydrological years, snowmelt ac-

counted for 37%, 40%, and 31% of the discharge in the Ohau, Pukaki, and Tekapo catchments, respectively. This stresses further the importance of the seasonal snow-pack to the water balance of the basins.

Finally, the research documents that during the severe drought of 2005, lake inflows were largely mitigated by ice melt from glaciers in the Pukaki basin. A contribution of glacier melt much larger than normal is believed to have sustained the discharge within 17% of the mean annual flow, even though the precipitation was reduced by 34%. This mitigating factor was less marked in Tekapo and not observed in the Ohau basin, in accordance with the relative proportion of glacierized areas in the catchments. This potentially provides a striking example of the contribution of long term storage to inflows during dry periods.

In conclusion, the application of SRM to these important catchments was successful and provided an operational tool for modelling their hydrology. Although the model was only assessed with historical data, it has the potential to provide short to medium term forecasts of water availability from hydro catchments. The lag between the production of free melt water in the watershed and the change of lake levels allows a forecast of two days ahead based on real data. Although this may not yet be sufficient to enable an operational use by water managers, it provides a modelling environment which can be coupled with forecasted meteorological data.

9.3 Future work

9.3.1 Image fusion

This thesis has shown how multispectral image fusion can be applied to MODIS data for the mapping of snow. This technique offers a new perspective towards the development of other datasets derived from MODIS. For instance, the classification of multiple land cover surfaces could equally benefit from such an improvement in spatial resolution.

Another approach to create a full set of MODIS land bands at 250m spatial resolution was proposed by [Trishchenko *et al.* \(2006\)](#). Unlike the multi-resolution technique proposed in this thesis, [Trishchenko *et al.*'s](#) approach is statistical and relied on multiple regressions between MODIS land bands. A competitive assessment could be conducted to further examine the advantages and disadvantages of each method. In such a context, [Section 3.4.3.2](#) potentially provides an experimental pro-

to col.

In the context of assessing the performance of image fusion, the modified directed Hausdorff distance was shown to be a useful indicator of quality. This measure can also be interpreted as a statistical assessment of the planimetric accuracy of natural pattern outlines. Although, the MDHD was used only to assess the classification of snow targets, there is scope for further investigations of this measure with more than two classes. By enforcing a “feature-based” approach, the MDHD is naturally in line with the framework of object-based classification. One direction could be to associate the MDHD with a more classical assessment of class confusions. The former can assess the position of feature boundaries, while the latter would measure the correct classification of the features on each side of the boundary.

9.3.2 ATOPCOR

The atmospheric model in the ATOPCOR module of MODImLab has the potential to take further advantage of the capability of MODIS. The sensor can provide spatial estimates of atmospheric parameters required for the correction. In this thesis, only water vapour content was retrieved from MODIS imagery, but algorithms to estimate other parameters from MODIS on a per pixel basis can be implemented. It can advantageously replace local observations to achieve a more accurate correction of the imagery. For instance, a MODIS ozone retrieval algorithm could be used to replace the daily observation by spatially varying estimations of total ozone (Seemann *et al.*, 2003). Similarly, aerosol optical depth retrieval from MODIS data can also be considered (Chu *et al.*, 2002; Liang *et al.*, 2006). Although ATOPCOR was originally implemented to enable a robust classification of snow targets, the radiometric correction of MODIS optical imagery can contribute to the classification of other land targets, as well as retrieval of physical properties in environments that are dominated by high relief.

There is also scope for further development of ATOPCOR. In particular, the physically based topographic correction algorithm provides a framework in which the anisotropic reflectance of the snow surface could be considered. This aspect was ignored in this thesis because the computational cost of such an implementation was not justified for the classification of well contrasted targets such as snow. However, once snow has been detected, the implementation of models of bidirectional reflectance (BRDF) would enable conversion of data measured at the top of the atmosphere to spectral albedo. A conversion from spectral to broadband surface

albedo would provide a valuable contribution to snowpack modelling and energy balance studies. Towards this goal, a collaboration is in progress within the framework of research at the *Laboratoire de Glaciologie et Géophysique de l'Environnement* (LGGE, Grenoble). Models of snow BRDF have been established and are now in the process of implementation in the ATOPCOR module of the processing chain.

9.3.3 Snow mapping from MODIS/AQUA data

All the data processed in this thesis originated from the MODIS sensor aboard the TERRA platform. Another MODIS sensor is operating aboard the AQUA platform that collects imagery in early afternoon, local time. The use of MODIS/AQUA data can reduce the repeat time of snow cover observations. However, the band 6 aboard this sensor has failed. This compromises the direct application of the unmixing algorithm to MODIS/AQUA data. One end-member at least should be removed to ensure the determination of the constrained linear system of equations. Some adaptations are thus needed to allow the use of these data in the future.

9.3.4 Hydrological modelling

Hydrological modelling of lake inflows should be made more durable. Towards this goal, the processing of hydrological years 2008 and 2009 will be undertaken. This will allow a further assessment of the model's robustness. With more simulated years, the time series of the snowmelt contribution to lake inflows can be further examined to enable the long-term contribution of melt components to be estimated more reliably. Despite the consistent evidence suggested by this research, too few years and not enough catchments were considered to establish with certainty the existence of a link between dry years and the release of long term water storage from glaciers. Further simulation of the daily discharge from the alpine catchments of New Zealand is desirable to elucidate this issue further.

Estimation of ice melt is indirect and empirical. A necessary improvement to hydrological modelling involves the estimation of glacier melt in a deterministic way, within the modelling framework. This could be done within a formulation of the SRM model by discriminating glacierized area from the snowy area, and associating different runoff coefficients and melt factors with each type of surface (see for example [Schaper *et al.*, 1999](#); [Seidel and Martinec, 2003](#)). This strategy could be improved by adding additional reservoirs capable of addressing ice melt originating

under the debris as well as from the calving into pro-glacial lakes. Remote sensing could further contribute to this strategy by monitoring the changes in debris and clear ice and the expansion of terminal lakes.

The SRM model is designed to function ultimately as a prediction tool. However, the current predictive ability of the model is limited to the lag of two days that was identified between the input of free water in the catchment (i.e., precipitation and melt) and the output (i.e., the lake level). In order to achieve more operational capabilities, the model should be tested with forecasted meteorological data to extend predictions. Towards this goal, Nagler *et al.* (2008) used prognostic equations to complete and extrapolate the time series of snow cover area along with predictions of meteorological variables. The use of ensemble forecasts of meteorological data can provide forecasted lake inflows with confidence intervals on the output.

Unlike SnowSim, the SRM model does not provide direct estimates of the snow storage. However, this information remains valuable to water managers for seasonal operation of lake storage. In questioning the quality of the output of SnowSim, the thesis naturally raises the question of its improvement. A possible direction is a dynamic calibration of the parameters of SnowSim so that its outputs match the repeated satellite observations. Another improvement could involve the use of a more physically based model instead of the current degree-day model whereby observed values of albedo obtained through remote sensing could be used (Molotch *et al.*, 2004). Furthermore, the convergence of both the storage output enabled by SnowSim and the hydrological output allowed by SRM could be achieved. This can be done by running both models with identical parameters and climatic data in an integrated framework.

Finally, the results presented in this thesis stress another aspect of water use sustainability in New Zealand. Global climate change is likely to affect the water cycle with potential changes in rainfall patterns, magnitude and area of seasonal snow cover, and glacier retreat. There is a risk of a major environmental impact on water resources that justifies ongoing monitoring using satellite imagery and runoff modelling as employed in this thesis. Scenarios of modified climate could be implemented in SRM to examine such impacts.

References

- Ackerman, S., Strabala, K., Menzel, P., Frey, R., Moeller, C., Gumley, L., Baum, B., Seemann, S. W., and Zhang, H. (2006). *Discriminating clear-sky from cloud with MODIS, Algorithm theoretical basis document (MOD35), version 5.0*. MODIS Cloud Mask Team. 88, 89, 91
- Ackerman, S., Strabala, K., Menzel, W., Frey, R., Moeller, C., and Gumley, L. (1998). Discriminating clear sky from clouds with MODIS. *Journal of Geophysical Research*, 103(D24), 32141–32157. 88, 89, 117
- Ackerman, S. A., Holz, R. E., Frey, R., Eloranta, E. W., Maddux, B. C., and McGill, M. (2008). Cloud detection with MODIS. Part II: validation. *Journal of Atmospheric and Oceanic Technology*, 25(7), 1073–1086. 47
- Adams, J. B., Sabol, D. E., Kapos, V., Almeida Filho, R., Roberts, D. A., Smith, M. O., and Gillespie, A. R. (1995). Classification of multispectral images based on fractions of end-members: Application to land-cover change in the Brazilian Amazon. *Remote Sensing of Environment*, 52(2), 137–154. 169, 172, 173
- Adams, J. B., Smith, M. O., and Johnson, P. E. (1986). Spectral mixture modeling: A new analysis of rock and soil types at the Viking Lander 1 site. *Journal of Geophysical Research*, 91(B8), 8098–8112. 169
- Ahlmann, H. W. (1924). Le niveau de glaciation comme fonction de l'accumulation d'humidité sous forme solide. Méthode pour le calcul de L'humidité condensée dans la haute montagne et pour l'étude de la fréquence des glaciers. *Geografiska Annaler*, 6, 223–272. 248
- Aiazzi, B., Alparone, L., Argenti, F., and Baronti, S. (1999). Wavelet and pyramid techniques for multisensor data fusion: a performance comparison varying with scale ratios. In S. B. Serpico (Ed.), *Proceedings of the SPIE Image Signal Process. For Remote Sensing V*, Volume 3871, 251–262. SPIE: SPIE. 76, 80
- Alados-Arboledas, L., Olmo, F. J., Alados, I., and Prez, M. (2000). Parametric models to estimate photosynthetically active radiation in Spain. *Agricultural and Forest Meteorology*, 101(2-3), 187–201. 123
- Alparone, L., Baronti, S., Garzelli, A., and Nencini, F. (2004). A global quality measurement of pan-sharpened multispectral imagery. *IEEE Geoscience and Remote Sensing Letters*, 1(4), 313–317. 82, 220
- Alparone, L., Wald, L., Chanussot, J., Thomas, Gamba, P., and Bruce, L. M. (2007). Comparison of pansharpening algorithms: outcome of the 2006 GRS-S data fusion contest. *IEEE Transactions on Geoscience and Remote Sensing*, 45(10), 3012–3021. 73, 80, 220
- Ambach, W. (1988). Interpretation of the positive-degree-days factor by heat balance characteristics – West Greenland. *Nordic Hydrology*, 19(4), 217–224. 249, 251
- Ambroise, B., Beven, K., and Freer, J. (1996). Toward a generalization of the TOPMODEL

- concepts: Topographic indices of hydrological similarity. *Water Resources Research*, 32(7), 2135–2145. 421
- Amolins, K., Zhang, Y., and Dare, P. (2007). Wavelet based image fusion techniques – An introduction, review and comparison. *Journal of Photogrammetry and Remote Sensing*, 62(4), 249–263. 72, 76, 77
- Amos, M. J., Featherstone, W. E., and Blick, G. H. (2005). Progress towards implementation and development of a New Zealand national vertical datum. In F. Sansò (Ed.), *A Window on the Future of Geodesy, Proceedings of the International Association of Geodesy*, Volume 128, Sapporo, Japan, 338–343. Springer. 56
- Andersen, T. (1982). Operational snow mapping by satellites. In J. W. Glen (Ed.), *Hydrological Aspects of Alpine and High Mountain Areas*, Wallingford, UK, 149–154. International Association of Hydrological Sciences: International Association of Hydrological Sciences. 29
- Anderson, D. A. (1981). Maximum likelihood estimation in the non-central chi-distribution. *Sankhya, Indian Journal of Statistics*, 43(Series B), 58–67. 391
- Anderton, P. W. (1973). The significance of perennial snow and ice to the water resources of the South Island, New Zealand. *Journal of Hydrology (NZ)*, 12(1), 6–18. 12, 313, 318
- Anderton, P. W. (1974a). Estimation of snow storage and melt in the catchment of Lake Pukaki. In *Proceedings of the New Zealand Hydrological Society Symposium*, Otago University, Dunedin, New Zealand. 24, 290
- Anderton, P. W. (1974b). Tasman glacier: Interpretation of multispectral photography. Unpublished report for Ministry of Works New Zealand. 27
- Anderton, P. W. (1975). Tasman Glacier 1971-73. Hydrological research. Annual Report 3, Ministry of Works and Development, Wellington, New Zealand. 23
- Andreadis, K. M. and Lettenmaier, D. P. (2006). Assimilating remotely sensed snow observations into a macroscale hydrology model. *Advances in Water Resources*, 29(6), 872–886. 28, 38
- Ångström, A. K. (1961). Techniques of determining the turbidity of the atmosphere. *Tellus*, 13(2), 214–223. 127
- Aoki, T., Aoki, T., Fukabori, M., Hachikubo, A., Tachibana, Y., and Nishio, F. (2000). Effects of snow physical parameters on spectral albedo and bidirectional reflectance of snow surface. *Journal of Geophysical Research*, 105(D8), 10219–10236. 31, 32, 101
- Archer, A. (1970). Studies of snow characteristics in the north-eastern Ben Ohau Mountains, New Zealand. *Journal of Hydrology (NZ)*, 9(1), 4–21. 23, 24, 248
- Arendt, A. and Sharp, M. (1999). Energy balance measurements on a Canadian high arctic glacier and their implications for mass balance modelling. In M. Tranter, R. Armstrong, E. Brun, G. Jones, M. Sharp, and M. Williams (Eds.), *Proceedings of the IUGG Symposium - Interactions Between the Cryosphere, Climate and Greenhouse Gases*, Volume 256, Birmingham, 165–172. IAHS Publication. 251, 252, 296
- Armstrong, R. L. and Brun, E. (2008). *Snow and climate : physical processes, surface energy exchange and modeling*. Cambridge, U.K.: Cambridge University Press. 30, 171, 242, 244, 247, 251
- Aslyng, H. C. and Stendal, M. M. (1965). Minimum, maximum, and mean temperatures obtained by various methods and at various heights in a natural sward. *Oikos*, 16(1/2),

- 70–77. 309
- Assaf, H. (2007). Development of an energy-budget snowmelt updating model for incorporating feedback from snow course survey measurements. *Journal of Engineering, Computing and Architecture*, 1(1), 1–25. 247
- Ballantine, J.-A. C., Okin, G. S., Prentiss, D. E., and Roberts, D. A. (2005). Mapping North African landforms using continental scale unmixing of MODIS imagery. *Remote Sensing of Environment*, 97(4), 470–483. 169
- Bandaragoda, C., Tarboton, D. G., and Woods, R. (2004). Application of TOPNET in the distributed model intercomparison project. *Journal of Hydrology*, 298(1-4), 178–201. 27
- Bannari, A., Pacheco, A., Staenz, K., McNairn, H., and Omari, K. (2006). Estimating and mapping crop residues cover on agricultural lands using hyperspectral and IKONOS data. *Remote Sensing of Environment*, 104(4), 447–459. 169
- Barnes, W. L., Pagano, T. S., and Salomonson, V. V. (1998). Prelaunch characteristics of the moderate resolution imaging spectroradiometer (MODIS) on EOS-AM1. *IEEE Transactions on Geoscience and Remote Sensing*, 36(4), 1088–1100. xvii, 41, 42, 66
- Barrett, A. P., Leavesley, G. H., Viger, R. L., Nolin, A. W., and Clark, M. P. (2001). A comparison of satellite-derived and modeled snow-covered area for a mountain drainage basin. In M. Owe, K. Brubaker, J. Ritchie, and A. Rango (Eds.), *Proceeding of the Santa Fe symposium - Remote sensing and hydrology*, Volume 267, Santa Fe, New Mexico, USA, 569–573. IAHS Publication. 260
- Barringer, J. R. F. (1989). A variable lapse rate snowline model for the remarkable, central otago, New Zealand. *Journal of Hydrology (NZ)*, 28(1), 32–46. 25, 254, 278
- Barsky, S. and Petrou, M. (2005). The shadow function for rough surfaces. *Journal of Mathematical Imaging and Vision*, 23(3), 281–295. 157
- Bartelt, P. and Lehning, M. (2002). A physical SNOWPACK model for the Swiss avalanche warning: Part I: numerical model. *Cold Regions Science and Technology*, 35(3), 123–145. 247
- Barton, J. S., Hall, D. K., and Riggs, G. A. (2000). Remote sensing of fractional snow cover using moderate resolution imaging spectroradiometer (MODIS) data. In *Proceedings of the 57th Eastern Snow Conference*, Syracuse, New York, USA, 171–183. 170, 203
- Barton, J. S., Hall, D. K., and Riggs, G. A. (2001). Thermal and geometric thresholds in the mapping of snow with MODIS. 46
- Baumgartner, M., Martinec, J., and Seidel, K. (1986). Large-area deterministic simulation of natural runoff from snowmelt based on Landsat MSS data. *IEEE Transactions on Geoscience and Remote Sensing*, GE-24(6), 1013–1017. 35
- Baumgartner, M., Seidel, K., and Martinec, J. (1987). Toward snowmelt runoff forecast based on multisensor remote-sensing information. *IEEE Transactions on Geoscience and Remote Sensing*, GE-25(6), 746–750. 29
- Beauchemin, M., Thomson, K. P. B., and G., E. (1998). On the hausdorff distance used for the evaluation of segmentation results. *Canadian Journal of Remote Sensing*, 24(1), 3–8. 197
- Beavan, J., Matheson, D., Denys, P., M., D., Herring, T., Hager, B., and P., M. (2004). A vertical deformation profile across the Southern Alps, New Zealand, from 3.5 years of continuous GPS data. In T. van Dam and O. Francis (Eds.), *Cahiers du centre Européen de Géodynamique et Simologie, Proceedings of the Workshop: The state of GPS vertical positioning: Separation of Earth processes by space geodesy*, Volume 23, Luxembourg, 111–123. 10

- Beer, A. (1852). Bestimmung der absorption des rothen lichts in farbigen flüssigkeiten. *Annalen der Physik*, 86, 78–87. 122
- Bendjoudi, H. (2002). The gravelius compactness coefficient: critical analysis of a shape index for drainage basins. *Hydrological Sciences Journal*, 47(6), 921–930. 154
- Bergström, S. (1976). Development and application of a conceptual runoff model for Scandinavian catchments. SMHI Reports RHO 7, Department of Water Resources Engineering, Lund Institute of Technology, University of Lund, Norrköping. 25, 249
- Berk, A., Bernstein, L. S., Anderson, G. P., Acharya, P. K., Robertson, D. C., Chetwynd, J. H., and Adler-Golden, S. M. (1998). MODTRAN cloud and multiple scattering upgrades with application to AVIRIS. *Remote Sensing of Environment*, 65(3), 367–375. 121
- Berthier, E., Arnaud, Y., Vincent, C., and Rémy, F. (2006). Biases of SRTM in high-mountain areas: Implications for the monitoring of glacier volume changes. *Geophysical Research Letters*, 33(8), L08502.1–L08502.5. 62
- Beven, K. J. and Kirkby, M. J. (1979). A physically based, variable contributing area model of basin hydrology. *Hydrological Sciences Journal*, 24, 43–69. 421
- Bird, R. E. and Riordan, C. (1986). Simple solar model for direct and diffuse irradiance on horizontal and tilted planes at the Earth's surface for cloudless atmosphere. *Journal of Climate and Applied Meteorology*, 25, 87–97. xviii, 96, 107, 123, 124, 125, 128, 129, 130, 133, 148, 398
- Birkeland, K. W. and Landry, C. C. (2002). Power-laws and snow avalanches. *Geophysical Research Letters*, 29(11), 49.1–49.3. 156
- Bishop, M. P., Jr., J. F. S., and Colby, J. D. (2003). Remote sensing and geomorphometry for studying relief production in high mountains. *Geomorphology*, 55, 345–361. 143
- Blair, R. W., J. (1994). Moraine and valley wall collapse due to rapid deglaciation in Mount Cook National Park, New Zealand. *Mountain Research and Development*, 14(4), 347–358. 14
- Blaschke, T. and Strobl, J. (2001). Whats wrong with pixels? Some recent developments interfacing remote sensing and GIS. *GIS-Zeitschrift für Geoinformationssysteme*, 6, 12–17. 151
- Blesius, L. and Weirich, F. (2005). The use of the Minnaert correction for land-cover classification in mountainous terrain. *International Journal of Remote Sensing*, 26(17), 3831–3851. 97, 98, 99
- Blöschl, G. (1999). Scaling issues in snow hydrology. *Hydrological Processes*, 13(14-15), 2149–2175. 151
- Blöschl, G., Kirnbauer, R., and Gutknecht, D. (1991). Distributed snowmelt simulations in an alpine catchment 1. Model evaluation on the basis of snow cover patterns. *Water Resources Research*, 27(12), 3171–3179. 260
- Boardman, J. (1994). Geometric mixture analysis of imaging spectrometry data. In *Proc. International Geoscience and Remote Sensing Symposium IGARSS '94. Surface and Atmospheric Remote Sensing: Technologies, Data Analysis and Interpretation*, Volume 4, 2369–2371. 169
- Boer, E. (2001). Kriging and thin plate splines for mapping climate variables. *International Journal of Applied Earth Observation and Geoinformation*, 3(2), 146–154. 278, 385
- Bonan, G. (2002). *Ecological Climatology: Concept and Applications*. New York: Cambridge Univ. Press. 107
- Bonett, D. G. and Seier, E. (2003). Confidence intervals for mean absolute deviations. *The*

- American Statistician*, 57(4), 233–236. 59, 387, 388
- Borcherds, P. H. and Sheth, C. V. (1995). Least squares fitting of a straight line to a set of data points. *European Journal of Physics*, 16(5), 204–210. 214
- Bouguer, P. (1729). *Essai d'optique sur la gradation de la lumière*. Paris: Claude Jombert. 122
- Bouguer, P. (1760). *Traité d'optique sur la gradation de la lumière* (H. L. Guerin & L. F. Delatour ed.). Paris: Nicolas Louis de la Caille. Ouvrage posthume de M. Bouguer, English translation by W. E. Knowles Middleton, Pierre Bouguer's optical treatise on the gradation of light (Toronto: University of Toronto Press, 1961). 122
- Boussinesq, J. (1877). Essai sur la theorie des eaux courantes. In *Mémoires présentés par divers savants à l'Académie des Sciences de l'Institut de France*, Volume XXIII, No 1, 680. Paris: Imprimerie Nationale. 417
- Boussinesq, J. (1904). Recherche théoriques sur l'écoulement des nappes d'eau infiltrées dans le sol et sur le débit des sources. *Journal de Mathématiques Pures et Appliquées, Série 5, Tome X, Fasc. I*, 5–78. 363, 417, 418, 420, 421, 422
- Bowden, D. T. (1994). Application of a snowmelt-runoff model to the Lake Pukaki basin, Mount Cook. Master's thesis, University of Canterbury. 4, 26, 39, 269, 310, 311, 324, 338
- Braithwaite, R. J. (1995). Positive degree-day factors for ablation on the Greenland ice sheet studied by energy-balance modelling. *Journal of Glaciology*, 41(137), 153–160. 244
- Braithwaite, R. J. and Olesen, O. B. (1989). *Calculation of glacier ablation from air temperature, West Greenland* (Oerlemans, J. ed.), 219–233. *Glacier Fluctuations and Climatic Change, Glaciology and Quaternary Geology*. Dordrecht: Springer. 248
- Braun, L. N. (1991). Modelling of the snow-water equivalent in the mountain environment. In *Snow, Hydrology and Forests in High Alpine Areas (Proceedings of the Vienna Symposium)*, Volume 205, 3–17. IAHS Publication. 308
- Brown, L., Thorne, R., and Woo, M.-K. (2008). Using satellite imagery to validate snow distribution simulated by a hydrological model in large northern basins. *Hydrological Processes*, 22(15), 2777–2787. 3, 28, 29, 261
- Brown, M., Gunn, S. R., and Lewis, H. G. (1999). Support vector machines for optimal classification and spectral unmixing. *Ecological Modelling*, 120(2-3), 167–179. 168
- Brun, E., Martin, E., Simon, V., Gendre, C., and Coléou, C. (1989). An energy and mass model of snow cover suitable for operational avalanche forecasting. *Journal of Glaciology*, 35(121), 333–342. 244, 245, 247
- Buhmann, M. D. (2003). *Radial Basis Functions, Theory and Implementations*. Cambridge: Cambridge University Press. 386
- Burrough, P. A. (1996). *Natural objects with indeterminate boundaries* (Peter A. Burrough and Andrew U. Frank ed.), Chapter 1, 3–28. *Geographic objects with indeterminate boundaries*. Bristol, PA: Taylor & Francis Inc. 150
- Cantor, G. (1955). *Contributions to the Founding of the Theory of Transfinite Numbers*. USA: Dover Publications. Translated from German by Philip E. B. Jourdain of "Beiträge zur Begründung der transfiniten Mengenlehre", *Mathematische Annalen*, 46(4), 1895, 481–512. 149
- Carlisle, B. (2002). *Digital elevation model quality and uncertainty in DEM-based spatial modelling*. Ph. D. thesis, University of Greenwich. 55, 60
- Carrara, A., Bitelli, G., and Carla, R. (1997). Comparison of techniques for generating digital

- terrain models from contour lines. *International Journal of Geographical Information Science*, 11(5), 451–473. 55, 60
- Casassa, G., Lopez, P., Pouyaud, B., and Escobar, F. (2009). Detection of changes in glacial run-off in alpine basins: examples from North America, the Alps, central Asia and the Andes. *Hydrological Processes*, 23(1), 31–41. 313
- Ca'zorzi, F. and Fontana, G. D. (1986). Improved utilization of maximum and minimum daily temperature in snowmelt modelling. In *Modelling Snowmelt-Induced Processes (Proceedings of the Budapest Symposium)*, Volume 155, 141–150. IAHS Publication. 309
- Chandrasekhar, S. (1960). *Radiative transfer*. New York: Courier Dover Publications. 121
- Chang, C.-I., Ren, H., Chang, C.-C., D'Amico, F., and Jensen, J. (2004). Estimation of sub-pixel target size for remotely sensed imagery. *IEEE Transactions on Geoscience and Remote Sensing*, 42(6), 1309–1320. 173
- Chavez, P. S. (1988). An improved dark-object subtraction technique for atmospheric scattering correction of multispectral data. *Remote Sensing of Environment*, 24(3), 459–479. 99
- Chavez, P. S. (1996). Atmospheric corrections-revisited and improved. *Photogrammetric Engineering and Remote Sensing*, 62(9), 1025–1036. 95
- Chavez, P. S. J., Sides, S. C., and Anderson, J. A. (1991). Comparison of three different methods to merge multiresolution and multispectral data: Landsat TM and SPOT Panchromatic. *Photogrammetric Engineering and Remote Sensing*, 57(3), 265–303. 72, 76
- Chen, H. and Varshney, P. K. (2007). A Human perception inspired quality metric for image fusion based on regional information. *Information Fusion*, 8(2), 193–207. 82
- Chen, J. and Ohmura, A. (1990). On the influence of Alpine glaciers on runoff. In *Proceedings of two Lausanne Symposia - Hydrology in Mountainous Regions. I - Hydrological Measurements; the Water Cycle*, Volume 193, Lausanne, Switzerland, 117–125. IAHS Publication. 313, 318
- Chen, Y., Hall, A., and Liou, K. N. (2006). Application of three-dimensional solar radiative transfer to mountains. *Journal of Geophysical Research*, 111(D21), D21111.1–D21111.13. 110, 115, 118, 119
- Chikita, K. A., Nishi, M., Fukuyama, R., and Hamahara, K. (2004). Hydrological and chemical budgets in a volcanic caldera lake: Lake Kussharo, Hokkaido, Japan. *Journal of Hydrology*, 291(1-2), 91–114. 301
- Chinn, T. J. (1979). How wet is the wettest of the wet west coast? *New Zealand Alpine Journal*, 32, 85–87. 12
- Chinn, T. J. (1989). *Satellite image atlas of glaciers: New Zealand* (Williams and J. G. Ferrigno ed.), 23–48. United States Geological Survey Professional Paper 1386-H. 14
- Chinn, T. J. (2001). Distribution of perennial snow and ice water resources in New Zealand. *Journal of Hydrology (NZ)*, 40(2), 139–187. 12, 14, 17, 290
- Chinn, T. J., McSaveney, M. J., and McSaveney, E. R. (1992). The Mount Cook rock avalanche of 14 December 1991. Information Brochure of the Institute of Geological and Nuclear Sciences. 14
- Chinn, T. J. H. (1969). Snow survey techniques, Waitaki Catchment, South Canterbury. *Journal of Hydrology (NZ)*, 8(2), 68–76. 23
- Chinn, T. J. H. (1981). Snowfall variations, hazards and snow melt. Technical Report WS 525, Ministry of Works and Development, Wellington, New Zealand. 23
- Chu, D. A., Kaufman, J., Ichoku, C., Remer, L. A., Tanré, D., and Holben, B. N. (2002).

- Validation of MODIS aerosol optical depth retrieval over land. *Geophysical Research Letters*, 29(12), 1617. 340
- Church, J. E. (1941). The melting of snow. In *Proceedings of the Central Snow Conference*, Volume I, 21–32. 248
- Civco, D. L. (1989). Topographic normalization of Landsat Thematic Mapper digital imagery. *Photogrammetric Engineering and Remote Sensing*, 55(9), 1303–1309. 97, 98
- Clark, M., rn Hreinsson, E., Martinez, G., Tait, A., Slater, A., Hendrikx, J., Owens, I., Gupta, H., Schmidt, J., and Woods, R. (2009). Simulations of seasonal snow for the South Island, New Zealand. *Journal of Hydrology (NZ)*, 48(2), 41–58. 3, 27
- Clark, M. P. (1993). Investigations in snow hydrology: an examination of energy balance influences on snow melt and characteristics of water movement through snow in the Craigieburn range, New Zealand. Master's thesis, University of Canterbury, Christchurch, New Zealand. 23, 246
- Clark, M. P., Rupp, D. E., Woods, R. A., Zheng, X., Ibbitt, R. P., Slater, A. G., Schmidt, J., and Uddstrom, M. J. (2008). Hydrological data assimilation with the ensemble Kalman filter: Use of streamflow observations to update states in a distributed hydrological model. *Advances in Water Resources*, 31(10), 1309–1324. 27
- Clark, M. P., Slater, A. G., Barrett, A. P., Hay, L. E., McCabe, G. J., Rajagopalan, B., and Leavesley, G. H. (2006). Assimilation of snow covered area information into hydrologic and land-surface models. *Advances in Water Resources*, 29, 1209–1221. 38, 337
- Cline, D. W., Bales, R. C., and Dozier, J. (1998). Estimating the spatial distribution of snow in mountain basins using remote sensing and energy balance modeling. *Water Resources Research*, 34(5), 1275–1285. 28
- Clyde, G. D. (1931). Snow-melting characteristics. *Utah Agricultural Experiment Station Bulletin*, 231, 1–23. 248
- Colbeck, S., Akitaya, E., Armstrong, R., Gubler, H., Lafeuille, J., Lied, K., McClung, D., and Morris, E. (1998). *The International Classification for Seasonal Snow on the Ground*. The International Commission on Snow and Ice. 30
- Colbeck, S. C. (1982). An overview of seasonal snow metamorphism. *Reviews of Geophysics and Space Physics*, 20(1), 45–61. 30
- Colby, J. D. (1991). Topographic normalization in rugged terrain. *Photogrammetric Engineering and Remote Sensing*, 57(5), 531–537. 98
- Coll, C., Caselles, V., Sobrino, J. A., and Valor, E. (1994). On the atmospheric dependence of the split-window equation for land-surface temperature. *International Journal of Remote Sensing*, 15(1), 105–155. 33
- Collins, E. H. (1934). Relationship of degree-days above freezing to runoff. *Transactions of the American Geophysical Union*, 15, 624–629. Reports and Papers, Hydrology. 248
- Congalton, R. G. (1991). A review of assessing the accuracy of classifications of remotely sensed data. *Remote Sensing of Environment*, 37(1), 35–46. 221
- Corripio, J. G. (2003). Vectorial algebra algorithms for calculating terrain parameters from DEMs and solar radiation modelling in mountainous terrain. *International Journal of Geographical Information Science*, 17(1), 1–23. 107, 109, 110
- Coutagne, A. (1948). Etude générale des variations de débits en fonction des facteurs qui les conditionnent, 2ème partie: les variations de débit en période non influencées par les

- précipitations. *La Houille Blanche*, 431–436. 422
- Cox, S. and Allen, S. (2009). Vampire rock avalanches of January 2008 and 2003, Southern Alps, New Zealand. *Landslides*, 6(2), 161–166. 14
- Crane, R. G. and Anderson, M. R. (1984). Satellite discrimination of snow / cloud surfaces. *International Journal of Remote Sensing*, 5, 213–223. 36, 70
- Craven, P. and Wahba, G. (1979). Smoothing noisy data with spline functions: estimating the correct degree of smoothing by the method of generalized cross-validation. *Numerische Mathematik*, 31, 377–403. 384
- Cucumo, M., Rosa, A. D., Ferraro, V., Kaliakatsos, D., and Marinelli, V. (2007). Experimental testing of models for the estimation of hourly solar radiation on vertical surfaces at Arcavacata di Rende. *Solar Energy*, 81(5), 692–695. 131
- Cutler, E. S. and Fitzharris, B. B. (2005). Observed surface snowmelt at high elevation in the Southern Alps of New Zealand. *Annals of Glaciology*, 40, 163–168. 2, 17, 252
- Dankers, R. and De Jong, S. (2004). Monitoring snow-cover dynamics in Northern Fennoscandia with SPOT VEGETATION images. *International Journal of Remote Sensing*, 25(17), 2933–2949. 29, 36
- Daubechies, I. (1990). The wavelet transform, time-frequency localization and signal analysis. *IEEE Transactions on Information Theory*, 36(5), 961–1005. 77
- Daubechies, I. (1992). *Ten Lectures on Wavelets*. Philadelphia, PA, USA: Society for Industrial and Applied Mathematics. 77
- de La Casinière, A., Bokoye, A. I., and Cabot, T. (1997). Direct solar spectral irradiance measurements and updated simple transmittance models. *Journal of Applied Meteorology*, 36(5), 509–520. 123
- de Ruyter de Wildt, M., Seiz, G., and Gruen, A. (2007). Operational snow mapping using multitemporal Meteosat SEVIRI imagery. *Remote Sensing of Environment*, 109(1), 29–41. 36
- de Zeeuw, J. W. (1973). *Hydrograph analysis for areas with mainly groundwater runoff*, Volume 2, Theories of field drainage and watershed runoff of *Drainage Principles and Applications*, Chapter 16, 321–258. Wageningen, Netherlands: International Institute for Land Reclamation and Improvement. 271, 419
- Deems, J. S., Fassnacht, S. R., and Elder, K. J. (2006). Fractal distribution of snow depth from Lidar data. *Journal of Hydrometeorology*, 7(2), 285–297. xxi, 158, 159
- DeGaetano, A. T. and Belcher, B. N. (2007). Spatial interpolation of daily maximum and minimum air temperature based on meteorological model analyses and independent observations. *Journal of Applied Meteorology and Climatology*, 46(11), 1981–1992. 277
- Dennison, P. E., Halligan, K. Q., and Roberts, D. A. (2004). A comparison of error metrics and constraints for multiple endmember spectral mixture analysis and spectral angle mapper. *Remote Sensing of Environment*, 93(3), 359–367. 180
- Dennison, P. E. and Roberts, D. A. (2003). Endmember selection for multiple endmember spectral mixture analysis using endmember average RMSE. *Remote Sensing of Environment*, 87(2-3), 123–135. 172
- Desmet, P. J. J. (1997). Effect of interpolation errors on the analysis of DEMs. *Earth Surface Processes and Landforms*, 22, 563–580. 58
- Dewalle, D. R. and Rango, A. (2008). *Principles of Snow Hydrology*. New York, USA: Cambridge University Press. 3, 8, 39, 239, 269, 292

- Dillard, J. P. and Orwig, C. F. (1979). Use of satellite data in runoff forecasting in the heavily forested, cloud-covered Pacific Northwest. In *Operational Applications of Satellite Snow Cover Observations (Proceedings of the Sparks, Nevada Workshop)*, Sparks, Nevada, 127–150. NASA. 39
- Dodson, R. and Marks, D. (1997). Daily air temperature interpolated at high spatial resolution over a large mountainous region. *Climate Research*, 8, 1–20. 277
- Dorren, L. K., Maier, B., and Seijmonsbergen, A. C. (2003). Improved Landsat-based forest mapping in steep mountainous terrain using object-based classification. *Forest Ecology and Management*, 183, 31–46. 97
- Dozier, J. (1980). A clear-sky spectral solar radiation model for snow-covered mountainous terrain. *Water Resources Research*, 16(4), 709–718. 118
- Dozier, J. (1981). A method for satellite identification of surface temperature fields of sub-pixel resolution. *Remote Sensing of Environment*, 11(3), 221–229. 127, 135
- Dozier, J. (1984). Snow reflectance from LANDSAT-4 Thematic Mapper. *IEEE Transactions on Geoscience and Remote Sensing*, GE-22(3), 323–328. 36
- Dozier, J. (1989). Spectral signature of alpine snow cover from the Landsat Thematic Mapper. *Remote Sensing of Environment*, 28, 9–22. 30, 31, 32, 36, 45, 70, 85, 174
- Dozier, J., Bruno, J., and Downey, P. (1981). A faster solution to the horizon problem. *Computers & Geosciences*, 7, 145–151. 108, 109, 113
- Dozier, J. and Frew, J. (1981). Atmospheric corrections to satellite radiometric data over rugged terrain. *Remote Sensing of Environment*, 11, 191–205. 99
- Dozier, J. and Frew, J. (1990). Rapid calculation of terrain parameters for radiation modeling from digital elevation data. *IEEE Transactions on Geoscience and Remote Sensing*, 28(5), 963–969. 104, 109, 110, 112, 113
- Dozier, J., Green, R. O., Nolin, A. W., and Painter, T. H. (2009). Interpretation of snow properties from imaging spectrometry. *Remote Sensing of Environment*, 113(Supplement 1), S25–S37. 5, 31, 32, 50
- Dozier, J. and Marks, D. (1987). Snow mapping and classification from Landsat Thematic Mapper data. *Annals of Glaciology*, 9, 97–103. 29, 36, 107
- Dozier, J. and Painter, T. H. (2004). Multispectral and hyperspectral remote sensing of alpine snow properties. *Annual Review of Earth and Planetary Sciences*, 32, 465–494. 3, 5, 31, 166, 167, 171
- Dozier, J., Painter, T. H., Rittger, K., and Frew, J. E. (2008). Time-space continuity of daily maps of fractional snow cover and albedo from MODIS. *Advances in Water Resources*, 31(11), 1515–1526. 185
- Dozier, J. and Warren, S. G. (1982). Effect of viewing angle on the infrared brightness temperature of snow. *Water Resources Research*, 18(5), 1424–1434. 33
- Du, Y., Vachon, P. W., and van der Sanden, J. J. (2003). Satellite image fusion with multiscale wavelet analysis for marine applications: preserving spatial information and minimizing artifacts (PSIMA). *Canadian Journal of Remote Sensing*, 29(1), 14–23. 80
- Dubayah, R., Dozier, J., and Davis, F. (1990). Topographic distribution of clear-sky radiation over the Konza prairie, Kansas. *Water Resources Research*, 26(4), 679–690. 110
- Dubayah, R. and Loechel, S. (1997). Modeling topographic solar radiation using GOES data. *Journal of Applied Meteorology*, 36(2), 141–154. 103, 110, 115, 119, 120

- Dubuisson, M.-P. and Jain, A. (1994). A modified Hausdorff distance for object matching. In *Pattern Recognition- Conference A: Computer Vision & Image Processing., Proceedings of the 12th IAPR International Conference on*, Volume 1, 566–568 vol.1. 198, 199, 228
- Duchon, J. (1976). Interpolation des fonctions de deux variables suivant le principe de la flexion des plaques minces. *R.A.I.R.O. Analyse Numérique*, 10, 5–12. 384
- Duchon, J. (1977). Splines minimizing rotation-invariant semi-norms in Sobolev spaces. In *Constructive Theory of Functions of Several Variables* (W. Schempp and K. Zeller ed.), Volume 571 of *Lecture Notes in Mathematics*, 85–100. Berlin / Heidelberg: Springer. 383
- Duckstein, L., Ambrus, S., and Davis, R. D. (1985). *Management forecasting requirements* (Anderson, M. G. and Burt, T. P. ed.), Chapter 16, 559–585. Hydrological Forecasting. New York: John Wiley and Sons. 300
- Duguay, C. R. (1993). Radiation modeling in mountainous terrain: review and status. *Mountain Research and Development*, 13(4), 339–357. 104, 108, 110, 115, 119, 146
- Dumont, M., Brissaud, O., Picard, G., Schmitt, B., Gallet, J.-C., and Arnaud, Y. (2009). High-accuracy measurements of snow Bidirectional Reflectance Distribution Function at visible and NIR wavelengths - comparison with modelling results. *Atmospheric Chemistry and Physics Discussions*, 9(5), 19279–19311. 32
- Duran, O. and Petrou, M. (2007). Anomaly detection using spectral unmixing with negative and superunity abundance weights. In *Proc. IEEE International Geoscience and Remote Sensing Symposium IGARSS 2007*, 4029–4032. 173
- Dwight, H. B. (1961). *Tables of Integrals and other Mathematical Data* (Fourth ed.). New York: The MacMillan Company. 396
- Dymond, J., Shepherd, J., and Qi, J. (2001). A simple physical model of vegetation reflectance for standardising optical satellite imagery. *Remote Sensing of Environment*, 75, 350–359. 98
- Dymond, J. R. and Shepherd, J. D. (1999). Correction of the topographic effect in remote sensing. *IEEE Transactions on Geoscience and Remote Sensing*, 37(5), 2618–2620. 98
- Efron, B. (1979). Bootstrap methods: another look at the jackknife. *The Annals of Statistics*, 7(1), 1–26. 59
- Ekstrand, S. (1996). Landsat TM-based forest damage assessment: correction for topographic effects. *Photogrammetric Engineering and Remote Sensing*, 1996(2), 151–161. 99, 143
- Elder, K., Dozier, J., and Michaelsen, J. (1991). Snow accumulation and distribution in an alpine watershed. *Water Resources Research*, 27(7), 1541–1552. 155
- Elder, K., Rosenthal, W., and Davis, R. E. (1998). Estimating the spatial distribution of snow water equivalence in a montane watershed. *Hydrological Processes*, 12(10-11), 1793–1808. 36, 161
- Etchevers, P., Martin, E., Brown, R., Fierz, C., Lejeune, Y., Bazile, E., Boone, A., Dai, Y.-J., Es-sery, R., Fernandez, A., Gusev, Y., Jordan, R., Koren, V., Kowalczyk, E., Nasonova, N. O., Pyles, R. D., Schlosser, A., Shmakin, A. B., Smirnova, T. G., Strasser, U., Verseghy, D., Yamazaki, T., and Yang, Z.-L. (2004). Validation of the energy budget of an alpine snow-pack simulated by several snow models (SnowMIP project). *Annals of Glaciology*, 38(9), 150–158. 157, 244, 247
- Evensen, G. (2006). *Data Assimilation: The Ensemble Kalman Filter*. New York: Springer-Verlag. 38

- Falconer, K. J. (2003). *Fractal Geometry: Mathematical Foundations and Applications*. (2nd ed.). Chichester, England: John Wiley & Sons. 153, 154, 155, 160
- Falls, L. W. (1974). The Beta distribution: A statistical model for world cloud cover. *J. Geophys. Res.*, 79(9), 1261–1264. 162
- Fawcett, T. (2006). An introduction to ROC analysis. *Pattern Recognition Letters*, 27(8), 861–874. 201, 223, 224
- Ferguson, R. (1999). Snowmelt Runoff Models. *Progress in Physical Geography*, 23(2), 205–227. 244, 245
- Fernandez, A. (1998). An energy balance model of seasonal snow evolution. *Physics and Chemistry of the Earth*, 23(5), 661–666. 247
- Ferner, S. and Sutherland, I. (1987). The utility of computer-processed NOAA imagery for snow cover mapping and streamflow simulation in Alberta. In *Proceedings of the Vancouver Symposium - Large Scale Effects of Seasonal Snow Cover*, Volume 166, Vancouver, Canada, 173–185. IAHS Publication. 29, 39
- Ferrari, S. and Cribari-Neto, F. (2004). Beta regression for modelling rates and proportions. *Journal of Applied Statistics*, 31(7), 799–815. 162
- Fierz, C., Riber, P., Adams, E. E., Curran, A. R., Föhn, P. M. B., Lehning, M., and Plüss, C. (2003). Evaluation of snow-surface energy balance models in alpine terrain. *Journal of Hydrology*, 282(1-4), 76–94. 247
- Fily, M., Dedieu, J.-P., and Durand, Y. (1999). Comparison between the results of a snow metamorphism model and remote sensing derived snow parameters in the Alps. *Remote Sensing of Environment*, 68(3), 254–263. 29, 33
- Finsterwalder, S. and Schunk, H. (1887). Der suldenferner. *Zeitschrift des Deutschen und Oesterreichischen Alpenvereins*, 18, 72–89. 248
- Fisher, P. (1997). The pixel: a snare and a delusion. *International Journal of Remote Sensing*, 18(7), 679–685. 151
- Fisher, R. A. (1921). On the “probable error” of a coefficient of correlation deduced from a small sample. *Metron*, 1, 3–32. 213
- Fitzgerald, G. J., Pinter, Jr., P. J., Hunsaker, D. J., and Clarke, T. R. (2005). Multiple shadow fractions in spectral mixture analysis of a cotton canopy. *Remote Sensing of Environment*, 97(4), 526–539. 169
- Fitzharris, B. B. (1978). Problems with estimating snow accumulation with elevation on New Zealand mountains. *Journal of Hydrology (NZ)*, 17(2), 78–80. 24, 28, 51
- Fitzharris, B. B. (1987). A method for indexing the variability of alpine snow cover over large areas. In *Proceedings of the Vancouver Symposium - Large scale effects of seasonal snow cover*, Volume 166, Vancouver, 139–50. IAHS Publication. 24, 25
- Fitzharris, B. B. (1992). The 1992 electricity crisis and the role of climate and hydrology. *New Zealand Geographer*, 48(2), 79–83. xix, 1, 21, 22, 23
- Fitzharris, B. B. and Garr, C. (1995). Simulation of past variability in seasonal snow in the Southern Alps, New Zealand. *Annals of Glaciology*, 21, 377–382. 2, 19, 25, 50, 239, 242, 254, 269, 283, 290, 296, 320
- Fitzharris, B. B., Lawson, W., and Owens, I. (1999). Research on glaciers and snow in New Zealand. *Progress in Physical Geography*, 23(4), 469–500. 2, 3, 12, 17, 19, 22, 23, 24, 27, 51, 292

- Fitzharris, B. B. and McAleve, B. (1999). Remote sensing of seasonal snow cover in the mountains of New Zealand using satellite imagery. *Geocarto International*, 14(3), 33–42. 28, 261
- Fitzharris, B. B. and McGann, R. (1989). Mapping seasonal snow cover from weather satellites. In R. Welch (Ed.), *Proceedings of the Fifteenth New Zealand Geography Conference*, Dunedin, New Zealand, 235–238. New Zealand Geographical Society. 28
- Fitzsimons, S. J. (1997). Late-glacial and early Holocene glacier activity in the Southern Alps, New Zealand. *Quaternary International*, 38–39, 69–76. 14
- Foppa, N., Hauser, A., Oesch, D., Wunderle, S., and Meister, R. (2007). Validation of operational AVHRR subpixel snow retrievals over the European Alps based on ASTER data. *International Journal of Remote Sensing*, 28(21), 4841–4865. 36, 175, 191, 203, 217
- Foppa, N., Wunderle, S., Hauser, A., Oesch, D., and Kuchen, F. (2004). Operational subpixel snow mapping over the Alps with NOAA-AVHRR data. *Annals of Glaciology*, 38(1), 245–252. 170, 175
- Foster, J. L., Sun, C., Walker, J. P., Kelly, R., Chang, A., Dong, J., and Powell, H. (2005). Quantifying the uncertainty in passive microwave snow water equivalent observations. *Remote Sensing of Environment*, 94(2), 187–203. 34
- Fountain, A. G. and Tangborn, W. V. (1985). The effect of glaciers on streamflow variations. *Water Resources Research*, 21(4), 579–586. 313
- Fourier, J.-B. J. (1822). *Théorie analytique de la chaleur*. Paris: Jacques Gabay. Reprod. in 1988. 418
- Frey, R. A., Ackerman, S. A., Liu, Y., Strabala, K. I., Zhang, H., Key, J. R., and Wang, X. (2008). Cloud detection with MODIS. Part I: Improvements in the MODIS cloud mask for collection 5. *Journal of Atmospheric and Oceanic Technology*, 25(7), 1057–1072. 87, 88
- Gabriel, P., Lovejoy, S., Schertzer, D., and Austin, G. L. (1988). Multifractal analysis of satellite resolution dependence. *Geophysical Research Letters*, 15(12), 1373–1376. 151
- Gao, B. C. and Kaufman, Y. J. (2003). Water vapor retrievals using Moderate Resolution Imaging Spectroradiometer (MODIS) near-infrared channels. *Journal of Geophysical Research*, 108(D13), ACH4.1–ACH4.10. 125
- Garen, D. C. and Marks, D. (2005). Spatially distributed energy balance snowmelt modelling in a mountainous river basin: estimation of meteorological inputs and verification of model results. *Journal of Hydrology*, 315(1–4), 126–153. 110, 247, 277
- Garguet-Duport, B., Girel, J., Chassery, J.-M., and Pautou, G. (1996). The use of multi-resolution analysis and wavelet transform for merging SPOT panchromatic and multispectral imagery data. *Photogrammetric Engineering and Remote Sensing*, 62(9), 1057–1066. 72, 76
- Garnier, B. J. (1958). *The climate of New Zealand*. London: Edward Arnold. 12
- Garzelli, A. and Nencini, F. (2006). PAN-sharpening of very high resolution multispectral images using genetic algorithms. *International Journal of Remote Sensing*, 27(15), 3273–3292. 72, 220
- GCOS (2006). Systematic observation requirements for satellite-based products for climate. <http://www.wmo.int/pages/prog/gcos/Publications/gcos-107.pdf>. 71
- Gerstenecker, C., Läufer, G., Steineck, D., Tiede, C., and Wrobel, B. (2005). Validation of digital elevation models around Merapi Volcano, Java, Indonesia. *Natural Hazards and*

- Earth System Sciences*, 5, 863–876. 62
- Gill, P. E., Murray, W., and Wright, M. H. (1981). *Practical Optimization*. London: Academic Press. 173
- Gillies, A. J. (1964). Review of snow survey methods, and snow surveys in the Fraser Catchment, Central Otago. *Journal of Hydrology (NZ)*, 3(1), 3–16. 22, 27
- Goetz, A. F., Vane, G., Solomon, J. E., and Rock, B. N. (1985). Imaging spectrometry for earth remote sensing. *Science*, 228(4704), 1147–1153. 169
- Gómez-Landesa, E., Rango, A., and Hall, D. K. (2001). Improved snow cover remote sensing for snowmelt runoff forecasting. In *Proceeding of the International Symposium on Remote Sensing and Hydrology 2000*, Volume 267, Santa Fe, New Mexico, 61–65. IAHS Publication. 36
- González-Audicana, M., Otazu, X., Fors, O., and Alvarez-Mozos, J. (2006). A low computational-cost method to fuse IKONOS images using the spectral response function of its sensors. *IEEE Transactions on Geoscience and Remote Sensing*, 44(6), 1683–1691. 75, 80
- González-Audicana, M., Saleta, J. L., Catalán, R. G., and García, R. (2004). Fusion of multispectral and panchromatic images using improved IHS and PCA mergers based on wavelet decomposition. *IEEE Transactions on Geoscience and Remote Sensing*, 42(6), 1291–1299. 72, 74
- Goodchild, M. F. and Mark, D. M. (1987). The fractal nature of geographic phenomena. *Annals of Association of American Geographers*, 77(2), 265–278. 151
- Graetz, R. D. and Gentle, M. R. (1982). The relationship between reflectance in the Landsat wavebands and the composition of an Australian semi-arid shrub rangeland. *Photogrammetric Engineering and Remote Sensing*, 48, 1721–1730. 169
- Granger, R. J., W., P. J., and Parviainen, J. (2002). Boundary-layer integration approach to advection of sensible heat to a patchy snow cover. *Hydrological processes*, 16(18), 3559–3569. 158
- Gregg, W. W. and Carder, K. L. (1990). A simple spectral solar irradiance model for cloudless maritime atmospheres. *Limnology and Oceanography*, 35(8), 1657. 128
- Grena, R. (2008). An algorithm for the computation of the solar position. *Solar Energy*, 82(5), 462–470. 102
- Greuell, W. and Oerlemans, J. (2004). Narrowband-to-broadband albedo conversion for glacier ice and snow: equations based on modeling and ranges of validity of the equations. *Remote Sensing of Environment*, 89(1), 95–105. 247
- Griffiths, G. A. and McSaveney, M. J. (1983). Distribution of mean annual precipitation across some steepland regions of New Zealand. *New Zealand Journal of Science*, 26, 197–209. 12, 256
- Grimmond, C. S. B. (1980). Runoff from seasonal snow in the Fraser catchment, Central Otago. BSc Hons dissertation. 26, 39, 338
- Grippa, M., Mognard, N., and Le Toan, T. (2005). Comparison between the interannual variability of snow parameters derived from SSM/I and the Ob river discharge. *Remote Sensing of Environment*, 98(1), 35–44. 29
- Gromov, M. (2007). *Metric Structures for Riemannian and Non-Riemannian Spaces*. Boston: Birkhäuser. 197
- Gross, H. N. and Schott, J. R. (1998). Application of spectral mixture analysis and image

- fusion techniques for image sharpening. *Remote Sensing of Environment*, 63(2), 85–94. 72
- Gu, D. and Gillespie, A. (1998). Topographic normalization of Landsat TM images of forest based on subpixel Sun–Canopy–Sensor geometry. *Remote Sensing of Environment*, 64(2), 166–175. 98
- Guangtao, Z., Wenjun, Z., Xiaokang, Y., and Yi, X. (2005). Image quality assessment metrics based on multi-scale edge presentation. In *Proceedings of the IEEE Workshop on Signal Processing Systems Design and Implementation*, Greece, 331–336. IEEE: IEEE. 196
- Gupta, R., Haritashya, U., and Singh, P. (2005). Mapping dry/wet snow cover in the Indian Himalayas using IRS multispectral imagery. *Remote Sensing of Environment*, 97(4), 458–469. 29, 36
- Gupta, R. P., Ghosh, A., and Haritashya, U. K. (2007). Empirical relationship between near-IR reflectance of melting seasonal snow and environmental temperature in a Himalayan basin. *Remote Sensing of Environment*, 107(3), 402–413. 29, 297
- Hale, G. M. and Querry, M. R. (1973). Optical constants of water in the 200 nm to 200 μ m wavelength region. *Applied Optics*, 12(3), 555–563. 30, 86
- Hale, S. R. and Rock, B. N. (2003). Impact of topographic normalization on land-cover classification accuracy. *Photogrammetric Engineering and Remote Sensing*, 69(7), 785–791. 97
- Hall, D. K., Foster, J. L., Salomonson, V. V., Klein, A. G., and Chien, J. Y. L. (2001). Development of a technique to assess snow-cover mapping errors from space. *IEEE Transactions on Geoscience and Remote Sensing*, 39(2), 432–438. 222
- Hall, D. K. and Martinec, J. (1985). *Remote sensing of ice and snow*. New York: Chapman and Hall. 28, 39, 293
- Hall, D. K., Riggs, G., Salomonson, V. V., DiGirolamo, N. E., and Bayr, K. J. (2002). MODIS snow-cover products. *Remote Sensing of Environment*, 83, 181–194. 3, 34, 36, 45, 46, 47, 51, 70, 149, 160, 166
- Hall, D. K. and Riggs, G. A. (2007). Accuracy assessment of the MODIS snow products. *Hydrological Processes*, 21(12), 1534–1547. 4, 47, 51
- Hall, D. K., Riggs, G. A., and Salomonson, V. V. (1995). Development of methods for mapping global snow cover using moderate resolution imaging spectroradiometer data. *Remote Sensing of Environment*, 54, 127–140. 45, 71, 160
- Hall, D. K., Riggs, G. A., and Salomonson, V. V. (2006, updated daily). MODIS/Terra Snow Cover 5-Min L2 Swath 500m V004 and V005 [March 2000 to May 2006]. Digital media.
- Hall, F. R. (1968). Base-flow recessions - a review. *Water Resources Research*, 4(5), 973–983. 417, 421
- Halley, J. M., Hartley, S., Kallimanis, A. S., Kunin, W. E., Lennon, J. J., and Sgardelis, S. P. (2004). Uses and abuses of fractal methodology in ecology. *Ecology Letters*, 7(3), 254–271. 155
- Hanley, J. A. and Mcneil, B. J. (1982). The meaning and use of the area under a receiver operating characteristic (ROC) curve. *Radiology*, 143(1), 29–36. 223
- Haran, T. M., Khalsa, S. S., Khalsa, S. S., Knowles, K., and Gumley, L. E. (2001). The MODIS Swath-to-Grid Toolbox. In *American Geophysical Union Abstracts*, Boston, AGU–U21A–22. American Geophysical Union. 67
- Harrison, A. R. and Lucas, R. M. (1989). Multi-spectral classification of snow using NOAA AVHRR imagery. *International Journal of Remote Sensing*, 10(4–5), 907–916. 35

- Harrison, W. (1986). Seasonal accumulation and loss of snow from a block mountain catchment in Central Otago. *Journal of Hydrology (NZ)*, 25, 1–17. 23
- Hay, J. E. and Fitzharris, B. B. (1988). The synoptic climatology of ablation on a New Zealand glacier. *International Journal of Climatology*, 8(2), 201–215. 245
- Hay, J. E. and McKay, D. C. (1985). Estimating solar irradiance on inclined surfaces: A review and assessment of methodologies. *International Journal of Sustainable Energy*, 3(4&5), 203–240. 107, 131, 132
- Heinz, D. C. and Chang, C.-I. (2001). Fully constrained least squares linear spectral mixture analysis method for material quantification in hyperspectral imagery. *IEEE Transactions on Geoscience and Remote Sensing*, 39(3), 529–545. 173
- Henderson, R. D. and Thompson, S. M. (1999). Extreme rainfalls in the Southern Alps of New Zealand. *Journal of Hydrology (NZ)*, 38(2), 309–330. 12, 16, 256, 283
- Hendrikx, J. (2005). *An examination of the snow and avalanche hazard on the Milford Road, Fiordland, New Zealand*. Ph. D. thesis, University of Canterbury, Christchurch, New Zealand. 24
- Hendrikx, J. (2007). The June 2006 Canterbury snowstorm. *Journal of Hydrology (NZ)*, 46, 33–49. 12
- Hickman, J. S. (1972). Estimates of snowline from meteorological satellite pictures. Technical Report research report 12, New Zealand Meteorological Service, Wellington. 27
- Hicks, D. M., Hill, J., and Shankar, U. (1996). Variation of suspended sediment yields around New Zealand: the relative importance of rainfall and geology. In *Proceedings of the Exeter Symposium: Erosion and Sediment Yield: Global and Regional Perspectives*, Volume 236, Exeter, 149–156. IAHS Publication. 14
- Ho, C. W. (1982). Snow avalanche studies in the Mount Cook region. Master's thesis, University of Otago, Dunedin, New Zealand. 24
- Hock, R. (2003). Temperature index melt modelling in mountain areas. *Journal of Hydrology*, 282(1-4), 104–115. 25, 242, 244, 249, 251, 252, 253, 296, 305
- Hock, R. (2005). Glacier melt: a review of processes and their modelling. *Progress in Physical Geography*, 29(3), 362–391. 249, 296
- Holzmann, H., Koboltschnig, G., Vollmann, M., and Schöner, W. (2007). Snow melt modelling and comparison with satellite images. In *Geophysical Research Abstracts*, Volume 9, Vienna, Austria, EGU2007–A–10504. European Geosciences Union: Copernicus Publications. 261, 273
- Hori, M., Aoki, T., Tanikawa, T., Motoyoshi, H., Hachikubo, A., Sugiura, K., Yasunari, T. J., Eide, H., Storvold, R., Nakajima, Y., and Takahashi, F. (2006). In-situ measured spectral directional emissivity of snow and ice in the 8–14 μm atmospheric window. *Remote Sensing of Environment*, 100(4), 486–502. 33
- Horowitz, H. M., Nalepka, R. F., Hyde, P., and Morgenstern, J. P. (1971). Estimating the proportions of unresolved objects within a single resolution element of a multispectral scanner. In *Proceedings of the Seventh International Symposium on Remote Sensing of Environment*, University of Michigan, Ann Arbor, MI, 1307–1320. 167
- Horton, R. E. (1915). The melting of snow. *Monthly Weather Review*, 43(12), 599–605. 248
- Hreinsson, E. Ö. (2008). Assimilation of snow covered area into a hydrologic model. Master's thesis, University of Canterbury, Christchurch, New Zealand. 38, 337

- Hudson, S. R., Warren, S. G., Brandt, R. E., Grenfell, T. C., and Six, D. (2006). Spectral bidirectional reflectance of Antarctic snow: measurements and parameterization. *Journal of Geophysical Research*, 111(D18), D18106.1–D18106.19. 31, 32, 100, 101
- Hutchinson, M. F. (1989). A new procedure for gridding elevation and stream line data with automatic removal of spurious pits. *Journal of Hydrology*, 106, 211–232. 55, 278, 284
- Hutchinson, M. F. (1995). Interpolating mean rainfall using thin plate smoothing splines. *International Journal of Geographical Information Science*, 9(4), 385–403. 385
- Hutchinson, M. F. (1998a). Interpolation of rainfall data with thin plate smoothing splines - part I: Two dimensional smoothing of data with short range correlation. *Journal of Geographic Information and Decision Analysis*, 2(2), 139–151. 284
- Hutchinson, M. F. (1998b). Interpolation of rainfall data with thin plate smoothing splines: II. Analysis of topographic dependence. *Journal of Geographic Information and Decision Analysis*, 2(2), 152–167. 284
- Huttenlocher, D., Klanderma, G., and Rucklidge, W. (1993). Comparing images using the Hausdorff distance. *IEEE Transactions on Pattern Analysis and Machine Intelligence*, 15(9), 850–863. 197
- Igawa, N., Koga, Y., Matsuzawa, T., and Nakamura, H. (2004). Models of sky radiance distribution and sky luminance distribution. *Solar Energy*, 77(2), 137–157. 131
- Immerzeel, W., Droogers, P., de Jong, S., and Bierkens, M. (2009). Large-scale monitoring of snow cover and runoff simulation in Himalayan river basins using remote sensing. *Remote Sensing of Environment*, 113(1), 40–49. 4, 29
- Iqbal, M. (1983). *An Introduction to Solar Radiation*. Toronto, New York: Academic Press. 106, 107, 108, 110, 112, 113, 122, 124, 126, 128, 131
- Ishikawa, N., Owens, I. F., and Sturman, A. P. (1992). Heat balance characteristics during fine periods on the lower parts of the Franz Josef Glacier, South Westland, New Zealand. *International Journal of Climatology*, 12(4), 397–410. 245, 246
- Islam, M. N. (2001). *Hydrological modelling of glacierized mountain watersheds in Southern Alps, New Zealand*. Ph. D. thesis, Lincoln University, Christchurch, New Zealand. 26, 50
- Itten, K. and Meyer, P. (1993). Geometric and radiometric correction of TM data of mountainous forested areas. *IEEE Transactions on Geoscience and Remote Sensing*, 31(4), 764–770. 97
- Jansson, P., Hock, R., and Schneider, T. (2003). The concept of glacier storage: a review. *Journal of Hydrology*, 282(1-4), 116–129. 313
- Jarvis, C. H. and Stuart, N. (2001a). A comparison among strategies for interpolating maximum and minimum daily air temperatures. Part I: the selection of 'guiding' topographic and land cover variables. *Journal of Applied Meteorology*, 40(6), 1060–1074. 277
- Jarvis, C. H. and Stuart, N. (2001b). A comparison among strategies for interpolating maximum and minimum daily air temperatures. Part II: The interaction between number of guiding variables and the type of interpolation method. *Journal of Applied Meteorology*, 40(6), 1075–1084. 277
- Jin, X. Y. and Davis, C. H. (2005). Automated building extraction from high-resolution satellite imagery in urban areas using structural, contextual, and spectral information. *EURASIP Journal of Applied Signal Processing*, 2005(14), 2196–2206. 72
- Johansson, B., Caves, R., Ferguson, R., and Turpin, O. (2001). Using remote sensing data

- to update the simulated snow pack of the HBV runoff model. In M. Owe, K. Brubaker, J. Ritchie, and A. Rango (Eds.), *Proceedings of the Santa Fe symposium - Remote Sensing and Hydrology*, Volume 267, Santa Fe, New Mexico, USA, 595–597. IAHS Publication. 37
- Johansson, B., J., A., and Jansson, J. (2003). Satellite data on snow cover in the HBV model. Method development and evaluation. Report no. 90, SMHI, Hydrology, Norrköping. 37
- Johnson, N. L., Kotz, S., and Balakrishnan, N. (1995). *Continuous univariate distributions* (2nd ed.), Volume 1–2. New York: Wiley & Sons. 388, 390
- Jönsson, P. and Eklundh, L. (2004). TIMESAT—a program for analyzing time-series of satellite sensor data. *Computers & Geosciences*, 30(8), 833–845. 293
- Jordan, R. (1991). A one-dimensional temperature model for a snowcover; Technical documentation for SN THERM.89. Technical Report ADA245493, Cold Regions Research and Engineering Lab, Hanover, Netherlands. 247
- Justus, C. G. and Paris, M. V. (1985). A model for solar spectral irradiance and radiance at the bottom and top of a cloudless atmosphere. *Journal of Applied Meteorology*, 24(3), 193–205. 129, 130
- Kasten, F. and Young, A. T. (1989). Revised optical air mass tables and approximation formula. *Applied Optics*, 28(22), 4735–4738. 124
- Kaufman, Y. J., Kleidman, R. G., Hall, D. K., Martins, J. V., and Barton, J. S. (2002). Remote sensing of subpixel snow cover using 0.66 and 2.1 μm channels. *Geophysical Research Letters*, 29(16), 28.1–28.4. 170
- Kavasseri, R. G. and Nagarajan, R. (2005). A multifractal description of wind speed records. *Chaos, Solitons & Fractals*, 24(1), 165–173. 155
- Kelliher, F., Owens, I., Sturman, A., Byers, J., Hunt, J., and Seveney, T. (1996). Radiation and ablation on the névé of Franz Josef Glacier. *Journal of Hydrology (NZ)*, 35(1), 129–148. 23, 246
- Kelly, R. E., Chang, A. T., Tsang, L., and Foster, J. L. (2003). A prototype AMSR-E global snow area and snow depth algorithm. *IEEE Transactions on Geoscience and Remote Sensing*, 41(2), 230–242. 34
- Kent, J. T. and Mardia, K. V. (1994). *The link between kriging and thin plate splines* (F. P. Kelly ed.), Chapter 24, 325–339. Probability, Statistics and Optimisation. Chichester: Wiley & Sons. 385
- Kent, K. M. (1972). *Travel time, time of concentration, and lag*, Chapter 15 Section 4, Hydrology, 1–16. National Engineering Handbook. Washington, DC: Natural Resources Conservation Service, U.S. Govt. 301
- Kerekes, J. (2008). Receiver operating characteristic curve confidence intervals and regions. *IEEE Geoscience and Remote Sensing Letters*, 5(2), 251–255. 224
- Kerr, T. (2005). Snow storage modeling in the Lake Pukaki catchment, New Zealand: an investigation of enhancements to the SNOWSIM model. Master's thesis, University of Canterbury, Christchurch, New Zealand. xxiii, 2, 3, 7, 23, 26, 50, 239, 242, 255, 256, 257, 259, 260, 267, 278, 283, 285, 286, 289, 290, 296, 300, 306, 309, 310, 311
- Kerr, T., Owens, I., and Henderson, R. (2007). An extreme average annual precipitation gradient measured in a lee mountain catchment, South Island, New Zealand. In *Geophysical Research Abstracts*, 1607–7962/gra/EGU2007–A–11607. 12, 255
- Keshava, N. (2003). A survey of spectral unmixing algorithms. *Lincoln Laboratory Jour-*

- nal*, 14(1), 55–78. 167, 168, 173
- Key, J. R. (1994). The area coverage of geophysical fields as a function of sensor field-of-view. *Remote Sensing of Environment*, 48(3), 339–346. 161, 163, 335
- Key, J. R., Collins, J., Fowler, C., and Stone, R. (1997). High-latitude surface temperature estimates from thermal satellite data. *Remote Sensing of Environment*, 61(2), 302–309. 33, 46, 247
- Khlopenkov, K. and Trishchenko, A. (2008). Implementation and evaluation of concurrent gradient search method for reprojection of MODIS Level 1B imagery. *IEEE Transactions on Geoscience and Remote Sensing*, 46(7), 2016–2027. 43, 67
- Khlopenkov, K. V. and Trishchenko, A. P. (2007). SPARC: New cloud, snow, and cloud shadow detection scheme for historical 1–km AVHRR data over Canada. *Journal of Atmospheric and Atmospheric Technologies*, 24(3), 322–343. 86, 87, 113
- Kienzle, S. (2004). The effect of DEM raster resolution on first order, second order and compound terrain derivatives. *Transactions in GIS*, 8(1), 83–111. 115
- Kirkbride, M. (1995). Relationship between temperature and ablation on the Tasman glacier, Mount Cook National Park, New Zealand. *New Zealand Journal of Geology and Geophysics*, 38, 17–27. 248, 251, 305
- Kitamoto, A. and Takagi, M. (2000). The area proportion distribution-relationship with the internal structure of mixels and its application to image classification. *Systems and Computers in Japan*, 31(5), 57–76. 162, 165, 335
- Klein, A. G., Hall, D., and Riggs, G. A. (1998). Improving snow-cover mapping in forests through the use of a canopy reflectance model. *Hydrological Processes*, 12, 1723–1744. 45, 46, 160
- Klein, A. G., Hall, D. K., and Riggs, G. A. (1997). Improving the MODIS global snow-mapping algorithm. In *Proceedings of the IEEE International Geoscience and Remote Sensing Symposium*, Singapore, 619–621. IEEE International: IEEE. 46
- Klein, A. G. and Isacks, B. L. (1999). Spectral mixture analysis of Landsat thematic mapper images applied to the detection of the transient snowline on tropical Andean glaciers. *Global and Planetary Change*, 22(1–4), 139–154. 169
- Klein, A. G. and Stroeve, J. (2002). Development and validation of a snow albedo algorithm for the MODIS instrument. *Annals of Glaciology*, 34, 45–52. 247
- Klinkenberg, B. (1994). A fractal analysis of shadowed and sunlit areas. *International Journal of Remote Sensing*, 15(5), 967–977. 157
- Kobayashi, S. and Sanga-Ngoie, K. (2008). The integrated radiometric correction of optical remote sensing imageries. *International Journal of Remote Sensing*, 29(20), 5957–5985. 123, 143
- Koboltschnig, G. R., Schoner, W., Zappa, M., and Holzmann, H. (2007). Contribution of glacier melt to stream runoff: if the climatically extreme summer of 2003 had happened in 1979. *Annals of Glaciology*, 46(1), 303–308. 313
- Kolberg, S., Rue, H., and Gottschalk, L. (2006). A Bayesian spatial assimilation scheme for snow coverage observations in a gridded snow model. *Hydrology and Earth System Sciences*, 10(3), 369–381. 38
- Kondratyev, K. Y. (1969). *Radiation in the Atmosphere*. University of Michigan: Academic Press. 106, 107

- König, M., Winther, J.-G., and Isaksson, E. (2001). Measuring snow and glacier ice properties from satellite. *Reviews of Geophysics*, 39(1), 1–27. 33, 34, 85, 87, 170, 247
- Kotchenova, S. Y., Vermote, E. F., Levy, R., and Lyapustin, A. (2008). Radiative transfer codes for atmospheric correction and aerosol retrieval: intercomparison study. *Applied Optics*, 47(13), 2215–2226. 123
- Kraijenhoff van de Leur, D. A. (1973). *Rainfall-runoff relations and computational models*, Volume 2, Theories of field drainage and watershed runoff of *Drainage Principles and Applications*, Chapter 15, 245–320. Wageningen, Netherlands: International Institute for Land Reclamation and Improvement. 419, 421
- Krenke, A. N. and Khodakov, V. G. (1966). On the relationship of surface melt of glaciers with air temperature. *Data on Glaciological Studies*, 12, 153–164. In Russian. 248
- Kuchment, L. S. and Gelfan, A. N. (2001). Statistical self-similarity of spatial variations of snow cover: verification of the hypothesis and application in the snowmelt runoff generation models. *Hydrological Processes*, 15(18), 3343–3355. 158
- Kulkarni, A., Randhawa, S., Rathore, B., Bahuguna, I., and Sood, R. (2002). Snow and glacier melt runoff model to estimate hydropower potential. *Journal of the Indian Society of Remote Sensing*, 30(4), 221–228. 29
- Kunin, W. E. (1998). Extrapolating species abundance across spatial scales. *Science*, 281(5382), 1513–1515. 156
- Kuusisto, E. (1980). On the values and variability of degree-day melting factor in Finland. *Nordic Hydrology*, 11(5), 235–242. 252
- Kuusisto, E. (1986). The energy balance of a melting snow cover in different environments. In *Proceedings of the Budapest Symposium - Modelling Snowmelt-Induced Processes*, Volume 155, Budapest, 37–45. IAHS Publication. 245
- Lam, N. S.-N. and Quattrochi, D. A. (1992). On the issues of scale, resolution, and fractal analysis in the mapping sciences. *Professional Geographer*, 44(1), 88–98. 151
- Lambert, J. H. (1760). *Photometria sive de mensura et gradibus luminis, colorum, et umbrae*. Ausburg. 122
- Land Processes DAAC (2006a). *MODIS Reprojection Tool Swath (MRTSwath) release notes version 2.1*. Land Processes DAAC. Available at https://lpdaac.usgs.gov/lpdaac/tools/modis_reprojection_tool_swath. 67
- Land Processes DAAC (2006b). *MODIS Reprojection Tool Swath users manual*. Land Processes DAAC. Available at https://lpdaac.usgs.gov/lpdaac/tools/modis_reprojection_tool_swath. 67
- Lang, H. and Braun, L. (1990). On the information content of air temperature in the context of snow melt estimation. In L. Molar (Ed.), *Proceedings of the Strbsk Pleso Worksho - Hydrology of Mountainous Area*, Volume 190, Czechoslovakia, 347–354. IAHS Publication. 249, 251
- Laporterie-Déjean, F., de Boissezon, H., Flouzat, G., and Lefèvre-Fonollosa, M.-J. (2005). Thematic and statistical evaluations of five panchromatic/multispectral fusion methods on simulated PLEIADES-HR images. *Information Fusion*, 6(3), 193–212. 80
- Lasaponara, R. and Masini, N. (2005). QuickBird-based analysis for the spatial characterization of archaeological sites: case study of the Monte Serico medieval village. *Geophysical Research Letters*, 32(12), L12313. 72

- Lavallée, S., Brissette, F. P., Leconte, R., and Larouche, B. (2006). Monitoring snow-cover depletion by coupling satellite imagery with a distributed snowmelt model. *Journal of Water Resources Planning and Management*, 132(2), 71–78. 3, 28, 37
- Lawson, C. L. and Hanson, R. J. (1974). *Solving least squares problems*. Prentice-Hall Series in Automatic Computation. Englewood Cliffs, New Jersey, USA: Prentice-Hall. 172
- Leckner, B. (1978). The spectral distribution of solar radiation at the Earth's surface—elements of model. *Solar Energy*, 20(2), 143–150. xviii, 122, 125, 126, 398
- Lehning, M. (2005). Energy balance and thermophysical processes in snowpacks. In M. G. Anderson (Ed.), *Snow and Glacier Hydrology*, Volume 4 of *Encyclopedia of Hydrological Sciences*, Part 14, Chapter 160, 1–16. Chichester: John Wiley & Sons, Ltd. 155, 244
- Lenoble, J. (Ed.) (1985). *Radiative Transfer in Scattering and Absorbing Atmospheres: Standard Computational Procedures*. Hampton, Va., USA: A. Deepak. 121, 127
- Leong, D. and Chesterton, J. (2005). Waitaki catchment, hydrological information. Report commissioned by the Ministry for the Environment for consideration by the Waitaki Catchment Water Allocation Board 582, Ministry for the Environment, Wellington, New Zealand. 16, 17
- Leprieur, C. E., Durand, J. M., and Peyron, J. L. (1988). Influence of topography on forest reflectance using Landsat Thematic Mapper and digital terrain data. *Photogrammetric Engineering and Remote Sensing*, 54(4), 491–496. 95
- Leroux, C., Deuzé, J.-L., Goloub, P., Sergent, C., and Fily, M. (1998). Ground measurements of the polarized bidirectional reflectance of snow in the near-infrared spectral domain: Comparisons with model results. *Journal of Geophysical Research*, 103(D16), 19721–19732. 32, 101
- Leroux, C., Lenoble, J., Brogniez, G., Hovenier, J. W., and Haan, J. F. D. (1999). A model for the bidirectional polarized reflectance of snow. *Journal of Quantitative Spectroscopy and Radiative Transfer*, 61(3), 273–285. 32
- Li, B., Zhu, A.-X., Zhou, C., Zhang, Y., Pei, T., and Qin, C. (2008). Automatic mapping of snow cover depletion curves using optical remote sensing data under conditions of frequent cloud cover and temporary snow. *Hydrological Processes*, 22(16), 2930–2942. 29, 292, 293
- Li, D. H. W. and Cheung, G. H. W. (2005). Study of models for predicting the diffuse irradiance on inclined surfaces. *Applied Energy*, 81(2), 170–186. 131
- Li, S., Kwok, J. T., and Wang, Y. (2002). Using the discrete wavelet frame transform to merge Landsat TM and SPOT panchromatic images. *Information Fusion*, 3, 17–23. 72, 77
- Li, X. and Williams, M. W. (2008). Snowmelt runoff modelling in an arid mountain watershed, Tarim Basin, China. *Hydrological Processes*, 22(19), 3931–3940. 4, 293, 296
- Li, Z. (1994). A comparative study of the accuracy of Digital Terrain Models (DTMs) based on various data models. *Journal of Photogrammetry and Remote Sensing*, 49(1), 2–11. 58
- Li, Z., Zhu, Q., Gold, C., and Gold, C. (2005). *Digital terrain modeling: principles and methodology*. CRC Press. 56, 58
- Liang, S., Zhong, B., and Fang, H. (2006). Improved estimation of aerosol optical depth from MODIS imagery over land surfaces. *Remote Sensing of Environment*, 104(4), 416–425. 340
- Liang, T. G., Huang, X. D., Wu, C. X., Liu, X. Y., Li, W. L., Guo, Z. G., and Ren, J. Z. (2008). An application of MODIS data to snow cover monitoring in a pastoral area: A case study

- in Northern Xinjiang, China. *Remote Sensing of Environment*, 112(4), 1514–1526. 29, 47, 85
- Liang, X., Lettenmaier, D. P., Wood, E. F., and Burges, S. J. (1994). A simple hydrologically based model of land surface water and energy fluxes for general circulation models. *J. Geophys. Res.*, 99(D7), 14415–14428. 37
- Lill, B. J. (2003). Climate change and alpine catchment discharge. Master's thesis, University of Otago, Dunedin, New Zealand. 27, 50
- Lillesand, T. M. and Kiefer, R. W. (2000). *Remote Sensing and Image Interpretation* (Fourth ed.). New York, USA: John Wiley & Sons, Inc. 97
- Lina, X., Jiancheng, S., Hongen, Z., and Shengli, W. (2005). Fractional snow cover estimation in Tibetan Plateau using MODIS and ASTER. In *Proceedings of the IEEE International Geoscience and Remote Sensing Symposium IGARSS '05*, Volume 3, 1940–1942. 29, 179
- LINZ (2004a). NZTopo data dictionary, Topographic data for GIS. Technical Report version 3.5, Land Information New Zealand. 54
- LINZ (2004b). Technical specification for the maintenance of NZTopo data. Technical Report version 1.6, Land Information New Zealand. 54
- Liu, J., Schaaf, C., Strahler, A., Jiao, Z., Shuai, Y., Zhang, Q., Roman, M., Augustine, J. A., and Dutton, E. G. (2009). Validation of moderate resolution imaging spectroradiometer (MODIS) albedo retrieval algorithm: Dependence of albedo on solar zenith angle. *Journal of Geophysical Research*, 114, D01106(11). 247
- Liu, P. (1994). A new phase function approximating to Mie scattering for radiative transport equations. *Physics in Medicine and Biology*, 39(6), 1025–1036. 127
- Liu, W. and Wu, E. Y. (2005). Comparison of non-linear mixture models: sub-pixel classification. *Remote Sensing of Environment*, 94(2), 145–154. 168
- Lopez, P., Sirguey, P., Arnaud, Y., Pouyaud, B., and Chevallier, P. (2008). Snow cover monitoring in the Northern Patagonia Icefield using MODIS satellite images (2000–2006). *Global and Planetary Change*, 61(3–4), 103–116. 3, 29, 36, 47, 85, 98
- Lovejoy, S. and Mandelbrot, B. B. (1985). Fractal properties of rain, and a fractal model. *Tellus Series A*, 37, 209–232. 155
- Lu, D. and Weng, Q. (2004). Spectral mixture analysis of the urban landscape in Indianapolis with Landsat ETM+ imagery. *Photogrammetric Engineering and Remote Sensing*, 70(9), 1053–1062. 169
- Luo, Y., Trishchenko, A. P., and Khlopenkov, K. V. (2008). Developing clear-sky, cloud and cloud shadow mask for producing clear-sky composites at 250-meter spatial resolution for the seven MODIS land bands over Canada and North America. *Remote Sensing of Environment*, 112(12), 4167–4185. 47, 71, 85, 87, 117
- Luo, Z., Wahba, G., and Johnson, D. R. (1998). Spatialtemporal analysis of temperature using smoothing spline ANOVA. *Journal of Climate*, 11(1), 18–28. 277
- Lyapustin, A., Tedesco, M., Wang, Y., Aoki, T., Hori, M., and Kokhanovsky, A. (2009). Retrieval of snow grain size over Greenland from MODIS. *Remote Sensing of Environment*, 113(9), 1976–1987. 29, 89
- Maillet, E. (1903). *Comptes Rendus Hebdomadaires des Séances de l'Académie des Sciences*, 136, 947. cited by Boussinesq (1904) but manuscript unavailable. 421
- Maillet, E. (1905). *Essai d'hydraulique souterraine et fluviale*. Librairie scientifique A. Paris: Herman. 418

- Malcher, P., Floricioiu, D., and Rott, H. (2003). Snow mapping in alpine areas using medium resolution spectrometric sensors. In *Proceedings of the IEEE International Geoscience and Remote Sensing Symposium*, Volume 4, Toulouse, France, 2835–2837. IEEE International: IEEE. 29
- Male, D. H. and Gray, D. M. (1981). *Handbook of snow: Principles, processes, management and use*. Toronto: Pergamon Press. 30, 242, 244, 251
- Mallat, S. (1989a). Multiresolution approximation and wavelet orthonormal bases of $L_2(\mathbb{R})$. *Transactions of the American Mathematical Society*, 315(1), 69–87. 77
- Mallat, S. (1989b). A theory for multiresolution signal decomposition: the wavelet representation. *IEEE Transactions on Pattern Analysis and Machine Intelligence*, 11(7), 674–693. 77
- Malpica, J. A. (2007). Hue adjustment to IHS pan-sharpened IKONOS imagery for vegetation enhancement. *IEEE Geoscience and Remote Sensing Letters*, 4(1), 27–31. 72, 75
- Mandelbrot, B. (1967). How long is the coast of Britain? Statistical self-similarity and fractional dimension. *Science*, 156(3775), 636–638. 152, 153
- Mandelbrot, B. (1975). *Les Objets fractals : forme, hasard et dimension*. Paris: Flammarion. English translation, *Fractals: Form, Chance, and Dimension* (San Fransico: W.H. Freeman, 1977). 152
- Mandelbrot, B. B. (1983). *The Fractal Geometry of Nature*. New York: W.H. Freeman. 151, 152, 153, 156
- Mangolini, M., Ranchin, T., and Wald, L. (1992). Procédé et dispositif pour l'amélioration de la résolution spatiale d'images à partir d'autres images de meilleure résolution spatiale. French Patent No 92-13961. 79
- Marks, D., Link, T., Winstral, A., and Garen, D. (2001). Simulating snowmelt processes during rain-on-snow over a semi-arid mountain basin. *Annals of Glaciology*, 32(1), 195–202. 245
- Martinec, J. (1960). The degree-day factor for snowmelt runoff forecasting. In *Proceedings of the IUGG General Assembly - Commission on Surface Runoff*, Volume 51, Helsinki, 468–477. IAHS Publication. 251, 252, 253
- Martinec, J. (1975). Snowmelt-runoff model for stream flow forecasts. *Nordic Hydrology*, 6(3), 145–154. 26, 39, 51, 249, 268, 269, 271, 417, 423, 425
- Martinec, J. (1982). Runoff modeling from snow covered area. *IEEE Transactions on Geoscience and Remote Sensing*, GE-20(3), 259–262. 269
- Martinec, J. and Rango, A. (1986). Parameter values for Snowmelt Runoff Modeling. *Journal of Hydrology*, 84(3-4), 197–219. 253, 296, 301, 303
- Martinec, J., Rango, A., and Roberts, R. (2005). *SRM Snowmelt Runoff Model, User's manual* (Enrique Gómez-Landesa ed.). 39, 51, 269, 273, 292, 299, 303, 304, 305, 306, 311, 423
- Martínez, P. J., Prez, R. M., Plaza, A., Aguilar, P. L., Cantero, M. C., and Plaza, J. (2006). Endmember extraction algorithms from hyperspectral images. *Annals of Geophysics*, 49(1), 93–101. 175
- Masuoka, E., Fleig, A., Wolfe, R. E., and Patt, F. (1998). Key characteristics of MODIS data products. *IEEE Transactions on Geoscience and Remote Sensing*, 36(4), 1313–1323. 43
- McAlevey, B. P. (1998). A distributed seasonal snow model for New Zealand. Master's thesis, University of Otago, Dunedin, New Zealand. 26, 28, 50, 255, 261, 283

- McGill, R., Tukey, J. W., and Larsen, W. A. (1978). Variations of box plots. *The American Statistician*, 32(1), 12–16. 218
- McGregor, G. R. (1990). Snowpack structure and avalanching, Craigieburn Range, New Zealand. *New Zealand Journal of Geology and Geophysics*, 33, 405–417. 24
- McGuire, M., Wood, A. W., Hamlet, A. F., and Lettenmaier, D. P. (2006). Use of satellite data for streamflow and reservoir storage forecasts in the Snake River basin. *Journal of Water Resources Planning and Management*, 132(2), 97–110. 3, 37
- McKerchar, A. and Pearson, C. (1997). Quality of long flow records for New Zealand Rivers. *Journal of Hydrology (NZ)*, 36(1), 15–41. 289, 290
- McKerchar, A. I., Pearson, C. P., and Fitzharris, B. B. (1998). Dependency of summer lake inflows and precipitation on spring SOI. *Journal of Hydrology*, 205, 66–80. 2, 19, 320, 321, 322, 338
- McNulty, D. and Fitzharris, B. B. (1980). Winter avalanche activity and weather in a Canterbury alpine basin. *New Zealand Journal of Geology and Geophysics*, 23, 103–111. 24
- McSaveney, M. J., Chinn, T. J., Horell, G. A., and K., L. C. (1978). The measured distribution of precipitation across the Southern Alps. Report WS 71, Ministry of Works and Development, Christchurch, New Zealand. 256
- Meridian Energy Ltd (2009). Discover the Waitaki hydro scheme. Wellington, New Zealand. xvii, 1, 19, 22
- Metsämäki, S., Vepsäläinen, J., Pulliainen, J., and Sucksdorff, Y. (2002). Improved linear interpolation method for the estimation of snow-covered area from optical data. *Remote Sensing of Environment*, 82(1), 64–68. 170, 188
- Meyer, P., Itten, K. L., Kellenberger, T., S., S., and R., S. (1993). Radiometric corrections of topographically induced effects on Landsat TM data in an alpine environment. *Journal of Photogrammetry and Remote Sensing*, 48(4), 17–28. 99, 143
- Miao, X., Gong, P., Swope, S., Pu, R., Carruthers, R., Anderson, G. L., Heaton, J. S., and Tracy, C. (2006). Estimation of yellow starthistle abundance through CASI-2 hyperspectral imagery using linear spectral mixture models. *Remote Sensing of Environment*, 101(3), 329–341. 169
- Middleton, W. E. K. (1964). The early history of the visibility problem. *Appl. Opt.*, 3(5), 599–602. 122
- Ministry of Economic Development (2004). Sustainable Energy. Wellington, New Zealand. 19, 22
- Ministry of Economic Development (2009). New Zealand energy data file, 2008 Calendar year edition. xix, 21
- Ministry of the Environment (2004). New Zealand land cover database 2. User Guide. Available at <http://www.mfe.govt.nz/issues/land/land-cover-dbase/>. xix, 15
- Minnaert, M. (1941). The reciprocity principle in lunar photometry. *Astrophysical Journal*, 93, 403–410. 98
- Mishra, A., Hata, T., and Abdelhadi, A. W. (2004). Models for recession flows in the upper Blue Nile River. *Hydrological Processes*, 18(15), 2773–2786. 422
- Mitáš, L. and Mitášová, H. (1988). General variational approach to the interpolation problem. *Computation and Mathematics with Applications*, 16(12), 983–992. 385
- Molotch, N. P. and Margulis, S. A. (2008). Estimating the distribution of snow water equiva-

- lent using remotely sensed snow cover data and a spatially distributed snowmelt model: A multi-resolution, multi-sensor comparison. *Advances in Water Resources*, 31(11), 1503–1514. 35
- Molotch, N. P., Painter, T. H., Bales, R. C., and Dozier, J. (2004). Incorporating remotely-sensed snow albedo into a spatially-distributed snowmelt model. *Geophysical Research Letters*, 31(3), L03501.1–L03501.4. 28, 247, 342
- Moore, R. D. (1983). A comparison of the snowmelt energy budgets in two alpine basins. *Archives for Meteorology, Geophysics, and Bioclimatology, Series B*, 33(1-2), 1–10. 23, 246
- Moore, R. D. and Owens, I. (1984a). Modelling alpine snow accumulation and ablation using daily climate observations. *Journal of Hydrology (NZ)*, 23(2), 73–83. 25, 253, 254, 277
- Moore, R. D. and Owens, I. F. (1984b). A conceptual runoff model for a mountainous rain-on-snow environment, Craigieburn Range, New Zealand. *Journal of Hydrology (NZ)*, 23(2), 84–99. 25
- Moore, R. D. and Prowse, T. D. (1988). Snow hydrology of the Waimakariri catchment, South Island, New Zealand. *Journal of Hydrology (NZ)*, 27(1), 44–68. 17, 23, 245, 246
- Morris, J. Y. and OLoughlin, C. L. (1965). Snow investigations in the Craigieburn Range. *Journal of Hydrology (NZ)*, 4, 2–16. 22
- Nagler, T. and Rott, H. (2000). Retrieval of wet snow by means of multitemporal SAR data. *IEEE Transactions on Geoscience and Remote Sensing*, 38(2), 754–765. 29, 34
- Nagler, T., Rott, H., Malcher, P., and Mller, F. (2008). Assimilation of meteorological and remote sensing data for snowmelt runoff forecasting. *Remote Sensing of Environment*, 112(4), 1408–1420. 4, 273, 342
- NASA (1976). *U.S. Standard atmosphere 1976*. Washington, D.C.: National Oceanic and Atmospheric Administration, National Aeronautic and Space Administration, United States Air Force. 124
- Nascimento, J. and Bioucas-Dias, J. (2007). Hyperspectral unmixing algorithm via dependent component analysis. In *Proc. IEEE International Geoscience and Remote Sensing Symposium IGARSS 2007*, 4033–4036. 175
- Nash, J. and Sutcliffe, J. (1970). River flow forecasting through conceptual models part I – A discussion of principles. *Journal of Hydrology*, 10(3), 282–290. 260, 299
- Neale, S. M. and Fitzharris, B. B. (1997). Energy balance and synoptic climatology of a melting snowpack in the Southern Alps, New Zealand. *International Journal of Climatology*, 17(14), 1595–1609. 23, 245, 246, 252
- Nencini, F., Garzelli, A., Baronti, S., and Alparone, L. (2007). Remote sensing image fusion using the curvelet transform. *Information Fusion*, 8(2), 143–156. 76
- Nichol, J. and Wong, M. S. (2005). Satellite remote sensing for detailed landslide inventories using change detection and image fusion. *International Journal of Remote Sensing*, 26(9), 1913–1926. 72
- Nishihama, M., Wolfe, R., Solomon, D., Patt, F., Blanchette, J., Fleig, A., and Masuoka, E. (1997). *MODIS Level 1A Earth Location: Algorithm Theoretical Basis Document, version 3.0*. MODIS Science Data Support Team. 151
- Nolin, A. W., Dozier, J., and Mertes, L. A. K. (1993). Mapping alpine snow using a spectral mixture modelling technique. *Annals of Glaciology*, 17, 121–124. 29, 36, 170, 172, 174
- Nunes, A. S. L., Maral, A. R. S., and Vaughan, R. A. (2008). Fast over-land atmospheric cor-

- rection of visible and near-infrared satellite images. *International Journal of Remote Sensing*, 29(12), 3523–3531. 123
- Oberto, L. and Pennechi, F. (2006). Estimation of the modulus of a complex-valued quantity. *Metrologia*, 43, 531–538. 391
- Ohmura, A. (2001). Physical basis for the temperature-based melt-index method. *Journal of Applied Meteorology*, 40(4), 753–761. 244, 249, 250
- Okaya, D., Stern, T., and Davey, F. (Eds.) (2007). *A continental plate boundary: tectonics at South Island, New Zealand*. Number 175 in Geophysical Monograph. American Geophysical Union. 10
- Olyphant, G. A. (1986). Longwave radiation in mountainous areas and its influence on the energy balance of alpine snowfields. *Water Resources Research*, 22(1), 62–66. 245
- Openshaw, S. (1984). *The Modifiable Areal Unit Problem*. Number 38 in Concepts and techniques in modern geography. Norwich: Geo Books. 193
- Ozdogan, M. and Woodcock, C. E. (2006). Resolution dependent errors in remote sensing of cultivated areas. *Remote Sensing of Environment*, 103(2), 203–217. 162
- Painter, T. H. and Dozier, J. (2004). Measurements of the hemispherical-directional reflectance of snow at fine spectral and angular resolution. *Journal of Geophysical Research*, 109(D18), D18115.1–D18115.21. 31, 32, 101
- Painter, T. H., Dozier, J., Roberts, D. A., Davis, R. E., and Green, R. O. (2003). Retrieval of subpixel snow-covered area and grain size from imaging spectrometer data. *Remote Sensing of Environment*, 85, 64–77. 29, 36, 170, 175, 178, 180, 191
- Painter, T. H., Rittger, K., McKenzie, C., Davis, R. E., and Dozier, J. (2009). Retrieval of subpixel snow-covered area, grain size, and albedo from MODIS. *Remote Sensing of Environment*, 113(4), 868–879. In Press. 29, 170, 176, 180, 191, 222, 224, 225, 247, 335
- Painter, T. H., Roberts, D. A., Green, R. O., and Dozier, J. (1995). Improving alpine-region spectral unmixing with optimal-fit snow endmembers. In R. O. Green (Ed.), *Summaries of the Fifth Annual JPL Airborne Earth Science Workshop*, Number 95N33764; Document ID: 19950027343, 125–128. Jet Propulsion Laboratory: JPL Publication 95-1. 170
- Painter, T. H., Roberts, D. A., Green, R. O., and Dozier, J. (1998). The effect of grain size on spectral mixture analysis of snow-covered area from AVIRIS data. *Remote Sensing of Environment*, 65(3), 320–332. 173
- Pardo-Igúzquiza, E., Chica-Olmo, M., and Atkinson, P. M. (2006). Downscaling cokriging for image sharpening. *Remote Sensing of Environment*, 102(1-2), 86–98. 220
- Pasqualini, V., Pergent-Martini, C., Pergent, G., Agreil, M., Skoufas, G., Sourbes, L., and Tsirika, A. (2005). Use of SPOT 5 for mapping seagrasses: An application to *Posidonia oceanica*. *Remote Sensing of Environment*, 94(1), 39–45. 72
- Perez, R., Stewart, R., Arbogast, C., Seals, R., and Scott, J. (1986). An anisotropic hourly diffuse radiation model for sloping surfaces: description, performance validation, site dependency evaluation. *Solar Energy*, 36(6), 481–497. 107, 131, 132
- Peters, E. J. (1996). *An integrated approach to inflow forecasting for reservoir management: The Upper Waitaki*. Ph. D. thesis, Lincoln University, Christchurch, New Zealand. 26, 50
- Peters, O. and Christensen, K. (2002). Rain: Relaxations in the sky. *Physical Review. E*, 66(3), 036120.1–036120.9. 155
- Petrovic, V. (2007). Subjective tests for image fusion evaluation and objective metric valida-

- tion. *Information Fusion*, 8(2), 208–216. 80
- Picard, G., Arnaud, L., Domine, F., and Fily, M. (2009). Determining snow specific surface area from near-infrared reflectance measurements: Numerical study of the influence of grain shape. *Cold Regions Science and Technology*, 56(1), 10–17. 30
- Platnick, S., King, M. D., Ackerman, S. A., Menzel, W. P., Baum, B. A., Riédi, J. C., and Frey, R. A. (2003). The MODIS cloud products: algorithms and examples from Terra. *IEEE Transactions on Geoscience and Remote Sensing*, 41(2), 459–473. 88
- Plüss, C. and Mazzoni, R. (1994). The role of turbulent heat fluxes in the energy balance of high alpine snow cover. *Nordic Hydrology*, 25(1-2), 25–38. 244, 245, 249, 252
- Pohl, C. and Genderen, J. L. V. (1998). Multisensor image fusion in remote sensing: concepts, methods and applications. *International Journal of Remote Sensing*, 19(5), 823–854. 72
- Policarpo, F., Oliveira, M. M., and Comba, J. L. D. (2005). Real-time relief mapping on arbitrary polygonal surfaces. In *Proceedings of the 2005 Symposium on Interactive 3D Graphics and Games SIGGRAPH05*, Washington, DC, 155–162. 109
- Polidori, L., Chorowicz, J., and Guillande, R. (1991). Description of terrain as a fractal surface and application to digital elevation model quality assessment. *Photogrammetric Engineering and Remote Sensing*, 57(10), 1329–1332. 153, 156
- Pratt, W. K. (1991). *Digital Image Processing* (2nd ed.). New York, NY, USA: John Wiley & Sons Inc. 115
- Prowse, T. D. (1981). *The snow environment of the Craigieburn Range*. Ph. D. thesis, University of Canterbury, Christchurch, New Zealand. 23
- Prowse, T. D. and Owens, I. F. (1982). Energy balance over melting snow, Craigieburn Range, New Zealand. *Journal of Hydrology (NZ)*, 21(2), 133–147. 23, 244, 245, 246
- Proy, C., Tanré, D., and Deschamps, P.-Y. (1989). Evaluation of topographic effects in remotely sensed data. *Remote Sensing of Environment*, 30(1), 21–32. 104, 107, 118, 119
- Pu, R., Gong, P., Michishita, R., and Sasagawa, T. (2008). Spectral mixture analysis for mapping abundance of urban surface components from the Terra/ASTER data. *Remote Sensing of Environment*, 112(3), 939–954. 169
- Pullianen, J. (2006). Mapping of snow water equivalent and snow depth in boreal and sub-arctic zones by assimilating space-borne microwave radiometer data and ground-based observations. *Remote Sensing of Environment*, 101(2), 257–269. 29, 34
- Purdie, J. and Fitzharris, B. (1999). Processes and rates of ice loss at the terminus of Tasman Glacier, New Zealand. *Global and Planetary Change*, 22(1-4), 79–91. 15, 290, 316, 318, 319
- Quarmby, N. A., Townshend, J. R. G., Settle, J. J., White, K. H., Milnes, M., Hindle, T. L., and Silleos, N. (1992). Linear mixture modelling applied to AVHRR data for crop area estimation. *International Journal of Remote Sensing*, 13(3), 415–425. 169
- Quick, M. C. and Pipes, A. (1977). UBC watershed model. *Hydrological Sciences Bulletin*, 22, 285–295. 26
- Quincey, D. and Glasser, N. (2009). Morphological and ice-dynamical changes on the Tasman Glacier, New Zealand, 1990-2007. *Global and Planetary Change, In Press, Corrected Proof*68(3), 185–197. 15
- Ranchin, T., Aiazzi, B., Alparone, L., Baronti, S., and Wald, L. (2003). Image fusion—the ARSIS concept and some successful implementation schemes. *Journal of Photogrammetry and Remote Sensing*, 58, 4–18. 72, 76, 332

- Ranchin, T. and Wald, L. (1993). The wavelet transform for the analysis of remotely sensed images. *International Journal of Remote Sensing*, 14(3), 615–619. 76
- Ranchin, T. and Wald, L. (2000). Fusion of high spatial and spectral resolution images: the ARSIS concept and its implementation. *Photogrammetric Engineering and Remote Sensing*, 66(1), 49–61. xx, 54, 78, 79, 82, 93
- Rango, A. and Itten, K. I. (1976). Satellite potentials in snowcover monitoring and runoff prediction. *Nordic Hydrology*, 7(4), 209–230. 35
- Rango, A. and Martinec, J. (1995). Revisiting the degree-day method for snowmelt computations. *Water Resources Bulletin*, 31(4), 657–669. 249, 252, 253, 296
- Rango, A. and Martinec, J. (1997). Water storage in mountain basins from satellite snow cover monitoring. In J. A. Baumgartner MF, Schultz GA (Ed.), *Proceedings of the International Symposium on Remote Sensing and Geographic Information Systems for Design and Operation of Water Resources Systems*, Volume 242, Rabat, Morocco, 83–91. IAHS Publication. 28
- Ranzi, R., Grossi, G., and Bacchi, B. (1999). Ten years of monitoring areal snowpack in the Southern Alps using NOAA-AVHRR imagery, ground measurements and hydrological data. *Hydrological Processes*, 13, 2079–2095. 29
- Raup, B., Racoviteanu, A., Khalsa, S. J. S., Helm, C., Armstrong, R., and Arnaud, Y. (2007). The GLIMS geospatial glacier database: A new tool for studying glacier change. *Global and Planetary Change*, 56(1–2), 101–110. 36
- Rees, G. (2006). *Remote Sensing of Snow and Ice*. CRC Press. 3, 30
- Riaño, D., Chuvieco, E., Salas, J., and Aguado, I. (2003). Assessment of different topographic corrections in Landsat-TM data for mapping vegetation types. *IEEE Transactions on Geoscience and Remote Sensing*, 41(5), 1056–1061. 98
- Rich, P. M., Dubayah, R., Hetrick, W. A., and Saving, S. C. (1994). Using Viewshed models to calculate intercepted solar radiation: applications in ecology. *American Society for Photogrammetry and Remote Sensing Technical Papers*, 524–529. 131
- Richter, R. (1998). Correction of satellite imagery over mountainous terrain. *Applied Optics*, 37(18), 4004–4015. 7, 96, 99, 103, 104, 107, 110, 113, 115, 119, 123, 131, 139, 141, 147, 333
- Richter, R. and Müller, A. (2005). De-shadowing of satellite/airborne imagery. *International Journal of Remote Sensing*, 26(15), 3137–3148. 113
- Riggs, G. and Hall, D. K. (2002). Reduction of cloud obscuration in the MODIS snow data product. In *Presented at the 59th Eastern Snow Conference, in proceedings of the 60th Eastern Snow Conference*, Stowe, Vermont, USA, 205–212. Eastern Snow Conference: Eastern Snow Conference. 47
- Riggs, G. A., Hall, D. K., and Salomonson, V. V. (2006). MODIS Snow Products user guide to collection 5. Technical report, National Snow and Ice Data Center. 46, 47, 85, 170, 185
- Riucklidge, W. (1996). *Efficient Visual Recognition Using the Hausdorff Distance*, Volume 1173 of *Lecture Notes in Computer Science*. New York: Springer. 197
- Roberts, D., Smith, M., and Adams, J. (1993). Green vegetation, nonphotosynthetic vegetation, and soils in AVIRIS data. *Remote Sensing of Environment*, 44(2-3), 255–269. 168, 169
- Roberts, D. A., Gardner, M., Church, R., Ustin, S., Scheer, G., and Green, R. O. (1998). Map-

- ping chaparral in the Santa Monica mountains using multiple endmember spectral mixture models. *Remote Sensing of Environment*, 65(3), 267–279. 169, 175
- Robinson, D. A., Dewey, K. F., and Heim, R. R. (1993). Global snow cover monitoring: an update. *Bulletin of the American Meteorological Society*, 74(9), 1689–1696. 160
- Robinson, G. D., Gross, H. N., and Schott, J. R. (2000). Evaluation of two applications of spectral mixing models to image fusion. *Remote Sensing of Environment*, 71(3), 272–281. 72, 173
- Rodriguez, E., Morris, C. S., Belz, J. E., Chapin, E. C., Martin, J. M., Daffer, W., and Hensley, S. (2005). An assessment of the SRTM topographic products. Technical Report D-31639, Jet Propulsion Laboratory, Pasadena, California. 62
- Rohl, K. (2006). Thermo-erosional notch development at fresh-water-calving Tasman Glacier, New Zealand. *Journal of Glaciology*, 52(11), 203–213. 15
- Romanov, P., Gutman, G., and Csiszar, I. (2000). Automated monitoring of snow cover over North America with multispectral satellite data. *Journal of Applied Meteorology*, 39(11), 1866–1880. 36, 46
- Romanov, P., Tarpley, D., Gutman, G., and Carroll, T. (2003). Mapping and monitoring of the snow cover fraction over North America. *Journal of Geophysical Research*, 108(D16), 8619. 170, 188
- Rosenthal, W. and Dozier, J. (1996). Automated mapping of montane snow cover at subpixel resolution from the Landsat Thematic Mapper. *Water Resources Research*, 32(1), 115–130. 29, 170, 174, 191
- Rosenthal, W. and Elder, K. (2003). Evidence of chaos in slab avalanching. *Cold Regions Science and Technology*, 37(3), 243–253. 156
- Ruddell, A. R. (1995). *Recent glacier and climate change in the New Zealand Alps*. Ph. D. thesis, School of Earth Sciences, University of Melbourne, Melbourne, Australia. 23
- Sabol, Jr., D. E., Adams, J. B., and Smith, M. O. (1992). Quantitative subpixel spectral detection of targets in multispectral images. *Journal of Geophysical Research*, 97, 2659–2672. 169, 173
- Salinger, M. (1980a). New Zealand climate: I. Precipitation patterns. *Monthly Weather Review*, 108(11), 1892–1904. 12
- Salinger, M. (1980b). New Zealand climate: II. Temperature patterns. *Monthly Weather Review*, 108(11), 1905–1912. 12
- Salisbury, J. W. and D’Aria, D. M. (1992). Emissivity of terrestrial material in the 8–14 μm atmospheric window. *Remote Sensing of Environment*, 42, 83–106. 33
- Salisbury, J. W., D’Aria, D. M., and Wald, A. (1994). Measurements of thermal infrared spectral reflectance of frost, snow, and ice. *Journal of Geophysical Research*, 99(B12), 24235–24240. 33
- Salomonson, V. V. and Appel, I. (2004). Estimating fractional snow cover from MODIS using the normalized difference snow index. *Remote Sensing of Environment*, 89, 351–360. 46, 170, 179, 191, 214
- Salomonson, V. V. and Appel, I. (2006). Development of the Aqua MODIS NDSI fractional snow cover algorithm and validation results. *IEEE Transactions on Geoscience and Remote Sensing*, 44(7), 1747–1756. 5, 36, 46, 170, 178, 179, 180, 191, 217
- Sandmeier, S. and Itten, K. I. (1997). A physically-based model to correct atmospheric and

- illumination effects in optical satellite data of rugged terrain. *IEEE Transactions on Geoscience and Remote Sensing*, 35(3), 708–717. 99, 103, 107, 110, 115, 119
- Savitzky, A. and Golay, M. J. E. (1964). Smoothing and differentiation of data by simplified least squares procedures. *Analytical Chemistry*, 36(8), 1627–1639. 293
- Schaaf, C. B., Gao, F., Strahler, A. H., Lucht, W., Li, X., Tsang, T., Strugnell, N. C., Zhang, X., Jin, Y., Muller, J.-P., Lewis, P., Barnsley, M., Hobson, P., Disney, M., Roberts, G., Dunderdale, M., Doll, C., D'Entremont, R. P., Hug, B., Liang, S., Privette, J. L., and Roy, D. (2002). First Operational BRDF, Albedo Nadir Reflectance Products from MODIS. *Remote Sensing of Environment*, 83, 135–148. 247
- Schaper, J., Martinec, J., and Seidel, K. (1999). Distributed mapping of snow and glaciers for improved runoff modelling. *Hydrological Processes*, 13(12-13), 2023–2031. 320, 341
- Schmidt, R. A. (1982). Properties of blowing snow. *Review of Geophysics*, 20(1), 39–44. 156
- Schneider, C., Kilian, R., and Glaser, M. (2007). Energy balance in the ablation zone during the summer season at the Gran Campo Nevado Ice Cap in the Southern Andes. *Global and Planetary Change*, 59(1-4), 175–188. 245
- Seemann, S. W., Li, J., Menzel, W. P., and Gumley, L. E. (2003). Operational retrieval of atmospheric temperature, moisture, and ozone from MODIS infrared radiances. *Journal of Applied Meteorology*, 42(8), 1072–1091. 340
- Seidel, K. and Martinec, J. (2003). Advances in remote sensing of snow and ice for modelling the runoff process. In *Geoinformation For European-Wide Integration, 22nd Symposium of the European-Association-of-Remote-Sensing-Laboratories*, Prague, Czech Republic, 193–200. Millpress SCI, Netherlands. 320, 341
- Seidel, K. and Martinec, J. (2004). *Remote sensing in snow hydrology. Runoff modelling, effect of climate change*. Springer Praxis Publishing Ltd. 28
- Settle, J. J. and Drake, N. A. (1993). Linear mixing and the estimation of ground cover proportions. *International Journal of Remote Sensing*, 14(6), 1159–1177. 172, 175
- Shensa, M. J. (1992). The discrete wavelet transform: wedding the a trous and Mallat algorithms. *IEEE Signal Processing Letters*, 40(10), 2464–2482. 77
- Shepherd, J. D. and Dymond, J. R. (2003). Correcting satellite imagery for the variance of reflectance and illumination with topography. *International Journal of Remote Sensing*, 24(17), 3503–3514. 97, 99, 103, 107, 108, 115, 119
- Shi, J., Dozier, J., and Rott, H. (1994). Snow mapping in alpine regions with synthetic aperture radar. *IEEE Transactions on Geoscience and Remote Sensing*, 32(1), 152–158. 29, 34
- Shi, W., Zhu, C., Tian, Y., and Nichol, J. (2005). Wavelet-based image fusion and quality assessment. *International Journal of Applied Earth Observation and Geoinformation*, 6, 241–251. 80
- Shimabukuro, Y. and Smith, J. (1991). The least-squares mixing models to generate fraction images derived from remote sensing multispectral data. *IEEE Transactions on Geosciences and Remote Sensing*, 29(1), 16–20. 173
- Shimabukuro, Y. E., Holben, B. N., and Tucker, C. J. (1994). Fraction images derived from NOAA AVHRR data for studying the deforestation in the Brazilian Amazon. *International Journal of Remote Sensing*, 15(3), 517–520. 169
- Shirley, P. and Morley, R. K. (2003). *Realistic Ray Tracing* (2nd ed.). A K Peters, Ltd. 109
- Shook, K. and Gray, D. M. (1996). Small-scale spatial structure of shallow snowcovers. *Hy-*

- drological Processes*, 10(10), 1283–1292. 157
- Shook, K. and Gray, D. M. (1997). Synthesizing shallow seasonal snow covers. *Water Resources Research*, 33(3), 419–426. 157
- Shook, K., Gray, D. M., and W., P. J. (1993). Temporal variation in snowcover area during melt in prairie and alpine environments. *Nordic Hydrology*, 24(2-3), 183–198. 158
- Shoshany, M. (1989). Secondary reflection effect on sensor response for a V-shaped valley. *International Journal of Remote Sensing*, 10(7), 1197–1206. 118
- Shrestha, D., Margate, D., Meer, F. v. d., and Anh, H. (2005). Analysis and classification of hyperspectral data for mapping land degradation: An application in southern Spain. *Int J Appl Earth Obs Geoinform*, 7(2), 85–96. 169
- Sibson, R. (1981). *A brief description of natural neighbor interpolation*, Chapter 2, 21–36. Interpolating multivariate data. New York: John Wiley & Sons. 56
- Sicart, J.-E., Hock, R., and Six, D. (2008). Glacier melt, air temperature, and energy balance in different climates: The Bolivian Tropics, the French Alps, and northern Sweden. *Journal of Geophysical Research*, 113, D24113(11). 249, 250
- Simpson, J. and Stitt, J. (1998). A procedure for the detection and removal of cloud shadow from AVHRR data over land. *IEEE Transactions on Geoscience and Remote Sensing*, 36(3), 880–897. 117
- Sinclair, M. R., Wratt, D. S., Henderson, R. D., and Gray, W. R. (1997). Factors affecting the distribution and spillover of precipitation in the Southern Alps of New Zealand – A case study. *Journal of Applied Meteorology*, 36(5), 428–442. 256, 283
- Singer, F. S. and Popham, R. W. (1963). Non-meteorological observations from weather satellites. *Astronautics and Aerospace Engineering*, 1(3), 89–92. 28, 35
- Singer, R. B. and McCord, T. B. (1979). Mars - Large scale mixing of bright and dark surface materials and implications for analysis of spectral reflectance. In N. W. Hinners (Ed.), *Lunar and Planetary Science Conference*, Volume 10 of *Lunar and Planetary Science Conference*, 1835–1848. 167
- Singh, P., Kumar, N., and Arora, M. (2000). Degree-day factors for snow and ice for Dokriani Glacier, Garhwal Himalayas. *Journal of Hydrology*, 235(1-2), 1–11. 249, 252
- Singh, P. and Singh, V. P. (2001). *Snow and Glacier Hydrology*. Dordrecht, The Netherlands: Kluwer Academic Publishers. 253, 300
- Singh, P., Spitzbart, G., Hübl, H., and Weinmeister, H. W. (1997). Hydrological response of snowpack under rain-on-snow events: a field study. *Journal of Hydrology*, 202(1-4), 1–20. 245
- Sirguy, P. (2009). Simple correction of multiple reflection effects in rugged terrain. *International Journal of Remote Sensing*, 30(4), 1075–1081. 96
- Sirguy, P., Mathieu, R., and Arnaud, Y. (2009). Subpixel monitoring of the seasonal snow cover with MODIS at 250 m spatial resolution in the Southern Alps of New Zealand: methodology and accuracy assessment. *Remote Sensing of Environment*, 113(1), 160–181. 109
- Sirguy, P., Mathieu, R., Arnaud, Y., and Fitzharris, B. B. (2009). Seven years of snow cover monitoring with MODIS to model catchment discharge in New Zealand. In *Proceedings of the IEEE International Geoscience and Remote Sensing Symposium*, Volume II, Cape Town, South Africa, 863–866. IEEE.

- Sirguey, P., Mathieu, R., Arnaud, Y., Khan, M. M., and Chanussot, J. (2007). Improved resolution for the detection of snow with MODIS using wavelet fusion. In *Proceedings of the IEEE International Geoscience and Remote Sensing Symposium*, Barcelona, Spain, 3975–3978. IEEE International: IEEE.
- Sirguey, P., Mathieu, R., Arnaud, Y., Khan, M. M., and Chanussot, J. (2008). Improving MODIS spatial resolution for snow mapping using wavelet fusion and ARSIS concept. *IEEE Geoscience and Remote Sensing Letters*, 5(1), 78–82. 217
- Sirguey, P., Oltmer, S., and Mathieu, R. (2007). Assessment of the performance of image fusion for the mapping of snow using Euclidean distance. In P. A. Whigham (Ed.), *19th Annual Colloquium of the Spatial Information Research Centre*, Dunedin, New Zealand, 13–24. The University of Otago.
- Sjoberg, R. W. and Horn, B. K. P. (1983). Atmospheric effects in satellite imaging of mountainous terrain. *Applied Optics*, 22(11), 1702–1716. 107, 115, 140, 141
- Slater, A. G., Clark, M. P., and Barrett, A. P. (2009). Comment on “Estimating the distribution of snow water equivalent using remotely sensed snow cover data and a spatially distributed snowmelt model: A multiresolution, multi-sensor comparison” by Noah P. Molotch and Steven A. Margulis. *Advances in Water Resources*, 32(11), 1680–1684. In Press, Corrected proof. 35
- Slater, M. T. (2001). ATSR/2 a British sensor on a European satellite monitoring Scandinavian snow cover. In M. F. Buchroithner (Ed.), *A Decade of Trans-European Remote Sensing Cooperation*, Balkema, Rotterdam, 127–130. Taylor & Francis. 36
- Slater, M. T., Sloggett, D. R., Rees, W. G., and Steel, A. (1999). Potential operational multi-satellite sensor mapping of snow cover in maritime sub-polar regions. *International Journal of Remote Sensing*, 20(15), 3019–3030. 35, 166
- Slater, P. N. (1980). *Remote Sensing, Optics and Optical Systems*. Massachusetts 01867, USA: Addison-Wesley Publishing Company. xxv, 397
- Slaymaker, O. and Kelly, R. E. J. (2007). *The Cryosphere and Global Environmental Change*. Environmental Systems and Global Change Series. Willey-Blackwell Publishing. 244, 245
- Small, C. (2001). Estimation of urban vegetation abundance by spectral mixture analysis. *International Journal of Remote Sensing*, 22(7), 1305–1334. 169
- Sobrino, J. A., Kharraz, J. E.-L., and Li, Z.-L. (2003). Surface temperature and water vapour retrieval from MODIS data. *International Journal of Remote Sensing*, 24(24), 5161–5182. 33
- Souza, C., Firestone, L., Silva, L. M., and Roberts, D. (2003). Mapping forest degradation in the Eastern Amazon from SPOT 4 through spectral mixture models. *Remote Sensing of Environment*, 87(4), 494–506. 169
- Spencer, J. W. (1971). Fourier series representation of the position of the Sun. *Search*, 2(5), 172. 102
- Staehelin, J., Schill, H., Höger, B., Viatte, P., Levrat, G., and Gamma, A. (1995). Total ozone observation by sun photometry at Arosa, Switzerland. *Optical Engineering*, 34(7), 1977–1986. 126
- Stahl, K., Moore, R., Floyer, J., Asplin, M., and McKendry, I. (2006). Comparison of approaches for spatial interpolation of daily air temperature in a large region with complex topography and highly variable station density. *Agricultural and Forest Meteorology*, 139(3–4), 224–236. 277, 281
- Staley, H. (2005). New Zealand three electricity crises. In *Saving electricity in a hurry*. Proceed-

- ings of the IEA workshop*, Paris, France, 41–45. [1](#), [22](#)
- Stamnes, K., Tsay, S.-C., Wiscombe, W., and Jayaweera, K. (1988). Numerically stable algorithm for discrete-ordinate-method radiative transfer in multiple scattering and emitting layered media. *Applied Optics*, 27(12), 2502–2509. [121](#)
- Stein, A. (2002). *Some basic elements of statistics* (Alfred Stein and van der Meer, Freek and Ben Gorte ed.), Chapter 2, 9–22. *Spatial Statistics for Remote Sensing*. Springer. [58](#)
- Stroeve, J. C., Box, J. E., and Haran, T. (2006). Evaluation of the MODIS (MOD10A1) daily snow albedo product over the Greenland ice sheet. *Remote Sensing of Environment*, 105(2), 155–171. [47](#), [85](#)
- Strong, D. (2008). Patterns and processes of ice loss at Tasman Glacier: an evaluation using historic data sources and remotely sensed imagery. Master's thesis, University of Otago, Dunedin, New Zealand. [15](#), [314](#)
- Sturman, A. P. and Tapper, N. J. (2006). *The weather and climate of Australia and New Zealand* (2nd ed.). Melbourne, Australia: Oxford University Press. [10](#)
- Sui, J. and Koehler, G. (2001). Rain-on-snow induced flood events in Southern Germany. *Journal of Hydrology*, 252(1-4), 205–220. [245](#)
- Sun, Y. and Baricz, A. (2008). Inequalities for the generalized Marcum Q-function. *Applied Mathematics and Computation*, 203(1), 134–141. [389](#)
- Swamy, A. N. and Brivio, P. A. (1997). Modelling runoff using optical satellite remote sensing data in a high mountainous alpine catchment of Italy. *Hydrological Processes*, 11(11), 1475–1491. [35](#), [166](#)
- Swanson, R. H. (1970). Local snow distribution is not a function of local topography under continuous tree cover. *Journal of Hydrology (NZ)*, 9(2), 292–298. [16](#)
- Tabler, R. D. (1980). Self-similarity of wind profiles in blowing snow allows outdoor modeling. *Journal of Glaciology*, 26, 421–434. [155](#)
- Tagirov, R. and Tagirov, L. (1997). Lambert formula Bouguer absorption law? *Russian Physics Journal*, 40(7), 664–669. [122](#)
- Tait, A., Henderson, R., Turner, R., and Zheng, X. (2006). Thin plate smoothing spline interpolation of daily rainfall for New Zealand using a climatological rainfall surface. *International Journal of Climatology*, 26(14), 2097–2115. [255](#), [256](#), [284](#)
- Tait, A. and Turner, R. (2005). Generating multiyear gridded daily rainfall over New Zealand. *Journal of Applied Meteorology*, 44(9), 1315–1323. [284](#)
- Takács, B. (1998). Comparing face images using the modified Hausdorff distance. *Pattern Recognition*, 31(12), 1873–1881. [199](#)
- Tallaksen, L. M. (1995). A review of baseflow recession analysis. *Journal of Hydrology*, 165(1-4), 349–370. [417](#)
- Tanré, D., Herman, M., and Deschamps, P. Y. (1981). Influence of the background contribution upon space measurements of ground reflectance. *Applied Optics*, 20(20), 3676–3684. [131](#)
- Tanré, D., Herman, M., Deschamps, P.-Y., and Lefé, A. D. (1979). Atmospheric modelling for space measurements of ground reflectances, including bidirectional properties. *Applied Optics*, 18(21), 3587–3594. [100](#), [120](#)
- Tchiguirinskaia, I., Schertzer, D., Lovejoy, S., and Veysseire, J.-M. (2006). Wind extremes and scales: multifractal insights and empirical evidence. In J. Peinke, P. Schaumann, and

- S. Barth (Eds.), *Wind Energy: Proceedings of the Euromech Colloquium*, 99–104. Springer-Verlag. 156
- Teillet, P. M. (1986). Image correction for radiometric effects in remote sensing. *International Journal of Remote Sensing*, 7(12), 1637–1651. 98
- Teillet, P. M., Guindon, B., and Goodenough, D. G. (1982). On the slope-aspect correction of multispectral scanner data. *Canadian Journal of Remote Sensing*, 8(2), 84–106. 98
- Tekeli, A. E., Akyürek, Z., Sorman, A. A., Sensoy, A., and Sorman, A. Ü. (2005). Using MODIS snow cover maps in modeling snowmelt runoff process in the Eastern part of Turkey. *Remote Sensing of Environment*, 97(2), 216–230. 4, 292
- Thomas, I. L., Lewis, A. J., and Ching, N. P. (1978). Snowfield assessment from Landsat. *Photogrammetric Engineering and Remote Sensing*, 44(4), 493–502. 28
- Thomas, W. (1997). A three-dimensional model for calculating reflection functions of inhomogeneous and orographically structured natural landscapes. *Remote Sensing of Environment*, 59(1), 44–63. 100
- Thompson, C. S. (1985). Maps of rainfall parameters for New Zealand. New Zealand Meteorological Service miscellaneous publication 187. 12, 256
- Thompson, S. M. (1997). Snow storage estimation for hydro-electricity catchments from monitored rainfall and river flow. Client report wlg97/7, NIWA, Wellington, New Zealand. 26, 50
- Thompson, S. M. (2002). River discharge from mountains with frequent rain. *Journal of Hydrology (NZ)*, 41(2), 125–144. 27
- Timoshenko, S. and Goodier, J. N. (1951). *Theory of Elasticity*. New York: McGraw-Hill International Book Co. 384
- Tippet, J. M. and Kamp, P. J. J. (1993). Fission track analysis of the late Cenozoic vertical kinematics of continental Pacific Crust, South Island, New Zealand. *Journal of Geophysical Research*, 136(B9), 16119–16148. 10
- Toet, A. and Franken, E. M. (2003). Perceptual evaluation of different image fusion schemes. *Displays*, 24(1), 25–37. 82
- Tokola, T., Sarkeala, J., and Van Der Linden, M. (2001). Use of topographic correction in Landsat TM-based forest interpretation in Nepal. *International Journal of Remote Sensing*, 22(13), 551–563. 97
- Toller, G. N., Isaacman, A., Kuyper, J., and Salomonson, V. (2006). *MODIS Level 1B Product Users Guide for Level-1B Version 5*. NASA/Goddard Space Flight Center, Greenbelt, MD 2077, USA: MODIS Characterization Support Team (MCST). 65, 69
- Torres, J. L., Blas, M. D., and García, A. (2006). New equations for the calculation of the horizon brightness irradiance in the model of Perez. *Solar Energy*, 80(7), 746–750. 131
- Toutin, T. (2002). Three-dimensional topographic mapping with ASTER stereo data in rugged topography. *IEEE Transactions on Geoscience and Remote Sensing*, 40(10), 2241–2247. 44
- Treidl, R. A. (1970). A case study of warm air advection over a melting snow surface. *Boundary-Layer Meteorology*, 1(2), 155–168. 245
- Trishchenko, A. P., Luo, Y., and Khlopenkov, K. V. (2006). A method for downscaling MODIS land channels to 250-m spatial resolution using adaptive regression and normalization. In *Proceedings of the SPIE - The International Society for Optical Engineering*, Volume 6366,

- Stockholm, Sweden, 636607–8. SPIE. 75, 339
- Tu, T.-M., Huang, P. S., Hung, C.-L., and Chang, C.-P. (2004). A fast Intensity–Hue–Saturation fusion technique with spectral adjustment for IKONOS imagery. *IEEE Geoscience and Remote Sensing Letters*, 1(4), 309–312. 72, 74, 75, 80
- Turner, A. E. (1986). Modelling snowmelt and rainfall runoff. Master’s thesis, University of Otago, Dunedin, New Zealand. 26, 39, 338
- Turpin, O., Ferguson, R., and Johansson, B. (1999). Use of remote sensing to test and update simulated snow cover in hydrological models. *Hydrological Processes*, 13(12-13), 2067–2077. 28, 37, 260
- Turpin, O. C., Ferguson, R. I., and Clark, C. D. (1997). Remote sensing of snowline rise as an aid to testing and calibrating a glacier runoff model. *Physics and Chemistry of the Earth*, 22(3-4), 279–283. 260
- Twaddle, D. G. (1995). Modelling snow cover in short tussock grassland. Master’s thesis, University of Otago, Dunedin, New Zealand. 25
- Udnæs, H.-C., Alfnes, E., and Andreassen, L. M. (2007). Improving runoff modelling using satellite-derived snow covered area? *Nordic Hydrology*, 38(1), 21–32. 38
- U.S. Army Corps of Engineers (1956). Summary report of the snow investigations : snow hydrology. Technical report, Department of the Army, Portland, Oregon. 248
- U.S. Army Corps of Engineers (1991). User manual SSARR Model, Streamflow Synthesis and Reservoir. Technical report, Department of the Army, Portland, Oregon. 38
- U.S. Army Corps of Engineers (1998). Runoff from Snowmelt. Technical Report DC 20314-1000, EM 1110-2-1406, Department of the Army, Washington. 242, 244, 249, 251, 252, 253
- van der Meer, F. (2002). *Image classification through spectral unmixing* (Alfred Stein and van der Meer, Freek and Ben Gorte ed.), Volume 1 of *Spatial Statistics for Remote Sensing*, Chapter 11, 185–193. Netherlands: Springer. 168
- van der Meer, F. and De Jong, S. M. (2000). Improving the results of spectral unmixing of Landsat Thematic Mapper imagery by enhancing the orthogonality of end-members. *International Journal of Remote Sensing*, 21(15), 2781–2797. 173
- van der Meer, F., Yang, H., and Land, H. (2001). *Imaging spectrometry and geological applications* (van der Meer, Freek and de Jong, Steven M. ed.), Chapter 7, 201–218. *Imaging Spectrometry: Basic Principles and Prospective Applications*. Netherlands: Springer. 169
- Vapnik, V. N. (2000). *The Nature of Statistical Learning Theory* (2nd ed.). New York: Springer. 168
- Vartiainen, E. (2000). A new approach to estimating the diffuse irradiance on inclined surfaces. *Renewable Energy*, 20, 45–64. 131
- Venteris, E. R. and Slater, B. K. (2005). A comparison between contour elevation data sources for DEM creation and soil carbon prediction, Coshocton, Ohio. *Transactions in GIS*, 9(2), 179–198. 58
- Vermote, E. F., El Saleous, N. Z., and Justice, C. O. (2002). Atmospheric correction of MODIS data in the visible to middle infrared: first results. *Remote Sensing of Environment*, 83(1-2), 97–111. 121
- Vermote, E. F., Saleous, N. E., Justice, C. ., Kaufman, Y. J., Privette, J. L., Remer, L., Roger, J. C., and Tanré, D. (1997). Atmospheric Correction of Visible to Middle-Infrared EOS-MODIS Data over Land Surfaces: Background, Operational Algorithm and Validation.

- Journal of Geophysical Research*, 102(D14), 17131–17141. 99, 121, 125, 140
- Vermote, E. F., Tanré, D., Deuzé, J.-L., Herman, M., and Mockette, J.-J. (1997). *Second Simulation of the Satellite Signal in the Solar Spectrum (6S): User guide version 2*. 126, 128, 133
- Vermote, E. F., Tanré, D., Deuzé, J.-L., Herman, M., and Morcette, J.-J. (1997). Second simulation of the satellite signal in the solar spectrum, 6S: an overview. *IEEE Transactions on Geoscience and Remote Sensing*, 35(3), 675–686. 96, 120, 121, 126, 131, 133
- Vermote, E. F. and Vermeulen, A. (1999). MODIS algorithm technical background document. Atmospheric correction algorithm: Spectral reflectances (MOD09). Technical Report Version 4.0, NASA. 123
- Vikhamar, D. and Solberg, R. (2003). Snow-cover mapping in forests by constrained linear spectral unmixing of MODIS data. *Remote Sensing of Environment*, 88(3), 309–323. 29, 170, 174, 191, 335
- von Hann, J. (1897). *Handbuch der Klimatologie* (2nd ed.). Stuttgart: Verlag von J. Engelhorn. English translation of the 2nd German edition by R. de Courcy Ward, Handbook of climatology, part I: General climatology (New York: The MacMillan Company, 1903). 248
- Wahba, G. (1990). *Spline models for observational data* (2nd ed.). Philadelphia: Society for Industrial and Applied Mathematics. 278, 383, 384, 385
- Wahba, G. and Wendelberger, J. (1980). Some new mathematical methods for variational objective analysis using splines and cross validation. *Monthly Weather Review*, 108(8), 1122–1143. 278, 383, 385
- Wahba, G. and Wold, S. (1975). A completely automatic french curve: fitting spline functions by cross validation. *Communications in Statistics - Theory and Methods*, 4(1), 1–17. 384
- Wald, L. (2002). *Data fusion: definitions and architectures (fusion of images of different spatial resolutions)*. Paris: Les Presses de l'École des Mines de Paris. 72, 73, 82, 93, 332
- Wald, L., Ranchin, T., and Mangolini, M. (1997). Fusion of satellite images of different spatial resolution: assessing the quality of resulting images. *Photogrammetric Engineering and Remote Sensing*, 63(6), 691–699. 80, 82, 191
- Wallace, S. J. (2001). Mapping glacial landforms in the Pukaki and Tekapo lake basins. Unpublished postgraduate diploma in science, University of Otago, Dunedin, New Zealand. 14
- Wan, Z., Zhang, Y., Zhang, Q., and Li, Z.-L. (2002). Validation of the land-surface temperature products retrieved from Terra Moderate Resolution Imaging Spectroradiometer data. *Remote Sensing of Environment*, 83, 163–180. 247
- Wan, Z. M. and Dozier, J. (1996). A Generalized split-window algorithm for retrieving land-surface temperature from space. *IEEE Transactions on Geoscience and Remote Sensing*, 34(4), 892–905. 33, 336
- Wang, J., Endreny, T. A., and Hassett, J. M. (2006). Power function decay of hydraulic conductivity for a TOPMODEL-based infiltration routine. *Hydrological Processes*, 20(18), 3825–3834. 422
- Wang, J. and Li, W. (2003). Comparison of methods of snow cover mapping by analysing the solar spectrum of satellite remote sensing data in China. *International Journal of Remote Sensing*, 24(21), 4129–4136. 36
- Wang, L., Sharp, M., Brown, R., Derksen, C., and Rivard, B. (2005). Evaluation of spring snow covered area depletion in the Canadian Arctic from NOAA snow charts. *Remote*

- Sensing of Environment*, 95(4), 453–463. 29
- Wang, Q., Tenhunen, J., Schmidt, M., Kolcun, O., and Droesler, M. (2006). A model to estimate global radiation in complex terrain. *Boundary-Layer Meteorology*, 119, 409–429. 103, 119, 123
- Wang, Q., Tenhunen, J., Schmidt, M., Kolcun, O., Droesler, M., and Reichstein, M. (2006). Estimation of total, direct and diffuse PAR under clear skies in complex alpine terrain of the National Park Berchtesgaden, Germany. *Ecological Modelling*, 196(1-2), 149–162. 110
- Wang, Z. and Bovik, A. C. (2002). A universal image quality index. *IEEE Signal Processing Letters*, 9(3), 81–84. 82, 201, 220, 333
- Wardle, P. (1991). *Vegetation of New Zealand*. New Jersey, USA: Blackburn Press. 16
- Warren, S. G. (1982). Optical properties of snow. *Reviews of Geophysics and Space Physics*, 20, 67–89. 31, 32, 33, 171, 174, 251, 297
- Warren, S. G. (1984). Optical constants of ice from the ultraviolet to the microwave. *Applied Optics*, 23(8), 1026–1225. 30, 86
- Warren, S. G., Brandt, R. E., and Hinton, P. O. (1998). Effect of surface roughness on bidirectional reflectance of Antarctic snow. *Journal of Geophysical Research*, 103, 25,789–25,807. 32
- Warren, S. G. and Wiscombe, W. J. (1980). A model for the spectral albedo of snow, II: snow containing atmospheric aerosols. *Journal of the Atmospheric Sciences*, 20, 2734–2745. 31
- Weingartner, R. and Pearson, C. (2001). A comparison of the hydrology of the Swiss Alps and the Southern Alps of New Zealand. *Mountain Research and Development*, 21(4), 370–381. 256, 283
- Werner, P. W. and Sundquist, K. J. (1951). On the groundwater recession curve for large watersheds. In *Proceedings of the IAHS General Assembly*, Volume 33, Brussels, 202–212. IAHS Publication. 421
- White, P. A. and Reeves, R. R. (2002). The volume of groundwater in New Zealand 1994 to 2001. Client report n 2002/79 prepared for statistics new zealand, Institute of Geology and Nuclear Sciences. 16
- Whitehouse, I. E. (1988). *Geomorphology of the central Southern Alps, New Zealand: the interaction of plate collision and atmospheric circulation* (Williams, Paul W. ed.), Volume 69 of *The Geomorphology of plate boundaries and active continental margins (Zeitschrift für Geomorphologie, Supplementbände)*, 105–116. 14
- Willmott, C. J., Ackleson, S. G., Davis, R. E., Feddema, J. J., Klink, K. M., Legates, D. R., O'Donnell, J., and Rowe, C. M. (1985). Statistics for the evaluation and comparison of models. *Journal of Geophysical Research*, 90(C5), 8995–9005. 57, 59, 135
- Willmott, C. J. and Matsuura, K. (2005). Advantages of the mean absolute error (MAE) over the root mean square error (RMSE) in assessing average model performance. *Climate Research*, 30(1), 79–82. 58, 59, 217
- Winther, J.-G. (1994). Spectral bi-directional reflectance of snow and glacier ice measured in Dronning Maud Land, Antarctica. *Annals of Glaciology*, 20, 1–5. 101
- Winther, J. G. and Hall, D. K. (1999). Satellite-derived snow coverage related to hydropower production in Norway: present and future. *International Journal of Remote Sensing*, 20(15-16), 2991–3008. 31, 32
- Wiscombe, W. J. and Warren, S. G. (1980). A model for the spectral albedo of snow, I: pure

- snow. *Journal of the Atmospheric Sciences*, 37(12), 2712–2733. 31, 101
- Wise, S. M. (2000). Assessing the quality for hydrological applications of digital elevation models derived from contours. *Hydrological Processes*, 14, 1909–1929. 55, 57, 59
- Wittenberg, H. (1999). Baseflow recession and recharge as nonlinear storage processes. *Hydrological Processes*, 13(5), 715–726. 422
- Wolfe, R. E., Nishihama, M., Fleig, A. J., Kuyper, J. A., Roy, D. P., Storey, J. C., and Patt, F. S. (2002). Achieving sub-pixel geolocation accuracy in support of MODIS land science. *Remote Sensing of Environment*, 83, 31–49. xx, 66
- Wolfe, R. E., Roy, D. P., and Vermote, E. (1998). MODIS land data storage, gridding, and compositing methodology: Level 2 Grid. *IEEE Transactions on Geoscience and Remote Sensing*, 36(4), 1324–1338. 43
- Woo, A., Poulin, P., and Fournier, A. (1990). A survey of shadow algorithms. *IEEE Computer Graphics and Applications*, 10(6), 13–32. 109
- Woo, M.-k. and Dubreuil, M.-A. (1985). Empirical relationship between dust content and Arctic snow albedo. *Cold Regions Science and Technology*, 10(2), 125–132. 255, 258, 296
- Woodcock, C. E. and Strahler, A. H. (1987). The factor of scale in remote sensing. *Remote Sensing of Environment*, 21(3), 311–332. 151
- Wu, C. and Murray, A. T. (2003). Estimating impervious surface distribution by spectral mixture analysis. *Remote Sensing of Environment*, 84(4), 493–505. 169
- Wu, J., Wang, D., and Bauer, M. E. (2005). Image-based atmospheric correction of QuickBird imagery of Minnesota cropland. *Remote Sensing of Environment*, 99(3), 315–325. 123
- Xia, Y., Fabian, P., Winterhalter, M., and Zhao, M. (2001). Forest climatology: estimation and use of daily climatological data for Bavaria, Germany. *Agricultural and Forest Meteorology*, 106(2), 87–103. 277, 281
- Xiao, X., Shen, Z., and Qin, X. (2001). Assessing the potential of VEGETATION sensor data for mapping snow and ice cover: a Normalized Difference Snow and Ice Index. *International Journal of Remote Sensing*, 22(9), 2479–2487. 36
- Xiao, X., Zhang, Q., Boles, S., Rawlins, M., and III, B. M. (2004). Mapping snow cover in the pan-Arctic zone, using multi-year 1998-2001 images from optical VEGETATION sensor. *International Journal of Remote Sensing*, 25(14), 5731–5744. 166
- Xydeas, C. S. and Petrovic, V. (2000). Objective image fusion performance measure. *Electronics Letters*, 36(4), 308–309. 82
- Zhan, Q., Molenaar, M., Tempfli, K., and Shi, W. (2005). Quality assessment for geo-spatial objects derived from remotely sensed data. *International Journal of Remote Sensing*, 26(14), 2953–2974. 196
- Zhang, H., Zhao, J., and Jiancheng, S. (2005). Comparing four sub-pixel algorithms in MODIS snow mapping. In *Proceedings of the IEEE International Geoscience and Remote Sensing Symposium IGARSS '05*, Volume 6, 3784–3787. 170
- Zhang, W. J. and Kang, J. Y. (2006). QuickBird panchromatic and multi-spectral image fusion using wavelet packet transform. *Intelligent Control and Automation*, 344, 976–981. 72
- Zhang, Y. (2004). Understanding image fusion. *Photogrammetric Engineering and Remote Sensing*, 70(6), 657–661. 72
- Zuzel, J. F. and Cox, L. M. (1975). Relative importance of meteorological variables in snowmelt. *Water Resources Research*, 11(1), 174–176. 248

Appendices

Appendix A

Thin plate spline

A.1 Problem statement

Consider $\{y_i : i = 1, \dots, n\}$ to be a set of real value observations, each associated with a d -dimensional vector of variables $\mathbf{x}_i = (x_{i,1}, \dots, x_{i,d})$ and a measurement variance σ_i^2 . A *thin plate smoothing spline* (TPSS) interpolator is a function f of the Sobolev space W^m , $m = 2, 3, \dots$ that minimizes the penalized least squares equation

$$E(f) = \frac{1}{n} \sum_{i=1}^n \left(\frac{y_i - f(\mathbf{x}_i)}{\sigma_i} \right)^2 + \lambda J_m(f), \quad (\text{A.1})$$

where the first term on the right-hand side of Equation (A.1) measures the fidelity of the interpolation to the data points, while the second term on the right-hand side

$$J_m(f) = \sum_{\alpha_1 + \dots + \alpha_d = m} \frac{m!}{\alpha_1! \dots \alpha_d!} \int_{\Omega} \dots \int_{\Omega} \left(\frac{\partial^m f}{\partial x_1^{\alpha_1} \dots \partial x_d^{\alpha_d}} \right)^2 dx_1 \dots dx_d \quad (\text{A.2})$$

is the penalty functional. Ω is a bounded interval of \mathbb{R}^d , m and $\lambda \geq 0$ are two parameters that control the “roughness” of the spline. A comprehensive mathematical background about spline interpolation can be found in Wahba (1990) and specific details about TPSS are provided by Duchon (1977) and Wahba and Wendelberger (1980).

A.2 Interpolating vs. smoothing thin plate spline

A noteworthy case of the penalty function is achieved when $m = 2$. For $d = 1$ and $d = 2$, $J_2(f)$ identifies to the strain energy of bending of a prismatic bar and a

rectangular plate with null Poisson's ratio, respectively (Timoshenko and Goodier, 1951, pg. 155 & 168). When $\lambda \rightarrow 0$, the observations are assumed to be free of errors and the spline must be a pure interpolator (i.e., $f(\mathbf{x}_i) = y_i$) that minimizes the bending energy $J_2(f)$. In this case, the name *thin plate spline* (TPS) is used as it originates from the 2-D physical analogy whereby f identifies to the elevation of a thin sheet of metal that would naturally accommodate irregularly spaced data points in the absence of gravity (Duchon, 1976). On the other hand, $\lambda \rightarrow \infty$ requires $J_2(f)$ to vanish. The resulting system of second-order partial differential equations imposes a hyperplane solution for f . Under this constraint, minimizing the fidelity term on the right-hand side of Equation (A.1) corresponds to an ordinary least squares fit of the solution to the data points. Intermediate values of λ provide a tradeoff between fitting the data points accurately and minimizing the bending energy. Thus, more weight given to $J_2(f)$ yields a smoother surface at the expense of the fidelity and justifies the naming of a "smoothing parameter" for λ . A higher order of regularity for f is required when $m > 2$, thus yielding smoother surfaces. In this research, only $m = 2$ is considered because of its physical meaning.

When it comes to determining f based on noisy observations, optimal fitting refers to the estimation of an appropriate value for λ so that f approaches the signal closely while accommodating the noise. This can be achieved by several means for which extensive details can be found in Wahba (1990, Chap. 4). The methods generally implement a *cross validation* (CV) technique that relies on the "leaving-out-one" lemma (Craven and Wahba, 1979). That is, for a given λ , the TPSS model is fitted to the dataset n times by ignoring one of the data points successively. Thus, the errors between the fitted models and the ignored data can be summarized into either the mean square (MSE) or the root mean square error (RMSE) that is aimed to be minimum for the appropriate λ . The optimum value for the smoothing parameter can be estimated on the basis of a Monte Carlo technique (Wahba and Wold, 1975). More efficient and less time-consuming algorithms have been designed and referred to as the *ordinary cross validation* (OCV), or the widely used *generalized cross validation* (GCV) technique. Nevertheless, although the GCV has been shown to be a robust method for the estimation of λ , it requires a large number of observations to ensure that enough information is available to separate the signal from the noise (Wahba, 1990, pg. 65). For example, in this research, the fields of temperature and rainfall needed to be spatially interpolated based on a sparsely distributed network of data (see Section 8.3). In such a case, it was relevant to assume that measurements were

free of errors and to implement the interpolating rather than the smoothing thin plate spline (i.e., TPS rather than the TPSS). Thus, the smoothing parameter could be ignored and f should only minimize J_2 .

A.3 Multivariate TP(S)S

TP(S)S interpolation has been largely used in Geographical Information Systems (GIS) due to its mathematical elegance and physical meaning. In the framework of geo-statistics, thin plate spline interpolation is based on a deterministic model with a local stochastic component. λ and m can be regarded as playing the role of an implicit prior covariance model. It was shown that, under certain conditions, thin plate interpolation compares to the purely stochastic Kriging technique (Kent and Mardia, 1994; Wahba, 1990, Chap. 3.2). The TP(S)S are often used in two dimensions to fit an interpolated surface (e.g., temperature, pressure) to observations that are simply associated with their bivariate set of geographical coordinates. However, TP(S)S interpolation enables the incorporation of more than two covariables in order to improve the accuracy of the prediction. Thus, Wahba and Wendelberger (1980) suggested the use of TP(S)S in multivariate approaches. Hutchinson (1995) took advantage of the height as a covariable in a trivariate TPSS to improve the spatial interpolation of rainfall. Boer (2001) showed that a trivariate thin plate spline approach performed similarly to trivariate regression-kriging and was an attractive alternative to the time-consuming co-kriging interpolation technique.

A.4 Solution

The general solution of the TP(S)S is given by Wahba (1990, Chap. 2.4). For $m = 2$, it takes the form

$$f(\mathbf{x}) = \sum_{k=0}^d a_k \phi_k(\mathbf{x}) + \sum_{i=1}^n \underbrace{\frac{y_i - f(\mathbf{x}_i)}{n\lambda\sigma_i^2}}_{w_i} \psi_2(\|\mathbf{x} - \mathbf{x}_i\|). \quad (\text{A.3})$$

$\mathbf{a} = (a_0, \dots, a_d)^T$ and $\mathbf{w} = (w_1, \dots, w_n)^T$ are the affine transformation and wrapping coefficients, respectively, $\phi = \{\phi_0, \phi_1, \dots, \phi_d\} = \{1, x_1, \dots, x_d\}$, and $\|\mathbf{x} - \mathbf{x}_i\| = \sqrt{\sum_{j=1}^d (x_j - x_{i,j})^2}$ is the Euclidean norm. ψ_m is Green's function for the penalty functional J_2 (Mitáš and Mitášová, 1988; Wahba, 1990, pg. 31), also known as the *radial*

basis function (RBF, Buhmann, 2003) or reproducing kernel. It is defined by

$$\begin{aligned}\psi_2(0) &= 0, \\ \psi_2(r) &= |r|^{4-d} \ln |r| \quad \text{if } d \text{ is even,} \\ \psi_2(r) &= |r|^{4-d} \quad \text{otherwise.}\end{aligned}\tag{A.4}$$

For $d = 1$, Equation (A.4) yields the well-known cubic spline interpolator whereby $\psi_2(|x - x_i|) = |x - x_i|^3$. It can be seen from Equation (A.4) that in 2-D (i.e., bivariate TPS) the reproducing kernel becomes $\psi_2(\|\mathbf{x} - \mathbf{x}_i\|) = \|\mathbf{x} - \mathbf{x}_i\|^2 \ln \|\mathbf{x} - \mathbf{x}_i\|$. For trivariate TPS, $\psi_2(\|\mathbf{x} - \mathbf{x}_i\|) = \|\mathbf{x} - \mathbf{x}_i\|$ is used.

From Equation (A.3) and using the notation $r_{ij} = \|\mathbf{x}_j - \mathbf{x}_i\|$ it can be proven that for all y_j

$$\begin{aligned}y_j &= f(\mathbf{x}_j) + n\lambda\sigma_j^2 w_j \\ &= \sum_{i=1}^n w_i \psi_2(r_{ij}) + n\lambda\sigma_j^2 w_j + \sum_{k=0}^d a_k \phi_k(\mathbf{x}_j).\end{aligned}\tag{A.5}$$

Equation (A.5) can be rewritten in the following matrix form:

$$\mathbf{y} = (\mathbf{\Psi} + n\lambda\mathbf{D}_\sigma^2) \mathbf{w} + \mathbf{\Phi} \mathbf{a},\tag{A.6}$$

where

$$\begin{aligned}\mathbf{y} &= \begin{pmatrix} y_1 \\ \vdots \\ y_n \end{pmatrix}, \mathbf{\Psi} = \begin{bmatrix} \psi_2(r_{11}) & \cdots & \psi_2(r_{1n}) \\ \vdots & \ddots & \vdots \\ \psi_2(r_{n1}) & \cdots & \psi_2(r_{nn}) \end{bmatrix}, \mathbf{D}_\sigma^2 = \begin{bmatrix} \sigma_1^2 & \cdots & 0 \\ \vdots & \ddots & \vdots \\ 0 & \cdots & \sigma_n^2 \end{bmatrix}, \\ \mathbf{w} &= \begin{pmatrix} w_1 \\ \vdots \\ w_n \end{pmatrix}, \mathbf{\Phi} = \begin{bmatrix} 1 & x_{1,1} & \cdots & x_{1,d} \\ \vdots & \vdots & \ddots & \vdots \\ 1 & x_{n,1} & \cdots & x_{n,d} \end{bmatrix}, \text{ and } \mathbf{a} = \begin{pmatrix} a_0 \\ \vdots \\ a_d \end{pmatrix}.\end{aligned}\tag{A.7}$$

In addition \mathbf{w} must fulfil

$$\mathbf{\Phi}^T \mathbf{w} = 0\tag{A.8}$$

in order to ensure that $\mathbf{\Psi}$ is strictly positive definite. In such a case, Equations (A.6) & (A.8) provide a determined system of $n + d + 1$ equations for as many unknowns whose solution is given by

$$\mathbf{a} = [\mathbf{\Phi}^T (\mathbf{\Psi} + n\lambda\mathbf{D}_\sigma^2)^{-1} \mathbf{\Phi}]^{-1} \mathbf{\Phi}^T (\mathbf{\Psi} + n\lambda\mathbf{D}_\sigma^2)^{-1} \mathbf{y},\tag{A.9a}$$

$$\mathbf{w} = (\mathbf{\Psi} + n\lambda\mathbf{D}_\sigma^2)^{-1} (\mathbf{y} - \mathbf{\Phi} \mathbf{a}).\tag{A.9b}$$

The solution of the TPS is obtained by having $\lambda = 0$ in the above equations.

Appendix B

Confidence intervals

Consider $\Delta_i = P_i - O_i$ being the error between a predicted and an observed value P_i and O_i , respectively, for $i = \{1, 2, \dots, n\}$, so that Δ_i are n independent identically distributed normal random variables with mean μ and variance σ^2 . The Mean Absolute Error (MAE) and the Root Mean Square Error (RMSE) are often used in this thesis to assess the performance of models, as well as to discriminate modelling strategies. In order to ensure that two or more models can be effectively discriminated, there is a need for estimating the confidence interval (CI) on estimators of these statistics. This appendix is aimed at providing parametric methods to compute such CIs.

B.1 Mean Absolute Error (MAE)

An estimator of the Mean Absolute Error (MAE) is defined as

$$\widehat{\text{MAE}} = \frac{1}{n} \sum_{i=1}^n |\Delta_i|. \quad (\text{B.1})$$

[Bonett and Seier \(2003\)](#) proposed a method to compute confidence intervals for Mean Absolute Deviation (MAD). The method was originally designed for its application to deviations (i.e., the digression between a random value and the mean or median of its population, or any other target). Nevertheless, it can be used to address the statistics of errors (i.e., the residual between the predicted and real value of a process), if these errors are random and of additive nature. If the errors are correlated with the predicted value (e.g., multiplicative error), then they must be normalized before applying [Bonett and Seier \(2003\)](#)'s formulas. The confidence in-

terval for the MAE is computed using

$$\hat{\tau} = \widehat{\text{MAE}} \quad (\text{B.2a})$$

$$\hat{\delta} = \frac{\hat{\mu} - \hat{\eta}}{\hat{\tau}} \quad (\text{B.2b})$$

$$\gamma = \frac{\hat{\sigma}^2}{\hat{\tau}^2} \quad (\text{B.2c})$$

$$c = \frac{n}{n-1} \quad (\text{B.2d})$$

$$\text{Var}[\ln \hat{\tau}] = \frac{\hat{\delta}^2 + \hat{\gamma} - 1}{n}, \quad (\text{B.2e})$$

where $\hat{\mu}$, and $\hat{\sigma}$, are the sample mean and standard deviation, respectively. $\hat{\eta}$ is the target from which the absolute deviation is sought. This can be the median, the mean, or other fixed target. In the case of MAE, the target is 0. $\hat{\delta}$ and $\hat{\gamma}$ measure the skewness and kurtosis of the distribution of errors, respectively. [Bonett and Seier \(2003\)](#) showed that the confidence interval for the MAE can be computed for distributions under moderate non-normality based on the standard normal table by

$$\text{Prob}\left(e^{\ln(\hat{c}\hat{\tau}) - z_{\alpha/2} \sqrt{\text{Var}[\ln \hat{\tau}]}} \leq \text{MAE} \leq e^{\ln(\hat{c}\hat{\tau}) + z_{\alpha/2} \sqrt{\text{Var}[\ln \hat{\tau}]}}\right) = 1 - \alpha, \quad (\text{B.3})$$

where α is the significance level (e.g., $\alpha = 0.05$ corresponds to a 95% CI).

B.2 Root Mean Square Error (RMSE)

An estimator of the Root Mean Square Error (RMSE) is defined as

$$\widehat{\text{RMSE}} = \sqrt{\frac{\sum_{i=1}^n \Delta_i^2}{n}}. \quad (\text{B.4})$$

The RMSE obeys a statistical distribution as illustrated in [Figure B.1](#). For each set of the parameters n , μ , and σ , the distribution was obtained from RMSE values calculated from 50,000 vectors of errors. In order to approach the RMSE distribution it can be noted that the random variable

$$Y = \sum_{i=1}^n \left(\frac{\Delta_i}{\sigma}\right)^2$$

is distributed according to a non-central chi-square distribution χ_{n, λ^2}^2 with n degrees of freedom and non-centrality parameter $\lambda^2 = n\left(\frac{\mu}{\sigma}\right)^2$ ([Johnson et al., 1995](#), chap. 18, pg. 450). The distribution of the square root of a random variable having a

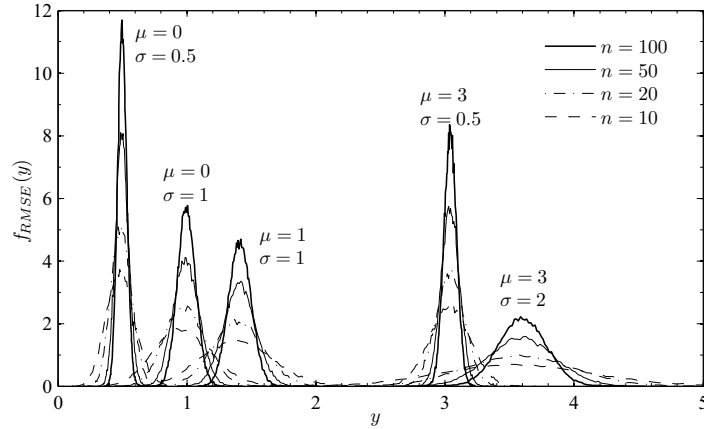


Figure B.1 Empirical distribution of RMSE values obtained from 50,000 independent random vectors of errors for various values of n , μ , and σ .

non-central chi-square distribution with n degrees of freedom and non-centrality parameter λ^2 is a non-central chi distribution $\chi'_{n,\lambda}$ with n degrees of freedom and non-centrality parameter λ (Sun and Baricz, 2008), hence,

$$Z = \sqrt{Y} \sim \chi'_{n,\lambda}.$$

It follows that the RMSE random variable is proportional to a non-central chi distributed variable:

$$\text{RMSE} = \frac{\sigma}{\sqrt{n}} Z. \quad (\text{B.5})$$

Non-central chi distribution

Probability density function

The probability density function of the non-central chi distribution $\chi'_{n,\lambda}$ is defined as

$$\begin{aligned} \chi'_{n,\lambda}: [0, \infty[&\rightarrow [0, \infty[\\ x &\mapsto \chi'_{n,\lambda}(x) = \lambda \left(\frac{x}{\lambda}\right)^{\frac{n}{2}} e^{-\frac{x^2+\lambda^2}{2}} I_{\frac{n}{2}-1}(\lambda x), \end{aligned} \quad (\text{B.6})$$

where $I_\nu(z)$ is the modified Bessel function of the first kind given by

$$I_\nu(z) = \left(\frac{z}{2}\right)^\nu \sum_{k=0}^{\infty} \frac{\left(\frac{z}{2}\right)^{2k}}{\Gamma(\nu + k + 1)k!}.$$

$\Gamma(a)$ is the gamma function defined by the integral¹

$$\Gamma(a) = \int_0^{\infty} e^{-t} t^{a-1} dt.$$

Relationship with RMSE

It is evident from Equation (B.6) that, although the RMSE is proportional to a non-central chi distributed variable [Equation (B.5)], its distribution is difficult to establish. Nevertheless, the mean (i.e., expectation) of the RMSE random variable (i.e., $\mu_{\text{RMSE}} = E[\text{RMSE}]$) can be obtained from that of Z (i.e., $\mu_{\chi'_{n,\lambda}} = E[Z]$) by

$$\mu_{\text{RMSE}} = \frac{\sigma}{\sqrt{n}} \mu_{\chi'_{n,\lambda}}. \quad (\text{B.7})$$

In addition, $\chi'_{n,\lambda}$ quickly approaches a normal distribution when n gets large (i.e., typically more than 30) as illustrated in Figure B.2 (Johnson *et al.*, 1995, chap. 18 & 29). Thus, the random variable RMSE also tends to a normal distribution (Figure B.1). For a large enough n , a confidence interval (CI) can be provided for a sample estimation $\hat{\mu}_{\text{RMSE}}$ of the RMSE, based on the variance of Z (i.e., $\text{Var}[Z] = \sigma_{\chi'_{n,\lambda}}^2$) and on the standard normal table. The variance of RMSE is given by

$$\sigma_{\text{RMSE}}^2 = \frac{\sigma^2}{n} \sigma_{\chi'_{n,\lambda}}^2, \quad (\text{B.8})$$

and for a statistical risk α ,

$$\text{Prob}(\hat{\mu}_{\text{RMSE}} - z_{\alpha/2} \hat{\sigma}_{\text{RMSE}} \leq \mu_{\text{RMSE}} \leq \hat{\mu}_{\text{RMSE}} + z_{\alpha/2} \hat{\sigma}_{\text{RMSE}}) = 1 - \alpha. \quad (\text{B.9})$$

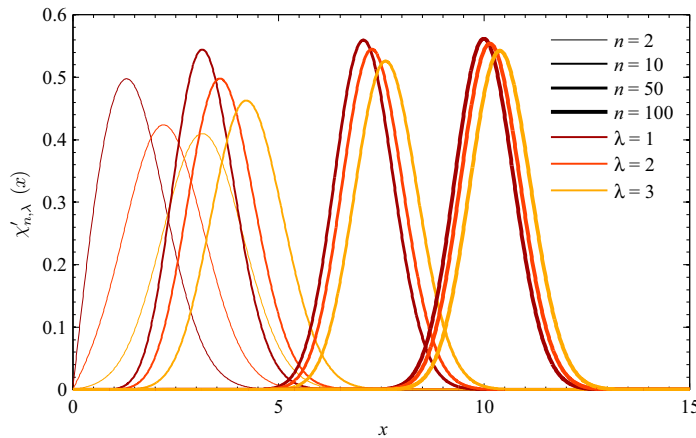


Figure B.2 Probability density function of the non-central chi distribution for several degrees of freedom and non-centrality parameters. $\chi'_{n,\lambda}$ quickly approaches normal distribution when n gets large.

¹If a is a positive integer, then $\Gamma(a) = (a - 1)!$.

Mean

According to Anderson (1981) and Oberto and Pennechi (2006), the mean of $\chi'_{n,\lambda}$ is given by

$$\mu_{\chi'_{n,\lambda}} = \sqrt{\frac{\pi}{2}} L_{1/2}^{(n/2-1)}\left(-\frac{\lambda^2}{2}\right), \quad (\text{B.10})$$

where $L_\nu^{(a)}(z)$ is the generalized Laguerre function defined by

$$L_\nu^{(a)}(z) = \frac{\Gamma(\nu + a + 1)}{\Gamma(\nu + 1)} {}_1\tilde{F}_1(-\nu; a + 1; z).$$

${}_1\tilde{F}_1(a; b; z)$ is the regularized confluent hypergeometric function of the first kind defined by

$$\begin{aligned} {}_1\tilde{F}_1(a; b; z) &= \sum_{k=0}^{\infty} \frac{(a)_k z^k}{\Gamma(b + k)k!} \\ &= \frac{{}_1F_1(a; b; z)}{\Gamma(b)}. \end{aligned}$$

${}_1F_1(a; b; z)$ is the confluent hypergeometric function of the first kind given by

$${}_1F_1(a; b; z) = \sum_{k=0}^{\infty} \frac{(a)_k z^k}{(b)_k k!},$$

where $(a)_k = \frac{\Gamma(a+k)}{\Gamma(a)}$ is the Pochhammer symbol.

Variance

The variance of $\chi'_{n,\lambda}$ is given by

$$\sigma_{\chi'_{n,\lambda}}^2 = n + \lambda^2 - \mu_{\chi'_{n,\lambda}}^2. \quad (\text{B.11})$$

Sample application

Consider a set of $n = 100$ data points whose errors of prediction are independent and known to be normally distributed with mean $\mu = 2$ and variance $\sigma^2 = 9$. Thus, the non-centrality parameter is $\lambda = \sqrt{n} \frac{\mu}{\sigma} \approx 6.667$. $\mu_{\chi'_{n,\lambda}} \approx 11.991$ is obtained from Equation (B.10). Equation (B.7) yields the expected value of the RMSE as $\mu_{\text{RMSE}} \approx 3.597$. $\sigma_{\chi'_{n,\lambda}} \approx 0.653$ is obtained from Equation (B.11). Equation (B.8) yields the standard deviation of the RMSE as $\sigma_{\text{RMSE}} \approx 0.242$. Figure B.3 shows the distribution of RMSE values obtained from 50,000 independent vectors of errors. There is a perfect agreement between the RMSE distribution and the normal distribution

whose parameters are calculated based on the statistics of the non-central chi distribution.

Now consider that the RMSE is estimated from a single vector of errors, whose sample mean $\hat{\mu} = 1.811$ and sample standard deviation $\hat{\sigma} = 3.136$. The non-centrality parameter is $\hat{\lambda} = \sqrt{n} \frac{\hat{\mu}}{\hat{\sigma}} \approx 5.775$. $\hat{\mu}_{\chi'_{n,\lambda}} \approx 11.521$ yields $\hat{\mu}_{\text{RMSE}} \approx 3.613$. $\hat{\sigma}_{\chi'_{n,\lambda}} \approx 0.790$ yields $\hat{\sigma}_{\text{RMSE}} \approx 0.248$. Finally, for at the .05 significance level (i.e., 95% confidence interval) $z_{\alpha/2} \approx 1.96$ and

$$\text{Prob}(3.613 - 1.96 \times 0.248 \approx 3.123 \leq \mu_{\text{RMSE}} \leq 3.613 + 1.96 \times 0.248 \approx 4.099) = 95\%. \tag{B.12}$$

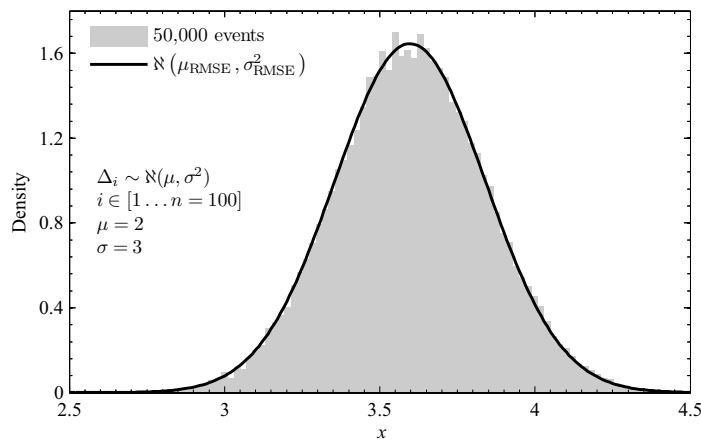


Figure B.3 Example of the distribution of 50,000 RMSE values obtained from $n = 100$ data points whose errors of prediction are independent and normally distributed with mean $\mu = 2$ and variance $\sigma^2 = 9$. The normal distribution whose parameters are calculated based on the statistics of the non-central chi distribution show a perfect agreement with the experimental distribution.

Appendix C

Illumination angle

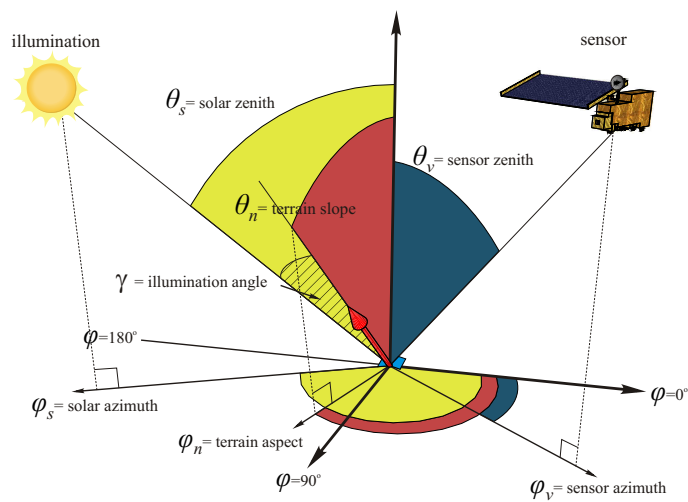


Figure C.1 Relative geometry of the sun, the sensor, and the target.

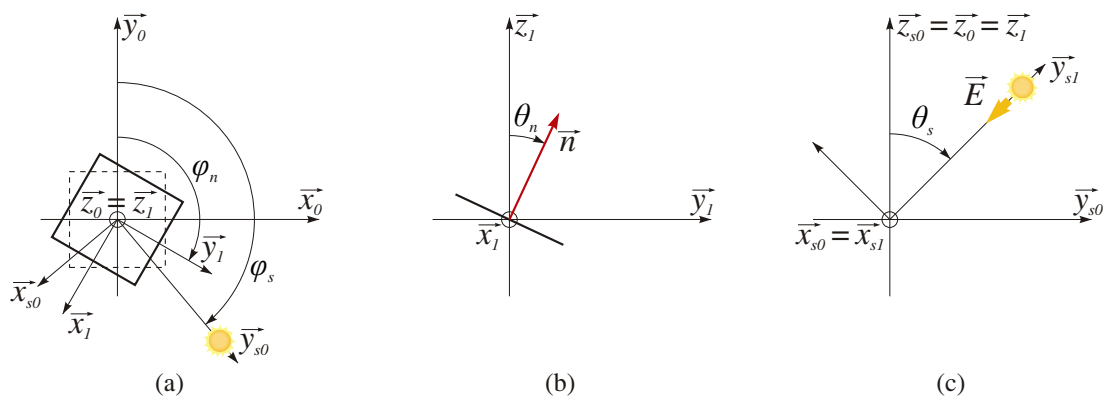


Figure C.2 Decomposition of the geometry using Euler's angles.

The radiative power received by an orientated plane surface $\vec{S} = S\vec{n}$ exposed to a radiant flux density $\vec{E} = -Ey_{s1}^{\vec{}}$ is given by the scalar product

$$W = \vec{E} \cdot \vec{S}. \quad (\text{C.1})$$

Using Euler's representation given in Figure C.2 (c), $y_{s1}^{\vec{}}$ is parameterized by the solar zenith angle θ_s and can be decomposed into the plan $(y_{s0}^{\vec{}}, z_{s0}^{\vec{}})$ as follows:

$$y_{s1}^{\vec{}} = \sin \theta_s y_{s0}^{\vec{}} + \cos \theta_s z_{s0}^{\vec{}}. \quad (\text{C.2})$$

Similarly, $y_{s0}^{\vec{}}$ is expressed in the plan $(y_0^{\vec{}}, z_0^{\vec{}})$ using the solar azimuth angle φ_s [Figure C.2 (a)]:

$$y_{s0}^{\vec{}} = \sin \varphi_s x_0^{\vec{}} + \cos \varphi_s y_0^{\vec{}}. \quad (\text{C.3})$$

Substituting $z_{s0}^{\vec{}} = z_0^{\vec{}}$ and Equation C.3 into Equation C.2 yields

$$y_{s1}^{\vec{}} = \sin \theta_s \sin \varphi_s x_0^{\vec{}} + \sin \theta_s \cos \varphi_s y_0^{\vec{}} + \cos \theta_s z_0^{\vec{}}. \quad (\text{C.4})$$

From Figure C.2 (b) the normal vector to the surface according to the slope θ_n can be expressed as

$$\vec{n} = \sin \theta_n y_1^{\vec{}} + \cos \theta_n z_1^{\vec{}}. \quad (\text{C.5})$$

Using the aspect parameter φ_n , $y_1^{\vec{}}$ is given in the plan $(y_0^{\vec{}}, z_0^{\vec{}})$ by

$$y_1^{\vec{}} = \sin \varphi_n x_0^{\vec{}} + \cos \varphi_n y_0^{\vec{}}. \quad (\text{C.6})$$

Substituting $z_1^{\vec{}} = z_0^{\vec{}}$ and Equation C.6 into Equation C.5 yields

$$\vec{n} = \sin \theta_n \sin \varphi_n x_0^{\vec{}} + \sin \theta_n \cos \varphi_n y_0^{\vec{}} + \cos \theta_n z_0^{\vec{}}. \quad (\text{C.7})$$

Finally, by substituting Equation C.4 & C.7 into Equation C.1, the scalar product between the irradiance vector and the surface vector can be written as:

$$\begin{aligned} \vec{E} \cdot \vec{S} &= -ES y_{s1}^{\vec{}} \cdot \vec{n} \\ &= -ES (\sin \theta_n \sin \varphi_n \sin \theta_s \sin \varphi_s + \sin \theta_n \cos \varphi_n \sin \theta_s \cos \varphi_s + \cos \theta_n \cos \theta_s) \\ &= -ES [\cos \theta_n \cos \theta_s + \sin \theta_n \sin \theta_s (\sin \varphi_n \sin \varphi_s + \cos \varphi_n \cos \varphi_s)] \\ &= -ES \underbrace{[\cos \theta_n \cos \theta_s + \sin \theta_n \sin \theta_s \cos(\varphi_s - \varphi_n)]}_{\cos \gamma}. \end{aligned} \quad (\text{C.8})$$

Appendix D

Analytical integration of Equation (4.25)

Equation (4.25) can be rearranged as

$$\begin{aligned}
 C_t = & \frac{1}{2\pi} \int_0^{2\pi} \frac{\cos \theta_n}{1 + \tan^2 \theta_n \cos^2(\varphi - \varphi_n)} \\
 & + \cos(\varphi - \varphi_n) \sin \theta_n \left[\arctan [\tan \theta_n \cos(\varphi - \varphi_n)] + \frac{\pi}{2} + \frac{\tan \theta_n \cos(\varphi - \varphi_n)}{1 + \tan^2 \theta_n \cos^2(\varphi - \varphi_n)} \right] d\varphi \\
 & - \underbrace{\frac{1}{2\pi} \int_0^{2\pi} \left[\cos \theta_n \sin^2 H_\varphi + \sin \theta_n \cos(\varphi - \varphi_n) (H_\varphi - \sin H_\varphi \cos H_\varphi) \right] d\varphi}_{V_d}. \quad (D.1)
 \end{aligned}$$

Consider separately each component of the previous integral that is not accounted in V_d and that has not a null contribution. It is evident that each integrand is periodic of period 2π with respect to φ , therefore it is possible to ignore the translation of φ_n when integrating over $[0, 2\pi]$. Thus, Equation (D.1) can be decomposed into

$$I_1 = \int_0^{2\pi} \frac{\cos \theta_n}{1 + \tan^2 \theta_n \cos^2 \varphi} d\varphi, \quad (D.2a)$$

$$I_2 = \int_0^{2\pi} \sin \theta_n \cos \varphi \arctan [\tan \theta_n \cos \varphi] d\varphi, \quad (D.2b)$$

$$I_3 = \int_0^{2\pi} \sin \theta_n \tan \theta_n \frac{\cos^2 \varphi}{1 + \tan^2 \theta_n \cos^2 \varphi} d\varphi, \text{ and} \quad (D.2c)$$

$$C_t = \frac{1}{2\pi} (I_1 + I_2 + I_3) - V_d. \quad (D.2d)$$

The following integrals can be used (Dwight, 1961):

$$\int \frac{dx}{a^2 + b^2 \cos^2 x} = \frac{1}{a \sqrt{a^2 + b^2}} \arctan \left(\frac{a \tan x}{\sqrt{a^2 + b^2}} \right), [a > 0] \quad (\text{D.3a})$$

$$\int \frac{\cos^2 x}{a^2 + b^2 \cos^2 x} dx = \frac{x}{b^2} - \frac{a}{b^2 \sqrt{a^2 + b^2}} \arctan \left(\frac{a \tan x}{\sqrt{a^2 + b^2}} \right), [a > 0] \quad (\text{D.3b})$$

$$\int \frac{\sin^2 x}{a^2 + b^2 \cos^2 x} dx = \frac{\sqrt{a^2 + b^2}}{ab^2} \arctan \left(\frac{a \tan x}{\sqrt{a^2 + b^2}} \right) - \frac{x}{b^2}, [a > 0] \quad (\text{D.3c})$$

Note that the integrations are computed for functions that have more than one branch, from a point on one branch to a point on another branch. Therefore, care should be taken in dealing with the value of \tan^{-1} .

Equation (D.3b) is used to compute I_1 :

$$\begin{aligned} I_1 &= 2\pi \frac{\cos \theta_n}{\sqrt{1 + \tan^2 \theta_n}} \\ &= 2\pi \cos^2 \theta_n. \end{aligned} \quad (\text{D.4})$$

Similarly, Equation (D.3c) is used to compute I_3 :

$$\begin{aligned} I_3 &= 2\pi \frac{\sin^2 \theta_n}{\cos \theta_n} \left(\frac{1}{\tan^2 \theta_n} - \frac{1}{\tan^2 \theta_n \sqrt{1 + \tan^2 \theta_n}} \right) \\ &= 2\pi (\cos \theta_n - \cos^2 \theta_n). \end{aligned} \quad (\text{D.5})$$

An integration by parts enables the computation of I_2 . Let

$$\begin{cases} u' = \cos \varphi & \Rightarrow u = \sin \varphi \\ v = \arctan(\tan \theta_n \cos \varphi) & \Rightarrow v' = -\frac{\tan \theta_n \sin \varphi}{1 + \tan^2 \theta_n \cos^2 \varphi} \end{cases}. \quad (\text{D.6})$$

Hence

$$I_2 = \tan \theta_n \int_0^{2\pi} \frac{\sin^2 \varphi}{1 + \tan^2 \theta_n \cos^2 \varphi} d\varphi, \quad (\text{D.7})$$

which can be found using Equation (D.3c)

$$\begin{aligned} I_2 &= 2\pi \sin \theta_n \tan \theta_n \left(\frac{\sqrt{1 + \tan^2 \theta_n}}{\tan^2 \theta_n} - \frac{1}{\tan^2 \theta_n} \right) \\ &= 2\pi (1 - \cos \theta_n). \end{aligned} \quad (\text{D.8})$$

From Equation (D.4), (D.5) and (D.8)

$$I_1 + I_2 + I_3 = 2\pi. \quad (\text{D.9})$$

Therefore,

$$C_t = 1 - V_d. \quad (\text{D.10})$$

Appendix E

Atmospheric absorption coefficients

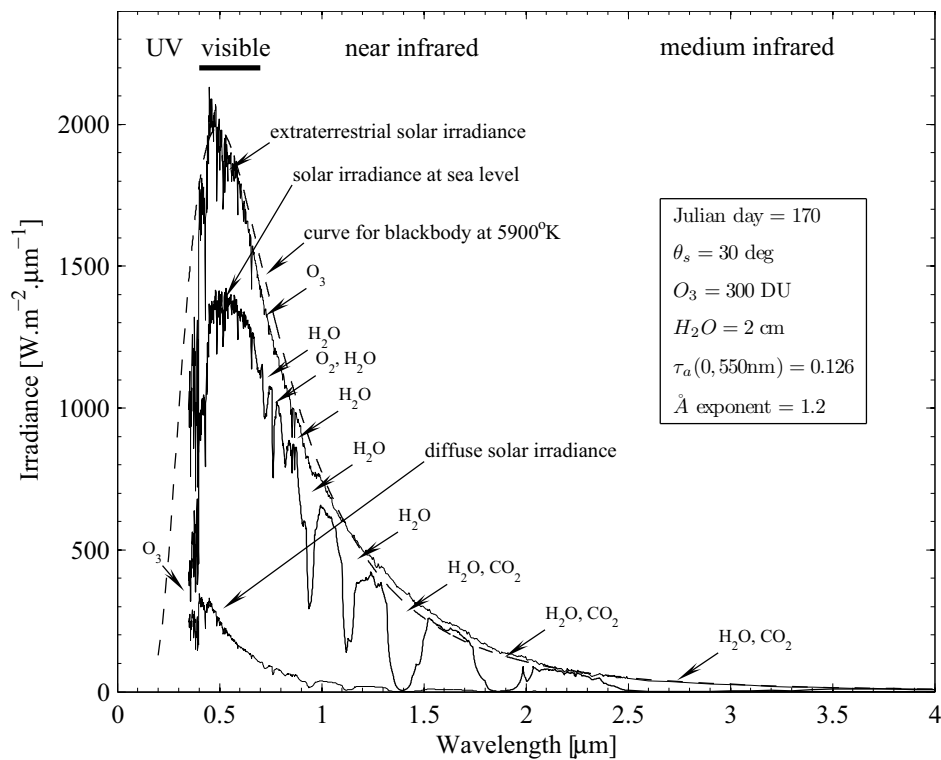


Figure E.1 Typical irradiance spectrum calculated with the atmospheric model described in Section 4.4 [adapted from Slater (1980)]. Absorption coefficients are provided on the verso of the page.

Table E.1 Extraterrestrial solar spectrum and atmospheric absorption coefficients at 122 wavelengths from [Leckner \(1978\)](#) with few additions and modification from [Bird and Riordan \(1986\)](#).

Wavelength λ [μm]	$^a E_0$ [W. $\text{m}^{-2}\cdot\mu\text{m}^{-1}$]	a_w [m^{-1}]	a_o [m^{-1}]	a_u	Wavelength λ [μm]	E_0 [W. $\text{m}^{-2}\cdot\mu\text{m}^{-1}$]	a_w [m^{-1}]	a_o [m^{-1}]	a_u
0.3	535.9	0.0	10.0	0.0	0.98	767.0	1.48	0.0	0.0
0.305	558.3	0.0	4.8	0.0	0.9935	757.6	0.1	0.0	0.0
0.31	622.0	0.0	2.7	0.0	1.04	688.1	0.00001	0.0	0.0
0.315	692.7	0.0	1.35	0.0	1.07	640.7	0.001	0.0	0.0
0.32	715.1	0.0	0.8	0.0	1.1	606.2	3.2	0.0	0.0
0.325	832.9	0.0	0.38	0.0	1.12	585.9	115.0	0.0	0.0
0.33	961.9	0.0	0.16	0.0	1.13	570.2	70.0	0.0	0.0
0.335	931.9	0.0	0.075	0.0	1.145	564.1	75.0	0.0	0.0
0.34	900.6	0.0	0.04	0.0	1.161	544.2	10.0	0.0	0.0
0.345	911.3	0.0	0.019	0.0	1.17	533.4	5.0	0.0	0.0
0.35	975.5	0.0	0.007	0.0	1.2	501.6	2.0	0.0	0.0
0.36	975.9	0.0	0.0	0.0	1.24	477.5	0.002	0.0	0.05
0.37	1119.9	0.0	0.0	0.0	1.27	422.7	0.002	0.0	0.3
0.38	1103.8	0.0	0.0	0.0	1.29	440.0	0.1	0.0	0.02
0.39	1033.8	0.0	0.0	0.0	1.32	416.8	4.0	0.0	0.0002
0.4	1479.1	0.0	0.0	0.0	1.35	391.4	200.0	0.0	0.00011
0.41	1701.3	0.0	0.0	0.0	1.395	358.9	1000.0	0.0	0.00001
0.42	1740.4	0.0	0.0	0.0	1.4425	327.5	185.0	0.0	0.05
0.43	1587.2	0.0	0.0	0.0	1.4625	317.5	80.0	0.0	0.011
0.44	1837.0	0.0	0.0	0.0	1.477	307.3	80.0	0.0	0.005
0.45	2005.0	0.0	0.003	0.0	1.497	300.4	12.0	0.0	0.0006
0.46	2043.0	0.0	0.006	0.0	1.52	292.8	0.16	0.0	0.0
0.47	1987.0	0.0	0.009	0.0	1.539	275.5	0.002	0.0	0.005
0.48	2027.0	0.0	0.014	0.0	1.558	272.1	0.0005	0.0	0.13
0.49	1896.0	0.0	0.021	0.0	1.578	259.3	0.0001	0.0	0.04
0.5	1909.0	0.0	0.03	0.0	1.592	246.9	0.00001	0.0	0.06
0.51	1927.0	0.0	0.04	0.0	1.61	244.0	0.0001	0.0	0.13
0.52	1831.0	0.0	0.048	0.0	1.63	243.5	0.001	0.0	0.001
0.53	1891.0	0.0	0.063	0.0	1.646	234.8	0.01	0.0	0.0014
0.54	1898.0	0.0	0.075	0.0	1.678	220.5	0.036	0.0	0.0001
0.55	1892.0	0.0	0.085	0.0	1.74	190.8	1.1	0.0	0.00001
0.57	1840.0	0.0	0.12	0.0	1.8	171.1	130.0	0.0	0.00001
0.593	1768.0	0.075	0.119	0.0	1.86	144.5	1000.0	0.0	0.0001
0.61	1728.0	0.0	0.12	0.0	1.92	135.7	500.0	0.0	0.001
0.63	1658.0	0.0	0.09	0.0	1.96	123.0	100.0	0.0	4.3
0.656	1524.0	0.0	0.065	0.0	1.985	123.8	4.0	0.0	0.2
0.6676	1531.0	0.0	0.051	0.0	2.005	113.0	2.9	0.0	21.0
0.69	1420.0	0.016	0.028	0.15	2.035	108.5	1.0	0.0	0.13
0.71	1399.0	0.0125	0.018	0.0	2.065	97.5	0.4	0.0	1.0
0.718	1374.0	1.8	0.015	0.0	2.1	92.4	0.22	0.0	0.08
0.7244	1373.0	2.5	0.012	0.0	2.148	82.4	0.25	0.0	0.001
0.74	1298.0	0.061	0.01	0.0	2.198	74.6	0.33	0.0	0.00038
0.7525	1269.0	0.0008	0.008	0.0	2.27	68.3	0.5	0.0	0.001
0.7575	1245.0	0.0001	0.007	0.0	2.36	63.8	4.0	0.0	0.0005
0.7625	1223.0	0.00001	0.006	4.0	2.45	49.5	80.0	0.0	0.00015
0.7675	1205.0	0.00001	0.005	0.35	2.5	48.5	310.0	0.0	0.00014
0.78	1183.0	0.0006	0.0	0.0	2.6	38.6	15000.0	0.0	0.00066
0.8	1148.0	0.036	0.0	0.0	2.7	36.6	22000.0	0.0	100.0
0.816	1091.0	1.6	0.0	0.0	2.8	32.0	8000.0	0.0	150.0
0.8237	1062.0	2.5	0.0	0.0	2.9	28.1	650.0	0.0	0.13
0.8315	1038.0	0.5	0.0	0.0	3.0	24.8	240.0	0.0	0.0095
0.84	1022.0	0.155	0.0	0.0	3.1	22.1	230.0	0.0	0.001
0.86	998.7	0.00001	0.0	0.0	3.2	19.6	100.0	0.0	0.8
0.88	947.2	0.0026	0.0	0.0	3.3	17.5	120.0	0.0	1.9
0.905	893.2	7.0	0.0	0.0	3.4	15.7	19.5	0.0	1.3
0.915	868.2	5.0	0.0	0.0	3.5	14.1	3.6	0.0	0.075
0.925	829.7	5.0	0.0	0.0	3.6	12.7	3.1	0.0	0.01
0.93	830.3	27.0	0.0	0.0	3.7	11.5	2.5	0.0	0.00195
0.937	814.0	55.0	0.0	0.0	3.8	10.4	1.4	0.0	0.004
0.948	786.9	45.0	0.0	0.0	3.9	9.5	0.17	0.0	0.29
0.965	768.3	4.0	0.0	0.0	4.0	8.6	0.0045	0.0	0.025

^aValues for extraterrestrial irradiance have been computed with the solar spectrum used at the World Radiation Center (WRC), Physikalisch-Meteorologisches Observatorium Davos (PMOD) Publication 615, 1985. The spectrum can be obtained from ftp://ftp.pmodwrc.ch/pub/data/irradiance/spectral_irradiance, last retrieved in October 2008.

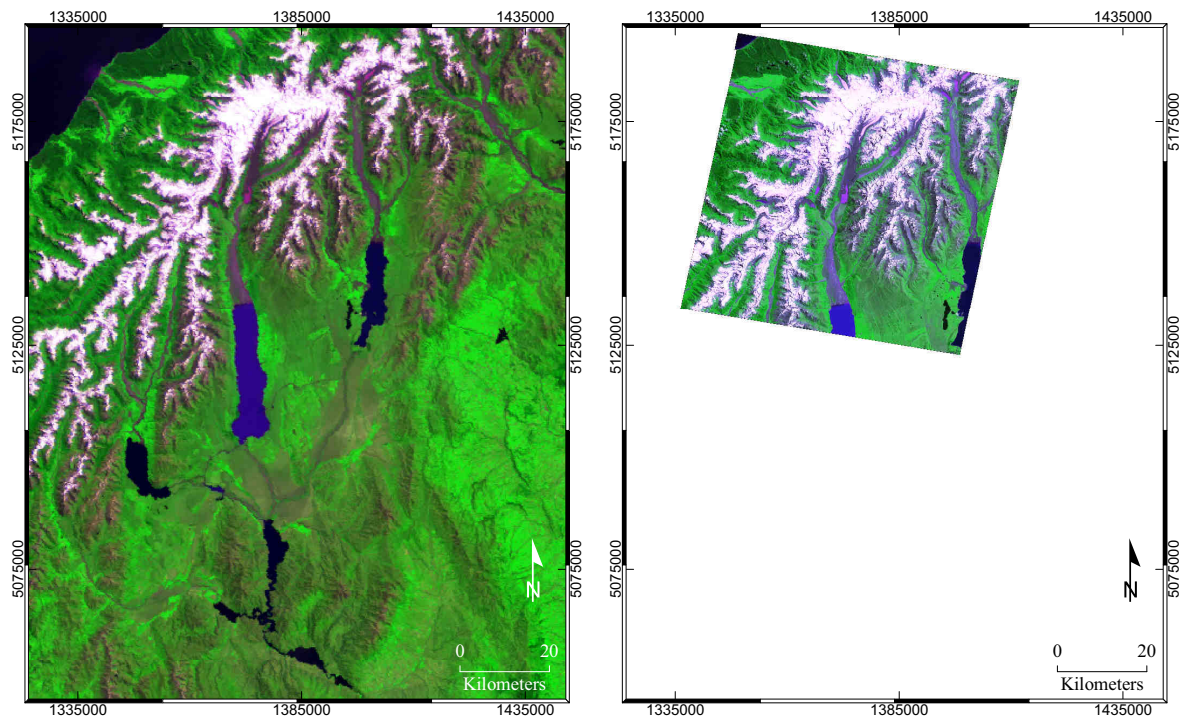
Appendix F

Snow maps for accuracy assessment

This appendix provides the MODIS- and ASTER-derived maps of fractional snowcover used for the assessment of the accuracy of MODIS products. Each double page corresponds to a date (Table 6.1) and shows:

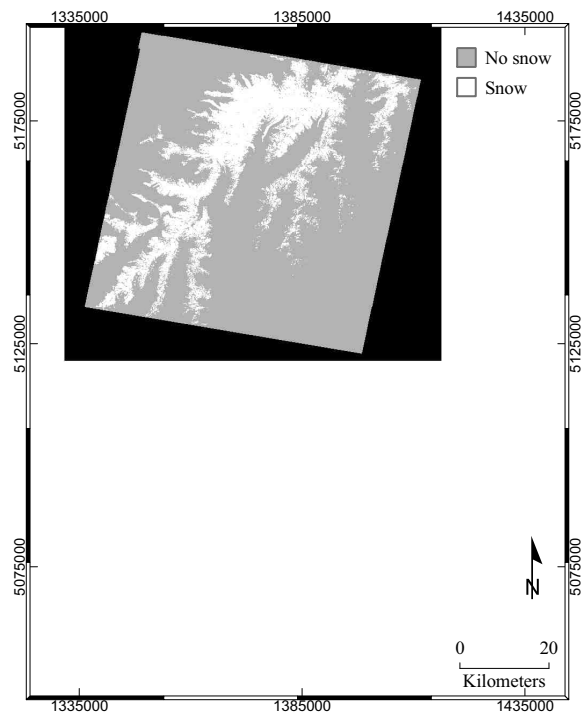
1. a false-colour RGB composite from MODIS bands 1, 2, and 3 at 250 m spatial resolution (i.e., band 3 is fused);
2. a false-colour RGB composite from ASTER bands 2, 3, and 1 at 15 m spatial resolution;
3. a binary classification of snow from the ASTER image based on the NDSI;
4. the MODIS derived maps of fractional snow cover at both 250 (M250) and 500 m (M500) spatial resolution along with the corresponding aggregation of ASTER snow classification used as a reference.

The difference between spatial resolutions is clearly visible when zooming into the .pdf version of the thesis. Note that only the ASTER images and the corresponding binary classifications of snow had to be exported at 60 m spatial resolution in order to limit the size of the file.



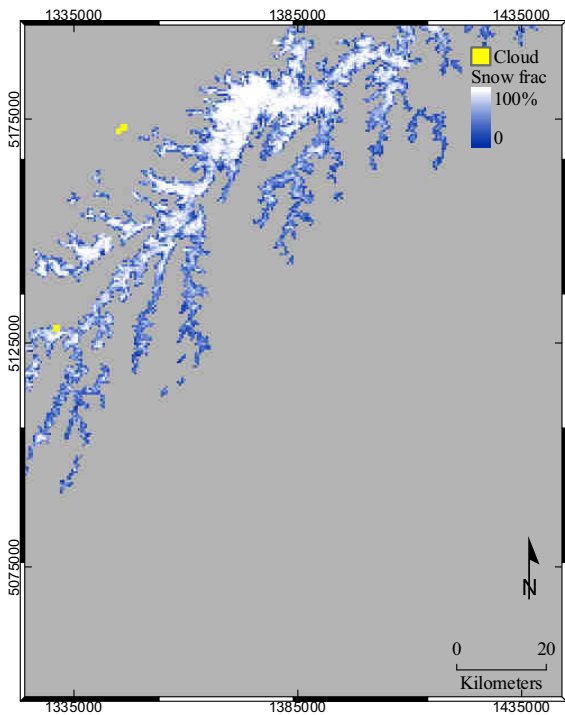
(a) MODIS bands 1, 2, and 3 (250 m)

(b) ASTER bands 2, 3, and 1 (15 m)

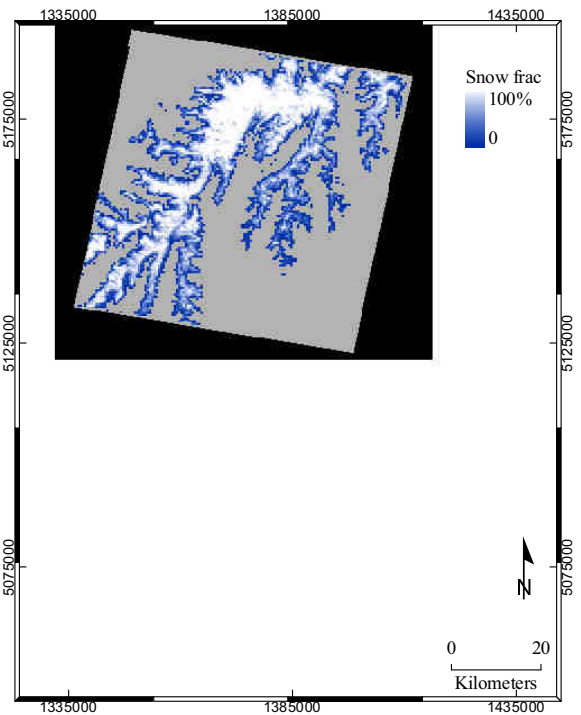


(c) ASTER binary snow map (15 m)

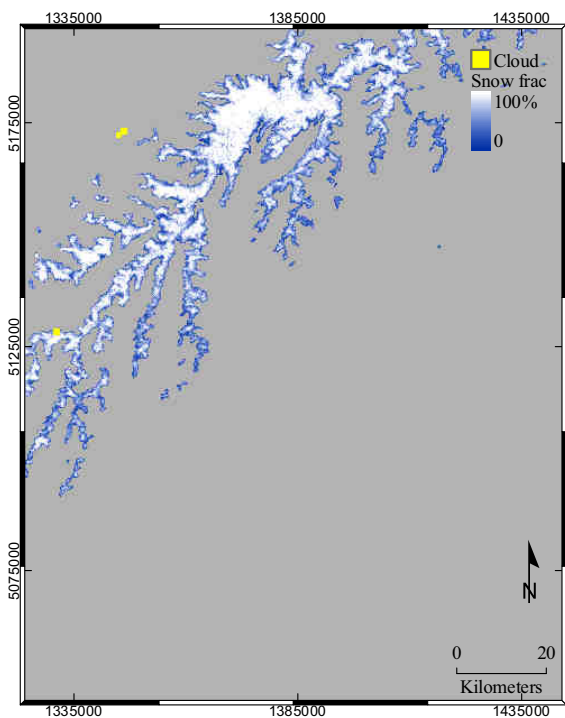
Figure F.1 Snow maps on 31 December 2002, 22:35 GMT.



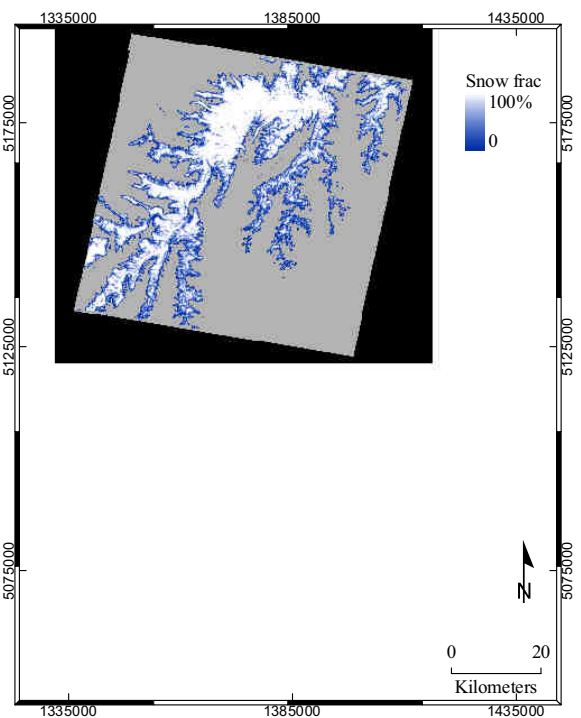
(d) MODIS fractional snow cover (500 m)



(e) ASTER fractional snow cover (500 m)

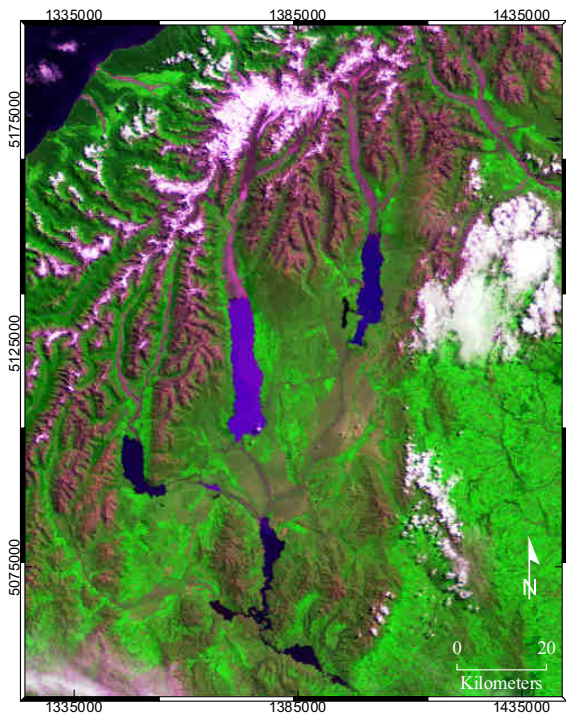


(f) MODIS fractional snow cover (250 m)

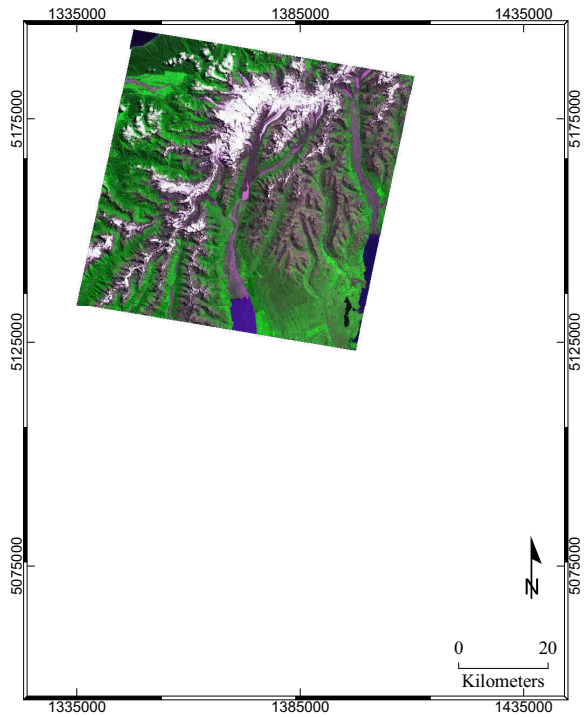


(g) ASTER fractional snow cover (250 m)

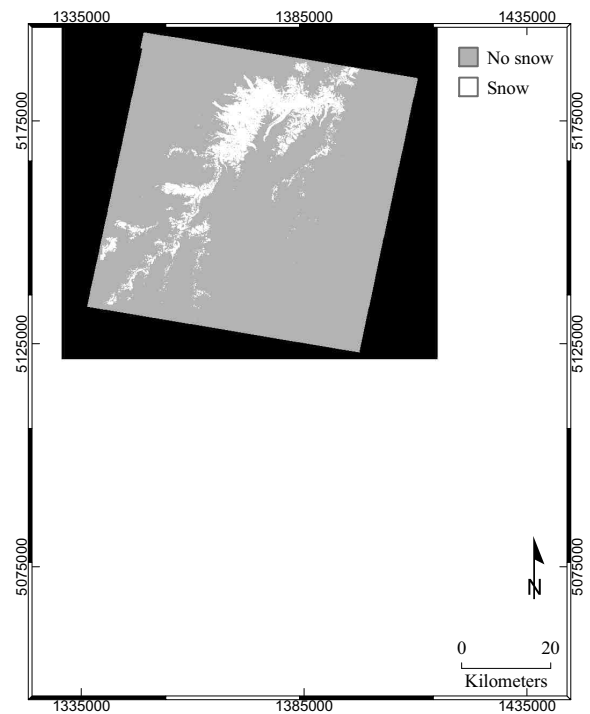
Figure F.1 (continued)



(a) MODIS bands 1, 2, and 3 (250 m)

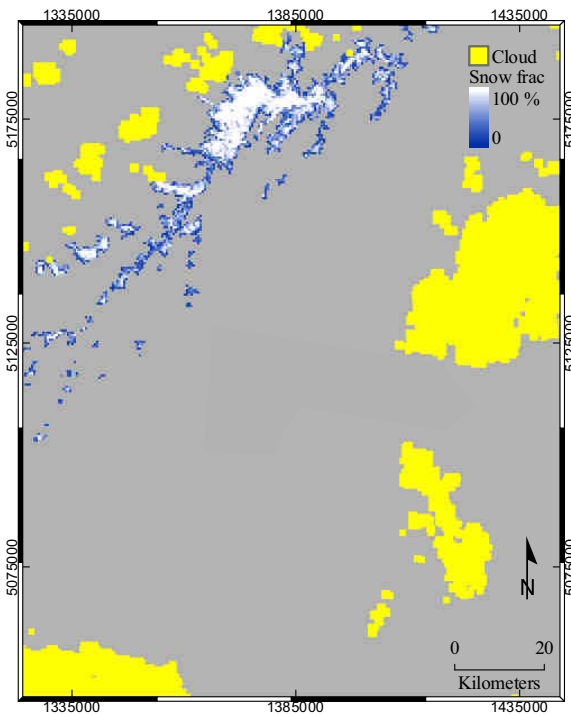


(b) ASTER bands 2, 3, and 1 (15 m)

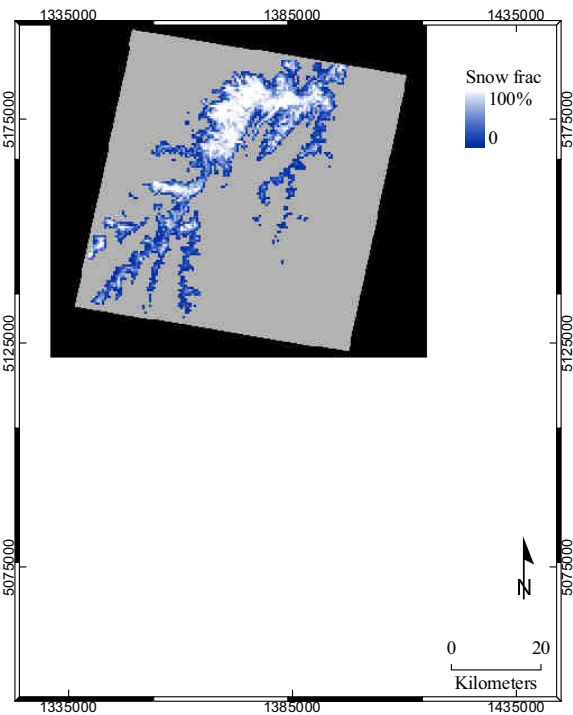


(c) ASTER binary snow map (15 m)

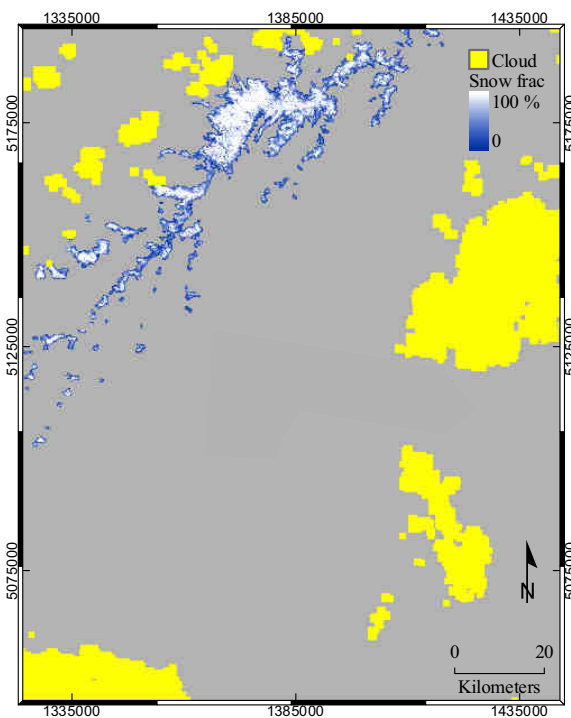
Figure F.2 Snow maps on 29 January 2002, 22:35 GMT.



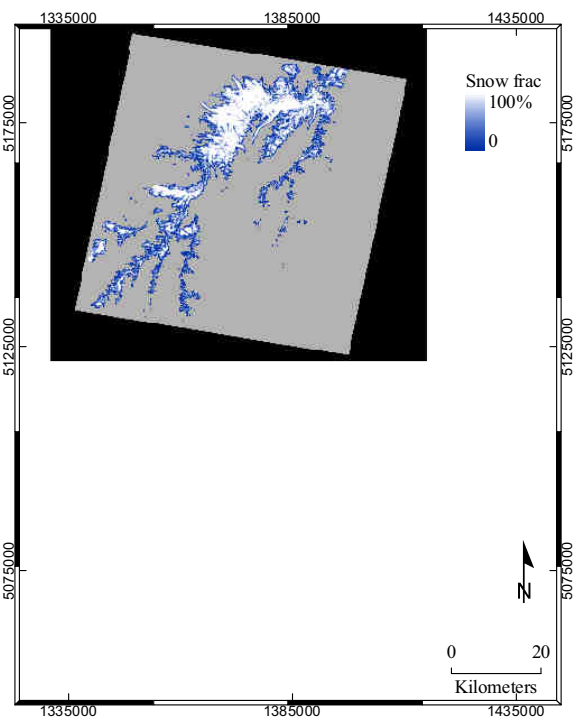
(d) MODIS fractional snow cover (500 m)



(e) ASTER fractional snow cover (500 m)



(f) MODIS fractional snow cover (250 m)



(g) ASTER fractional snow cover (250 m)

Figure F.2 (continued)

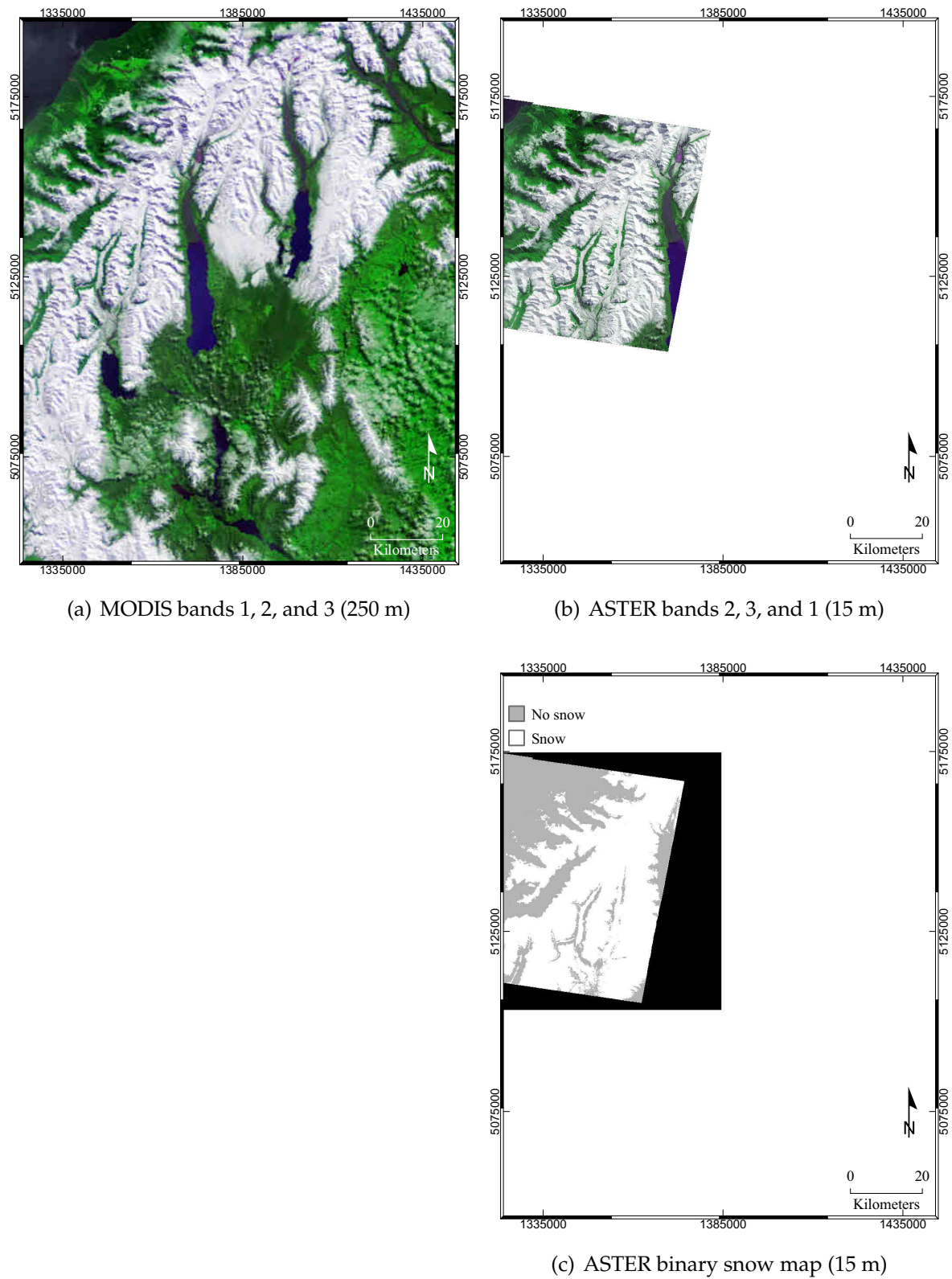
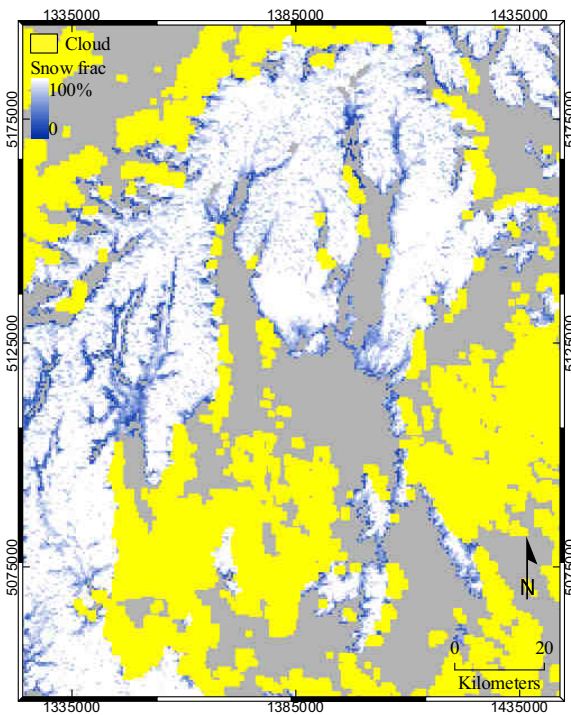
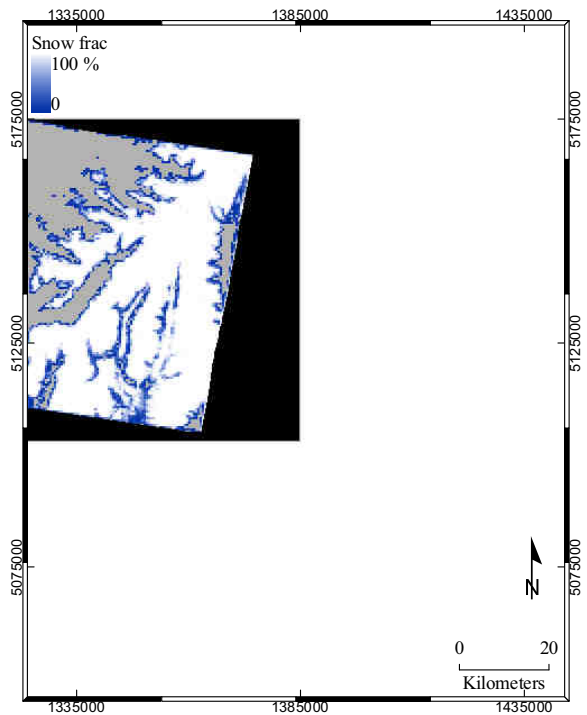


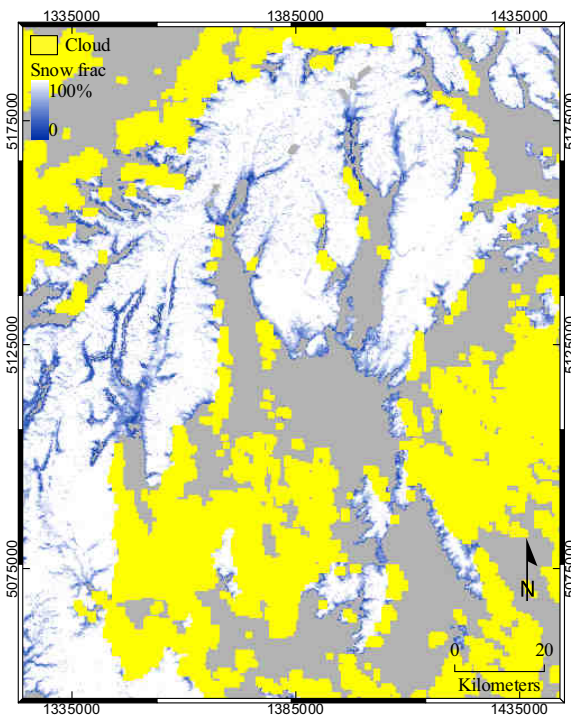
Figure F.3 Snow maps on 11 September 2000, 22:55 GMT.



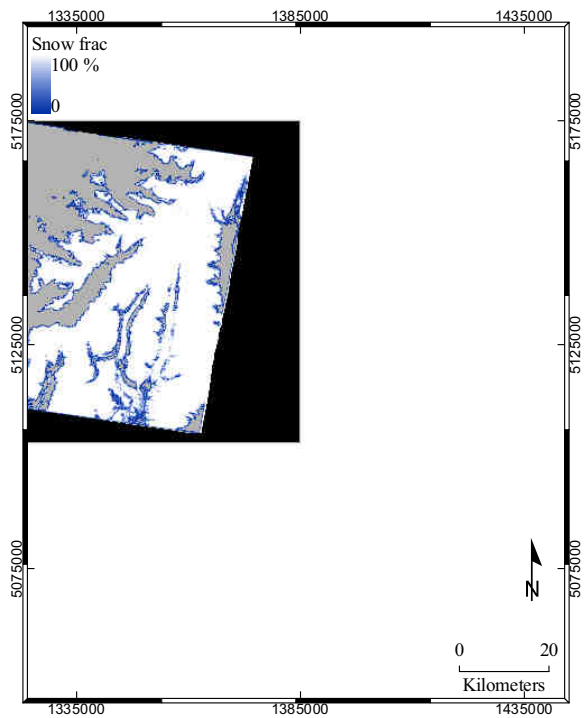
(d) MODIS fractional snow cover (500 m)



(e) ASTER fractional snow cover (500 m)



(f) MODIS fractional snow cover (250 m)



(g) ASTER fractional snow cover (250 m)

Figure F.3 (continued)

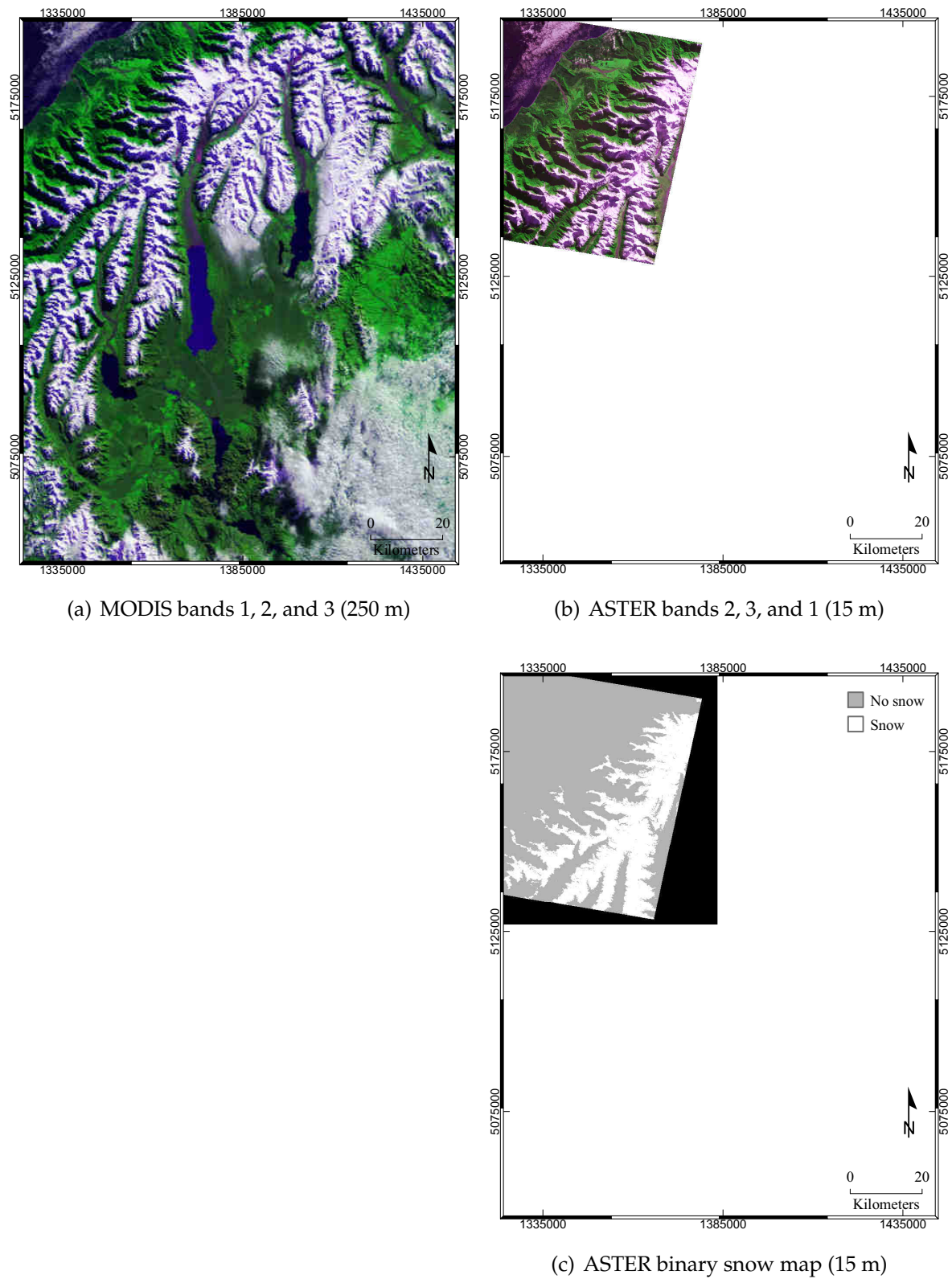
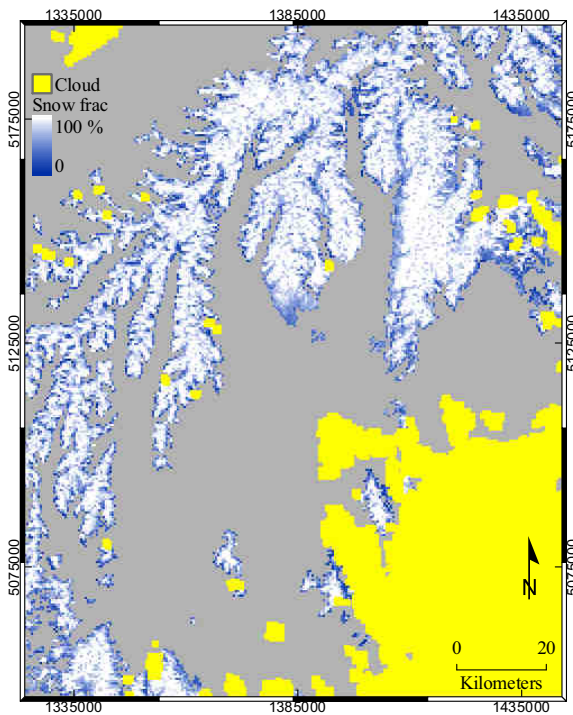
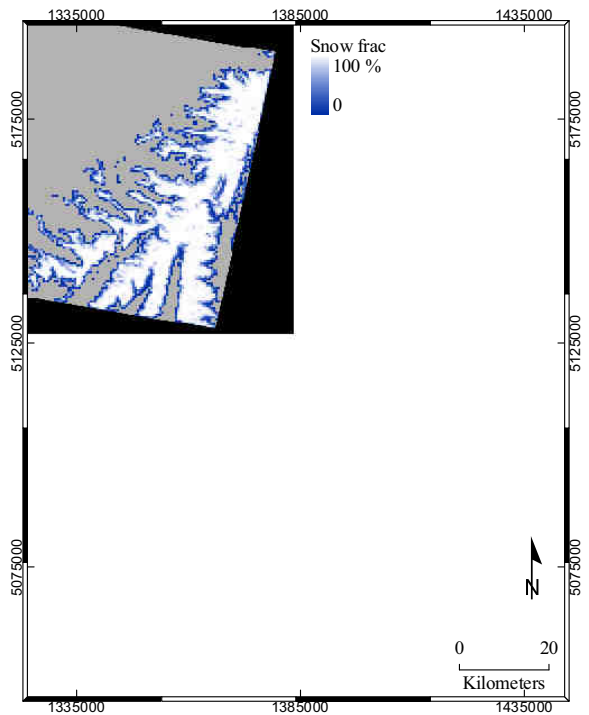


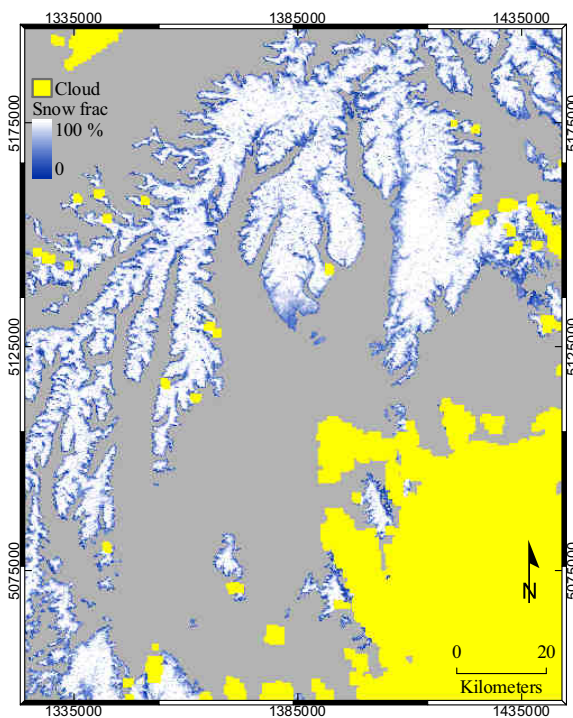
Figure F.4 Snow maps on 16 May 2006, 22:35 GMT.



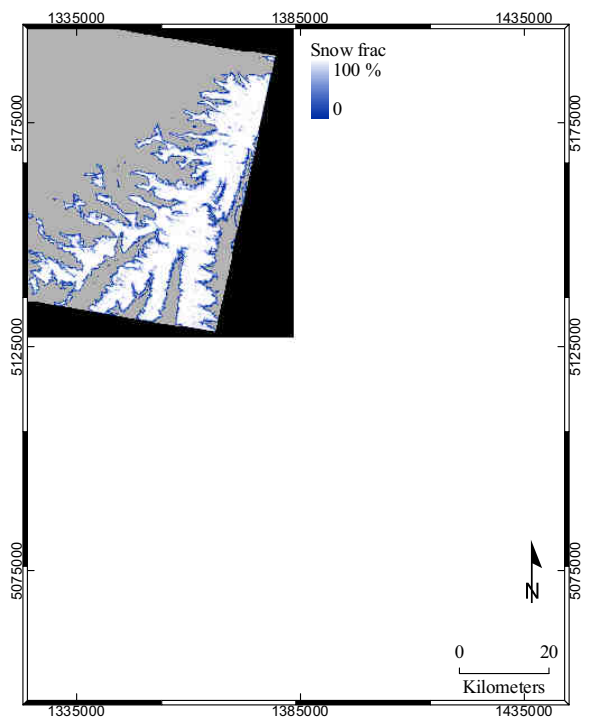
(d) MODIS fractional snow cover (500 m)



(e) ASTER fractional snow cover (500 m)



(f) MODIS fractional snow cover (250 m)



(g) ASTER fractional snow cover (250 m)

Figure F.4 (continued)

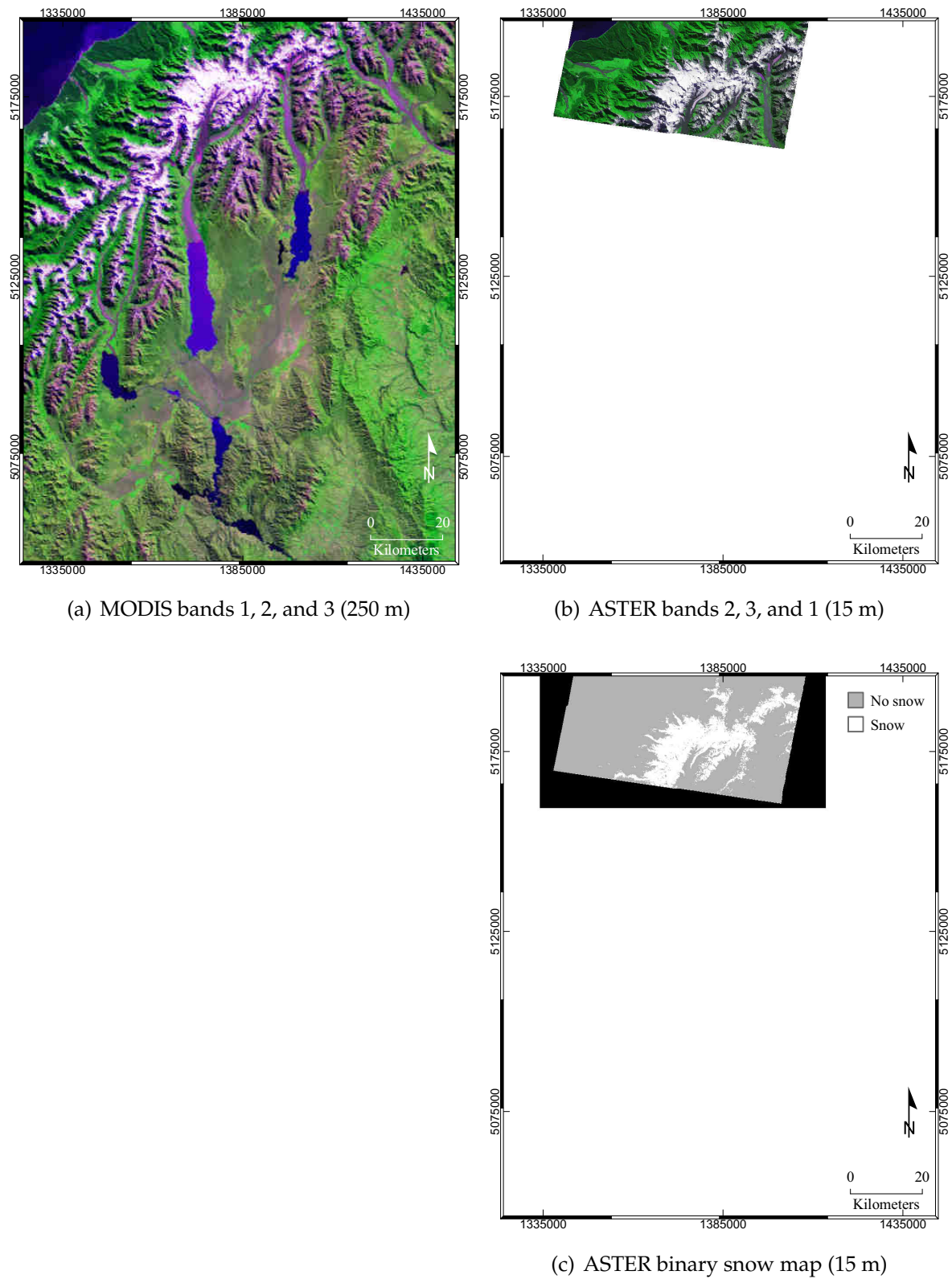
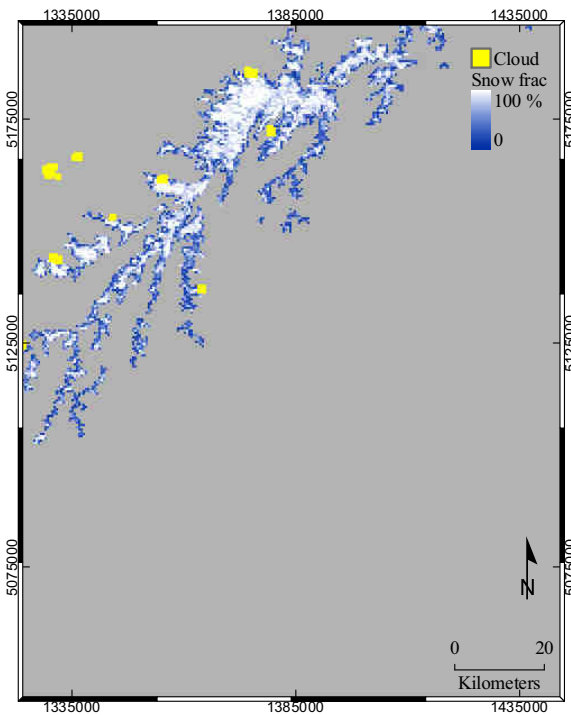
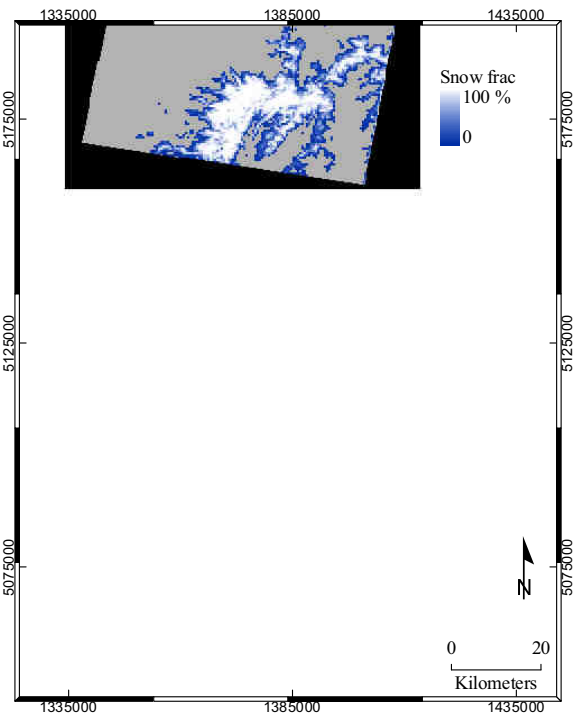


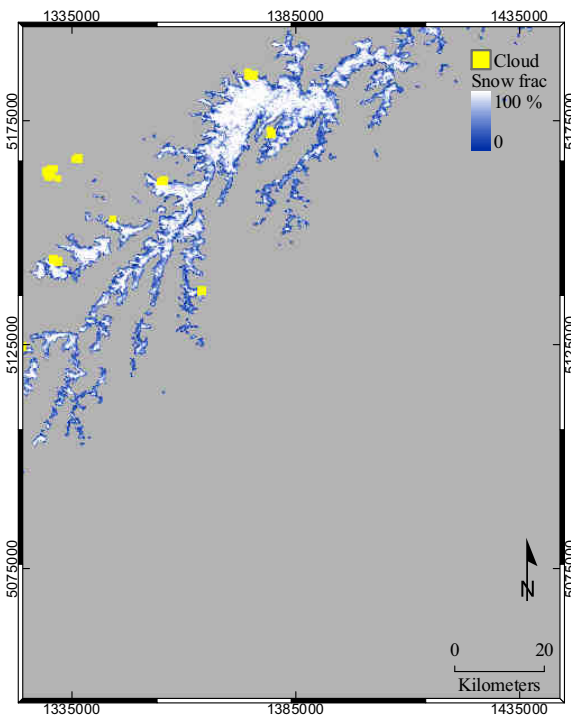
Figure F.5 Snow maps on 7 April 2001, 22:50 GMT.



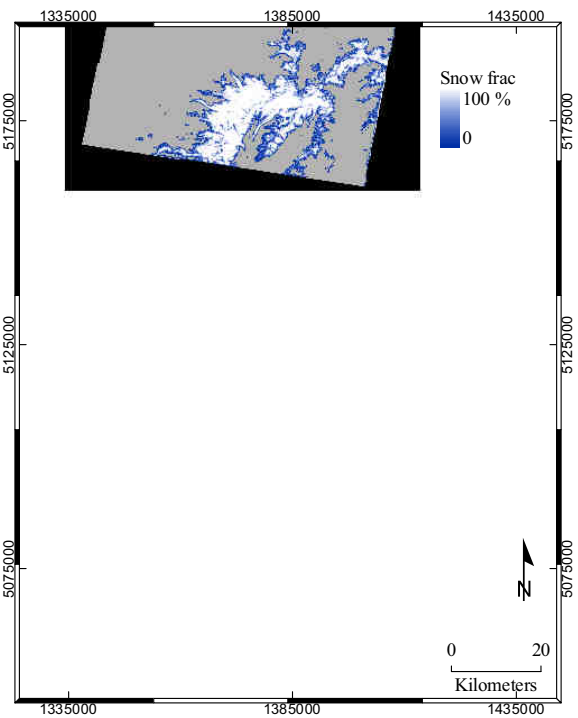
(d) MODIS fractional snow cover (500 m)



(e) ASTER fractional snow cover (500 m)

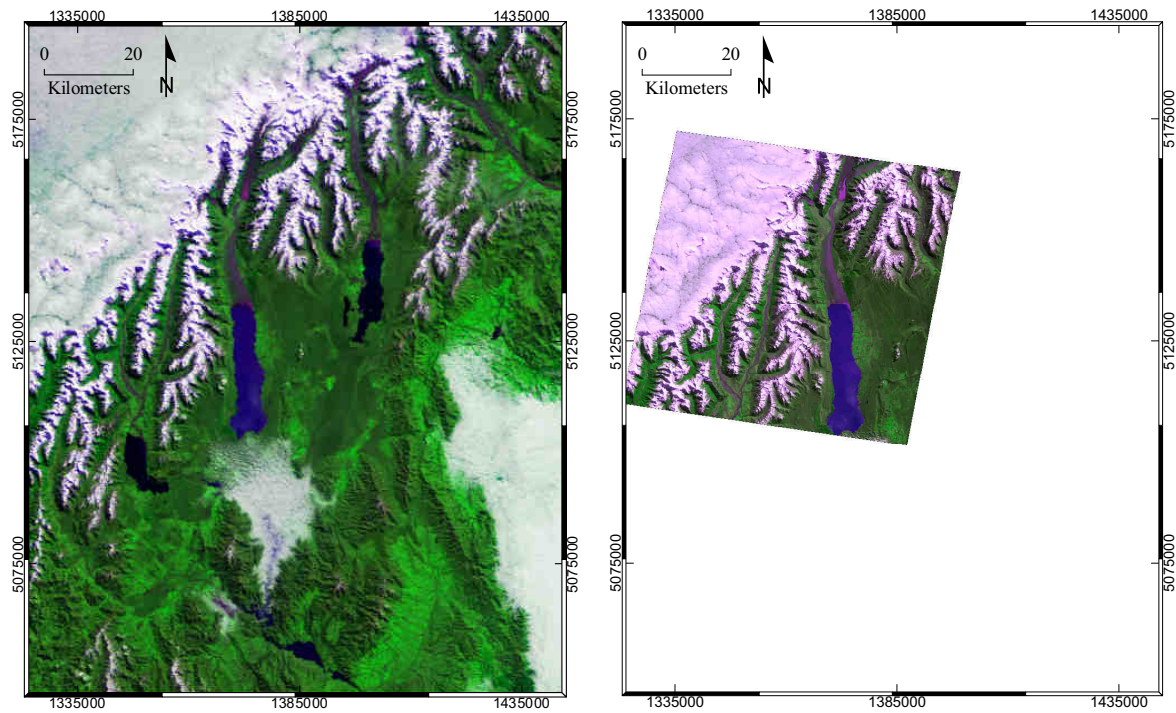


(f) MODIS fractional snow cover (250 m)



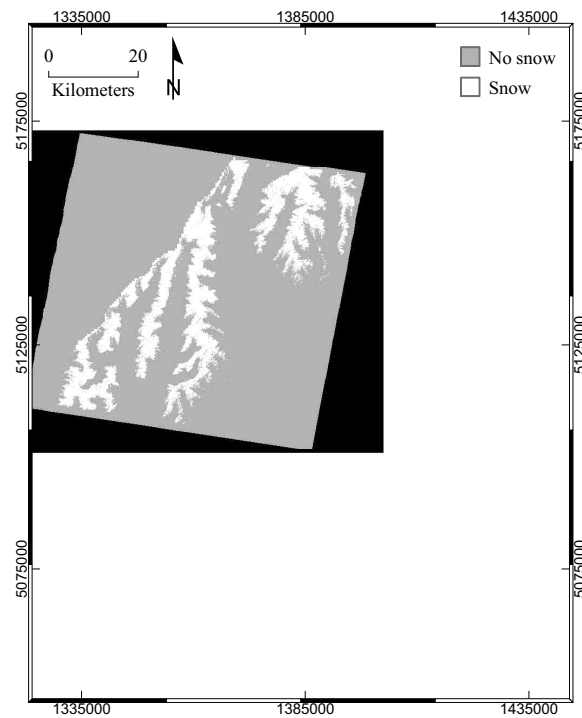
(g) ASTER fractional snow cover (250 m)

Figure F.5 (continued)



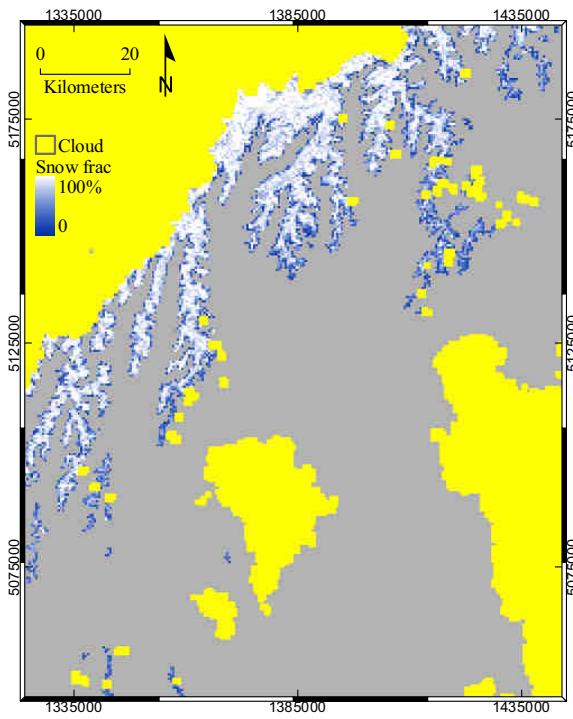
(a) MODIS bands 1, 2, and 3 (250 m)

(b) ASTER bands 2, 3, and 1 (15 m)

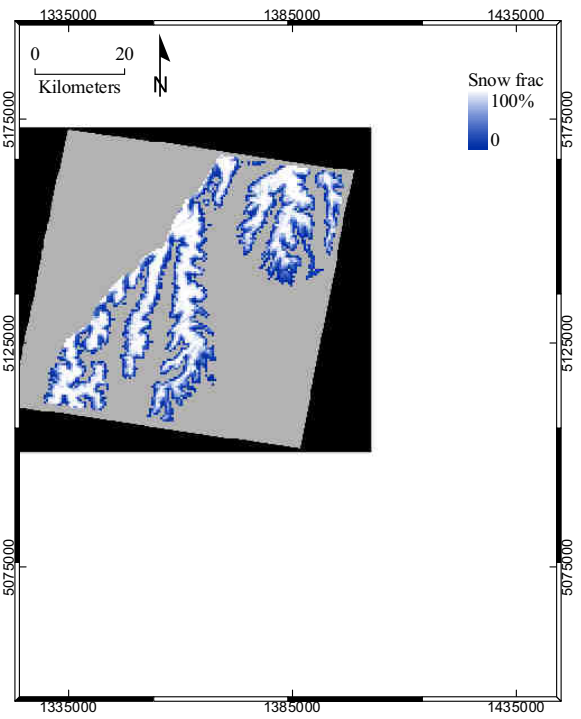


(c) ASTER binary snow map (15 m)

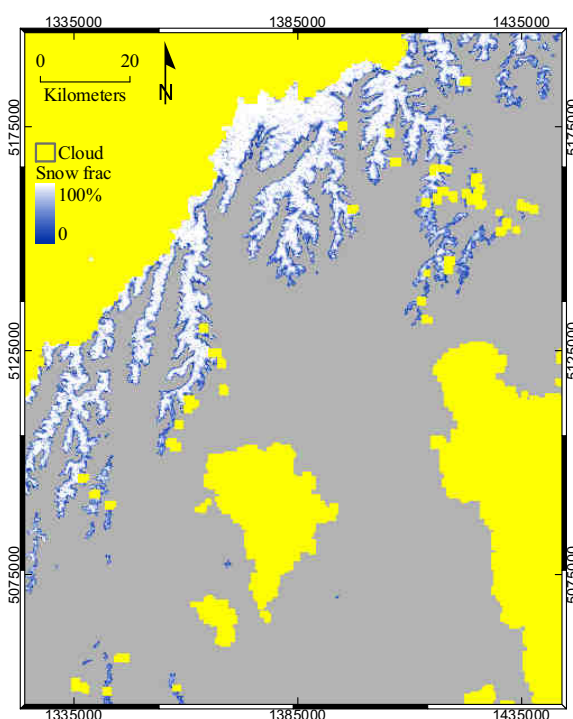
Figure F.6 Snow maps on 9 September 2005, 22:40 GMT.



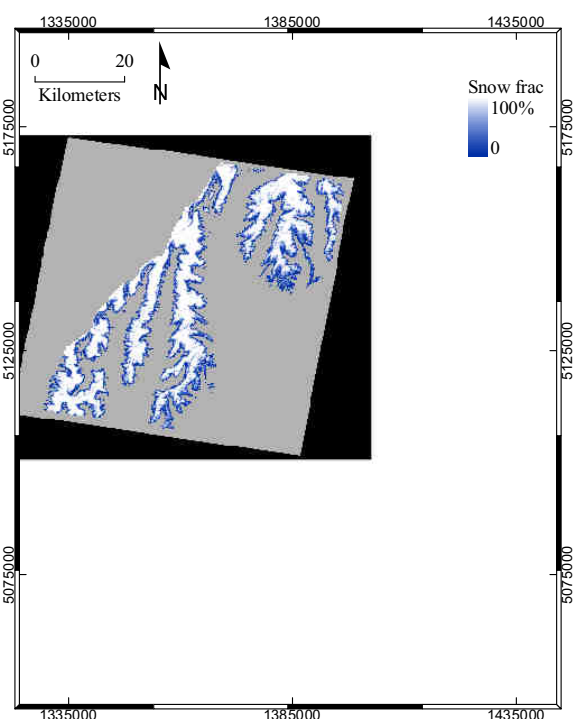
(d) MODIS fractional snow cover (500 m)



(e) ASTER fractional snow cover (500 m)



(f) MODIS fractional snow cover (250 m)



(g) ASTER fractional snow cover (250 m)

Figure F.6 (continued)

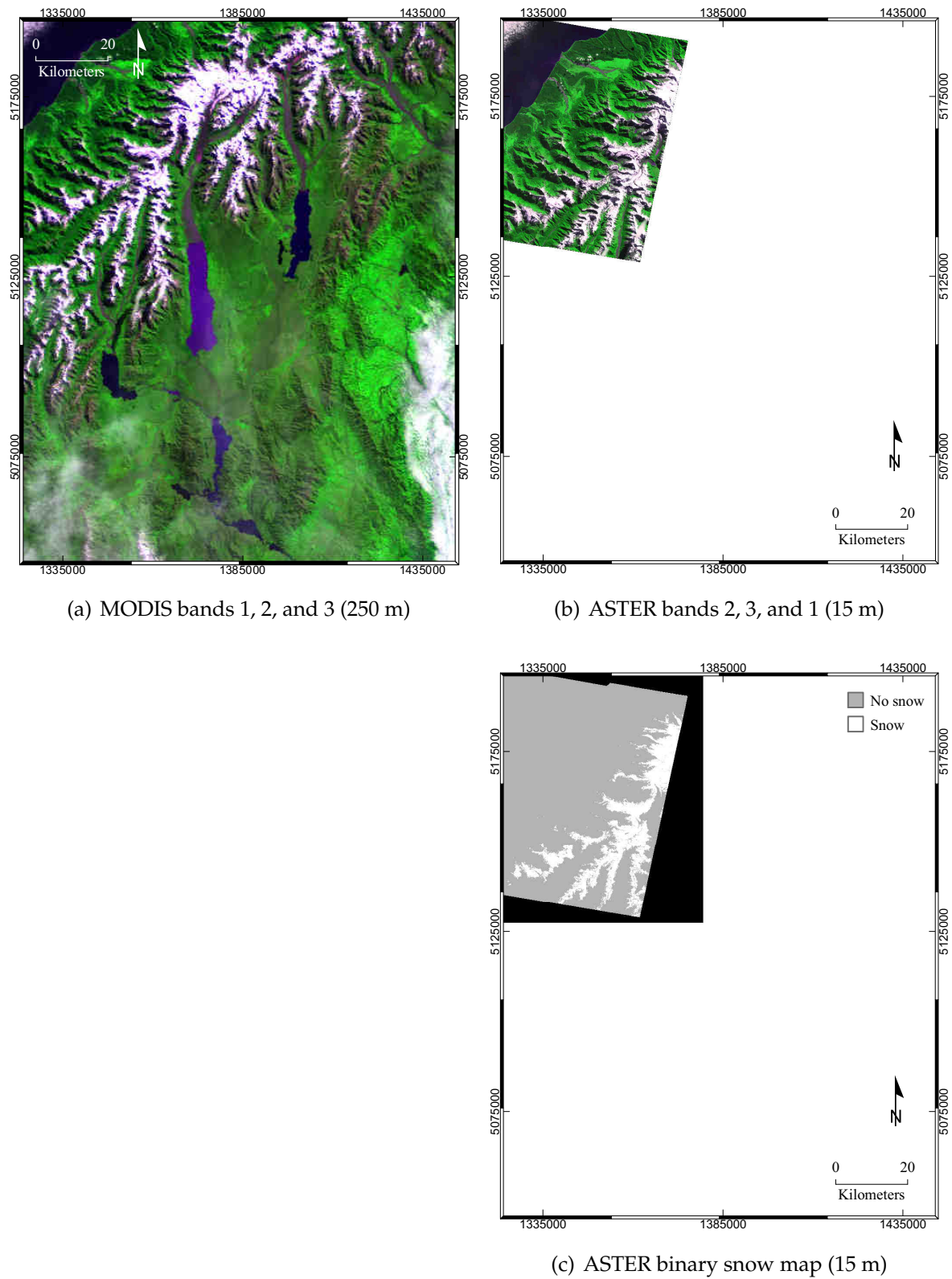
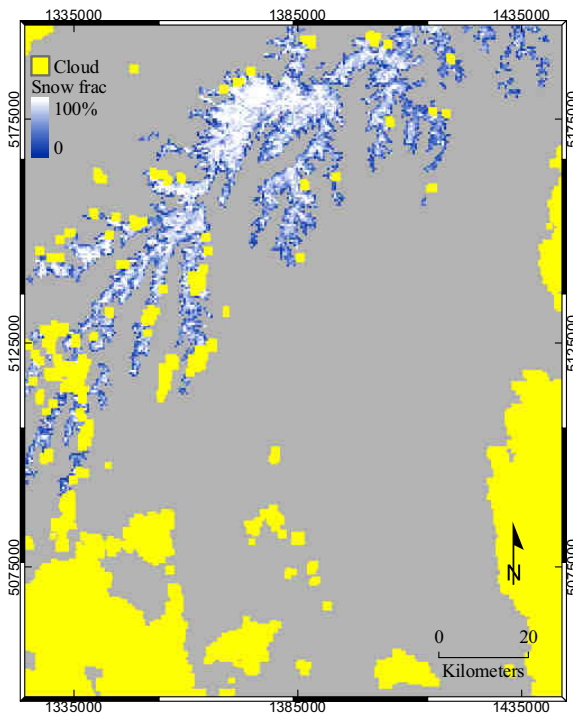
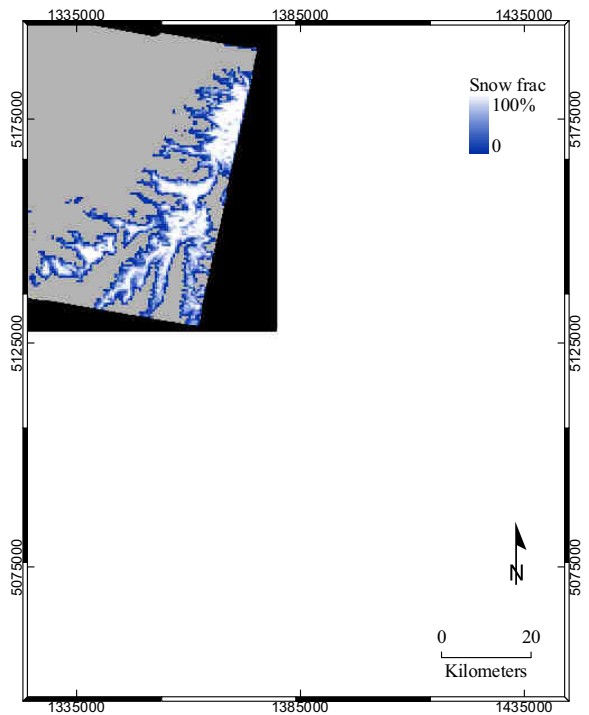


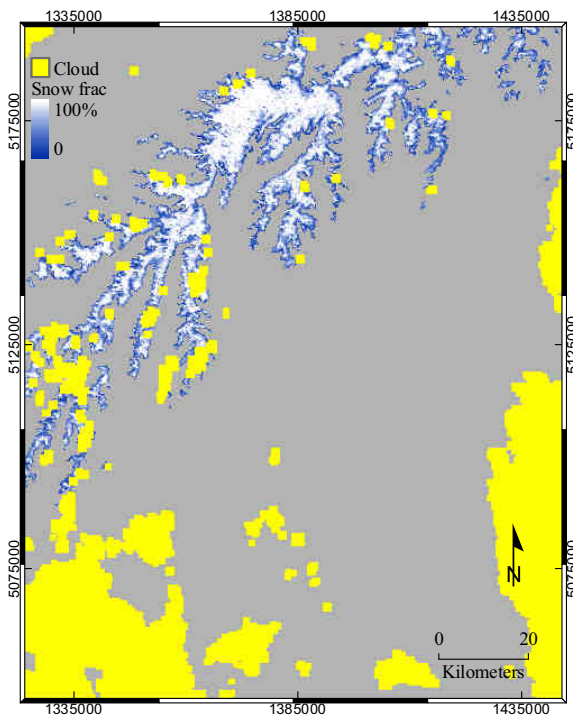
Figure F.7 Snow maps on 3 April 2002, 22:35 GMT.



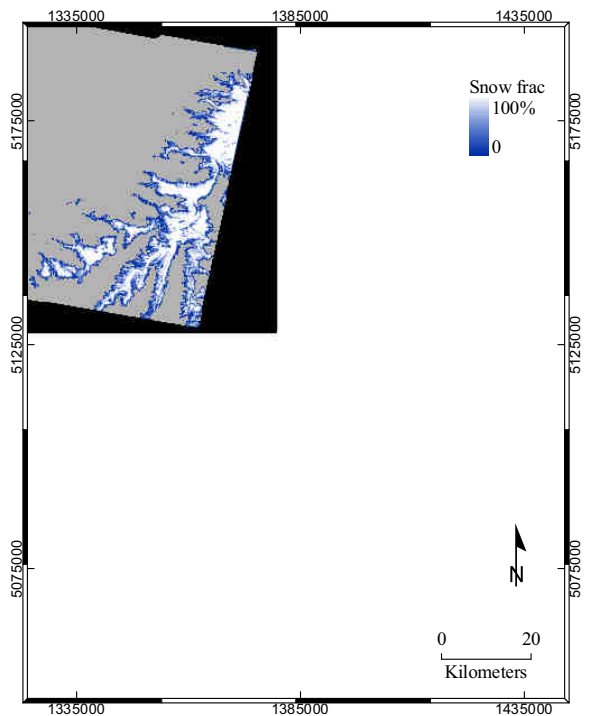
(d) MODIS fractional snow cover (500 m)



(e) ASTER fractional snow cover (500 m)



(f) MODIS fractional snow cover (250 m)



(g) ASTER fractional snow cover (250 m)

Figure F.7 (continued)

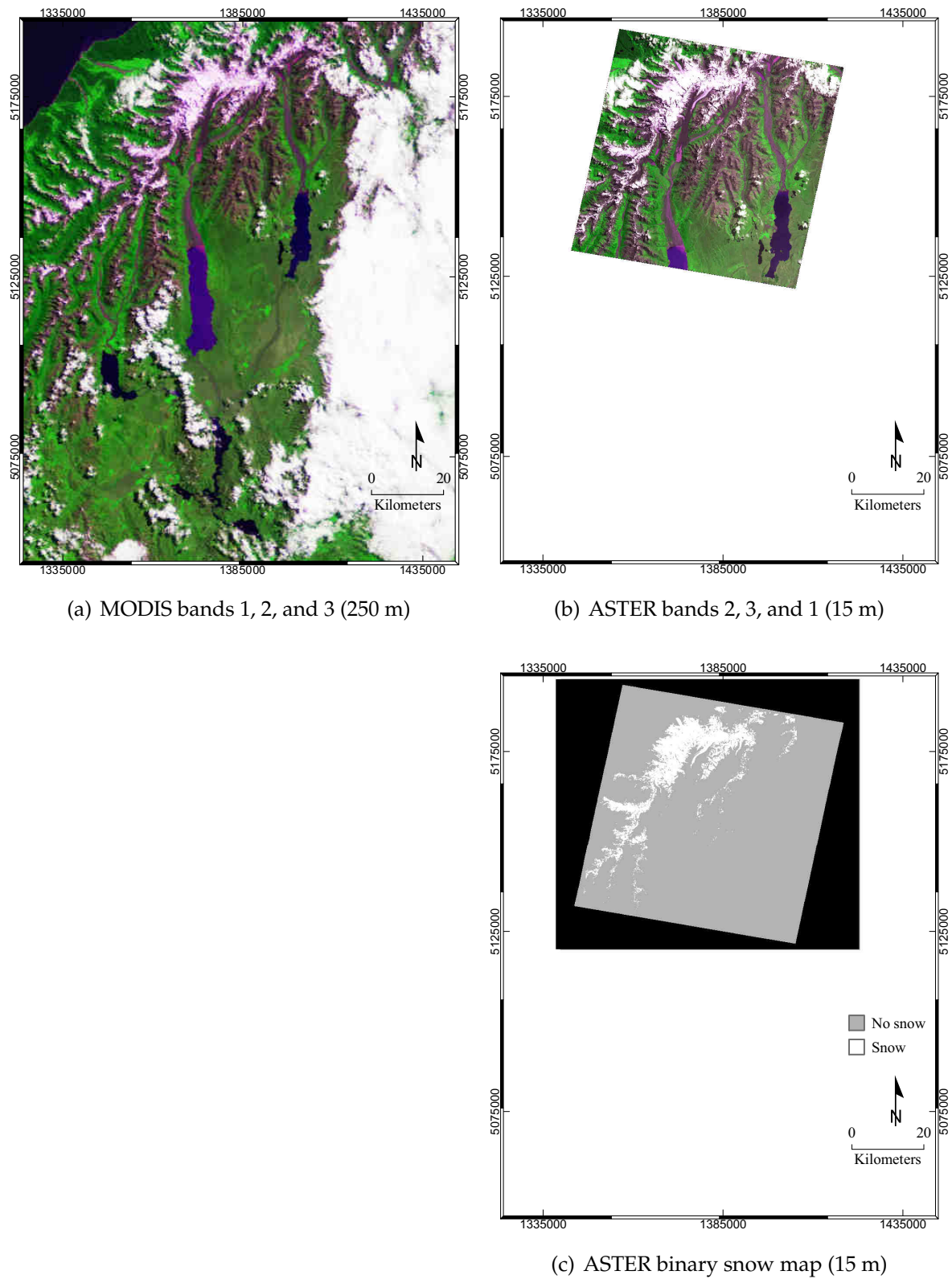
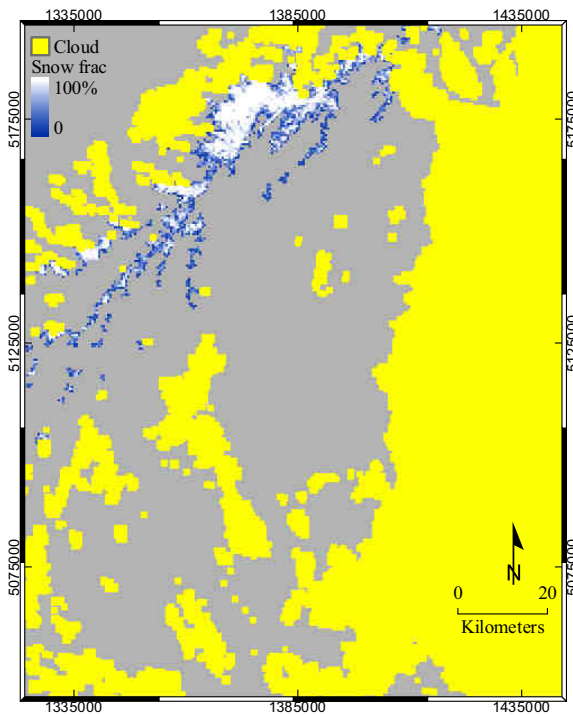
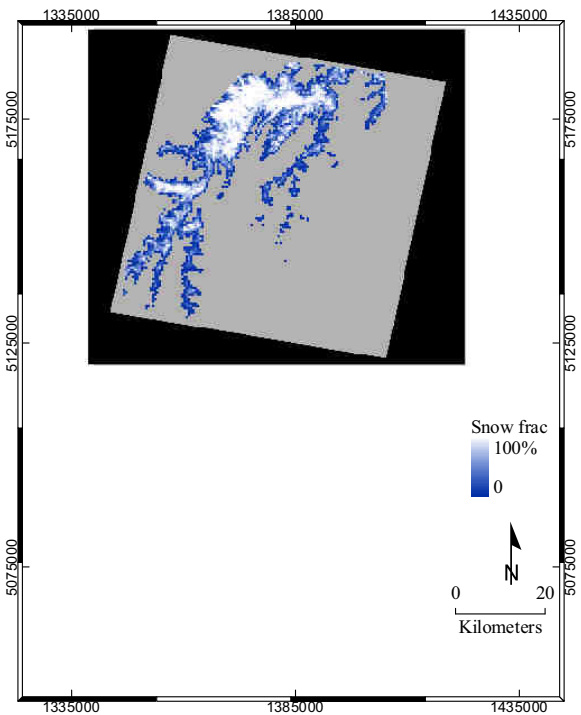


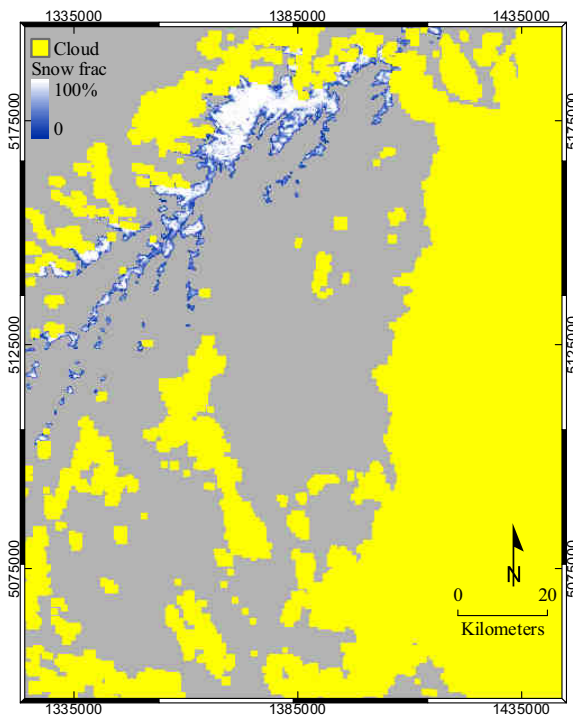
Figure F.8 Snow maps on 24 January 2006, 22:35 GMT.



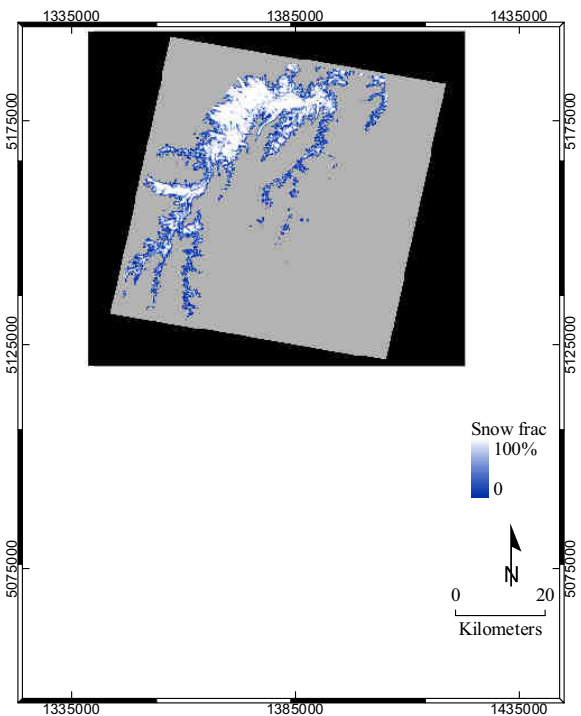
(d) MODIS fractional snow cover (500 m)



(e) ASTER fractional snow cover (500 m)



(f) MODIS fractional snow cover (250 m)



(g) ASTER fractional snow cover (250 m)

Figure F.8 (continued)

Appendix G

Note about the recession law

G.1 The Snowmelt Runoff Model (SRM) and the recession law

In order to simulate streamflow, SRM relies on a single recession law which aims at describing the falling limb of the hydrograph (Figure G.1). It assumes that, in the absence of supply, the discharge Q follows an exponential decrease characterized by the recession coefficient k and the geometric progression (Martinec, 1975)

$$k = \frac{Q_{n+1}}{Q_n}, \quad (\text{G.1})$$

where n is the index corresponding to the time step (e.g., days). Assuming that k is constant yields a recurrence relation referred to as the *recession law* which can be written as

$$Q_n = Q_0 k^n. \quad (\text{G.2})$$

The streamflow is formed by the superposition of separate recession events (Figure G.1). Two comprehensive reviews (Hall, 1968; Tallaksen, 1995) provide substantial detail about the analysis of runoff recession, including its historical origins and physical implications. The above relationship [Equation (G.2)] is simply a discretization of one of the recession laws established by Boussinesq (1904), who linearized the physically-based differential equations that govern the groundwater flow of a single source (Boussinesq, 1877), by making simplifying assumptions with regard to the aquifer (Tallaksen, 1995).

Apart from general restrictions about the homogeneity, uniformity, isotropy, and specific boundary conditions of the system under consideration, the main

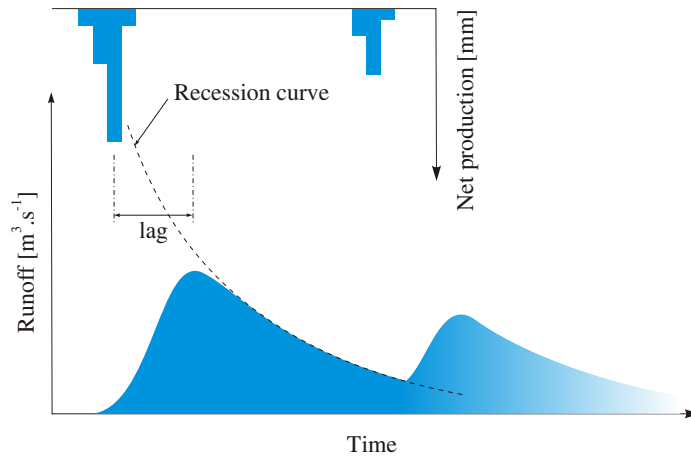


Figure G.1 The basin hydrograph, recession, and lag.

assumptions that permit the linearization of the non-linear differential equations (Equations (2) & (3), pg. 14 in [Boussinesq, 1904](#)) are that the height difference between the ground-water level and the stream must be negligible compared to the depth of the groundwater itself, and that the vertical component of the flow can be ignored. Thus, the linearization is generally valid only for a relatively flat terrain and in periods of drought. In this case, the differential equation governing the height h of the ground-water level simplifies to the diffusion equation

$$\mu \frac{\partial h}{\partial t} = C \nabla^2 h, \quad (\text{G.3})$$

where C is a given function of the position \vec{r} . Equation G.3 permitted an analogy to be drawn with the process of heat transfer, for which [Fourier \(1822\)](#) provided a solution. Under the assumption that the dependence of $h(t, \vec{r})$ to the variables time t and position \vec{r} can be separated [i.e., $h(t, \vec{r}) = X(\vec{r})T(t)$], it can be deduced that h is proportional to $e^{-\alpha t}$, and thus is the discharge Q ([Boussinesq, 1904](#)):

$$Q(t) = Q_0 e^{-\alpha t}, \quad (\text{G.4})$$

where α is the recession constant¹ and Q_0 is the initial discharge. The latter can be calculated using the law of conservation of mass to balance the net production (i.e., the water available for runoff) and the discharge integrated over an infinite time. This exponential decay proved its relevance in a successful application by [Maillet \(1905\)](#). Plotting $\log(Q_{t+\Delta t})$ versus $\log(Q_t)$ of the observed hydrograph for an arbitrary

¹From the French *coefficient de tarissement* suggested by [Boussinesq \(1904\)](#).

time difference Δt (e.g., 1 day) allows empirical determination of the recession coefficient. If the linearization assumptions are valid, such a plot should reveal a linear relationship of slope 1 and intercept $-\alpha\Delta t$ (de Zeeuw, 1973).

G.2 The “reservoir” conceptualization of the recession

From Equation G.4 it can be shown that in the absence of production, Q satisfies the following linear first-order ordinary differential equation:

$$\frac{dQ}{dt} + \alpha Q = 0. \quad (\text{G.5})$$

It can be conceptualized practically by a cylindrical reservoir of diameter D that is drained through a capillary tube of length L and diameter d , while assuming that all the resistance to the flow is concentrated in the capillary pipe as illustrated in Figure G.2 (Kraijenhoff van de Leur, 1973). According to Poiseuille’s law that describes the laminar flow in a capillary pipe, the field of velocity of the fluid at the outlet of the pipe obeys a radial quadratic law given by

$$v(r, \theta) = \frac{d^2 \rho g h}{16 \eta L} \left(1 - \frac{4r^2}{d^2} \right), \quad (\text{G.6})$$

where ρ is the density of water, g is the acceleration due to gravity, and η is the dynamic viscosity of water. Hence,

$$\begin{aligned} Q &= \int_0^{\frac{d}{2}} \int_0^{2\pi} v(r, \theta) r dr d\theta \\ &= \frac{\rho g h \pi d^4}{128 \eta L}. \end{aligned} \quad (\text{G.7})$$

By calling S the total storage of the reservoir,

$$h = \frac{4S}{\pi D^2}. \quad (\text{G.8})$$

Finally, substituting Equation (G.8) into Equation (G.7) yields

$$Q = \underbrace{\frac{\rho g d^4}{32 \eta L D^2}}_{\alpha} S. \quad (\text{G.9})$$

On the other hand, it is evident that the system’s operation is governed by the equation of conservation of mass in the reservoir:

$$Q = -\frac{dS}{dt} + \Pi, \quad (\text{G.10})$$

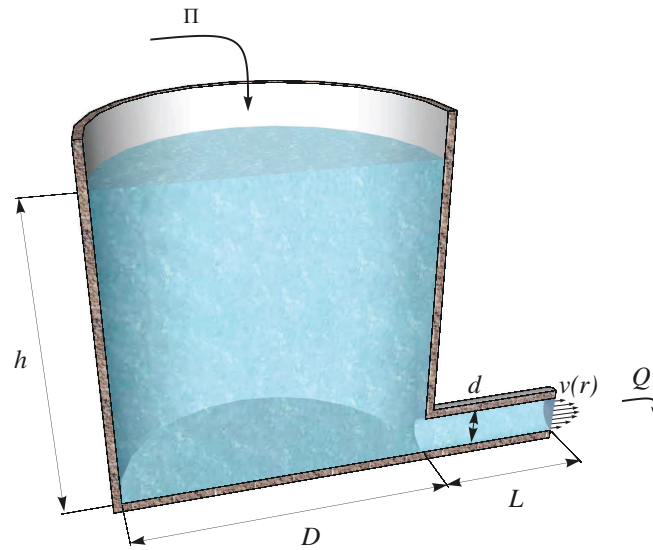


Figure G.2 Conceptualisation of Equation G.5 by a reservoir.

where Π is the production of water by the basin. Combining Equations (G.9) & (G.10) yields

$$Q + \frac{1}{\alpha} \frac{dQ}{dt} = \Pi. \quad (\text{G.11})$$

Consequently, in the absence of production (i.e., $\Pi = 0$), Equation G.11 is directly identifiable to Equation (G.5) with α being the characteristic time of the system. Thus, under the assumption made by Boussinesq (1904), the drainage of an aquifer can be simply conceptualized by the drainage of a reservoir of constant section through a capillary pipe that would allow a laminar regime of the flow (i.e., Reynolds number $Re < 2000$). The proportionality between the discharge Q and the storage S in the reservoir makes this conceptualization referred to as the *model of the linear reservoir*.

G.3 Non linear systems

Relatively strict assumptions are needed to linearize the equations governing the groundwater flow, and to satisfy the simple conceptualization by a linear reservoir [Equation (G.9)]. However, nonlinearities remain in real systems and such a simplification can hardly be met entirely. Boussinesq (1904) acknowledged that the linear response could not always approach experimental hydrographs. To reflect

better reality, he proposed a solution to the non-linear physically-based equations for a stream that would sit on the upper boundary of the ground's impermeable layer. [Boussinesq](#) found that, in such a case, the discharge would obey a recession of the form

$$Q(t) = \frac{Q_0}{1 - kt^2}, \quad (\text{G.12})$$

where k is the recession constant ([Hall, 1968](#)). This solution still relies on the assumption that the slope of the underlying impermeable layer is relatively small, as well as, as noted by [Hall \(1968\)](#), on the disputable assumptions that there is no recharge of the aquifer during the recession, and that the discharge originates from a single source.

From observation, [Maillet \(1903\)](#) suggested that the non linear response of the hydrograph of a source¹ could be modelled by Equation (G.12) augmented by a constant flow. In response, [Boussinesq \(1904\)](#) argued that the solution proposed by [Maillet](#) can be approached by the superposition principle applied to the linear theory. In other words, the non-linear response of a system can be the sum of the recessions of a number of linear sub-systems as shown in Equation (G.13). This was later confirmed by [Werner and Sundquist \(1951\)](#) in the case of artesian aquifers and it became the basis of hydrological models that represent complex systems by a succession of inter-connected linear reservoirs with different time characteristics ([Kraijenhoff van de Leur, 1973](#)):

$$Q(t) = \sum_{i=0}^n Q_{0,i} e^{-\alpha_i t}. \quad (\text{G.13})$$

It is evident that using an appropriate recession law is crucial in hydrological modelling, whether it is assumed that the system is linear or not. For instance, a widely used and accepted hydrological model such as TOPMODEL ([Beven and Kirkby, 1979](#)) was originally developed based on a non-linear reservoir.² [Beven and Kirkby \(1979\)](#) assumed that the flow could be approached by an exponential function of the storage. It yields a recession that follows a first-order hyperbolic function of time. This form departs from the physically-based solutions presented previously and was later criticised by [Ambroise et al. \(1996\)](#) for being not appropriate in some catchments. [Ambroise et al. \(1996\)](#) generalized the TOPMODEL approach to allow

¹Maillet studied the source of Cérilly for which he is supposed to have published the results in 1903. This work is mentioned in [Boussinesq \(1904\)](#), but a copy of the publication could not be found.

²Note that a non-linear reservoir is simply a conceptualisation similar to the linear reservoir but whose section is not constant.

use of the forms suggested in Equations (G.9) & (G.12), while permitting also more complex forms of recession, such as the power function decay of the discharge relatively to the storage (Wang *et al.*, 2006).

Other non linear relationships have been studied such as the one proposed by Coutagne (1948) and further used by Wittenberg (1999) to discriminate base flow from direct flow, or by Mishra *et al.* (2004) to model discharge in the upper Blue Nile river. Both considered that the discharge and the storage were related by

$$S = aQ^b, \quad (\text{G.14})$$

where a and b are the two parameters of the recession. Substituting Equation (G.14) into the flow equation [Equation (G.10)] yields that in the absence of recharge

$$\frac{dQ}{dt} + \frac{1}{ab}Q^{2-b} = 0. \quad (\text{G.15})$$

The integration of Equation (G.15) (Wittenberg, 1999) yields

$$Q(t) = Q_0 \left[1 + t \frac{(1-b)Q_0^{(1-b)}}{ab} \right]^{\frac{1}{(b-1)}} \quad (\text{G.16})$$

Again, the parameters a and b can be found from analysis of the experimental hydrograph.

G.4 SRM and the linear assumption

In a gauged basin, this recession phenomenon can be studied from the hydrograph by plotting $\log(Q_{n+1})$ versus $\log(Q_n)$. Such a scatter plot accounts for all discharge values, most being affected by new precipitations, snowmelt, or ice melt. The points that depict the true recession tend to form the lower envelope of the scatter plot (i.e., the smallest Q_{n+1} for a given Q_n). Most often, the linearization assumptions of Boussinesq (1904) are not fulfilled and the plot exhibits a substantial departure from that expected from a linear reservoir. For example, Figure G.3 shows, for each of the three catchments considered in this thesis, the discharge observed at day $n + 1$ versus the discharge observed the previous day n , over the hydrological years 2000–2006 displayed in a logarithmic scale. Despite the noise that can be attributed to the indirect method for gauging the catchment's discharge¹, the lower envelopes are approximately linear but not parallel to the 1:1 ratio line. It reveals a non-linear

¹The discharge is obtained by monitoring lake levels and water transfers between the lakes.

behaviour of the catchments, at least for the range of inflows considered. It also indicates that the recession coefficient k is not constant, but rather depends on the discharge itself.

Such variable recession factors are expected (Martinec, 1975; Martinec *et al.*, 2005) and SRM allows for a power law parameterization as follows

$$k_{n+1} = xQ_n^{-y}, \quad (\text{G.17})$$

where x , and y are constants retrieved from the linear fitting to the lower envelop of the hydrograph plotted in Figure G.3. In this thesis, a robust linear regression was fitted to the scatter plot for each catchment (i.e., a weighted linear regression that gives lower weight to possible outliers). The lower bound of the 99% confidence interval of the linear fit (Figure G.3) provided preliminary values of x and y . The final values were refined during the calibration of SRM until the modelled recession matched the observed values reasonably well. It must be noted that, in this case, the recurrence becomes

$$Q_n = x^{\sum_{i=0}^{n-1} (1-y)^i} Q_0^{(1-y)^n} \quad (\text{G.18})$$

$$= x^{\frac{1}{y}} \left[\frac{Q_0}{x^{\frac{1}{y}}} \right]^{(1-y)^n}. \quad (\text{G.19})$$

A proof of this relationship is given as follows.

Proposition G.4.1. $\frac{Q_{n+1}}{Q_n} = xQ_n^{-y} \Rightarrow Q_n = x^{\frac{1}{y}} \left[\frac{Q_0}{x^{\frac{1}{y}}} \right]^{(1-y)^n}$

Proof. This is equivalent to proving that $x^{\sum_{i=0}^{n-1} (1-y)^i} Q_0^{(1-y)^n} = x^{\frac{1}{y}} \left[\frac{Q_0}{x^{\frac{1}{y}}} \right]^{(1-y)^n}$. It corresponds to proving that the statement $P(n) : \frac{1}{y} [1 - (1-y)^n] = \sum_{i=0}^{n-1} (1-y)^i$ is true for all n using mathematical induction.

Basis: $P(1)$ is clearly true.

Inductive step: If $P(n)$ holds, then:

$$\begin{aligned} \sum_{i=0}^n (1-y)^i &= \sum_{i=0}^{n-1} (1-y)^i + (1-y)^n \\ &= \frac{1}{y} [1 - (1-y)^n] + (1-y)^n \\ &= \frac{1}{y} [1 - (1-y)^{n+1}] \end{aligned} \quad (\text{G.20})$$

Therefore $P(n+1)$ is true. \square

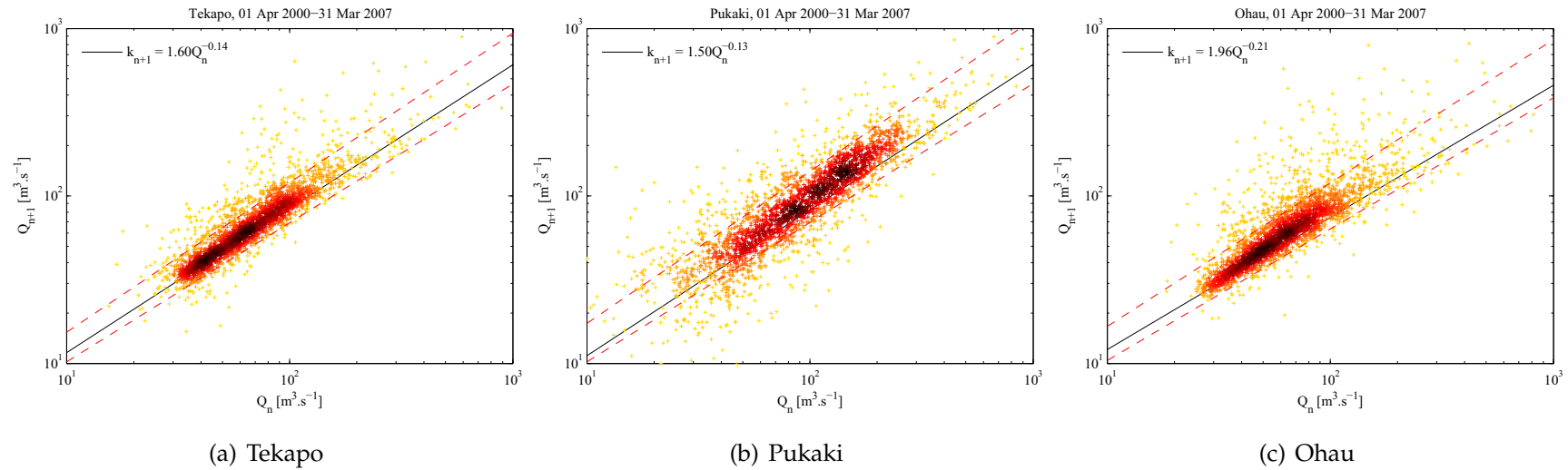


Figure G.3 Recession analysis: scatter plot of Q_{n+1} vs. Q_n for the hydrological years 2000–2006. Plots are drawn in logarithmic scale and colour coded to depict the density of points. Red (gray) dotted lines represent the 99% confidence interval of a robust linear regression of the data. The black solid line corresponds to the calibrated recession coefficients of the catchments.

Two main issues arise from this parameterization. From Equation (G.19), $Q_n \xrightarrow{n \rightarrow \infty} x^{\frac{1}{y}}$. The recession model does not converge to null flow at infinite time, and thus it does not uphold the principle of conservation of mass. If $Q < x^{\frac{1}{y}}$, then $k > 1$ and the recession becomes invalid. Despite the fact that SRM bounds k within an acceptable range (i.e., $k < 1$), the choice of x and y can only satisfy the modelling within a limited range of discharge values and set artificially the minimum flow that can be simulated. Hence, care must be taken during the calibration of the two parameters for a specific catchment so that $x^{\frac{1}{y}}$ is smaller than the lowest flow to be expected. Figure G.4 shows an example of flow recessions based on the calibrated coefficients of each catchment. The horizontal asymptotes indicate the limit below which the flow cannot be modelled.

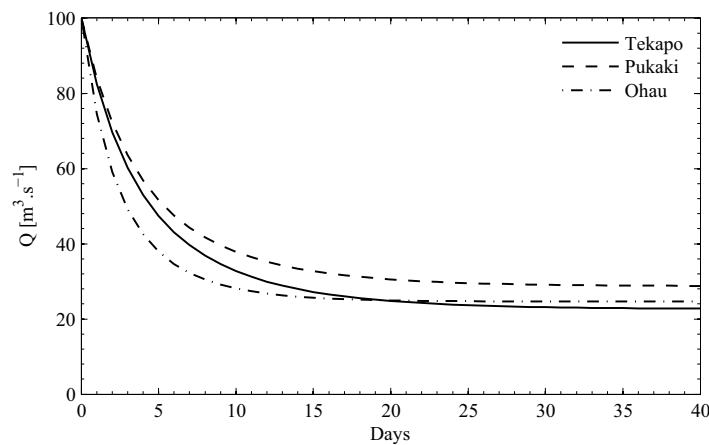


Figure G.4 Flow recessions after calibration of the non linear recession relationship. The non null horizontal asymptote must be lower than the minimum flow expected in each catchment.

The other main criticism that can be made of SRM is structural. As described in Section 8, the cornerstone of SRM is based on the assumption of a linear reservoir since the SRM formula [Equation (8.5)] relies on the convergence of the geometric series permitted by the constant recession factor. Martinec (1975) acknowledged that most catchments may exhibit nonlinearities in terms of flow recession (this clearly includes the ones of interest in this thesis) and thus implemented a variable recession coefficient. However, Martinec, as well as users of SRM, never mentioned that, in this case, the recurrence relationship [Equation (G.20)] does not permit a convergence that upholds the original formula. In other words, the model was designed using an assumption (i.e., the linear reservoir model) that was immediately con-

tradicted in practical applications. Nevertheless, only the recession coefficient was amended and the general formulation was retained. In theory, a new formulation should be established on the basis of the new recurrence relationship. However, finding an analytical solution of the infinite sum of the timely discharge under the assumption of non-linearity is complicated. In the case of the proposed recession relationship, this sum does not even converge, thus preventing any alternate formulation. It stresses an intrinsic and somewhat important flaw of SRM. It is beyond the scope of this thesis to address this issue and no attempt is conducted to modify the formulation of SRM to satisfy the model of flow recession. It is believed that, at least, this intrinsic flaw of SRM should be explained and clarified. This area potentially provides opportunities for further development of SRM.

Appendix H

Simulation results without long term storage

This appendix provides the simulated discharge results over the hydrological years 2000–2006, as well as the contribution of the stored water components (i.e., the seasonal and the short lived snow). The time series shows the simulations obtained from the optimal set of parameters determined in Section 8.4.

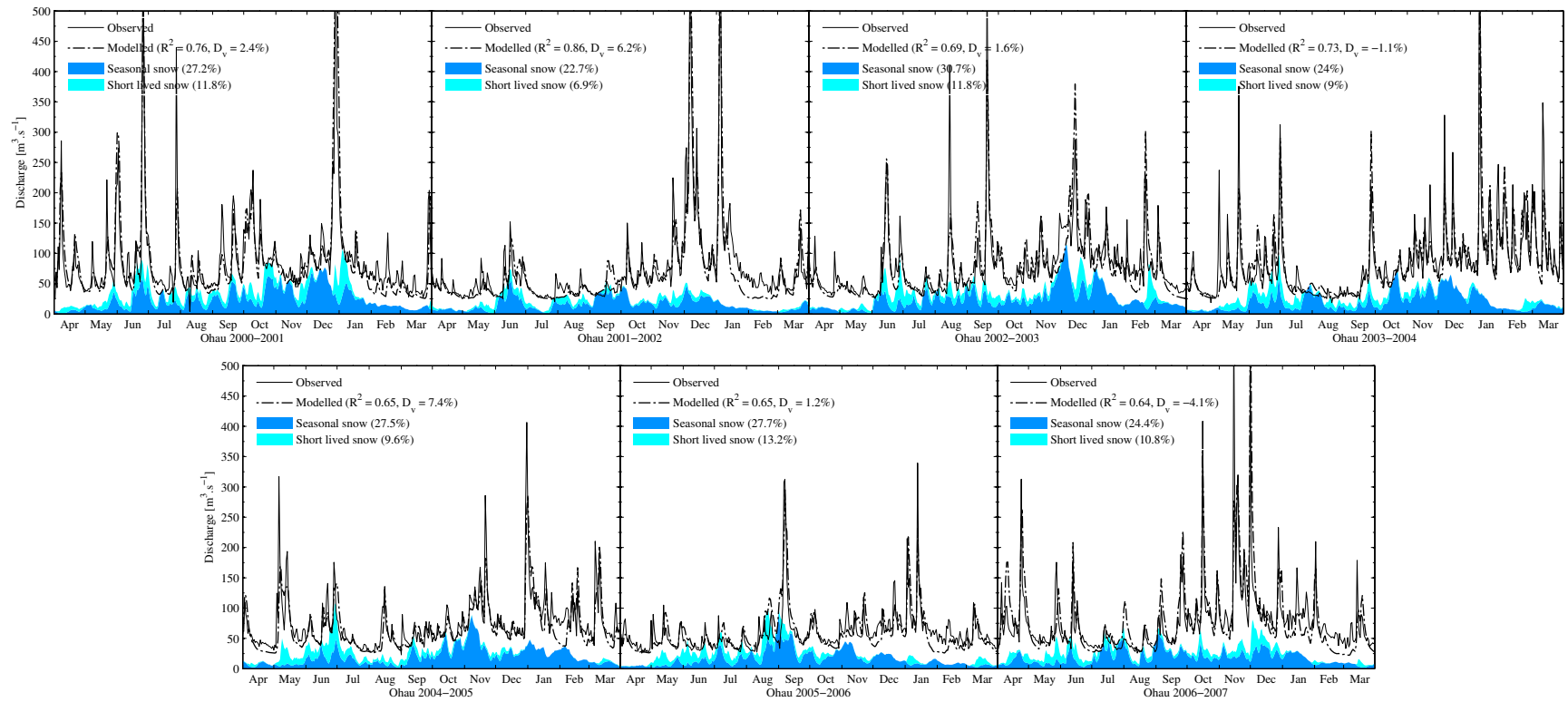


Figure H.1 Results of discharge simulation without long term storage in Ohau 2000–2007

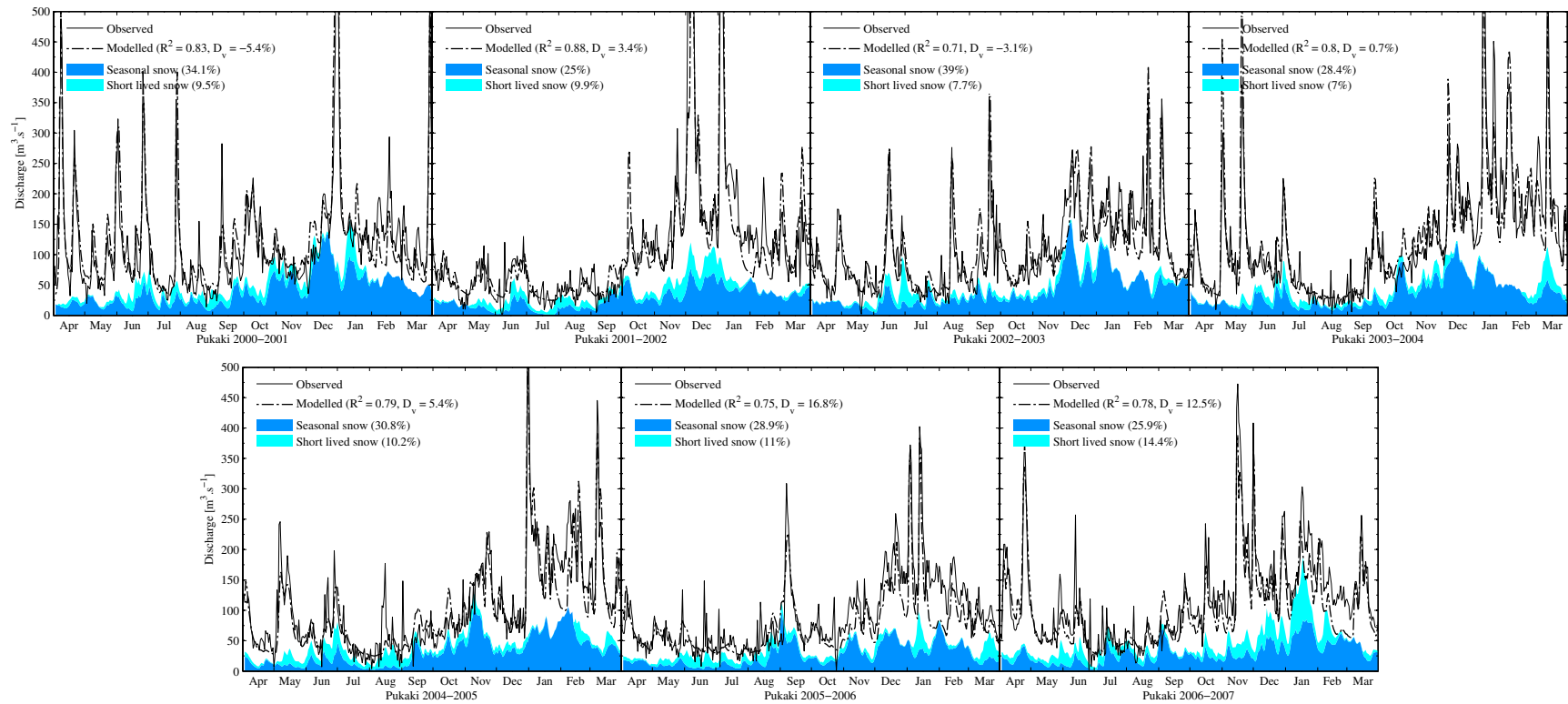


Figure H.2 Results of discharge simulation without long term storage in Pukaki 2000–2007

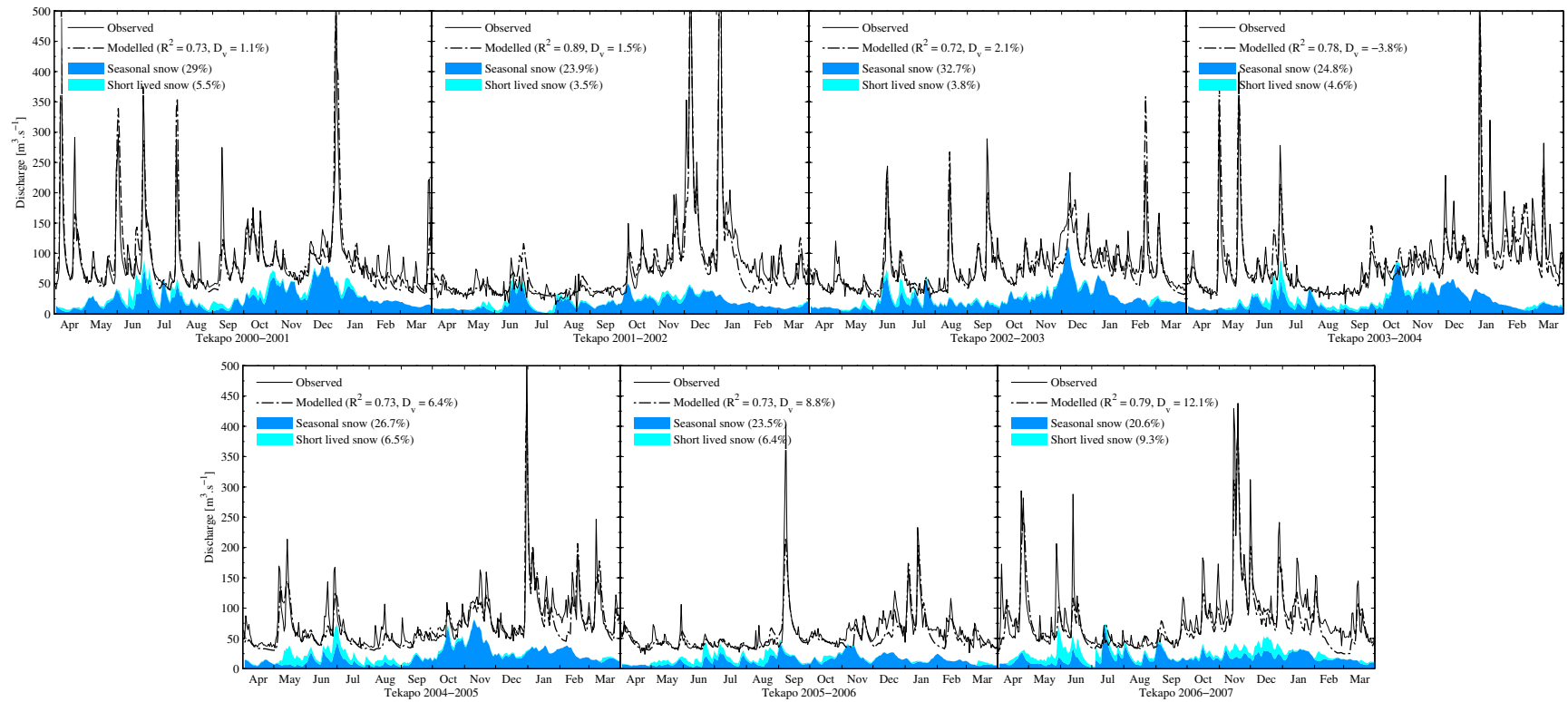


Figure H.3 Results of discharge simulation without long term storage in Tekapo 2000–2007

Appendix I

Simulation results with long term storage adjustment

This appendix provides the simulated discharge over the hydrological years 2000-2006, as well as the contribution of the stored water components (i.e., the seasonal snow, the short lived snow, and the long term storage). The time series corresponds to the simulation obtained from the optimal set of parameters determined in Section 8.4 with a manual adjustment of the snow runoff coefficient c_s in the ablation season to accommodate the deviation of the total runoff volume.

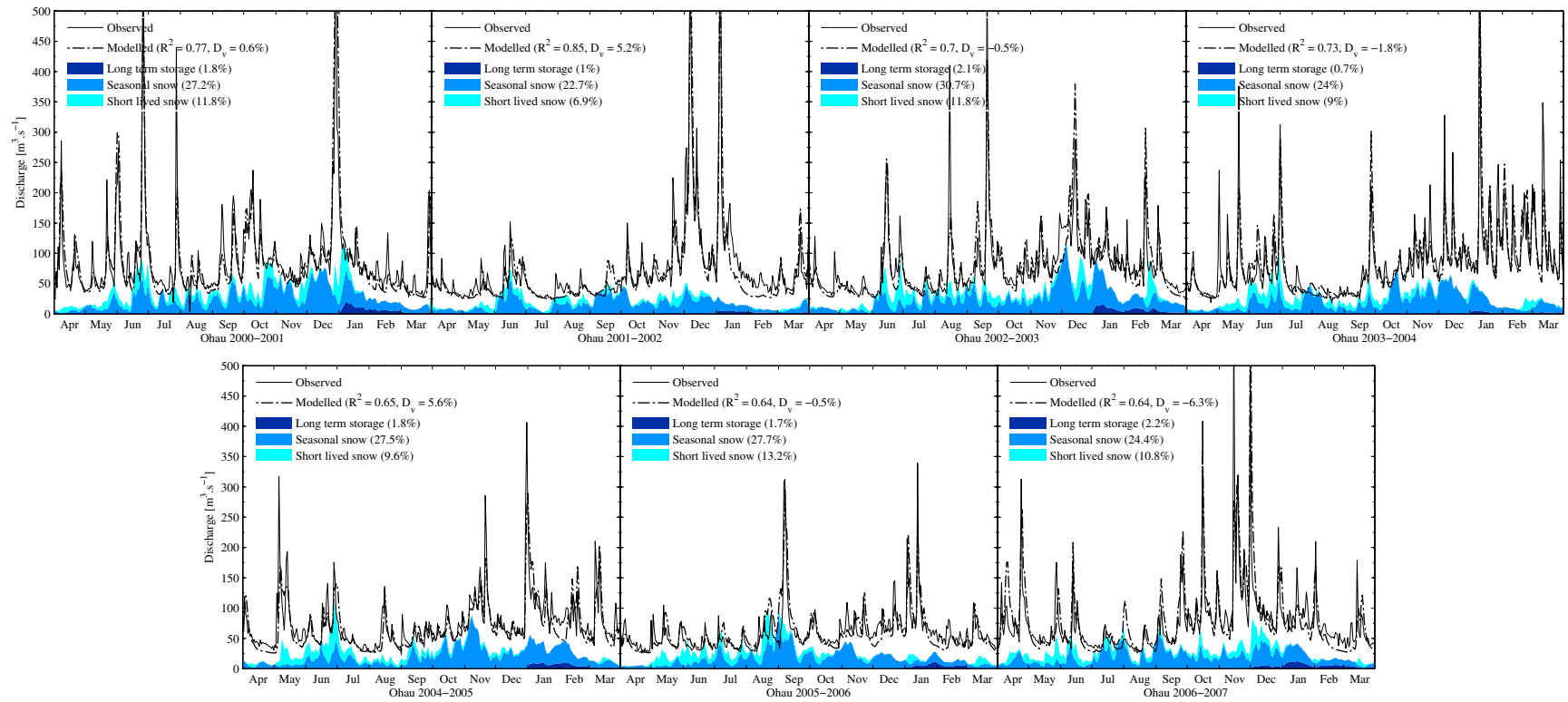


Figure I.1 Results of discharge simulation with long term storage adjustment in Ohau 2000–2007

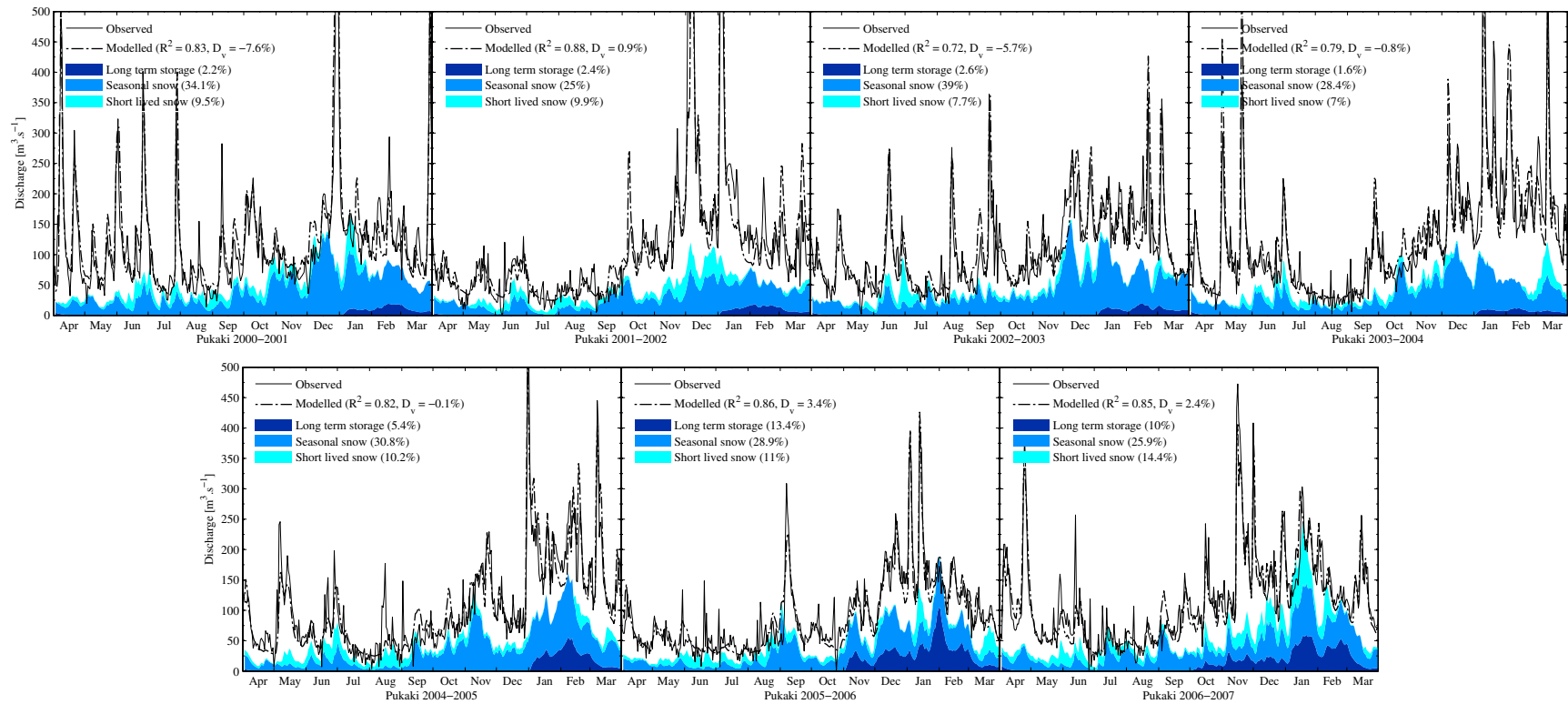


Figure I.2 Results of discharge simulation with long term storage adjustment in Pukaki 2000–2007

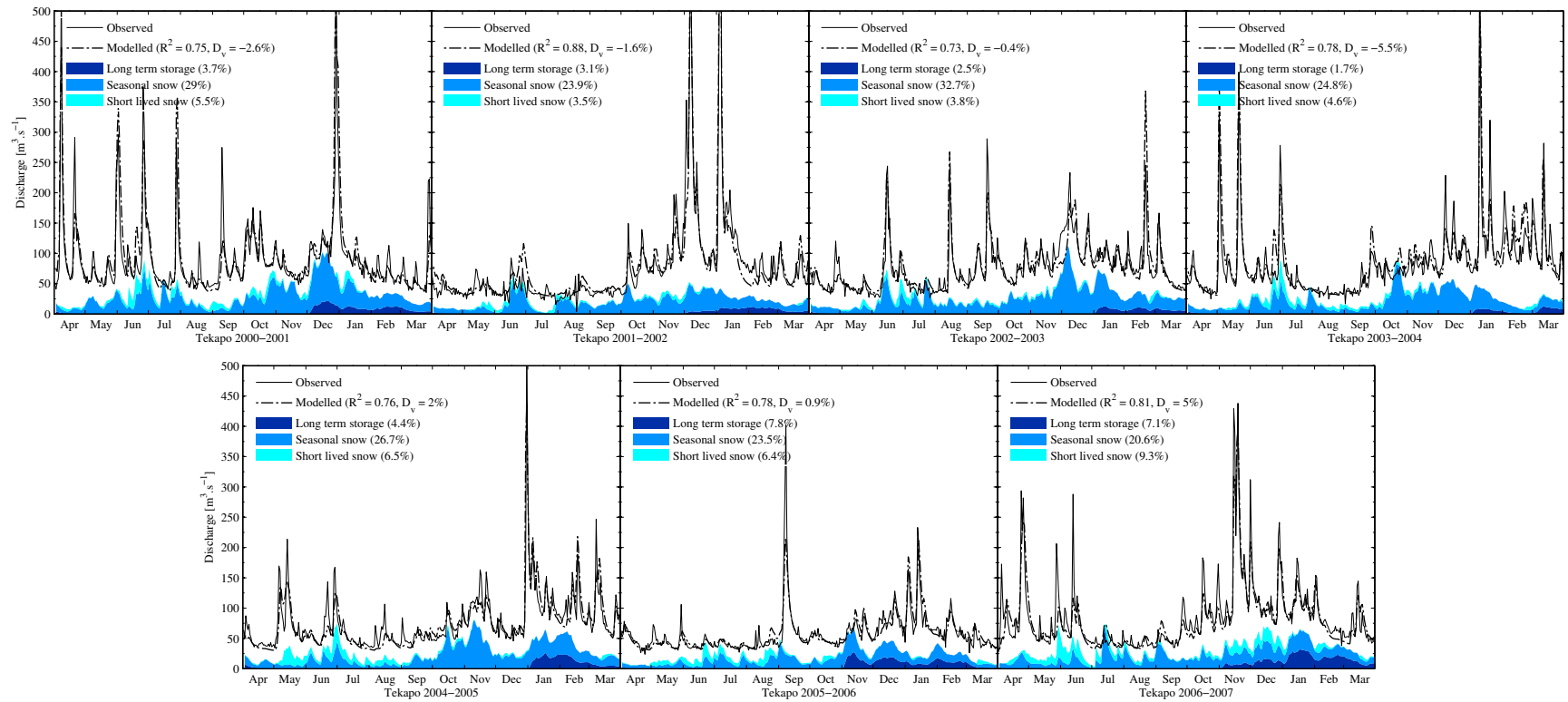


Figure I.3 Results of discharge simulation with long term storage adjustment in Tekapo 2000–2007

Appendix J

MODImLab

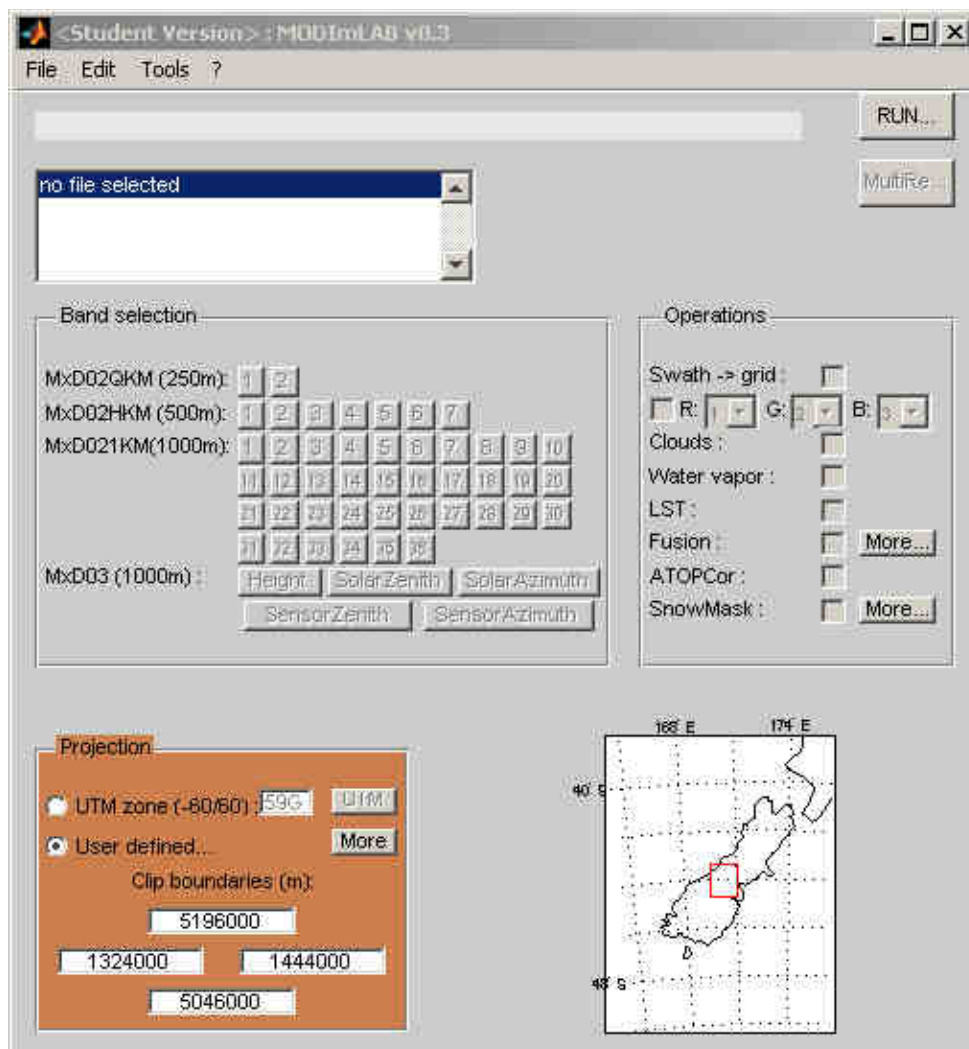


Figure J.1 Front panel of the MODImLab toolbox.

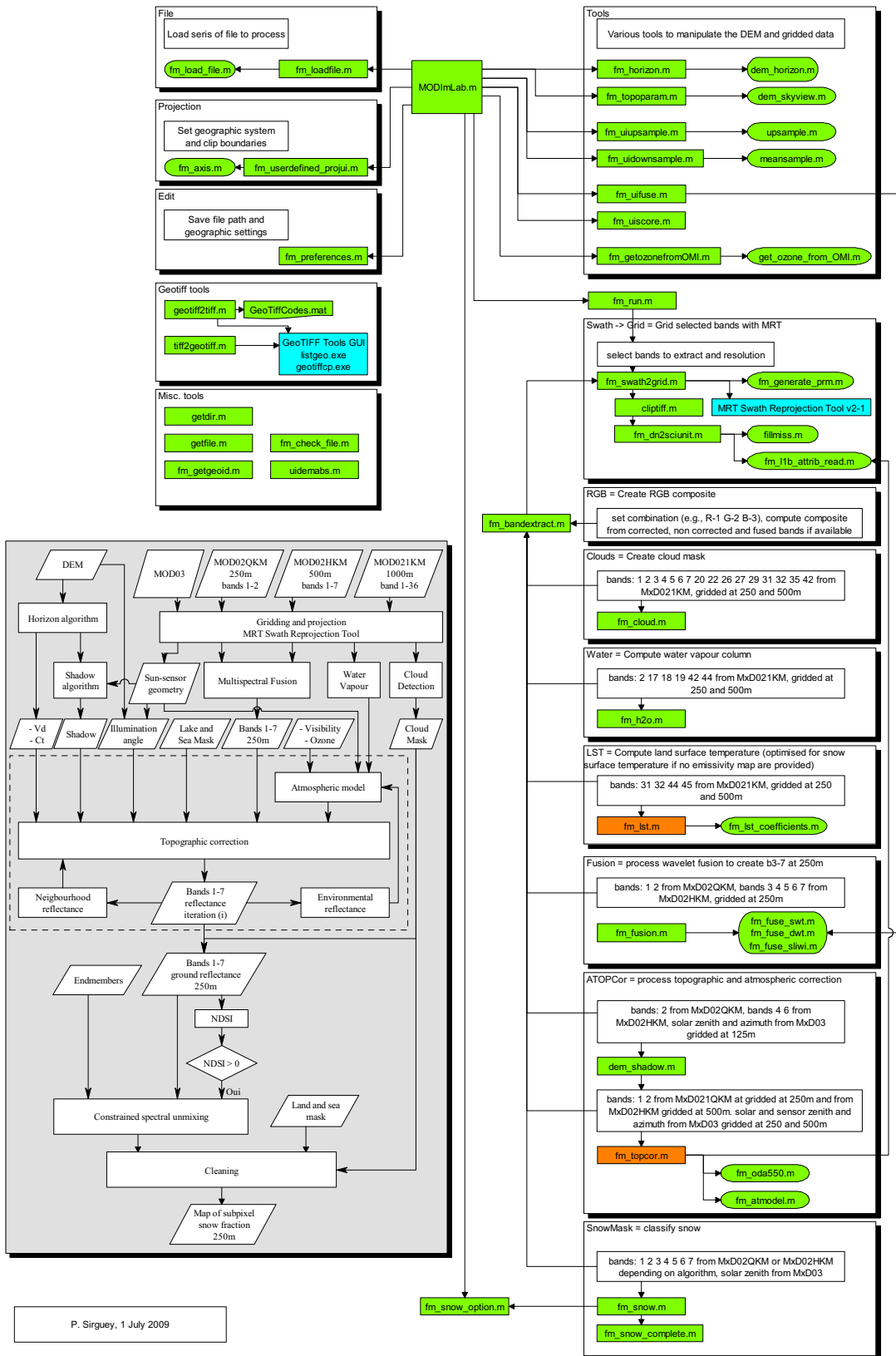


Figure J.2 Flowchart of the MODImlab Toolbox.

